Preparation of Silica Nanoparticles for Biomedical Applications: Bacterial Detection, Oral Drug Delivery and Colloidal Stability

GIORGIA GIOVANNINI

A thesis submitted in partial fulfilment of the requirements of the University of Kent and the University of Greenwich for the Degree of Doctor of Philosophy

August 2017

Declaration

I certify that this degree has not be accepted in substance for any degree, and is not concurrently being submitted for any degree other than that of Doctor of Philosophy being studied at the Universities of Kent and Greenwich. I also declare that this work is the result of my own investigations except where otherwise identified by references and that I have not plagiarised the work of others.

Signed: _____ (Student)

Mr Giorgia Giovannini

Signed: _____ (Supervisor)

Dr Andrew J. Hall

Date: _____

ACKNOWLEDGEMENTS

"It's all mind over matter. If you don't mind, it doesn't matter".

(Albert Einstein)

ABSTRACT

The new branch of medicine, nanomedicine, implies the use of engineered devices and nanostructures in order to accelerate the knowledge of biomolecular-biological processes, to improve the efficiency of disease therapeutics and to develop novel diagnostic techniques. In the present work, three aspects related to the use of nanoparticles (NPs) in biomedical applications have been investigated. Overall, NPs can be applied for *in vivo* and *in vitro* bio-applications and the results achieved are strongly related with the stability of the material in suspension and in biological fluids. In particular, silica nanoparticles (SiNPs) have been synthesised and used for (I) the development of a probe for the fluorescent detection of bacteria (II) as carriers in oral drug delivery and (III) they have been used as proxy for the evaluation of a novel storage method to retain long-term colloidal stability of NPs suspensions.

I) Addressing the need of cheap devices capable of detecting bacteria, here we investigated the use of NPs for bacterial detection. An "on-off" fluorescent substrate was firstly synthesised by glycosylic bond formation between a carbohydrate and a switchable fluorophore and its efficiency in detecting the presence of microorganisms was evaluated. 'Nanoprobes' were then developed by functionalising the surface of particles (silica, gold nanoparticles and streptavidin-coated magnetic nanoparticle) with the synthesised substrates. The nanoprobes successfully detected bacteria as proof-of-concept and the developed detection strategy provides a platform upon which further improvements in bacterial detection can be made in the future.

II) The second research challenge proposes to take advantage of the pH-sensitivity of SiNPs for the design of drug delivery systems suitable for oral administration. SiNPs were synthesised from tetraethyl orthosilicate (TEOS) and ethyl triethoxysilane (ETEOS) using different ratios of the two precursors. The degradation and model-drug release profiles from the NPs were analysed in the context of oral drug delivery. The NPs were exposed to pH's found in the GI tract and indicated that silica NPs can be suitable carriers as they avoided degradation at pH4 found in the fed stomach and began releasing model-drug in small intestine-like pH's (pH6 and pH7.4). It was also shown that covalently binding model-drug (fluorescein isothiocyante) inside the NPs led to greater molecule retention inside the NPs over time compared to those physically entrapped in the particle matrix (fluorescein sodium salt and methylene

blue). In addition, the dissolution of the NPs was also proved to proceed via different mechanisms depending on the TEOS:ETOS formulation, which presents future avenues for drug release studies.

III) Finally, we addressed the colloidal stability issues that are still limiting the real application of nanoparticles on the market. With this aim, a novel approach to stabilise nanoparticles during storage was explored. By trapping the NPs in the matrix of a reversible hydrogel we showed that the physico-chemical proprieties are better maintained over time compared to NPs stored in solution. *In vitro* and *ex ovo* assays proved that the gel-NPs were non-toxic and suggested that NPs stored in gel can be used for biological experimentations without require further purification steps. Studies of gel strength allow considering the proposed method as a promising alternative to the storage techniques currently available, such as surface-coating or lyophilisation methods. The evaluation of the efficiency and versatility of the proposed storage method has been recently published.

Overall the applicability of NPs as platform for bacterial detection, for oral drug delivery have been evaluated and a novel versatile and efficient approach to stabilise NPs in suspension during storage have been developed and evaluated. The findings will hopefully contribute positively to the field of nanomedicine and helping the translation of materials from the laboratory bench to the market.

TABLE OF CONTENTS

LIST OF FIGURES

LIST OF TABLES

LIST OF ABBREVIATIONS

SiNPs: Silica nanoparticles

AuNPs: Gold nanoparticles

4-MU: 4-methylumbelliferone; 7-hydroxy-4-methyl coumarin

4-AAU: Umbelliferone-4-acetic acid; 7-hydroxy-4-coumarin acetic acid

4-MUD: 4-Methylumbelliferyl β-D-glucopyranoside

4-AAUG: 4-umbelliferone-β-D-glucopyranoside acetic acid

APTMS: 3-aminopropyltrimethoxysilane

THPMP: 3-(Trihydroxysilyl)propyl methylphosphonate, monosodium salt solution

TEOS: Tetraethyl orthosilicate

ETEOS: Eethyltriethoxysilane

DI water: Deionised water

DMF: N,N--dimethyformamide

DMSO: Dimethylsulfoxide

PBS: phosphate buffer saline

LB broth: Luria-Bertani broth

DLS: Dynamic light scattering

TEM: Transmission electron microscopy

SEM: Scanning electron microscopy

NTA: Nanoparticles tracking analysis

PDI: polydispersity index

LOD: Limit of detection

DMEM: Dulbecco's Modified Eagle Medium

Chapter 1

General introduction

1.1 Nanotechnology and Nanomedicine

The interest in nanotechnology started to grow in the early 1990s when the application of pure physics to advanced technology opened the borders of science, spreading the use of new tools that unveiled ultra-small mysterious worlds. Indeed, thanks to the development of ultra-precise analytical tools, became possible to visualise and analyse material at the nanoscale. Finally, it has become possible to understand the conditions required to assemble matter into nano-shapes and to evaluate the unique properties acquired by macro-materials when shaped into nano-structures[1]. The more these new techniques were improved, the higher the confidence became in controlling phenomena occurring in the broad and intriguing nano-size world, where nano refers to 1-100 nm, as specified by the definition of nanotechnology[2].

The development of nanotechnology led to the design of a wide set of nanomaterials bearing a huge assortment of intrinsic properties which make them suitable for various applications starting from solar energy storage to personalised therapies. Year by year, new nanomaterials are added to this collection and this trend seems unlikely to stop. The growth in nanotechnology has been rapid and intense worldwide, and it has even strongly influenced the medical field. Nanomaterials are attracting the interest of material scientists and medical staff due to their size-dependent physical and chemical properties and their favourable surface/volume ratio. For instance, nanomaterials have been extensively used as carriers to deliver drug to the target. These unique

properties have led to hypotheses that advanced nanotherapies, for example, will reduce the need for surgical procedures and they will limit the negative effects of drugs, ultimately enhancing the cost/efficiency of treatments. Many further possibilities are foreseen in the development of faster, smaller and highly sensitive diagnostic and imaging tools that will ultimately lead to improvements in human health[3].

Nowadays, creative combinations of nanomaterial and targeting agents have been designed and proposed for biological applications (bionanotechnology) leading to the rise of a new branch of medical science based on nanomaterials. Nanomedicine indeed is defined as the application of nanotechnology in the process of developing new medical tools, such as pharmaceuticals, medical imaging and diagnostics, cancer treatments, implantable materials, and tissue regeneration[4]. Nanomedicine is a broad, ever-emerging research field, in which the physical and chemical properties of materials at the nanoscale are exploited to improve human health and wellbeing, leading to the development of highly accurate and sensitive diagnostic tests, novel carriers for drug delivery and *in vivo* bio-imaging. Nanomedicine is mainly interested in developing treatments using nanomaterials as carriers for drug and cell delivery and in developing biomedical devices, in which point-of-care devices and bioimaging can be further distinguished (*Figure 1*).
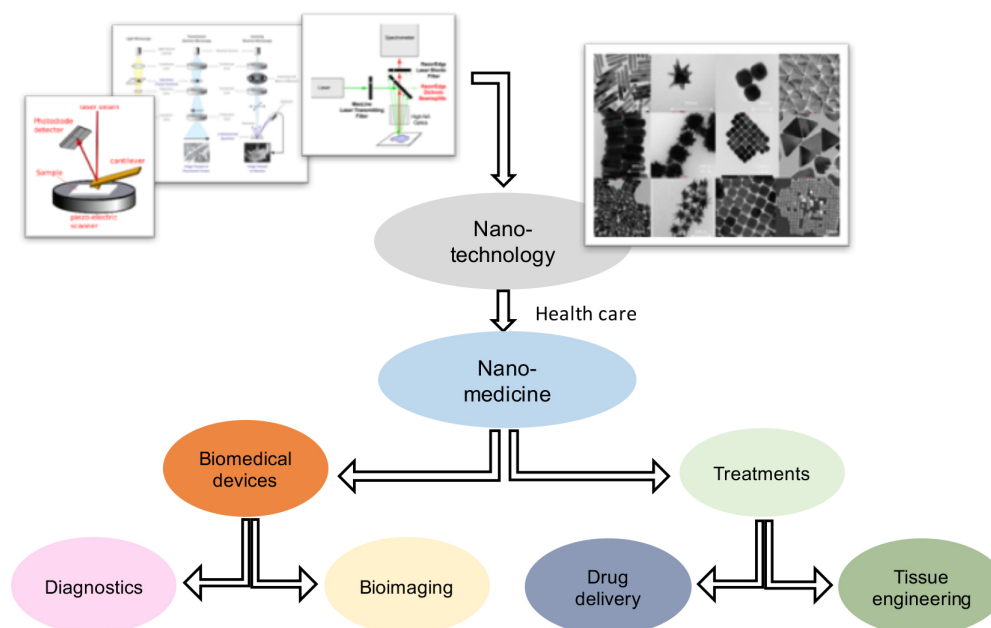
Figure 1: Schematic representation of the development of nanotechnology which allowed understanding and control of matter at the nanoscale. By applying the nanomaterial in medicine, a new field or research was developed: nanomedicine. It aims to enhance efficiency of already existing drugs, to develop new treatments to cure diseases or for regenerative treatments while at the same time develops new devices for bioimaging and diagnose.

At the beginning of the 21st century, formal government programmes were established around the world and highlighted confidence that nanotechnology-driven science will be at the forefront of future breakthroughs. For example, in the USA, the National Nanotechnology Initiative (NNI) was launched in 2001 with the purpose of funding the establishment of 'centres of excellence' focused on the development of new nanomaterials, enhancing knowledge regarding their interaction with living cells, and highlighting advantages and disadvantages related to their use in nanomedicine. Similarly, in Europe, with the funding scheme Horizon2020, millions of euros have been invested in supporting nanomedicine projects involving industrial and academic partners distributed across the continent[4, 5].

1.2 Biomedical applications

1.2.1 Treatment

Drug delivery

Depending on the biomedical application, it is possible to choose between all the different nanomaterials available according to physico-chemical characteristics. For instance, the advantages of using nanoparticles as carriers for drug delivery are numerous: the nanoparticles can enhance the bioavailability of the drug by reducing its metabolism and excretion, in the case of hydrophilic drugs, or by enhancing the adsorption of hydrophobic active compound. In the example given in *Figure 2*, silica NPs are used as a carrier for pro-apoptotic miR-34a. The particles were conjugated with anti-GD2 specific for GD2, an overexpressed biomarker on neuroblastoma cell surfaces, in order to deliver the anticancer drug (miR34a) directly to the targeted neuroblastoma cancer cells. Mice bearing two different types of neuroblastoma tumours (*1* and *2*) have been treated with anti-GD2-miRneg-NP (particles with anti-GD2 but without miR34a: *1a* and *2a*) and with anti-GD2-miR34a-NP (particles with both anti-GD2 and miR34a: *1b* and *2b*). In both cases, the nanoparticles showed to be targeted to the tumour since both are functionalised with the specific antibody, but only the one bearing miR34a showed to be effective in reducing the tumour growth (*Figure 2-1b, 2b and c*)[6].
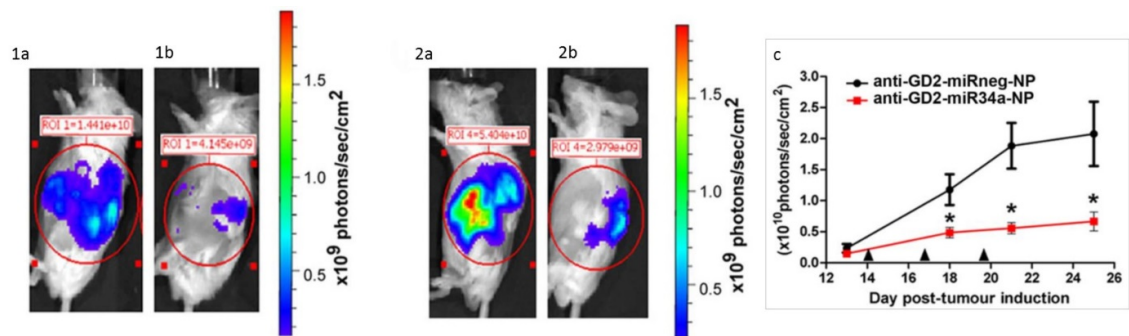
Figure 2: In the presented work silica NPs are used as a carrier for pro-apoptotic miR-34a: the nanoparticles coated with the specific antigen GD2 were efficiently targeted to the tumour and miR34a was confirmed to be effective in reducing the tumour growth. Adapted from reference[6].

Drug delivery typically involves incorporating drugs inside the carrier whereby the nanomaterial can protect the therapeutic from degradation/inactivation and, by changing the formulation of the nanomaterial, it is possible to trigger the drug release in close proximity to the target. For instance, peptides-based therapies showed to be efficient in the treatment of different disease ranging from cancer to diabetes. However, peptides are difficult to work with due to their tendency to degrade during formulation and administration, therefore their development has been limited. Rasekh *et al*. successfully encapsulated angiotensin II into tristearin-base nanocarriers by electrospraying technology. Both synthetic procedure and the material chose for the nanocarrier design proved to maintain the integrity of the active compound. Indeed, the effect observed using angiotensin II-loaded nanoparticles for *in vivo* and *in vitro* studies were comparable with the effect induced by the active compound administered alone but prolonged over time due to the gradual release of the peptide from the tristearin-based nanocarrier[7].

The NPs surface can be functionalised with molecules that help in delivering the carrier to a specific tissue/organ, driving the drug directly to the target[8, 9]. An example is given in *Figure 3,* were QDs have been conjugated with specific antibody for the prostate-specific membrane antigen (PSMA) in order to enter and image a specific type of cell lines (*Figure 3-i*). Figure 3-ii shows the different fate of particles functionalised for a specific target: QDs-PSMA showed to be selectively internalised only by cells presenting the specific antigen (C4-2 cell) (a), while no internalisation was observed in other type of cells (b). PEG-coated QDs did not interact with the cells since they were not functionalised with the specific antibody GD2(c)[10].
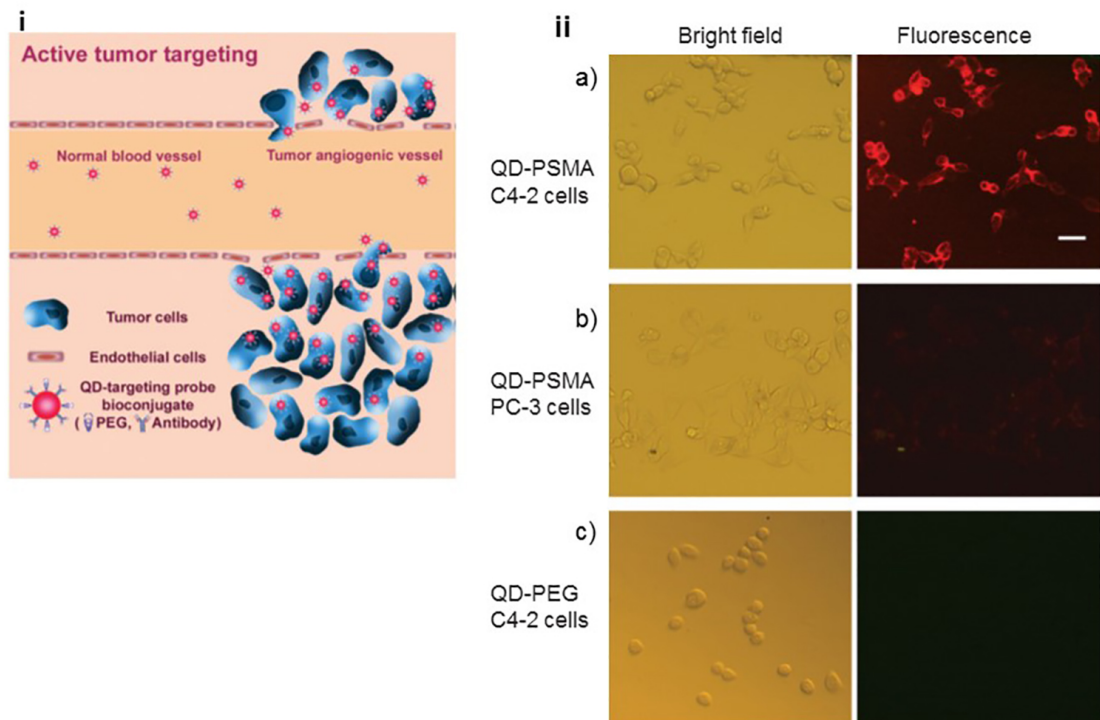
Figure 3: i) Designed QDs that have been conjugated with specific antibody for the prostate-specific membrane antigen (PSMA). ii) Shows the fate of particles differently functionalised QDs-PSMA interacts with the specific cell (a) and do not interact with other cells (b) while if functionalised with PEG (c) do not interact with the cells. Adapted from reference[10].

Tissue engineering

Tissue engineering is an interdisciplinary filed focused in the development of biological substituents to replace or maintain damaged tissues. Implantable tissues such as skin and cartilage are already used in human and more are under clinical trials. Tissues engineering strategies is based on the principle that under appropriate conditions cells can re-organise themselves into functional structure[11]. Nanotechnology has been applied not only for design systems carrying small molecules, but the protection effect offered by nanoparticles has been exploited by bioengineers in the field of regenerative medicine as well. Nanomaterial specifically designed as three-dimensional scaffold which provide an extracellular matrix-like environment supporting the cells during seeding and rearrangement[12]. Nanocarriers have been employed to improve cell viability and engraftment into the damaged tissue, fundamental for cell therapies to be effective. For example, De Chavalho *et al.* encapsulated OSTEO-1 into nanofibrillar cellulose beads. Cell viability assays proved that after 7 days cells started to adhere at the bottom of the microplate well and they enter the cell cycle. Nanofibrillar cellulose

5

showed to maintain cell viability for at least 2 weeks allowing cells to receive nutrients, and once the cellulose derivate is degraded the cells are free to proliferate[13].

1.2.2 Biomedical devices

Bioimaging

While for drug delivery purposes nanomaterials are mainly used as carriers, in developing biomedical devices their intrinsic properties are exploited. The possibility to image biological events *in vivo*, *in vitro* and *ex ovo* is required to decipher mechanisms underlying numerous disease processes and the reaction of cells to specific stimuli. The ability to observe internal mechanisms in fine detail has allowed scientists to understand human physiology and biochemistry.

The intrinsic fluorescence of quantum dots (QD) and fluorescent-labelled NPs has been widely investigated for use for bioimaging[14]. Magnetic resonance imaging (MRI) is one of the most powerful biomedical imaging techniques, allowing to visualise deep into tissues, and its sensitivity is enhanced by using contrast agents. The alternative nano-MRI is now attracting much interest since it allows to further improve the sensitivity of the technique compare to the commonly used gadolinium-base MRI contrast agents[15]. The intrinsic fluorescence properties of nano-graphene oxide have been recently intensively explored as imaging[16,17,18].

When the nanomaterial does not have intrinsic photo-chemical properties (silica NPs for instance), they can be loaded or labelled with dyes enhancing their photo-stability, protecting the compounds from inactivation and favouring cellular internalisation. Furthermore, multimodal particles can be designed by loading the cargo inside the nanoparticles and simultaneously functionalising the surface with molecules which allow targeting or enhance cellular uptake. Shi *et al.*, for instance, designed fluorescent silica NPs (RBITC-DSFNPs) for early-stage apoptosis detection and imaging. RBITC-DSFNPs were loaded with rhodamine B isothiocyanate and labelled with Annexin V (protein which selectively binds phosphatidylserine exposed on the outer membrane during cellular apoptosis). Compared with the conventional fluorochrome used (Cy3-labelled Annexin V) the designed NPs showed to have an excellent photostability

offering a promising alternative for the evaluation of the efficiency of anti-cancer treatment. *Figure 4-A* the MCF-7cells were treated with paclitaxel (to induce cell apoptosis) and RBITC-DSFNPs, while *Figure 4-B* the cells were only treated with particles. Cells were stained in order to allow their fluorescence visualisation (A-ii and B-ii) and cells were optically imaged as well (A-i and B-i). Importantly, images A-iii and B-iii prove that RBITC-DSFNPs selectively imaged only cells at the early-stage of apoptosis (A-iii) and not the healthy one (B-iii)[19].
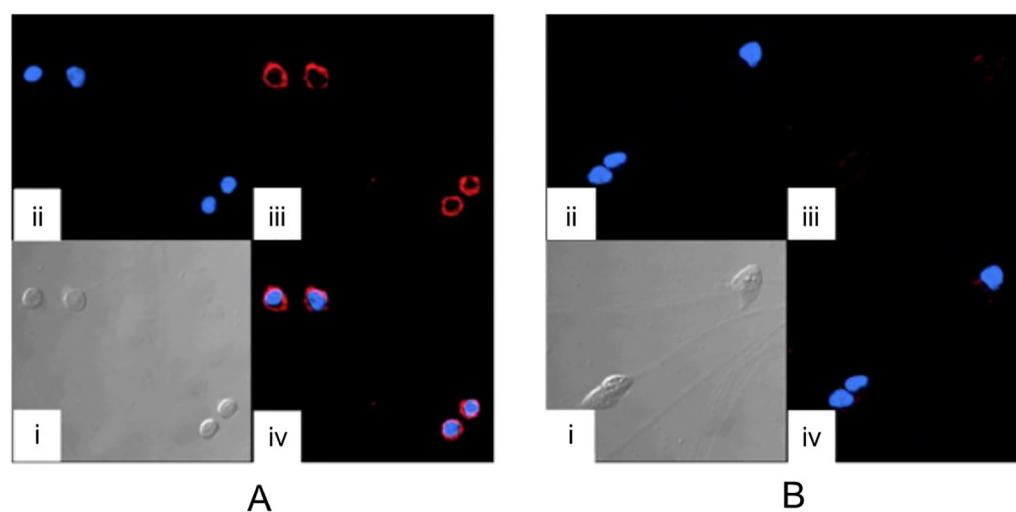
Figure 4: Fluorescent silica NPs (RBITC-DSFNPs) for early-stage apoptosis detection and imaging. RBITC-DSFNPs were loaded with rhodamine B isothiocyanate for fluorescent visualisation and with Annexin V for targeting. RBITC-DSFNPs prove to selectively image only cell at the early-stage of apoptosis (A-iii) and not the healthy one (B-iii). Image A-iv and B-iv marge images ii and iii. Adapted from reference[19]

Diagnostic devices - biosensors

Similarly, nanoparticles have been exploited for the development of advanced diagnostic devices. In such cases, the nanoprobe could be used only as platform on which the detection of a specific target occurs or it can actively take part in the process, mainly by transducing the recognition of the targeted molecule into a measurable signal or enhancing that signal. An overview of the concept of biosensors will be presented later in the second chapter of the present work, but *Figure 5* gives an idea of the role played by nanomaterials when involved in diagnostics development. The figure presents one of the most used point-of-care devices: the pregnancy test. The biomarker detected by this device is the hormone secreted by the placenta shortly after fertilisation (human chorionic gonadotropin, hCG). Antibody-coated gold NPs, which are red in colour, are incorporated into the device and specifically bind the hormone,

and the complex then flows to the test line (*Figure 5-a*). Here, the complex is bound at the test line and produces a red line that indicates the presence of the hormone in the urine (*Figure 5-b*)[20].
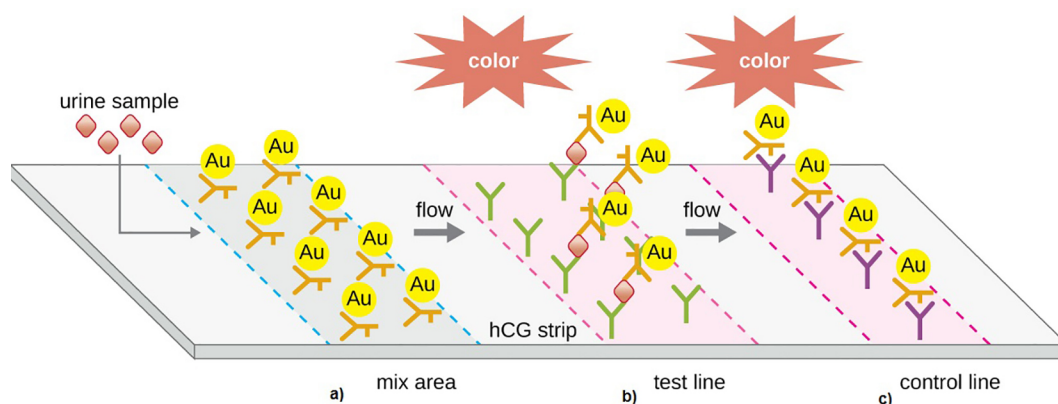
Figure 5: Schematic design of a lateral flow test (LFT) which can be used to describe a pregnancy test. a) The sample (urine) is loaded and it flows along the strip encountering, at the conjugate pad, the antihCG-coated AuNPs. b) the antigen-antibody AuNP complexes are then captured by immobilised anti-hCG at the 'test line', where a red line will be visible due to the intrinsic colour of the AuNPs. c) anti-hCG conjugated AuNP not bound to the hormone hCG will continue flowing, interacting with antibodies immobilised at the control line. Adapted from reference[20].

Another property of AuNPs widely exploited in designing sensor devices is the change in colour upon agglomeration. For instance, Schofield *et al.* used lactose-stabilised AuNPs to develop a colorimetric system for the detection of bacteria. The lactose on the AuNP surface has two fundamental roles: i) stabilises the particles maintaining them monodispersed in suspension and ii) it will selectively bond the toxin released form cholera. As shown in *Figure 6-a* in absence of the toxin the suspension of lactose-coated AuNPs is red but it turns into a purple colour when cholera toxin is added (b) due to particles agglomeration induced by the presence of the toxin as represented in *Figure 6-c*[21].
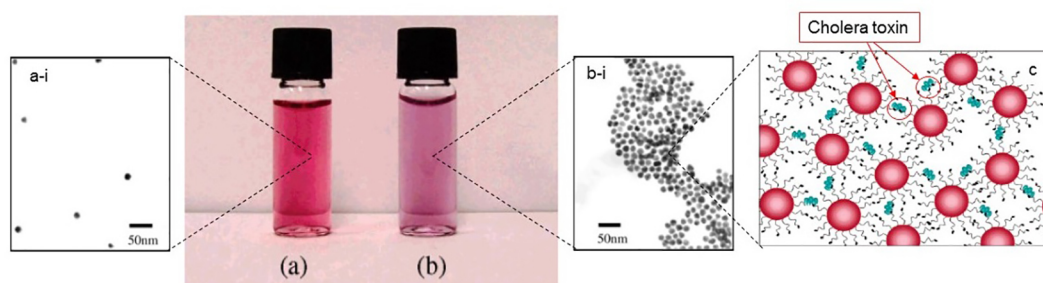
Figure 6: Lactose-stabilised AuNP a) before addition of cholera toxin and b) after addition. The change in colour of the sample indicate particles agglomerated binding the toxin. The TEM images of the sample in the two situations show the well dispersed particles before addition (a-i) and the formation of the agglomerates after addition of the toxin (b-i). The agglomeration is induced by the interaction of the lactose-coated AuNPs with the toxin (c). Adapted from reference[21].

Multifunctional nanoparticles can be achieved when materials having different properties are combined. This possibility has been particularly exploited in developing biomedical devices, as is the case, for instance, in the nanoprobe designed by Fun *et al.* coating iron magnetic particles with a gold plasmonic shell. The shell has been further functionalised with Cy3 (fluorescent dye) and with aptamer S6 in order to allow the selective recognition and imaging of SK-BR-3 cancer cells. The iron magnetic core allows the isolation of the cells, which can then be visualised by fluorescence microscopy due to the dye labelled on the surface. Once the cells have been isolated and imaged, they additionally proved that, due to the presence of the gold shell, most of the cancer cells can be killed by irradiation with near-IR light (*Figure 7*)[22] .
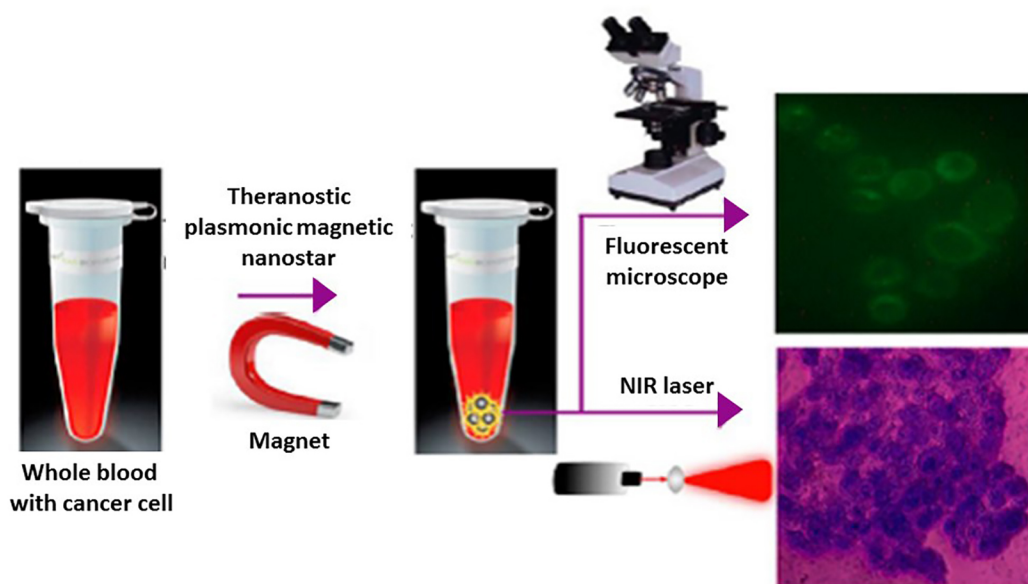
Figure 7: Gold-coated iron NPs functionalised with Cy3 and with aptamer S6 proved to selective recognise SK-BR-3 cancer cells. The iron magnetic core allows the isolation of the cells, which can then be visualised by fluorescence microscope and eventually killed by irradiation with near-IR light. Adapted from reference[22].

1.3 Current limitations

1.3.1 Interaction with biological environment

One of the big advantages possible through the use of nanomaterials in nanomedicine is the unique capability of these nanomaterial to interact with the biological environment and, in particular, with cells. The physico-chemical properties of nanoparticle size, surface charge and surface roughness strongly determine the behaviour of the nanoparticles once applied *in vivo*. However, one of the limitations of

nanomedicine is the uncertain behaviour of the nanomaterial once in contact with a biological environment. It is well known that proteins present in complex biological media (e.g. blood) adsorb onto the nanoparticles surface, forming the so-called 'protein corona'. This thick layer of protein alters the physico-chemical properties, which are not only fundamental for their activity, but their alteration could lead even to toxic effects. Many research groups have investigated this topic and even though many doubts have been resolved, many other questions have not yet been answered[23,24,25,26]

1.3.2 Colloidal stability issues

A similar, though less complicated, issue is sometimes encountered when NPs need to be stored for a short/long period of time. NPs in suspensions tend to be unstable depending on their physico-chemical properties and the solvent in which they are stored. Considering the difficulties in predicting the behaviour of the particles when applied in biological applications, guaranteeing that NPs maintain their properties during storage has become a challenge. This is fundamental in order to ensure that when used they still have the morphology and properties expected. Zaloga *et al*. observed for instance that the effectiveness of super-magnetic iron oxide NPs (SPIONs) in targeting cancer cells can be affected during storage. By using a magnet, SPIONs can be 'driven' inside the tumour but it was proved that the magnetic properties of the particles decrease if stored at different temperature (*Figure 7-A*)[27]. Lyophilisation is a common technique used to stabilise particles during storage. It requires the use of cryoprotectants in order to preserve the morphology of NPs during the exposure at very low temperature. Although it is still considered an efficient storage method, lyophilisation can lead to undesired outcomes such as changes in morphology of the nanomaterial, difficulties in redispersion of the sample or NPs are not anymore usable. An example is shown in *Figure 8-B* where SEM image shows polymeric nanocapsules lyophilised using 5% w/v of PVA as stabiliser after reconstitution. The particles are well separated, but some of them are included in the PVA film and therefore they are no longer available in suspension[28].
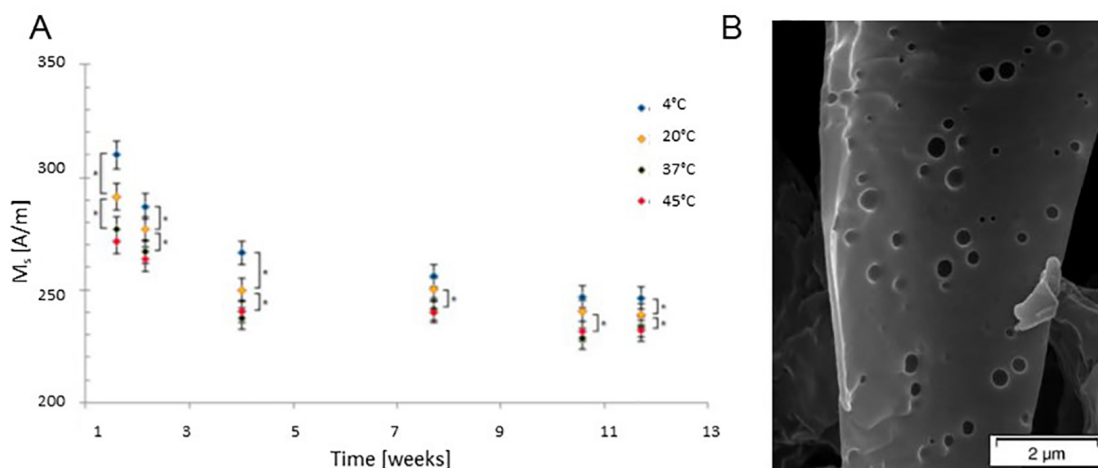
Figure 8: A) The efficacy of SPIONs in targeting anti-cancer drugs inside the tumour decreases after 4 weeks of storage at different temperatures due to changes in their magnetic properties. Adapted from reference[27] . B) SEM image of polymeric nanocapsules lyophilised using 5% w/v of PVA partially included in a PVA film after reconstitution. Adapted from reference[28].

Many strategies have been developed in order to obtain stable nanomaterial suspensions. Some of these require complicated surface chemistry, others require quite expensive instrumentation and, even though good results have been achieved at least for certain type of colloidal systems, issues related to colloidal stability still represent a limitation for the success of nanomedicine. Chapter 5 will explore this issue further.

1.4 Thesis organisation

The present work aims to address three aspects all related to nanomedicine. As shown in *Figure 9* the three main subjects of the thesis are related to (i) the development of nanoprobes for bacterial detection, (ii) the evaluation of the possibility to control drug release using silica nanoparticles as carriers, and (iii) addressing the issue of colloidal stability, which interests the nanotechnology field in general.
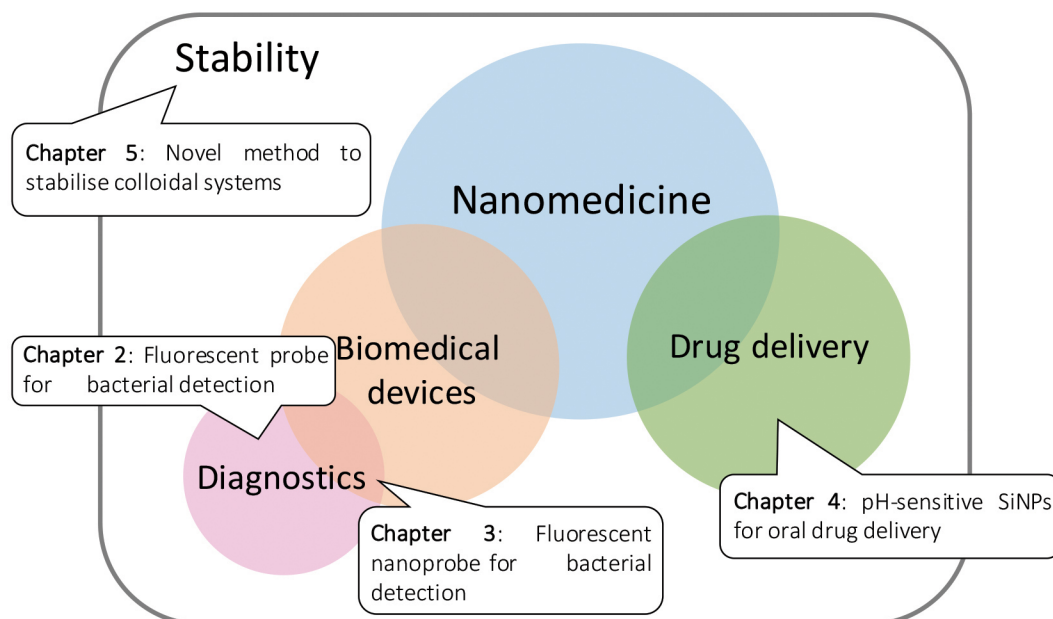
Figure 9: Thesis structure. The thesis addresses three main topics all related to the nanomedicine

Chapter 1: The present chapter aimed to give a brief taste of the topics which will be exhaustively discussed separately.

Chapter 2: This section addresses the need to fight one of the most concerning health problems related with bacterial infection and the constant increase of bacterial resistance to antibiotics. The chapter presents the synthesis and evaluation of a fluorescent "on-off" substrate capable of detecting bacteria and its comparison with similar substrates available on the market.

Chapter 3: The fluorescent substrate studied in the previous chapter has then been used to functionalise the surface of nanoparticles. The nanoprobes have been tested in enzymatic assays and in presence of bacteria. Advantages and disadvantages achieved by using the so synthesised nanoprobe are discussed and critically evaluated.

Chapter 4: Oral administration is the first choice for the development of new drug formulations due to some important advantages compared with the other administration ways. The possibility of designing pH-responsive SiNPs for oral drug delivery is evaluated in this chapter.

Chapter 5: Given the need to deal with the instability of nanoparticles and problems related to their storage, herein a novel method to stabilise colloidal systems is presented. The physico-chemical theory behind the idea and its experimental

translation is outlined in the presented chapter. The efficiency of the method proposed has been tested using different types of nanoparticles and its applicability has been evaluated using different toxicity assays *in vitro* and *ex ovo*.

Chapter 6: In conclusion, I would like to give personal reflections related to topics discussed, pointing out which are the "missing pieces" of the promising puzzle as such the application of nanotechnology in medicine.

Chapter 2

Fluorescent probe for bacterial detection

2.1 Introduction

2.1.1 Biosensors

The demand for fast, reliable and low-cost systems for the selective detection of analytes has always been ample. The interest in such topics comes from different research fields, starting from medicine through environmental health to national security for the detection of harmful compounds. In the last decade, researchers have invested a great deal of efforts in enhancing the efficiency and reliability of devices already existing or in developing new detection methods exploiting advanced technologies. Sensors are commonly defined as analytical devices used for the recognition of target. Many definitions have been given regarding sensors and biosensors in the last decade. Two commonly cited articles regarding the topic refer to a biosensor as either "a chemical sensing device in which a biologically derived recognition entity is coupled to a transducer, to allow the quantitative development of some complex biomedical parameters"[29] or as "an analytical device incorporating a deliberate and intimate combination of specific biological element (that creates a recognition event) and a physical element (that transduces the recognition event)"[30].

Nowadays, the terms 'sensor' and 'biosensor' are sometimes confused, but chemical sensors and biological sensors have different definitions, which changed with the time[31]. Previously a biosensor was considered a chemical sensor in which the recognition system utilises biochemical mechanisms, while today this term refers to a sensor that measures qualitatively/quantitatively the presence of the analyte in a biological system, linking the definition more to the application of the device rather than its structure. Curiously, the first example of biosensors are canaries used in mines as an early-warning system, alerting miners to the presence of toxic gases. The technology was very simple: the gas would kill the bird before the miners[32]. The official definition of biosensor, given by IUPAC, is "a device that uses specific biochemical reactions mediated by isolated enzymes, immune systems, tissues, organelles or whole cells to detect chemical compounds usually by electrical, thermal or optical signals"[33].

Independently of which definition is considered, all of them give a clear description of the composition of a biosensor. Indeed, all definitions make clear the presence of two main components: the biological recognition part, responsible for the specific interaction with analyte, and the transducer which converts the recognition event into a measurable signal, normally connected to an output system *(Figure 10).*
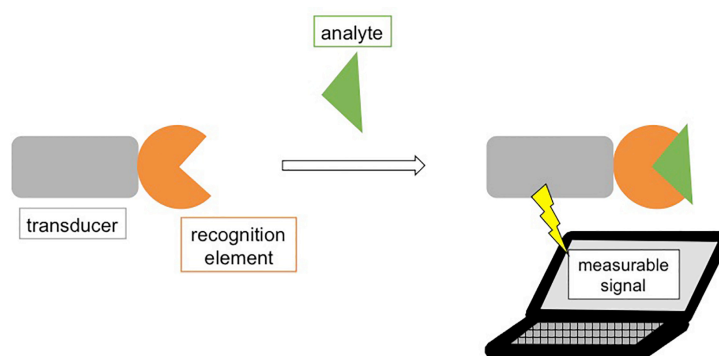
Figure 10: Schematic representation of biosensor. The biosensor is formed by the transducer, which emit a measurable signal when the recognition part of the biosensor interacts with the analyte signalling the recognition event.

Much work has been done in developing new biosensors in the medical field to improve global health. Particularly interesting is the area of prevention and early diagnosis of disease, in which government investment is rising considerably every year. Since many different methods of detection have been successfully developed, the current goal is to miniaturise these technologies in order to have portable, user-friendly, efficient and reusable devices called point-of-care (POC) diagnostics. The idea behind POC devices

is the decentralisation of the healthcare centres controlling the public health by spreading, all over the territory, the tools and knowledge needed. POC are thought as tests that can be done in proximity to the patient, investing into the role of General Practitioner (GP) and pharmacists as intermediates between hospitals and patients. The POC market is expected to reach almost $28 billion by 2018 and the total molecular diagnostics market is estimated to grow up to > $9 billion by 2020, which attracts public and private funding to explore this wide field[34].

Classification

Biosensors can be classified based on their application, e.g. in food safety, environmental monitoring, clinical analysis and medical diagnosis, but most commonly they are subdivided into classes according to their recognition element and transducer moieties. According to the recognition element, it is possible to distinguish, for instance, immunosensors, that are considered as biosensors in which antibodies constitute the biological recognition element[35]. Other type of biosensors used enzymes and nucleic acids as biological recognition element. More used and meaningful is the classification related to the transducer, the moiety that converts the event recorded by the recognition element into a measurable signal. Depending on the fundamentals of the physical or chemical changes that occur at the transducer when the event takes place, the device can be recognised as a resonant, optical, electrochemical, acoustic (piezometric) or thermal biosensor[36] *(Figure 11)*.
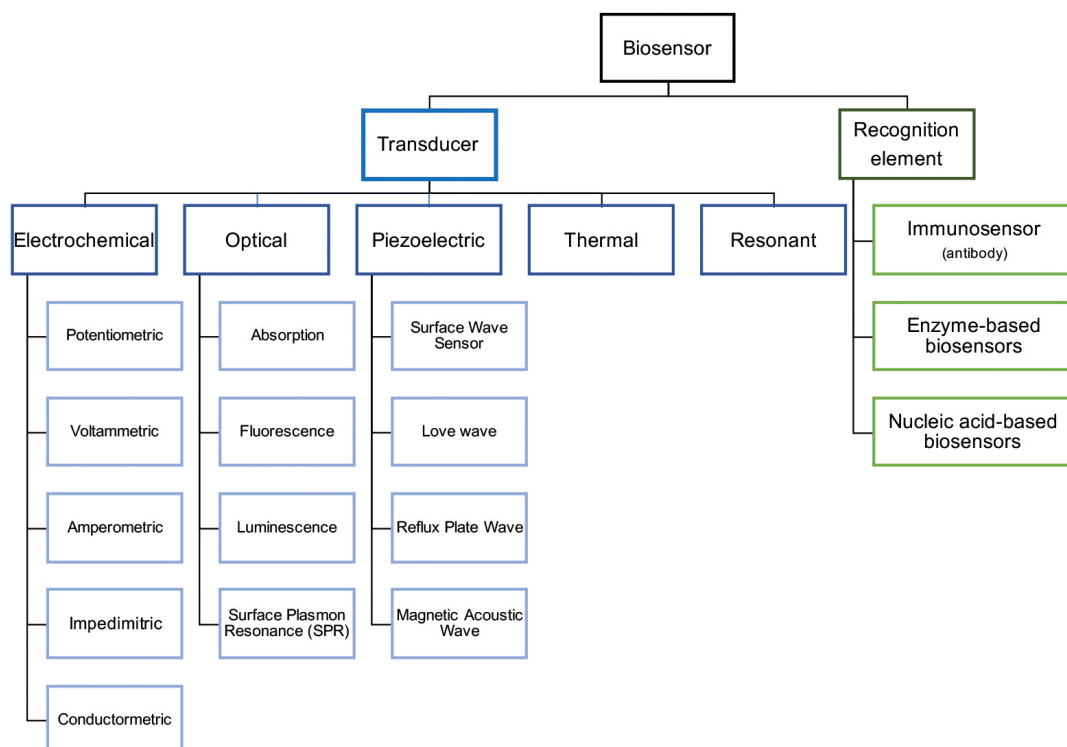
Figure 11: Classification of biosensors accordingly to their transducer or element recognition moieties. Each family is further classified in subclasses.

For instance, an electrochemical biosensor can provide semi- or fully quantitative information through measuring the electro-active species produced or consumed during the recognition, while in a resonant biosensor the resonant frequency measured is the result of a change in mass of the electrode when the analyte becomes attached to it[32]. Optical biosensors have been exploited and developed greatly in the last years thanks to advantages that include speed of the detection, reproducibility of measurement and applicability to different fields. This group can be further subdivided according to the properties applied in sensing; indeed the recognition event can be transduced into different optical properties such as absorption, reflectance, luminescence, fluorescence and surface plasmon resonance (SPR).

2.1.2 Fluorescent-based biosensors

Fluorescent-based biosensors have been greatly explored in the last years due to their high sensitivity and the simplicity of the sensor itself. As shown in *Figure 12* some fluorophores can act simultaneously as transducer and as detection element (e.g. when metals are detected by complexation with the fluorophore for instance), otherwise the two moieties are distinguished. In the latter case, it is possible to distinguish between

direct or indirect detection. While in the direct detection recognition element and transducer have to be connected together, in the case of indirect detection they can be individual components in contact with the same environment.
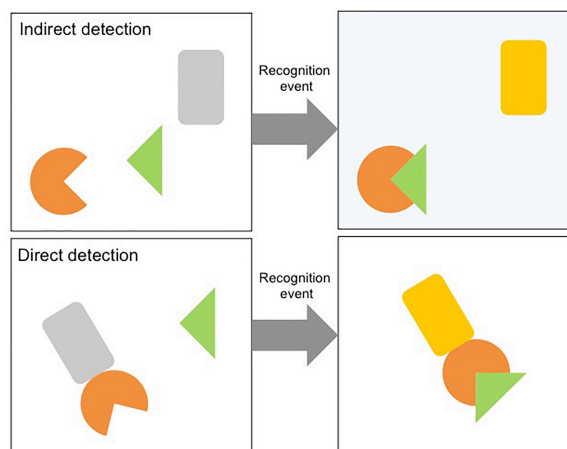
Figure 12: Schematic representation of indirect and direct detection of the analyte. As shown, the interaction between recognition element and analyte induces changes in the surrounding environment (normally changes in pH), which the transducer emits as a measurable signal. In direct detection, it is effectively the interaction between recognition element and analyte which is transduced.

The possibility of direct and indirect detection of the target along with the characteristics of being generally inexpensive and easily implemented, make fluorochromes interesting for biosensor construction[37]. Depending on the molecule chosen, the sensing can take place through observing changes in different properties such as the steady-state of the fluorescent intensity, the lifetime of the signal, spectral shifts (Internal Charge Transfer - ICT), fluorescence enhancement (Förster Resonance Energy Transfer - FRET)[38] or fluorescence quenching (Photoinduced Electron Transfer – PET)[39][40]. The huge variety of fluorophores available allows the development of biosensors having different principles of detection and different intrinsic characteristics.

Switchable-fluorescent sensors

Switchable fluorogenic probes, which are characterised by an *on-off* fluorescence state, are attracting considerable attention as new tools for biological sensing and imaging, since they can provide specific and selective detection/labelling producing low-background and high-contrast imaging[41] *(Figure 13).*
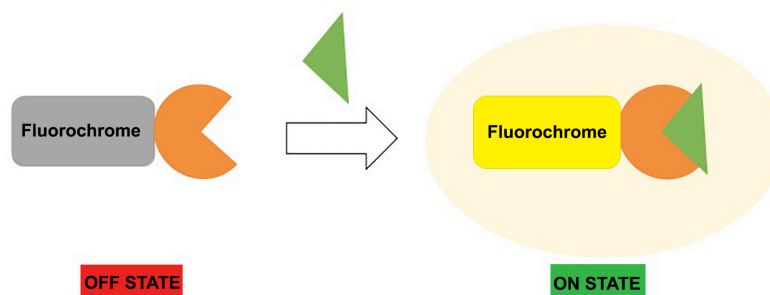
Figure 13: Switchable fluorescent probes indicate the presence of the analyte by changing in the fluorescent properties of the transducer. Normally the signal is quenched, but once the analyte is recognised, the signal increases due to physio-chemical changes, which occur in the transducer's structure.

Different mechanisms can be involved in the switch between the *on* and *off* state of the dye. *Table 1* summarizes the main switching mechanisms. They can be related to environmental changes such as is the case of polarity and viscosity sensing dyes, or to external stimuli that alter the molecular structure, such as *cis-trans* isomerisation, ring-closing/ring-opening, molecular proton-transfer process, structural folding/unfolding and many others.

Table 1: Brief summary of switching mechanisms.

Type of change	Triggering phenomenon	Type of dye
Environmental changes	The *on/off* mechanism is due to charge/electron transfer[42]	Polarity sensitive
	The *on/off* mechanism occurs when the energy is not dissipated as kinetic energy since the structure of the molecule is looked by the viscosity of the environmet[43,44]	Viscosity sensitive
	Protonation and deprotonation of the molecule induce the *on/off* state of the fluorescence[45][46]	pH sensitive
Structural changes	The presence of metal ions leads to the formation of complexes inducing or quenching the fluorescence	Metal ions
	The formation/cleavage of the linkage between two molecules induces/quenches fluorescence[47]	Bond formation/cleavage

One example of a switchable fluorophore is that proposed by Wang *et al*. This group synthesised a switchable fluorophore where fluorescence is turned on due to chemical alteration of the molecular structure when the interaction with ATP occurs. This compound allowed observation of the decrease in mitochondrial ATP under glucose

starvation conditions and the increase of ATP levels in the early stage of cell apoptosis[48].

Han *et al.* synthesised a probe formed from two molecules of fluorescein that behave as donor in a FRET process linked to an acceptor (BODIPY). When fluorescein is in the phenolic form (pH < 6) the energy is given to the acceptor and FRET occurs, while normal fluorescein fluorescence is measured at pH > 6.5. At this pH the fluorescein moieties are in the phenolate form therefore the energy is released as fluorescence and FRET doesn't occur. This switchable probe enters cells and doesn't leach out as easily as other fluorescein pH sensitive probes due to the high negative charge, allowing a ratiometric detection of the pH in different cell compartments[49]. In another example, coumarin fluorophores were introduced as FRET donors into a xanthene-Zn complex acting as FRET acceptor. Under normal conditions the probe only shows signals related to coumarin since the fluorescence of xanthene is quenched by the Zn-complex. Interaction of ATP with the fluorophore disrupts the complex and, as consequence, FRET occurs. The coumarin peak decreases while the xanthene peak greatly increases[50].

The capability of some switchable fluorescent molecules to form complexes with metal ions has been widely exploited. In this case the *on/off* switch can occur when the complex is formed or when another metal ion displaces the one forming a complex. The increase/decrease of fluorescence can therefore indicate the presence of metal ions. Majzoub *et al.* synthesised a selective probe for the detection of Zn(II) in living cells taking advantage of the photon electron transfer (PET) phenomenon and competitive displacement. The fluorochrome had weak or no fluorescence when complexed with Cu(II) since PET occurs. In presence of Zn(II), Cu is displaced since the affinity of the fluorophore for the new metal is higher. The complex formed with Zn(II) inhibits PET and therefore the fluorescence increases greatly[51]. Many other works have been done for the detection of metal ions exploiting PET and competitive displacement phenomena[4852]. They main disadvantages in metal detection are the interference of the pH for the complex formation and the difficulty to make the probe selective for a specific metal since complex formation is mainly related to the valence of the metal.

It is clear that many possible switching mechanisms can be used to develop a probe. Each of them can be more suitable for specific purposes. Depending on the analyte that

is targeted, the fluorophore has to be carefully chosen in order to have a readily detected signal change without interference with the background or non-specific detection.

Switching mechanism: formation/cleavage of covalent bond

Formation of covalent bonds has long been used to develop switchable fluorogenic probes for various analytes, although it is manly used for chromogenic sensing. Usually it takes advantages of nucleophilic addition reactions between fluorophore and analytes, which are usually amines, phenols, thiols, sulphides, cyanide *etc.*, or it can be used to detect metal ions that catalyse ligand reactions. Although they lack specificity, many probes have been developed, for instance for the detection of amino acids and dopamine[47,53]. However, this limitation has been sometimes overcome. For instance, Li *et al.* presented two fluorescent probes capable of selective detection of histidine even at low concentration[54,55].

The cleavage of covalent bonds is a technique very often used since it is related with high affinity and selectivity for the analyte. Usually in the normal state the probe has no fluorescence or the signal is very weak, but once the bond is cleaved upon addition of the analyte, the fluorophore is released and its fluorescence increases remarkably. The cleavage can be induced by different analytes, such as metal ions[56,57], reactive oxygen species (ROS)[58,59], anions and small molecules[60,61,62] or the covalent bond can be enzymatically cleaved.

One possible switching mechanism, which has attracted much attention for the development of biosensors, is the enzymatic cleavage of covalent bonds (*Figure 14*). For these types of probes, 7-hydroxy coumarin derivatives, fluorescein, rhodamine and resorufin derivatives were usually used as fluorophores. The development of various types of probes has allowed the detection of many different enzymes, such as β-galactopyranoside, β-lactamase, β-glucoronidase, α-glucosidase, protease, glutathione transferase, monoamine oxidase, esterase, tyrosinase and many others. The detection of specific types of enzyme can lead to information such as a cell's metabolic activity and can be useful for diagnosis of diseases, for example to detect bacterial infections.
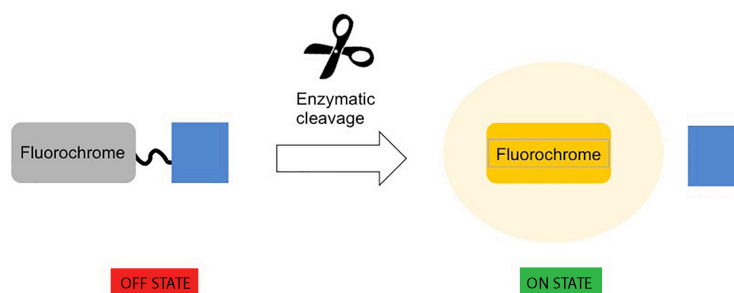
Figure 14: Schematic representation of the mechanism by which switchable probes switch to the "on state" emitting fluorescence: the recognition part is recognised by a specific enzyme which cleaves its connection with the transducer leading to the appearance of the measurable signal.

2.1.3 Coumarin derivatives for biosensors development

Coumarin derivatives have been widely used in the development of accurate, low-cost, rapid detection methods for metal ions (Hg, Cu, Fe, *etc.*), anions (cyanides, fluorides, etc.), ROS (NO_2, H_2O_2) and enzymes, with good sensitivity and selectivity. Coumarin derivatives, due to their benzopyrone structure, have many advantages, including high fluorescence quantum yield, large Stokes shift, excellent light stability and lower toxicity compared to other fluorophores. The heterocyclic benzopyrone is formed by the fusion between pyrone and benzene rings. Depending on the position of the carbonyl group, two different families of compounds can be identified: benzo-α–pyrones, named coumarins, and benzo-β-pyrones, that are instead indicated as chromones (*Figure 15-a*). The high fluorescent quantum yield and the photostability of most coumarin derivatives can be rationalised by through consideration of the stilbene structure to which coumarin is strongly related. Stilbene has high fluorescence only in the *trans* conformation, in which the fluorescence occurs due to the formation of conjugated double bonds in the structure. Under UV-light, *trans-cis* transformation occurs leading to a loss of fluorescence (*Figure 15-b*). The structures of coumarin and stilbene are relatively similar, the only difference being that the lactone structure fixes the *trans* conformation into a *trans*-stilbene making coumarin a fluorophore with higher photostability and switchability. The fluorescence properties of coumarins can be varied noticeably changing the pH[63] and polarity[64] of the solvent or by modifying the structure by placing different substituents on the structure.
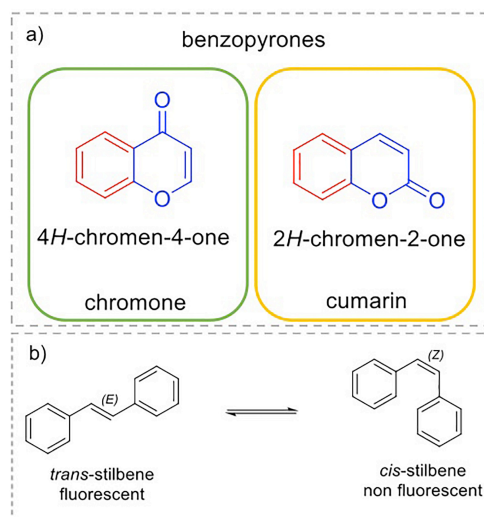
Figure 15: a) Structure of chromones and coumarins. b) The similarity with stilbenes structure determines the coumarin's fluorescent properties. However, the presence of the lactone in the coumarin structure locks the compound into a favourable conformation giving to the compound high photostability.

The most common modification is oxygenation at position 7, the so-reached 7-hydroxycoumarin is named umbelliferone. The positions at which coumarin is chiefly modified are 3, 4, 6 and 7 of the benzopyrone ring, although some examples of modification at positions 5 and 8 have also been reported. Interestingly, adding an electron donor group at positions 4, 6, 7 or, alternatively, an electron-acceptor on position 3, shifts the fluorescence band to longer wavelengths[65] (*Figure 16*).
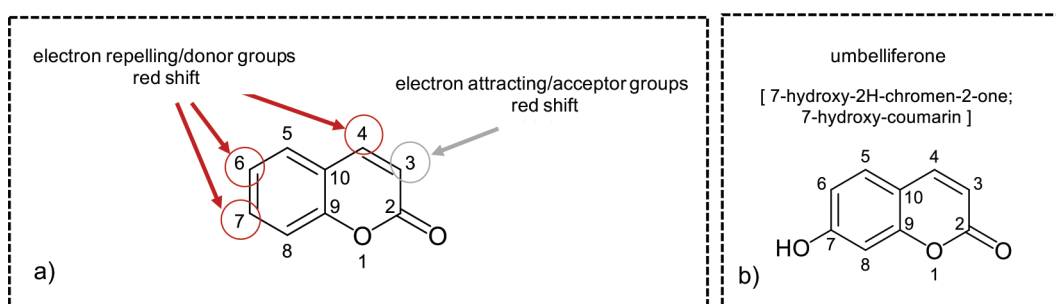
Figure 16: a) The image shows the position of the ring which are often modified in order to enhance the fluorescence properties of the compound. b) The structure of 7-hydroxy-coumarin is presented. All compounds with similar structure are considered umbelliferone derivatives.

The blue light emission, which characterises coumarins, represents a limitation for some applications. For instance, proteins and cell components emit green light, which is very close to the coumarin emission peak, leading to background interferences. The variety of coumarin derivatives designed comes from the need to synthesise molecules with more suitable fluorescent properties (higher Stokes Shift, better quantum

efficiency) and additional characteristics (selectivity, cell permeability, biocompatibility, etc.), while maintaining the basic structure of the benzopyrone.

The switchable properties of coumarins have been exploited to design probes to detect metal ions, anions, small molecules, biological material (proteins, DNA, RNA etc.) and enzymes. Some examples include the following: Romieu developed an *on-off* probe for the selective detection of penicillin G acylase[66] and penicillin amidase[67], while Singh *et al*. developed a probe capable of detecting and defining the affinity of histone deacetylase inhibitors; this enzyme is involved in epigenetic regulation and is a therapeutic target for cancer treatment[68]. Two switch-on long wavelength probes have been designed for the detection of nitroreductase[69] and salicylate hydroxylase-coupled dehydrogenase assay[70]. Chen *et al.* successfully developed a non-fluorescent amino-coumarin as a switch-on probe for the detection of monoamine oxidase A and B[71].

2.1.4 Bacterial infections

Worldwide, bacterial infections account for nearly 40% of the total 50 million annual estimated deaths. Besides advance technologies, various antibiotics have been developed, but bacterial infections are still one of the most concerning health problems worldwide. One of the reasons that make the treatment of bacterial infection inefficient is the difficulty of diagnosis, since very often microorganisms are only identified when they have reached a systemic stage or when anatomical damage occurs. Another reason that has led to the current situation is related to the length of time needed for a drug to step from the laboratory to the pharmaceutical market. Most importantly, besides the lack of new antibiotics, those already available are becoming less effective due to bacterial resistance[72,73,74,75]. Antimicrobial resistance (AMR) has been accelerated by the misuse and over- prescription of antibiotics[76,77]. There is increasing concern about the threat posed by AMR to health, food production and economic prosperity. In Europe alone, about 25,000 people die each year from drug-resistant microbial infections, similar to the number who die in road traffic accidents, with an estimated economic impact of at least €51.5 billion[78]. Early and specific diagnosis is considered a potential solution. Such devices could be used by medical practitioners to rapidly choose appropriate therapies rather than prescribing broad-spectrum antibiotics and enhancing the possibility of AMR.

The most important requirements for this new type of diagnostic are specificity and accuracy. Traditional methods for the detection of bacteria involve the following basic steps: pre-enrichment, selective enrichment, biochemical screening and serological confirmation. Some new techniques are very sensitive but analysis time is lengthy (e.g. PCR), thus making the process time-consuming. Furthermore, current methods used for microbiological tests require complex instrumentation and qualified staff. In recent years, intensive research has been undertaken to develop methods that can rapidly detect low concentrations of pathogens in water, food and clinical samples.

2.1.5 Bacterial extracellular enzymes

Bacteria must utilise energy sources from their environment to produce ATP fundamental for their maintenance and reproduction. Different bacteria use different types of source of energy: autotrophic bacteria produce energy using inorganic carbon and sunlight while heterotrophic bacteria use carbohydrates (organic carbon) present in the surrounding environment to produce energy. Carbohydrates are then oxidised by endoenzymes to produce ATP, but only few bacteria can directly use disaccharides (lactose and sucrose) and polysaccharides (starch) to produce energy. Most bacteria need to hydrolyse these macromolecules into smaller monosaccharides, which can then be transported across the cellular membrane and be oxidised. Disaccharides and polysaccharides are formed by simple sugar molecules linked by a glycosydic bonds. Heterotrophic bacteria release exoenzymes to the environment which cleave these bonds, forming monosaccharides that can be then internalised and used as source of energy to produce ATP[79]. Extracellular enzymes are classified according to the substrate that they process and, therefore, the type of reaction that they catalyse. Some of these enzymes are expressed constitutively while others are induced only under specific circumstances. In the latter case, the regulation of the enzymatic expression takes place in three different manners: by positive control (an activator induces the production of the enzyme), by negative control (the enzymatic expression is normally inhibited, it is produced only in presence of the substrate) and by feedback inhibition (the further expression of the enzyme is inhibited by the accumulation of the product of the reaction catalysed). Exo-enzymes are normally hydrolases (glycosidase if they process carbohydrates, peptidase if they hydrolyse proteins, etc.) and they are classified according to the type of carbohydrate hydrolysed. For instance, the

glycosidase family can be subdivided in smaller groups according to the carbohydrate processed and its structural molecular conformation. As shown in *Figure 17,* bacteria produce galactosidase or glucosidase to hydrolyse galactose and glucose respectively but, to hydrolyse α-glucose, the bacteria will have to release the specific α-glucosidase, while for the β-glucose the β-glucosidase enzyme is needed.
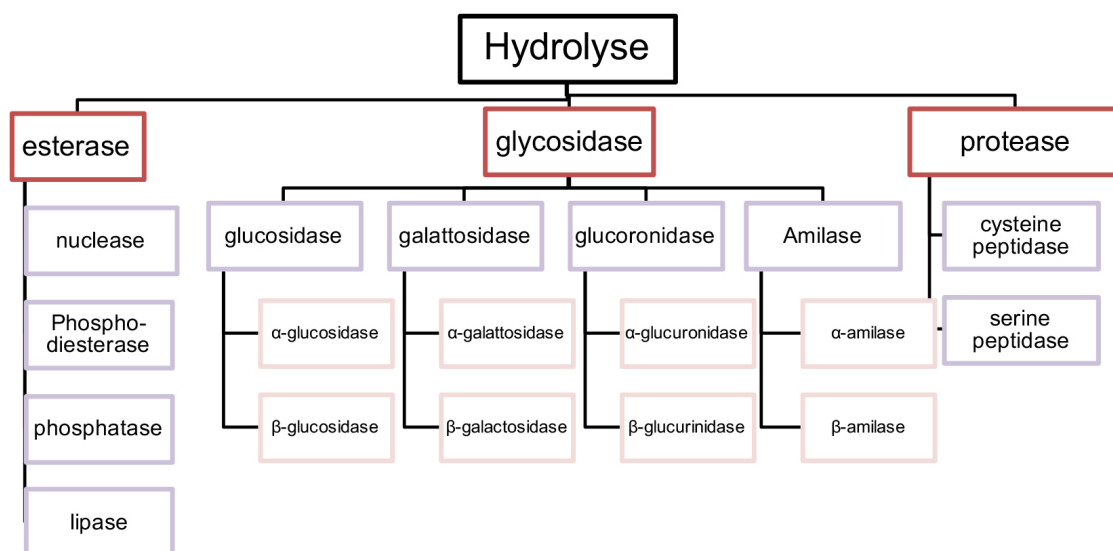
Figure 17: Hydrolase enzymes mainly cleave C-C, C-O and C-N bonds, but also other such as S-S, C-P. Glycosidases cleave the C-O bond. They can be divided into subfamilies according to the type and conformation of the carbohydrate.

Each bacterium has a set of constitute exoenzymes, which allow it to preferentially use specific types of carbohydrates as sources of energy. For this reason, exoenzymes have been exploited for the detection and identification of microorganisms in the environment, water, in food and in animal/human samples.

β-glucosidase

β-glucosidases are widely distributed among animals, plants, fungi and bacteria and they have been studied intensively for their important roles in a variety of fundamental biological and biotechnological processes. They are common members of the cellulose enzyme system.   β-glucosidase catalyses the hydrolysis of the glycosydic bonds to terminal non-reducing residues in β-D-glucosides and oligosaccharides, releasing glucose (*Scheme 1-a and -b*).
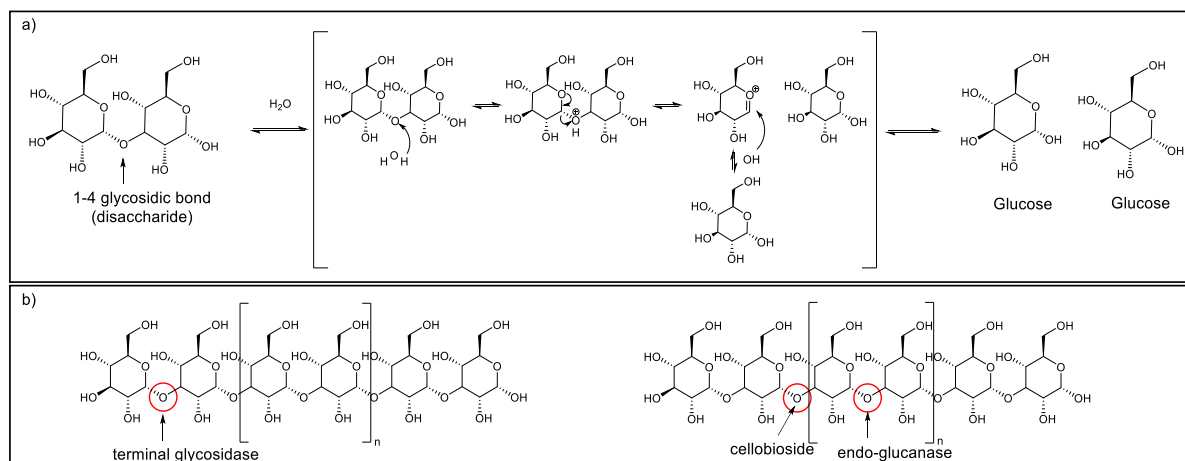
Scheme 1: a) Hydrolysis of the glycosidic bond in presence of water with formation of two molecules of glucose. b) Hydrolytic enzymes are classified according to the position of a polysaccharide on which they act. Glycosidase is a terminal enzyme; therefore it hydrolyses glycosidic bonds at the terminal end of the polymeric chain. Cellobioside and endo-glucanase hydrolyse the internal bonds between glucose monomers.

The mechanism of hydrolysis presented above is very similar to the process which occurs inside the protein. Indeed, the water, being an amphoteric medium, induces nucleophilic attack on the anomeric carbon, leading to the same structural rearrangement that occurs in the presence of the enzyme. The difference is that the enzymatic hydrolysis can retain the structure of the glucose or it can induce an inversion of the anomeric configuration to create, from β-glucose, the corresponding α-anomer. This exoenzyme is produced by different types of heterotrophic bacteria. It has been proved that its activity increases at higher pH (from pH 6 to pH 7 its activity increases from 5 to 10-fold higher) but its production is reduced by the presence of other type of sugars, like lactulose, in the environment[80]. β-glucosidases are important for the terminal hydrolysis of complex polymers, they are produced by a wide array of microorganisms and they can be exo-enzymes, endo-enzymes or ecto-enzymes (membrane bound enzymes, common in yeast)[81]. *Figure 18* gives an example of the structure of the protein-substrate interaction which can be observed by X-Ray analysis[82]. The enzyme is a homodimer, which means that it is a protein formed by two chains A and B which are chiral. The hydrolysis of the substrate requires the presence of a proton donor and proton acceptor residues, which are normally called nucleophile/base. Aspartame and glutamate have been found to be the mentioned residues
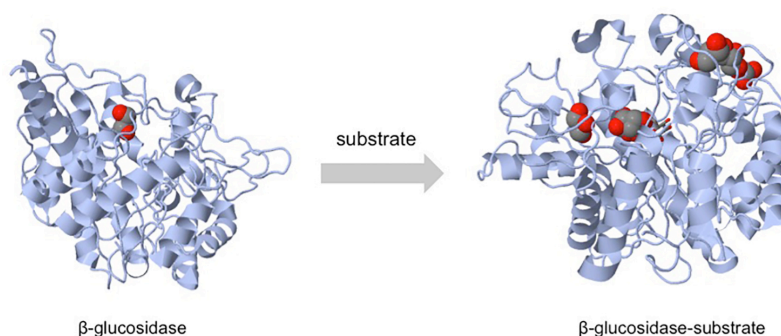
Figure 18: 3D structure of the enzyme β-glucosidase before and after complexation with its specific substrate β-glucose. Adapted from reference[82].

Chromogenic substrates have been used for the detection of extracellular β-glucosidase in bacteriological culture since the beginning of the 1900s and the most common substrate used was the natural glucoside esculin. In 1987, James and Yeoman proved that the detection of the enzyme using 8-hydroxy-quinoline-β-D-glucoside is equivalent with that given by esculin[83]. In subsequent years, many other substrates have been used for the detection of this exoenzyme, like dihydroxiflavone and ginesenosides. Parry *et al.* evaluated the efficiency of 5 different classes of chromogenic β-glucosidase substrates with different bacterial strains belonging to three families, *Enterobacteriaceae*, *Enterococcus* and *Listeria spp. (Figure 19)*[84].
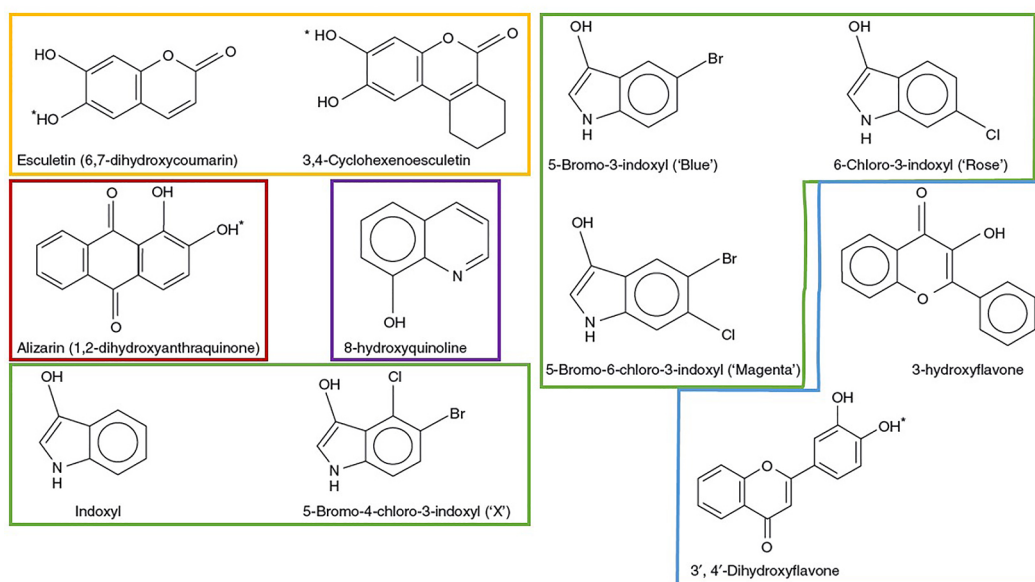
Figure 19: Six different classes of chromogens which have been synthesised and evaluated for their capability to detect different types of bacteria. Adapted from reference[84].

It is noteworthy that different substrates showed differences in their activity in detecting the same enzyme produced by different bacteria. It appears that the affinity

of the substrate for the β-glucosidase can vary within different bacterial species and this could be explained by the capability of some substrates to induce the enzymatic activity[84]. The same research group carried out similar experiments testing different fluorochromic β-glucosidase substrates, based on the 4-methylumbelliferone structure, for the detection of different bacterial strains and species. Differences were noticeable in the β-glucosidase activity produced by different strains in response to different substrates, confirming the variation in the affinity of this specific enzyme for substrates that differ by only small structural changes[85]. A chromogenic probe for β-glucosidase was used to develop a paper strip test for a rapid detection of bacteria synthesising this enzyme. The test was surprisingly quick, the change in colour occurring within 10 minutes, and it showed that it is possible to distinguish between Streptococci and Enterococci, since the latter produces more of the analyte being tested for[86]. *Streptococcus bovis,* which is related with gastrointestinal neoplasia, was selectively detected among other strains of Streptococci and Enterococci taking advantage of its ability to produce both β-glucosidase and β-galactosidase. Using both a fluorescent probe and a chromatic probe, both enzymes were respectively detected within 30 minutes, allowing the identification of the *S. bovis*[87]. Recently, Wei *et al.* developed a precipitating chromogenic and fluorogenic agar medium assay for the detection of *Klebsiella pneumonia, Streptococcus faecalis and Bacillus cereus.* Using β-glucose and β-galactose as recognition elements, their work showed the possibility of distinguishing between different foodborne bacteria without interferences between colorimetric and fluorimetric signals[88].

Overall, β-glucosidase has proved to be a good target for exploitation in the detection and identification of bacteria. In the last decade, a wide variety of substrates has been designed, conjugating β-D-glucose with chromophores/fluorophores. The activity of β-glucosidase is inducible and related to the substrate used; therefore, by changing the structure of the substrates, it is possible to enhance the speed of the identification and to improve the limit of detection (LOD).

2.1.6 Coumarin-based *on-off* fluorescent probes for bacterial detection

As described previously (*Section 2.1.3*), many switchable fluorescent probes have been designed in the last decades, usually based on 4-methylumbelliferone (4-MU) (*Figure 20*).

4-MU
4-methylumbelliferone
[7-hydroxy-4-methylcoumarin;
7-hydroxy-4-methyl-2*H*-chromen-2-one]
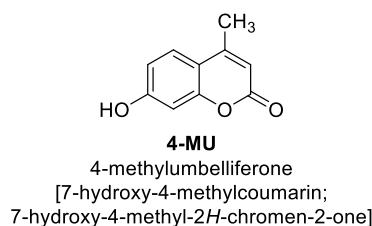
Figure 20: Structure of 4-MU and corresponding scientific names

Umbelliferone derivatives (7-hydroxycoumarins) have been shown to be suitable as switchable fluorophores by enzymatic cleavage due to their easy hydrolysis and the intense blue fluorescence generated after cleavage occurs. Umbelliferone has several features that make it suitable for the design of substrates capable of analyte detection. First, the presence of the hydroxyl group in position 7 of the benzylpyrone ring allows the compound to exist in an *on* or *off* state. Indeed, when the hydroxyl group is substituted, the derivate is weakly fluorescent, but when the bond is cleaved and the hydroxyl group becomes available again, the fluorescence is enhanced[89,90]. This *on-off* switching property of umbelliferone derivatives can be justified by the alteration of their electronic properties and electron distribution in the molecule depending on the atom to which the oxygen is linked. Furthermore, the fluorescence intensity increases in alkaline environment due to anion formation at the 7-hydroxyl group. After excitation, the unpaired electron delocalises on the structure leading to the conjugation of double bonds, which in turn leads to fluorescence. Low toxicity and good photo-physical and photo-chemical properties are features that make coumarins even more intriguing, alongside the fact that they are relatively inexpensive compared with other switchable dyes. In the last years, researchers have used coumarins due to the possibility of modify the fluorescence properties of this compounds simply changing the substituents on the benzopyrone ring.

Different enzymatically-switchable fluorescent substrates based on 4-methyl umbelliferones are commercially available and prove to be efficient in indicating the

presence of enzymes. However, 4-MU suffers from a few disadvantages. Firstly, it has a relatively high pK$_a$ (7.8[91]) leading to only partial dissociation to the phenolate under the conditions where enzymes (proteins) are effective. When using 4-MU for enzymatic assays, a basification step (addition of "stop buffer") is therefore often needed at the end of the experiment in order to increase the fluorescent signal and obtain better signal-to-noise ratio (S/N). Furthermore, 4-MU is relatively insoluble in aqueous solutions. This is undesirable considering the wide range of concentrations required when enzymatic kinetics are evaluated.

2.1.7 Project aims

Herein, we present the synthesis of seven different umbelliferone derivatives which could be used to indicate the presence of bacteria in a sample by detecting the presence of the enzyme β-glucosidase released by the microorganism (*Figure 21*). The photo-chemical and photo-physical properties of the synthesised compounds have been evaluated and compared with the properties of 4-MU as the standard. In particular, these derivatives showed to have a lower pK$_a$. This is particular important in order to give a reasonably high fluorescent signal at neutral pH, without the need of an additional basification step as it is often required by 4-MU. Moreover, substrates having better solubility than 4-MU in aqueous solvents allow for testing at high concentrations in assays. One of the substrates synthesised was further modified by glycosylation with β-D-glucose to obtain the substrate responsive to specific enzymes produced by bacteria and allowing a 'retro detection' of the microorganism. The activity of the substrate was tested using enzymatic assays to determine its specificity and selectivity. Furthermore, its activity was tested in presence of different types of bacteria.
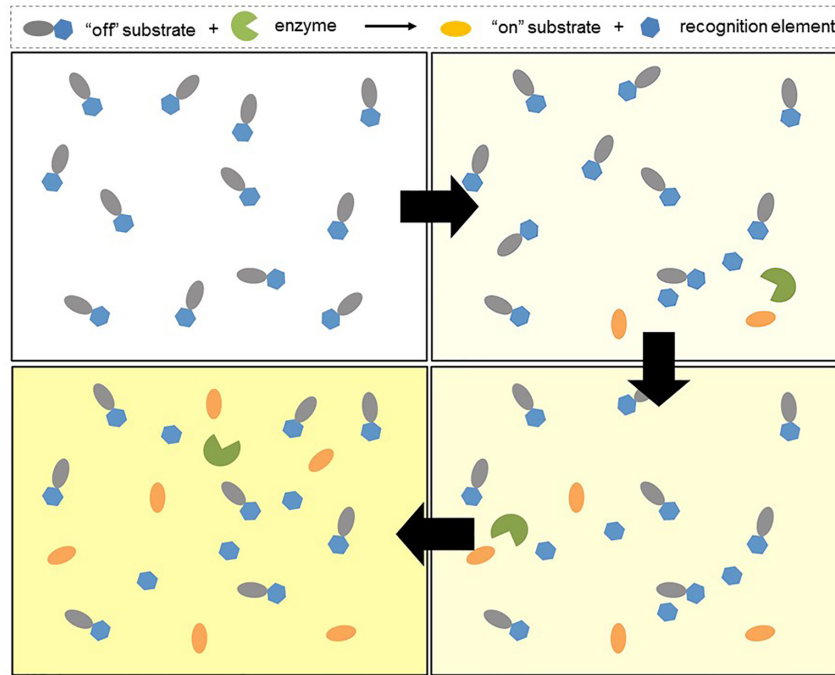
Figure 21: Increase of the fluorescence in a sample were bacteria are present. Ideally, the bacteria release the β-glucosidase enzyme, which can be detected by the substrate synthesised by measuring the fluorescent signal. Higher is the amount of substrates hydrolysed by the enzyme and higher is the fluorescent signal detectable.

2.2 Experimental

2.2.1 Materials

Acros organics: 7-hydroxycoumarin-4-acetic acid (97%), ammonia, (*ca.* 7N solution in methanol, Acroseal®), lithium aluminium hydride (1M solution in THF, Acroseal®) and 2,3,4,6-Tetra-O-acetyl-α-D-glucopyranosyl bromide (98.5% stabilised) were purchased from Acreos organics. EDC (> 98.0%) and D-biotin (>98.0%) were purchased from Tokyo Chemical Industries (TCI) (Oxford, UK). All following reagent were purchased from Sigma-Aldrich (Gillingham, UK): 4-aminophenol, resorcinol (99%), barium chloride (99.9%), acetone (anhydrous), methanol (puris. ≥99.8%), 6-mercapto-hexanol, iodine puriss., sodium sulfate, sodium methoxide reagent grade (95%), toluene anhydrous (99.8%), tetrahydrofuran (THF-99.5% extra dry over molecular sieves stabilised Acroseal®), N,N-dimethylformimide (DMF-99.8% extra dry over molecular sieves Acroseal®), dimthyl sulfoxide (anhydrous 99.9%), trimethylamine (≥99%), 1-butanol ACS reagent (≥99.4%), sodium hydroxide (≥98%),sulfuric acid ACS reagent (95-98%), sodium hydrate (NaH), thionyl chloride reagentPlus® (≥99%), β-glucosidase (from almonds ≥2 unitits/mg solid), LB broth with agar (Miller), LB broth, α-glucosidase (from Saccharomyces cerevisiae ≥100 units/mg protein),4-methylumbelliferyl α-D-glucopyranoside, biotin (5-fluorescien) conjugate. N-hydroxysuccinimide (NHS) was purchased from Fluka while pentafluorophenyl trifluoroacetate, T3P and TBTU were purchased from Fluorochem. Nunclon Delta sterile flat bottom 96-well plate and Micro BCA™ were purchased from Thermo Fisher Scientific (Loughborough, UK). Dimethyl Sulphoxide-d6 (99.9%) for NMR analysis was purchased from Goss Scientific Instruments Ltd (Cheshire, UK). MERCK silica gel 60, 230-400 mesh ASTM was used for column chromatography. Thin-layer chromatography (TLC) was performed on aluminium-backed plates MERCK silica gel 60 or on aluminium-backed plates aluminum oxide F254 (Fluka Analytics). Acetic acid glacial, chloroform, dichloromethane, absolute ethanol, ethyl acetate, sodium acetate, 2-isopropanol, n-hexane were purchased from Fisher Scientific. Silica gel 60 was purchased from Millipore. Bacteria were isolated from midstream sample urine (MSU) given by women with OAB (over-acute bladder) attending an outpatient clinic for urinary problems at Medway Maritime Hospital, Gillingham, Kent.

2.2.2 Synthetic methods

Synthesis of coumarin derivatives:
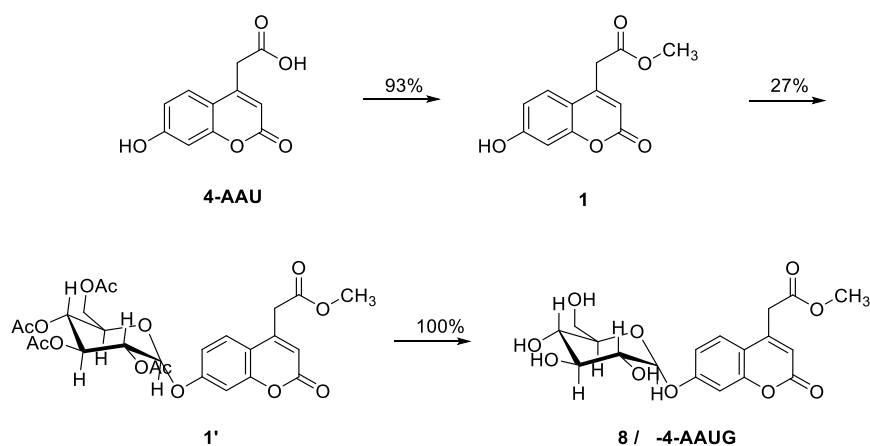
Synthesis of methyl 2-(7-hydroxy-2-oxo-2H-chromen-4-yl)acetate: **(7-hydroxy-4-coumarin methoxy acetic acid)(1):** 7-hydroxy-4-coumarin acetic acid (1 g, 4.54 mmol) was dissolved in methanol (200 mL). Thionyl chloride (1 mL) was added under stirring at 0°C, then at room temperature (RT). The reaction was left to react overnight at RT. Next day, the solvent was removed under vacuum and EA was consequently added to the residue. After 3 hours in the fridge the formed precipitate was filtered and dried under vacuum overnight reaching compound **1** as pale yellow solid (0.99 g, 93%, MW 234.18 gmol^{-1}). **^{1}H NMR** (400 MHz, DMSO-d_6): δ 10.6 (s, 1H), 7.50 (d, ^{3}J = 8.7 Hz, 1H), 6.81-6.78 (q, 1H), 6.73 (d, ^{3}J = 2.3 Hz, 1H), 6.24 (s, 1H), 3.95 (s, 2H), 3.64 (s, 3H), ppm. **^{13}C NMR** (100 MHz, DMSO-d_6): δ 170.34 (C-Ar), 161.84 (C-Ar), 160.61 (C-Ar), 155.56 (C-Ar), 150.08 (-C-OH), 127.22 (CH-Ar), 113.62 (CH-Ar), 112.73 (CH-Ar), 111.76 (C=O), 102.92 (CH-Ar), 52.73 (-CH$_3$), 37.21 (-CH$_2$-) ppm. **HR-MS (ESI-TOF):** m/z for $C_{12}H_{10}O_5^+$ [M+H]$^+$ calculated 234.18 found 234.0. **FT-IR**: 3108, 1684, 1599 cm^{-1}. **M.p.**: 219-222 °C.

Synthesis of (2R,3R,4S,5R)-2-(acetoxymethyl)-6-((4-(2-methoxy-2-oxoethyl)-2-oxo-2H-chromen-7-yl)oxy)tetrahydro-2H-pyran-3,4,5-triyl triacetate (7-aceto-β-glucopyranoseide-4-coumarin acetyl methoxide) (1') : compound **1** (0.99 g, 4.22 mmol) was dissolved in acetone (30 mL) and a NaOH 1M solution was added (6 mL). After 15 minutes the aceto-α-glucopyranoside-bromide (2.6 g, 6.33 mmol), dissolved in acetone (50 mL), was added to the reaction dropwise over 30 minutes in the dark. The reaction was left to react for 24 hours under inert atmosphere in dark. After 24 hours the solvent was evaporated under vacuum, the yellow oil reached. After solubilisation in

water (50 mL) the aqueous layer was washed 4 times with chloroform (100 mL). The combined organic layers were distilled under vacuum, and the obtained brown oil was re-crystallised from EA reaching clean product *(1')* as pale yellow solid (0.639 g, 27%, MW 564.18 gmol^{-1}). **^{1}H NMR** (400 MHz, DMSO-d_6): δ 7.68 (d, J = 2.5 Hz, 1H), 7.08 (m, J = J = 2.5 Hz, 1H), 7.01-6.98 (dd, J = 2.50, 8.85 Hz, 1H), 6.41 (s, 1H), 6.99 (dd, J = 8.9, 2.5 Hz, 1H), 5.73 (d, J = 7.93, Hz, 1H), 5.44 – 5.37 (m, 1H), 5.14-5.08 (m, 1H), 5.0-5.05 (m, 1H), 4.33 (m, J = 10.2, 5.8 , 2.5 Hz, 1H), 4.17-4.22 (dd, J = 12.3, J = 5.8 Hz, 1H), 4.13-4.08 (q, 1H), 4.02 (s, 2H), 3.65 (s, 3H), 2.02(s, 9H), 1.98 (s, 3H), ppm. **^{13}C NMR** (100 MHz, DMSO-d_6): δ 170.56 (C=O), 170.17 (C=O), 170.11 (C=O), 169.90 (C=O), 169.69 (C-Glu), 160.26 (Ar-C), 159.38 (Ar-C), 155.05 (Ar-C), 127.53 (Ar-CH), 149.72 (Ar-C), 114.90 (Ar-CH), 114.65 (Ar-CH), 114.03 (C=O), 103.98 (Ar-CH), 97.08 (C-Glu), 68.5-72.47 (C-Glu), 62.19 (-CH$_2$-),52.77 (-CH$_3$), 37.16 (-CH$_2$-), 20.87 (-CH$_3$), ppm. **MS (ES-):** m/z 563.2 [M$^-$ - H$^+$]; **MS (ES+):** m/z 587.0 [M$^+$ + Na$^+$].

Synthesis of methyl 2-(2-oxo-7-(((2S,3R,4S,5S,6R)-3,4,5-trihydroxy-6-(hydroxymethyl)tetrahydro-2H-pyran-2-yl)oxy)-2H-chromen-4-yl)acetate **(8/β-4-AAUG):** compound **1'** (100 mg, 0.177 mmol) was suspended in dried methanol (3 mL) and stirred for 15 minutes under nitrogen. Ammonia 7 N methanol solution (5 mL) was added and stirred under nitrogen in the dark. After 4.5 hours no starting material was present analysing the crude by TLC. The sample was concentrated under vacuum reaching compound **8/β-4-AAUG** as yellow solid (70.15 mg, 100%, MW 396.31 gmol^{-1}). **^{1}H NMR** (400 MHz, DMSO-D6) δ 7.63 (d, J = 8.9 Hz, 1H), 7.07 (d, J = 2.4 Hz, 1H), 7.04 (d, J = 11.5 Hz, 1H), 6.36 (s, 1H), 5.39 (d, J = 4.7 Hz, 1H), 5.13 (d, J = 4.5 Hz, 1H), 5.05 (t, J = 12.2 Hz, 2H), 4.59 (t, J = 5.45, 1H), 3.70 (d, J = 15.3 Hz, 1H), 4.01 (s, 2H), 3.70 (m, J = 15.3, 1H), 3.65 (s, 2H), 3.45 (m, J = 18.2 Hz, 2H), 3.28 (m, J = 18.72, 2H), 3.17 (m, J = 5.2 Hz, 1H) ppm. **^{13}C NMR** (101 MHz, DMSO-D6) δ 170.17 (C-Ar), 160.79 (C-C), 160.51 (C-C), 155.17 (C-Ar), 149.89 (C-Ar), 127.12 (Ar-CH), 114.27 (Ar-CH), 113.83 (C=O), 103.96 (Ar-CH), 100.55 (C-Glu), 77.73 (C-Glu), 77.06 (C-Glu), 73.68 (C-Glu), 70.21 (C-Glu), 61.22 (-CH$_2$-), 52.79 (-CH$_3$-), 37.16 (-CH$_2$-) ppm. HR-MS (ESI-TOF): m/z for C$_{17}$H$_{18}$O$_{10}$$^+$. **HR-MS (ESI-TOF):** m/z for C$_{17}$H$_{18}$O$_{10}$$^+$ [M+H]$^+$ calculated 396.31 found 396.0.. **IR**: 3408, 3214, 2884, 1704, 1614, 1397, 1334, 1206, 1077, 1013, 837 cm^{-1}. **M.p.:** 219-225 °C.
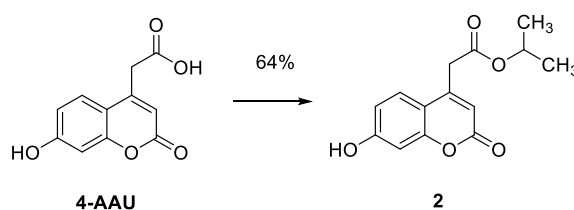
Synthesis of isopropyl 2-(7-hydroxy-2-oxo-2H-chromen-4-yl)acetate (2), 7-hydroxycoumarin-4-acetic acid (0.5 g, 2.27 mmol) was solubilised under sonication in 2-propanhol (150 mL). H_2SO_4 (1.5 mL) was added drop wise under stirring. The reaction was left react overnight RT. After 24 h the solvent was evaporated under vacuum obtaining a brown/red oil which was solubilised in water (50 mL). The aqueous layer was extracted with EA (50 mL) several times. The combined EA layers were concentrated under vacuum and a pale-yellow solid (**2**) precipitated overnight from the EA solution, which was filtered and dried under vacuum (0.38 g, 64%, MW 262.18 gmol^{-1}). **^{1}H NMR** (400 MHz, DMSO-D6) δ 10.6 (s, 1H), 7.49 (d, J = 8.7 Hz, 1H), 6.80 (dd, J = 8.7, 2.4 Hz, 1H), 6.73 (d, J = 2.4 Hz, 1H), 6.22 (s, 1H), 4.92 (m, J = 25.0 Hz, 1H), 389 (s, 2H), 1.19 (s, 3H), 1.17 (s, 3h) ppm. **^{13}C NMR** (101 MHz, DMSO-D6) δ 169.25 (C=O), 161.89 (-C-C-), 160.71 (-C-C-), 155.61(Ar-C), 150.32 (C=O), 127.22 (Ar-C), 113.58 (Ar-C), 112.58 (Ar-C), 111.74 (Ar-C-OH), 102.91 (Ar-C), 68.97 (-CH=), 37.78 (-CH$_2$-), 22.01 (-CH$_3$) ppm. **HR-MS (ESI-TOF):** m/z for $C_{14}H_{14}O_5^+$ [M+H]$^+$ calculated 262.18 found 262.0. **IR**: 3188, 2979, 1719, 1684, 1596 cm^{-1}. **M.p.**: 215-216 °C.
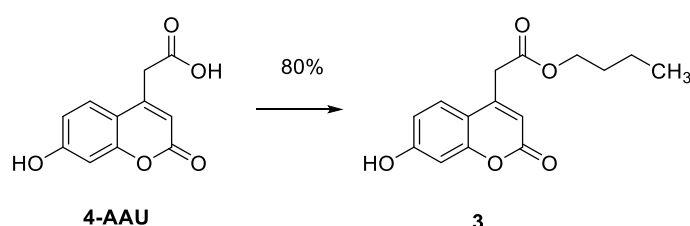
Synthesis of butyl 2-(7-hydroxy-2-oxo-2H-chromen-4-yl)acetate (3), 7-hydroxycoumarin-4-acetic acid (1 g, 4.5 mmol) was solubilised in 1-butanol (150 mL). Concentrated H_2SO_4 (2.4 mL) was added drop wise under stirring. After 24 h the crude was concentrated under vacuum reaching brown/red oil which was solubilised in water (50 mL) and the aqueous layer was extracted with EA (50 mL) several times. After extraction, the combined organic layers were concentrated under vacuum, and the pure compound **3** was crystalized from EA as a pale-orange powder. (0.995 g, 80%,

MW 276.29 gmol^{-1}). **^{1}H NMR** (400 MHz, DMSO-D6) δ 10.6 (s, 1H), 7.51 (d, J = 8.7 Hz, 1H), 6.79 (dd, J = 8.72, 2.38, 1H), 6.73 (d, J = 2.3 Hz, 1H), 6.23 (s, 1H), 4.05 (t, J = 6.5 Hz, 1H), 3.93 (s, 1H), 1.50 (m, J = 12.6 Hz, 2H), 1.24 (m, J = 14.9 Hz, 2H), 0.82 (t, J = 7.4 Hz, 3H) ppm. **^{13}C NMR** (101 MHz, DMSO-D6) δ 169.75 (C=O), 161.88 (-C-C-), 160.71 (-C-C-), 155.61 (Ar-C), 150.23 (C=O), 127.25 (Ar-C), 113.56 (Ar-C), 112.63 (Ar-C), 111.75 (Ar-C-OH), 102.90 (Ar-C), 65.03 (-CH$_2$-), 37.52 (-CH$_2$-), 30.59 (-CH$_2$-), 19.04 (-CH$_2$-), 14.01 (-CH$_3$) ppm**. HR-MS (ESI-TOF):** m/z for C$_{15}$H$_{16}$O$_5^+$ [M+H]$^+$ calculated 276.29 found 276.0. **IR**: 3377, 2962, 1698, 1608, 1400, 1252, 1210, 1139, 857, 624 cm^{-1}. **M.p.:** 152-154 °C.
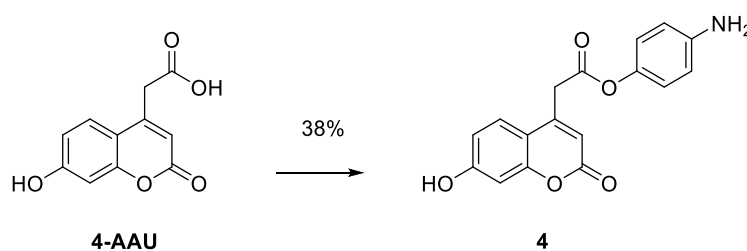
*Synthesis of 4-aminophenyl 2-(7-hydroxy-2-oxo-2H-chromen-4-yl)acetate (**4**)*. 7-hydroxycoumarin-4-acetci acid (0.5 g, 2.27 mmol), 4-amino-phenol (0.247 g, 2.27 mmol) and EDC (0.653 g, 3.4 mmol) were dried under vacuum for 2 hours. All compounds were solubilised in the same flask at RT in anhydrous DMF (10 mL) and flashed with N$_2$ several times. The reaction was left to react firstly in an ice bath at 0°C, then at RT overnight under nitrogen condition. The reaction mixture was concentrated under vacuum and suspended in 0.1 M NaOH solution (50 mL). The aqueous layer was extracted five times with EA (50 mL). The organic layers were concentrated and the yellow solid purified by silica gel chromatographic column using DCM 100% increasing gradually up to DCM/MeOH 8%. The obtained yellow solid was additionally precipitated in EA overnight reaching compound **4** as yellow fine powder (0.4 g, 38%, MW 311.29 gmol^{-1}). **^{1}H NMR** (400 MHz, DMSO-*d$_6$*): δ 10.04 (s, 1H), 7.66 (d, J = 8.8 Hz, 1H), 7.35 (m, 2H), 6.82 (dd, J = 2.38, 8.73 Hz, 1H), 6.74 (d, J = 2.36 Hz, 1H), 6.70 (m, 2H), 6.23 (s, 1H), 3.83 (s, 2H), ppm. **^{13}C NMR** (100 MHz, DMSO-*d$_6$*): δ 165.93 (C=O), 161.31 (C=O), 160.30 (Ar-C-OH), 155.12 (C=C), 153.66 (Ar-CH$_2$-), 151.22 (Ar-NH$_2$), 130.52 (Ar-O), 126.81 (Ar-C), 121.16 (Ar-C), 115.19 (Ar-C), 113.07 (Ar-C), 11.92 (Ar-C), 111.60 (C=C), 102.41 (Ar-C), 59.83 (-CH$_2$-) ppm. **MS (ES+):** m/z 312.0 [M$^+$ + H$^+$]. **IR:** 3290, 1698, 1603, 1512, 1440, 1267, 1206, 838 cm^{-1}. **M.p.:** 256-257 °C.
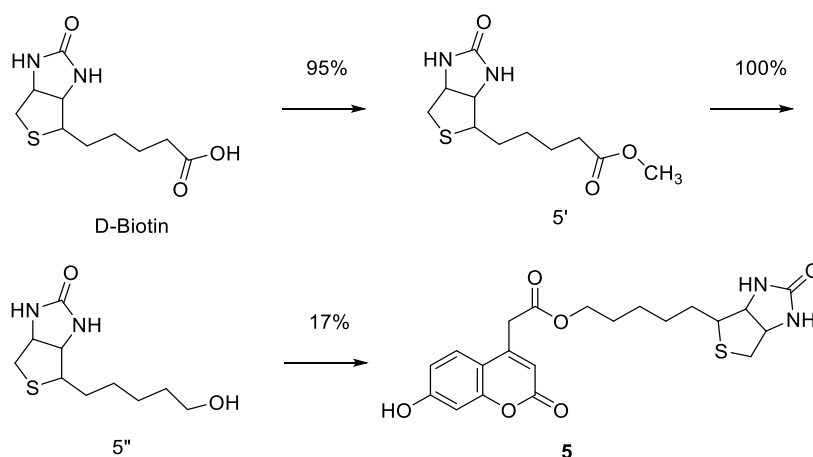
Synthesis of methyl 5-(2-oxohexahydro-1H-thieno[3,4-d]imidazol-4-yl)pentanoate (5'): D-biotin (2 g, 8.19 mmol) was dissolved in methanol (260 mL). Concentrated sulfuric acid (2.18 mL) was added under stirring at RT overnight. Next day, the solvent was evaporated under vacuum and the received residue was dispersed in water (100 mL) and extracted five times with EA (100 mL). The organic layer was concentrated under vacuum reaching compound **5'** as white solid (2 g, 95%, MW 258.32 gmol^{-1}). **^{1}H NMR** (400 MHz, DMSO-d_6): δ 6.43 (s, 1H), 6.35 (s, 1H), 4.30 (dd, J = 7.7, 5.0 Hz, 1H), 4.13 (m, 1H), 3.58 (s, 3H), 3.10 (m, 1H), 2.82 (dd, J = 12.4, 5.1 Hz, 1H), 2.57 (d, J = 12.4 Hz, 1H), 2.30 (t, J = 7.5 Hz, 2H), 1.61 (m, 1H), 1.53 (m, 2H), 1.45 (m, 1H), 1.33 (m, 2H). ppm. **^{13}C NMR** (100 MHz, DMSO-d_6): δ 173.88 (C=O), 163.27 (C=O), 61.59 (C-H), 59.74 (C-H), 55.90 (C-H), 51.76 (CH$_3$), 40.42 (C-H$_2$), 33.66 (CH$_2$), 28.56 (CH$_2$), 28.53 (CH$_2$), 25.04 (CH$_2$) ppm. **HR-MS (ESI-TOF):** m/z for C$_{11}$H$_{18}$O$_3$N$_2$S$^+$ [M+H]$^+$ calculated 258.32 found 258.0. **IR**: 3271, 3191, 2924, 1699, 1464, 1432, 1237 cm^{-1}.

Synthesis of 4-(5-hydroxypentyl)tetrahydro-1H-thieno[3,4-d]imidazol-2(3H)-one (5''): compound **5'** (2 g, 7.8 mmol) was dissolved in anhydrous THF (50 mL), LiAlH$_4$ (34 mL) was then added and the reaction was stirred under nitrogen. Reaction was monitored by TLC and when all starting material was consumed (3 h) the reaction was stopped by addition of MeOH and water (15 mL each) drop wise at 0°C. A saturated solution of sodium sulfate (20 mL) was added and the mixture was stirred for 20 min. A solution of DMC/MeOH 4:1 (300 mL) was added and stirred for a few minutes. The white solid formed was filtered and the filtrate concentrated reaching the product **5''** as white fluffy solid. (1.8 g, 100%, MW 230.23 gmol^{-1}). **^{1}H NMR** (400 MHz, DMSO-d_6): δ 4.27 (m, 1H), 4.10 (dd, J= 7.70, 4.52, 1H), 3.36 (t, J = 6.5 Hz, 2H), 3.08 (m, 1H), 2.80 (dd, J = 12.27, 5.2 Hz, 1H), 2.55 (d, J = 12.2 Hz, 1H), 1.62 (m, 1H), 1.47 (m, 1H), 1.41 (m, 2H),

1.30 (m, 4H) ppm. **¹³C NMR** (126 MHz, DMSO-d_6): δ 164.49 (C=O), 62.35 (C-H), 61.03 (CH$_2$), 60.83 (C-H), 56.23 (C-H), 40.5 (CH$_2$), 32.84 (CH$_2$), 29.07 (CH$_2$), 26.11 (CH$_2$) ppm. **HR-MS (ESI-TOF):** m/z for C$_{10}$H$_{18}$O$_2$N$_2$S$^+$ [M+H]$^+$ calculated 230.32 found 230.0. **IR**: 3197, 2924, 2851, 1695 cm^{-1}.

*Synthesis of 5-(2-oxohexahydro-1H-thieno[3,4-d]imidazol-4-yl)pentyl 2-(7-hydroxy-2-oxo-2H-chromen-4-yl)acetate**(5):*** compound **5"** (1 g, 4.3 mmol), 7-hydroxy-4-coumarin acetic acid (0.95 g, 4.3 mmol) and EDC (1.24 g, 6.45 mmol) were dried under vacuum for a few hours and then solubilised in anhydrous DMF (20 mL). The reaction was left react under nitrogen at 0°C and then at RT wrapped in tin foil overnight. After 24 hours the crude was concentrated under vacuum reaching a brown oil which was dissolved in 0.01M NaOH (100 mL) and extracted with EA (100 mL) five times. The orange solid was purified by silica gel column chromatography starting from EA 100% increasing gradually up to EA/MeOH 50%. The first fractions were collected, concentrated, reaching the final product **5** as pale yellow solid (0.32 g, 17%, MW 432.29 gmol^{-1}). **¹H NMR** (400 MHz, DMSO-d_6): δ 10.66 (s, 1H), 7.51 (d, J = 8.7 Hz, 1H), 6.80 (dd, J = 8.7, 2.4 Hz, 1H), 6.73 (d, J = 2.3 Hz, 1H), 6.44 (s, 1H), 6.38 (s, 1H), 6.24 (s, 1H), 4.31 (dd, J = 7.6, 5.2 Hz, 1H), 4.12 (m, 1H), 4.05 (t, J = 6.5 Hz, 2H), 3.39 (s, 2H), 3.06 (m, 1H), 2.82 (dd, J = 12.4, 5.1 Hz, 1H), 2.58 (d, J = 12.4 Hz, 1H), 1.54 (m, 3H), 1.45 (m, 1H), 1.25 (M, 4h) ppm. **¹³C NMR** 169.74 (C=O), 163.33 (C=O), 161.92 (C=O), 160.72 (Ar-OH), 155.62 (C=C), 150.23 (Ar-C), 127.24 (Ar-H), 113.60 (Ar-H), 112.65 (C=O), 111.74 (Ar-H), 102.92 (Ar-H), 65.27 (CH$_2$), 61.60 (C-H), 59.79 (C-H), 55.98 (C-H), 40 (CH$_2$), 37.56 (CH$_2$), 28.74 (CH$_2$), 28.68 (CH$_2$), 28.38 (CH$_2$), 25.86 (CH$_2$) ppm. **MS (ES$^+$):** m/z 433.1 [M$^+$ + H$^+$]. **IR**: 3349, 2936, 1705, 1612, 1138 cm^{-1}. **M.p.**: 185-190 °C.
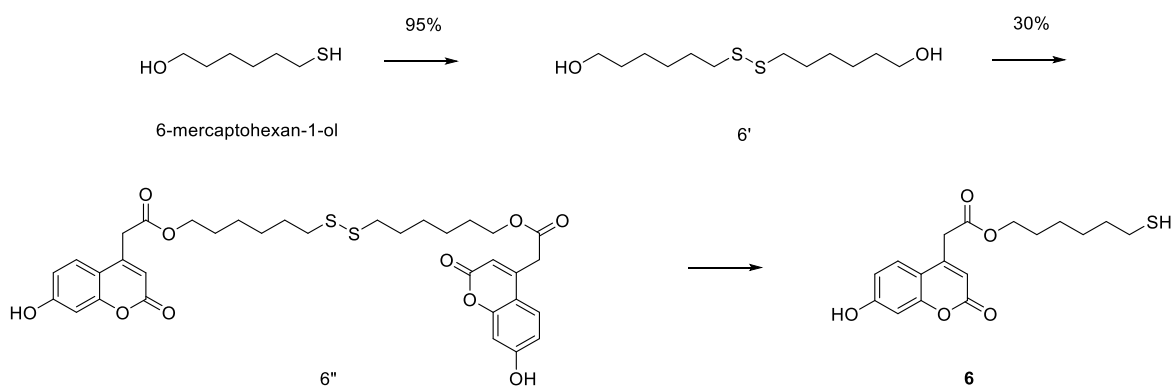
Synthesis of 6,6'-disulfanediylbis(hexan-1-ol) (6'): to 6-mercapto hexanol (3 mL, 0.022 mol) was added under stirring a saturated solution of I_2 in methanol until the reaction turned from a white suspension to a yellow solution (4 mL), and then stirred for 4 hours at RT. The brown oil obtained after removal of the solvent under vacuum, was redispersed in DCM (50 mL) and washed several times with water. The organic layer was concentrated under vacuum reaching compound **6'** as transparent oil (5.57 g, 95%, MW 266.48 gmol^{-1}). **¹H NMR** (400 MHz, DMSO-d_6): δ 4.32 (s, 2H), 3.37 (t, J = 6.5 Hz, 4H), 2.69 (t, J = 8, 2H), 2.46 (q, J = 8 Hz, 2H), 1.61 (m, 2H), 1.53 (m, 2H), 1.40 (m, 4H), 1.30 (m, 8H) ppm. **¹³C NMR** (100 MHz, DMSO-d_6): δ 61.22 (C-OH), 38.42 (CH-S-S), 34.01 (CH$_2$), 33.00 (CH$_2$), 32.94 (CH$_2$), 29.18 (CH$_2$), 28.24 (CH$_2$), 25.62 (CH$_2$), 25.56 (CH$_2$), 24.29 (-S-S-CH) ppm. **HR-MS (ESI-TOF):** m/z for C$_{12}$H$_{28}$O$_2$S$_2^+$ [M+H]$^+$ calculated 266.48 found 266.0. **IR**: 3331, 2928, 2853, 1050 cm^{-1}.

Synthesis of disulfanediylbis(hexane-6,1-diyl) bis(2-(7-hydroxy-2-oxo-2H-chromen-4-yl)acetate) (6"): compound **6'** (0.55 g, 2.06 mmol), 7-hydroxy-4-coumarin acetic acid (1 g, 4.54 mmol) and EDC (1.5 g, 8.24 mmol) were dried under vacuum for a few hours and then solubilised in anhydrous DMF (50 mL). The reaction was left react under nitrogen and at 0°C and then at room temperature overnight. After 48 hours the crude was concentrated under vacuum and dissolved in water and extracted with EA (100 mL). The organic layer after concentration was purified by silica gel column chromatography starting from hexanol 100% increasing gradually up to EA 100%. The fractions with the product were collected. After precipitation in EA the product **6"** was isolated as white solid (0.437 g, 30%, MW 670.19 gmol^{-1}) **¹H NMR** (400 MHz, DMSO-d_6): 10.62 (S, 2H), δ 7.50 (d, J = 8.7 Hz, 2H), 6.78 (dd, J = 8.7, 2.3 Hz, 2H), 6.72 (d, J = 2.3 Hz, 2H), 6.23 (s, 2H), 4.05 (t, J = 4.0 Hz, 4H), 4.02 (s, 4H), 2.64 (t, J = 8.0 Hz, 4H), 1.55 – 1.51 (m, 8H), 1.28-1.17 (m, 8H) ppm. **¹³C NMR** (100 MHz, DMSO-d_6): δ 169.72 (Ar-C-OH), 161.89 (C-C), 160.71 (C-C), 155.62 (Ar-C=O), 150.24 (Ar-C-CH$_2$), 127.26 (Ar-CH-),

113.57 (Ar-CH-), 112.65 (Ar-CH-), 111.76 (-O-C=O), 102.90 (Ar-CH-), 65.23 (CH$_2$), 37.57 (Ar-CH$_2$), 33.81 (CH$_2$), 28.44 (CH$_2$), 27.81 (CH$_2$), 25.29 (CH$_2$), 24.19 (CH$_2$) ppm. **MS (ES$^-$): m/z** 335.1 [M/2$^-$ - H]$^+$; **MS (ES$^+$):** m/z 337.1 [M/2 + H]$^+$. **IR**: 3222, 2916, 1688, 1600, 1392, 1234, 1164 cm^{-1}. . **M.p.:** 119-121 °C

*Synthesis of 6-mercaptohexyl 2-(7-hydroxy-2-oxo-2H-chromen-4-yl)acetate **(6):*** compound 6 was synthesized prior analysis and NPs functionalization without isolation. And it will be discussed in the following section.
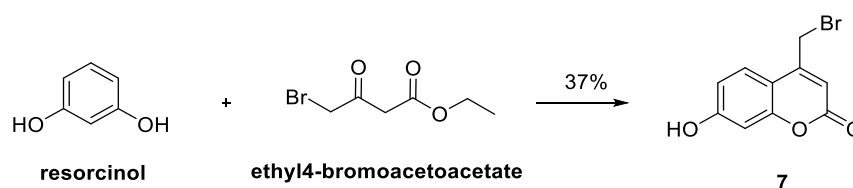
*Synthesis of 4-(bromomethyl)-7-hydroxy-2H-chromen-2-one **(7):*** resorcinol (0.55 g, 5 mmol) and ethyl-4-bromoacetoacetate (0.65 mL, 4.7 mmol) were mixed together and dissolved in H$_2$SO$_4$ 70% (20 mL) at RT. After 24 hours the crude was poured in crashed ice and the brown/orange solid was filtered. The solid was solubilized in EtOH and water was added drop wise until some solid precipitated. Compound **7** was isolated as pale yellow solid (0.45 g, 37%, 255 gmol^{-1}) **^{1}H NMR** (400 MHz, DMSO-d_6): δ 10.65 (s, 1H), 7.71 (d, J = 8.8 Hz, 1H), 6.85 (dd, J = 8.8, 2.4 Hz, 1H), 6.75 (d, J = 2.4 Hz, 1H), 6.46 (s, 1H), 4.81 (s, 2H) ppm. **^{13}C NMR** (100 MHz, DMSO-d_6): δ 162.04 (Ar-CH), 160.75 (-C-C-), 156.01 (-C-C-), 152.09 (Ar-C=O), 127.30 (Ar-CH), 113.59 (Ar-CH), 112.03 (Ar-CH), 109.89 (Ar-C-), 103.11 (Ar-CH), 28.64 (-CH$_2$-). ppm. **MS (ES$^-$):** m/z 255 [M$^-$ - 2H$^+$]; **MS (ES$^+$):** m/z 256.9 [M$^-$ + H$^+$]. **IR**: 3202, 1692, 1607, 1556, 1313, 1128, 855 cm^{-1}. **M.p.**: 186-190°C

2.2.3 Instruments and analytical methods

UV-Vis analysis:

A Tecan Infinite M200 Pro microscope reader and Tecan i-control 1.10.4.0 software were used for all the absorbance and fluorescent emission measurements. Samples were added to Nunc Maxisorb 96-well plates before being read or, in the case of microbiological/cellular experiments, Nunclon Delta sterile flat bottom 96-well plate were used instead. For fluorescence evaluation of the umbelliferone derivatives, quartz slides were used to obtain the absorbance and fluorescence spectrum. A scan range of

260-400 nm and a wavelength step size of 1 nm were employed for the absorbance spectra measurements. The maximum absorbance value determined for each compound was used as excitation wavelength for fluorescence spectrum. Fluorescent emission was scanned in the range of 400-600 nm with wavelength step size of 1 nm and gain setting of 60.

$\lambda_{ex}/ \lambda_{em}$ 327/460 nm were used for both enzymatic and bacterial assays. Absorbance at 690 nm was used for the quantification of bacteria in the sample.

Fluorescence analysis of umbelliferone-derivatives at different pH: The pH of sodium phosphate buffers was adjusted using solution 0.1 M NaOH or 0.1 M HCl reaching pH 4, 5, 5.5, 6, 6.5, 7, 7.5 and 8. For each derivative, a stock solution of 1 mM was prepared in water. 0.1 mL of the stock was added to 0.9 mL of buffer at different pH. For each derivative were prepared 0.1 mM solutions at the different pH tested.

Mass Spectroscopy analysis (MS):

Low-resolution mass spectra (m/z) were recorded using electrospray ionisation (ESI) in positive and/or negative mode (as stated). ESI mass spectra were measured on a Waters Ultima mass spectrometer using direct injection (1 mL). All samples were prepared at concentration of 1 mg/mL in analytical grade methanol.

Infra-Red spectroscopy (FT-IR):

IR spectra were recorded in the range of 4000-400 cm^{-1} in attenuated total reflaction (ATR) mode using a Perkin Elmer Spectrum One FT-IR spectrometer.

Nuclear Magnetic Resonance spectroscopy (NMR):

^{1}H and ^{13}C NMR spectra were recorded in the deuterated solvent stated on a Jeol ECP 400 MHz FT NMR spectrometer, incorporating a tuneable H (5) 400 probe (1H: 400 MHz and 13C: 100 MHz) or on a Jeol ECA, 500 MHz FT NMR Spectrometer, incorporating a NM-50TH5AT/FG2 probe. All chemical shifts (δ) are quoted in ppm and coupling constants (J), where given, in averaged Hz. Residual signals from the solvents or TMS signal were used as an internal reference. 1H resonances were assigned with the aid of 2D techniques such as COSY and HMQC. 13C resonances were assigned using a DEPT 135 sequence. Spectra were processed using MestReNova or Jeol software.

Incubators:

Bacteria samples were grown in Petri dishes on solid LB agar in a Genlab incubator at 37°C overnight. Bacteria were harvested in liquid LB broth under agitation (166 rpm) at 37°C in a New Brunswick Scientific incubator.

Autoclave:

All tools used for the bacterial culturing and experiments were sterilised using an INUCLAV 18/23 class B autoclave purchased form UniEquip. Solid and liquid materials were autoclaved at 134°C.

2.2.4 Assays

Enzymatic assays:

All enzymatic assays here presented were accomplished using sodium acetate buffer 0.2 M at pH 6.5 unless otherwise specified. The amount of protein was quantified by Micro BCA Protein Assay Kit after purification by centrifugation. All assays have been performed in 96-well plates using as maximum volume of 100 μL in each well. Once prepared, the plate was incubated at 37°C and shaken at 600 rpm. The increase of fluorescence was measured every 15 minutes using as excitation and emission wavelengths, respectively, 327 and 460 nm. In assay IV, a mixture of unknown enzymes was used. The powder was purified by centrifugation and the total amount of protein was quantified by BCA Protein Assay Kit.

Table 2: Concentrations of substrate and enzyme used in the selectivity assays.

	Substrate (conc. mM)	Enzyme (conc. μg/mL)
Assay I	β-4-AAUG (0.006-2)	β-glucosidase (50)
Assay II	β-4-AAUG (0.1)	α-glucosidase (25-500)
Assay III	β-4-AAUG, α-4-MUD (0.1)	α-glucosidase (250)
Assay IV	β-4-AAUG, α-4-MUD (0.1)	Unknown enzyme (2.5 mg/mL)

Preparation of sodium acetate buffer 0.2 M pH 6.5: 2.722 g of sodium acetate was solubilised in 100 mL of DI water and the pH was adjusted adding glacial acetic acid.

Bacterial assays:

Culturing bacteria and harvesting: All bacteria have been cultured in Petri dishes on Luria-Bertani broth solid (LB with agar) and incubated at 37°C overnight. A few isolated colonies were then harvested in liquid LB broth at 37°C under shaking at 650 rpm for 4 hours. The suspension of bacteria was diluted until the desired concentration was obtained, determined by McFarlan turbidity standards, measuring the opacity of the sample and by plate counting backwards. McFarlan standards have been prepared by mixing a 1% w/v solution of barium chloride and 1% v/v solution of sulfuric acid according to available protocols. To the 96-well microplate was firstly added the substrate solution at appropriate concentrations and, after the fluorescent signal at t0 was measured, the bacterial samples were quickly added to each well and the increase of fluorescence was measured over time, shaking the plate at 600 rpm at 37°C. All concentration analysed were calculated accordingly to the final volume of 200 µL/well: 100 µL were constituted by bacterial suspension in LB broth and 100 µL of sterile aqueous solution of the substrate. The increase in fluorescence was measured using as $\lambda_{ex}/\lambda_{em}$ wavelength 327/460 nm respectively every 15 minutes. The spectra of the kinetic achieved were normalised with the auto-hydrolysis in broth-water (1:1) solution obtained for each substrate in each experiment.

E. coli, Enterococcus, K. pneumonia, P. aeruginosa, and S. areus bacteria were tested at different concentrations when treated with the substrates at different concentrations (250 or 50 µM). The respective concentrations of substrate/bacteria are shown in *Table 3*.

Table 3: Concentrations of substrates and bacteria used for bacterial experiments.

	Substrate (µM)	Bacteria (CFU/mL)
Assay I	β-4-AAUG (50)	1, 20, 75
Assay II	β-4-MUD (50)	1, 20, 75
Assay III	α-4-MUD (50)	1, 20, 75
Assay IV	β-4-AAUG (250)	1.17, 2.5, 5, 10, 20, 37.5, 75, 150
Assay V	β-4-MUD (250)	1.17, 2.5, 5, 10, 20, 37.5, 75, 150
Assay VI	α-4-MUD (250)	1.17, 2.5, 5, 10, 20, 37.5, 75, 150

Toxicity of substrates induced on E.coli: The assays were carried out in sterile 96-well plates. 100 μL of 500, 50 and 5 μM solutions of each substrate diluted in water were mixed with 100 μL of 0.2 CFU/mL *E.coli* in LB broth, reaching 200 μL as the final volume for each well. Final concentrations of the substrates and *E.coli* assayed are reported in *Table 4*. The plates were incubated at 37°C under shaking and the bacterial growth was evaluated by measuring the absorbance at 690 nm every 20 minutes.

Table 4: Concentrations of substrates and *E.coli* used in the toxicity experiment.

Conc. (μM) of each substrate	Conc. (CFU/mL) of *E.coli*
500	0.1
50	0.1
5	0.1
0 (0.1 mL of water)	0.1

2.3 Results and discussion

2.3.1 Synthesis of umbelliferone derivatives and fluorescence study

As mentioned in the introduction, a few enzymatically switchable fluorescence substrates (analogues of 4-MU) are available on the market. The project goal was to synthesise new coumarin derivatives with better fluorescent properties than the fluorophore currently available, 4-MU, along with the intention of making them suitable for nanoparticle functionalisation. Photochemical and photo-physical properties of the synthesised substrates have been evaluated and their solubility in aqueous solvent tested. The substrates have been also designed with the purpose of developing a nanoprobe formed by nanoparticles decorated with the synthesised substrates on the nanoparticle surface. One fundamental characteristic that a compound must have in order to be covalently linked to nanomaterials is the presence of reactive chemical groups in its structure. Through appropriate reactions, the compound can then be conjugated with the anchor groups available on the NP's surface. Considering this, it can be noticed that the available analogues of 4-MU structure would not be adequate for this purpose, since the only reactive group is the hydroxyl group in position 7, which is needed for the connection with the detection element (in this case β-D-glucose, which allows the substrate to be recognised by the enzyme β-glucosidase). For this reason, all the derivatives here presented were obtained using 7-hydroxy-4-coumarin acetic acid (4-AAU) as a starting material. 4-AAU has two possible modification sites: the hydroxyl group and the acetic acid group, respectively, in positions 7 and 4 on the benzopyrene ring (*Figure 23*).

4-MU
4-methylumbelliferone
[7-hydroxy-4-methyl-2*H*-chromen-2-one]

4-AAU
7-hydroxycoumarin-4-acetic acid
umbelliferon-4-acetic acid
[2-(7-hydroxy-2-oxo-2*H*-chromen-4-yl)acetic acid]
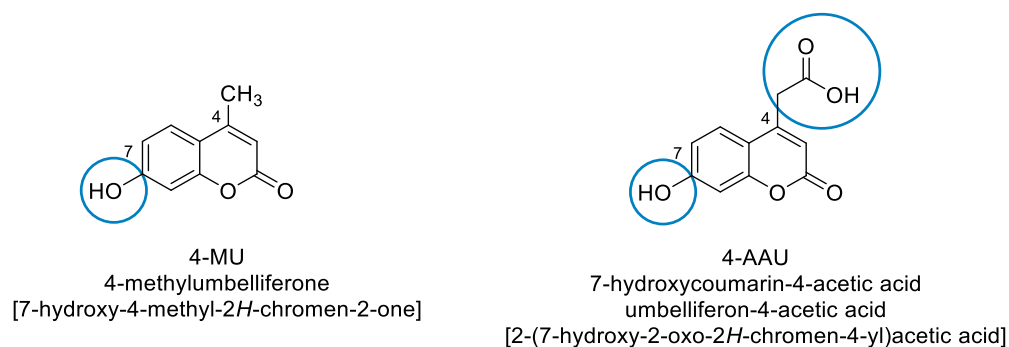
Figure 22: Structure of 4-MU and 4- AAU are compared highlighting the available sites of modification.

Only the engagement of the hydroxyl group in bond formation/cleavage leads to the *on/off* state, while changes at position 4 do not alter the switchable property of the compound. All derivatives have been therefore synthesised by modifying the carboxyl group of the 4-AAU. The only exception is compound **7**, for which the umbelliferone ring has been synthesised *ex novo (Figure 23).*

	R
1	$-CH_3$
2	isopropyl $(CH_3)_2$
3	$-CH_2CH_2CH_2-CH_3$
4	$-C_6H_4-NH_2$
5	biotin chain
6	$-(CH_2)_6-SH$
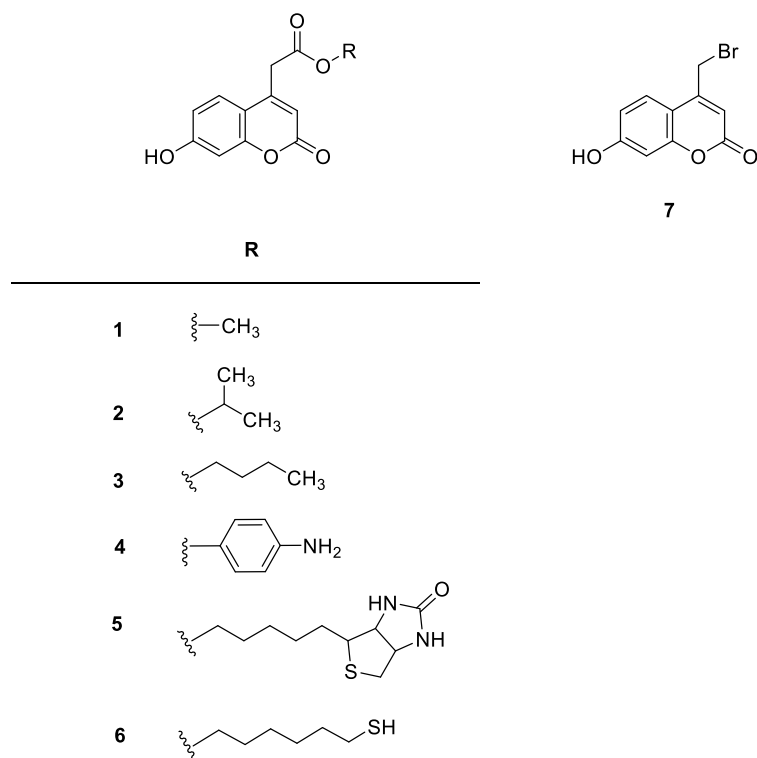
Figure 23: Structures of the synthesised umbelliferone derivatives.

For compounds **2** and **3**, 2-propanol and *n*-butanol were used to protect the acidic group during the synthetic procedures and to evaluate the possibility to enhance fluorescent properties of the compounds. The two conjugates with D-biotin and mercaptohexanol, compounds **5** and **6** respectively, were prepared primarily for use in NP's surface functionalisation. Due to the characteristic low solubility in aqueous solvents of both the mercaptohexanol and biotin moieties, the solubility of the corresponding umbelliferone derivatives was found to be quite poor in water. The solubility was instead enhanced with *p*-aminobenzene derivate (compound **4**) due to the possible protonation of the amino group in aqueous environment at the condition tested. The bromo derivative **7** was synthesised in order to have a reactive halogen suitable for the NP's surface functionalisation.

Compounds **1-4** were synthesised by one-step reactions. In the case of compounds **1-3,** the carboxylic group of the umbelliferone was esterified using a Fisher-Speier reaction, in which the acidification of the methanol, 2-propanol and *n*-butanol solutions of 4-AAU led to the formation of the ester bond between the starting material and the alcohol *(Scheme 2).*
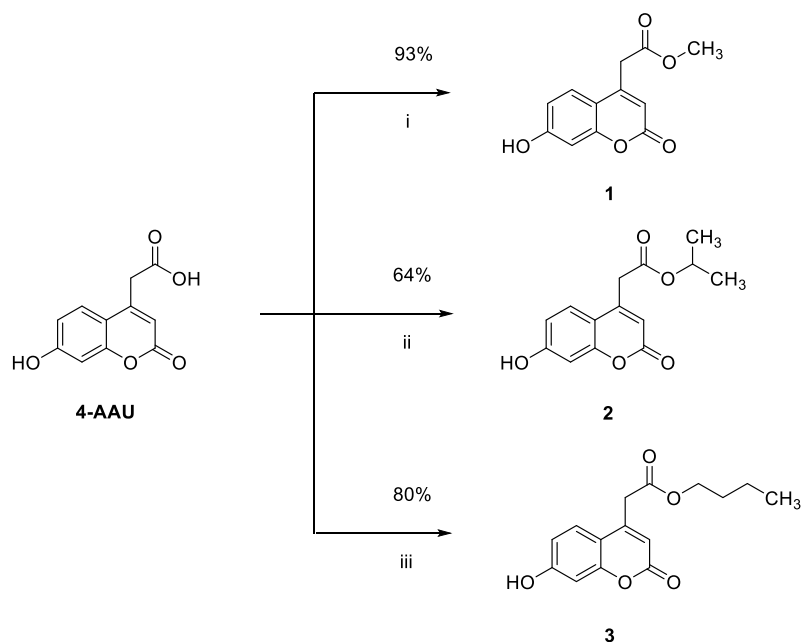
Scheme 2: i) MeOH, SOCl$_2$, RT, overnight ii) 2-propanol, H$_2$SO$_4$, RT, overnight iii) 1-butanol, H$_2$SO$_4$, RT, overnight

The ester formation between 4-AAU and 4-amino-phenol *(*compound **4**) was instead achieved by activating the carboxyl group with EDC (N-(3-dimethylaminopropyl)-N′-ethylcarbodiimide hydrochloride) as shown in *Scheme 3.*
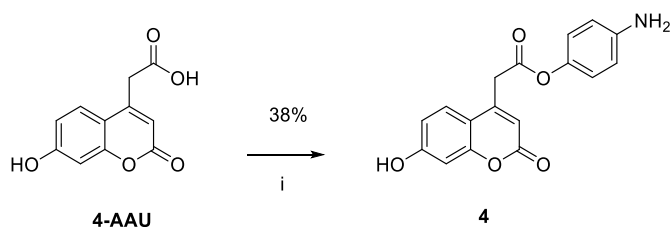
Scheme 3: i) EDC, DMF, under N$_2$, in ICE-bath for 15 minutes then RT overnight

In the case of compounds **5** and **6**, the synthetic pathways consisted of a few different steps. As shown in *Scheme 4*, for the synthesis of compound **5,** D-biotin was firstly methylated and reduced to give a terminal hydroxyl group, which was then used for the ester bond formation with the 4-AAU under EDC coupling reaction conditions.
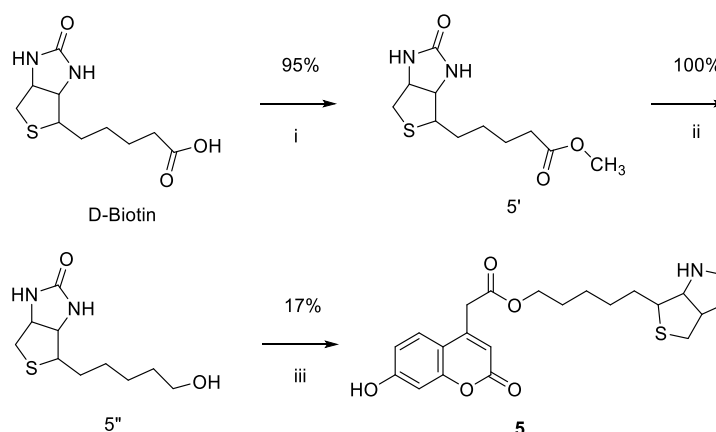
Scheme 4: i) MeOH, H_2SO_4, RT, overnight ii) LiAlH$_4$, THF, 3h, RT iii) 4-AAU, EDC, DMF, under N_2, overnight, RT

In order to avoid the formation of side products due to interaction between thiol groups and the hydroxyl/carboxyl groups of the coumarin during the synthesis of compound **6**, the thiol groups were protected by formation of disulfide bonds between two molecules of 6-mercapto-ethanol to give the dimer. This dimer was mixed with two equivalents of 4-AAU and EDC to give a dimeric coumarin derivate. The disulfide bond was maintained until the compound was used in order to avoid any possible intermolecular reactions during storage (*Scheme 5*). The final compound **6** was therefore produced only when needed, by addition of dithiothreitol (DTT).
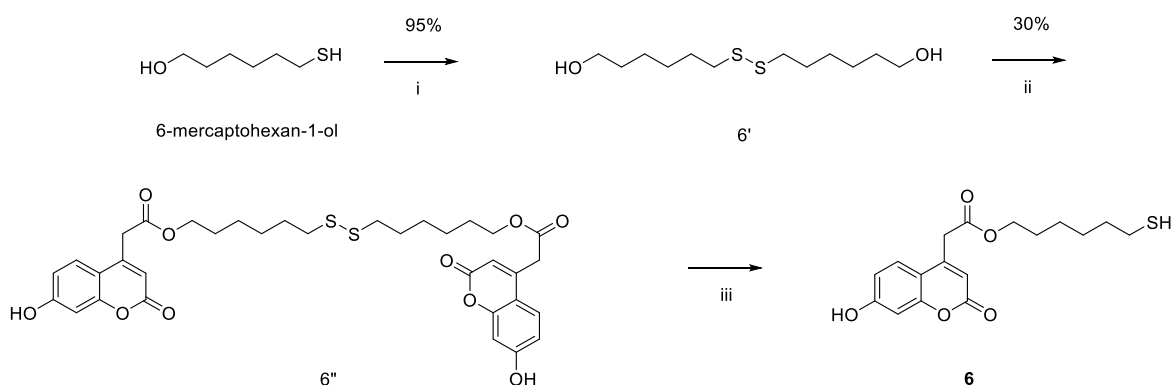
Scheme 5: a) i) I_2 in MeOH saturated sol., H_2O, 2h, RT ii) 4-AAU, EDC, DMF, under N_2, overnight, RT iii) DTT prior use.

In the case of compound **7** the synthesis differs from those mentioned above. The bromo derivate was synthesised *ex novo* via a Pechmann condensation by mixing resorcinol with ethyl 4-bromoacetoacetate in 70% aqueous sulfuric acid (*Scheme 6*).
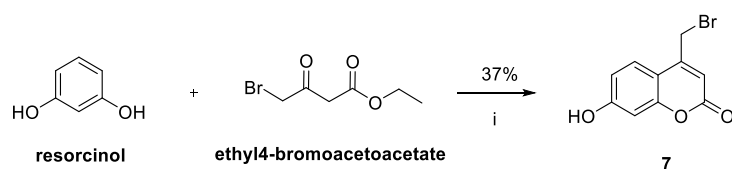
Scheme 6: a) i-H$_2$SO$_4$ 70%, RT, 24h.

The esterification protocols mentioned here have been selected after several trials, in which other coupling reactions were unsuccessful. Although most coupling reactions require the activation of the carboxyl group followed by the subsequent addition of the compound with the phenol group, it was found that in order to avoid intra- or intermolecular reaction of the starting material, with formation of secondary by-products, all reagents and the coupling agents had to be mixed together simultaneously and under anhydrous conditions.

The solubility and fluorescence properties for all compounds described above were evaluated and compared with 4-MU. The solubility of the compounds has been tested in water (pH 6.5) and the values are reported in *Table 5.* As expected, compounds **2**, **3, 5** and **7** were poorly soluble in water, with compound **6** requiring the addition of DMSO. The solubility was enhanced for compound **4** due to the presence of amino groups and even the solubility of compound **1** was reasonably good.

Table 5: Solubility of all compounds valuated as mg/mL in water. DI water pH 6.5 was added under constant stirring until the compound was completely solubilised.

	4-AAU	4-MU	1	2	3	4	5	6	7
Solubility mg/mL in water (pH 6.5)	0.66	0.16	0.73	0.28	0.24	0.81	0.32	Insoluble (DMSO required)	0.33

In order to determine the optical properties of compounds synthesised, excitation/emission spectra were recorded for all compounds in water at a concentration of 100 μM, with the results shown in *Figure 24*. The absorbance peaks were broad and showed a slight red shift compared to 4-MU (from 322 to 332 nm of absorbance of 4-MU and compound **7** respectively). Considering the proximity of the excitation wavelengths for the compounds analysed, in the further experiments λ$_{ex}$ =

327 nm and λ_{em} = 460 nm has been used for all compounds and the Stokes shift (the difference between the λ_{ex} and λ_{em}) can be thus be considered equal for all compounds (133 nm).
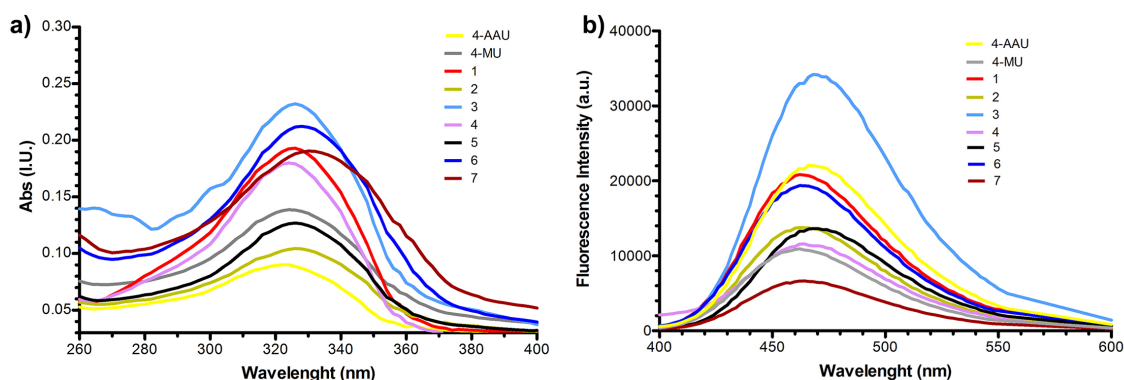
Figure 24: a) excitation b) emission spectrums of all compounds at concentration 100 μM in water (pH 6.5). The fluorescent spectrums were obtained using as excitation wavelength the one corresponding to the maximum peak for each compound. In particularly: 322 nm for compound 1 and 4; 326 nm for compound 3, 5 and for 4-AAU; 328 nm for compound 2, 6 and 4-MU and finally 332 nm for compound 7. The maximum fluorescent peak was the same for each compound and it is measured at 460 nm.

One limitation of 4-MU is the low pK$_a$, meaning that its fluorescence is reasonably good only above pH 7. Therefore, the fluorescence properties of the synthesised compounds have been evaluated in the pH range 4 to 8. From *Figure 25*, it is noticeable that, for all compounds, the fluorescence signal increases with increasing pH. For all synthesised compounds the fluorescent signal start increasing at pH 6.5 ad exception for compound **7** for which the signal raised at pH 7.5 as for **4-MU.** All synthesised compounds appeared to have a better fluorescence profile than **4-MU** with the exception of compound **7** whose fluorescence increases only at pH 7.5-8. The fluorescence signal of all synthesised substrates is almost constant below pH 6 but it starts to increase between pH 6-6.5 rather than at pH 7-7.5 as it is in the case of **4-MU** (grey line). This means that the fluorescence signal would be measured during biologically relevant conditions (i.e. usually at pH 6-6.5) without the need for later basification, as is required for **4-MU**. In particular, while for 4-MU no increase in fluorescence was observed between pH 6.5-7, the signal for compound **1** raised from intensity 8000 to 14000.
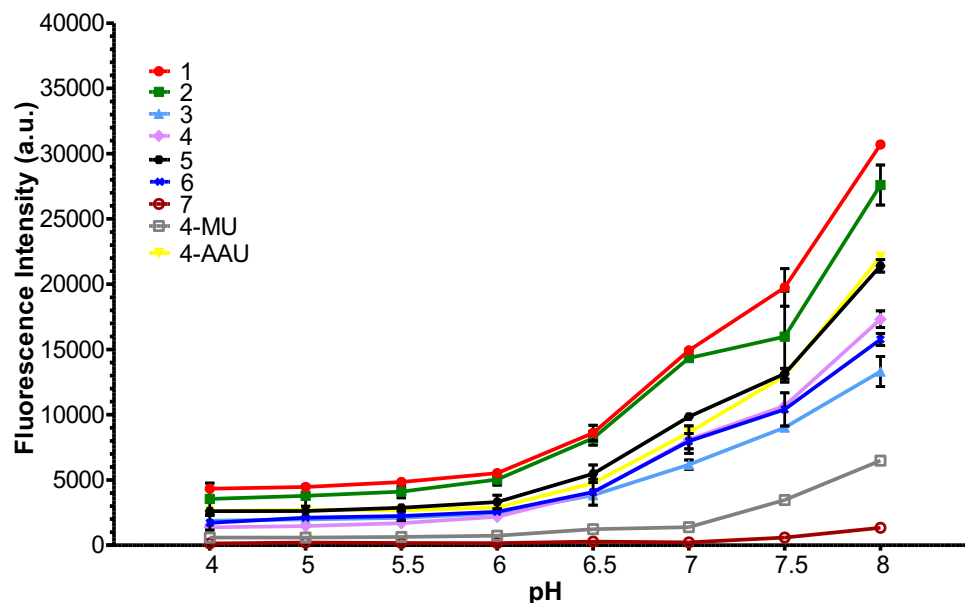
Figure 25: Fluorescence measured for each compound (0.1 mM) at pH 4, 5, 5.5, 6, 6.5, 7, 7.5 and 8. The values have been compared with the starting material 4-AAU and especially with 4-MU. compounds showed a better fluorescent profile than 4-MU since signal increases around pH 6-6.5 rather then 7-7.5.

In addition, the possible inhibitory effect on bacterial cell grow was evaluated for each of the umbelliferone derivatives in order to determine if the fluorophores itself induce bactericidal or bacteriostatic effect. *E. coli* was treated with three different concentrations of each derivative and their effect was evaluated by determining the growth curves of the bacteria. In particular, 0.1 CFU of *E.coli* was treated with 500, 50 and 5 µM of each substrate, incubated while shaking at 37°C and the absorbance was recorded every 20 minutes at 690 nm. An increase of signal indicates an increase of turbidity, which indicates that the bacteria are growing over time. As shown in *Figure 26,* only compound **7** relatively inhibits the bacterial growth, as is evident at a concentration of 500 µM (burgundy line). Compound **7** might have some activity as a bacteriostatic compound. The remaining compounds only limited the maximum amount of bacterial growth, since the plateau of the growth curve is achieved at lower concentrations of bacteria compared with the reference (red line).
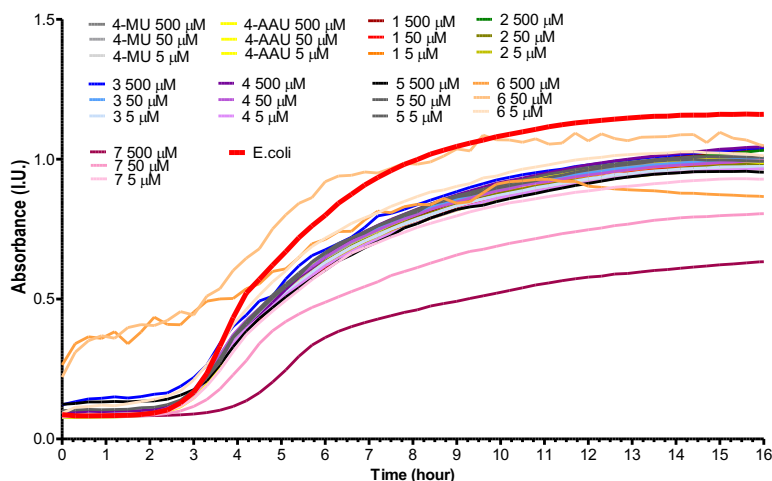
Figure 26: 0.1 CFU of *E.coli* were plated in a 96-well plate and incubated at 37°C under constant shaking and treated with 500, 50 and 5μM of each substrates. The bacterial cell growth was evaluated measuring the increase in absorbance read at 690 nm. An increase of absorbance, therefore an increase of opacity of the sample, indicates an increase of cell number in the sample.

2.3.2 Synthesis of the substrate for bacterial detection

In *Scheme 7*, the theoretical pathway chosen for the synthesis of the substrate is presented. The glycosydic bond between compound **1** and the protected α-glucose bromide was introduced by a Williamson reaction, in which the hydroxyl group is first activated to its anion form by NaOH. Once activated, it reacts with the bromo-derivate leading to the formation of the glycosydic bond (compound **1'**). After deacetylation of the hydroxyl groups of the sugar using sodium methoxide, compound **8** is obtained. The ultimate goal of the project was to develop a nanoprobe for bacterial detection; therefore, the carboxyl group in position 4 of the umbelliferone derivate is needed for the particle surface functionalisation. Following protocols found in literature, the hydrolysis should occur under basic conditions, after which the free acid is obtained (compound **c**). Although different procedures were attempted, the reaction was unsuccessful and, instead, the 4-methyl derivate was found (compound **9**) as highlighted by the ^{1}H-NMR spectrum (*Figure 27*).
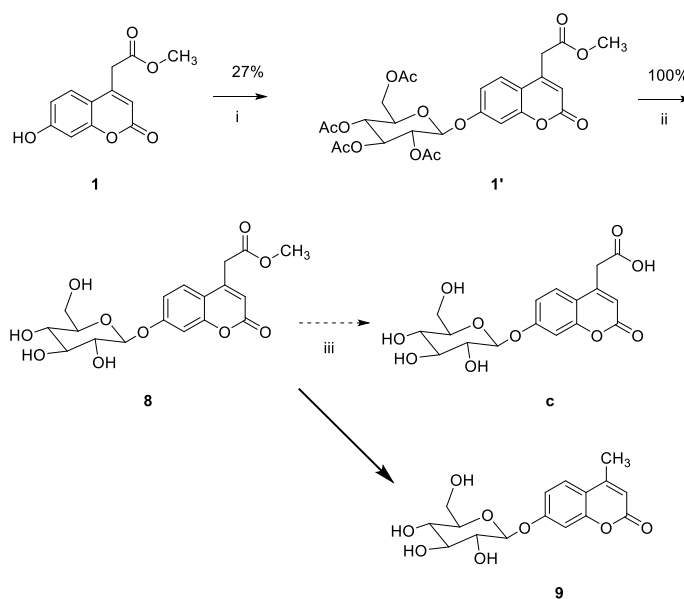
Scheme 7: Pathway planned for the synthesis of the glucose-umbelliferone derivate with the free carboxylic acid that can be used for the functionalisation of the particle surface. i) NaOH 1M, 2,3,4,6-Tetra-O-acetyl-α-D-glucopyranosyl bromide, N₂, RT, 24h ii) NaOMe in anhydrous MeOH, RT, 4h iii) NaOH 1 M, water, RT, 2h.
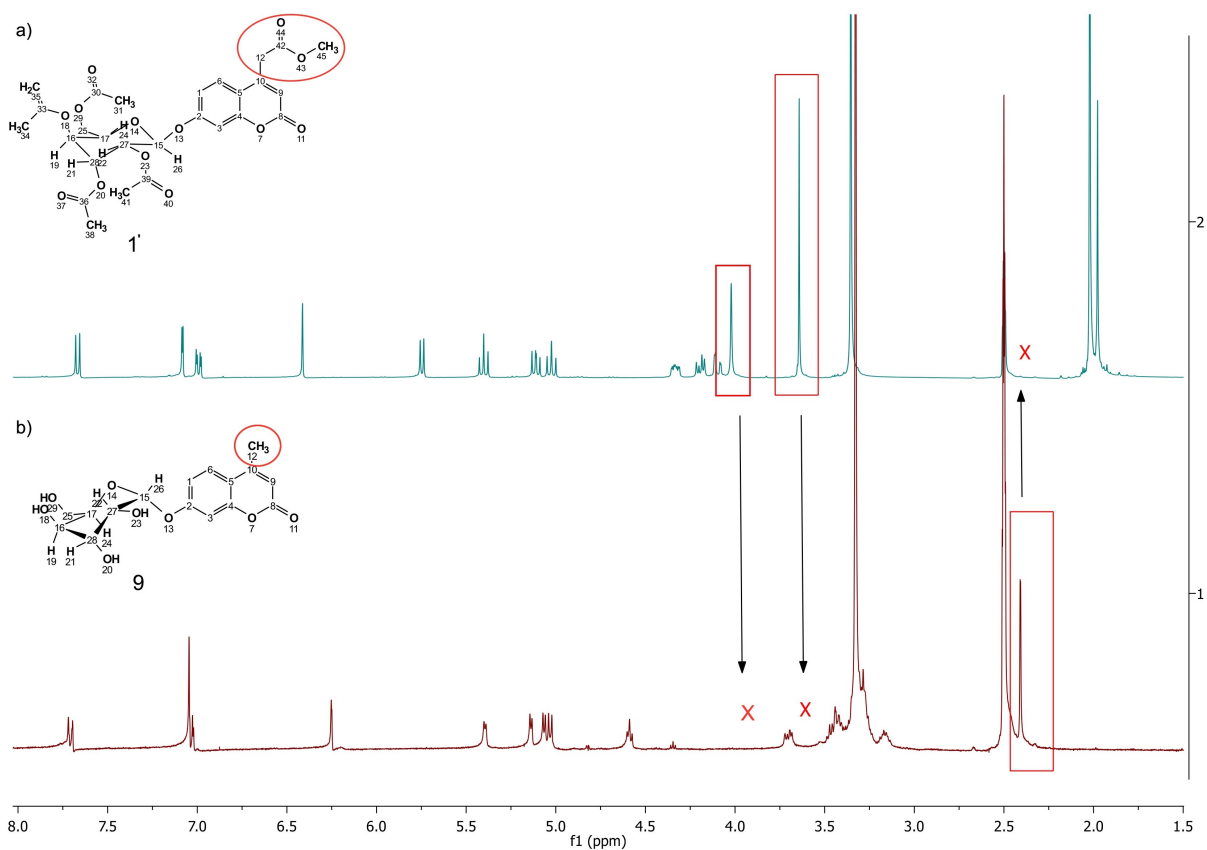
Figure 27: Comparison between ¹H-NMR spectrum of compound before and after demethylation/deacetylation. Red rectangles indicate in a) the -CH₂- and the -CH₃ of the methylated acetic group, signals that are not present instead in b) in which the signal of the –CH₃ in position 4 of the umbelliferone appears in the spectrum.

A possible explanation of this side reaction is presented in *Scheme 8,* where presumably a decarboxylation reaction could have occurred with the release of methanol and CO_2.
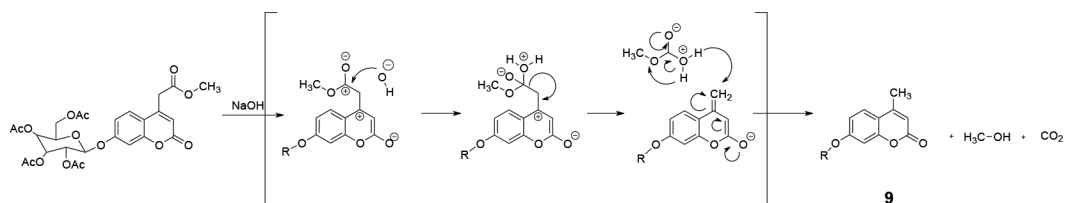
Scheme 8: Decarboxylation mechanism proposed which could occurs during the demethylation reaction.

Compounds **2** was synthesised in order to address the issue related to the difficulties in the demethylation step. 2-isopropanol was used to protect the acidic hydroxyl group in position 4 of the umbelliferone since it is a better leaving group compared with the methyl group. Unfortunately, the hydrolysis occurred during the glycosylation reaction leading to the formation of a mixture of unidentified by-products. Using NaOMe for deacetylation of the sugar, likely due to its basic property, compound **9** was often identified in certain amounts. Ammonolysis was therefore chosen as alternative deacetylation protocol, which allowed isolation of compound **8** in high yield and purity. The final reaction pathway followed for the synthesis of compound **8** is shown in *Scheme 9*.
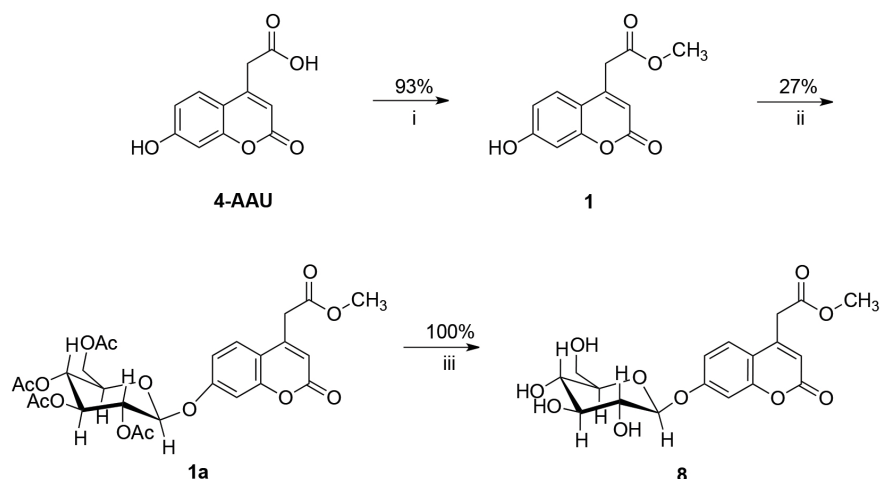
Scheme 9: i) SOCl₂, MeOH, overnight, RT ii) NaOH 1M, a-acetoglucopyarnosylbromide, RT, 24h iii) NH₃/MeOH, RT, 4.5 h.

In the synthesis shown above, α-glucose was used as starting material. However, to our surprise, no recognition event was observed when using the α-glucosidase enzyme. It was subsequently discovered that compound **8** was instead recognised by β-

glucosidase, indicating that the α-glucose had changed configuration during the synthesis, effectively becoming β-glucose. It was hypothesised that anomerisation occurred under the basic conditions of the Williamson and/or the deacetylation reaction, which lead to the ring-opening of the carbohydrate allowing rotation of the asymmetric centre (the carbon in position 1) (*Figure 28*). Polarimetry measurements have been performed in order to confirm the anomerisation. The values achieved for the synthesised compounds are showed in *Table 6* and they are in agreement with the above hypothesis. For the α-anomer, the specific optical rotation ([α]) values were expected to be highly positive, while for the β-anomer they were expected close to 0°. The measured values for synthesised compounds **8** and **9** [α] were -1.258° and -2.958° respectively. This corresponds to the value expected for the β anomer. On the other hand, the starting material acetobromo-α-D-glucose and compound α-4-MUD (purchased and introduced later in the chapter) gave values of 174° and 148°, respectively, when measured under the same conditions, in accordance with values found in literature and provided by the manufacturers.

Table 6: Optical rotation values measured for each compound.

	Compound **8**	Compound **9**	Acetobromo-α-D-glucose	4-MUD
$[\alpha]_D^{20}$ (c [w/v]= 0.8, pyridine)	-1.258°	-2.958°	147°	148°
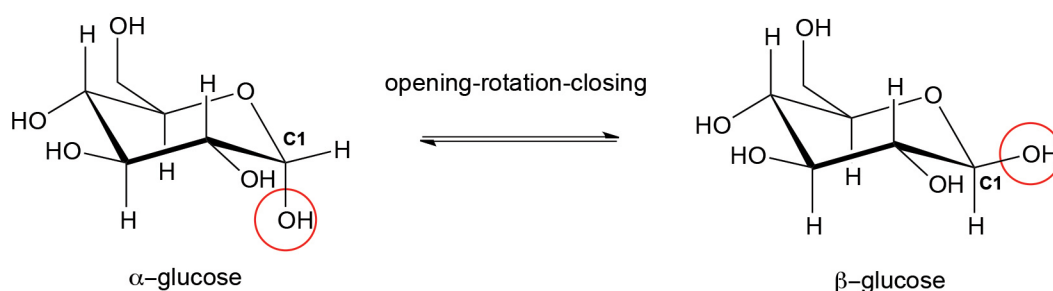
Figure 28: In the case of aldohexoses (6C and an aldehyde group in the open form) the rotation occurs in C1(asymmetric centre) of the open form of the glucose.

Although it is not often clearly stated, in other works found in literature α-glucose was used as starting material for the synthesis of the substrate, but was then also recognised by β-glucosidase[92, 93] supporting our results.

The conjugation between fluorophore and carbohydrate was attempted even for the remaining synthesised compounds but the reactions were problematic. Presumably, the alteration of the umbelliferone structure leads to a redistribution of electron on the ring making the hydroxyl group in position 7 less reactive. In order to overcome the limited reactivity of the hydroxyl group, the glycosylation was attempted using a stronger base such as sodium hydrate (NaH), catalysing the reaction using Cupper bromide (CuBr) or increasing the temperature. It was found that the harsh conditions tested tend to destabilise the carbohydrate, rather than increase the reactivity of the hydroxyl group as desired. Indeed, one of the common side products was the compound **d** shown in *Figure 29,* for which formation E2 (elimination with one step reaction) has been proposed (see *Appendix A2.1* for details).
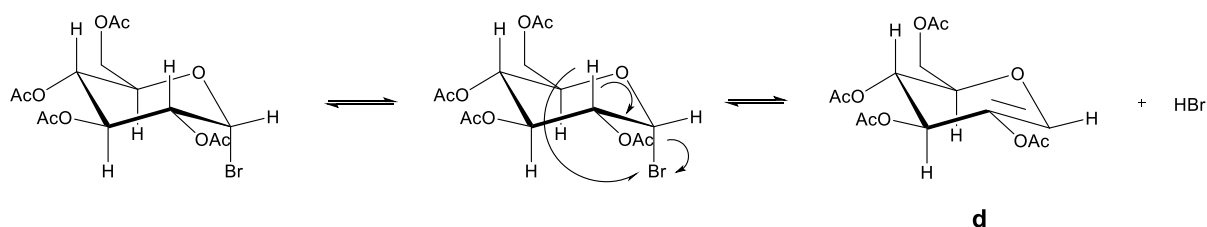
Figure 29: Mechanism proposed to explain the formation of side product d which refers to the E2 reaction, in which the elimination mechanism occurs in only one step and it is favoured by strong bases.

Unfortunately, none of the mentioned alternative reactions leaded to satisfying results therefore only compound **8** was further investigated regarding its activity in detecting the enzyme β-glucosidase.

2.3.3 Enzymatic assays

For greater clarity, in the next paragraphs compound **8** is referred as **β-4-AAUG** to highlight the differences during the enzymatic and bacterial assays. For the same reason, compound **9** is referred as **β-4-MUD.** Different assays have been tested to define whether **β-4-AAUG** represents a valid alternative to the commercially available compound in detecting the activity of β-glucosidase. **β-4-AAUG** has been compared with **α-4-MUD** (purchased) to define its selectivity for the enzyme β-glucosidase. Preliminary studies have been accomplished in order to compare the affinity of the enzyme for the synthesised substrate and **β-4-MUD** having glucose in the same

conformation. *Figure 30* shows the structure of the two compounds compared in the following sections.
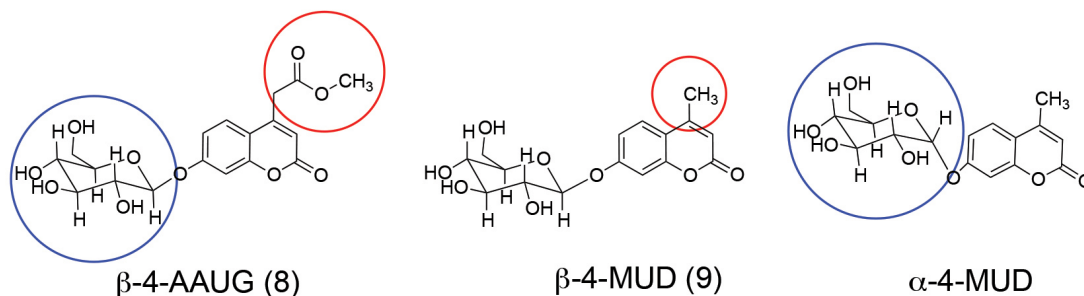
	Sobstituent in 4	Enzyme
β-4-AAUG (8)		β-glucosidase
β-4-MUD (9)	CH₃	β-glucosidase
α-4-MUD	CH₃	α-glucosidase

Figure 30: Structure of the three compounds tested in the enzymatic assays. All compounds were compared in order to define selectivity and sensitivity of β-4-AAUG for the enzyme β-glucosidase.

Selectivity

Enzymes are usually very specific for a particular substrate. Even a small conformational/configurational difference in the substrate's structure can change the enzyme's affinity for it. In this case, depending on the configuration of the sugar linked to the fluorophore, the final substrate will be recognised by a particular enzyme. In particular, substrates having α-glucose linked to the fluorophore will be recognised by the corresponding α-glucosidase (**α-4-MUD**), while compounds formed with β-glucose will be processed selectively by β-glucosidase (**β-4-AAUG**). The specific glucosidase, being a hydrolytic enzyme, cleaves the glycosydic bond between the corresponding carbohydrate and fluorophore, leading to an increase in the fluorescence signal.

In order to prove the specificity of the synthesised substrate, **β-4-AAUG** and **α-4-MUD** have been tested in presence of both α-glucosidase and β-glucosidase, varying either the concentration of the enzyme or the concentration of the substrate.

The enzymatic activity can vary with changes in environmental conditions. Hence, the affinity of the enzymes in detecting the substrates has also been evaluated in different

types of buffered media. Sodium acetate buffer 0.2 M at pH 6.5 was found to create the best conditions for the present work and it has been used for all enzymatic assays presented. *Figure 31* shows the fluorescence measurements of the synthesised **β-4-AAUG** when treated with 50 μg/mL of β-glucosidase, which was previously found to be the optimal concentration for this type of assay. It can be noticed that the amount of substrate used in the assay is important in order to have a detectable signal. The ideal range of substrate **β-4-AAUG** in enzymatic assays was found to be between 25 and 100 μM. An increase of fluorescence, which indicates the presence of the enzyme, was detected after only a few minutes even at low concentration of substrate, indicating good affinity.
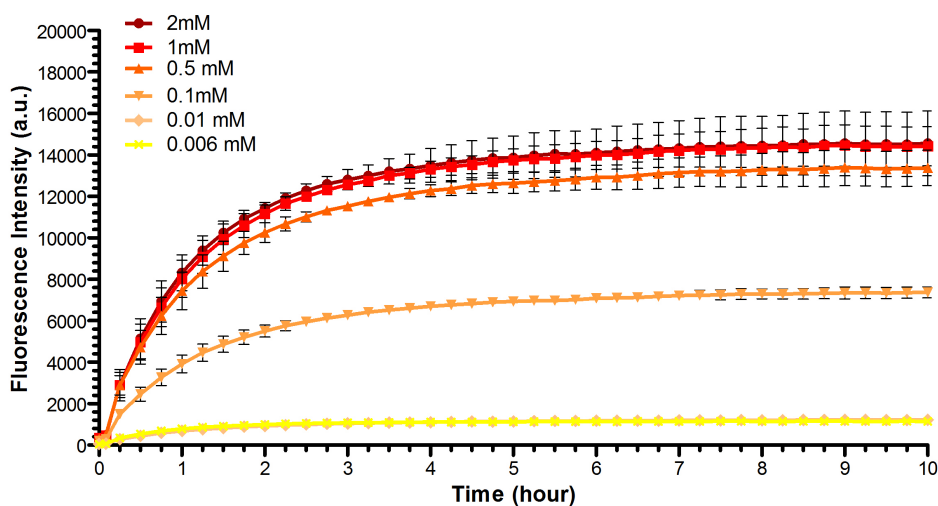
Figure 31: Different concentrations of substrate β-4-AAUG from 0.006 to 2 mM were tested in the presence of 50 μg/mL of β-glucosidase. Data are presented as average values ± SD (n=3).

In order to define the selectivity of the substrate for the specific enzyme, 0.1 mM of **β-4-AAUG** was also treated with different concentration of the other enzyme, α-glucosidase. *Figure 32* shows the result of this assay and it is evident that the substrate was not recognised by the enzyme. Only at very high concentrations 500 μg/mL (which is ten-fold higher than that used in the previous experiment) a small increase in signal was observed, which could be related to spontaneous hydrolysis of the glyosidic bond in the aqueous environment rather than to the enzymatic activity.
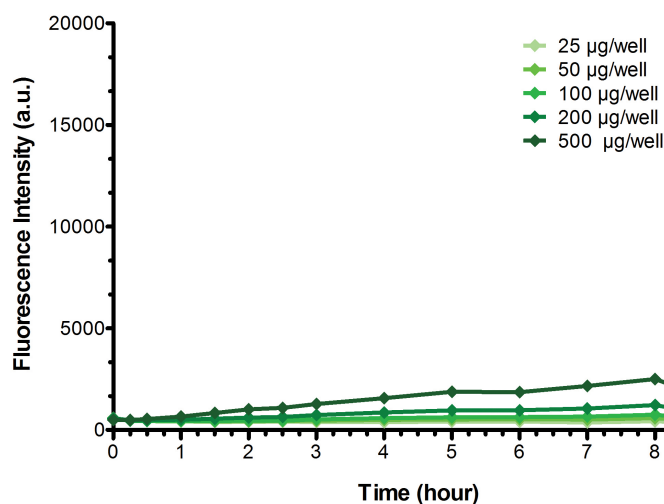
Figure 32: Different concentrations of enzyme α-glucosidase (25-500 μg/well) were treated with 0.1 mM of β-4-AAUG. Data are presented as average values ± SD (n=3).

As a proof of concept, the same assay was carried out treating the specific substrate for the enzyme **α-4-MUD** (0.1 mM) with 250 μg/mL of α-glucosidase (black line). As expected, the fluorescence signal increased quickly after addition of the enzyme. The obtained fluorescence data are shown in *Figure 33,* along with the one for the β-anomeric substrate **(β-4-AAUG)** treated under the same conditions (red line). The selectivity of the specificity of the recognition event is even more evident in this case, as only for **α-4-MUD**, the specific substrate for the enzyme tested, an increase of fluorescent signal measured.
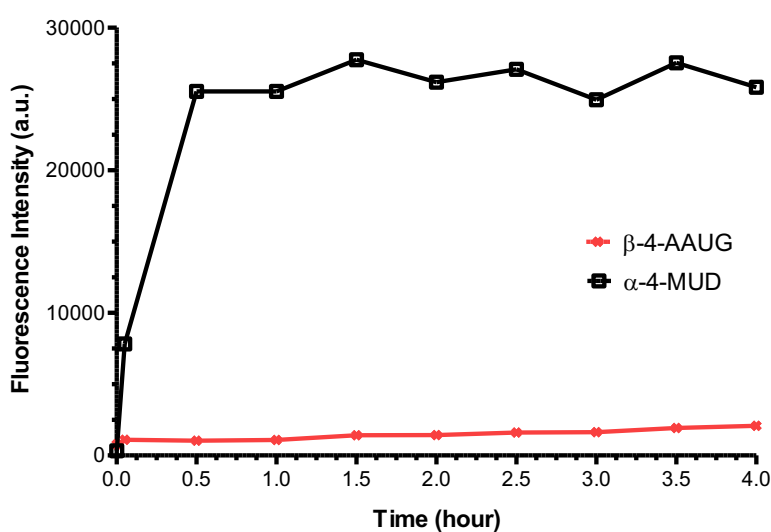
Figure 33: α-MUD and β-AAUG were tested at concentration 0.1 mM in presence of α-glucosidase (250 μg/mL).

The same experiment was carried on with a mixture of unknown enzymes commonly used for baking. The assays proved that the main component of the product was β-glucosidase, while the α-type was present in a lower amount (*Figure 34*). The result achieved with this assay proved that the high selectivity of the substrates for the respective enzyme allows to distinguish between the two hydrolytic enzymes α- and β-glucosidase. This selectivity could be eventually exploited for the quantification of the β-glucosidase in a sample.
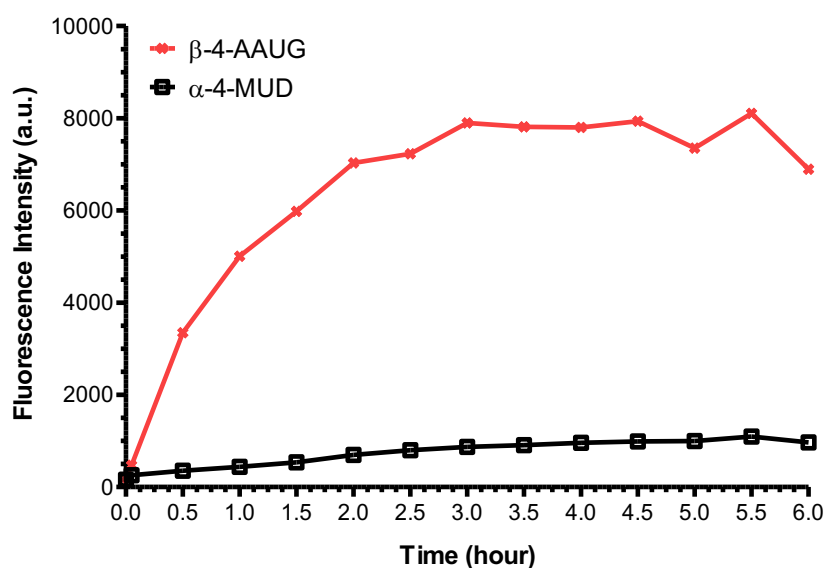
Figure 34: Evaluation of the composition of mixture of unknown enzymes by treating it with substrates α-4-MUD and β-4-AAUG which are specific for respectively α and β glucosidase. 2.5 mg of the mixture were treated with 0.1 mM of each substrate.

Sensitivity

Preliminary experiments have been accomplished in order to determine whether there is or not a difference between the substrates **β-4-AAUG** and **β-4-MUD** in detecting the activity of the specific enzyme β-glucosidase. Some parameters are used to accurately define the affinity of the recognition between enzyme and substrate. All parameters derive from the Michaelis-Menten equation, by which the kinetic rate of an enzymatically catalysed reaction is related to the concentration of the substrate used, as shown in the equation below:

$$v = \frac{V_{max}[S]}{K_m + [S]}$$

Where V_{max} indicates the maximum rate achievable by the system (and therefore the point of enzyme saturation) and K_m (Michaelis constant) defines the substrate concentration [S] that gives the half-maximum velocity of the reaction. The lower is K_m, the lower is the amount of substrate required to reach the saturation of the enzyme, hence K_m is one of the parameters used to indicate the affinity of the enzyme for the substrate; in particular, the higher is K_m, the lower is the affinity protein-substrate. Evaluating the V_{max} and K_m values calculated using GraphPad software, it was notice that the affinity of the enzyme for **β-4-AAUG** is greater than that for **β-4-MUD** at the concentration tested (from 15 μM to 2 mM), since the K_m is lower (804 and 4032 μM, respectively) as shown in *Figure 35.* Other parameters can be obtained from the Michaelis-Menten equation. One of them is the catalytic efficiency parameter (k_{cat}/K_m), which is a measure of how efficiently the enzyme converts a substrate into the product. While K_m is calculated from the Michaelis-Menten equation, k_{cat} can be calculated as follows:

$$k_{cat} = \frac{V_{max}}{E_0}$$

Where E_0 is the concentration of enzyme used, in this case 50 μg/mL. The calculated values are presented in *Figure 35* and they confirm that the considered enzyme has higher affinity to **β-4-AAUG** since K_m is lower and this substrate is more efficiently converted into the product.

	V_{max}	K_m	k_{cat}	k_{cat}/K_m
β-4-AAUG	0.022	804	$4.5 \; 10^{-4}$	$5.6 \; 10^{-7}$
β-4-MUD	0.027	4032	$5.4 \; 10^{-4}$	$1.3 \; 10^{-7}$
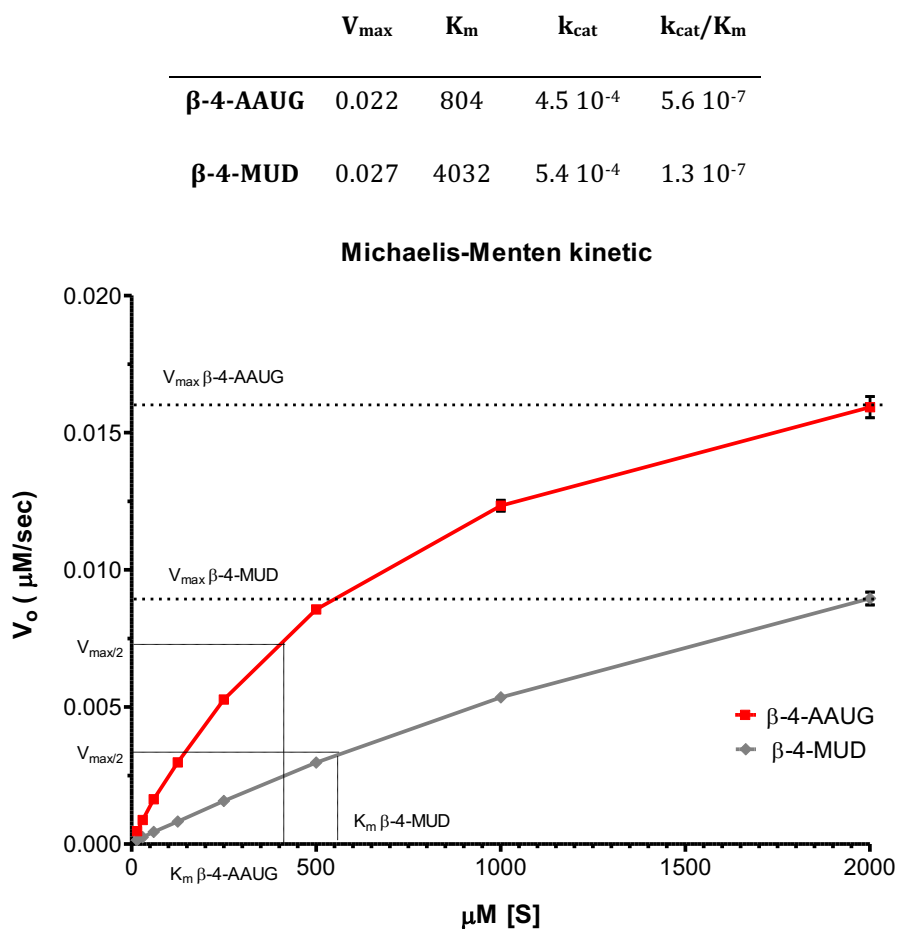
Figure 35: Michaelis-Menten kinetic allows to determine values which indicate the affinity of the substrate for β-glucosidase. Values are reported as average values ± SD (n=3).

2.3.4 Bacterial detection

The main goal of the project was to synthesise a substrate capable of bacterial detection. This could then have been used to functionalise nanoparticle surfaces, thus enhancing its sensitivity. Bacteria show preferences in terms of the carbohydrates used as a source of energy. For instance, some preferentially use galactose and others glucose; therefore, the former mainly produces galactosidase while in the latter glucosidase is produced in order to break the polysaccharide into absorbable monosaccharaides. By changing the carbohydrate used for the substrate design, selective detection of the two different bacteria can be therefore achieved. Unfortunately, this selectivity is only partial, since glucosidases are usually inducible enzymes, which means that even if they are not usually produced, their synthesis can

be induced in the presence of the specific substrate, especially in case of deprivation of nutrients in the environment.

Herein, the activity of the substrate has been tested in the presence of different types of bacteria: *Escherichia coli (E. coli), Enterococcus, Klebsiella pneumonia, Pseudomonas aeruginosa and Staphylococcus aureus.*

E.coli is a coliform bacterium belonging to the genus that is mostly found in the intestine of warm-blooded organisms. It is a Gram-negative bacterium, facultative anaerobic bacteria and it has rod-shaped cell. Most *E.coli* strains are harmless and are components of the normal flora of the gut; however there are other pathogenic strains of *E.coli* which represent the main cause of food poisoning. Some virulent strains of *E.coli* can cause not only problems in the gut (abdominal cramps, diarrhea, vomiting, etc.) but they can also spread to the near urinary tract, causing infections (uropathogenic *E.coli* – UPEC). Approximately 1-100 CFU is the estimated dose of *E.coli* needed to induce infection, although this is an approximation, since different strains possess different virulence and, therefore, the infectious dose can vary widely from one strain to another[94,95]

The members of the genus *Enterococcus* are Gram-positive cocci, which appear in pairs or short chains. *Enterococcus* are particularly resistant to a broad range of temperature, pH and disinfectants. These bacteria are commensal organisms in the human intestine and they can cause opportunistic infections, e.g. when the host's resistance is lowered or when it colonised other organisms. They are indeed responsible for about 16% of the nosocomial urinary tract infections (infections which occur in hospitals). The infectious dose is unknown and it can vary from one strain to another[96,97,98].

Klebsiella pneumonia (K. pneumonia) belongs to the Enterobacteriaceae family, which are Gram-negative bacteria, and are encapsulated, rod-shaped and non-motile. *K. pneumonia* is the medically most important species, representing one of the most common causes of bacterial pneumonia and, due to the antibiotic resistance developed and its opportunistic behaviour, it is responsible for numerous nosocomial bacterial infections of urinary and respiratory tracts. The infectious dose is unknown for *K. pneumonia*, although apparently 100 CFU/g of bacteria are required to produce damage[99,100].

Pseudomonas aeruginosa (P. aeruginosa) belongs to the Pseudomonadaceae family, genus Pseudomonas. This family are Gram-negative bacteria, facultative anaerobe, having polar flagella. The possibility of move is fundamental for the pathogenicity of this type of bacteria while the virulence is related to the releases of toxins and other substances. *P.aeruginosa*, being an opportunistic pathogen, often causes infections in immuno-compromised hosts (HIV/AIDS, cystic fibrosis, chronic pulmonary diseases, etc.) and it mainly colonises the respiratory tract. The infectious dose is unknown, but some worms-tests showed that the concentration of bacteria cell to induce infection is reasonably high[101]. *P. aeruginosa* can adapt very well to different environmental conditions, which has helped them to resist antibiotics, such that nowadays multi-drug resistant strains are emerging[102,103] .

Staphylococcus aureus (S. aureus) is a Gram-positive, round-shaped bacterium, a facultative anaerobe, which belongs to the Firmicutes family. *S. aureus* are opportunistic bacteria and a common cause of skin and respiratory tract infections. In humans, at least 100,000 organisms (1CFU) are required for the infection to occur. *S. aureus* can survive after exposure to different conditions and it can easily develop antibiotic resistance[104,105].

All bacteria used in this work were isolated and identified from human samples from patients hospitalised for urinary infections. They have some common characteristics which make them interesting for our purpose: they are opportunistic pathogens and, therefore, cause infection only when colonising specific organs or when the host's defence is lower. They are therefore common nanosomic infections and they have developed resistance against those antibiotics routinely used. In the present work, these bacteria have been used to test the activity of the substrate synthesised and the designed nanoprobe.

Evaluation in selectivity between different bacteria

Detecting bacteria by enzyme recognition could lead to a better LOD since a single bacterium can produce more enzymes. On the other hand, since different type of bacteria can produce the same enzymes this approach leads to a lower selectivity in the detected bacteria. However, exploiting the metabolic preference of bacteria for a specific carbohydrate, a reasonable grade of selectivity can still be achieved. Substrates

α-4-MUD, **β-4-MUD** and **β-4-AAUG** were compared in order to evaluate the eventual selectivity for specific bacteria, with regard to the recognition element (α or β-glucose) and/or the type of fluorophore used.

The efficacy in detecting bacteria (e.g. *E.coli, Enterococcus, K.pneumoniae, P.aeruginosa and S.aureu*s) at different concentrations was evaluated using the substrates at a concentration of 50 μM. All bacteria were cultured on LB solid broth and harvested in liquid LB prior to the assay. The desired concentration was determined by McFarlan turbidity standards, measuring the opacity of the sample, and by plate counting backwards. From the stock sample, each of the bacterial solutions was diluted with LB broth and analysed at concentrations of 75, 20 and 1 CFU/well, respectively when incubated with of 50 μM substrate solution. All experiments were carried in sterile 96-well plates, measuring the increase of fluorescence after incubation at 37°C under shaking over time. Preliminary experiments were accomplished to evaluate the stability of the substrates in sodium acetate buffer and in broth (see *Appendix A2.2* for details). Since the substrates appeared to be less stable in broth, all data in the following experiments are normalised for the auto-hydrolysis of the corresponding substrate in broth during each experiment.

As seen in *Figure 36*, 50 μM of **β-4-AAUG** can be useful for the detection of *E. coli, Enterococcus and K. Pneumoniae*. Using this substrate, detection of these three bacteria at a concentration of 75 CFU/well was achieved in 1 hour, while 2 hours were required for the detection of 1 CFU/well (corresponding to 10^6 cells/well) (*Figure 36-i, ii and iii*). **β-4-AAUG** appeared to be less sensitive to the presence of *P. aeruginosa*, given that 3 hours were required for its detection at 75 CFU/well, while 3.5 and 5 hours were required for the detection at the bacteria at 20 and 1 CFU/well respectively (*Figure 36-iv*). In the case of *S. aureus,* little difference was found between the detection of the bacteria at the different concentrations used, but the overall signal was relatively low. (*Figure 36-v*). The low signal limits the possibility of using this substrate for the detection of *S.aureus.*
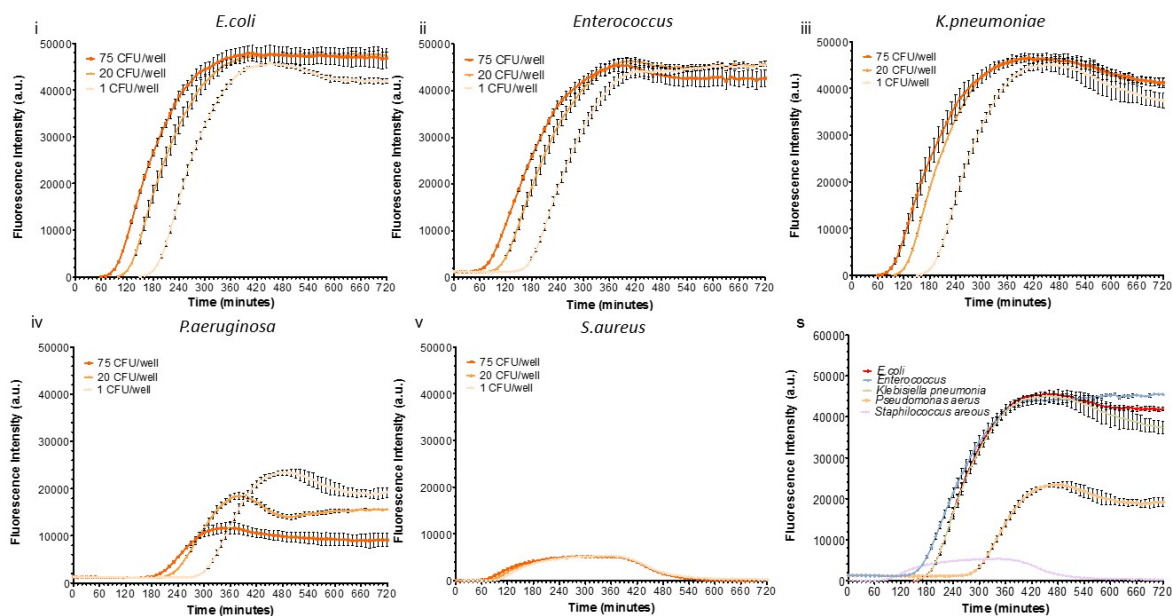
Figure 36: 50 µM of β-AAUG were treated with 75, 20 and 1 CFU/mL of each type of bacteria (i-v). In graph-s are compered the curves obtained for the detection of 1 CFU/mL of each type of bacteria (scale fixed at 60000 A.U.). Data are presented as average values ± SD (n=3).

Figure 37 presents the data obtained for the detection of the same concentrations of the five different bacteria using 50 µM of **β-4-MUD**. The curves describing the increase of fluorescence are comparable with those for **β-4-AAUG**. Indeed, in about 1 hour, the substrate indicated the presence of *E. coli, Enterococcus and K. Pneumoniae* at 75 CFU, while 3 hours were required for the identification of *P. aeruginosa (Figure 37-i, ii, iii, iv).* This confirms that the recognition of the substrates occurs through the activity of the enzyme β-glucosidase, which processes the β-glucose present in both substrates. However, it is fundamental to highlight that the scale used to show the fluorescence signal for the two substrates is different. They have been changed to better evaluate the time at which the detection occurs but the intensities of the signals are remarkably different: the maximum signal obtained using the substrate **β-4-AAUG** is almost 5-fold higher than that reached with **β-4-MUD**. This can be noticed more readily by observing the summary graph reporting the data recorded for substrate incubated with 1 CFU of different bacteria (*Figure 36-s* and *Figure 37-s*). For these graphs the scale bar was fixed at 60000 A.U. It is clear that fluorescent profile of **4-MUD**, which requires elevation of the pH in order to reach a better signal, is less favourable. Interestingly, **β-4-MUD** appeared to be better at detecting *S. aureus* than was **β-4-AAUG,** which confirms that the fluorophore partially determines the enzyme-substrate affinity (*Figure 37-v).*
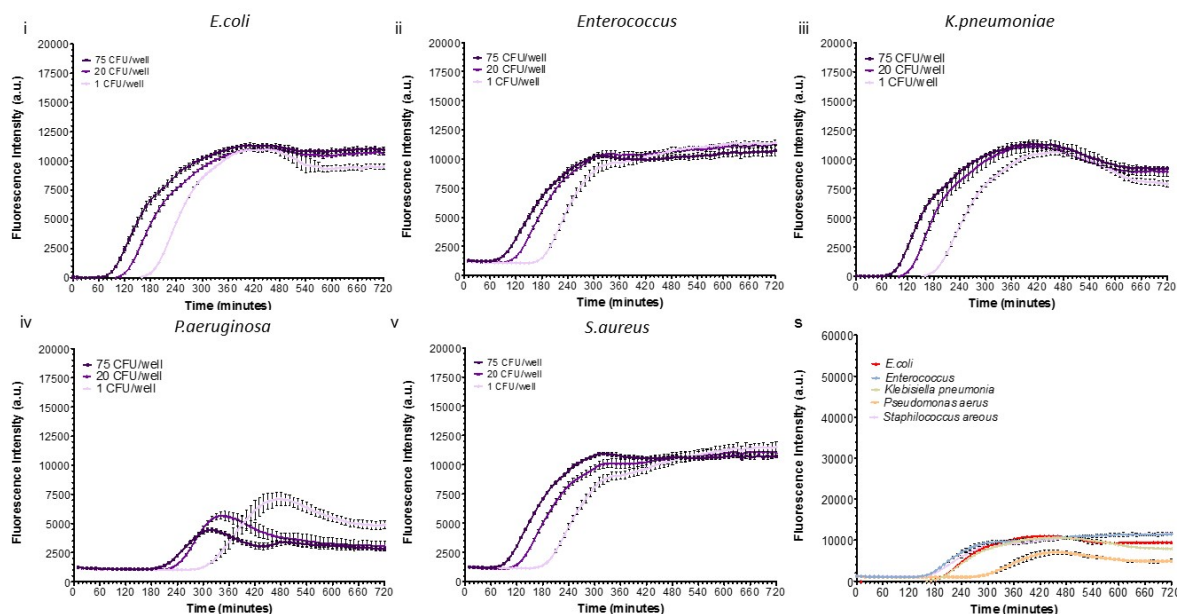
Figure 37: 50 μM of β-MUD were treated with 75, 20 and 1 CFU/mL of each type of bacteria (i-v). In graph-s are compered the curves obtained for the detection of 1 CFU/mL of each type of bacteria (scale fixed at 60000 A.U.). Data are presented as average values ± SD (n=3).

In *Figure 38,* the results of treating a 50 μM solution of **α-4-MUD** with 75, 20 and 1 CFU/mL of bacteria are shown and the increase of fluorescence was again observed over time as indication of bacterial detection. Again, noteworthy that the scale used in the graphs has been adjusted to better evaluate the signal increase. *Figure 38-s* allows comparison of the different signal intensities measured for each substrate, again confirming the unfavourable fluorescent features of 4-MU. After 2 hours, an increase in fluorescence was noticeable in the presence of *E. coli, K. Pneumoniae* and *S. aureus (Figure 38- i, iii, v),* while after 3 hours the signal increased in presence of *Enterococcus (Figure 38-ii).* Even using the substrate selective for α-glucosidase, the detection of *P. aeruginosa* failed (*Figure 38-iv)* indicating that presumably these particular bacteria do not process glucose in any of its conformations.
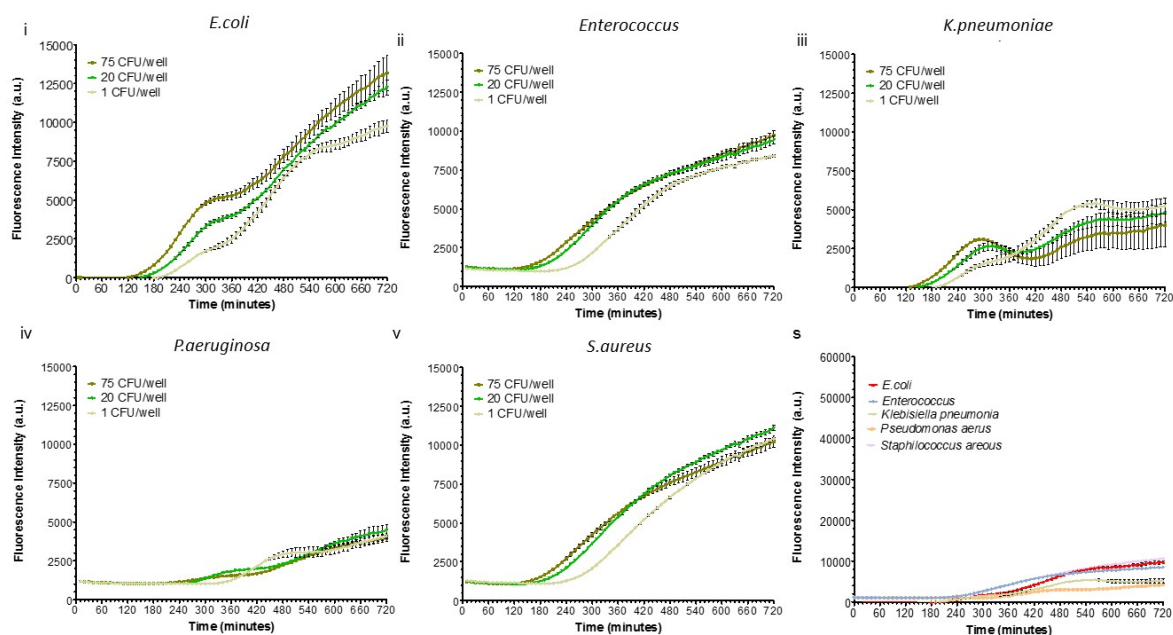
68

Figure 38: 50 μM of α-MUD were treated with 75, 20 and 1 CFU/mL of each type of bacteria (i-v). In graph-s are compered the curves obtained for the detection of 1 CFU/mL of each type of bacteria (scale fixed at 60000 A.U.). Data are presented as average values ± SD (n=3).

Analysing the data obtained in treating the bacterial samples at concentration of 2.5 CFU/mL (*Table 7-white section)* and 150 CFU/mL (*Table 5-yellow section*) with 250 μM of each substrate two considerations can be made. **β-4-MUD** and **β-4-AAUG** detect the bacterial with similar efficacy although as mentioned before **β-4-AAUG** has an advantageous fluorescence profile.

Table 7: Approximated time at which 250 μM of each substrate detected the presence of bacterial when present at concentration of 2.5 CFU/mL (white section) or 150 CFU/mL (yellow section).

2.5 CFU/mL	E. coli	Enterococcus	K. pneumonia	P. aeruginosa	S. aureus
β-4-AAUG	2.5 h	2.5 h	2.5 h	\	\
β-4-MUD	2 h	2 h	2 h	\	6 h
α-4-MUD	3 h	\	\	\	3 h
150 CFU/mL					
β-4-AAUG	1 h	1 h	1 h	\	\
β-4-MUD	1.5 h	1 h	1 h	\	1.5 h
α-4-MUD	2 h	\	\	\	2 h

By comparing the detection activity of the different substrates, it was noticeable that exploiting the selectivity for β-glucosidase *E.coli, K.pneumonia and Enterococcus* were successfully detected at low concentration (2.5 CFU/mL) by **β-4-AAUG** and **β-4-MUD**.

E.coli use carbon as main source of energy and in particular it firstly consumes glucose and only when this carbohydrate is completely consumed the bacteria start to use alternative source of carbon[106,107]. Due to the strong 'greed' by which it consumes glucose, *E.coli* didn't show relevant specificity for the two anomers α and β.

Enterococcus use glucose as fist source of energy as well. However, this type of bacteria are characterized by a high level of adaptability, therefore they can adjust their metabolism depending on the conditions available[108].

K.pneumonia have two different metabolisms depending on the external conditions: they fix nitrogen if in anaerobic condition, while in presence of oxygen the main source of energy is carbon and in particular glucose. Since the experiments here presented were done in aerobic conditions the bacteria were[109] easily detected by using the substrates having glucose has recognition element. In particular, it appeared that *K.pneumonia* preferentially produce β-glucosidase since **α-4-MUD** failed in detecting this bacteria.

Data indicated that *P.aeruginosa* can not be detected with any of the substrates tested as expected considering that this type of bacteria preferentially use amino acids or organic acid as source of energy[110] and not carbon as *E.coli* or *Enterococcus.* However, even *P.aeruginosa*, if no amino acid are available can use glucose, which is metabolised by anaerobic fermentation. Following this metabolic pathway glucose is transformed

in pyruvate, which is then converted in a mixture of acid. Obviously the higher is the concentration of the acid in the sample, the lower is the environmental pH. The fluorophores released after cleavage of the glycosidic bond are sensitive to pH, therefore a decrease of the environmental pH leads to a decrease in the fluorescent signal, which would in this case explain why the substrates tested failed in the detection of *P.aerouginosa*[111] .

This hypothesis is supported by the results achieved for *S.aureus* but it is in contrast with the behavior of *Enterococcus*. *S.aureus* use glucose as main source of energy as well but the fermentation of sugar leads to accumulation of lactate which can causes a decrease in the pH[112]. This could explain the reason why all fluorescent substrates failed in detecting these bacteria. On the other hand, *Enterococcus* is lactic acid bacteria (LAB) therefore the main product accumulate after glucose-metabolism is lactic acid, howbeit it was quickly and easily detected by the substrates. Observing the data achieved for *S.aureus* seams to preferentially produce α-glucosidase considering that the bacteria were successfully detected by using **α-4-MUD** while **β-4-AAUG** instead failed completely. The structure of the fluorophore seams to interfere partially with the recognition as well since **β-4-MUD** detected, although with low efficiency, *S.aureus*.

Further comments can be made comparing the detection curves obtained by enzymatic assay or in the bacteria study. It can be noticed indeed that the fluorescence increases following either a hyperbolic function or a sigmoidal function, depending on the assay. *Figure 39* compares these two functions. While in the enzymatic assays the kinetic of detection is described by a hyperbole, the recognition event in the bacterial experiment can be related to a sigmoidal curve[113].
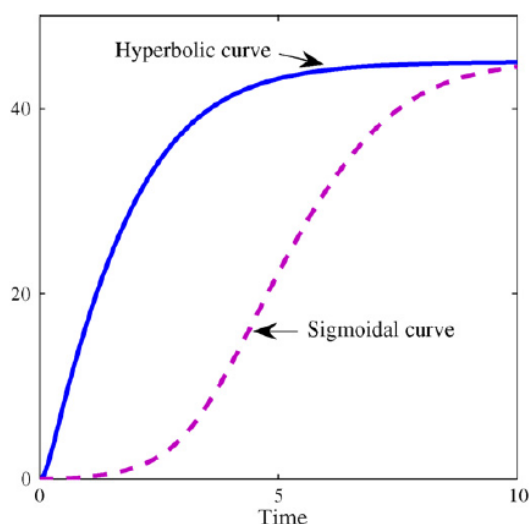
Figure 39: Differences between a hyperbolic and sigmoidal function. Adapted from reference[113].

The two curves describe the difference between a non-allosteric enzyme and an allosteric enzyme. A non-allosteric enzyme has only the active site where the analyte interacts. On the other hand, an allosteric enzyme has an allosteric site as well, which modulate the protein-analyte interaction by inducing conformation changes of the active site. This indicates that proteins isolated from difference sources are structurally different and therefore they give different responses. However, the difference between the immediate and constant increase of fluorescence recorded with the enzyme 'pure' and "on-off" behaviour of the bacterial enzyme could be explained as well by a few considerations. i) While in the enzymatic assay the enzyme is already available to recognise the substrate, in the bacteria assay it needs to be produced and released by the bacterial and this can be related to the delay in the fluorescence signal detected; ii) the enzyme is inducible, therefore the bacteria could be stimulated to produce it only when the nutrient present in the LB broth have been consumed.

2.4 Conclusions

Several novel umbelliferone derivatives have been synthesised and their fluorescence properties compared with the compound commonly used for the development of enzymatic substrates (i.e. 4-MU). Data showed that all the tested compounds, with the exception for compound **7**, were more suitable for the development of switchable probes since their fluorescence increases between pH 6 and 6.5, which are conditions at which enzymatic and bacterial assays are normally carried out. This means that using these novel substrates for the development of switchable probes would allow avoiding the additional basification step required when 4-MU is used. Compound **1** was further glycosylated to give the substrate **β-4-AAUG**, which was then tested in the enzymatic and bacterial assays. The synthesised substrate was shown to be highly selective for the enzyme β-glucosidase, since no increase of fluorescence signal was observed when it was treated with α-glucosidase.

The results observed with the bacterial experiments highlighted few important advantages when using the synthesised fluorophores. Indeed, the two substrates having the same carbohydrate, β-glucose, but different fluorophores showed similar detection capabilities in detecting *E. coli, K. pneumonia and Enterococcus.* Although the increase of fluorescence signal requires the same incubation time in order to occur, at the concentrations tested the intensity of that signal was almost 5 times higher using **β-4-AAUG** when compared to **β-4-MUD**. An additional basification step would be required to enhance the signal when using 4-MU, which will, on the other hand quench the enzymatic reaction. Therefore, using a better fluorophore, such as the one synthesised here, would make the analysis less laborious, likely more accurate, robust and reliable due to the better fluorescent properties at the pH close to neutrality.

2.5 Future works

The limitations recognized using umbelliferone-based fluorophores, i.e. low reactivity and chemical stability, could be avoided by choosing an alternative fluorophore, if affordable. In this case it would be interesting to choose a fluorophore which absorbs at longer wavelength in order to enhance the S/N ratio when human samples are analysed, e.g. urine, since biological material present in these samples can interfere with the fluorescence measured. Alternatively, the 'on-off' fluorescent detection can be achieved even using different recognition elements e.g. amino acids, instead of carbohydrates considering that they suffer of chemical instability, especially the switching between the α and β anomer can lead to a lost in specificity for the targeted enzyme. Furthermore, using glucose as recognition element, a relatively large range of bacteria can be detected since lots of microorganism produces glucosidase and preferentially use this carbohydrate as source of energy. However, the selectivity of the detection can be enhanced choosing a different recognition element. For instance, enzymes such as oxidases or azoreducates are produced by a relative limited type of bacteria, therefore targeting these enzymes rather than glycosidases could potentially improve the selectivity of the detection, allowing a better discrimination between different bacteria.

Chapter 3

Fluorescent nanoprobe for bacterial detection

3.1 Introduction

During the process of developing new biosensors, a few parameters should be considered in order to properly evaluate their properties and to compare them accordingly to their efficiency. These parameters are described in *Table 8* and they allow estimation of analytical performance characteristics such as the reliability, capacity and variability of the biosensor being evaluated[114].

Table 8: Description of parameters used to evaluate reliability, capacity and efficiency of a biosensor.

Properties	Definition
Sensitivity	A small change in the analyte concentration causes a large change in the detected signal
Selectivity	The response from the analyte can be differentiated from the response given by undesired elements
Limit of detection (LOD)	Quantity of analyte derived from the smallest signal detectable with an acceptable degree of certainty
Repeatability	Closeness of agreement between measurements taken under the same conditions
Reproducibility	Closeness of agreement between measurements taken under different conditions
Signal-to-noise ratio (S/N)	Ratio of the useful analytical signal to the background noise

Different approaches can be exploited in order to enhance the values of these parameters, hence improving the quality of the biosensor. For example, nanoparticles have been applied to enhance the sensitivity, which is defined by the ratio between the signal measured in response to a specific amount of analyte and the amount of analyte itself. The higher this value is, the better is the sensitivity of the biosensor. Considering the large surface-to-volume ratio offered and their small size, nanoparticles offer the possibility to increase the number of available binding sites, favouring the recognition event[115-117]. Moreover, other features that make the application of nanoparticles intriguing in developing biosensors include their tailorable chemical and physical properties, their biocompatibility and the additional properties that they can add to the biosensor itself [118]. Thanks to their excellent electronic, optical, mechanical and thermal properties, nanoparticles have been widely used for the construction of nanosensors. Carbon nanotubes[119,120], metal nanomaterials[121,122], magnetic nanoparticles[123,124], quantum dots[125] and silica nanoparticles have been exploited for their large surface area/volume ratio, grate electron conductivity, magnetic and photo-physical properties. *Table 9* briefly summarises some of the nanomaterials commonly exploited for the design of nano-biosensors and the properties that make them suitable for sensing purposes.

Table 9: Brief description of some common nanomaterials used for the design of nano-sensors.

Nanomaterial	Intrinsic properties
Metal NPs (gold and silver)	Colorimetric probe, enhancing/quenching fluorescence signal, enhancement of electromagnetic filed (enhancement Raman scattering intensity), localised surface plasmon resonance.
Magnetic NPs	Capture probe, magnetic relaxation
Quantum dots	Intrinsic fluorescent properties with high quantum yield and fluorescent photostability, FRET donor
Carbon nanotubes/Graphene	Nanoelectrode, Fluorescent quenching, photoluminescent (graphene)
Silica NPs	Surface modification, high loading capacity, low toxicity, fluorescent probes

The possibility of functionalising the nanoparticle surface with different substrates allows multiple detection[126,127] and, additionally, depending on the nanomaterial chosen, optical, electronic and magnetic properties can be added to the biosensor, enhancing the signal detected and therefore reducing the S/N ratio, or it can be actively involved in the recognition event.

3.1.1 Nanoprobes for bacterial detection

Due to their unique physical and chemical properties, nanomaterials have been extensively used for the development of biosensors for the rapid detection of microorganisms. The variety of nanoparticles used for the development of such detectors depends on the signal transduction method and the recognition element. For this purpose, bacterial toxins and the microbial cell itself have been used as targets. The detection of a specific bacterial strain relies on the binding between specific molecular receptors (antibody/aptamer) and bacterial antigens present on the bacterial cell wall, such as proteins or lipopolysaccharides (LPS)[128,129]. If selectivity is not required in the recognition between different bacterial strains, the presence of saccharides on the bacterial cell wall and the negative charge of the cell surface can be exploited for the general detection of bacteria[130-133]. An alternative target for bacterial detection are toxins, which are mostly proteins or peptides. These proteins are normally detected by using antibody/aptamers[134]. As previously mentioned, the intrinsic properties of the nanomaterial used for the nanprobe design can be directly

involved in the recognition event or they are exploited to enhance the signal measurable, ultimately improving the sensitivity of the method. There are many examples available in literature and some are listed *Table 10*.

Table 10: Examples of nanotechnology application in bacteria detection and the role of the nanomaterial in defining the detection method.

Bacteria detected	Nanomaterial	Detection method	Recognition element	LOD (CFU/mL)
S.enterica[135]	Magnetic NPs	Relaxation time	Antibody	10^2
E. coli[136]	Magnetic NPs/AuNPs	Separation/electrochemical measurement	Antibody	10^1-10^6
Salmonella typhimurium[137]	Carbon dots	Fluorescence	Aptamers	50
S. typhimurium and *S. aureus*[138]	Magnetic NPs/AuNPs	Surface-enhanced Raman spectroscopy (SERS)	Aptamers	35-15
Bacillus subtilis[139]	AuNPs	Colorimetric assay	Lysosyme	4.3×10^3
L. monocytogenes[140]	Magnetic NPs	Relaxation time (NMR)	Antibody	10^3
E.coli[141]	SiNPs	Fluorescence	Antibody/ Protein A	N/A
E. coli and *S. aureus*[142]	AuNPs	Electrochemical measurement	Enzymatic activity	10^2

When designing nanoprobes for bacterial detection there are a few aspects that should be considered: sensitivity, speed, reliability and selectivity. Different research groups have developed nanoprobes capable of selectively and rapidly detecting low concentrations of bacteria. Commonly, these requirements can be achieved by using antibodies/aptamers as the recognition element and electrochemical techniques for the transduction of the binding event. Despite the advantages of these types of nano-sensor, they tend to be expensive due either to the material required for their synthesis or the instrumentation needed for signal transduction. Although aptamers are considered to be a cheap alternative to antibodies, it is utopic to scale up the synthesis of such nanoprobes for an eventual marketization of the product while maintaining an accessible price.

3.1.2 Project aims

Herein, we present the design of a fluorescent nanoprobe for bacterial detection, which ensures a prompt and sensitive detection of bacteria. In the ideal scenario, the designed nanoprobe will meet the requirements for a point of care (POC) device. We hypothesise that the developed nanoprobe and the resulting detection tests would be rapid, robust and accurate, such that they could be used at the point-of-care in order to detect the pathogen causing the infection, allowing the GP to prescribe the correct antibiotic for the specific infection. The surface of the nanoprobe are functionalised with the substrates described and analysed in the previous section (*2.3.2*). Using carefully designed nanoprobes, we expect to achieve an enhancement in the sensitivity when compared with the substrate alone. As shown in *Figure 40*, if one single bacterium is present in the sample, only a limited amount of antigens will be available for the interaction with the antibodies on the nanoprobe. As consequence, the signal induced by the recognition even will be low and eventually amplification strategies or a more highly sensitive transduction method will be needed to allow detection. On the other hand, the single bacterium will produce a large amount of enzymatic proteins, which will be recognised by the nanoprobe, giving a detectable signal without the need for amplification or sophisticated equipment.
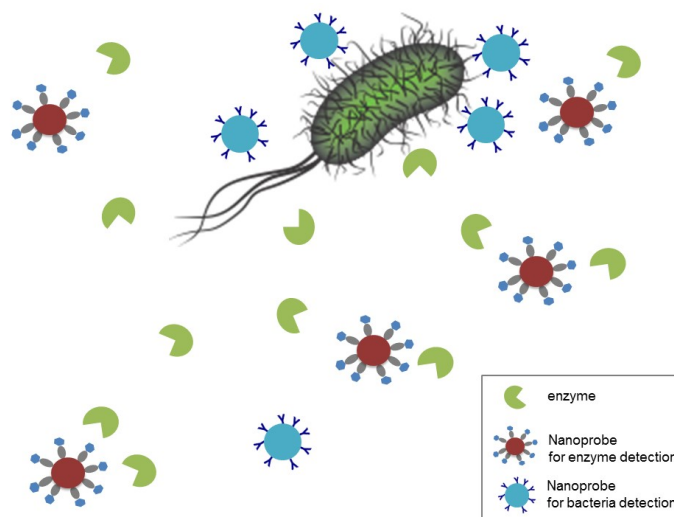
Figure 40: Schematic representation of the different sensitivity between the antibody-mediated detection and the enzymatic-mediated detection. A single bacterium can produce many enzymes that can be detected by the nanoprobe responsive to the enzymatic activity.

The advantage of using the nanoprobe instead of the substrate is illustrated in *Figure 41*. When the substrate is free in solution the enzyme will have to 'look for' the

compound in the sample to process them. Instead, if the substrates are closed to each other, on the nanoparticles surface the enzyme could ideally pass from one to the substrate immediately after hydrolysing each of them quicker and more efficiently. In this way, even though not many bacteria, and therefore no many enzymatic proteins are present in the sample, the detection of the sensitivity and LOD could be considered relatively good.
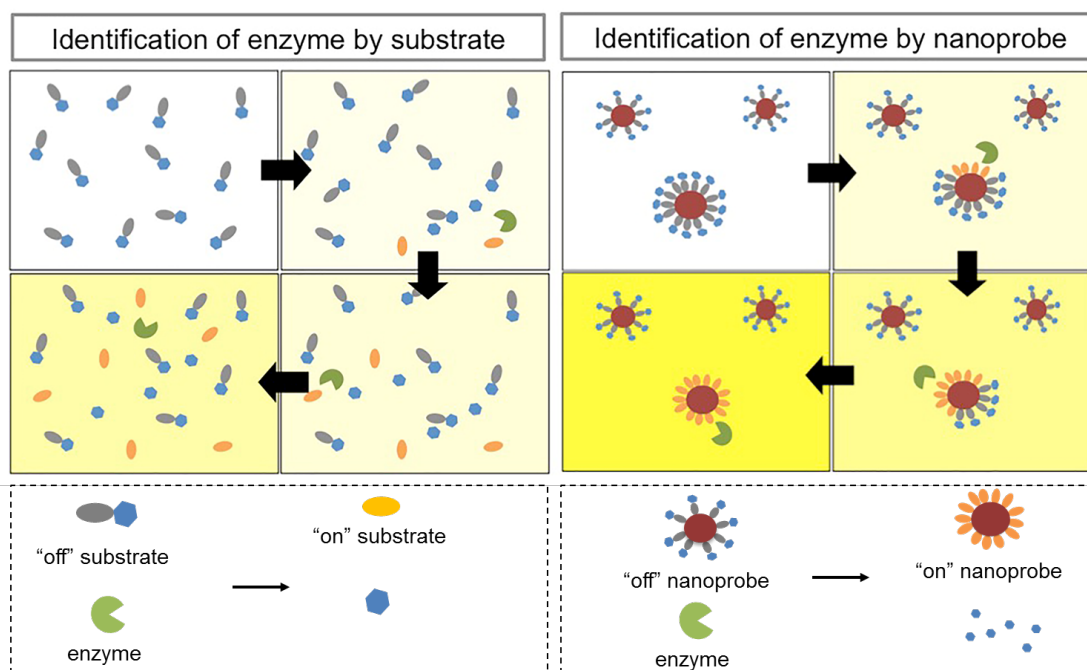
Figure 41: Schematic representation of how the sensitivity of the detection method can be improved by functionalising the nanoparticle surface with the substrate.

In the following paragraphs, the pathways chosen for the development of the nanoprobe are discussed. Issues encountered during the preparation and attempts in overcome these problems will be presented. Nanoprobes based on different nanomaterials have been designed and evaluated for their enzymatic selectivity and for detecting different types of bacteria.

3.2 Experimental

3.2.1 Materials

Cyclohexane (anhydrous, 99.5%), 1-hexanol (anhydrous, ≥99%), Triton® X-100, tetraethyl orthosilicate [TEOS] (99,99%), ammonium hydroxide solution (28% w/v in water, ≥99.99%), Glucose Assay Reagent Kit, DL-dithiothreitol (DTT) ≥99.5%, gold nanoparticles 50 nm stabilised suspension in 0.1 mM PBS reactant free. All mentioned were purchased from Sigma Aldrich. Nunclon Delta sterile flat bottom 96-well plate from Thermo Fisher Scientific. Absolute ethanol, phosphate buffer saline tablets (one tablet dissolved in 200mL DI water yields 0.01M phosphate buffer, pH 7.4) were purchased from Fisher Scientific. Here after, the use of 'PBS' refers to 0.01 M PBS, pH 7.4. Deionised water was prepared from 200 nm nylon membrane filters from Millipore. Streptavidin magnetic particles 0.7-0.9 μm were purchased from Kisker Biotech GmbH & Co. KG.

3.2.2 Synthetic methods

Synthesis of α-D-glucopyranoside bromide (bromo-D-glucose): MeONa (1.3 g, 24 mmol) was dissolved in anhydrous methanol (35 mL) and the reaction was flashed several times with nitrogen. Aceto-α-D-glucopyranoside bromide (1 g, 2.4 mmol) was added to the reaction and the mixture flashed several times with nitrogen and left react at RT for 5 hours under N_2. The reaction was then neutralised by addition of HCl 0.1 M reaching pH 6.5-7. The solid obtained after concentration *in vacuum* was directly used for NP modification.

Synthesis of Glu-5-strept-MPs:

Synthesis of 5-strept-MPs: 0.75 mg streptavidin-coated polystyrene magnetic particles (strept-MPs; 100 μL of stock particles) were centrifuged and the isolated pellet was washed twice with water. The pellet was then re-suspended in PBS and a pre-prepared PBS solution of compound **5** was added, reaching a final concentration of 1mM. The reaction was shaken at 700 rpm at 25°C. After 12 hours the suspension was centrifuged and the pellet was washed several times with water until no fluorescence was measured in the supernatant.

Synthesis of Glu-5-strpt-MPs: 0.75 mg of 5-strept-MPs were centrifuged and re-dispersed in 1 mL of NaOH 0.1 mM pH 8. After 1 hour of shaking at 700 rpm, an 11 mM solution of compound bromo-D-glucose was added to the particle suspension to give a final concentration of 5.5 mM. The mixture was shaken overnight at 700 rpm, in the dark and at RT. After 24 hours, the Glu-5-strpt-MPs were washed with water several times until no glucose was measured in the supernatant, as quantified using a Glucose Assay Kit.

Procedure followed for the glucose quantification with the Glucose Assay Kit: In a 96-well plate, 100 µL of the supernatant were mixed with 100 µL of the kit solution for each well. The plate was incubated at 37°C, shaken and the absorbance was measured after 2 hours at 340 nm. The concentration of sugar in the supernatant was quantified according to the calibration curve obtained with solution of D-glucose at known concentration[143].

Synthesis of Glu-6-AuNPs:

Synthesis of 6-AuNPs: compound **6** (17 mg, 0.024 mmol) was treated with DTT (7.4 mg, 0.048 mmol) in 2.4 mL of water buffered at pH 7.7 with NaOH. The reaction was stirred for 2 hours, and then another 5 mg of compound **6** were added to quench any unreacted DTT. After 30 minutes, the solution was used to re-disperse 0.5 mg/mL AuNP 50 nm diameter (5 mL of stock particles), which had been previously centrifuged, and the isolated pellet was washed once with water. The reaction was shaken at 700 rpm and 25°C. After 24 hours, the suspension was centrifuged and the pellet washed several times with water until no fluorescence was measured in the supernatant.

Synthesis of Glu-6-AuNPs: 0.5 mg of 6-AuNPs were centrifuged and re-dispersed in 1 mL of NaOH solution pH 7.7. After 1 hour of shaking at 700 rpm, 11 mM solution of compound bromo-D-glucose was added to the particles suspension to give a final concentration of 5.5 mM. The mixture was shaken overnight at 700 rpm, in the dark, at room temperature. After the following day, the Glu-6-AuNPs were washed with water until no glucose was measured in the supernatant, as quantified using a Glucose Assay Kit (see procedure above).

Synthesis of Glu-7-SiNPs:

Synthesis of SiNPs: SiNPs were synthesised using the micro-emulsion quaternary method. Briefly: 1.89 g of Trtion-X 100, 7.8 mL of cyclohexane, 1.133 mL of hexanol, 100 µL of TEOS were mixed and after 30 minutes 40 µL of ammonia solution was added. The mixture was stirred at room temperature and after 24 hours the micro-emulsion was broken by addition of ethanol and the particles were purified by repeated washes with ethanol (3 cycles of centrifugation/re-dispersion in ethanol).

Synthesis of 7-SiNPs: NaH (5 mg, 0.2 mmol) was added in 5 mL of toluene and the suspension was stirred in a vial under nitrogen and vacuum for a while. 10 mg of SiNPs were isolated and re-dispersed in 1 mL of toluene and added to the NaH solution to activate the hydroxyl groups present on the surface of the particles. After 1 hour of stirring, compound **7** (3 mg, 0.012 mmol) was added to the mixture and the reaction was stirred for 24 hours in the dark under nitrogen. The following day, the particles were washed with water until no fluorescence was measured in the supernatant.

Synthesis of Glu-7-SiNPs: Again NaH (5 mg, 0.2 mmol) was added in 5 mL of toluene and the suspension was stirred under nitrogen and vacuum for a while. 10 mg of 7-SiNPs were isolated and re-dispersed 1 mL of toluene and added to the NaH solution. After 1 hour of stirring, compound bromo-D-glucose (deacetylated sugar, 5 mg, 0.029 mmol) was solubilised in DMSO 0.5 mL and added to the particles in suspension. The mixture was stirred overnight under nitrogen in the dark and at room temperature. The following day, the Glu-7-SiNPs were washed with water until no glucose could be measured in the supernatant, as quantified by using a Glucose Assay Kit (see procedure above).

3.2.3 Instruments and analytical methods

Dynamic Light Scattering (DLS):

DLS experiments were performed using a Malvern Zetasizer and the measurements were evaluated using the Zetasizer software. Data are reported as average of three measurements (n = 3) ± SD. NP diameter, PDI and zeta potential were used to characterise the particles after synthesis and to assess their evolution after the various surface functionalisations. If not otherwise mentioned, nanoparticles were analysed at

a concentration of 0.25 mg/mL in water at 25°C in DTS1070 disposable cuvettes. Using water as dispersant at 25°C, 0.8872 was used as density value. Depending on the type of particles different parameters were used for material. Silica nanoparticles: refractive index (RI) 1.55, abs 0.01. Gold nanoparticles: RI 0.2, abs 3.32. Streptavidin-coated magnetic particles RI 1.59, abs 0.01.

UV-Vis analysis (as in Section 2.2.3)

$\lambda_{ex}/ \lambda_{em}$ 327/460 nm were used for both enzymatic and bacterial assays. Absorbance at 690 nm was used for the quantification of bacteria in the sample. 340 nm was the absorbance used for the glucose quantification assay.

Incubator (as in Section 2.2.3)

Autoclave (as in Section 2.2.3)

3.2.4 Assays

Quantification of surface functionalisation - method 1:

0.1 mg of each type of NP (5-strept-MPs, 6-AuNPs and 7-SiNPs) were isolated and re-dispersed in 1 mL of water. The fluorescence values were measured at excitation/emission wavelength 327/460 nm, respectively. Using the calibration curves for compounds **5**, **6** and **7,** in water the amount of fluorophore present on the NP surfaces was quantified for 5-strept-NPs, 6-AuNPs and 7-SiNPs, respectively.

Table 11: Quantification of surface functionalisation by method 1.

	5-strept-MPs	6-AuNPs	7-SiNPs
Fluorescence (A.U.)	25936	6853.32	693.32
mM of dye/0.1 mg of NPs	0.127	0.053	0.064
mM of dye/1 mg of NPs	1.27	0.53	0.64

Quantification of surface functionalisation - method 2:

0.2 mg of each type of NP (Glu-5-strept-MPs, Glu-6-AuNPs and Glu-7-SiNPs) were isolated and re-dispersed in 1 mL of water. The samples were incubated at 37°C under shaking with 100 ug/mL of both α and β-glucosidase, to give a final concentration in each well of 0.1 mg/mL. The increase in fluorescence was measured every 20 minutes.

After 12 hours, a plateau was reached and the experiment was stopped. The fluorescence values were measured at $\lambda_{ex}/ \lambda_{em}$ wavelength 327/460 nm, respectively. Using the calibration curves for compounds **5**, **6** and **7,** the amount of fluorophore present on the NP surfaces was quantified for each particle's type considering the highest fluorescent intensity measured.

Table 12: Quantification of surface functionalisation by method 2.

	Glu-5-strept-MPs	Glu-6-AuNPs	Glu-7-SiNPs
Max. fluorescence (A.U)	13377	1086.33	143
mM of dye/0.1 mg of NPs	0.065	0.0074	0.0066
mM of dye/1 mg of NPs	0.65	0.074	0.066

Determination of the amount of particles to be used for enzymatic and bacterial assays:

The amount (mg) of particles per mL of sample was determined by weighing the dried pellets isolated by centrifugation.

Table 13: Concentration of particles and amount of substrate present per mg of particles.

	mg/mL	Average mM of dye/mg of NPs
Glu-5-strept-MPs	7.5	0.963
Glu-6-AuNPs	0.16	0.304
Glu-7-SiNPs	0.35	0.351

The amount of NP suspension (mL) required for the preparation of the samples used in the assays was determined for each type of particle using the concentrations and the amounts (mM) of fluorophore per mg of particles shown in *Table 14*. The mM/mg value considered for this calculation is the average of the values determined by methods 1 and 2 for each type of particles. The amount of particles used for the assays is related to the amount of substrate on their surface, in order to have comparable fluorescent values.

Table 14: Amount of particles used for enzymatic and bacterial experiments accordingly to the amount of substrate calculated on their surface.

	NPs needed for 0.1 mM	
	mg	mL
Glu-5-strept-MPs	0.208	0.028
Glu-6-AuNPs	0.658	4.11
Glu-7-SiNPs	0.57	0.42

Enzymatic assays:

For both α-glucosidase and β-glucosidase, the amount of protein present in the stock solution was quantified when needed using a Micro BCA Protein Assay Kit, using known BSA dilutions for the calibration curve. All assays were performed in sodium acetate buffer 0.2 M, adjusted to pH 6.5 by addition of glacial acetic acid. Both enzyme-NP dilutions were prepared using this buffer. To the 96-well plate was firstly added NP suspension and, after the fluorescent signal at t_0 was measured, the enzyme solution was quickly added to each well and the increase of fluorescence measured over time while shaking the plate at 600 rpm at 37°C. All concentrations analysed were calculated according to the final volume of 100 µL/well. The increase of fluorescence was measured using as $\lambda_{ex}/\lambda_{em}$ wavelength 327/460 nm respectively.

Table 15: Concentrations of nanoprobes and enzymes used in the enzymatic assay.

	µM/well of dye for calc. for all particles	µg/well of enzyme α and β-glucosidase
Assay I	100, 50, 25	100

Bacterial assay:

Bacteria were cultured in Petri dishes on solid broth (LB with agar) and incubated at 37°C overnight. A few isolated colonies were then harvested in liquid LB broth at 37°C under shaking at 650 rpm for 4 hours. This suspension of bacteria was diluted to the desired concentration according to the McFlander standards. The stock solution was used for the preparation of the bacterial samples tested in the assay. The samples tested were obtained by dilution of the bacterial stock solution with LB. These samples

were further cultured on solid broth at 37°C overnight to confirm the concentration of bacteria used.

To sterile 96-well microplate was firstly added NP samples at appropriate concentrations and, after the fluorescent signal at t_0 was measured, the bacterial samples were quickly added to each well and the increase of fluorescence was measured over time, shaking the plate at 600 rpm at 37°C. All concentration analysed were calculated accordingly to the final volume of 200 µL/well. The increase in fluorescence was measured using as $\lambda_{ex}/\lambda_{em}$ wavelength 327/460 nm respectively.

Table 16: Concentrations of particles and microorganisms used in the bacterial experiment.

	µM/well of dye for calc. for all particles	CFU/well of each bacteria type
Assay I	50, 25 (only Glu-5-strept-MPs)	75

Determination of inhibitory activity of NPs:

The concentration of strept-MPs, AuNP and SiNPs in mg/mL was determined by weighing the dried pellet isolated by centrifugation of particles per known volume.

Table 17: Concentrations of particle's stocks.

	mg/mL
strept-MPs	6.8
6-AuNPs	0.14
7-SiNPs	1.21

Considering these values, the particles were tested for the inhibitory effect they induced in presence of the enzymes or bacteria at the final concentrations specified for each experiment.

Enzymatic assay: The assays were carried in 96-well plates. 200 µL of 2 mg/mL of strept-MPs and SiNPs particles were added to three different wells and diluted by factor 2, directly on plate, with sodium acetate buffer. In the case of AuNPs, the same procedure was followed but using 0.5 mg/mL as the starting concentration. To each well were subsequently added 50 µL of 400 µg/mL solution of enzyme α-glucosidase and 50 µL of 200 µM solution of α-MUD, reaching 200 µL as final volume for each well.

The final concentration of NPs, enzyme and substrate assayed are reported in the *Table 18*. The plates were incubated at 37 °C under shaking and the increase of fluorescence was determined every 15 minutes. The same concentrations were used for strept-MPs and SiNPs while lower for AuNPs due to lower availability.

Table 18: Concentration of particles used in the assay used to test the inhibitory effect of particles during the enzymatic assay.

mg/mL of strept-MPs and SiNPs / AuNPs	μg/mL of enzyme	μM of substrate
1 / 0.25	100	50
0.5 / 0.125	100	50
0.25 / 0.0625	100	50
0.125 / 0.0312	100	50
0.0625 / 0.0156	100	50
0.0312 / 0.0078	100	50
0.0156 / 0.0039	100	50
0 (0.1 mL of buffer)	100	50

Bacterial assay: The assays were carried in sterile 96-well plates. 200 μL of 2 mg/mL of strept-MPs and SiNPs particles were added to three different wells and diluted by factor 2, directly on plate with water. In the case of AuNPs the same procedure was followed but using 0.5 mg/mL as the starting concentration. To each well were subsequently added 50 μL of 300 CFU/mL of *E.coli* in LB broth and 50 μL of 1 mM solution of α-MUD, reaching 200 μL as final volume for each well. The final concentration of NPs, *E.coli* and substrate assayed are reported in *Table 19.* The plates were incubated at 37 °C under shaking and the increase of fluorescence was determined every 15 minutes. The same concentrations were used for strept-MPs and SiNPs while lower for AuNPs due to lower availability.

Table 19: Concentration of particles used in the assay accomplished to evaluate the inhibitory effect of particles during the bacterial assay.

mg/mL of strept-NPs and SiNPs / AuNPs	CFU/mL of *E.coli*	µM of substrate
1 / 0.25	75	250
0.5 / 0.125	75	250
0.25 / 0.0625	75	250
0.125 / 0.0312	75	250
0.0625 / 0.0156	75	250
0.0312 / 0.0078	75	250
0.0156 / 0.0039	75	250
0 (0.1 mL of buffer)	75	250

Determination of toxicity effect of NPs induced on E.coli:

The assays were carried in sterile 96-well plates. 100 µL of 2, 1 and 0.1 mg/mL of strept-MPs and SiNPs particles were added to three different wells in the plate. AuNPs were used at concentration of 0.5, 0.25 and 0.125 mg/mL. To each well were subsequently added 100 µL of 0.2 CFU/mL of *E.coli* in LB broth, reaching 200 µL as final volume for each well. The final concentration of NPs and *E.coli* assayed are reported in *Table 20*. The plates were incubated at 37 °C under shaking and the bacterial growth was evaluated by measuring the absorbance at 690 nm every 15 minutes.

Table 20: Concentration of particles used in the test accomplished to evaluate the toxicity of particles on *E.coli*.

mg/mL of strept-MPs and SiNPs / AuNPs	CFU/mL of *E.coli*
1 / 0.25	0.1
0.5 / 0.125	0.1
0.5 / 0.0625	0.1
0 (0.1 mL of buffer)	0.1

3.3 Results and discussion

3.3.1 Nanoprobe design

Different strategies have been considered in order to design nanoprobes capable of bacterial detection. The first was a linear strategy, where the different moieties were sequentially attached on the surface of SiNPs (*Figure 42*).
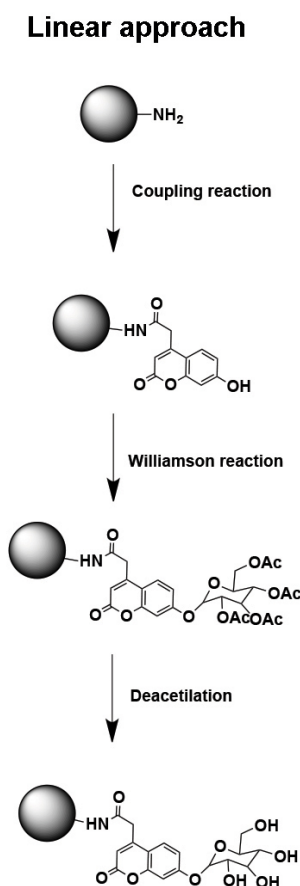
Figure 42: Linear approach for the nanoprobe design. In this approach, the SiNPs surface is functionalised firstly with 4-AAU by coupling reaction (i). Subsequently they are treated with aceto-α-D-glucopyranoside bromide (ii) which is then deacetylated (iii).

4-AAU was firstly covalently linked to the nanoparticle surface by a coupling reaction (EDC/NHS, SOCl$_2$, TBTU/base) between the carboxylic group of the 4-AAU and the amino groups available on the SiNPs. During the work up of the reaction, different centrifugation/redispersion steps, it was noticed that some fluorescence signal was constantly detectable in the supernatants. This suggested that the fluorophore is not covalently attached on the surface or that it was subsequently released into the supernatant during the washing process. Due to the coupling problem and the

difficulties of proving that 4-AAU was covalently attached on the particle surface, an alternative convergent strategy has been developed. In this case, the substrate is first synthesised and characterised using standard analytical techniques (NMR, Mass spec, FTIR, etc.), proving the success of the reaction, and it is then covalently attached to the nanoparticle surface (*Figure 43*).
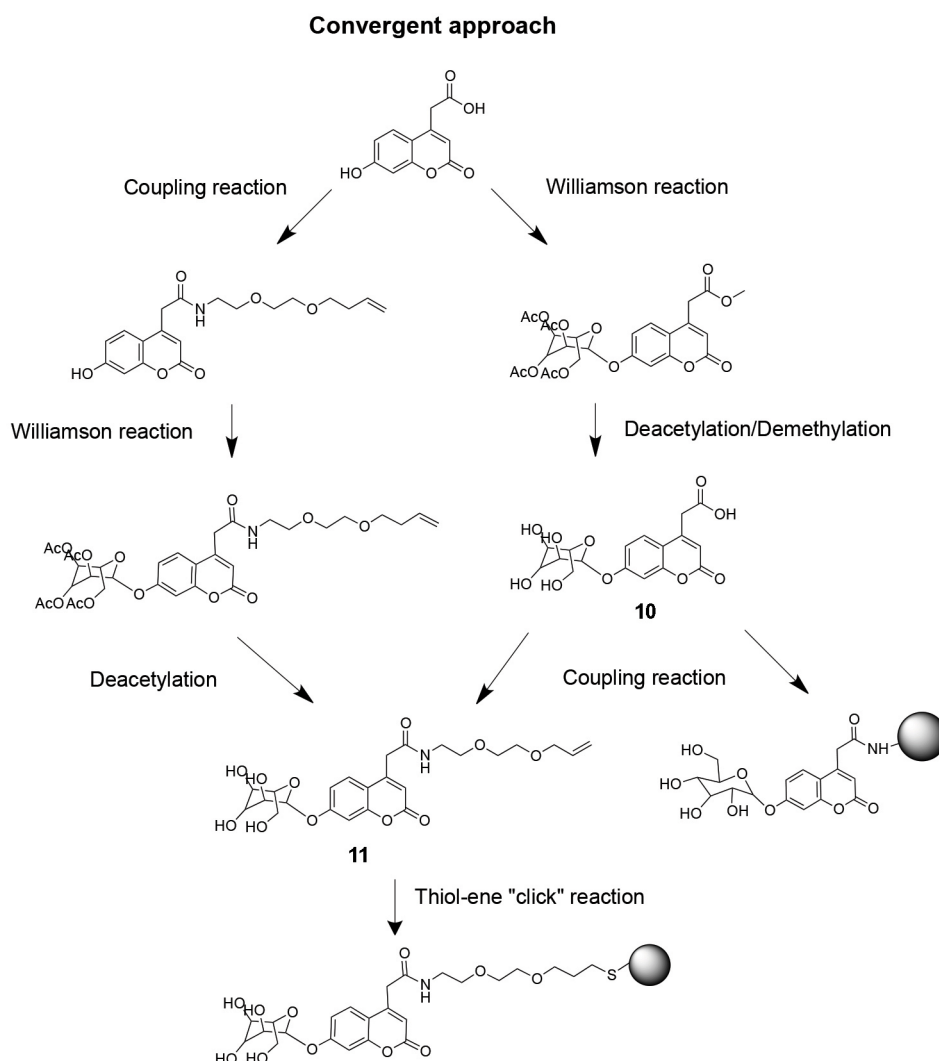
Figure 43: Two convergent approaches allow the synthesis of substrates; its characterisation by chemical analytical techniques can be done proving the efficiency of the reactions. The substrates are then used to functionalise the nanoparticle surface.

Following this new approach, we attempted to prepare compound **10** and compound **11.** The reaction scheme shown in *Scheme 10* focuses on one of the two pathways. However, compound **10** could not be successfully synthesised due to the difficulties encountered with the demethylation step. Details of this reaction were presented in *section 2.3.2* as well.

91
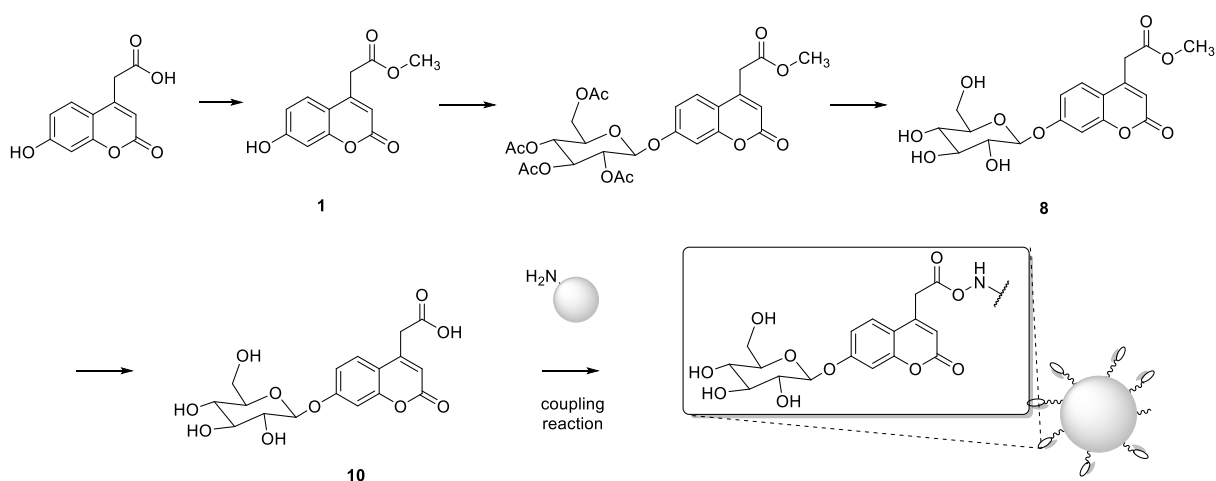
Scheme 10: Due to the difficulties encountered in the demethylation step, no free carboxyl group was available for the NPs-NH$_2$ functionalisation.

In order to make the functionalization more efficient, compound **11** was designed to possess an ethylene group, whose reactivity with thiol groups could have been exploited to functionalise the surface of thiolated-NPs using the thiol-ene "click" reaction. "Click" chemistry is characterised by easy, quick and complete reactions, in which the formation of secondary products is limited, properties that make them very useful for surface functionalisation purposes. For this pathway, thiolated-SiNPs were prepared by creating a thin shell made of APTMS and MTPMS in different ratios (*Scheme 11*). A linker (allyloxy)ethoxy)ethan-1-amine was needed to introduce the ethylene group into the structure. The linker was required for the thiol-ene"click" reaction but additionally, it would have acted as a spacer between the nanoparticle surface and the 4-AAU derivate. This spacer, according to the literature, allows for better recognition of NP-attached substrates by the enzyme. It also enhances the surface functionalisation efficiency, reducing steric hindrances between molecules attached on the surface.
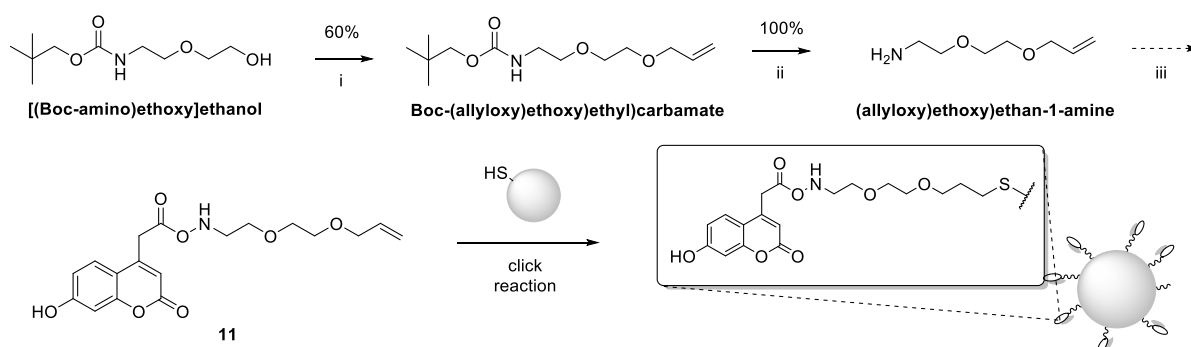
Scheme 11: i) KOH, allyl bromide, THF anhydrous, stirred under nitrogen, RT, overnight ii) 30% TFA in DCM, in ice bath then at RT for 4 hours iii) coupling between 4-AAU and the amine followed by iv) "click" reaction.

Unfortunately the coupling reaction between the 4-AAU and the amino group of the linker (allyloxy)ethoxy)ethan-1-amine was not successful, despite the numerous attempts and changes to the reaction conditions. Therefore, compound **11** could not be obtained. In order to form the amide bond between fluorophore and linker, many coupling reactions were considered. For example, the carboxylic group was activated by EDC, EDC/NHS, NHS/DCC, T3P, TBTU, SOCl$_2$ and by using pentafluoro phenyl trifluoroacetate (5Fphenyl-3Facetate). The protocols used are briefly summarised in *Table 21.* In some cases, the reaction occurred, but only after the laborious purification steps and the product was not of the required purity. Furthermore, the reaction yields were low (the maximum obtained was 45%) and they varied greatly from one reaction and the other one, even when exactly the same procedure was followed. The low yields and irreproducibility indicated that the pathway followed was unfavourable from a cost-efficiency point of view and it was therefore abandoned.

Table 21: Brief description of the coupling reactions attempted for the synthesis of compound 11. The carboxyl group of the 4-AAU was activated by using different type of common reagents. In the table yield and comments are reported for the protocol that leaded to the better results.

Reagents	Yield %	Comments
EDC	0	No product observed
EDC/NHS	10	Complicated purification leading to low yield
T3P/base	8	Purification by column chromatography needed
TBTU/base	44	By column chromatography the product was isolated but impurities remained.
DCC/NHS/base	45	Best result, but not reproducible; other experiments yielded 7, 13 and 2% product, respectively.
HOBt/base	0	No product observed.
5Fphenyl-3Facetate	0	No product observed.
SOCl$_2$	4-36	Purification very difficult, impure product isolated. The reaction leads to the formation of several side products

The difficulties encountered during the coupling reaction between the 4-AAU derivate and the linker may be explained by the instability of 4-AAU. Inter- and intramolecular reactions can occur between the hydroxyl and carboxyl groups of 4-AAU. Some of the hypothesised secondary products obtained during reactions are shown in *Figure 44*.
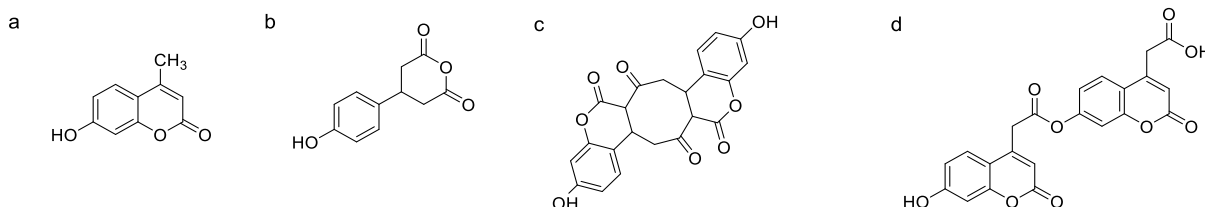
Figure 44: The secondary product a) has been isolated and characterised. The formation of the other compounds has been only hypothesised. b) Could be achieved after opening-closing of the lactone group in acidic or basic environment, while c) and d) are two possible inter-molecular interaction which could occur particularly in alkaline conditions.

This issue has been discussed in the *section 2.3.2* related to the substrate synthesis where similar problems were observed. Additionally, it has been proven that coumarin suffer from dimer formation and lactone-ring opening, even under mild conditions. One of the earliest studies focusing on the stability of coumarin is almost 100 years old, when coumarin became known and the first photo-dimers was characterised. Coumarin suffers from photochemical [π2s + π2s] cycloaddition reactions for the double bond derivate from pyrone ring, which leads to formation of 2 structural isomers, head-to-head and head-to-tail, each of which can exist in *cis* and *trans* configuration *(Figure 45)*. These photodimers can form when coumarin molecules are

solubilised in polar organic solvents and irradiated, but it can also arise when irradiated in ethanol/water solution with sunlight for longer times. It has been proven that cross-cycloaddition on the pyrone C=C bond occurs under irradiation and in the presence of simple alkanes as well[144-148]. Furthermore, coumarin and its dimers can suffer from lactone ring opening at high temperatures under alkaline conditions[149].
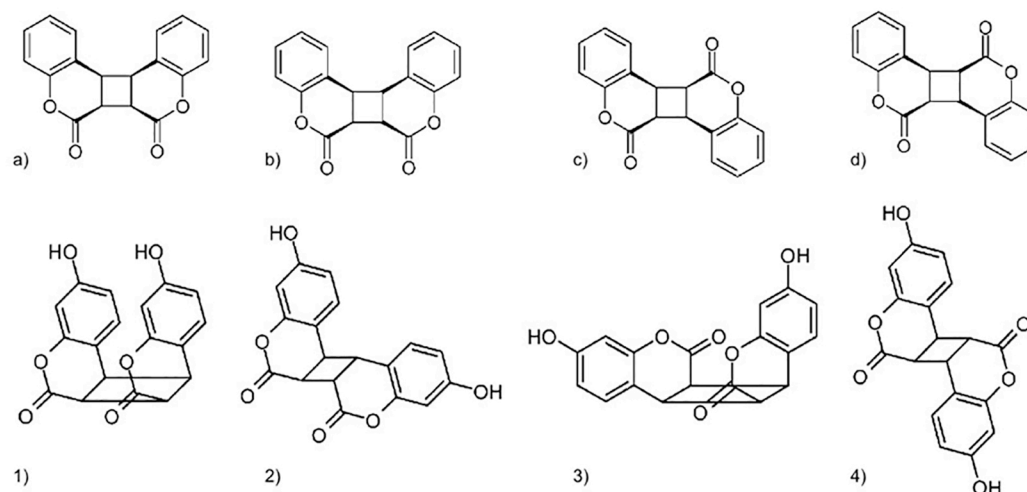
Figure 45: Structure of coumarin photodimers (a-d) and their spatial configuration (1-4). Adapted from reference[148].

Considering the problems encountered, three additional alternative strategies for the nanoprobe design were undertaken. They involved the synthesis of three other 4-AAU derivatives, compounds **5**, **6** and **7** discussed in *section 2.3.1*. These three derivatives have been chosen to facilitate the functionalisation of nanoparticle surfaces. In particular, compound **5** was used to functionalise streptavidin-coated polystyrene-magnetic particles (strept-MPs of 1000 nm diameter) enabling the synthesis of **5-strpt-MPs**. The affinity of streptavidin for biotin is the strongest non-covalent biological interaction known, formed by several hydrogen bonds, hydrophobic interactions and van der Waals forces. Even though the affinity can be reduced after modification of the biotin (o avidin) structure the binding constant commonly remains very high. With compound **6**, we exploited the affinity of thiol groups for gold. The surface functionalisation of AuNPs with thiol derivatives is usually a very efficient and easy procedure, and enabled us to obtain functionalised **6-AuNPs** (AuNPs with 50 nm diameter). In addition, compound **7** was used to functionalise SiNPs (100 nm diameter) through a Williamson reaction, using NaH toluene for the activation of hydroxyl groups

on the particle surface, allowing the formation of **7-SiNPs** (*Figure 46*).
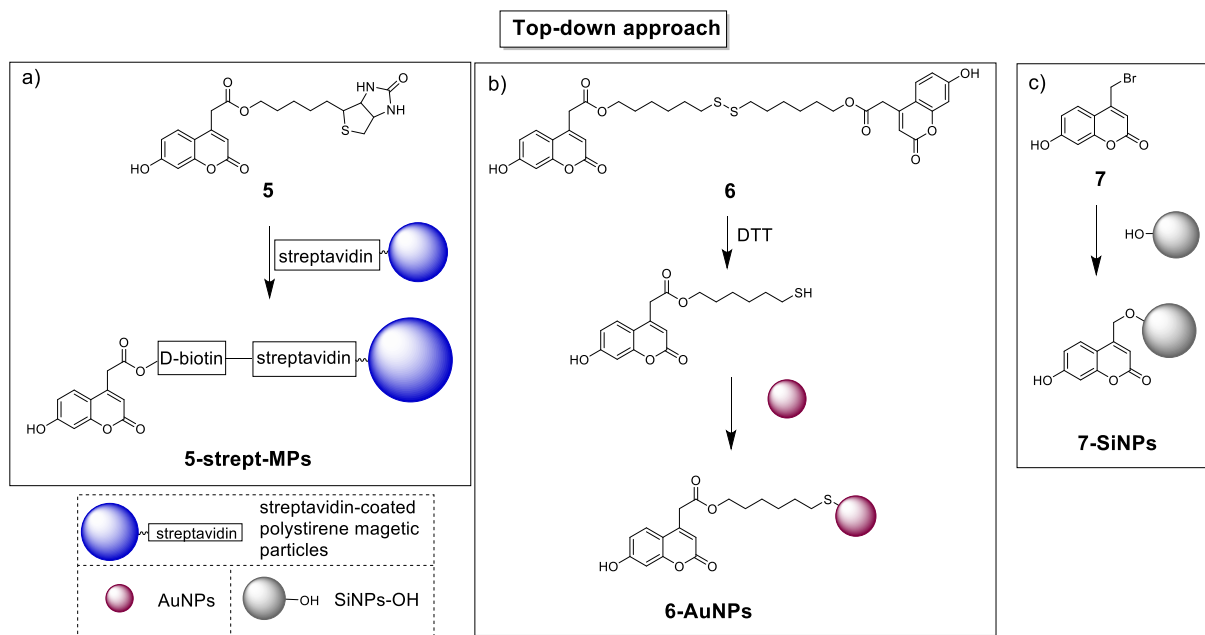
Figure 46: Three alternative top-down approaches. a) strept-MPs, compound **5,** in PBS at 25°C 700 rpm in dark overnight. b) Compound **6,** DTT for 2 h in aqueous solution pH 7.7; the mixture was directly added to the suspension of 100 nm AuNPs, stirred at RT for 24h. c) SiNP, NaH in toluene, after 30 min compound **7** was added, 24 h RT under N_2 in dark.

After functionalization, all particles were intensively washed with repeated cycles of centrifugation and re-dispersion in water until no fluorescence signal was measured in the supernatant. The fluorescent signal detected in the supernatants isolated at each wash step during the purification of the functionalised particles for all three particles types is shown in *Appendix section A2.3*. Using the calibration curve for each of the 4-AAU derivatives, the total amount of fluorophore attached on the nanoparticle surface was determined. The values are reported in *Table 22*. The low functionalisation of the AuNPs nanoparticles could be due to the reversibility of the interaction between thiolated compounds and the nanoparticle surface.

Table 22: Quantification of dyes (compound 5, 6 and 7) on the surface of the respective type of nanoparticles.

	5-strpt-MPs	6-AuNP	7-SiNPs
µmol of compound	1.2 µmol/mg	0.124 µmol/mg	0.46 µmol/mg

The second step of the synthesis involved the formation of the glycosydic bond between α-D-glucopyranoside bromide (compound bromo-D-glucose) and the functionalised particles. The deacetylation of the sugar ring was accomplished prior the coupling reaction. The reaction used for the glycosylic-bond formation was, in each case, a Williamson reaction as shown in the *Figure 47*. This was performed in NaOH 0.1 mM pH 8 solution for **5-strept-MPs**, in NaOH solution pH 7.7 for **6-AuNPs** and in NaH/toluene for **7-SiNPs**.
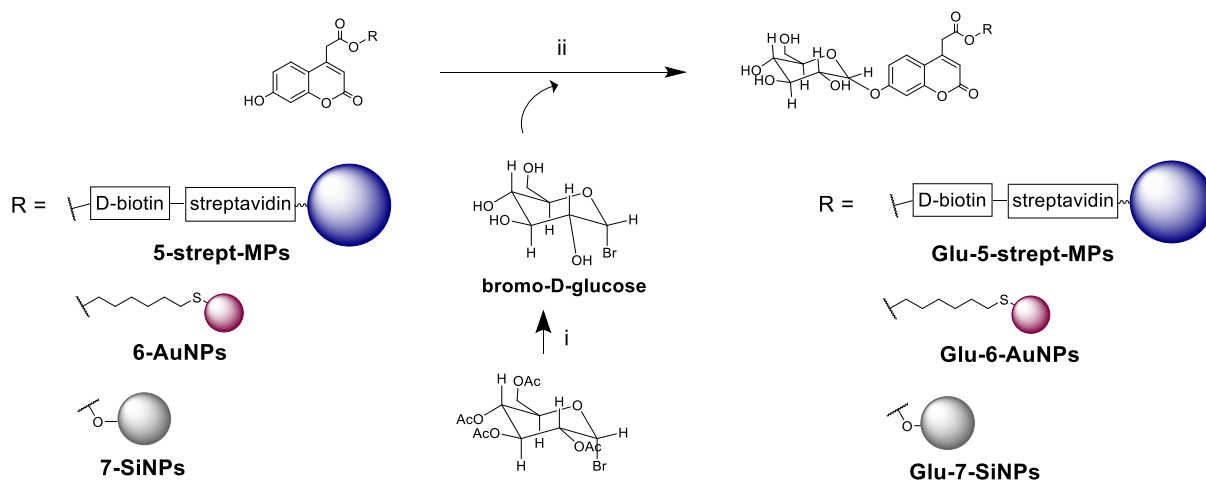
Figure 47: i) MeONa in dry MeOH, anhydrous condition, RT. After 3h the reaction mixture was neutralised with HCl and concentrated under vacuum ii) NP suspension stirred for 30 minutes in NaOH 0.1 mM pH 8 (5-strept-MPs), in NaOH solution pH 7.7 (6-AuNPs) or toluene with NaH (7-SiNPs) at RT in dark for 24 hours.

After 24 hours, the particles were washed several times until no glucose was found in the solution. The quantification of the glucose in the supernatants was accomplished by measuring the absorbance at 340 nm after treatment with a solution of 1.5 mM NAD, 1.0 mM ATP and 1 unit/mL of hexokinase. This mixture allows the production of NADH which is quantified by measuring the absorption at 340 nm (for details see *Appendix A2.4*)[143].

The particles were characterised after each step of surface functionalisation by DLS and by fluorescence. The presence of fluorescence signal on the NPs and the increase

in particle diameter could indicated successful coupling in all cases. Results are summarised in *Table 23*.

Table 23: Values reported for all particles were measured at concentration of 20 µg/mL in water. The table shows the diameter (Ø) and surface charge (ζ-potential) measured by DLS and fluorescence properties (Fluo) after each step of synthesis for each nanoporbe (NPs - uncoated particle; Flu-NPs – dye-labelled particle; Glu-Flu-NPs - final nanoprebes). Values are reported as average ± SD, n=3.

	Strept-MPs			AuNPs			SiNPs		
	Fluo(A.U.)	Ø (nm)	ζ(mV)	Fluo(A.U.)	Ø(nm)	ζ(mV)	Fluo(A.U.)	Ø (nm)	ζ(mV)
NPs	1869.67 ± 45.17	1023.67 ± 24.28	/	550.33 ± 20.68	61.37 ±1.39	-15.2 ± 0.5	198 ±1.41	113.07 ± 0.205	-42.13 ± 0.62
Flu-NPs	6484.33 ± 237.4	3174.33 ±346.73	/	1713.33 ± 86.76	89.66 ± 1.13	-21.1 ± 1.92	1733.33 ± 58.52	209.5 ± 1.43	-33.63 ± 0.90
Glu-Flu-NPs	4378 ± 50.41	>10000	/	1732.67 ± 79.71	243.67 ±7.21	-28.37 ± 1.35	232.33 ± 2.5	1943 ± 126.2	-20.3 ± 0.21

As expected, the fluorescence signal for **strept-MPs** increased when the surface was functionalised with the biotinylated **4-AAU** derivate (6484.33 ± 237.4 A.U), but decreased when the hydroxyl group of compound **5** was glycosylated (4378 ± 50.41 A.U.). Similar consideration could be done for SiNP: **7-SiNPs** were fluorescent (1733.33 ± 58.52 A.U.) while **Glu-7-SiNPs** were not (232.33 ± 2.5 A.U.). In both case the glycosylated particles (**Glu-5-strpt-MPs** and **Glu-7-SiNPs**) still have a higher fluorescent signal compared with the plane particles (**strept-MPs** and **SiNPs**). This could indicate that (i) glycosylation occurred only partially or (ii) the fluorescence is partially but not completely quenched. More difficult is the interpretation of the data obtained in the case of the AuNPs, since the fluorescence of **Glu-6-AuNPs** was the same as that of the **6-AuNPs** (1732.67 ± 79.71 and 1713.33 ± 86.76 A.U. respectively) which indicates that the glycosylation was not successful. The increase in diameter after glycosylation (from 89.66 ± 1.13 nm of **6-AuNPs** to 243.67± 7.21 nm of **Glu-6-AuNPs**) could indicate particle agglomeration during glycosylation. It was reasoned that the glucose may have been physically adsorbed on the particle surfaces rather than covalently linked to the hydroxyl group of compound **6.** Surface charge was measured for AuNPs and SiNPs. The AuNPs, usually neutral, became more negative after the surface coatings. **Glu-7-SiNPs** became instead more positive which, considering the remarkable increase in diameter, was a possible indication of aggregation/agglomeration. The ζ-potential of strept-MPs was not measured since these types of particles, having magnetic properties and large diameter, could

eventually affect the instrument. Observing the wide increase of the particles dimeter after glycosylation it appeared that all particles types tend to aggregate.

Quantification of NP's functionalisation

The quantification of the substrates on the particle surfaces for **Glu-5-strept-MPs, Glu-6-AuNPs** and **Glu-7-SiNP** was not an easy task. However, two methods have been accomplished in order to have at least an indication of the amount of particles to use in the subsequent assays.

The first method used is based on the assumption that the glycosylation occurred only at the hydroxyl group for the **5-strept-MPs, 6-AuNPs** and **7-SiNPs**. The amount of compound **5**, **6** and **7** presents on the surface of **5-strpt-MPs, 6-AuNPs** and **7-SiNPs** was therefore used as the amount of glycosylated substrate. Due to the partial detachment of the dye from the surfaces which could potentially occur during the following glycosylation step and washing procedures, this method could overestimate the real amount of substrate that is actually available.

The second method used was based on the quantification of the fluorescence signal obtained after treating the particles with hydrolytic enzymes at high concentration to avoid saturation, both α- and β-glucosidase. The increase in fluorescence was measured until a plateau was reached, indicating that the enzyme had cleaved all the substrates on the particle surface. This method is more accurate, but could lead to an underestimation of the amount of substrate, since the values reached strongly depend on the enzymatic activity.

As expected, values obtained with the first method are higher than those calculated with the second. As such, the average of the values achieved with the two methods have been considered to determine the concentration used in the enzymatic and bacterial experiments. *Table 24* shows the average values calculated for each particle in terms of μmol of substrate for each mg of nanoprobe. Using these values, the amount of particles needed to prepare the samples used for the enzymatic assay and the bacterial detection experiment was calculated (value highlighted in yellow in *Table 24*). Values achieved with the two separate methods are reported in *Appendix section A2.5.* Although the difference between the type of particles used makes the comparison

difficult, the result achieved seems to indicate that the functionalisation occurs better for strept-MPs.

Table 24: Average of the quantification values calculated for each nanoprobe (µmol/mg) and concentration of the nanoprobe in the stock (mg/mL) are reported. In the yellow section are reported the amount of particles needed to have 100 µM.

	Glu-5-strpt-MPs	Glu-6-AuNPs	Glu-7-SiNPs
[substrate] µmol/mg	0.965	0.097	0.264
[nanoprobe] mg/mL	7.5	0.16	1.35
mg nanoprobe for **[substrate] 100 µM**	0.1 mg (13 µL)	1 mg (6.25 mL)	0.378 mg (0.28 mL)

The difference between the value obtained for **Glu-7-SiNPs** by using the first method (0.636 mM) and the second (0.066 mM) suggested that compound **7** was only adsorbed on the surface. The fluorescence values achieved with the second method confirmed the failure of the functionalisation of SiNPs.

3.3.2 Evaluation of nanoprobe activity

The following studies were accomplished in order to exclude the interference of the particles used for the nanoprobe design on the biologic components, such as proteins and bacteria. If any inhibitory effect on the enzymatic activity and bacteria grow is observed, the failure in detecting the presence of bacteria can be related only to the inefficiency of the nanoprobe.

First of all, the inhibition effect of each particle type on the enzymatic activity was evaluated. Substrate **α-4-MUD** (50 mM) was treated with the enzyme α-glucosidase (100 µg/mL) in the presence of different concentrations of the three types of NPs used (**strept-MPs**, **AuNP** and **SiNPs**). As a reference, the efficacy of the recognition between enzyme and substrate was measured in the absence of NPs (red line in *Figure 48*). As shown the highest concentrations of particles used (1 mg/mL for strept-MPs and SiNPs; 0.25 mg/mL for AuNP) can limit the enzyme-substrate recognition. This phenomenon was particularly clear using strept-MPs, where a strong correlation with the particle concentration was observed (*Figure 48-a*). The inhibition induced by the presence of AuNPs was almost irrelevant and it was not related to the concentration of particles (*Figure 48-b*). Using SiNPs, the inhibitory effect was observed only for the

highest concentration (1mg/mL) while at lover concentrations the effect was negligible (*Figure 48-c*). It can be observed that a certain correlation between the NP size and the inhibition effect exists. The greater the size of the particles (strept-MPs > SiNP > AuNP; 1000, 100 and 50 nm diameter), the more profound was the observed inhibitory effect. The induction of protein denaturation or the alterations of the fluorescence signal are possible mechanisms by which the NPs tests (in particular strept-MPs) could inhibit the enzyme-substrate recognition.
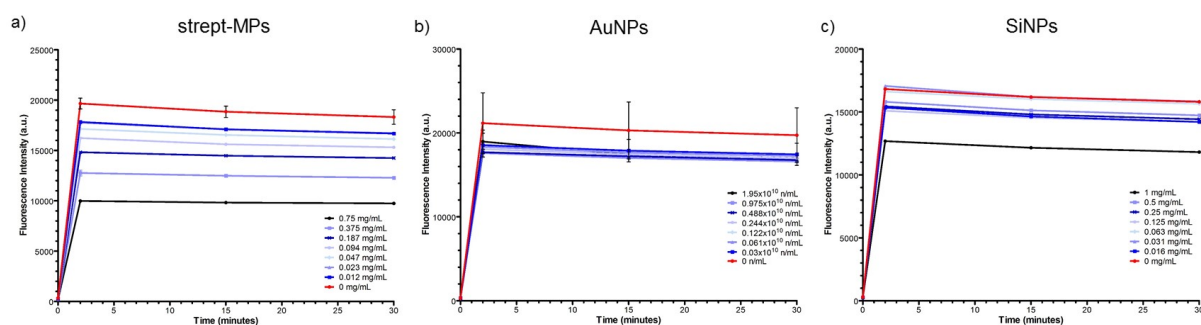
Figure 48: Inhibitory effects of the particles on the enzyme-substrate recognition event. The activity of the enzyme α-glucosidase (100 μg/mL) in processing the substrate α-4-MUD (50 mM) when particles are absent (red line) is compared with its activity in presence of (a) strept-MPs, (b) AuNPs and (c) SiNPs at different concentrations of nanoparticles (highest concentration tested- black line; remaining concentrations-graduated blue). Values are reported as average ± SD, n=3.

Similar experiments were conducted by treating α-4-MUD with *E. coli* in the presence of different concentrations of **strept-MPs**, **AuNPs** and **SiNPs** in order to determine if the presence of NPs can inhibit or limit the efficacy of the substrate in detecting bacteria. The presence of 25 CFU/mL of *E.coli* was detected with 250 μM of α-4-MUD in the presence of different concentrations of NPs. As in the previous experiment, 1 mg/mL was the maximum amount of **strept-MPs** and **SiNPs**, while 0.25 mg/mL was used for the **AuNPs**. As a reference, the efficacy of the substrate in detecting *E. coli* was measured in the absence of NPs (red line in *Figure 49*). Even in case it was evident that the presence of particles can limit the reaction enzyme-substrate, especially when particles were tested at high concentration (black lines in *Figure 49*). This inhibitory effect was more relevant in the case of strept-MPs and SiNPs (*Figure 49-a*), supporting the interpretation of the previous experiment.
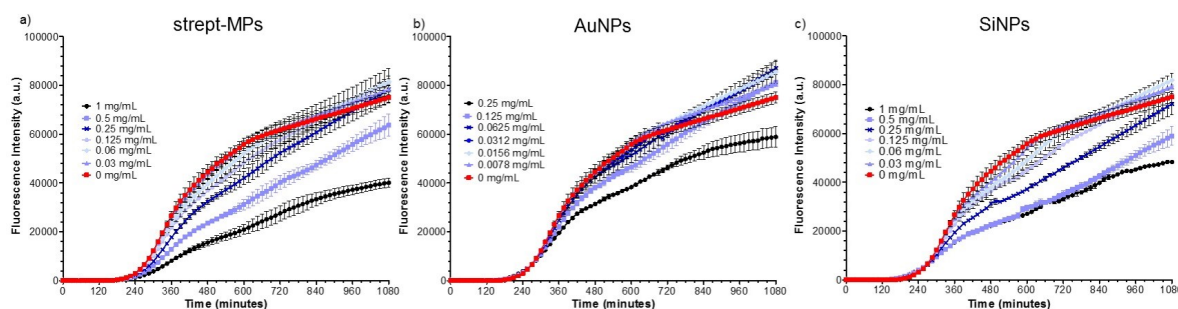
Figure 49: The activity of α-4-MUD (250 μM/mL) in the recognition of 25 CFU/mL of *E.coli* in absence of particles (red line) or in presence of (a) strept-MPs, (b) AuNPs and (c) SiNPs at different concentrations (black lines - higher concentration tested: 1 mg/mL for strpt-MPs and SiNPs and 0.25 mg/mL for AuNP. Blue graduated lines - lower concentrations). Values are reported as average ± SD, n=3.

Additionally, all three types of nanoparticle, **strept-MPs, AuNPs** and **SiNPs**, were evaluated for their possible effect on bacterial cells growth. In order to do this, 0.1 CFU/mL of *E.coli* was treated with three different concentrations of each type of particle and the toxicity of the particles was evaluated by determining the growth inhibition. **Strep-MPs** and **SiNPs** were used at concentrations of 1, 0.5 and 0.05 mg/mL while for **AuNPs** were used at 0.25, 0.125 and 0.0625 mg/mL. As shown in *Figure 50*, the presence of nanoparticles did not inhibit the growth of bacterial cells initially. However, the plateau of the growth curve was reached earlier when nanoparticles were present. When *E. coli* was incubated alone (red line *in Figure 50*), the maximum absorbance signal reached was higher when compared with the bacteria incubated in the presence of nanoparticles. This could be attributed to the fact that the presence of particles limits the physical space available for the cells to grow rather than to a toxic effect. This is true for **SiNPs** and **AuNPs,** while in the case of **strept-MPs**, a relevant inhibition of the cell grow can be noticed only at the highest concentration (1 mg/mL, dark-blue line *in Figure 50*). This could be related either to the large size of these particles (1 μm compared with the 100 nm and 50 nm SiNPs and AuNPs) or to the high amount used.
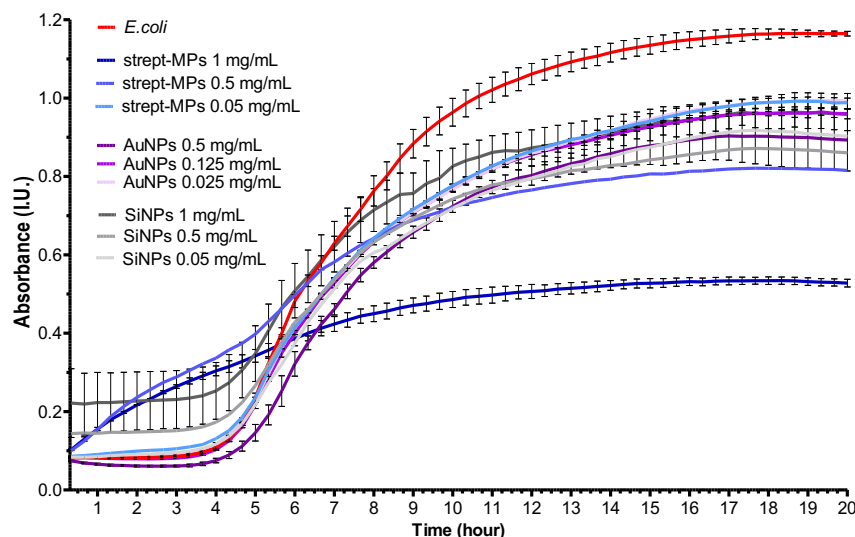
Figure 50: Evaluation of the effect induced by the three types of particles used for the nanoprobe design, strept-MPs (blue shade lines), AuNPs (violet shade lines) and SiNPs (grey shade lines) on the bacterial cells growth. The red line is referred to the growth of bacteria not treated over time. Values are reported as average ± SD, n=3.

The experiments above highlighted possible issues with the use of nanomaterials, such as inhibition of the enzymatic activity or cell growth. However, it is possible that these limitations can be overcome by choosing the optimum concentration of nanoprobe.

During the presented inhibitory and toxicity experiments, the concentration of particles has been chosen discounting the fact that they are different types of particles. The comparison between the different particles is difficult, given that they differ largely in their size and in the material from which are formed. For example, the number of particles in 1 mg of 1000 nm **strep-MPs** will not be the same as in 1 mg of 100 nm of **SiNPs.** Furthermore, **AuNPs** were used in lower concentration due to lower availability.

Enzymatic assay

All particles were tested individually in the presence of both α-glucosidase and β-glucosidase. Different concentrations of particles were incubated with the same amount of enzymes (100 μg/mL) and the kinetics of the recognition event was tracked by measuring the fluorescence output. All nanoprobes, **Glu-5-strept-MPs**, **Glu-6-AuNPs** and **Glu-7-SiNPs** were tested at concentrations of 100, 50 and 25 μM, respectively. The raw data were normalised considering the auto-hydrolysis of the glycosidic bond, which occurs spontaneously in aqueous environment. This

phenomenon was more intense with substrates on the particle surface than when the substrate was in solution. The lowest concentration (25 μM) provided for each particle a very weak signal after normalisation and, therefore, the results cannot be seen in the graph.

The results obtained for **Glu-5-strept-MPs** are shown in *Figure 51.* Analysis of this data leads to a few observations. First of all, it is evident that increasing the amount of particles increased the signal but, interestingly, the enzyme also started to react faster with the substrates on the particle surface. An increase of fluorescence was detectable after only 5 minutes when the particles were used at 100 μM concentrations, while a few more minutes were needed for the enzyme to process the particles at the lower concentration (50 μM) (*Figure 51)*. This phenomenon was not observed when the substrate alone was used at different concentrations (*Figure 32*) and it was not observed for **Glu-6-AUNPs** as well (*Figure 52*). A second important message from the data is that with this type of particle, the selectivity of the detection for the type of glucosidase used is lost. Exactly the same increase of fluorescence is measurable with both enzymes, which could be explained by inversion of stereochemistry during the deacetylation (giving a mixture of α and β glucose), therefore the NPs are recognised by both α-glucosidase and β-glucosidase (green lines and purple lines respectively in *Figure 51*).
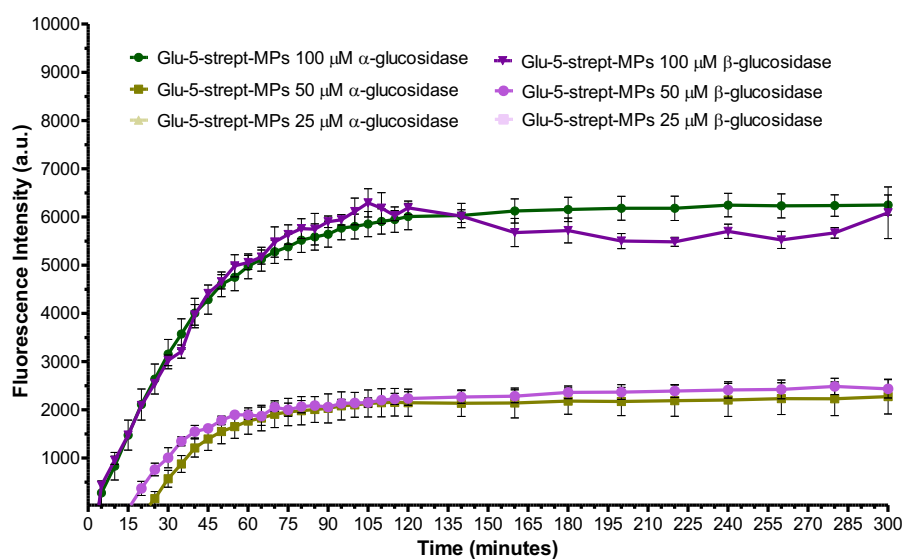
Figure 51: The increase of fluorescence was measured for the particles at each concentration 100, 50, 25 μM was normalised considering the hydrolysis that spontaneously occurred in aqueous environment. Glu-5-strpt-MPs treated with α (green lines) and β-glucosidase (purple lines). Values are reported as average ± SD, n=3.

Figure 52 shows the data obtained using **Glu-6-AuNPs,** which was normalised with the increase of fluorescence for particles that were not treated enzymatically. As expected, the higher the concentration of particles, the higher the fluorescent signal, but no delay was noticeable using a lower amount of particles. Interestingly, in this case, a difference was observed in the activity of the two enzymes. When treated with α-glucosidase (green lines in *Figure 52*) the increase in fluorescence measured was somewhat lower than when treated with the β-glucosidase (purple lines in *Figure 52*). This indicates that, during the synthesis of the **Glu-6-AuNPs**, the anomerisation process takes place more intensively and, therefore, the glucose present at higher amount is likely the one in β-configuration. This could be due to the different conditions used for the glycosylation experiment: 0.1 mM NaOH solution at pH 8 for the **Glu-5-strept-MPs** and NaOH pH 7.7 for **Glu-6-AuNPs**.
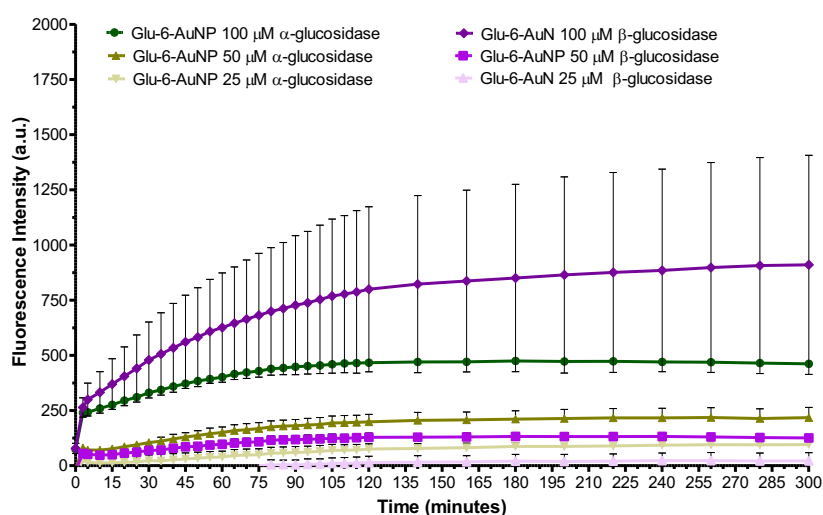
Figure 52: Increase of fluorescence was measured for the particles at each concentration 100, 50, 25 μM was normalised considering the hydrolysis that spontaneously occurred in aqueous environment. AuNP were treated with 100 μg/mL of each type of enzyme: α-glucosidase (green lines) and β-glucosidase (purple lines). Values are reported as average ± SD, n=3.

Glu-7-SiNPs were also tested in the enzymatic assay but, unfortunately, no increase in fluorescence was observed with either enzyme (*Figure 53*). Only the values for the higher concentration (100 μM) were positive after normalisation. This supported the conclusion made before: the functionalisation did not succeed and therefore the increase in size was only indicating the aggregation of the particles.
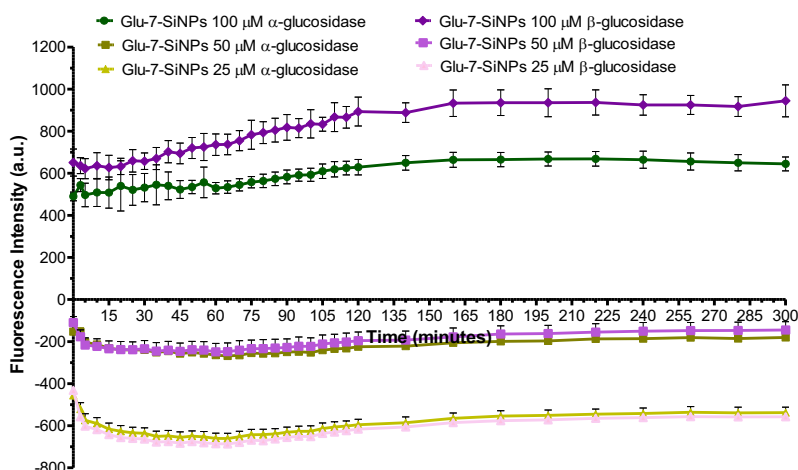
Figure 53: Increase of fluorescence was measured for the particles at each concentration 100, 50, 25 μM was normalised considering the hydrolysis that spontaneously occurred in aqueous environment. No relevant increase in fluorescence was measurable and the particles at 50 and 25 μM after normalisation gave only negative values. Values are reported as average ± SD, n=3.

Bacteria detection activity

All particles were tested for their ability to detect the following types of bacteria: *E. coli, Enterococcus, K. pneumonia, P. aeruginosa and S. aureus* at concentration of 75 CFU/mL in LB broth. The raw data collected were normalised for each type of nanoprobe to account for auto-hydrolysis. All nanoprobes, **Glu-5-strept-MPs**, **Glu-6-AuNPs** and **Glu-7-SiNPs** were tested at a concentration of 50 μM (concentration of NPs defined regarding the substrate). NP samples and bacterial samples were added to sterile 96-well plate and incubated at 37°C under shack measuring fluorescent signal every 10 minutes.

As shown in *Figure 54,* after about 1.5 h of incubation of bacteria with **Glu-6-AuNPs**, the fluorescence increased, signalling the presence of *E.coli, K. pneumonia* and *S. aureus* at 75 CFU/mL. Only after more than 4 h an increase in fluorescence was observed in the samples of *Enterococcus* and *P. aeruginosa*. Considering the long time required for the identification and the very weak fluorescence signal, it can be concluded that **Glu-6-AuNPs** are not suitable for the detection of the last two mentioned types of bacteria. However, they may be useful for the detection of *E. coli, K. pneumonia* and *S. areous.* It is important to highlight that the fluorescence was relatively low and thus the S/N ratio was low.
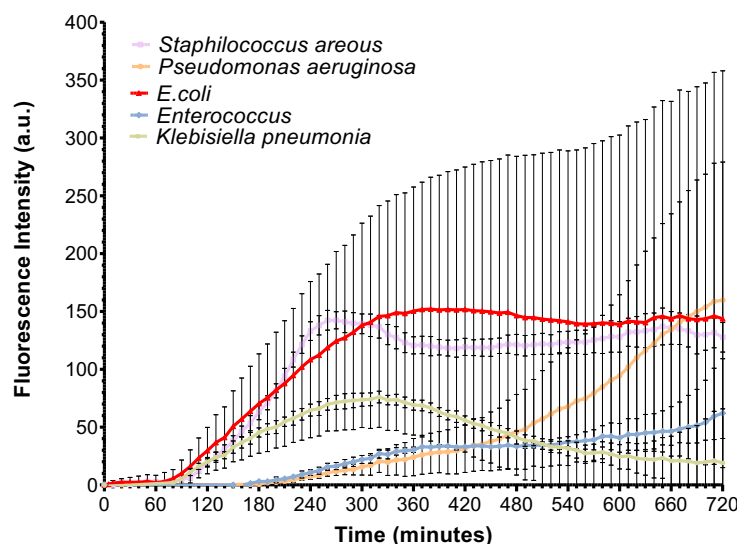
Figure 54: 75 CFU/mL of each type of bacteria was treated with 50 µM of substrate present on the Glu-6-AuNPs surface. Values are reported as average ± SD, n=3.

The same experiments were accomplished using **Glu-5-strept-MPs** at two concentrations, 50 and 25 µM (referred to the substrate on the surface) and incubated with again 75 CFU/mL of each type of bacteria. As seen in *Figure 55*, with this type of particles *E. coli, K. pneumonia* and *S. aureus* were readily detected. An increase in signal was also detectable when incubating *Entercoccus* and *P. aeruginosa* with **Glu-5-strept-MPs**, but the signal was lower and the detection occurred only after about 3 hours. The fluorescent signal at both concentrations increased relatively rapidly. Considering the results achieved for **Glu-6-AuNPs** and **Glu-5-strept-MPs** when treated with *E.coli* it can be clearly noticed the difference in the signal intensity: by using **Glu-5-strept-MPs** the signal was 20 times higher than that one measured for **Glu-6-AuNPs** (*c.a.* 3250 and 150 respectively).

a)

b)
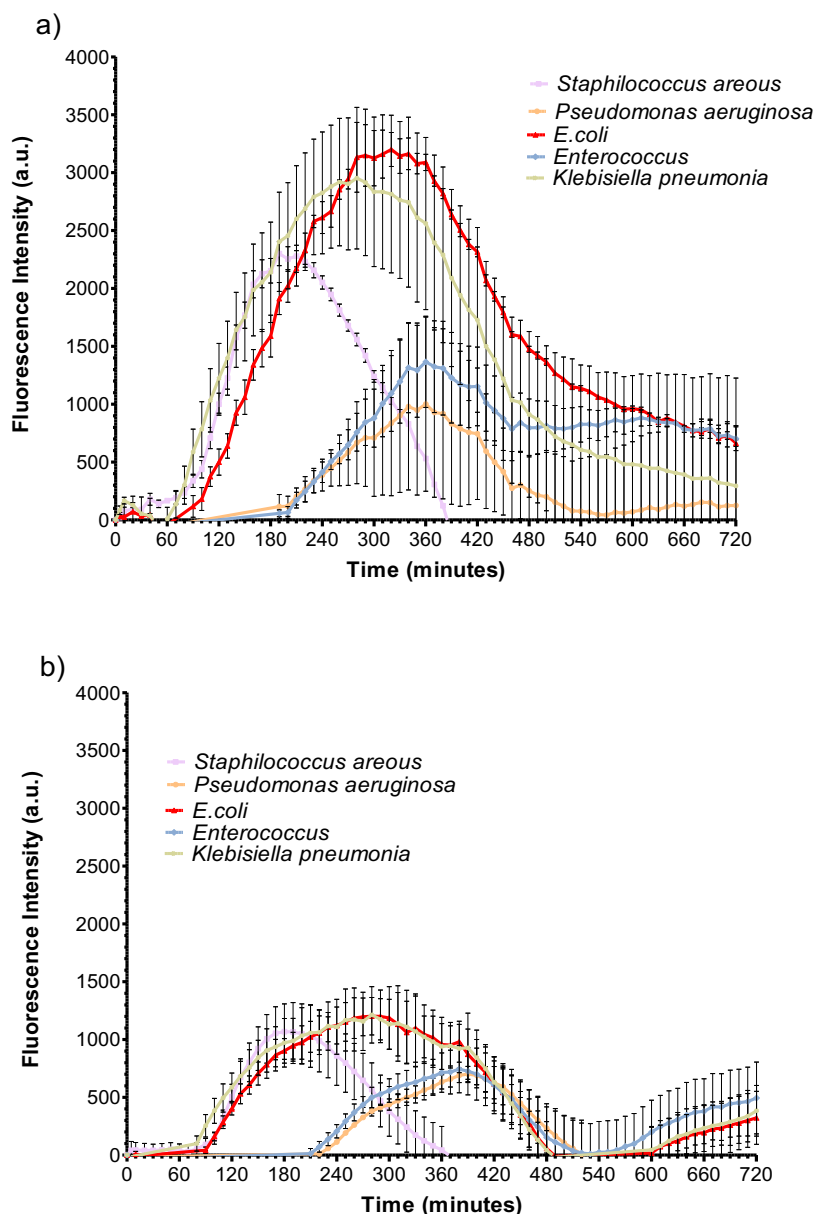
Figure 55: 75 CFU/mL of each type of bacteria was treated with a) 50 μm and b) 25 μm and incubated at 37°C. Values are reported as average ± SD, n=3.

When the bacteria were incubated with **Glu-7-SiNPs,** the increase in fluorescence was insignificant, confirming the negative results achieved in the enzymatic assay (data showed in *Appendix section A2.6*).

Table 25 summarises the detection times required for the detection of the bacteria with each of the different nanoprobes. It can be seen that **Glu-5-strpt-MPs** and **Glu-6-AuNPs** have similar detection capabilities for *E. coli, K. pneumoni* and *S. aureus*, for which the increase in fluorescence was detected after 1 and 1.5 hours, respectively, although the fluorescence signal obtained with **Glu-5-strpt-MPs** was remarkably

higher, translating to a better S/N ratio. The signal detected for **Glu-6-AuNPs** in the presence of *Enterococcus* and *P. aeruginosa* was too low to be considered reliable, while these bacteria can be properly detected by **Glu-5-strpt-MPs.**

Table 25: Detection time required for the detection of different bacteria at concentration of 75 CFU/mL when treated with three different types of nanoprobe tested.

	E.coli	*Enterococcus*	*K.pneumonia*	*P.aeruginosa*	*S.aureus*
Glu-5-strpt-MPs	1 h	3 h	1 h	3 h	1 h
Glu-6-AuNPs	1.5 h	\	1.5 h	\	1.5 h
Glu-7-SiNPs	\	\	\	\	\

3.3.3 Comparison between LOD of substrate and nanoprobe

The efficacy of nanoprobes and substrates in detecting bacteria was evaluated comparing the time required for the detection to occur. *Table 26* compares detection times required for nanoprobes and substrates used at the same concentration, i.e. 50 µM (referred to the substrate on the surface in the case of the nanoprobes) in detecting bacteria at a concentration of 75 CFU/mL. The data disproved the hypothesis given in the introduction regarding the possibility to improve the LOD by attaching the substrate to the surface of nanoparticles. With the particles tested here, no improvement was achieved since no relevant difference was found between the substrate and the nanoprobe in terms of detection time. The table points out even different selectivity for bacteria between nanoprobes and substrates. For instance, **Glu-5-strpt-MPs** were capable of detecting all types of bacteria, although after different incubation times (E*. coli, K. pneumonia* and *S. aureus* were detected after about 1 h, while 3 h were required for the detection of *P. aeruginosa* and *Enterococcus*). **β-4-AUUG** showed to be selective for *E. coli, Enterococcus* and *K. pneumonia* since no relevant increase in fluorescence was observed when it was tested with *P. aeruginosa* and *S. aureus.*

Table 26: Detection time required by substrates and nanoprobe to detect at the concentration of 50μM different type of bacteria at concentration of 75 CFU/mL.[ab] fluorescence value relatively low and *P.areuginosa* were detected only at this low concentration of substrate.

	E.coli	*Enterococcus*	*K.pneumonia*	*P.aeruginosa*	*S.aureus*
Glu-5-Strpt-MPs	1 h	3 h	1 h	3 h	1 h
Glu-6-AuNPs	1.5 h	\	1.5 h	\	1.5 h
Glu-7-SiNPs	\	\	\	\	\
β-4-AUUG	1 h	1 h	1 h	3 h[a]	\
β-4-MUD	1.5 h	1-1.5 h	1.5 h	3 h[b]	1.5 h
α-4-MUD	2 h	2 h	3 h	\	3 h

A few considerations could explain the lack of improvement when applying nanotechnology to the design of new tools for bacterial detection. (i) The loss of specificity of the substrate when linked to the NP surface; (ii) the inhibitory effect on the enzymatic activity that the particles themselves induced; (iii) the material type and size of particles could interfere with the bacterial growth, especially if used at high concentration. However, the intensity of the signal recorded can be relevant in defining the efficacy in the detection method since the higher the signal, the higher the S/N ratio. From this point of view, **Glu-5-Strpt-MPs** and **β-4-AUUG** showed to have a better fluorescent profile in compared to **Glu-6-AuNPs** and **α-4-MUD/β-4-MUD**.

3.4 Conclusions

During the fabrication of the nanoprobes, many issues were encountered. These were mainly related to the low reactivity and high instability of the fluorophore, 4-AAU. Among the three nanoprobes, only for two did the functionalization steps succeed: **Glu-5-strpt-MPs** and **Glu-6-AuNPs**. For **Glu-7-SiNPs** the functionalisation did not occur, as indicated by DLS data which provided clues that the surface of the particles was not functionalised with the substrate after all. This could be due to the low reactivity of compound **7** with the hydroxyl groups on the SiNPs surface. Alternatively, the fluorophore could be only absorbed by electrostatic interaction on the surface rather than been covalently attached on the particles, which leads to the removal of the compound during the washing steps. Good results were achieved with the other two nanoprobes, in particular with **Glu-5-strpt-MPs.** The results achieved during

enzymatic assay and bacteria experiments for the **Glu-5-strpt-MPs** and **Glu-6-AuNPs** nanoprobes showed that, during the glycosylation step, not all α-glucose was converted to the β-anomer, which instead occurred with 100% yield during the synthesis of the substrate. As a result, the nanoprobe surface was functionalised with both α- and/or β-glucose substrates. This became obvious when an increase of fluorescence was observed testing **Glu-5-strpt-MPs** with both α- and β-glucosidase. This lack of specificity decreases the possibility to distinguish between different bacteria. The difference between the type of bacteria detectable using the substrate **β-4-AAUG** and that using the nanoprobe is noteworthy. In particular, **Glu-5-strpt-MPs** required more time to detect *Enterococcus,* which was quickly detected by using **β-4-AAUG.** On the other hand, the substrate was not successful in detecting *S. aureus*, while incubating it with **Glu-5-strpt-MPs** an increase of fluorescence was easily detected. This is likely related to the combination of both α- and β-glucose on the surface of **Glu-5-strpt-MPs,** which leads ultimately to a reduction in the specificity of the detection.

3.5 Future work

The issues related with the instability and/or low reactivity of the fluorophore chosen, 7-hydroxy-4-coumarin acetic acid (4-AAU), could be presumably solved using a different switchable fluorophore. Further stability issues were observed with carbohydrate used. Indeed, isomerisation led to unexpected results, when using and α-glucose for the synthesis the substrate reached was instead selective for the β-glucosidase, or to the loss of selectivity for the specific enzyme during the functionalisation of the nanoparticles. For this reason, the carbohydrate could be replaced with a different molecule, e.g. amino acid, or other compounds easier to handle. Carefully choosing a different recognition element would allow even to enhance the selectivity for specific bacteria.

Magnetic particles functionalised with the switchable substrate (**Glu-5-strpt-MPs**) seemed to be a promising way for the development nanoprobes capable of bacterial detection. In particular, it is important to avoid the anomerisation process in order to preserve the desired selectivity in the detection. The inhibitory and toxicity effect observed using magnetic particles is a concern, since it could limit the efficiency in

detecting the enzymatic activity. Size appeared to be a possible source of inhibitory effect, it may be sensible to evaluate the possibility of using smaller streptaviding-coated magnetic particles. The sensitivity of detection given by using NPs could be remarkably improved by enhancing the efficiency of the functionalisation and preserving the selectivity for a specific enzyme.

The possibility of multiple functionalization of nanomaterials could be exploited for a multiple detection. Labelling and /or functionalising NPs with different substrates specific for different targets would be eventually possible to enhance the specificity for specific type of bacteria. For instance, by designing SiNPs loaded with pH-responsive dye (e.g. methylene red) and coating them with the 'on-off' fluorescent substrate (β-4-AAUG) present in chapter 2, it might be possible to distinguish between bacteria that preferentially use glucose as main source of energy and how the carbohydrate is metabolised. In particular, an increase in fluorescence would indicate the presence of the bacteria (glycosidic bond cleavage) while the colour of the pH-indicator used will indicate if the glucose is then metabolised with formation of acids. This would give an extra information regarding the bacteria detected, ultimately restrict the range of the possible candidate.

Chapter 4

pH-responsive SiNPs for oral drug delivery

4.1 Introduction

Therapies can be administered in different ways, depending on the chemical properties of the active compound, the type of disease, the age of the patient, whether the treatment can be administered orally or through the respiratory tract or injected intravenously, etc. Each of the administration pathways possesses advantages and disadvantages. Oral administration represents the most suitable dosage method and is usually the preferred choice, due to its simplicity, convenience and minimal invasiveness. Besides these advantages, formulating active compounds for oral administration represents a challenge due to the harsh environments which characterise the gastrointestinal (GI) tract. The stomach is characterised by acidic pH (pH 1-5) and metabolic enzymes which are essential for digestion. The intestine is divided into different sections having slightly different pH and different roles in the digestive process. However, it can be generally said that in the small intestine, nutrients and elements are absorbed entering directly the blood stream through which they will reach the organs of interest. The residual material that reaches the large intestine is then excreted as faeces thanks to peristaltic movements which occur in this tract of intestine (*Figure 56*).
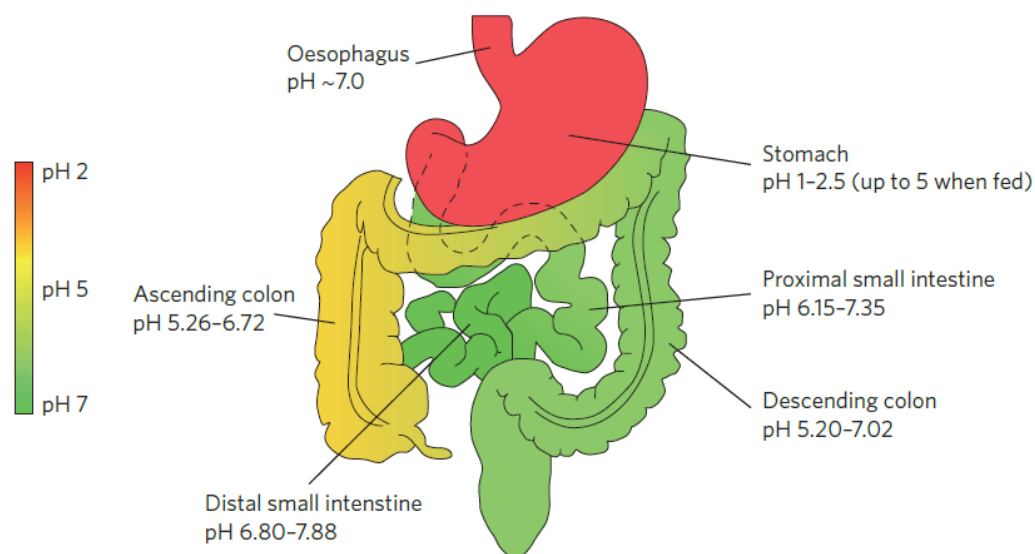
Figure 56: Representation of the GI track divided into the different environments of which it is formed. The low gastric pH (pH 1-5) and various enzymes are fundamental for the demolition of food in the essential components, which can then be absorbed in the intestine where pH values increase up to 6-8. Adapted from reference[150].

The endothelial cells and mucous form a thick barrier which allows to discriminate between what needs to be absorbed and what can be cleared as faeces. Small compounds can be adsorbed via passive transcellular transport and specific molecules can be actively internalised into the endothelial cells (transcytosis, receptor-mediated or carrier-mediated endocytosis). For macromolecules having unfavourable properties, the only way to be adsorbed and to avoid faecal clearance is to permeate between adjacent cells (paracellular transport via cell-cell junctions). Considering this, it has become evident that for a drug to be orally administered it needs to overcome two main obstacles: (i) it should be resistant to the low pH and to the enzymes present in the stomach, and (ii) the active compound should be able to permeate the enteric barrier and enter the bloodstream. The advantages and disadvantages of oral administration are summarised in *Table 27.*

Table 27: Advantages and disadvantages of oral administration of treatments.

Advantages	Disadvantages
• Good patient compliance ○ better suits life-routine ○ less invasive and painless	• Dose dumping ○ ingestion of food/beverage of particular substances can alter drug release and therefore the plasma concentration
• Cost/effective manufacturing ○ relatively cheap production (equipment, personal and material)	• Limited drug bioavailability ○ drug solubility ○ MW

Even though more than 60% of drugs available on the pharmaceutical market are formulated for oral administration, this route is often hampered by low solubility of the drug in aqueous environment, vulnerability to degradation in the gastric environment and low permeability through the different membranes present along the GI tract. Solubility and permeability determine the bioavailability of the drug *in vivo* and, ultimately, its efficacy. Additionally, some types of molecule can be particular unsuitable for oral administration, as is the case of proteins and peptides. These types of macromolecule often suffer from degradation/denaturation in the stomach, due to the low pH and enzymatic activity (peptidases), and they permeate the intestinal endothelium with difficulty due to their hydrophilicity and high molecular weight (MW).

Improvements have been made in oral formulations which led to the development of matrices capable of controlling drug release. Oral controlled release matrices have become an integral part of the pharmaceutical industry and they have been the centre of research thanks to the benefits over conventional dosage forms. In comparison with parenteral routes, oral delivery for instance allows for a better pharmacokinetic profile of the active compounds. Using oral formulation, the release of the drug can be prolonged, thus reducing the dosage intervals, which is crucial for treatment of chronic diseases. As mentioned already, oral therapies are better accepted by patients since they are less invasive in terms of life-routine, easier to administer and painless[151,152].

4.1.1 Strategies to enhance oral bioavailability

In order to overcome the pharmacokinetic-related issues, drugs have often been conjugated with other molecules, forming active derivatives or so called 'pro-drugs'. Linking specific moieties to the active compound can achieve an enhancement of hydrophilicity, extension of half-life in blood and a reduction in clearance. However, the added moiety should not alter the biological activity of the drug and, ideally, especially in the case of the pro-drugs, the linkage should be cleaved in order to give the active compound that induces the expected biological effect [151-155]. One of the limitations observed by using this strategy to enhance the pharmacokinetic of active compound is that some solubility/permeability enhancers have shown cytotoxicity to the endothelium, as is the case, for instance, when surfactants are used[156].

This strategy of conjugating the drug to enhance its pharmacokinetics has been shown to be especially effective in the case of proteins. For instance, an oral glucagon-like peptide-1 (GLP-1) analogue (NN9924) produced by Novo Nordisk is currently under phase III clinical trial[157]. GLP-1 is a peptide which, by activating the specific receptor (GLP-1R), induces the production of insulin and it is thus used as a treatment for type II diabetes[158,159]. The oral formulation was developed by Novo Nordisk in collaboration with other two pharmaceutical companies, Emisphere Technlogy Inc. and Merrion Pharmaceuticals, which developed unique technologies, Eligen[160] and GIPET[161], respectively, which enhance adsorption and therefore the efficiency of used compounds.

4.1.2 Nanotechnology-based oral drug delivery systems

With the advent of nanomedicine, the properties of nanoparticles have been exploited to overcome pharmacokinetic limitations observed for some drugs[162]. Taking advantage of the high surface/volume ratio and the high loading capacity of nanoparticles made from different biodegradable materials, active compounds can be internalised in the matrix or linked on their surface, enhancing the pharmacokinetics and bioavailability of the active compound[163,164]. Nanomaterials have proven to be efficient in protecting the drug in unfavourable environments, such as those in the stomach, avoiding inactivation due to acidic pH and/or enzymatic activity. Furthermore, it has been proven that nanoparticles can interact more easily with cells,

thus enhancing the permeability of the drug and its efficacy[165]. By changing the formulation and modifying the chosen nanomaterial's surface chemistry, it is possible to develop carriers which actively determine the pharmacokinetics of the drug considered[166]. By rationally choosing the composition of the NPs, the carrier can be formulated in order to have a specific kinetics of drug release, while they can be directed to the specific biological target by placing recognition moieties on their surface. In this way, the efficiency of the active compound can be enhanced and its potential toxicity decreased. The advantages reached by applaying nanotechnology to oral drug delivery compared with the oral administration of the simple drug are summarised in *Table 28*[167,168].

Table 28: Advantages acquired exploiting nanotechnology for the development of oral drug delivery systems compared to the direct oral administrations of drugs.

Advantages	Applications/achievements
Improved solubility	Delivery of poorly water-soluble drugs
Protection	Sensitive drugs are protected from low gastric pH and enzymatic degradation
Improved permeability	Transcytosis of drug across the tight intestinal barrier
Targeting	Delivery of drug to specific part of the GI track
Cellular uptake	Large molecules can be delivered inside cells
Delivery tracking	Combining therapeutic agents with imaging tools allows to track the site of drug delivery and give the possibility of 'real-time evaluation' of the *in vivo* drug delivery

Improved solubility, permeability and drug protection

It has been estimated that roughly 40% of investigated active compounds fail the transition to the clinical product due to poor aqueous solubility, which leads ultimately to a low bioavailability[163]. One possible strategy is to alter the chemical structure of the compounds in order to make its properties more favourable. Alternatively, if loaded inside particles, an insoluble drug can successfully be carried to the target and it is also protected from unfavourable environmental conditions as the one in the GI tract. This is crucial for peptides and proteins, which are particularly vulnerable. Importantly, even poorly soluble drugs, such as 5-fluorouracil[169], risperidone[170] and paclitaxel[171,172]

have been successfully encapsulated, showing a valuable alternative to exploit their remarkable therapeutic effects[173].

Delivery tracking

Understanding the fate of NPs during *in vivo* and *in vitro* experiments is essential to determine the efficiency of the formulation when used in therapy. It is important to have a clear picture of the path followed by the particles *in vivo* and their interactions with cells. Inert nanomaterials, such as liposomes and SiNPs, which don't have fluorescence or magnetic properties for instance, offer the possibility of multi-functionalisation. Aside from the active compound they can for instance be loaded/functionalised at the surface with dyes which make them fluorescent and allowing the tracking of the particles with sophisticated fluorescent microscopy techniques. Using NPs with intrinsic properties, e.g. graphene, quantum dots and magnetic particles, multiple functionalisation is not required since the properties of the nanomaterial itself can be exploited to evaluate the nanocarrier fate, as for instance the fluorescent properties of graphene and quantum dots[174-177].

Drug-NPs absorption

When using NPs as carriers for drug delivery, it is essential that the drug, once the target is reached, is released from the particles becoming available to induce the desired effects. There are three possible scenarios using NPs as delivering systems: i) the drug can be released from the particles in the proximity of the target, thus inducing its biological effect locally or being absorbed by cells and diffusing into the body through the circulatory system. ii) NPs can anchor to the cell surface and release the drug or iii) the NPs loaded with drug can be internalised by cells, which is desired especially when the drug itself has low cellular permeability (*Figure 57*). In the following sections, these possibilities are evaluated.
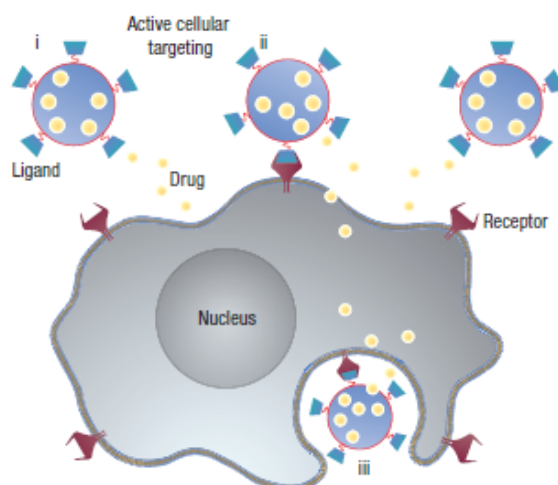
Figure 57: Once in proximity of cells the NPs can: (i) release their carrier contents in close proximity to the target; (ii) attach the membrane of the cell acting as an extracellular sustained-release drug depot; (iii) be internalise into the cell. Adapted from reference[178].

Delivery and controlled release

The concept of targeted drug delivery refers to the possibility of directing the active compound to the desired organ, whilst avoiding undesired accumulation in 'healthy' tissue. This can be achieved by functionalising the nanocarrier's surface with bio-relevant molecules, such as antibodies, carbohydrates, receptor substrates, which bind selectively to the target. In the case of therapies administered orally, targeting refers mainly to directing drugs to specific parts of the GI tract, usually to the intestinal epithelium. In particular, the small intestine is the site where absorption occurs, therefore the drug will enter the blood stream system and diffuse in the body. Alternatively, in the case of inflammatory diseases and bowel/colon cancers, the enteric lumen represents the actual target for the oral therapy. The main challenge in oral delivery is to formulate the treatment so that it can avoid degradation in the unfavourable gastric environment and can reach the intestinal lumen where the drug can be absorbed. Nanotechnology promises to be efficient in protecting the drug from both the acidic environment and enzymatic activity in the stomach, but once the intestine is reached, the drug needs to be released from the carrier.

In order to achieve this, pH-responsive nanomaterials have been designed which guarantee the protection of the loaded cargo at low pH (pH 1-4 in the stomach) and its release in natural/basic environments (pH 6-7 in the intestine). Different strategies are

available for imparting pH-responsive behaviour to nanomaterials: the introduction of ionisable groups, which determine solubility/structural changes in response to environmental pH-changes, the use of hydrophobic/hydrophilic polymers or acid/basic sensitive bonds, situations that all result in the release of the drug from the carrier[179]. Different pH-responsive NPs have been made by using, for instance, polyanions,[180-182] such as the Eudragits, hydroxypropyl methyl cellulose phthalate (HPMCP) and hyaluronic acid (HA), which can dissolve at different pH ranges. Moreover, combining polyanions and polycations, it is possible to reach the desired pH sensitivity required for each application.[183,184] For example, Makhlof *et al.* developed colon-specific nanospheres bycombining poly(lactic-co-glycolic acid) (PLGA) with a methacrylate copolymer into which budesonide was incorporated[185]. Changing the formulation of the NPs it was possible to design a carrier from which the drug was released slowly but continuously, maintaining the active compound in the therapeutic window and ultimately diminishing the number of administrations required. Han *et al.* designed pH-sensitive HA-nanoparticles (HA-NPs) for oral administration of insulin. They showed that the protein is protected and not released in the gastric environment, reaching the intestinal lumen where the HA-NPs significantly increase the insulin transport through enterocytes. Data showed that using HA-NPs, the pharmacokinetics of insulin were improved, stabilising the level of glucose for a longer time in comparison with the solution of insulin administered orally or intravenously (*Figure 58*)[186].
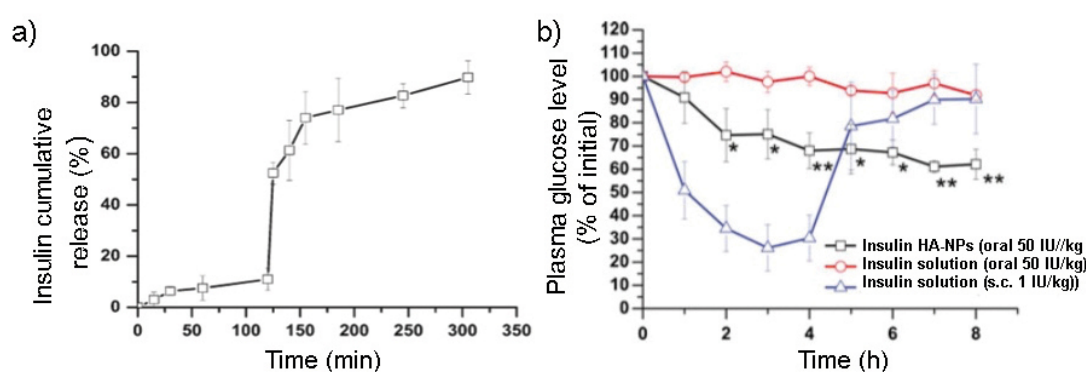
Figure 58: a) HA-NPs kinetic release of insulin over time when exposed at pH 1.2 and subsequently pH 6.8 mimicking the environments of the GI tract. b) Plasma glucose level (% of initial): insulin-loaded HA-NPs administered orally (black line) showed to reduce and maintain constant the level of glucose in a more desired way compared with insulin solution administered orally (red line) or subcutaneously injected (blue line). Adapted from reference[186].

Cellular uptake

Depending on their physical-chemical properties, NPs can interact more or less efficiently with cells. This is a crucial aspect which must be considered when developing nanoparticles for oral administration due to the issues related with the enteric barrier discussed. There are three main mechanisms by which drugs and even NPs can be absorbed in the intestine: (i) the paracellular route, (ii) active receptor-mediated endocytosis, and (iii) passive endocytosis (*Figure 59*).
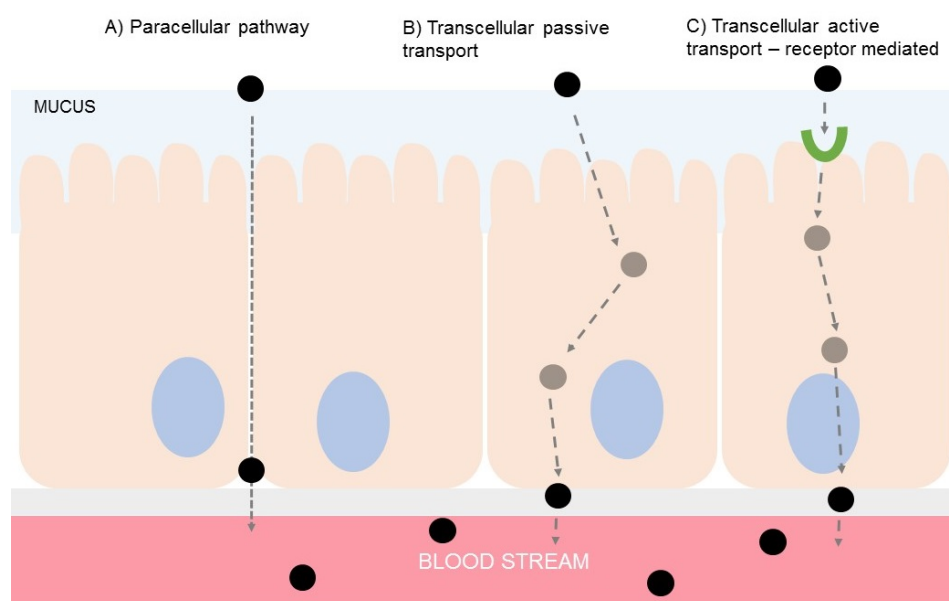
Figure 59: Representation of the three main up-take strategies available for nanoparticles: A) paracellular transport between the thin cellular junctions B) passive transcellular transport occurs when particles interact with cells. C) receptor mediated transcellular transport requires the specific receptor-NPs interaction.

The paracellular route is unlikely for macromolecules and NPs, since the junction between adjacent cells in the enteric endothelium is particularly narrow. The use of some polymers in solution or assembled as nanoparticles, such as chitosan, poly(acrylic acid)-based nanoparticles, surfactants and thiolated polymers, can enhance paracellular transport in the intestinal lumen, but not without a certain risk of toxicity[187-190].

Particles can be instead internalised by passive or receptor-mediated transcellular transport. Different attempts have been made to functionalise the surface of nanoparticles with specific molecules capable of binding to receptors available on the intestinal lumen. For instance, particles have been coated with lectins, proteins or glycoproteins capable of binding sugars on the cell surface, which are involved in

recognition processes. Some interesting results were achieved but, unfortunately, lectins proved to be highly immunogenic, often inducing irritation of the GI tract[191-193]. For example, NPs actively uptaken by intestinal cells were designed by coating the surface of particles with biotin, clathrin and vitamin B_{12}, for which specific receptor-mediated endocytosis mechanisms have been observed on cells, but no relevant achievement have been documented to date[194-198].

Unspecific uptake of NPs instead occurs once particles interact with the cell surface, according to the size of the particles and their surface properties. By coating NPs with polyvinyl alcohol (PVA) or vitamin E, the absorption of the particles is enhanced due to their adhesion properties[199-201]. NPs coated with PEG and chitosan have been widely investigated for their ability to interact with enterocytes and be internalised[202-205].

The ability of NPs to adhere to the mucin can enhance drug bioavailability. By interacting with the mucin, the carrier prolongs its permanence in the intestinal lumen, which increases the amount of drug that can be released in proximity to the enterocytes, reaching a favourable gradient for its absorption. Alginate and chitosan have been largely exploited for their adhesive properties to formulate oral preparations[206,207]. Many works can be found in the literature regarding NPs coated with chitosan in order to enhance the uptake of the particles and it seems to prolong the release of the active component, allowing reduced the intake of the medication required for the therapy[168,208]. Alongside the use of chitosan to develop mucin-adherent nanocarriers, good results have also been achieved using PEG or alginates. Comparing chitosan-coated NPs with PEG-coated NPs for their efficiency in delivering salmon calcitonin, results showed that a better pharmacokinetic is reached using chitosan due to the burst release observed using PEG[209,210].

In order to develop better carriers for oral delivery, NPs have been coated with combination of polymers. For instance, Prego *et al.* synthesised new nano-capsules composed of chitosan grafted with PEG, such that the resultant PEGylated chitosan NPs exhibited the combined properties of both materials, e.g. stability in the gastric environment, low cytotoxicity and enhanced bioavailability[211]. Despite the positive results achieved by using adherent particles (chitosan especially), different limitations are related to this adhesive property. In particular, the adhesion is often unspecific and can therefore occur on the gastrointestinal mucous, such that the particles never reach

the intestinal epithelium. Moreover, the adhesion effect depends on the turnover of the mucous; indeed, the particles will be removed as soon as the fresh mucin replaces the old one.

It is well known that cell-NPs interaction and cell internalisation are strongly related to the physico-chemical properties of the particles. Many studies have focused on the relationship between NPs and internalisation and results indicate that mainly NPs having diameters between 50-150 nm are better accumulated inside cells[212-214]. The hydrophilicity of the NPs surface has also been shown to determine the cellular internalisation efficiency, as well as the surface charge and the material from which they are made. Win *et al.* found that ultra-small NPs (d < 50 nm) are less efficiently internalised by cells, indicating a diameter of 100-200 nm as the better range [215]. Tang *et al.* compared 50 nm and 200 nm camptothecin-loaded SiNPs during *in vivo* experiments and found that since smaller particles are better internalised by cells, they can effectively improve cancer therapy by delivering efficiently the active compound inside the neoplastic cells (*Figure 60*)[216].
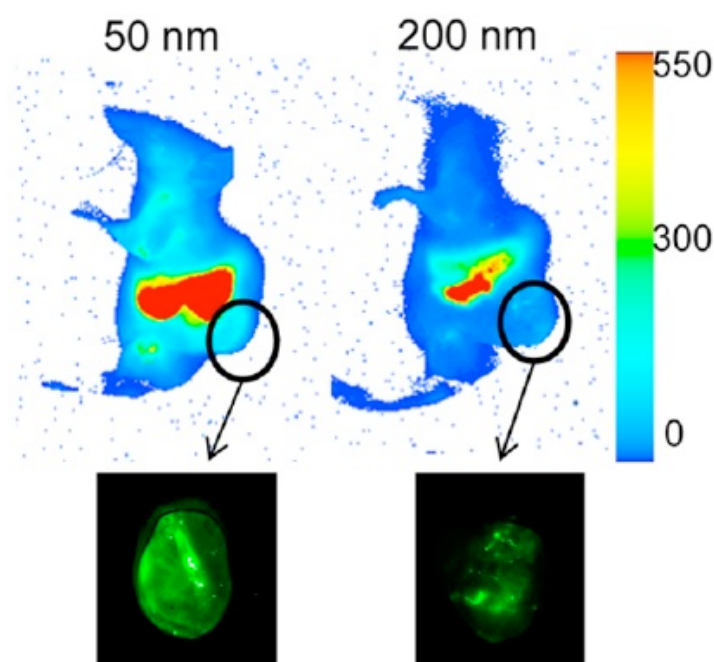
Figure 60: Difference efficiency of treatment using 50 and 200 nm of camptothecin-loaded SiNPs. The black circles indicate the tumour position. The higher efficiency of the treatment with 50 nm SiNP is observed by the size-decrease of the tumour and by the brighter signal in the tumour which indicates a better internalisation of the particles. Adapted from reference[216].

4.1.3 Some examples of nanomaterials applied for oral drug delivery

Liposomes

One of the first types of nanoparticles used for oral drug delivery were liposomes, which are vesicles of diameter between 30 to 1000 nm. They comprise one or more lipid bilayers formed by reorganisation of synthetic or natural phospholipids and are biodegradable and biocompatible. The possibility to scale up the reaction while maintaining good control on the particle size drove the attention of pharmaceutical industry, which has invested greatly in these materials. By changing the formulation of liposomes, it has been possible to overcome some of the limitations encountered when using these materials, e.g. the low loading capacity, the fast leakage of cargo and the rapid clearance. While the loading properties of drug in liposomes are mainly related to the drug itself (normally weak bases which should precipitate in the liposome), the retention capability was enhanced using cholesterol in the formulation to tighten the fluid phospholipid bilayers[217-219]. In order to obtain release of the drug when needed, pH-responsive liposomes were achieved by using different lipids, such as palmitoyl homocysteine. Alternatively, other mechanisms of release have been achieved by changing the formulation of the liposome (thermo-responsive liposome, enzyme-triggered release and ultrasound sensitive liposome)[220-223]. 'Stealth' liposomes, with improved half-life, have been made by increasing the amount of oligosaccharides on the carrier surface or by grafting PEGs[224-226]. A disadvantage often observed when using liposomes is their instability during storage and they are not often used for oral administration since they tend to suffer from degradation once in the GI track[227]. One of the few examples of liposomes applied to oral administration is the work of Situ *et al.* evaluating the difference in efficiency of melatonin delivery using liposomes synthesised by supercritical carbon dioxide (SO-CO_2) or by thin-film hydration (TFH); they showed that the technique used for the synthesis can affect the behaviour of the nanocarrier [228].

Solid lipid nanoparticles

Solid lipid nanoparticles (SLN) are a more recent discovery than liposomes; indeed, they have been designed in an attempt of overcome the limitations observed with

liposomes[229]. The difference between them is that SLN are formed from solid lipids. They share with liposomes some important characteristics, such as the possibility of large scale production, biodegradability and biocompatibility. However, SLN guarantee a better protection of the drug, a prolonged release and they better retain the cargo during storage. Their use is limited by their colloidal instability, their unpredictable gelation tendency and the fact that incorporation of drugs is usually low[168,230,231]. Baek *et al.* developed chitosan-coated SLN for oral delivery of curcumin. Using these chitosan-coated curcumin-loaded SLN, the bioavailability was fund to be 6- to 9-fold higher than that of curcumin solution and the chitosan-coating reduced remarkably the burst release of the compound in the acid stomach observed using plain SLN[168]. Rawat *et al.,* using combining different types of complex lipids in the formation of the solid lipid core, developed a novel oral carrier for repaglinide (anti-diabetic drug) having better loading capacity, improved drug retention and better stability during storage in comparison to SLN formed from a single lipid[232]. In order to overcome the above limitations, the modification of their formulation led to a new generation of liposomes, called nanostructured lipid carriers (NLC), which are formed by a combination of both liquid and solid lipids[233-235].

Polymeric nanoparticles

Polymeric nanoparticles (PNPs) have attracted the interest of many research groups and pharmaceutical companies for the development of novel carriers for oral drug delivery[236]. What make these particles attractive is that they are easy to prepare and there is a wide flexibility in their formulation thanks to the variety of polymers available (chitosan, alginate, PLGA, PLA, PEG, Eudragit, etc.)[181,237,238], which are mostly biocompatible and approved for human use by the FDA. By changing the type of polymer used, or by combining different types of polymer, it is possible to achieve PNPs having the desired size, surface charge and hydrophobicity[210,239]. Their surfaces can also be easily functionalised in order to direct the nanomaterial to a specific target and, by using certain types of polymer (Eudragit, HPMCP), pH-responsive PNPs can be synthesised to obtain a specific pharmacokinetics of drug release[186]. The interest in the application of PNPs for oral administration is the protection of the cargo that can be achieved and their tendency to adhere to the mucous, enhancing the bioavailability of the drug[240,241]. There are, unfortunately, a few limitations related with their used: PNPs

are commonly characterised by low loading capacity, low bioavailability and high burst release.

In *Figure 61* a schematic representation of the structural differences between liposomes, SLN and polymeric NPs is given. Liposomes are spherical vesicles having at least one lipid bilayer which allow them to incorporate water. Thus, while liposomes can incorporate both hydrophilic and hydrophobic compounds SLN can only be loaded with lipophilic compound since the core of the particles is formed by solid lipids. Polymeric nanoparticles are characterised by a considerable design-flexibility thanks to the possibility of choose between different type of polymers and self-assembly conditions, enabling modulation of physico-chemical parameters (size, surface charge, hydrophobicity) and drug release properties[242].
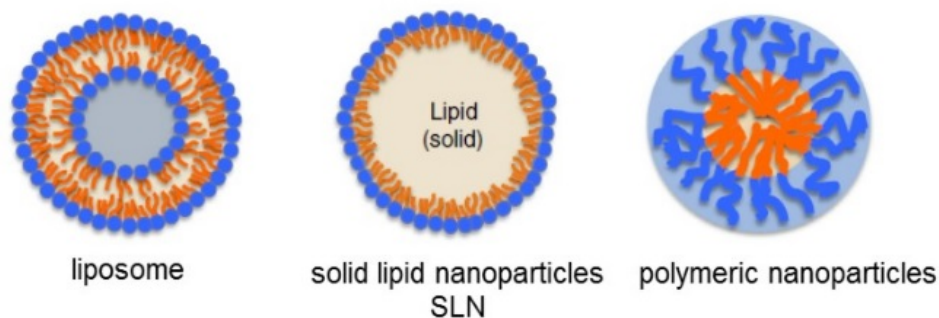
Figure 61: Structural differences between liposome, solid lipid nanoparticles and polymeric nanoparticles. Adapted from reference[242].

Silica nanoparticles

Among those functional materials developed in the last two decades for drug delivery, diagnostic sensors, imaging agents and labelling probes, silica nanoparticles (SiNPs) have gained special attention due to their straightforward synthesis, uniform morphology, controllable diameter, modifiable surface charge, easy functionalisation and significant biocompatibility. Many research groups have proved that by modifying the synthetic conditions, SiNPs of specific size and morphology can be obtained[243,244], while positively or negatively charged particles can be reached simply changing the silanes used for their synthesis. Due to the presence of positively/negatively charged groups on the surface, the functionalisation by conjugation or electrochemical absorption is regarded as simple and led to the development of various type of SiNPs. Indeed, linking antibodies or molecules capable of specifically interacting with

biological targets, a wide assortment of nanoparticles for drug delivery systems (especially for cancer treatment) has been developed. Lu *et al.* evaluated the efficiency of the anticancer drug comptothecin (CPT) when loaded in mesoporous SiNPs (MSN/CPT) or in mesoporous SiNPs functionalised with folic acid (FMSN/CPT). No increase of weight was measured (*Figure 62-A*) but a decrease of the tumour volume was instead visible after 14 days of daily treatment with 1 mg of FMSN/CPT (*Figure 62-B*). The images of the mice at the last day of treatment highlight the efficacy of FMSN/CPT in treating the tumour in comparison with MSN/CPT and CTP treatments (*Figure 62-C*). Not only folic acid showed to be useful to improve the bioavailability of the active compound targeting it to cancer cells, but the functionalised particles showed to be better biocompatible inducing less side effects[245]. Coating the particles with polymers (PEG and dextran) can modify the NP-cell interactions, leading to particles having a longer half-life, slower clearance and, ultimately, better bioavailability[246].
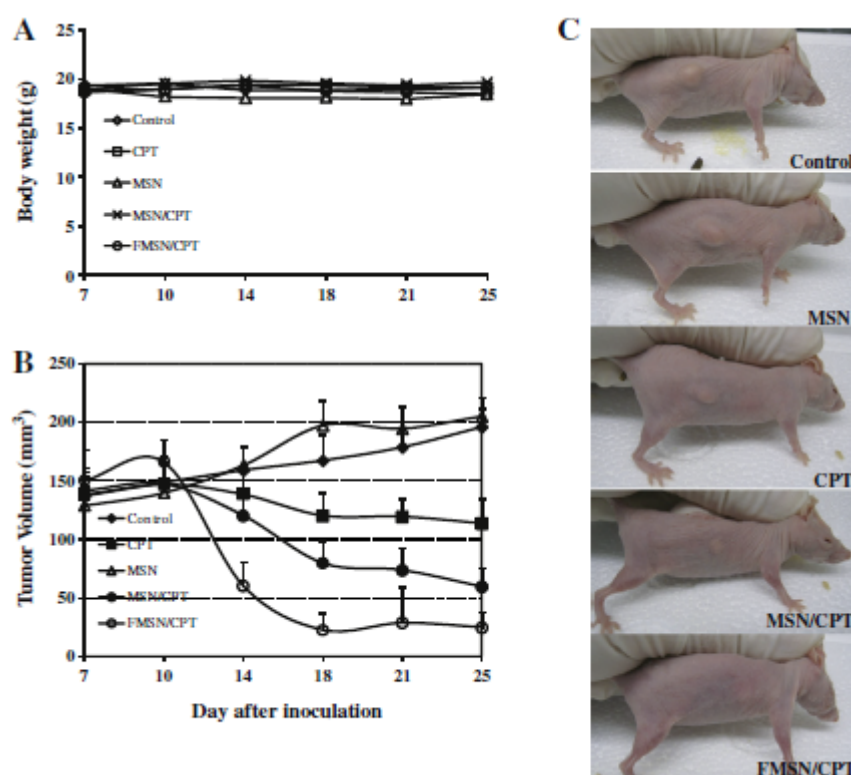
Figure 62: Human pancreatic cell line (MicaPaca-2) have been injected subcutaneously. The experiment started after 7 days when the tumour was palpable. Evaluation of the different efficiency of the anticancer drug comptothecin (CPT) when loaded in mesoporous SiNPs (MSN/CPT) or in mesoporous SiNPs functionalised with folic acid (FMSN/CPT). A) no increase of weight is measured with all type treatment but using FMSN/CPT the volume of the tumour decreased visibly after 14 days (B and C). Adapted from reference[245].

SiNPs are considered biodegradable and biocompatible, and are widely used in the food and cosmetic industries. However, it has been largely studied and confirmed by independent studies that the physico-chemical properties of SiNPs can affect their biocompatibility dramatically. For instance, small particles (< 50 nm) induce higher cytotoxicity, likely due to the higher cell internalisation compared with larger particles[247,248]. At the same time, smaller particles have been shown to be useful in improving the activity of drugs, especially anticancer drugs, by enhancing the cell uptake of compounds.

The above considerations refer to SiNPs in general, but they can be divided into two types: microporous SiNPs (SiNPs) and mesoporous SiNPs (MSN). SiNPs have pores < 2 nm and are therefore regarded as 'non-porous', while MSN have pores between 2 and 50 nm, which are even visible by TEM as shown in *Figure 63*.
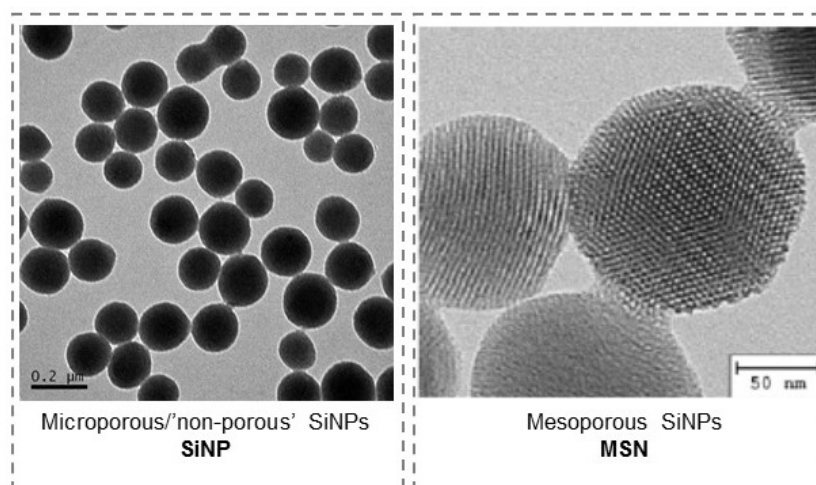
Figure 63: TEM images of non-porous/microporous SiNPs on the left and mesoporous SiNPs (MSN) on the right highlighting the difference in the matrix between the two well-known types of SiNPs. TEM of SiNPs is a self-acquired image while TEM of MSN is adapted from reference[90].

The possibility to functionalise the internal surface of pores exposing terminal groups available for conjugation makes MSN particularly attractive for drug delivery. The drug can be loaded inside the particles after synthesis, by diffusion of the solubilised cargo through the pores, from where it can then be released with different kinetics depending on the design of the MSN[249]. In the case of microporous SiNPs, the loading takes place during the formation of the particles itself and, thanks to their high loading capacity, the protective effect on the cargo and the transparent properties, their find greater application in bioimaging[17].

Although there are few studies available in the literature regarding microporous SiNPs applied to drug delivery[6,250,251], it was rationalised that the better protection of the cargo that can be achieved using microporous SiNPs could be exploited for the development of carriers for oral drug delivery, where, as discussed earlier, the protection of the drug from the harsh gastric environment remains a challenge. Peng *et al.* proved this protective effect using microporous SiNPs to deliver an antisense oligonucleotide capable of interfering with gene expression, with possible application in treating viral infections and cancer[252]. Studies proved that the spectroscopic properties of a photosensitizer can be retained better when covalently loaded into microporous SiNPs, reducing their toxicity to undesired cells[253,254]. The protective role played by microporous SiNPs has attracted the attention of researchers looking at oral delivery, especially for proteins. For example, Andreani *et al.* designed microporous SiNPs coated with muco-adhesive polymers for the oral delivery of insulin,[255] proving that even when changing the type of polymer used, the biocompatibility is maintained when testing the nanocarrier *in vitro* with Caco-2 and HepG2 cell lines[256]. Furthermore, the diameter and level of porosity of MNS can limit the type and amount of drug loaded, while even bulky molecules can be carried in high amounts by microporous SiNPs[257].

4.1.4 Project aims

Herein, we evaluate the possibility to exploit the pH-sensitivity of SiNPs to develop an alternative carrier for oral drug delivery. In particular we evaluated the different drug release from NPs having slightly different composition of the silica matrix. The release and degradation profiles of microporous SiNPs formulated using different ratios of different silane derivatives have been evaluated when exposed to different physiological environments, mimicking the conditions encountered along the GI tract (acidic stomach and basic intestinal lumen). The designed particles should retain the cargo when exposed at pH 4, which corresponds to the gastric conditions, but the release should occur at pH 7.4, allowing selective drug release in the intestinal lumen. Gastric pH is around 1.5-3 in a fasted stomach while it can rise up to pH 4-5 in a fed stomach. Since we noticed higher instability of SiNPs with the increase in pH, we chose to accomplish the experiment at pH 4 (fed stomach) in order to test particles in an environment where they more likely degrade, with the assumption that if exposed at lower pH as the one of fasted stomach (pH 1.5-3), the results would be comparable. In

particular, five types of NPs have been synthesised using different ratios of two different silane derivatives. The structural difference between the two derivatives should lead to different polymerisation degrees during the formation of the NP's matrices. The desired result is to obtain particles having higher or lower crosslinking density, which could lead to a different dissolution and, therefore, different drug release profiles.

Further, three different dyes, with varying levels of hydrophobicity, have been loaded inside the NPs during formation of the silica core. The different dyes have been even loaded following two different methods, covalent linkage and physical entrapment, in order to evaluate whether the proprieties of the cargo and the loading technique can determine the efficiency of the loading and the release profile.

For simplicity, from now on, the simple term of 'SiNPs' will be applied to 'microporous SiNPs'.

4.2 Experimental

4.2.1 Materials

Cyclohexane (anhydrous, 99.5%), 1-hexanol (anhydrous, $99%), Triton® X-100, aminopropyl trimethoxysilane [APTMS] (97%), tetraethyl orthosilicate [TEOS] (99.99%), ethyltriethoxysilane (96%)[ETEOS], ammonium hydroxide solution (28% w/v in water, ≥99.99%), 3-(trihydroxysilyl)propyl methylphosphonate monosodium salt (42% w/v in water) [THPMP], fluorescein isothiocyanate isomer I (≥90%)[FITC], fluorescein sodium salt [NaFlu], sodium phosphate dibasic (>98.5%), sodium phosphate monobasic (>98%), sodium carbonate (≥99.5%), sodium bicarbonate (≥99.5%), were purchased from Sigma Aldrich (Gillingham, Kent). Sodium carbonate (0.1M) combined with sodium bicarbonate (0.1M) yielded the pH 8.8 (1:9 v/v respectively) and pH 10.6 (9:1 v/v respectively) solutions used for NP degradation, and are hereafter referred to as 'pH 10.6' solutions. Methylene blue hydrate was purchased from Acros Organics (Fischer Scientific). Absolute ethanol, Transparent Nunc Maxisorb 96 well plates, phosphate buffer saline tablets (one tablet dissolved in 200 mL DI water yields 0.01 M phosphate buffer, pH 7.4) were purchased from Fisher Scientific (Leicestershire, UK). Hereafter, 'PBS' refers to 0.01 M PBS, pH 7.4. Carbon Films on 400 Mesh Grids Copper were purchased from Agar Scientific (Stansted, UK).

4.2.2 Synthetic methods

SiNPs synthesis

Dye precursor formation: In a dried glass vial, FITC (2.5 mg) was dissolved in 2 mL of 1-hexanol and APTMS (5.6 µL) was added. The reaction was allowed to proceed over 2 hours under a N_2 and then 0.162 mL of the mixture was collected and added into the prepared microemulsion, which preparation is described as follow.

Synthesis of FITC-SiNPs series: All nanoparticles were formed in a microemulsion prepared by combining cyclohehexane (7.5 mL), 1-hexanol (1.133 mL), Triton® X-100 (1.894 g) and DI water (0.48 mL) in a 30 mL plastic bottle under constant stirring. For the formation of the silica core, different types of silane (TEOS and ETEOS) in different ratios were used, considering as 100% the number of mmol of TEOS used in the

protocol usually followed. Five different types of SiNPs with differently-formulated silica matrices were synthesised: 100% TEOS (FITC-SiNP$_{100TEOS}$), 75% TEOS-25% ETEOS (FITC-SiNP$_{75TEOS}$), 50% TEOS-50% ETEOS (FITC-SiNP$_{50}$), 25% TEOS-75% ETEOS (FITC-SiNP$_{75ETEOS}$) and 100% ETEOS (FITC-SiNP$_{100ETEOS}$).

Table 29: TEOS/ETEOS ratio used for the silica core formation

	TEOS % (µL)	ETEOS % (µL)
FITC-SiNP$_{100TEOS}$	100% (100)	/
FITC-SiNP$_{75TEOS}$	75% (75)	25% (24)
FITC-SiNP$_{50}$	50% (50)	50% (48)
FITC-SiNP$_{75ETEOS}$	25% (25)	75% (72)
FITC-SiNP$_{100ETEOS}$	/	100% (92)

Once the silanes were added, 0.162 mL of the dye precursor solution was added. After 30 minutes, 40 µL of ammonium hydroxide was added to trigger polymerisation. The mixture was stirred for further 24 hours. Nanoparticle shells were synthesised by adding 50 µL of TEOS, followed by 40 µL of THPMP and 10 µL of APTMS after 20min and 5min between each other. After 24h, the microemulsion was broken by adding 30 mL ethanol. Formed SiNPs were purified by centrifugation (14000 rpm, 10 min) and re-dispersion in ethanol (3x). After purification, the nanoparticles were stored in ethanol at 4°C.

Synthesis of MB-SiNPs and NaFlu-SiNPs series:

3 mM solutions of methylene blue (MB) and fluorescein sodium salt (NaFlu) were prepared and used as the aqueous phase of the microemulsion to prepare MB-SiNPs and NaFlu-SiNPs, respectively. The silica core was formed using the TEOS/ETEOS ratios detailed above. 30 minutes after addition of the silanes, 40 µL of ammonium hydroxide was added to trigger polymerisation. The mixture was stirred for a further 24 hours. Nanoparticle shells were synthesised by adding 50 µL of TEOS, followed by 40 µL of THPMP and 10 µL of APTMS after 20min and 5min between each other. After 24h the microemulsion was broken by adding 30 mL ethanol. Formed SiNPs were purified by centrifugation (14000 rpm, 10 min) and re-dispersion in ethanol (3x). After purification the nanoparticles were stored in ethanol at 4°C.

Buffers preparation:

Phosphate buffers at different pH were prepared mixing 0.2 M sodium phosphate dibasic and 0.2 M sodium phosphate monobasic and adjusting the pH to 4, 6 and 7.4 using 5 M NaOH and 5 M of HCl.

4.2.3 Analytical methods

Dynamic Light Scattering (DLS):

SiNPs characterization: NPs of different series (SiNP-FITC, SiNP-NaFlu and SiNP-MB) were dispersed at a concentration of 500μg/mL in DI water. Their size and ζ-potential were analysed in a disposable folded capillary cell (DTS1070) at RT (~ 25°C) using Malvern Zetasizer. Final values are reported as average of three measurements (n = 3) ± SD.

SiNP-FITC stability study during 1 week of incubation in different pHs: 250μg/mL of SiNP-FITC$_{100TEOS}$, SiNP-FITC$_{75TEOS}$, SiNP-FITC$_{50}$, SiNP-FITC$_{75ETEOS}$ and SiNP-FITC$_{100ETEOS}$ were isolated and re-dispersed in 1 mL of each buffer (pH 4, 6 and 7.4) and incubated at 37°C. Size and ζ-potential were measured for each sample every day for 7 days. The values are reported as average (n = 3) ± SD.

Transmission Electron Microscopy (TEM):

Images were taken on a Joel JEM-3200FS transmission electron microscope at 250, 200, 150 and 100kV magnification.

SiNPs characherisation: 5μL of NPs in water (500μg/mL) was added on 'Carbon Films on 400 Mesh Grids Copper' and allowed to evaporate. Using ImageJ software, at least 100 NPs per image were analysed statistical values for NP diameter.

SiNPs dissolution – Eppendorf assay: The pellet isolated after centrifugation, for each particles, incubated at different conditions, was washed 3 times with water in order to remove residues salts from the buffer. The pellet was finally re-dispersed in 200 μL of DI filtered water, added to on 'Carbon Films on 400 Mesh Grids Copper' and allowed to evaporate.

UV-Vis analysis:

A Tecan Infinite M200 Pro Safire microplate reader was used for the majority of absorbance and fluorescence emission measurements. Samples were added to Nunc Maxisorb 96 well plates before being read.

Quantification of dye loaded: In order to quantify the amount of dye loaded during the synthetic procedure, 200 µg of each type of SiNPs were shaken (600 rpm) at 37°C in sodium carbonate/sodium bicarbonate (1:9) buffer at pH 10.6. After 5 hours, the samples were centrifuged (14000 rpm, 10 min) and no pellet was observed, meaning that the particles had dissolved. 24 hours were required for the complete dissolution of MB-SiNPs. Three wells of the 96-well plate were filled with 200 µL of the supernatant isolated after centrifugation. The signal was read at:

- FITC-SiNPs: 490-525 nm (λ_{ex}- λ_{em})

- NaFlu-SiNPs: 456-518 nm (λ_{ex}- λ_{em})

- MB-SiNPs: 660 nm (Abs)

The signal given by FITC, NaFlu and MB molecules free in solution was compared to a fluorescence/absorbance-based calibration curve of known concentrations of each dye (FITC, NaFlu and MB, respectively) at pH 10.8. The amount of dye loaded in 200 µg of particle were calculated and expressed as a concentration (µM). From the values obtained, the number of molecules per NP was calculated (Appendix A3.1 for details).

Degradation assay: Two methods have been used to define the kinetics of degradation and, therefore, dye release, from the SiNPs with different silica matrices. Both experiments were carried out in phosphate buffer at three different pHs, namely 4, 6 and 7.4, to mimic different physiological environments. The degree of drug release was evaluated by measuring the amount of dye present in the supernatant comparing the values measured with the calibration curve (fluorescent-based or absorbace-based) achieved for each dye (FITC, NaFlu and MB) at the corresponding pH. Depending of the NPs analysed, the quantification of the dye in the supernatant was accomplished using the wavelengths mentioned above. All experiments were accomplished in triplicates using three different batches of particles. The values achieved from the independent experiments are reported as average (n = 3) ± SD.

Eppendorf method (for FITC-SiNPs, MB-SiNPs and NaFluSiNPs): 250 µg of SiNP were washed once by centrifugation and re-dispersion in water before dispersion in 1 ml of each phosphate buffer (pH 4, 6 and 7.4). For each sample in each buffer, 7 samples were prepared, one for each checkpoint. The samples were shaken at 37°C at 600 rpm. After 1, 2, 4, 6, 8, 10 and 24 hours, the samples were centrifuged (14000rpm, 10 min) and 700 µL of the supernatant were removed and the remainder discarded. The pellet isolated after centrifugation was washed twice by centrifugation and re-dispersion in water, then used for TEM analysis.

Dialysis method (only for FITC-SINPs): 500 µg of FITC-SiNPs were washed once by centrifugation and re-dispersion in water before dispersion in 1 mL of each buffer. The samples were loaded in the dialysis bag and submerged in 30 mL of each phosphate buffer (pH 4, 6 and 7.4) in a plastic battle. The samples were stirred at 37°C for 7 days and the dye release was checked every day. For the analysis, 2 mL of buffer were withdrawn from the bottle and replaced with 2 mL of fresh buffer.

GI tract-like assay (only for FITC-SiNPs): 200 µg of FITC-SiNPs were washed once by centrifugation and re-dispersion in water before dispersion in 1 mL of phosphate buffer at pH 4. The samples were shaken at 37°C, at 600 rpm. After 2 hours the samples were centrifuged, 300 µL of the supernatant were used to fill three wells of a 96-well plate and the fluorescence was measured (490-525 nm). The remaining NP suspensions were filled with 300 µL of fresh buffer pH 4 and incubated again. Again, after 2 hours the samples were centrifuged and the supernatants completely removed and used for the fluorescence analysis, while the pellets were re-dispersed in 1 mL of buffer at pH 7.4. The samples were incubated under shaking and the above procedure was repeated every 2 hours. The experiment was stopped after 14 hours.

4.3 Results and Discussion

The formation of SiNPs is based on the sol-gel method, where the silica derivative is firstly hydrolysed under basic conditions and then the thus-formed reactive intermediates condense as shown in *Figure 64*. [258]
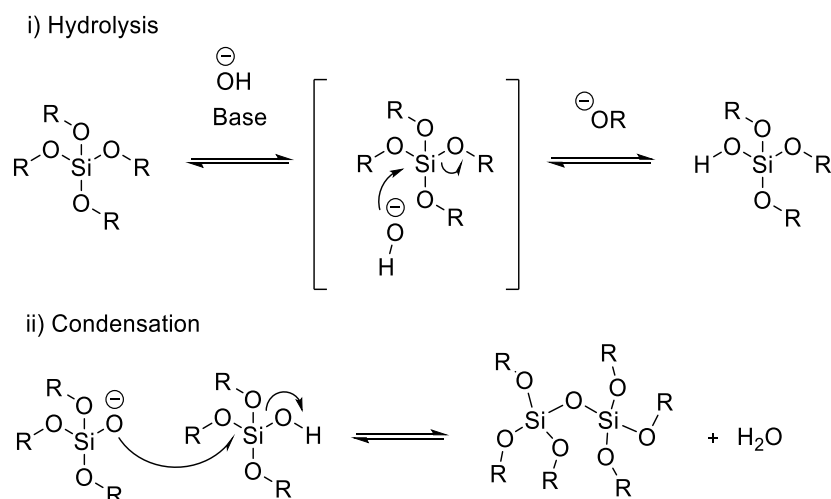
Figure 64: i) Hydrolysis of silica derivative in basic conditions and subsequently ii) condensation between hydrolysed monomers.

The Stöber and reverse microemulsion methods are the two most popular and largely studied protocols developed for the synthesis of SiNPs. The Stöber method allows the preparation of SiNPs on a large scale, the production is easy and the hydrolysis/condensation occurs in a water/alcohol mixture without need for surfactants, which are often difficult to remove completely. The diameter of particles synthesised by the Stöber method can vary between in the range 50-2000 nm[259]. While the NP size can be controlled by changing the synthesis parameters, it is complicated to control the dispersity and morphology of the particles[259,260].

In the present work, SiNPs have been synthesised using the reverse microemulsion method by which spherical, monodisperse SiNPs of diameter 50-100 nm can be synthesised. The precise control of size and properties of the particles is important, since these parameters determine NP-cell interactions, e.g. cytotoxicity, as previously discussed. In this method, a water-in-oil microemulsion is formed and stabilised by the addition of surfactants, as shown in *Figure 65-i.* The silane derivative used (e.g. tetraethyl orthosilicate– TEOS) and the catalytic base (e.g. ammonium hydroxide solution) are confined in the water droplets where the hydrolysis/condensation

process occurs. The first small micelles formed will fuse together and exchange their contents to promote the growth of SiNPs (*Figure 65-ii and iii*). It has been proven that nanoparticle size can be tuned by changing the water/surfactant ratio, the type of surfactant used, and by varying the amounts of ammonium hydroxide and TEOS[261]. A silica shell can be grafted around the silica core by adding further amounts of silanes to give core/shell microporous SiNPs (*Figure 65-iv*). The type of silane used for the shell formation plays two important roles: firstly, it can help to electrostatically stabilise the particles in suspension and, secondly, their chemical groups exposed on the particle surface (such as amino groups, thiol groups, etc.) can be used as anchors for further functionalisation of the particles. 3-(Trihydroxysilyl)propyl methylphosphonate (THPMP) and (3-aminopropyl)trimethoxysilane (APTMS) have been used for the shell formation, leading to the presence of negatively charged phosphate groups and positively charged amino groups on the nanoparticle surfaces, respectively (*Figure 65-vi*). Negatively charged particles were synthesised using THPMP and APTMS at a molar ratio 2:1. The final negative charge is due to the higher amount of THPMP used and to its higher reactivity. Presumably, this is because THPMP presents hydroxyl groups already available for the condensation, while with APTMS methoxy groups need to be hydrolysed first (*Figure 65-v*). The negative surface charge of the particles ensures electrostatic stabilisation of the particles in suspension.
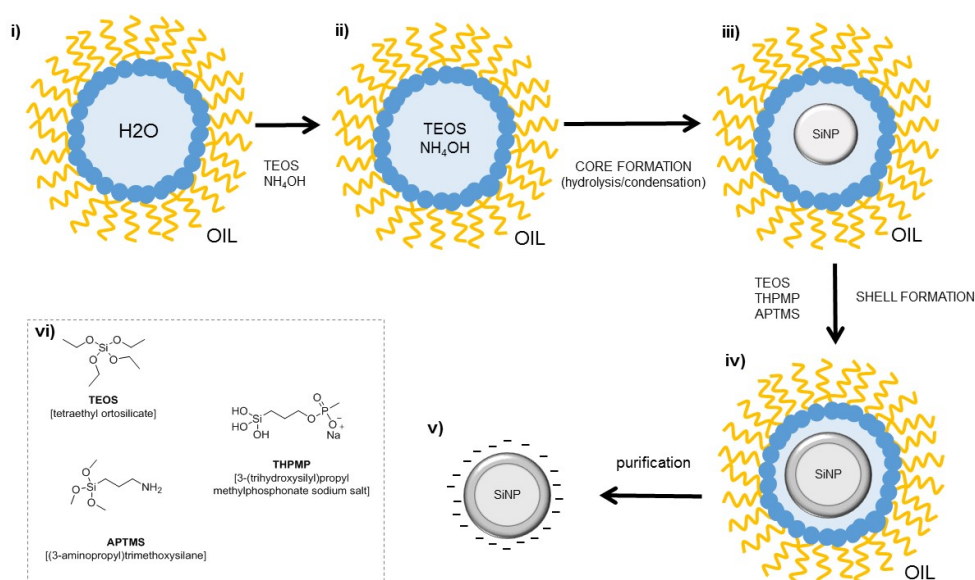
Figure 65: Reverse microemulsion method for the synthesis of SiNPs. Once added to the W/O microemulsion (i) TEOS and the catalyst (NH$_4$OH) move to the water droplets (ii) were polymerisation starts forming the core of the particles (iii). Adding further silica derivatives (TEOS, THPMP and APTMS) the shell can be form around the core (iv). After purification negatively charged SiNPs are isolated (v).

Along with the normal procedure, in the present work the cores of the SiNPs were synthesised using different ratios of TEOS and (ethyltriethyloxysilane) ETEOS (*Figure 66*). As can be seen, the two silica derivatives differ in the number of sites available for the hydrolysis/condensation process: 4 in TEOS, but only 3 in ETEOS. Therefore, it was hypothesised that the silica matrix formed from ETEOS would have lower crosslinking densities than those formed from TEOS, as depicted in *Figure 66*. In order to prove this hypothesis, 5 different types of SiNPs were synthesised using 100:0, 75:25, 50:50, 25:75 and 0:100 as the TEOS:ETEOS ratio for the core formation. The shells were formed according to the standard protocol[262], with TEOS:THPMP:APTMS were added in the molar ratio 4:2:1.

ID sample	TEOS %	ETEOS %
FITC-SiNP$_{100TEOS}$	100	/
FITC-SiNP$_{75TEOS}$	75	25
FITC-SiNP$_{50}$	50	50
FITC-SiNP$_{75ETEOS}$	25	75
FITC-SiNP$_{100ETEOS}$	/	100
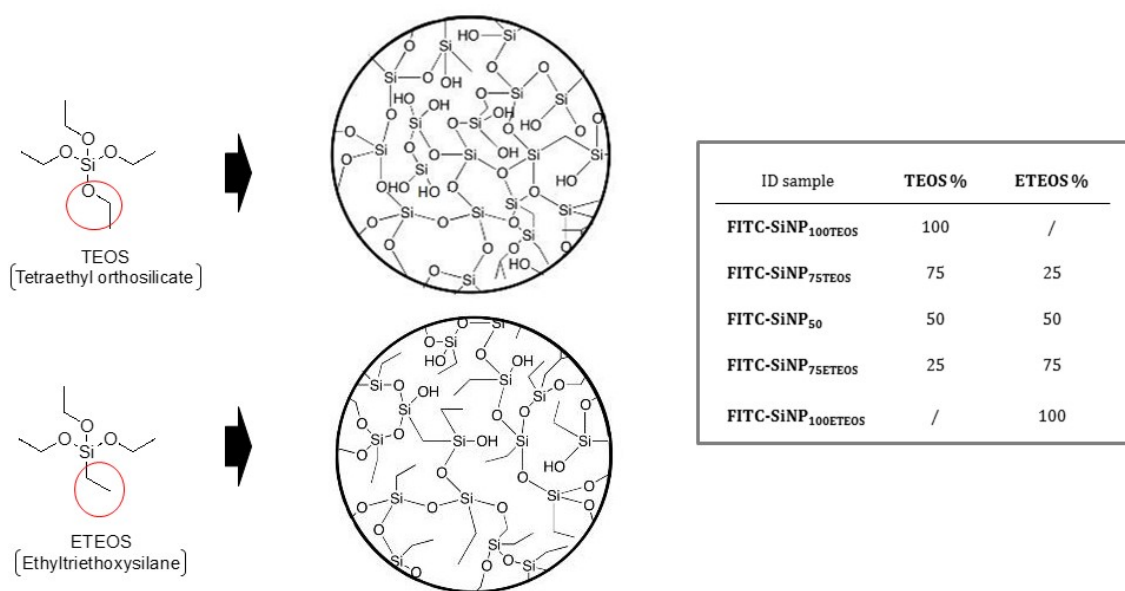
Figure 66: Structure of TEOS and ETEOS with the difference circled. In the table are indicated the ration (%) of TEOS/ETEOS used for the synthesis of each type of particles and the corresponding name.

Three different sets of particles have been synthesised, loading different dyes with different hydrophilicity in the silica core using different methods. The comparison between the results achieved with the different set of particles allow to determine if the hydrophilicity of the cargo and the technique used for the loading could determine the loading capacity of the particle and the release profile. Therefore, fluorescein sodium salt (NaFlu), fluorescein isothiocyanate (FITC) and methylene blue (MB) having different hydrophilicity (NaFlu>FITC>MB) were loaded into the silica matrix by covalent loading (FITC) or physical absorption (NaFlu and MB). The covalent loading requires the conjugation of the dye with a silane derivative which can be involved in

the matrix formation during polymerisation. Indeed, the conjugate formed by FITC and APTMS can actively participate in the silica core formation (Figure 67-i). The hydrophilic fluorescein sodium salt (NaFlu) and the hydrophobic methylene blue (MB) were instead simply added into the microemulsion system and were therefore simply physically entrapped in the matrix without chemical reaction (Figuere 67-ii).
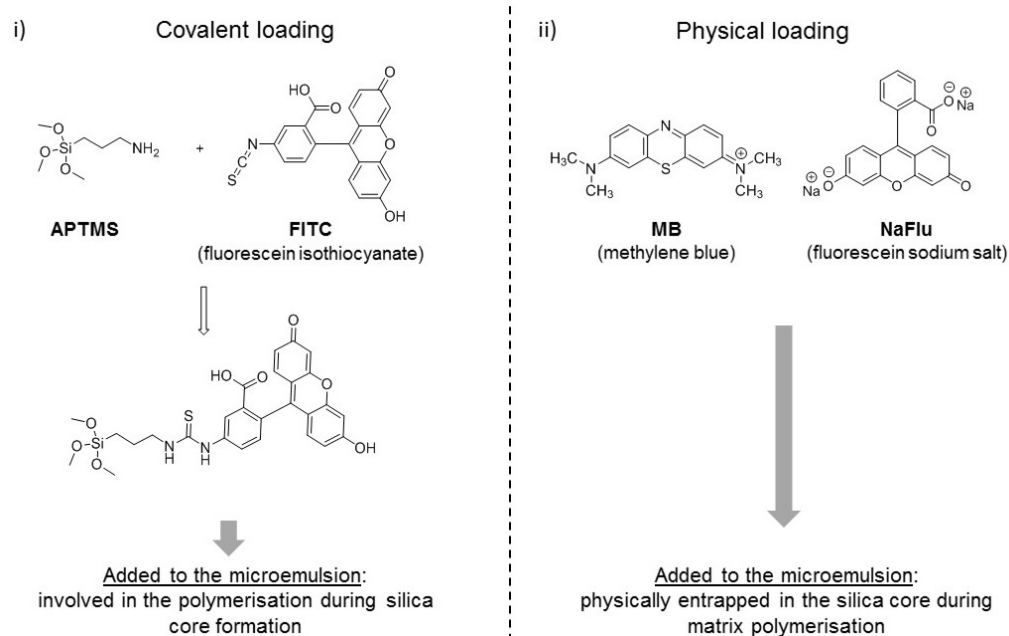
Figure 67: Schematic representation of the covalent loading method (i) in which FITC is firstly conjugated with a silica derivative (APTMS) thus the conjugate will participate at the hydrolysis/condensation process. In the physical loading method (ii) the dyes (MB and NaFlu) are simply entrapped in the matrix during the NPs formation.

Herein, the drug release is evaluated considering therefore three variables: 1) the composition of the silica matrix of the particles, 2) the properties of the dye loaded and 3) the method used for the dye loading.

4.3.1 Synthesis and characterisation of FITC-SiNPs

SiNPs used for the present work have been synthesised by the reverse microemulsion method following a procedure described by Bagwe et al.[263] and developed by our group[262,264,265]. In this case, FITC was covalently loaded into the matrix by previous conjugation with APTMS, forming a thiourea linkage as shown in *Figure 67-i.*

The microemulsion is formed by mixing DI water, cyclohexane as the oil phase, and Triton X-100 and hexanol as surfactant and co-surfactant, respectively. Five different ratios of TEOS:ETEOS (respectively 100:0, 75:25, 50:50, 25:75 and 0:100) were used

for the core formation. Immediately after silane derivative, FITC-APTMS solution and ammonium hydroxide are added to the microemulsion and the hydrolysis-condensation starts in the water droplets. After 24 hours, TEOS, THPMP and APTMS were added and left to react for another 24 hours, allowing the synthesis of the silica shell around the core. Once the particles were washed via cycles of centrifugation and re-dispersion in ethanol, FITC-loaded SiNPs were isolated whose structure is summarised in *Figure 68*.
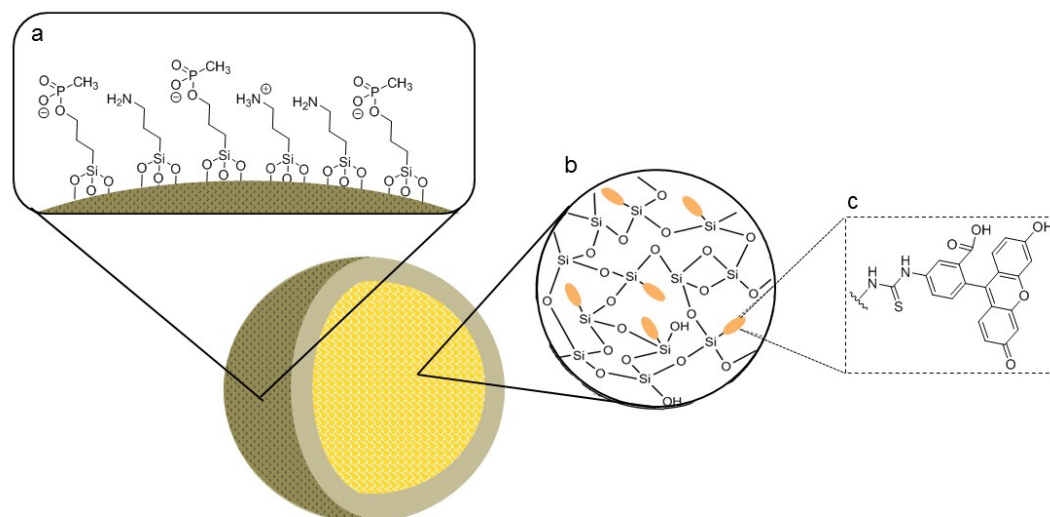
Figure 68: Schematic representation of the final structure of FITC-SiNPs. a) The surface is negatively charged due to the use of THPMP/APTMS for the shell formation. b) The matrix of the particle is formed by polymerisation (hydrolysis/condensation) of different ratios of TEOS:ETEOS. FITC-APTMS conjugate is covalently loaded in the NPs core (c).

All particles were characterised by DLS and TEM, confirming that they were spherical, monodisperse and relatively small (*Table 30*). According to DLS measurements, the particles have diameters ranging from 132.5 to 222.9 nm. It is noticeable slightly larger particles were obtained on increasing the amount of ETEOS used for the core (e.g. 222.9 nm measured for **FITC-SiNP$_{100ETEOS}$** compared with 132.5 nm of **FITC-SiNP$_{100TEOS}$**). Using ETEOS, a decrease in monodispersity and an increase of surface charge was noticed; for **FITC-SiNP$_{100TEOS}$** and **FITC-SiNP$_{100ETEOS}$** the PDIs were 0.177 and 0.275 and the ζ-potential were -27.8 mV and -22.3 mV, respectively. The diameter of the particles was also evaluated from TEM images, giving a different perspective compared to the DLS measurements. The average diameters of the particles measured by TEM are reported in *Table 30.*

Table 30: DLS values measured for each sample at concentration 0.5 mg/mL in water at RT. For each measurement, diameter, PDI and ζ-potential are reported as average ± SD, n=3. TEM images were processed using ImageJ software and the diameter (nm) was determined for each sample as average values (n = *c.a.* 100) ± SD. The ratio between the values measured by DLS and the one calculated from TEM are reported as well.

	DLS			TEM	Ratio
	Ø (nm)	PDI	ζ(mV)	Ø (nm)	ØDLS/ ØTEM
FITC-SiNP$_{100TEOS}$	132.5 ± 1.25	0.177 ± 0.016	-27.8 ± 0.80	72 ± 8	1.8
FITC-SiNP$_{75TEOS}$	144.1 ± 1.46	0.139 ± 0.013	-25.9 ± 1.01	79 ± 16	1.8
FITC-SiNP$_{50}$	170.0 ± 2.15	0.147± 0.005	-24.0 ± 0.27	80 ± 13	2.1
FITC-SiNP$_{75ETEOS}$	163.7 ± 1.72	0.102 ± 0.038	-26.4 ± 1.26	58 ± 20	2.8
FITC-SiNP$_{100ETEOS}$	222.9 ± 6.04	0.275 ± 0.030	-22.3 ± 0.65	50 ± 31	4.5

A clear discrepancy between values obtained by DLS and TEM can be observed. By DLS the diameter measured for **FITC-SiNP$_{100ETEOS}$** is larger compared with the other types of particles tested (222.9 nm compared with the 132.5 nm of **FITC-SiNP$_{100TEOS}$**). However, when measured by TEM the same particles are actually the smallest (albeit with the widest distribution) having 50 nm compared with the 80 nm diameter of **FITC-SiNP50**; the latter appeared to be the largest by this technique. In particular, the difference between the DLS and TEM values increases with the amount of ETEOS used for the core formation. The ratio between the diameter of **FITC-SiNP$_{100TEOS}$** measured by DLS and TEM is indeed 1.8, while the value calculated for **FITC-SiNP$_{100ETEOS}$** is higher, at 4.5, as reported in *Table 30.* The difference in the data obtained from the two analytical methods is related mainly to the different procedure required for sample preparation. DLS requires particles in suspensions and therefore it measures the hydrodynamic diameter, which leads to a slight overestimation of the particle size. Conversely, samples measured by TEM have to be dried. However, the largest particles at DLS should be the largest even when measured by TEM. Therefore, the increase in the ratio between DLS and TEM values with the increase in ETEOS used in the core formation may support the hypothesis that the matrix formed using ETEOS is characterised by a lower crosslinking density and is less dense in comparison to the one formed by TEOS. Indeed, the difference between DLS and TEM diameters could indicate that the solvent can diffuse better in **FITC-SiNP$_{100ETEOS}$** which swells when in suspension (DLS) and shrinks when dried (TEM). Conversely, the thick matrix of **FITC-SiNP$_{100TEOS}$** does not allow solvent diffusion and so the difference between TEM and DLS diameters is less evident. Another reasonable explanation for the differences in

the values observed by using the two techniques is related to the limitation of DLS in analysing polydisperse samples. Due to the presence of different populations in **FITC-SiNP$_{100ETEOS}$**, the diameter measured by DLS could be overestimated. Since the larger particles scatter light to a greater extent, the instrument tends to misinterpret the heterogeneous samples, prioritising large values of diameters not considering the presence of small particles (this topic will be discussed deeper in the *Chapter 5*).

TEM images (*Figure 69-a)* showed the spherical shape of all particles and, from them, the normal distribution was determined for each sample in which the broader the bell of the Gaussian curve, the more the diameter varies between the particles in the sample. Observing the TEM images in *Figure 69-a* and the normal distribution in *Figure 69-b* it is noticeable that the monodispersity of the samples decreases using ETEOS in the formulation, supporting the PDI values measured by DLS. In the TEM of **FITC-SiNP$_{100ETEOS}$** different populations are clearly visible, which is not the case for the other samples. The broad shapes of **FITC-SiNP$_{100ETEOS}$** and **FITC-SiNP$_{75ETEOS}$** curves confirms the presence of different populations in the samples, while the sharp bell determined for the remaining samples indicates that the particles in the samples are of similar diameter. TEM analysis indicated that the sample with the better size distribution was **FITC-SiNP$_{100TEOS}$**, which had the sharper bell (red line) in the normal distribution analysis, supporting the better PDI valued measured by DLS (0.177).
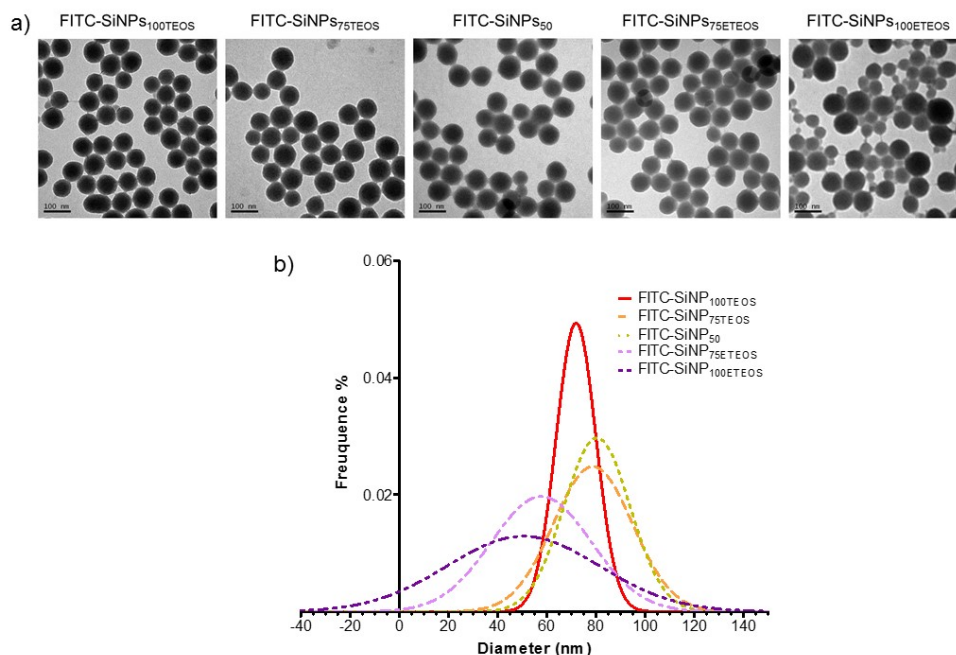
Figure 69: a) TEM images of each sample of 0.5 mg/mL in water. As noticeable, FITC-SiNP100ETEOS presents different populations of particles having different dimeter compared with the other particles synthesised. b) Normal distribution determined for each sample analysing TEM images.

The amount of FITC covalently loaded has been quantified for each type of synthesised particle. Since it is known that dyes inside the particles suffer from self-quenching[265], the quantification of the amount dye loaded would not be trustworthy if determined by measuring the fluorescence of the particles. Furthermore, considering that the amount of dye is calculated according to a calibration curve obtained using dye free in solution, it is important to make sure that the fluorescence measurement occurs in the same condition for a robust method. Therefore, the particles were first dissolved by incubation at 37°C in buffer pH 10.6 before quantification of the amount of dye loaded. The particles were incubated/shaken until no pellet was visible after centrifugation (usually 5 hours). Only when no pellet was visible after centrifugation the fluorescence of the samples was measured. This corresponds to the amount of dye incorporated in the matrix of a known amount of particles, but that it is free in solution after particles degradation. In *Table 31*, quantification of the dye loaded is reported as µM/200µg of NPs and as number of molecules of FITC internalised per individual particle. No relevant difference was observed between the loading capacities of **FITC-SiNP100TEOS, FITC-SiNP75TEOS** and **FITC-SiNP50**, for which respectively 1256, 1755 and 1578 molecules of dye per particle were calculated. Instead, a remarkable decrease in loading capacity was observed when ETEOS was the main component of the silica core:

550 and 122 are the molecules of dye per particles calculated, respectively, for **FITC-SiNP75ETEOS** and **FITC-SiNP100ETEOS**. In particular, the loading capacity of **FITC-SiNP100ETEOS** is ten times lower than that of **FITC-SiNP100TEOS** (122 *versus* 1256). This is probably related to the properties of ETEOS, which presents in its structure only three sites available for the polymerisation compared with the four ethoxy groups present in TEOS. Therefore, on increasing the amount of ETEOS, the polymerisation of the FITC-APTMS conjugate, and therefore its incorporation into the matrix, can also be hindered, leading to a lower loading capacity in the **FITC-SiNP100ETEOS** and **FITC-SiNP75ETEOS** particles.

Table 31: Quantification of dye-loading. In the first column are reported either the amount of FITC measure after dissolution of 200 μg of particles (μM) from which have been then calculated the number of molecules of FITC per nanoparticles (second column). Data are reported as average value ± SD, n=3.

	μM	molecules/NP
FITC-SiNP$_{100TEOS}$	0.89 ± 0.27	1256 ± 389
FITC-SiNP$_{75TEOS}$	0.98 ± 0.32	1755 ± 576
FITC-SiNP$_{50}$	0.81 ± 0.3	1578 ± 574
FITC-SiNP$_{75ETEOS}$	0.74 ± 0.12	550 ± 92
FITC-SiNP$_{100ETEOS}$	0.61 ± 0.61	122 ± 27

4.3.2 Evaluation of pH-responsiveness of FITC-SiNPs

The synthesised SiNPs are being proposed as vehicles for oral drug delivery. As consequence, they need to protect the cargo in the gastric environment (pH 4) and release it in the intestinal lumen (pH 6-7.4). Generally speaking, the release of the cargo from particles can occur in different ways. (i) It can leak out by simply solubilisation in the solvent that penetrates the matrix, (ii) the core of the NPs can swell, allowing the active compound to move between the loose frame and leave the carrier, or (iii) the matrix can be dissolved and, with this loss in consistency, the drug is released. These three possibilities are depicted in *Figure 70*.
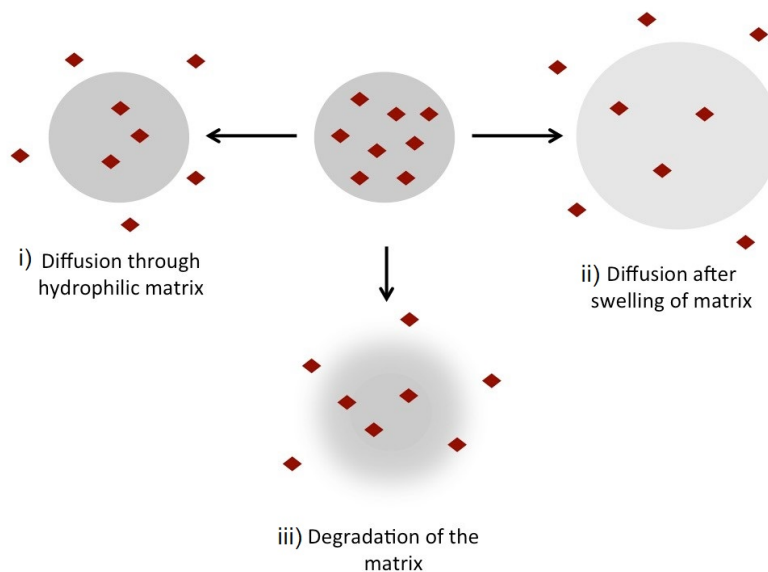
Figure 70: Schematic representation of drug release from the silica matrix. i) The aqueous environment can diffuse through the matrix of the particles; ii) the solvent can induce a swelling, loosen the matrix from which the cargo can easier diffuse through. iii) Alternatively, the matrix can be degraded once in contact with the solvent.

It has been shown that SiNPs tend to change morphology when exposed to slightly alkaline environment[266]. This phenomenon is related to the weakening effect that hydroxyl groups induce on the –Si-O-Si- bond, as shown in *Figure 71*.
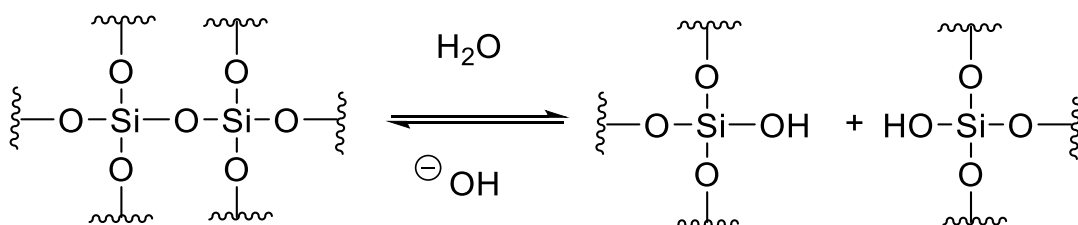
Figure 71: Hydroxide ions catalyses breakage of Si-O bond in aqueous environment inducing hydrolysis.

Due to the progressive hydrolysis of the silica matrix, hollow particles can be obtained starting from solid particles. Two are the theories given to explain the mechanism upon which hollow particles form after base-catalysed etching. Zhang *et al.* found that SiNPs, when exposed to $NaBH_4$, become hollowed spheres, a process which they showed to be dependent to the temperature and the concentration of $NaBH_4$ used. They observed that, when treated at room temperature with $NaBH_4$, the SiNP's shells start to dissolve, while the cores of the particles remain intact; this was supported by the reduction in NP diameter. Only once $NaBH_4$ is converted into $NaBO_2$ and H_2 does the hollowing process occur, due to the re-deposition of the silica induced by $NaBO_2$[267] (*Figure 72 blue rectangle*). Conversely, Park *et al.* suggested that the base-catalysed etching of particles

starts in the inner part of the core, forming small pores. The remainder of the particle then rearranges via Ostwald ripening,[268] reaching a stable situation with a lower surface energy, i.e. hollowed SiNPs[266] (*Figure 72 green rectangle*). Between these two hypotheses, other groups have found that the particles dissolve simultaneously from the inner and the outer part and maintain, at least initially, their morphology during the degradation[269] (*Figure 72 orange rectangle*).
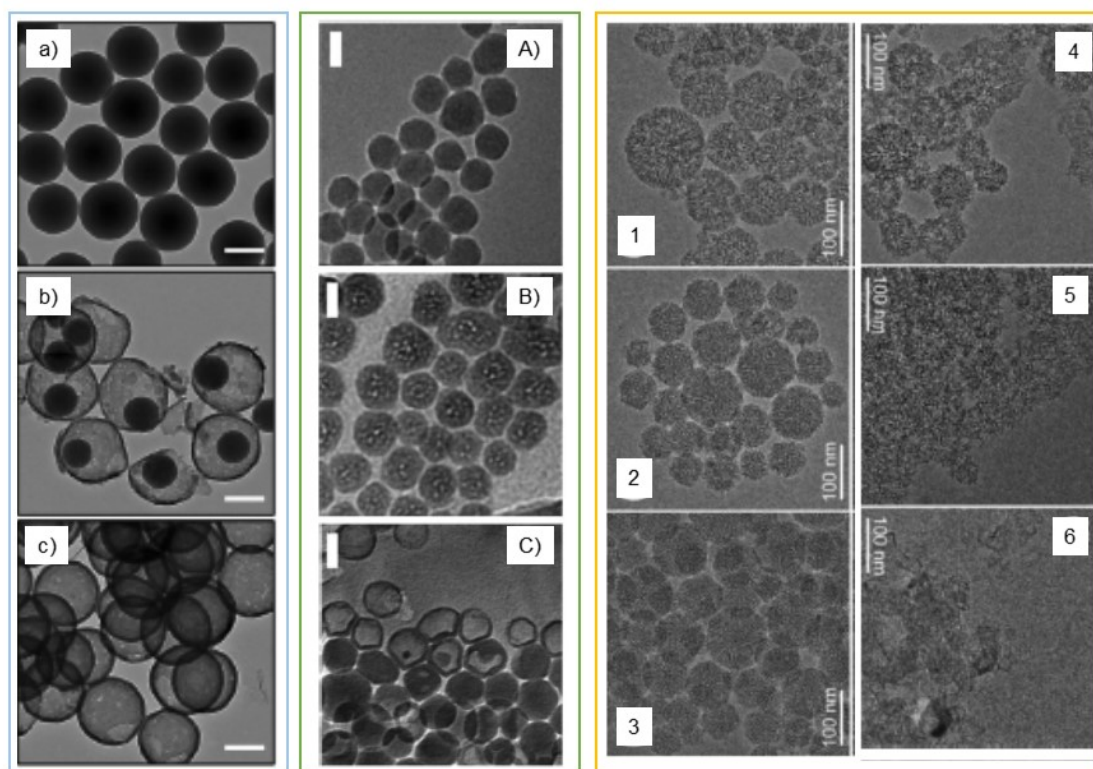
Figure 72: Representation of the three hypothesis given regarding the mechanism which lead to the change of SiNPs morphology. BLUE RECTANGLE: a) SiNPs treated with NaBH₄ became weak (b) and then re-deposition occurs and hollow particles forms (c). Adapted from reference[267]. GREEN RECTANGLE: the basic etching starts in the core of the particles (B) and after rearrangement of the material NPs become hollowed (C). Adapted from reference[266]. ORANGE RECTANGLE: SiNPs maintain their morphology while dissolution of the silica matrix occurs in the inner and outer part at the same time (1-6). Adapted from reference[269].

The dissolution of the SiNPs can therefore be considered the main aspect which determines the release of the cargo. According to the literature, the rate of dissolution is strongly related to the environmental conditions. As can be imagined, aggregates will dissolve more slowly compared to single particles, considering the lower surface area in contact with the environment,[269] while there are no differences in dissolution between particles synthesised following different synthetic procedures[266]. The cargo can leach out of the SiNPs simply by diffusion, especially if it is not covalently bound to

the matrix, however the dissolution of the particles is certainly important in determining the kinetics of the drug release.

The synthesised FITC-doped SiNPs have been evaluated as to their dissolution and drug release profile when exposed to buffers at different pH, mimicking the environmental conditions that would be encountered during their journey along the GI track: pH 4 which represents fed stomach, pH 6 which corresponds to the duodenum (initial part of the intestine), while pH 7.4 mimics the pH in the jejunum. The dissolution process was evaluated by TEM, while the amount of cargo released was determined by measuring the amount of FITC present in the supernatant once isolated from NPs. The dissolution kinetic studies were accomplished using (i) Eppendorf tubes, where the NP's suspensions were incubated under agitation, and (ii) by dialysis, where the particles are placed in a dialysis bag and immersed in a stirred aqueous environment. Apart from the volume of buffer used in the assay, the important difference between the two methods is that, while in the dialysis bag the particles are static and only the surrounding buffer is stirred, in the "Eppendorf" assay, the particles are constantly agitated, which better represents the *in vivo* situation (*Figure 73*).
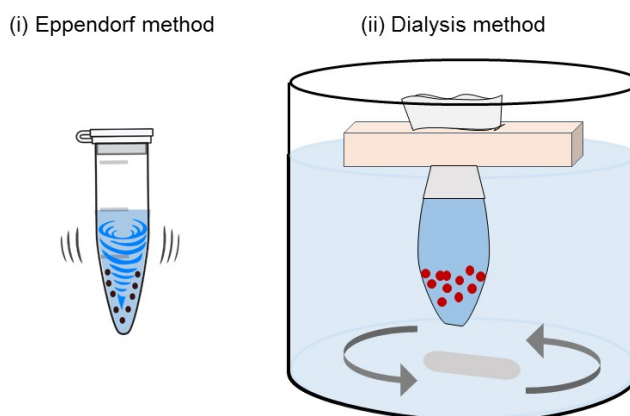
Figure 73: Representation of the two methods used in the present study: (i) the "Eppendorf" experiment in which the particles are incubated under constant agitation and (ii) the dialysis method in which the particles are stable and only the surrounding environment is mixed constantly.

"Eppendorf" method

Evaluation of dye release

For this experiment, 250 μg of nanoparticles were re-dispersed in 1 mL of sodium phosphate buffer at pHs 4, 6 and 7,4. The solutions were incubated at 37°C and agitated. Every two hours the particles were isolated by centrifugation and analysed by TEM, while the fluorescence of the supernatant was measured to quantify the amount of FITC released compering the values achieved with the fluorescent-based calibration curve of known FITC concentrations.

The fluorescence measurements clearly indicate that the dissolution of all formulated particles is pH-dependent (*Figure 74*). It is evident that a negligible amount of dye was released at pH 4. Even after 24 hours incubation, the maximum amount of FITC leached from the particles was below 10% of the total dye loaded. This indicates that using the synthesised SiNPs for oral delivery, no drug would be released in the acidic environment of the stomach (*Figure 74-i)*. Some differences were noticed in the release kinetics of the differently formulated particles when exposed at pH 6 (*Figure 74-ii)*. After 2 hours incubation, the drug release calculated for each type of particles was below 10%, but with differences in the release kinetics. After 8 hours, the amount of FITC that had leached from **FITC-SiNP$_{75TEOS}$**, **FITC-SiNP$_{50}$** and **FITC-SiNP$_{75ETEOS}$** was 20%, while it was only 10% for **FITC-SiNP$_{100TEOS}$** and **FITC-SiNP$_{100ETEOS}$**. After 24 hours incubation, it was determined that for **FITC-SiNP$_{75TEOS}$**, **FITC-SiNP$_{50}$** and **FITC-SiNP$_{75ETEOS}$** 40-60% of FITC had leached, very different from the 20% measured for **FITC-SiNP$_{100ETEOS}$**. Interestingly, for **FITC-SiNP$_{100TEOS}$**, which seemed to have a good retention of the dye, after 24 hour the amount of FITC leached reached 40%, similarly to the other types of particle. When incubated at pH 7.4, the dye instead leaches from the particles immediately. All particles tested **(FITC-SiNP$_{100TEOS}$, FITC-SiNP$_{75TEOS}$, FITC-SiNP$_{50}$, FITC-SiNP$_{75ETEOS}$** and **FITC-SiNP$_{100ETEOS}$**) were found to show similar release kinetics, despite the difference in the formulation of the silica cores (*Figure 74-iii)*. After only 1 hour of incubation, 10% of FITC was released into the supernatant, rising to 30% and 50% after 3 and 5 hours, respectively. After 6 hours, the dye leached from the particles less quickly, increasing by only *ca.* 20% in 18 hours (60% and 80% release of FITC was observed after 6 and 24 hours, respectively). The plateau in the dye leaching was reached around 80%. It is possible that some dye leached out during

storage or during the washes required to prepare the particles for the assay (*Figure 74-iii*).
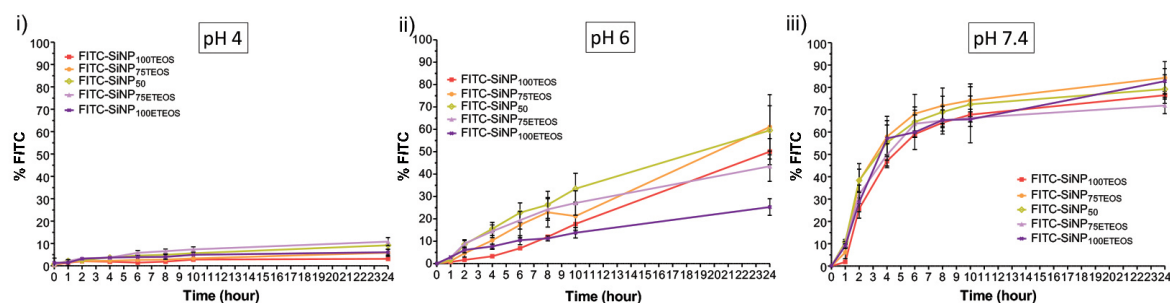
Figure 74: Results obtained by the Eppendorf experiment showing the clear difference in dissolution kinetic of the particles when exposed to different pHs while no relevant different was noticed between the particles differently formulated if not when exposed at pH6. Data are reported as average value ± SD, n=3.

Observing closely the release kinetics at pH 6 (*Figure 75*), it can be noticed that the dye is released more rapidly from **FITC-SiNP$_{50}$**, **FITC-SiNP$_{75TEOS}$** and **FITC-SiNP$_{75ETEOS}$** when exposed to this conditions in comparison with **FITC-SiNP$_{100ETOES}$**. In the latter case, after 24 hours only 20% of dye leached out, while the leaching from **FITC-SiNP$_{50}$** and **FITC-SiNP$_{75TEOS}$** reached 60%. **FITC-SiNP$_{100ETOES}$** and **FITC-SiNP$_{100TOES}$** have similar dissolution kinetics up to 8 hours but, after 24 hours a difference is noticeable, since the dye leached into the supernatant is twice as much in the case **FITC-SiNP$_{100TOES}$** (respectively 25% and 50% is the amount of FITC leaked at the end of the experiment) (*Figure 75)*. These results confirm the advantages to be gained by using SiNPs for oral drug delivery. The drug will be only partially released in the duodenum, characterised by pH 6-6.5. This is particularly important considering that in this section of the intestine, digestive enzymes are released in the lumen in order to prepare the catabolism of nutrients. The drug released in the duodenum will suffer from the high concentration of enzymes, while inside the particles the active compound can be protected from degradation/inactivation. The low release observed at pH 6 proved the efficiency of SiNPs for oral drug delivery. Considering the quick transition in the duodenum, it can be expected that less than 20% of the drug (corresponding to the amount of FITC release after 4 hours) would be released, while most of the drug will be delivered intact to the second section of the small intestine, the jejunum, were the absorption occurs.
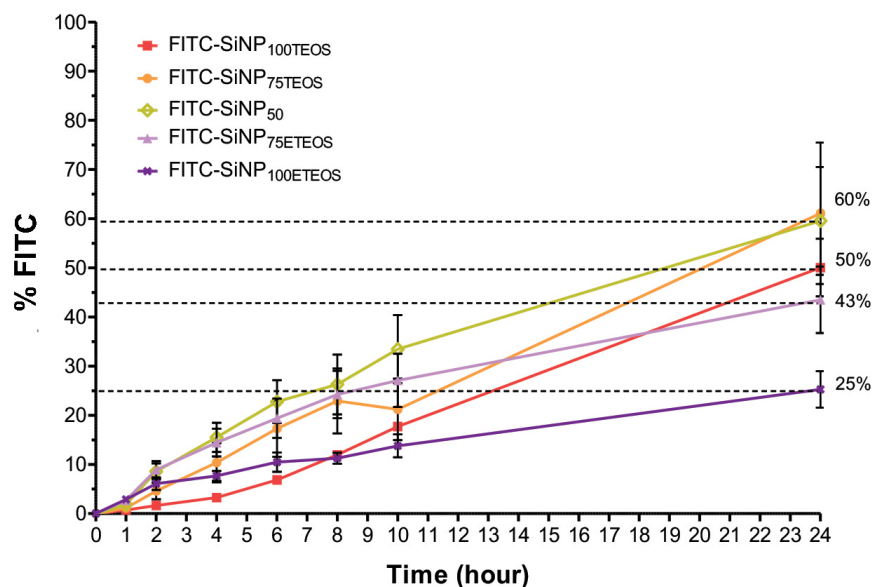
Figure 75: Kinetic release determined for each SiNPs type when incubated under agitation at pH 6. When expose to this condition some differences between the different types of SiNPs tested was noticed in their kinetic of release. In particular FITC-SiNP$_{100ETEOS}$ seemed to have a low release at pH 6. Data are reported as average value ± SD, n=3.

Degradation of the silica matrix

During the Eppendorf experiment, at each time point, the pellet isolated after centrifugation was washed several times to remove the salts of the buffer before TEM analysis (*Figure 76)*. It can be clearly seen that no changes in morphology were observed for all types of particle at any time point of analysis when incubated at pH 4. Only for **FITC-SiNP$_{100TEOS}$** and **FITC-SiNP$_{75TEOS}$** some small hollows were visible after 24 hours incubation. The TEM images supported the release profile observed by measuring the FITC signal in the supernatant at pH 4. All particles tested (**FITC-SiNP$_{100TEOS}$, FITC-SiNP$_{75TEOS}$, FITC-SiNP$_{50}$, FITC-SiNP$_{75ETEOS}$** and **FITC-SiNP$_{100ETEOS}$**) maintained their integrity and are intact even after long exposure at low pH and therefore the drug release in the acid gastric environment (pH 4) would be negligible.
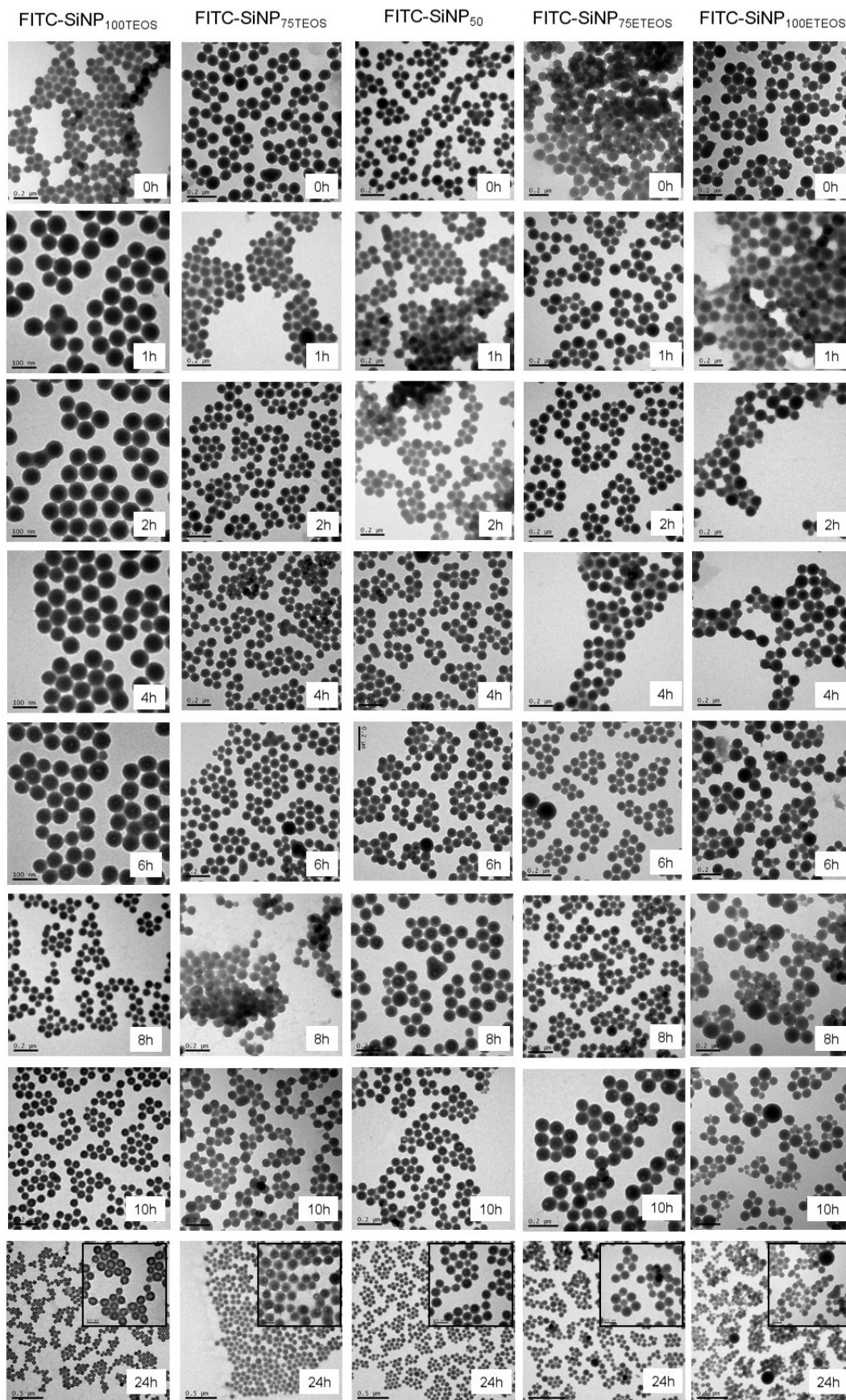
Figure 76: TEM images of FITC-SiNPs incubated at pH 4.

The TEM images of particles suspended in buffer at pH 6 confirm the results achieved from measuring the amount of FITC in the supernatant. Indeed, as shown in *Figure 77*, **FITC-SiNP$_{50}$**, **FITC-SiNP$_{75TEOS}$** and **FITC-SiNP$_{75ETEOS}$** dissolved more rapidly when incubated at this pH, in accordance with the prompt increase in dye measured in the supernatant. For these particles, holes began to be visible in the TEM images after 4 hours incubation. The different fate of **FITC-SiNP$_{100TEOS}$** and **FITC-SiNP$_{100ETEOS}$** exposed at pH 6 during the 24 hours is noteworthy and confirms the fluorescent data discussed previously. Both types of particle maintain their integrity until 8 h, in agreement with the fact that only 10% of loaded FITC was found in the supernatant. While no relevant changes in morphology were visible for **FITC-SiNP$_{100ETEOS}$** after 24 hours, in the case of **FITC-SiNP$_{100TEOS}$**, a few hollows were found after 10 hours, which become more evident after 24 hours. The difference in the amount of FITC leached after 24 hours from **FITC-SiNP$_{100TEOS}$** and **FITC-SiNP$_{100ETEOS}$** (40% and 20% respectively) is confirmed by the presence of hollows in the first case and the better stability of **FITC-SiNP$_{100ETEOS}$** when exposed at pH 6. The agreement between the results obtained from the fluorescence measurements and TEM images indicates a relationship between dissolution and drug release kinetics at pH 6.
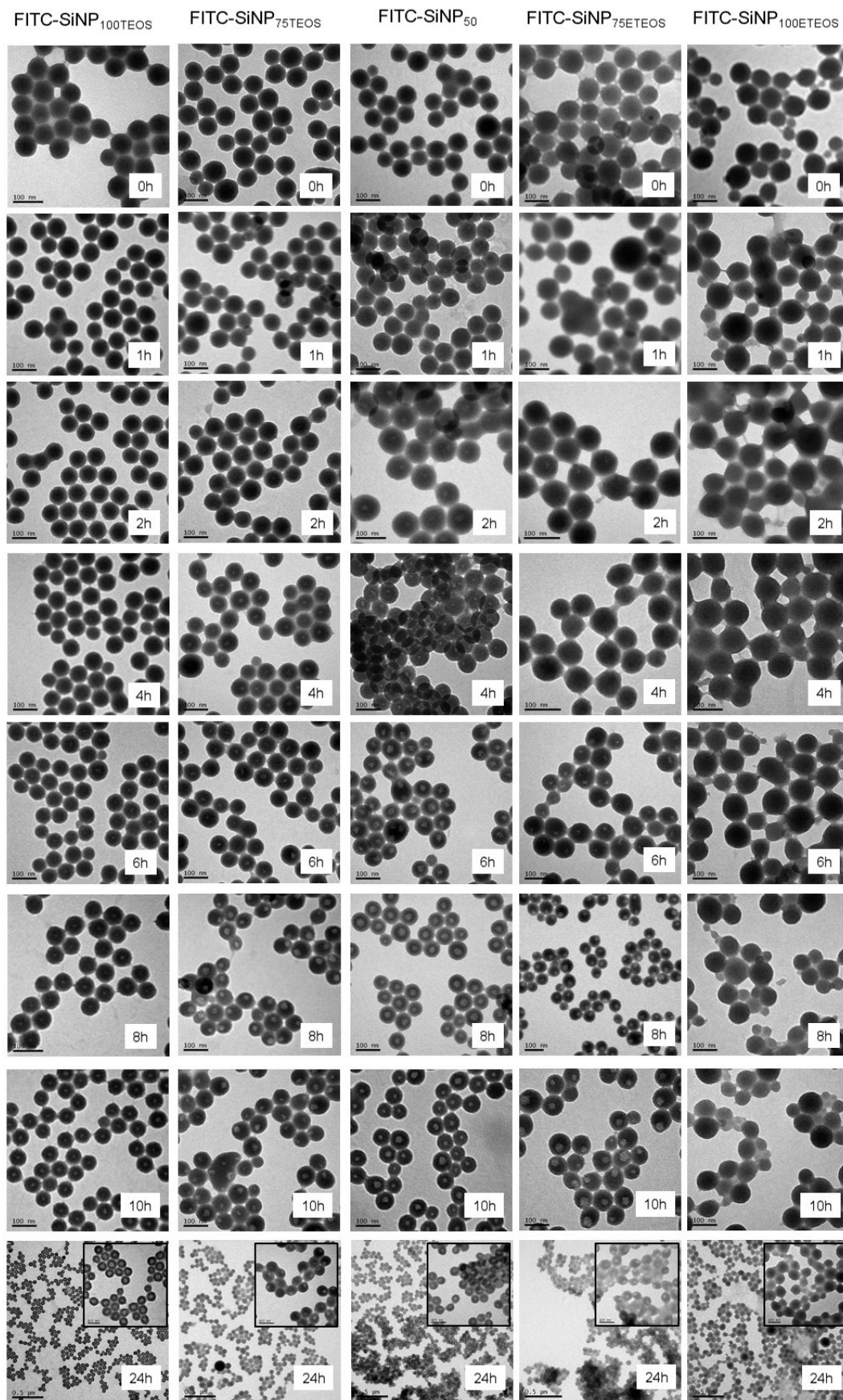
Figure 77: TEM images of FITC-SiNPs incubated at pH 6.

The base-catalysed etching of the silica matrix is evident at pH 7.4, where the dissolution of the particles is clearly defined after only 2 hours (*Figure 78*). The dye quantified in the supernatant and the TEM images partially support each other. Indeed, it can be seen that after 6 hours, the particles are deeply hollowed or partially dissolved, supporting the high fluorescence signal measured at this time point, as shown previously in *Figure 74*. However, this is not true for all types of particle. In the case of **FITC-SiNP$_{100TEOS}$** and **FITC-SiNP$_{100ETEOS}$**, the changes observed in the morphology of the particles would not lead one to think that they correspond to the point of maximum dye release. After 6 hours, both **FITC-SiNP$_{100TEOS}$** and **FITC-SiNP$_{100ETEOS}$** appear to be only partially degraded, but at this time the plateau of FITC released was essentially reached (around 60% of the loaded FITC had leached from the particles). This indicates that the leaching is not always related to the dissolution of the particles, but that it can also occur by diffusion of the dye through the matrix at pH 7.4, in which the dye has a better solubility.

The dye release curves are approximately the same for all types of particle exposed at pH 7.4, but the mechanism of dissolution appears to depend on the formulation of the particles. It can be observed that **FITC-SiNP$_{100ETEOS}$** did not suffer the hollowing process; this type of NPs appears to degrade slowly and the process seems to proceed from the exterior toward the interior. As dissolution proceeds, the particles seem to become "wrapped" in a faint network of silicate residues, which is the only material remaining after 24 hours. It is interesting to notice that, after 24 hours incubation at pH 7.4, spherical particles are replaced by faint entities in which only the shape of the initial particles is maintained, but not the consistency. These entities then fuse together, forming a thin layer of silica on the grid.

The fast release kinetics are supported by an almost complete degradation of particles after 10 hours at pH 7.4 and would ensure the prompt release of the drug in the second region of the small intestine, the jejunum. This section of the GI tract is designed for the absorption of nutrients and components. The internal lumen is formed by projections of epithelium, called villi, which increase the surface area and enhance the absorption process. Additionally, the completed dissolution of the particles after 24 hours confirms the biocompatibility of SiNPs. Presumably, the layer of silica observed after 24 hours can be simply excreted with faeces without accumulation in the body and any related toxicity.
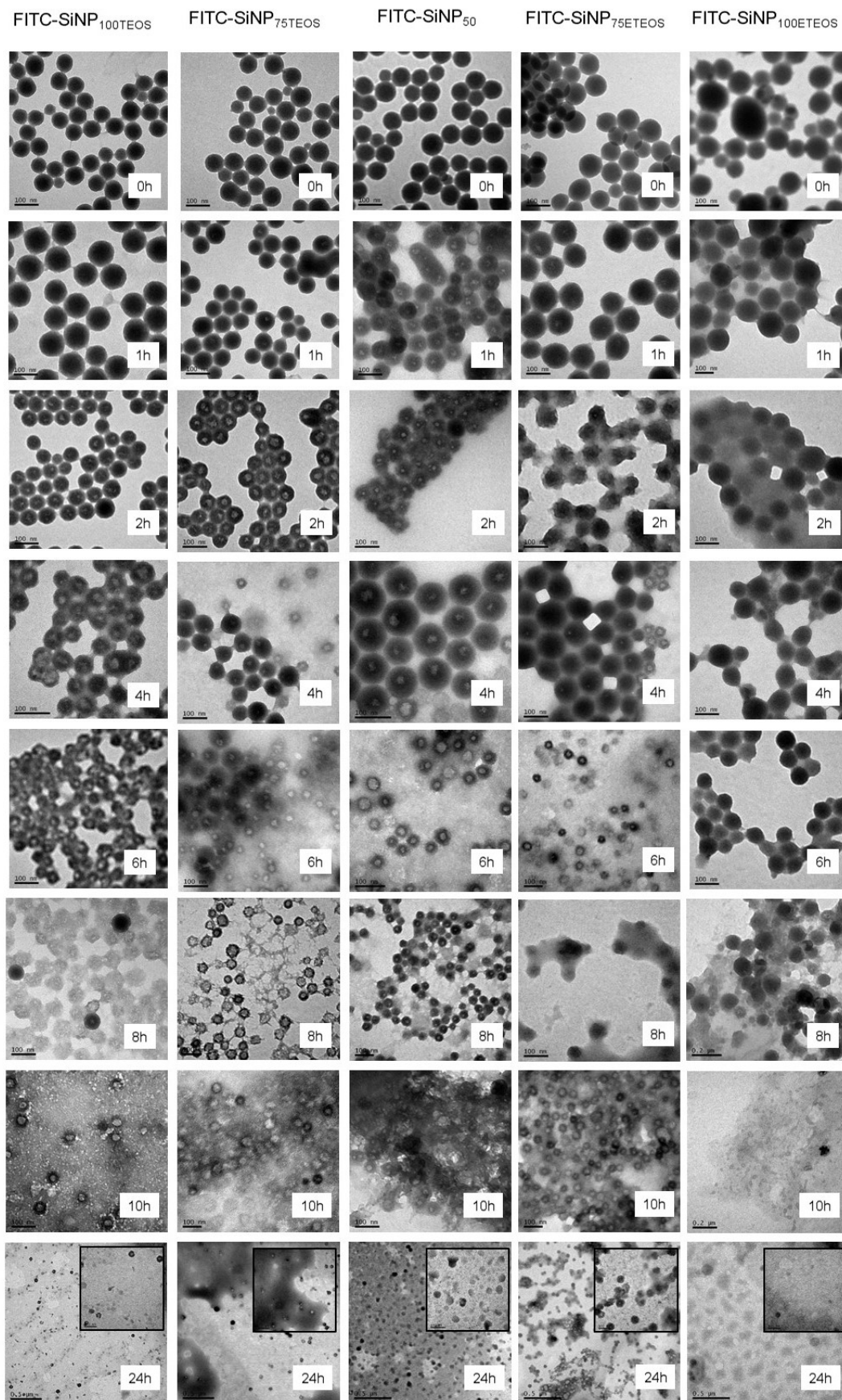
Figure 78: TEM images of FITC-SiNPs incubated at pH 7.4.

Figure 79 shows a better comparison between the dissolution mechanisms observed for **FITC-SiNP$_{100ETEOS}$** and **FITC-SiNP$_{100TEOS}$**. It can be observed that both types of NPs are stable at pH 4 since no morphological alteration is observed on incubation at this pH. The difference is instead noticeable after incubation at pHs 6 and 7.4. After 24 hours of incubation at pH 6, the difference in the dissolution mechanism is clear: holes are easily visible in the case of **FITC-SiNP$_{100TEOS}$**, while no hollowing process occurred for **FITC-SiNP$_{100ETEOS}$**. In the latter case, the particles appeared to simply dissolve when incubated at pH 6 for 24 hours. The same consideration can be made on comparing the TEM images obtained after **FITC-SiNP$_{100ETEOS}$** and **FITC-SiNP$_{100TEOS}$** were incubated at pH 7.4. In these cases, the hollowing process observed for **FITC-SiNP$_{100TEOS}$** and the dissolution phenomenon visible for **FITC-SiNP$_{100ETEOS}$** can be highlighted after 4 hours of incubation, while after 24 hours the particles were completely dissolved in both cases.
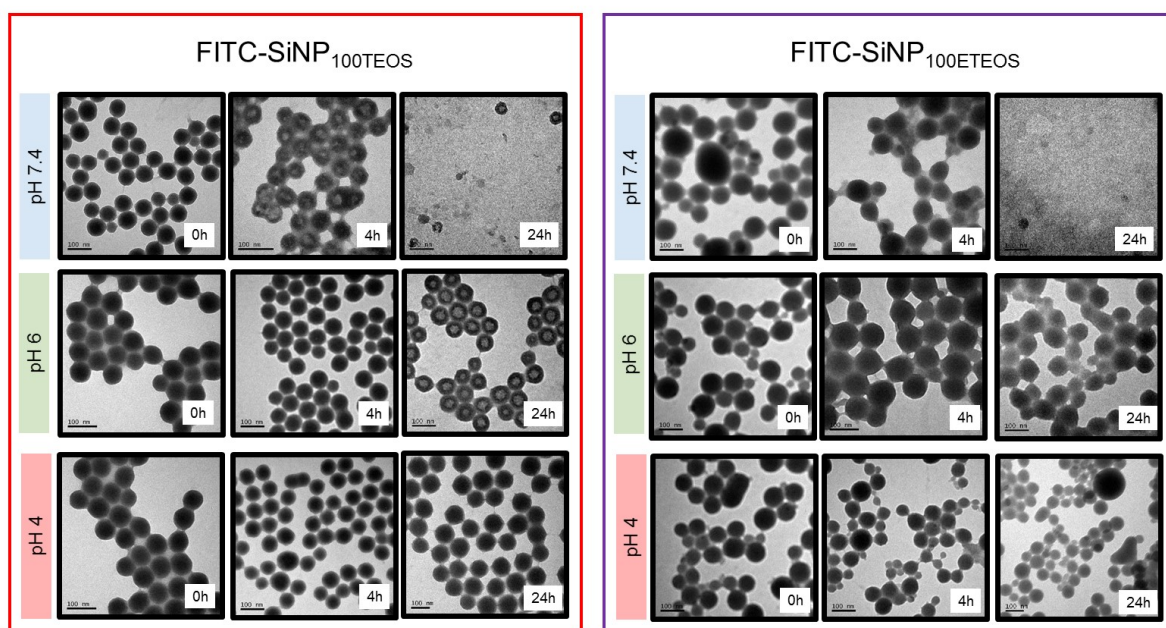
Figure 79: Close comparison between the dissolution mechanisms observed for FITC-SiNP$_{100TEOS}$ FITC-SiNP$_{100ETEOS}$ highlighting the hollowing process in the first case and the dissolution in the latter.

Dialysis method

For the dialysis experiments, 500 µg of particles were re-dispersed in 1 mL of each buffer. The solutions were then loaded in dialysis bags, closed and immersed in 30 mL of the same buffer, which was stirred continuously to facilitate diffusion of the cargo

following the concentration gradient from inside to outside the dialysis bag. The fluorescence was measured every day up to seven days.

The limitation of the method is clearly visible, since even at pH 7.4 no leaching was observed. The static situation created using the dialysis method is unfavourable for the release of the drug from the carrier, as well as differing from the situation that would be encountered by the particles in a physiological situation. Additionally, even the large amount of buffer used, into which the dye is released, could represent a limitation; the dye could have leached out, but the concentration in the surrounding environment could be too low to be measurable. The maximum released was measured for **FITC-SiNP$_{100ETEOS}$** at pH 6, reaching 5% (*Figure 80*). Such results can be explained through the need for flow/movement of the particles being fundamental for the release of the cargo or else the release takes much longer. Furthermore, in a static solution, SiNPs could aggregate in the dialysis bag affecting the dissolution of the particles, since less NP surface is in contact with the buffer.
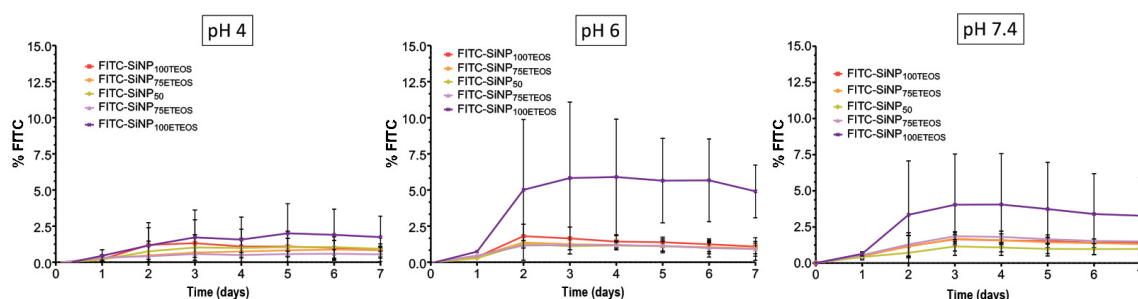
Figure 80: Quantification of FITC released by the particles by dialysis method. The leaching is very low, the 5 % of FITC in the buffer is barely reached at pH 6 and it is the maximum released measured. Values are reported as average ± SD, n=3.

GI tract-like assay

Although the dissolution profile results showed previously already proved the pH-responsiveness of the SiNPs, an additional proof of the applicability of SiNPs for oral delivery applications was given by exposing the particles to conditions that better represent the GI tract. Food, once ingested, follows a particular route along the GI tract, encountering different environments, which play specific roles in the digestion process. Accordingly, food will spend more or less time in each compartment. The fate of particles would be similar when administered orally. The present assays allow mimicking of the route along the GI tract. The particles were indeed incubated at pH 4

for 4 hours, approximately the time that food stays in the stomach. After this time, the same particles were incubated at pH 7.4 while agitated. This situation corresponds to the continuation of the journey from the stomach to the small intestine. The time required by food to pass through the intestine is approximately 10 hours. After this time, what has not been absorbed, is excreted as faeces.

All particles were incubated at 37°C at a concentration of 200 μg/mL in buffer pH 4. The samples were agitated and, every 2 hours, the concentration of the dye in the supernatants was quantified. After 4 hours the particles were centrifuged, re-dispersed in 1 mL of buffer pH 7.4 and the experiment proceeded as previously: the samples were incubated under agitation and the amount of dye in the supernatant was quantified every 2 hours. The experiment was terminated after a total amount of 14 hours. The results shown in *Figure 81* confirm the pH-sensitivity of SiNPs and their possible applicability for oral delivery. For all particles tested, negligible amounts of dye released at pH 4, while the leaching increases once the pH increases to 7.4. Translating these results to a real situation, it can be foreseen that no drug would be released in the fed stomach (pH 4) while the active compound will be progressively released in the intestine (pH 7.4).
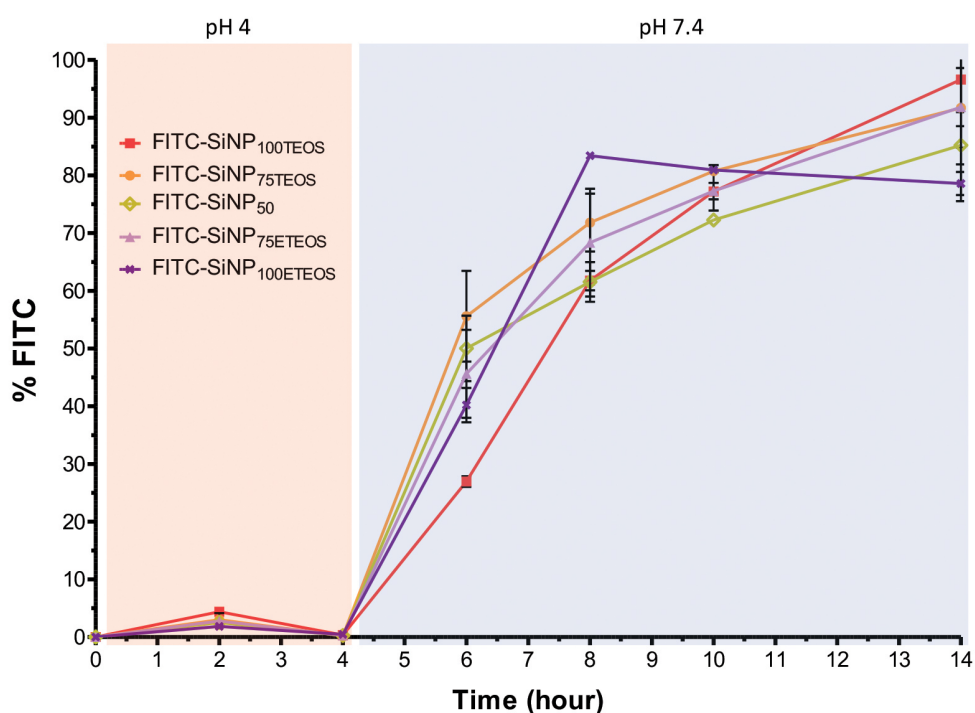
Figure 81: Each type of particle was incubated at concentration of 200 μg/mL in buffer at pH 4 for 4 hours and for other 10 hours at pH 7.4 for a total of 14 hours. Values are reported as average ± SD, n=3.

4.3.3 FITC-SiNPs stability study

The stability of the particles when incubated in each buffer was evaluated by DLS daily for 7 days and the values are presented in *Figure 82*. The DLS data indicate that the particles having ETEOS (**FITC-SiNP$_{100ETEOS}$** and **FITC-SiNP$_{75ETEOS}$**) in the core tend to aggregate at pH 4, while their diameter decreases at pH 6 and pH 7.4, which could indicate that they tend to dissolve. Particles formed mainly from TEOS are relatively stable at pH 4 and 6 but tend to aggregate at pH 7.4. In particular, **FITC-SiNP$_{100TEOS}$** remarkably aggregated at the 3th day when the dimeter of the particles increased ten times from the previous day (around 200 nm and 2250 nm at day 2 and 3 respectively).

The aggregation of particles which has been observed in some cases in the present study is not concerning and does not represent an issue for the use of SiNPs in oral delivery. If observed, aggregation occurred after more than 24 hours of incubation at any pH. Considering that all particles were degraded when incubation at pH 7.4 for less than a day, the possibilities of aggregation to occur are very limited.
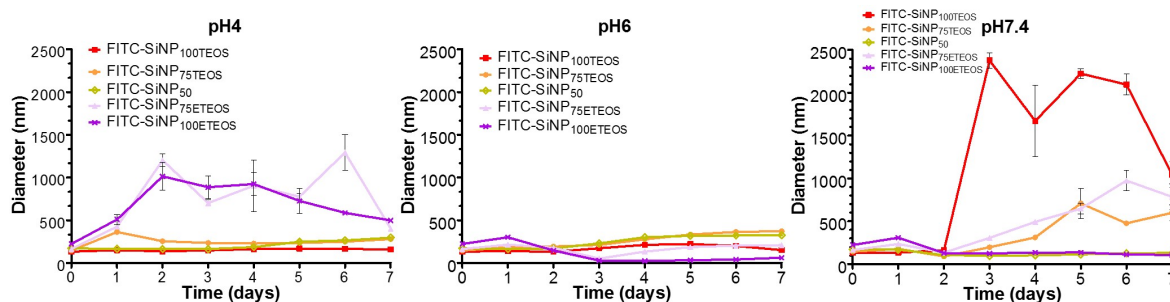
Figure 82: Diameter of particles incubated at 37°C in different buffers measured every day for 7 days. The samples were measured at concentration of 250 µg/mL. Data are reported as average value ± SD, n=3.

Closer analysis of the graph related to the pH 6 experiments reveals some relevant information (*Figure 83*). It can be seen that the diameter of **FITC-SiNP$_{100ETEOS}$** decreases rapidly between 24-60 hours, while when TEOS is present this tendency is not observed. In the case of **FITC-SiNP$_{75ETEOS}$**, an initial decrease in size is observed but, on the fourth day, they start to aggregate. Interestingly, the tendency to dissolve of **FITC-SiNP$_{100ETEOS}$** and the tendency to aggregate observed for particles formulated with TEOS could support the hypothesis proposed previously, according to which the formation of aggregates limits the dye release due to the decrease in NP surface area. Indeed, for **FITC-SiNP$_{100ETEOS}$** a connection can be presumed between the dissolution

indicated by the decrease in the diameter measured and the release (although low) of FITC at pH 6 and 7.4.
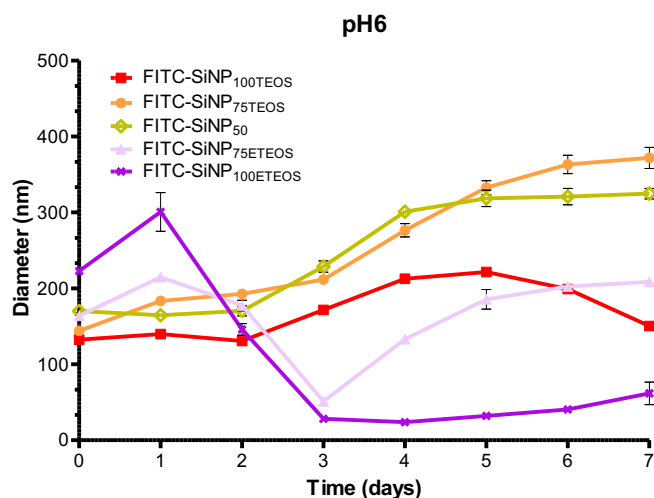
Figure 83: DLS measurement of particles incubated in pH 6 for one week and evaluated every day. Data are reported as average value ± SD, n=3.

Figure 84 shows the ζ-potential measured for each type of NP and indicates a common tendency for each of particles to become more positively charged under all conditions tested. The trend becomes more evident with the increase of pH values and, at pH 7.4, the particle charge increased quickly over the first two days until a plateau was reached. Although an increase in surface's charge usually indicates aggregation, in this case it was not related to any particular aspect of aggregation or dissolution.
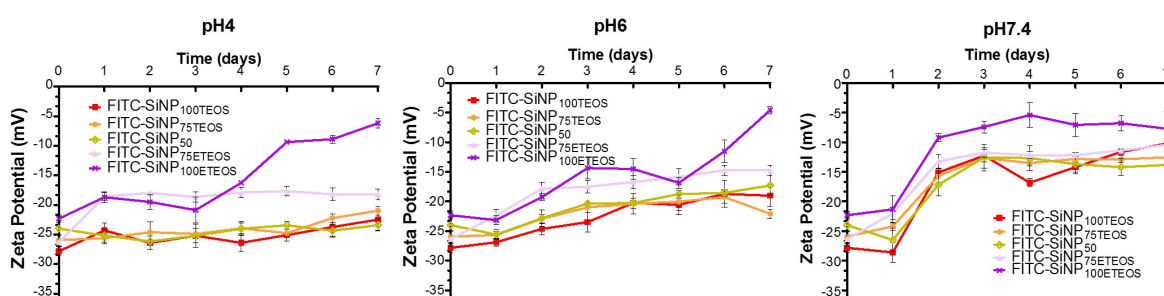
Figure 84: ζ-potential of samples incubated at 37°C in different buffers measured every day for 7 days. The samples were measured at concentration of 250 µg/mL. Data are reported as average value ± SD, n=3.

This is again important to highlight that the results gave only an indication of the stability of the particles under the conditions used in the study. Since the transition in the GI tract takes approximately one day and the particles will degrade after a certain

amount of time in the alkaline intestinal lumen, the stability of the particles should not be a reason for concern.

All particles tested (**FITC-SiNP$_{100TEOS}$, FITC-SiNP$_{75TEOS}$, FITC-SiNP$_{50}$, FITC-SiNP$_{75ETEOS}$** and **FITC-SiNP$_{100ETEOS}$**) were seen to properly protect the cargo from leaching when exposed to a gastric-like environment (pH 4 as the one in fed stomach), while the release increases with the increase of pH. At pH 6 the leaching increases but it is still limited, which means that more cargo will be released at pH 7.4, allowing the drug to proceed further through the small intestine and be released in the jejunum, where nutrient absorption takes place. No relevant difference was observed in terms of drug release between the different ratios of TEOS:ETOES used for the core formation. The main difference was noticed at pH 6, where **FITC-SiNP$_{100ETEOS}$** released the drug more slowly than the other NPs. After 24 h of incubation at pH 6, 20% and 50% was the amount of FITC released from **FITC-SiNP$_{100ETEOS}$** and **FITC-SiNP$_{100TEOS}$** respectively. At the same condition, 60% of FITC was released from **FITC-SiNP$_{75TEOS}$** and **FITC-SiNP$_{50}$** after 24 h of incubation. This difference could become valuable when considering certain active compounds, either very expensive or delicate, for which even a small improvement in the efficiency of delivery could represent a step forward. Although there were minimal differences observed in the dissolution kinetics, the different combination of TEOS/ETEOS used for the core formation were observed to determine the degradation mechanism undergone by each particle type. In particular, the presence of ETEOS in the matrix seemed to lead to dissolution of the particles from the exterior to the core, without the formation of holes in the particles. Conversely, the hollowing process occurred for those particles formulated with TEOS: small holes were first formed in the inner part leading, due to an Ostwald ripening process, to the formation of hollowed SiNPs characterised by thinner and thinner shells as the experiment proceeded.

4.3.4 Evaluation of SiNP's versatility as carrier for different cargos

In this section two important parameters related to the drug properties are evaluated: (i) the method used to load the cargo inside the SiNPs matrices, and (ii) the influence of the cargo's properties in the loading efficiency and kinetic of release. To this end, fluorescein sodium salt (NaFlu) and methylene blue (MB) were used as respectively hydrophilic and hydrophobic drug models and they were physically adsorbed rather than covalently entrapped in the NP matrices.

Synthesis of MB and NaFlu-SiNP series

SiNPs were synthesised following a similar procedure describe for the FITC-SiNPs series, with the difference that as aqueous phase a solution 3 mM of either NaFlu and MB were used to synthesise the NaFlu-SiNPs and MB-SiNPs series, respectively. TEOS and ETEOS were added in the same ratio and TEOS, THPMP and APTMS were used for the shell formation such that each series differs according only to the dye loaded and the method of loading.

Figure 85 shows the different types of particle synthesised in the MB-SiNPs and NaFlu-SiNPs series. As shown, the two series differ only by the dye physically incorporated. Each series consisted of five particle formulations, using different ratios of TEOS/ETEOS for the core formation, but all exhibit the same shell, therefore they are all negatively charged.

ID sample	TEOS %	ETEOS %
MB-SiNP$_{100TEOS}$	100	/
MB-SiNP$_{75TEOS}$	75	25
MB-SiNP$_{50}$	50	50
MB-SiNP$_{75ETEOS}$	25	75
MB-SiNP$_{100ETEOS}$	/	100

ID sample	TEOS %	ETEOS %
NaFlu-SiNP$_{100TEOS}$	100	/
NaFlu-SiNP$_{75TEOS}$	75	25
NaFlu-SiNP$_{50}$	50	50
NaFlu-SiNP$_{75ETEOS}$	25	75
NaFlu-SiNP$_{100ETEOS}$	/	100
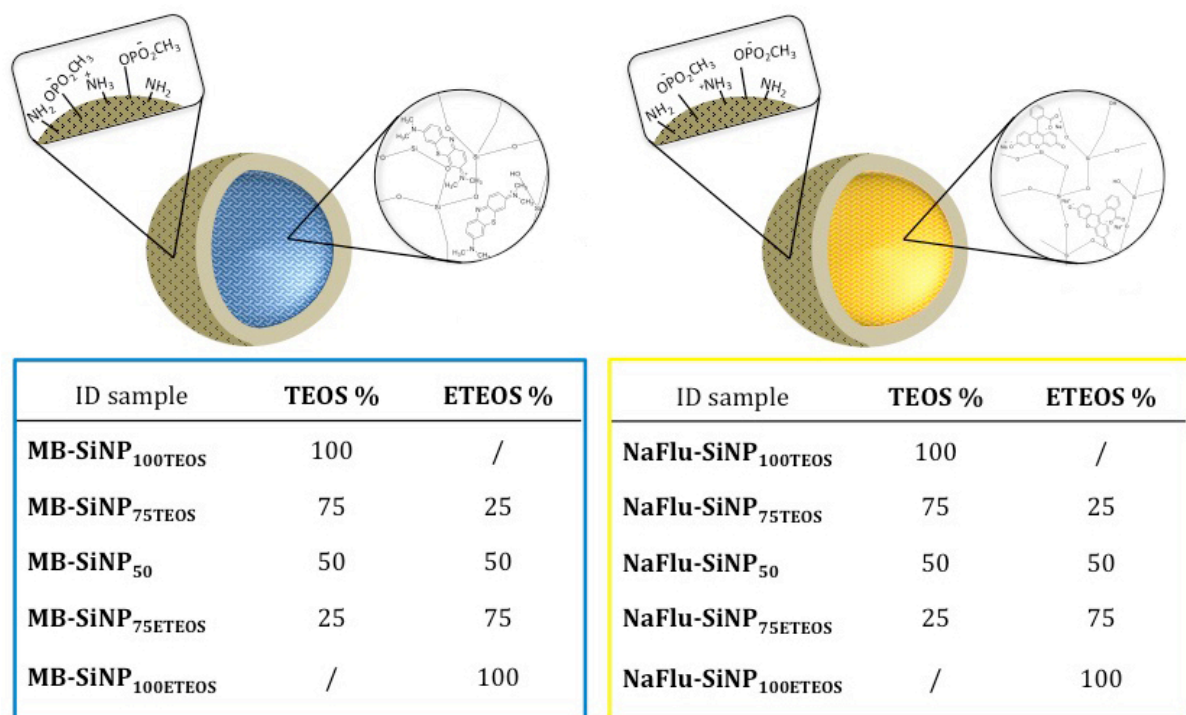
Figure 85: Structure of the MB-SiNPs (left) and of the NaFlu-SiNPs (right) series.

All particles were characterised after synthesis by DLS and TEM and the results are reported in *Tables 32* and *Table 33*. For these series, as well as for the FITC-SiNPs series discussed in Section 4.3.1, the use of ETEOS for the core formation leads to polydisperse samples, while with TEOS the samples are monodisperse. This is particularly evident for NaFlu-SiNPs where the PDI measured for **NaFlu-SiNP$_{100ETEOS}$** and **NaFlu-SiNP$_{100TEOS}$** were 0.328 and 0.039 respectively. DLS data were supported by the TEM analysis where different populations are clearly visible in the **MB-SiNP$_{100ETEOS}$** and **NaFlu-SiNP$_{100ETEOS}$** samples. DLS data indicate a correlation between the amount of ETEOS used in the core formulation and the hydrodynamic diameter measured for both series. The diameter increases from 138.1 nm for **MB-SiNP$_{100TEOS}$** to 190.4 nm for **MB-SiNP$_{100ETEOS}$** and for the other types of particle the diameter increases from 105.3 nm to 139.5 nm for **NaFlu-SiNP$_{100TEOS}$** and **NaFlu-SiNP$_{100ETEOS}$**, respectively. This increase is however noticeable only when considering the hydrodynamic diameter since, measuring the diameter from TEM images, the particles composed of 100 % ETEOS for both series are the smallest despite the high SD. From the TEM images, 67 nm and 63 nm were found the average diameters for **MB-SiNP$_{100ETEOS}$** and **NaFlu-SiNP$_{100ETEOS}$**, respectively (*Figure 86-i*).

Table 32: DLS values measured for each sample of the MB-SiNPs series at concentration 0.5 mg/mL in water at room temperature. For each measurement, diameter, PDI and ζ-potential are reported as average ± SD, n=3. The diameter of the TEM was determined directly measuring the diameter of the particles visible at the TEM image. Values are reported as average (n = *ca.* 100) ± SD.

	DLS			TEM
	Ø (nm)	PDI	ζ(mV)	Ø (nm)
MB-SiNP$_{100TEOS}$	138.1 ± 2.27	0.185 ± 0.037	-23.2 ± 0.85	73 ± 8
MB-SiNP$_{75TEOS}$	147.2 ± 2.07	0.142 ± 0.007	-28.6 ± 3.62	65 ± 8
MB-SiNP$_{50}$	144.5 ± 2.92	0.139 ± 0.014	-28.7 ± 0.53	65 ± 11
MB-SiNP$_{75ETEOS}$	185.2 ± 2.60	0.099 ± 0.015	-18.6 ± 0.61	73 ± 15
MB-SiNP$_{100ETEOS}$	190.4 ± 2.66	0.199 ± 0.020	-23.4 ± 0.51	67 ± 21

Table 33: DLS values measured for each sample of the NaFlu-SiNPs series at concentration 0.5 mg/mL in water at room temperature. For each measurement, diameter, PDI and ζ-potential are reported as average ± SD, n=3. The diameter of the TEM was determined directly measuring the diameter of the particles visible at the TEM image. Values are reported as average (n = *ca.* 100) ± SD.

	DLS			TEM
	Ø (nm)	PDI	ζ(mV)	Ø (nm)
NaFlu-SiNP$_{100TEOS}$	105.3 ± 1.72	0.039 ± 0.012	-36.6 ± 2.04	79 ± 8
NaFlu -SiNP$_{75TEOS}$	112.5 ± 2.56	0.124 ± 0.032	-32.9 ± 2.82	81 ± 11
NaFlu -SiNP$_{50}$	109.8 ± 0.81	0.125 ± 0.026	-41.1 ± 2.5	77 ± 9
NaFlu -SiNP$_{75ETEOS}$	125.0 ± 1.12	0.127 ± 0.013	-36.1 ± 4.25	98 ± 25
NaFlu -SiNP$_{100ETEOS}$	139.5 ± 3.92	0.328 ± 0.027	-32.2 ± 0.32	63 ± 24

Figure 86-*ii* shows the normal distribution determined for each type of particle using the values of the TEM analysis. At first glance, the difference between the sharp bell of SiNPs having cores made from 100TEOS, 75TEOS and 50TEOS for both series (respectively red, orange and green curves) and the broad bell of particles whose cores are composed of 75ETEOS and 100ETEOS (respectively pink and violet curves) is immediately evident. The width of the Gaussian curve for **MB/NaFlu-SiNP$_{100ETEOS}$** and **MB/NaFLu-SiNP$_{75ETEOS}$** (purple and pink line respectively in the graphs) indicates the presence of different populations in the samples, supporting DLS data.
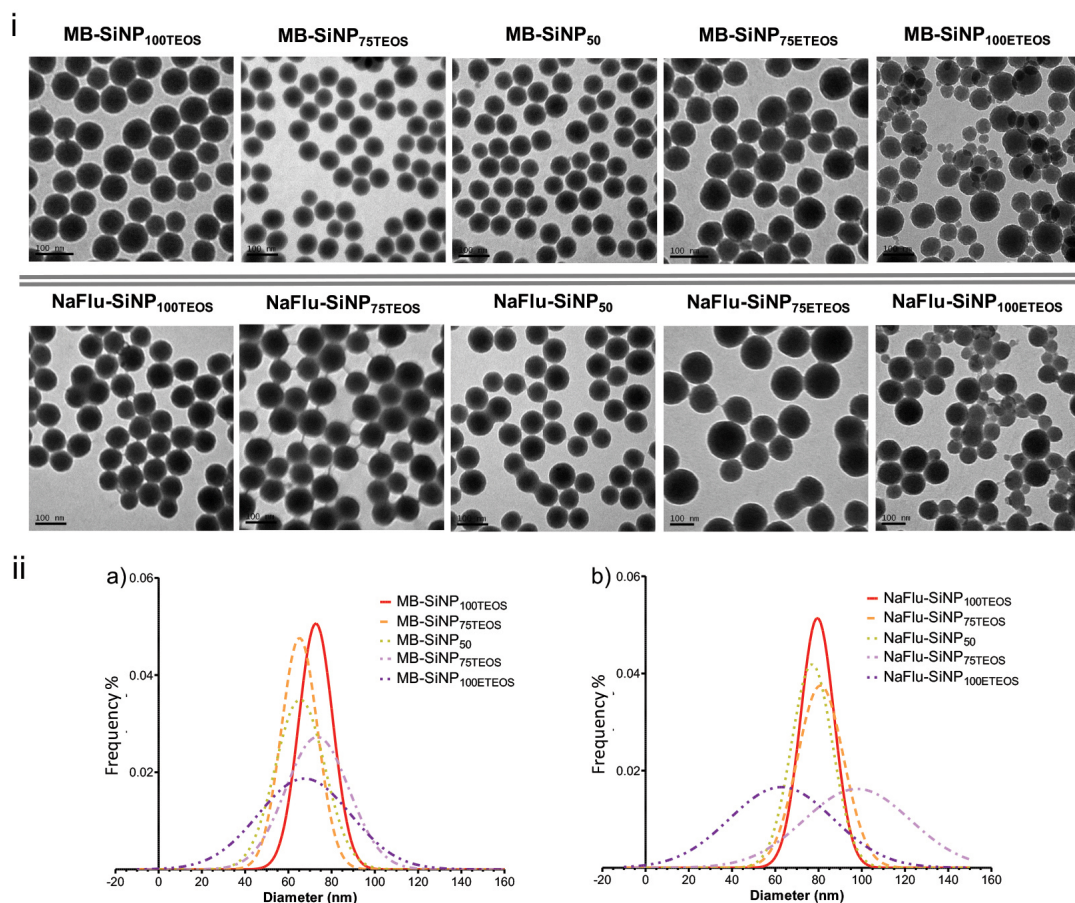
Figure 86: i) TEM images for the MB-SiNPs series particles (first row) and for NaFlu-SiNPs series (second row). ii) Normal distribution of the diameter of particles measure for MB-SiNPs (a) and NaFlu-SiNPs (b) series determine considering the average diameter of the particles measured on the TEM images.

The ratio between the DLS and TEM values was calculated for each sample (*Table 34*). The values have the same tendency as the one observed for FITC-SiNPs: increasing the amount of ETEOS, the difference between the hydrated state and the dried state increases too. Although the difference is not as evident as for the FITC-SiNPs series (2.2 and 2.8 for respectively MB-SiNPs and NaFlu-SiNPs series against 4.5 value found for FITC-SiNPs series) the same explanations given for can be applied for this type of particles as well. The difference in the values achieved could indicate that the presence of different types of dye in the matrix can alter the characteristics of the particle itself.

Table 34: Ratio between the hydrodynamic diameter measured by DLS and the diameter measured by TEM (dried particles).

	MB-series	NaFlu-series
X-SiNP$_{100TEOS}$	1.2	1.3
X-SiNP$_{75TEOS}$	2.3	1.4
X-SiNP$_{50}$	2.2	1.4
X-SiNP$_{75ETEOS}$	2.5	1.2
X-SiNP$_{100ETEOS}$	2.8	2.2

The quantification of the dye loaded for the MB-SiNPs and NaFlu-SiNPs series was performed after dissolution of the particles at 37°C under agitation in buffer pH 10.6, as described for FITC-SiNPs. It is noteworthy that while 5 hours incubation at 10.6 pH was enough for complete degradation of the NaFlu-SiNPs, in the case of MB-SiNPs only after 24 hours there was no pellet visible after centrifugation, indicating that MB somehow changes the properties of the silica matrix. Once the particles were completely degraded, the dye released into the buffer was quantified by measuring the absorbance (660 nm) for the MB-SiNPs series and the fluorescence (λ_{ex}-λ_{em} = 456-518 nm) for NaFlu-SiNPs series (*Table 35*). In both cases, the loading capacity calculated is lower compared to those determined for the FITC-SiNPs. These results confirmed what was expected, i.e. that covalent attachment gives better loading than simple physical entrapment. However, comparing the two cases in which the dye was physically entrapped, the low efficiency in loading of the NaFlu-SiNPs is evident. There are a few possible explanations for these result: (i) the internalisation of NaFlu, being negatively charged, could be limited due to the repulsive interaction with the negatively charged NP surface. (ii) NaFlu is highly soluble in water and therefore it may be that dye retention is a greater problem than actual loading, or (iii) the low photostability of fluorescein could be an additional problem when exposed to such high values of pH. MB was physically entrapped in the silica matrix, but since it is hydrophobic, the loading was more successful, although it is still lower when compared with the FITC-SiNPs. As expected, covalently loading the cargo appears to be a more successful method compared with the physical incorporation.

Table 35: Quantification of loading capacity. From the concentration of dye µM (reported as average values n = 3 ± SD) achieved the number of molecules of dye per NPs was calculated. Values are reported as average ± SD, n=3.

	µM	molecules/NP		µM	molecules/NP
MB-SiNP$_{100TEOS}$	0.069 ± 0.001	100 ± 2	NaFlu-SiNP$_{100TEOS}$	0.0004 ± 0.00003	0.7 ± 0.06
MB-SiNP$_{75TEOS}$	0.052 ±0.001	54 ± 1	NaFlu-SiNP$_{75TEOS}$	0.0002 ± 0.00003	0.36 ± 0.06
MB-SiNP$_{50}$	0.058 ± 0.001	61 ± 1	NaFlu-SiNP$_{50}$	0.0005 ± 0.00005	0.86 ± 0.09
MB-SiNP$_{75ETEOS}$	0.062 ± 0.001	91 ± 2	NaFlu-SiNP$_{75ETEOS}$	0.0003 ± 0.00003	1.2 ± 0.06
MB-SiNP$_{100ETEOS}$	0.039 ± 0.001	45 ± 1	NaFlu-SiNP$_{100ETEOS}$	0.0006 ± 0.00006	0.51 ± 0.05

Evaluation of pH-responsiveness – "Eppendorf" method

Evaluation of dye release

The kinetics of release for MB-SiNPs and NaFlu-SiNPs series were evaluated using only the "Eppendorf" method. The particles were incubated at pH 4, 6 and 7.4 in order to mimic the three environments encountered in the sections of the GI tract, as previously.

For this purpose, 250 µg/mL of particles were incubated in buffer solutions at pH 4, 6 and 7.4 pH at 37°C under constant agitation. Every time point the amount of dye in the supernatant was quantified by measuring the absorbance (600 nm) for the MB-SiNP series and the fluorescence signal for the NaFlu-SiNPs series (λ_{ex}-λ_{em} = 456-518 nm).

Figure 87 shows the data for the MB-SiNPs series. It is clear that dye is released randomly from the particles, no trend is observed and additionally the amount of MB released is very low. The maximum percentage of MB which leached from particles is 30%, the value calculated for **MB-SiNP$_{75ETEOS}$** after 10 hours of incubation at pH 7.4. MB was measured in the supernatant for all particles incubated at pH 6, although at low levels, normally below 10% (with the exception of **MB-SiNP$_{50}$** from which 20% of MB leached after 24 hour of incubation). There are a few possible reasons which could explain this behaviour: (i) the relative hydrophobicity of MB, especially in alkaline solutions, and (ii) its tendency to precipitate at pH lower then 5 (in such case, no absorbance would be measured). Yeo and co-workers recently showed that when *in vitro* release kinetic studies of poorly water-soluble drugs are designed without

considering the solubility limitations, results can lead to underestimation of the drug release. They suggest that the drug/volume ratio should be adjusted during the studies in order facilitate the dispersion of the compound analysed[270]. Presumably, the Eppendorf method does not represent a reliable system for the evaluation of drug release using methylene blue as drug-model.
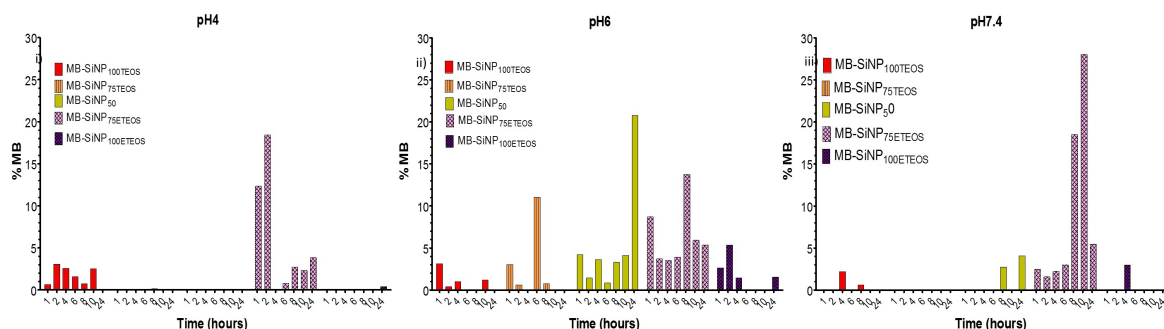
Figure 87: Drug release of MB from MB-SiNPs when exposed at different pH.

Conversely, the release of NaFlu from the carrier was immediate, indicating the low retention capabilities of the particles when loaded with highly hydrophilic compounds (*Figure 88*). After 1 hour of incubation, at all pHs tested, all available dye had leached from the particles. Only in the case of **NaFlu-SiNP$_{75TEOS}$** was the end-point was calculated as 100% of the dye loaded. The difference between the amount of dye loaded and the maximum amount of dye released observed in all the remaining types of particle is likely related with the processes followed for the preparation of the samples, which required one aqueous wash step in order to remove residual traces of the ethanol in which the particles were stored, as well as any dye that leached during storage.
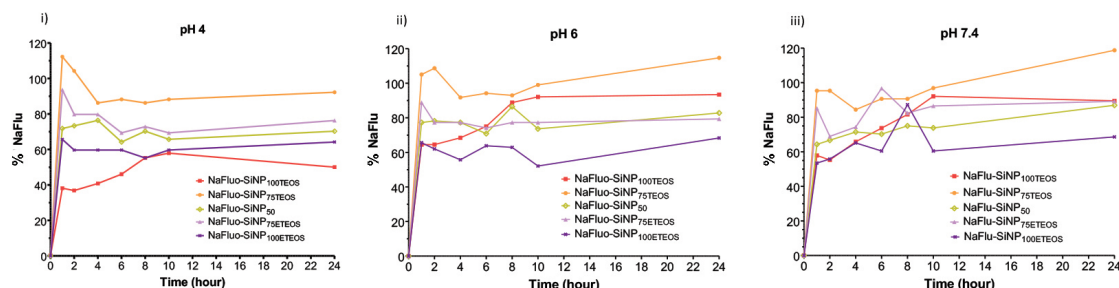
Figure 88: Drug release of NaFlu from NaFlu-SiNPs when exposed at different pH.

Degradation of the silica matrix

After 6 and 24 hours the particles of both series were isolated and analysed by TEM.

The results obtained with the MB-SiNPs are particularly interesting and are reported in *Figures 89, 90 and 91*. **MB-SiNP$_{100TEOS}$** and **MB-SiNP$_{75TEOS}$** appeared to be particularly resistant to degradation under the conditions tested, though some holes were observed only for **MB-SiNP$_{75TEOS}$** after 24 hours at pH 6. Even when incubated at pH 7.4 for 24 hours, no holes were visible in the matrix and no dissolution was observed. Conversely, for **MB-SiNP$_{100ETEOS}$** a few indications of dissolution were visible after 7 hours and, after 24 hours incubation at pH 4, the particles were completely dissolved. A similar situation was observed when **MB-SiNP$_{100ETEOS}$** were incubated at pH 6 and pH 7.4, although the dissolution was more evident. This particular behaviour of the particles can be related to the use of ETEOS in the core formulation. Indeed, even **MB-SiNP$_{75ETEOS}$** showed some tendency to dissolve when exposed at pH 4; this become more evident at pH 6 and especially at pH 7.4. It is worth highlighting the peculiar degradation mechanism observed for **MB-SiNP$_{75ETEOS}$**. When incubated at pH 4, after 6 and 24 hours, but in particular after 24 hours at pH 6, a faint layer of silica was observed at the outer surface of the particles while the core appeared solid and intact. This degradation mechanism could be similar to the process observed by Zhang *et al.* when treating SiNPs with NaBH$_4$ (see Section 4.3.2). However, the same particles, incubated at pH7.4 became hollowed after 6 hours end even more so after 24 hours, which suggests that these particles degrade differently depending on the conditions. For **MB-SiNP$_{50}$** the formation of the faint layer around the solid core of particles was observed when incubated at pH 4 and 6, but at pH 7.4 the particles completely dissolved without formation of any holes. For this type of particles there is no apparent correlation between the dissolution and release kinetics since, at least for **MB-SiNP$_{100ETEOS}$** and **MB-SiNP$_{75ETEOS}$**, from observing the TEM analysis we should expect MB to be present in the supernatant in higher concentrations compared to those measured.
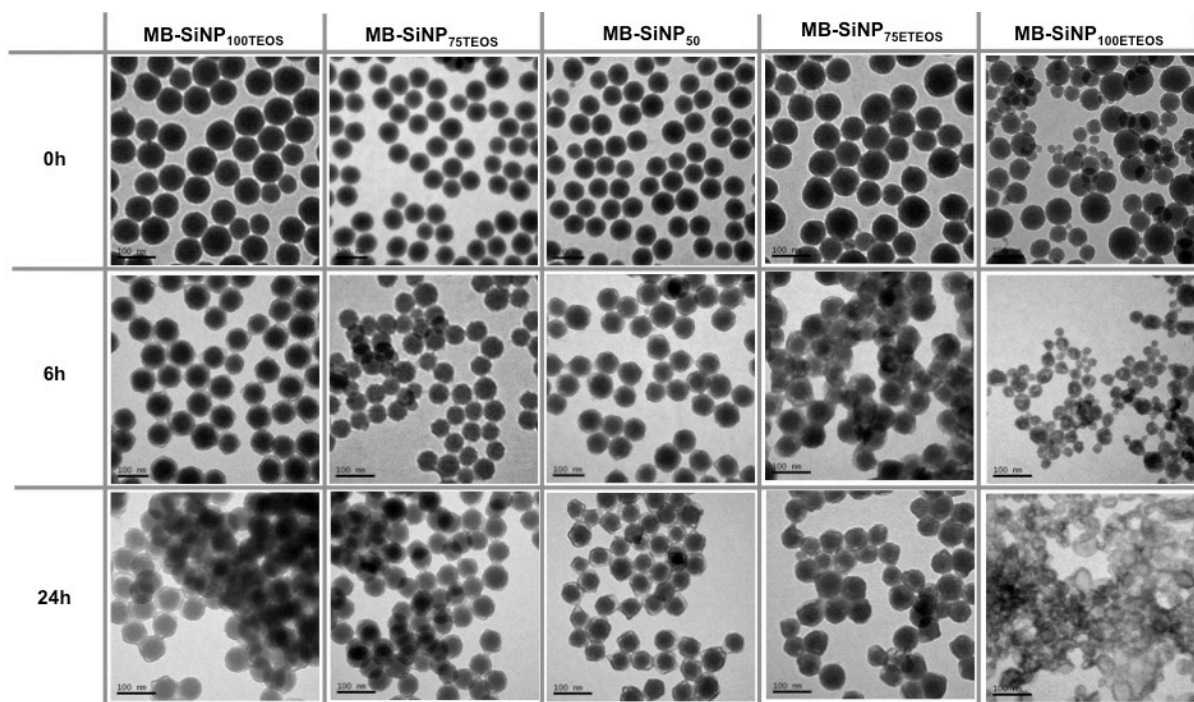
Figure 89: TEM analysis of MB-SiNPs series when 250 μg/mL of particles in buffer pH 4.
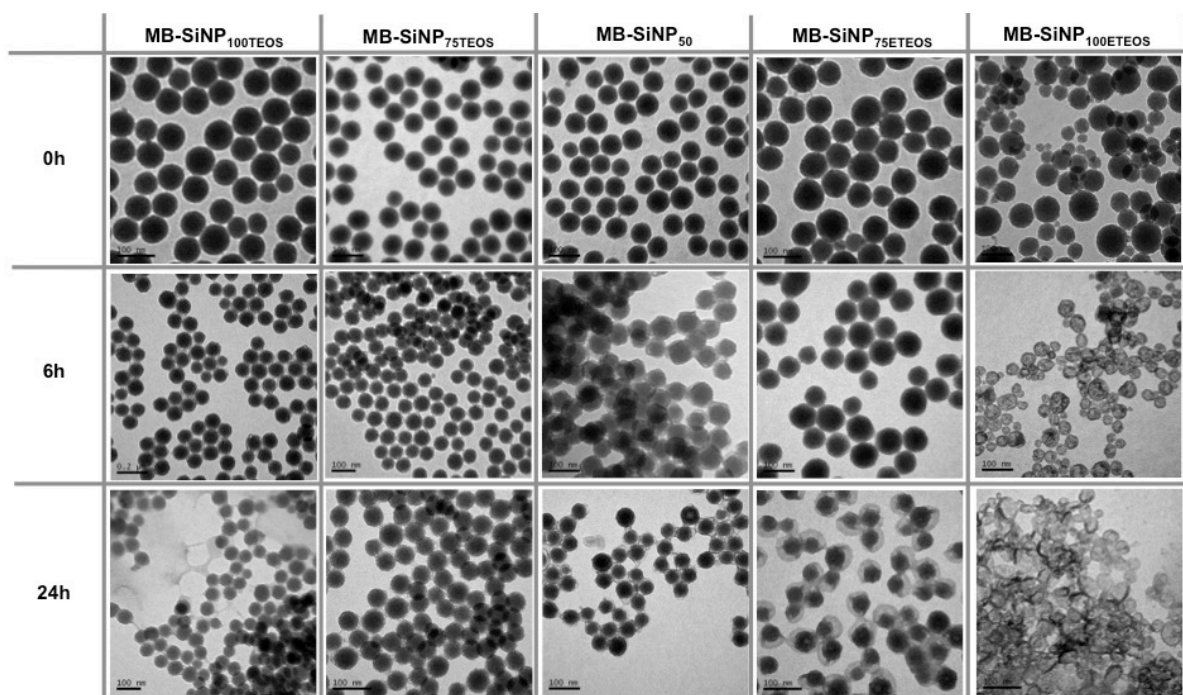
Figure 90: TEM analysis of MB-SiNPs series when 250 μg/mL of particles in buffer pH 6.
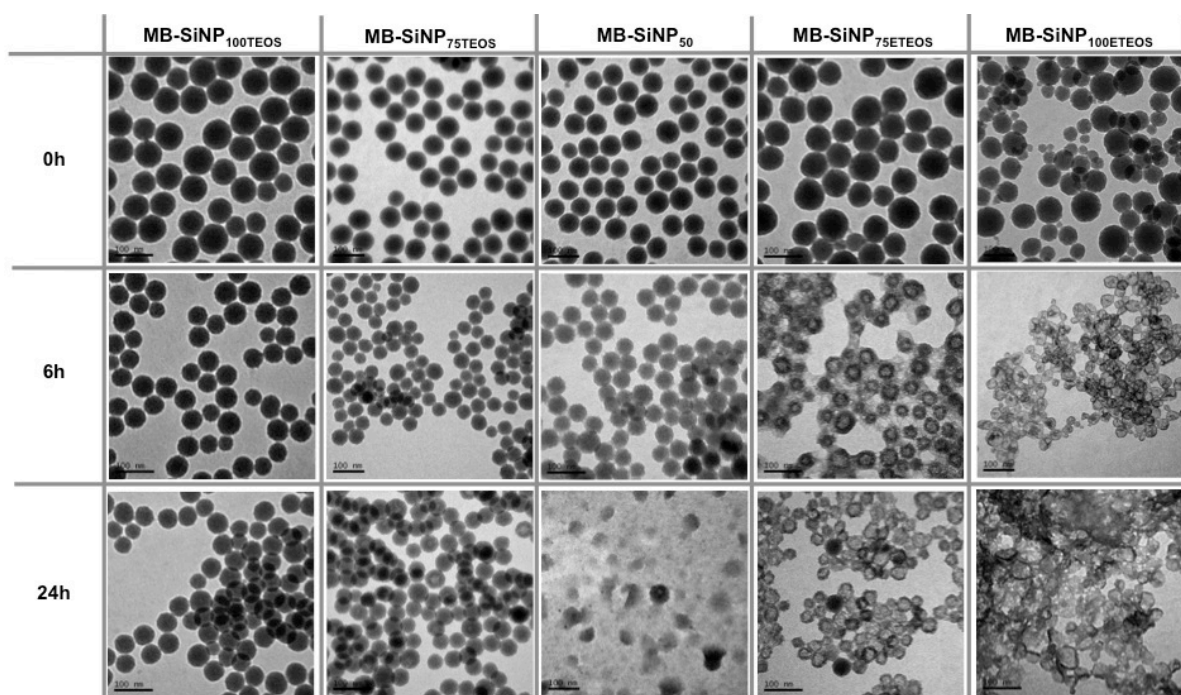
Figure 91: TEM analysis of MB-SiNPs series when 250 µg/mL of particles in buffer pH 7.4.

TEM analysis of the NaFlu-SiNPs series instead led to similar results to those observed for the FITC-SiNPs series, indicating that in this case the dye, NaFlu, does not interfere with the silica matrix formation (*Figure 92, 93 and 94*). All particles maintained their morphology at pH 4. When exposed at pH 6 for 6 hours almost all types of particle developed some holes in the inner part of the particles, which became larger after 24 hours, especially for **NaFlu-SiNP₁₀₀ₜₑₒₛ** and **NaFlu-SiNP₅₀**. As observed for the FITC-SiNPs series, the hollowing process did not occur for **NaFlu-SiNP₁₀₀ₑₜₑₒₛ**. This type of particles simply dissolved after incubation at pH 6 after 24 hours. The dissolution of **NaFlu-SiNP₁₀₀ₑₜₑₒₛ** appeared even more evident at pH 7.4 considering that after only 6 hours of incubation only a few SiNPs were noticeable on the grid. Generally speaking, all types of particle appeared to be particularly sensitive to the basic etching; indeed, after 6 hours of incubation all the NPs show evidence of degradation, in particular **NaFlu-SiNP₁₀₀ₑₜₑₒₛ** and **NaFlu-SiNP₇₅ₑₜₑₒₛ**, for which the dissolution was observed after only 6 hours. As for the MB-SiNPs, no relationship between dissolution and dye release kinetics was observed, which is due to the fact that in this case the dye simply diffused into the surrounding environment without the need for the matrix to actively take part to the release.
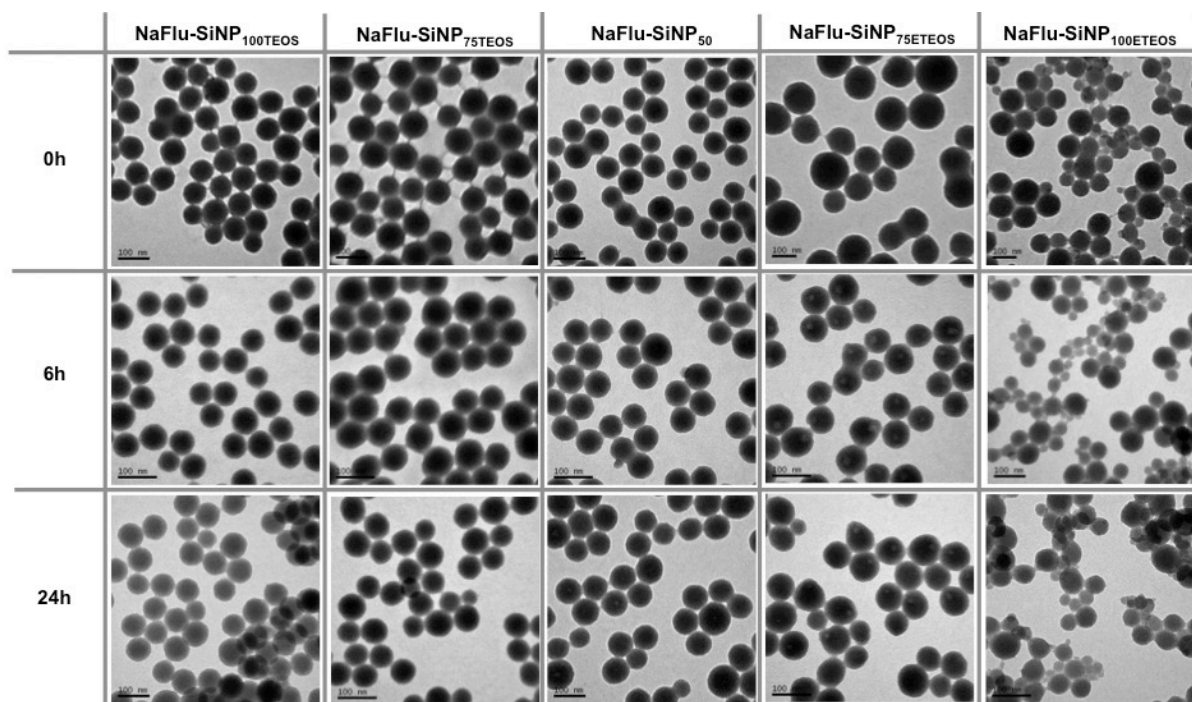
Figure 92: TEM analysis of NaFlu-SiNPs series when 250 µg/mL of particles in buffer pH 4.
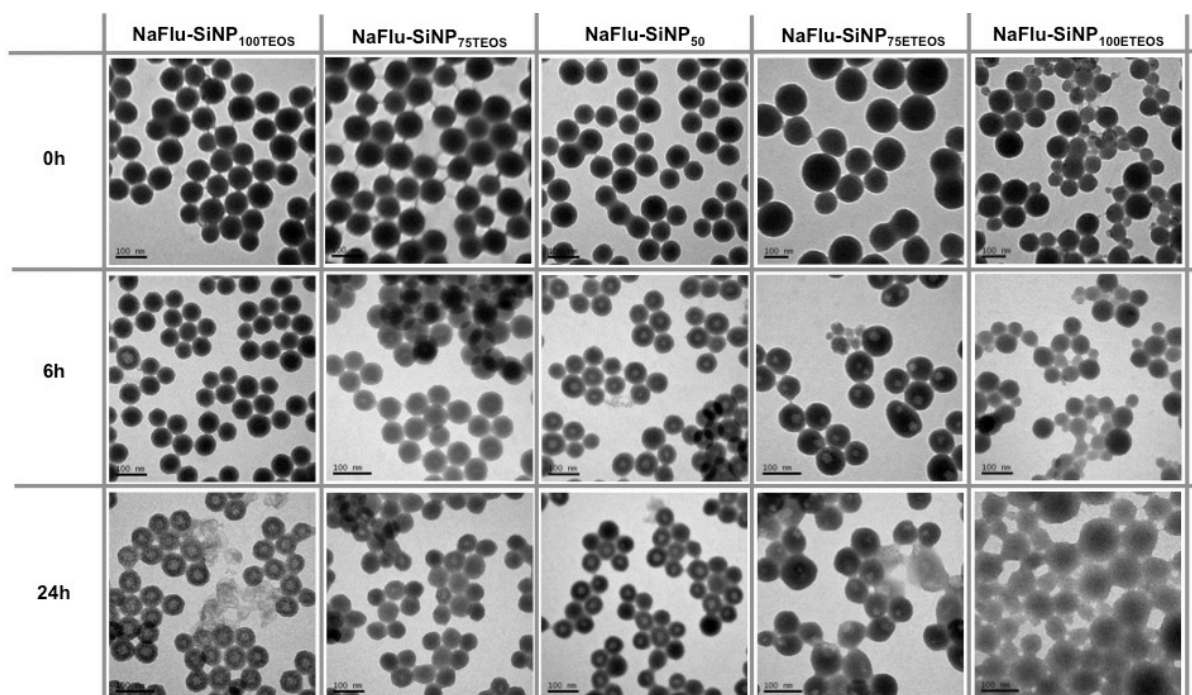
Figure 93: TEM analysis of NaFlu-SiNPs series when 250 µg/mL of particles in buffer pH 6.

172
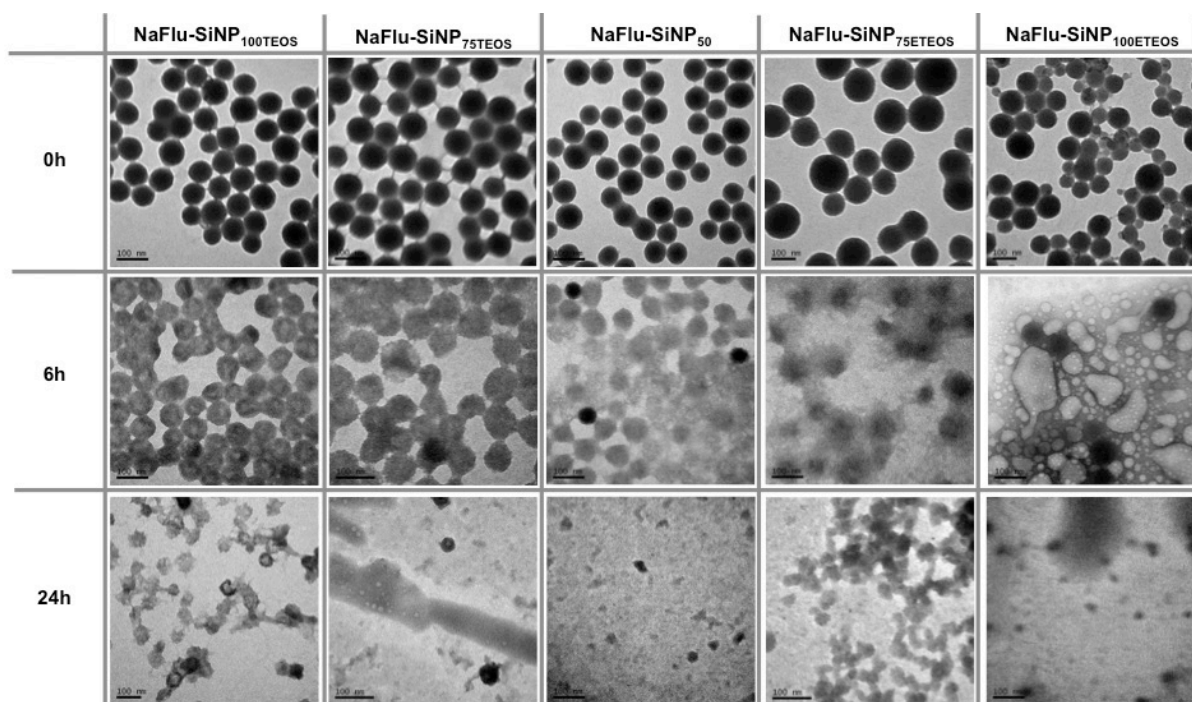
Figure 94: TEM analysis of NaFlu-SiNPs series when 250 µg/mL of particles in buffer pH 7.4.

MB-SiNPs and **NaFlu-SiNPs** proved to be unfavourable as drug delivery systems due to the low/absent control in the release kinetics. Data showed that highly hydrophilic molecules (NaFlu) are very poorly loaded inside the silica matrix and that the low amount loaded leaches immediately and independently to the surrounding environment. When a less water-soluble compound was internalised in the particles (MB) the loading efficiency improved, even if only the dye was physically entrapped, but the drug release was very limited and inconsistent. In particular, the release of the hydrophobic dye from **MB-SiNPs** appeared to be random and very low, even lower than 30% of the total dye loaded. In the case of **NaFlu-SiNPs**, the issue is exactly the opposite: the cargo is released too quickly, even at pH 4, which indicates that the drug would be released directly in the stomach, where the active compound would be degraded, therefore making the system unfavourable for oral administration.

A possible solution to overcome the issues with **NaFlu-SiNPs** could be to covalently load the dye into the matrix, which will surely retard the release. This method requires the conjugation of the drug with a silane derivative, which can then be involved in the hydrolysis/condensation process during the formation of the silica core. The issues related to the **MB-SiNPs** are unfortunately more complicated. Although, chemically changing the dye and loading it covalently inside the particle would improve the kinetics of release, MB appeared to interfere with the silica matrix formation, leading

ultimately to an alteration of the particles dissolution. This highlights the importance of evaluating the properties of the particles when used as carriers for specific compounds, since the release and degradation kinetics may be altered by the physico-chemical properties of the cargo. Using larger volumes than the one allowed by the "Eppendorf" assay would presumably assist in the solubilisation of the poorly water-soluble compound in the surrounding environment, enhancing its release and allowing for a better evaluation of the process.

The observed weakness of **MB-SiNP$_{100ETEOS}$** compared with the resistance to degradation of **MB-SiNP$_{100TEOS}$** is noteworthy. The unique degradation properties of **MB-SiNP$_{100ETEOS}$** and **MB-SiNP$_{100TEOS}$** could potentially lead to the formulation of different SiNPs, which do not suffer from basic etching or that can be degraded at low pH respectively, making them useful for other applications.

4.4 Conclusions

In the present study shows that SiNPs maintain their structure and morphology at pH 4 and degrade at pH 7.4, which makes them efficient carriers for oral delivery. The cargo is protected from the acidic environment of the stomach and it is then released in the intestine where absorption occurs. The covalent loading method (**FITC-SiNPs**) was the most advantageous compared to the physical entrapment of the dye, considering both the loading efficiency and drug retention, and it would be recommended for delivery high hydrophilic drugs. Little difference in the release profile was observed between the particles formulated varying the ration TEOS:ETEOS when the SiNPs were evaluated in the single buffer. However, evaluating the release profile in a GI-like model, the release of the cargo from **FITC-SiNP$_{100TEOS}$** appeared to be slower than with **FITC-SiNP$_{100ETEOS}$.** It was also interesting to observe the differences in the dissolution process depending on the silica derivate used for the matrix formation: **FITC-SiNP$_{100TEOS}$** degraded via a hollowing process, while **FITC-SiNP$_{100ETEOS}$** simply dissolved without the formation of holes.

Two different situations were observed with the NaFlu and MB loaded SiNPs. In the case of NaFlu-SiNPs the loading efficiency is very low and additionally the dye is immediately released after 1 hour in any buffer teste (pH 4, 6 and 7.4). This suggests

that highly hydrophilic dye should be covalently loaded inside the particles. At the contrary, in the case of MN-SiNPs the dye was released in very little amount at any buffer used, although MB was physically entrapped in the silica matrix. Interestingly even the dissolution of the particles is different compared with FITC-NPs and NaFLu-NPs. **MP-SiNP$_{100TEOS}$** showed to be highly stable even at pH 7.4 while **MP-SiNP$_{100ETEOS}$** started to degrade even when exposed at pH 4. These results can be related to a possible interaction between the cargo and the silica matrix of the particles. This could lead to (i) an alteration of the cargo's properties and/or (ii) to the alteration of the carrier's characteristics. This highlight the fact that each formulation requires specific and appropriate studies in order to evaluate its applicability. SiNPs and, presumably, other types of nanomaterial, should not be considered as carriers bearing the same features and applicability in any situation. Since cargo and carrier can interact with each other, it is important to consider them in combination as a new entity, a complex material, whose behaviour needs to be defined according to the desired application.

4.5 Future work

The present work proves the potential of pH-sensitive SiNPs for oral drug delivery. The possibility of loading the particles with hydrophilic/hydrophobic compounds should be further investigated, along with the possibility of improving both loading capacity and release kinetics by taking advantage of the covalent loading method. To better prove the efficiency as oral carrier, the capability of SiNPs in protecting the cargo from enzymatic activity should be tested as well. A similar GI-model experiment should be therefore accomplished with the addition of enzymes in buffers. The release profile should be defined for each case by using appropriate methods, considering the different properties of the compounds loaded. In the case of hydrophobic compounds, for instance, the use of greater volumes could be useful to better evaluate their release from carriers. Cytotoxicity studies should be accomplished using cell lines belonging to the GI tract and if the *in vitro* tests are positive, the efficiency of SiNPs as carrier for oral drug delivery should be further investigated *in vivo* experiments. Furthermore, different mechanisms of degradation observed for the SiNPs formulated using ETEOS or TEOS should be deepen.

Chapter 5

Improving colloidal stability of NPs stored in aqueous suspension

5.1 Introduction

Colloidal systems have been significantly investigated for drug delivery, cell imagining and sensing devices, but the difficulties in controlling the behaviour of the particles, during long storage and once surrounded by a biological environment, have limited their translation into clinical use. The efficacy of the nanomaterial is strongly related to the physico-chemical properties of the "nano" entities. It is therefore fundamental to keep in mind that any possible morphological changes or alteration of the properties of the material could reduce its activity or/and increase its toxicity in the case of biological applications[271,272]. For these reasons, results obtained using colloidal suspensions for *in vitro* and *in vivo* applications cannot be considered trustworthy and reproducible if the properties of the material used vary over time. The physico-chemical characteristics of the particles in solution are constant only for a certain amount of time after their synthesis, but often short/long term storage is required *(Figure 95)*.
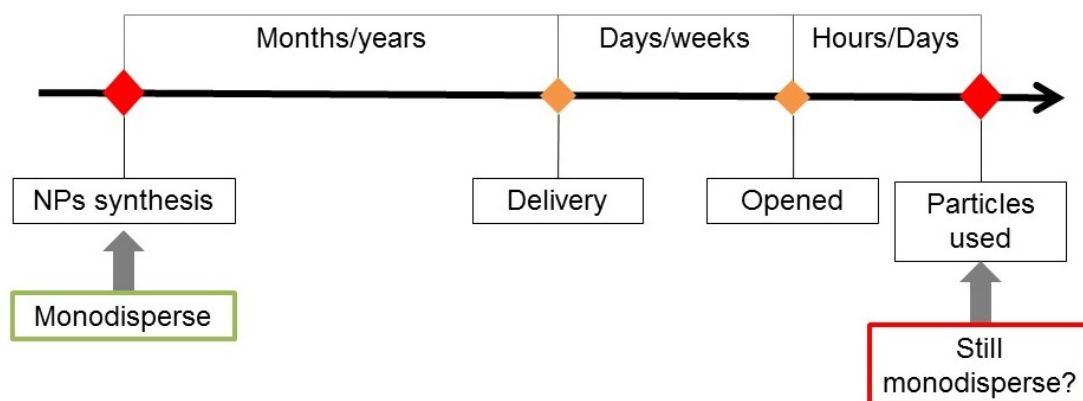
Figure 95: The figure shows the possible fate of monodisperse NPs after synthesis.

While some nanomaterials, such as AuNPs, are stable in aqueous solution, other type of particles are suspended in organic solvent (i.e. ethanol), as is the case for SiNPs. However, organic solvents are not suitable for biological purposes, hence several steps of washing and re-dispersion in aqueous solvents (water, PBS, etc.) are required prior to use, which can induce aggregation. Furthermore, proteins, genetic material and antibodies experience denaturation if in contact with organic solvents, thus nanomaterials loaded or functionalized with them need to be stored in aqueous solutions. It has been often observed, on the other hand, that most types of nanomaterial show physical instability (aggregation/particles fusion) and/or chemical instability (hydrolysis of the material forming particles, drug leaking and chemical reactivity between components), once in an aqueous environment (e.g. SiNPs), if not stabilised with specific additives (e.g. AuNPs, which are often stabilised in citrate buffer). These considerations have led researchers to look for suitable ways to store colloidal systems for short/long term, while maintaining their physico-chemical proprieties.

Two main opposing forces determine the stability of a colloidal suspension. The first is Brownian motion and involves a random change of direction as result of collisions between particles in suspension and the container walls[273]. The Brownian motion keeps the particles in constant movement avoiding them precipitate/fuse together under the gravitational force which leads to sedimentation *(Figure 96).*
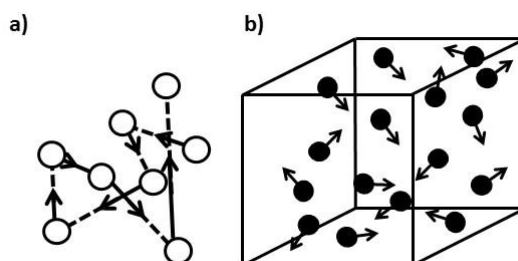
Figure 96: Representation of Brownian motion of particles. Each particle moves casually in the solvent (a) and randomly compared with the other particles in the sample (b).

While the Brownian motion depends mainly on the system in which the particles find themselves (temperature, viscosity of the solvent, etc.), the gravitational force is related to the size and density of the particles themselves. An unstable suspension can lead to two main situations: agglomeration and aggregation. IUPAC recommends two specific definitions in order to distinguish between these two terms which are often confused. An agglomerate is formed when particles interact with each other through weak physical interactions, forming precipitates larger than the colloidal size. If the colloidal particles are instead bonded through strong interactions, the process is named aggregation. By fusing together, the particles form an aggregate that is considered a new entity, having a different morphology and proprieties to the individual particles[274] *(Figure 97)*. It is not easy to distinguish between aggregates and agglomerates, but the difference is important, as while agglomeration is a reversible process, aggregation is not[275].
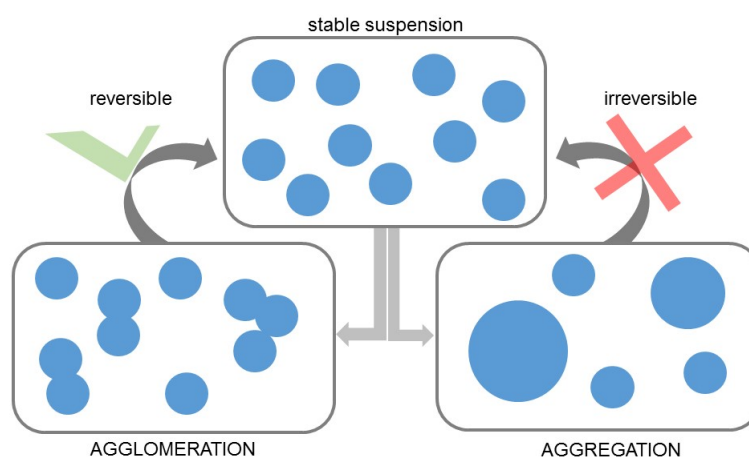
Figure 97: Illustration of the concepts of agglomeration and aggregation.

In the last years, many different approaches have been developed with the common purpose of stabilizing colloidal suspensions. All of them have some pros and cons, which make them suitable for a specific type of nanomaterial, but not for others.

5.1.1 Stabilisation techniques commonly used for NPs storage

Colloidal systems can be stored as suspension or as powder in order to preserve the physical-chemical properties of the particles and of the compounds eventually loaded inside the nanomaterial or attached at the surface. Although improvements can be achieved by choosing the appropriate storage method, different issues need to be faced with this two formulations. However, these issues can be, at least partially, overcame by the stabilisation techniques developed and presented in the following paragraphs.

Electrostatic and steric stabilisation: the DLVO theory

The most common method to stabilize colloidal systems is based on electrostatic repulsion. The interpretation of aggregation between particles in suspension is summarized in the DLVO theory[273,276], which defines the interaction of particles as a balance between attractive and repulsive forces. Once particles come close to each other, they behave depending on both their effective radius and their free energy. Two forces determine the free energy: van der Waals and the double layer interactions. Van der Waals forces are the result of the fluctuation of dipoles in molecules and they are often involved into the interactions between particles. These are normally attractive forces and they increase with the decrease of the distance between particles, with increasing the surface area of contact and with the increase of salt concentration in the solvent. The double layer interactions are instead repulsive, especially when the concentration of salt is low and when the density of surface charge increases *(Figure 98)*[276].
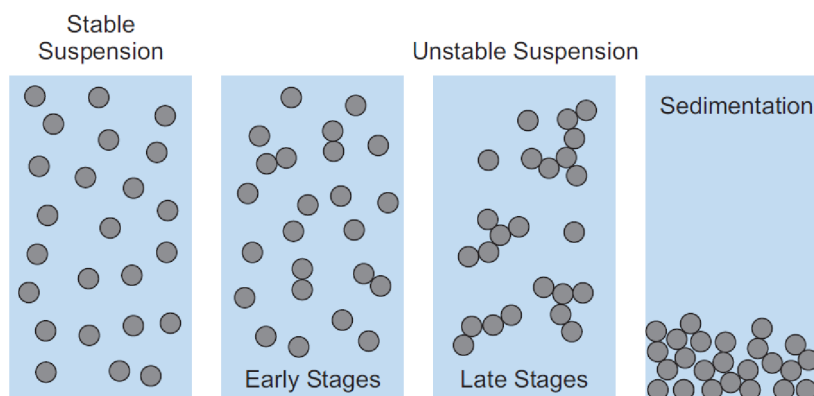
Figure 98: The scheme represents two possible situations which occur when colloidal particles are suspended in water. When the free energy is mainly driven by repulsive forces the suspension can be considered stable, while if the energy profile in the system is attractive the particles will approach each other forming initially dimers and trimers. As the aggregation proceeds the particles form larger cluster until they sediment. Adapted from reference[276].

As described by Coulomb's law, particles with similarly charged electric double layers and/or with a particular solvent affinity will repel each other[277]. It becomes clear that promoting the ionic adsorption on the particles surface, which induces the formation of an electronic double layer, leads to a decrease in the interfacial tension and, therefore, to a thermodynamically stable colloidal suspension[278,279]. The electrostatic stabilization of colloidal suspensions is limited by the concentration of salt in the solvent. It is known that the use of highly salted solvent destabilizes these systems due to changes in the surface charge of particles. A modification of the DLVO theory has been proposed in which greater value is given to the presence of ions in the environment surrounding the particles. In the proposed alternative equation, both the Coulomb law and the Debye-Hückel theory (which is a linearization of the Poisson-Boltzmann model) are taken into consideration. These theories define that particles (Coulomb's law) and electrolytes (for Debye theory) repel each other if they have the same charge, where instead an attraction occurs if they have opposite signs. With these modifications, the thickness of the double layer, which determines the stabilization effect, is related to the concentration of ions in the solution[280-282]. As shown in *Figure 99* double layer (t) around a positively charged particle is formed by anionic cloud where cations are present in much less amount. The density of ions forming the double layer is much higher closer to the particles surface, and it rarefies with the increase of distance from the surface. The DLVO energy profile (*Figure 99-b* graph above) and the force profile (graph below) is the result of the van der Waals and double layer contributions. The primary minimum corresponds to the minimum distance between

particles where there are only a bit of repulsive forces, therefore the resulting force is deeply attractive and the particles aggregate. In order to reach the primary minimum the particles need to overcome the energy barrier formed by the maximum energy peak of the DLVO profile. To do this a specific kinetic energy (related to the particle velocity and mass) is required. The high of the maximum, thus the energy required to aggregate, depends on the zeta potential and the thickness of the double layer (t). High concentration of salt decreases the stability of suspension because it decreases the energy that the particles need to overcome in order to fuse together. The second minimum, occurs when the repulsive electrostatic forces vanishes due to the high distance between particles. At this point particle weakly interact between each other forming agglomerates that can be re-dispersed.
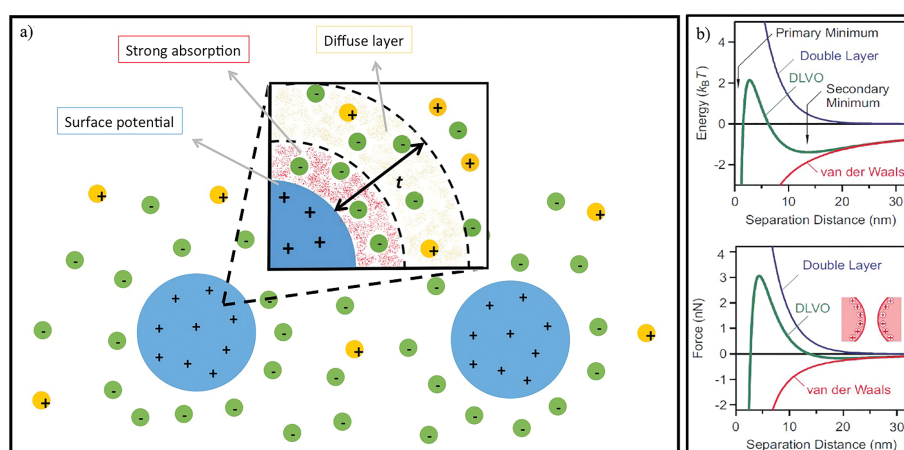
Figure 99: a) Representation of the electric double layer (t) around positively charged particles. b) DLVO energy profile (graph above) and the force profile (graph below). Partially adapted from reference[283].

The electrostatic stabilization approach is commonly used with metallic nanoparticles, which are uncharged and are therefore unstable when dispersed in aqueous solution. AuNPs are usually stabilised by using citric acid, the so-called Turkevich method, resulting in negatively charged particles that are stable in aqueous suspension[284]. Skoglund *et al.* evaluated the possibility of stabilising silver nanoparticles (AgNPs) by superficial absorption of surfactants. It was proven that, depending on the type and concentration of the surfactant, an enhancement or reduction of the agglomeration can be observed[285]. MacCuspie *et al.*[286] evaluated the destabilization effect produced by sodium chloride (NaCl), which is the most abundant salt in PBS and physiological fluids, when added to the suspension of AgNPs. They showed that on adding NaCl to citrate-stabilised AgNPs, the particles aggregate immediately, confirming the limits of

stabilizing the colloidal system when only electrostatic repulsive forces are involved. As a result, they proposed a further modification of the DLVO theory: the stability of colloids in solution is not considered dependent only on the balance between attractive van der Waals forces *(Figure 100-a)* and the electrostatic repulsive forces (double layer, *Figure 100-b*) but a third element, steric repulsive interactions, is also taken in consideration. Indeed, they explained that AgNPs are better stabilized by the surface adsorption of BSA due the steric hindrance that the bulky proteins cause on the NP's surface (*Figure 100-c*).

$$F = Fa\ (vdW) + Fer\ (double\ layer) + Fs(\ steric\ repulsions)^{286}.$$
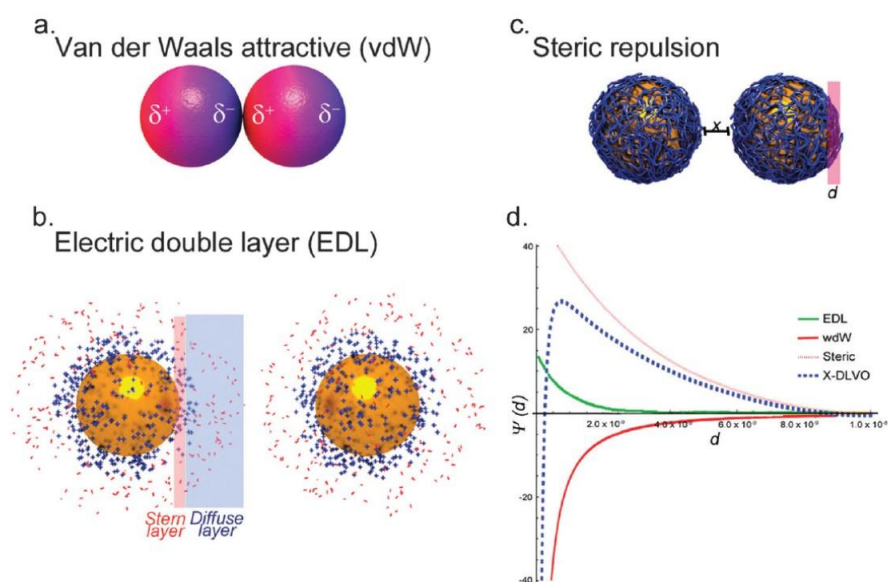
Figure 100: Summary of colloidal interaction that governs particle stability in solution. a) van der Waals interactions; c) Steric hindrance - repulsive forces; c) Electrostatic double layer - repulsive forces. d) DLVO energy profile which can be used to predict the contribution of different stabilization approach. Adapted from reference[287].

The electrostatic stabilization is not affected by pH and salt concentration in few cases. For instance, Hajdù *et al.* managed to stabilise iron oxide particles in aqueous medium by coating them with humic acid, which interestingly eliminates the pH sensitivity of the stabilised system and significantly enhances its tolerability of salt. Comparing this result with those obtained using slightly smaller molecules (citric acid), they concluded that humic acid stabilises iron oxide particles by both the electrostatic effect and through steric hindrance[288]. To summarise, although in some cases the electrostatic approach has been shown to be an effective method to stabilize colloidal systems, it is considered reliable only under specific conditions in which the surface charge of the colloids is not altered. Furthermore, if the nanomaterial is stored under vacuum, in

buffers or media where the superficial charge is neutralized/altered, or if the concentration of particles is high, then the presented technique shows limitations that must be taken into consideration.

As previously introduced, the repulsion between particles in suspension can be obtained through steric hindrance. This means that, by coating the particle surface with specific polymers or other materials, it is possible to physically avoid that particles come close enough to form aggregates. Stearic repulsion can occur between nanoparticles with low density coverage (*Figure 101*-a). In such case the distance between particles (H) is less than the double of the thickness of the layer (L) but bigger than the thickness of a single polymeric layer [L<H<2L]. Therefore the polymers of the two interacting particles tend to penetrate into each other resulting in a reduction of the free energy and therefore leading to an unstable suspension. If the coverage density is high (*Figure 101*-b) the suspension is better stabilised since the polymeric layer do not interpenetrate between each other. The energy profile in *Figure 101-c* shows that the higher is the distance between particles and the higher is the stability of the suspension.
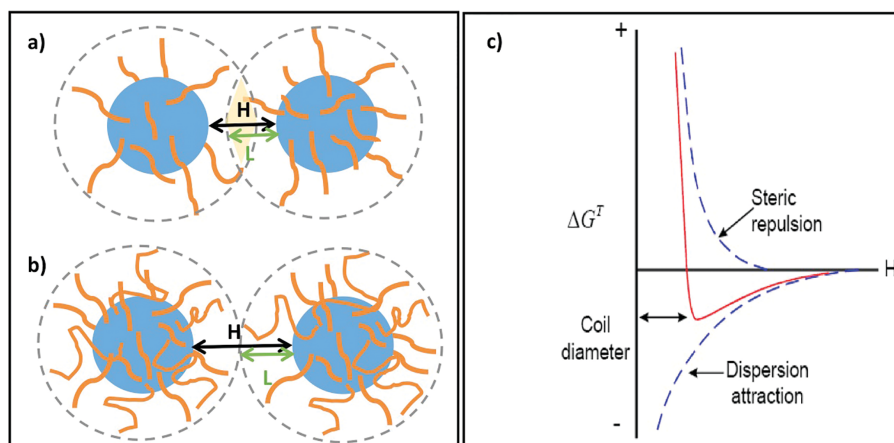
Figure 101: Representation of stearic repulsion between nanoparticles with low (a) or (b) high density coverage. c) DLVO explanation of the potential energy profile. Partially adapted from reference[283].

Different surface chemistry strategies have been applied in order to shield nanomaterials. The shell can be formed during the synthesis of the nanomaterial (*in situ*)[289] or post-synthesis[290,291]. In the latter case, the building material can simply be absorbed on the particle surface or covalently bound. For the covalent coating, functional groups, which can be used as anchor for the bound formation, are needed on the surface [292]. The bulky material used for the functionalization can vary depending

on the type of particle used, the type of solvent and the final use of the nanomaterial, where biocompatibility and toxicity must be considered. Large molecules are normally used to create steric hindrance on the surface, such as bulky proteins[293] (e.g. BSA[286,294,295]), copolymers[296], PEGylates[297,298], carbohydrates[299] and phospholipids[289,291]. *Figure 102* shows two examples were SiNPs were stabilised using lipids (*a*) or BSA (*b*).
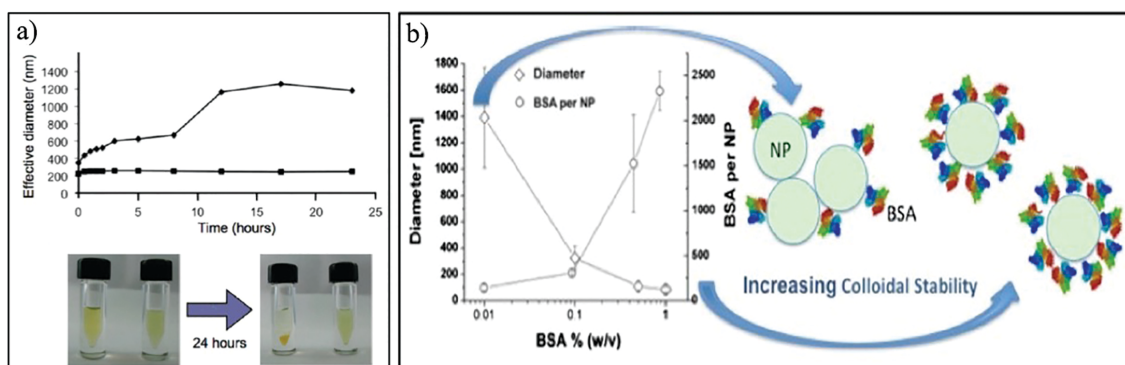
Figure 102: Two examples of steric stabilisation of NPs. a) mesoporous silica nanoparticles have been stabilised with lipids; DLS measurements and visual evaluation of samples proved the stabilisation effect reached in PBS. Adapted from reference[298]. b) The graph shows that the stabilization effect increases with the increase of the BSA adsorbed on the SiNPs surface. Adapted from reference[295].

Depending on the physico-chemical proprieties of the coating material (hydrophilicity/hydrophobicity, charge, etc.), along with stabilization, the biocompatibility, loading capacity, half-life in the bloodstream, targeting and up-take can also be enhanced. However, coating the nanoparticle surface can limit the intrinsic activity of the nanomaterial. It has been pointed out, for instance, that coating supermagnetic iron oxide nanoparticles with lauric acid and albumin, an alteration of the saturation magnetization and biocompatibility occurred, although there was no evidence of colloidal instability[24]. Conversely, Barbu and co-worker exploited the biocompatibility and stabilisation effect of dextran designing NPs capable of permeate the blood-brain barrier (BBB) due to the presence of alkylglycerol. Alkylglycerol-based polymeric NPs are known to enhance drug availability to the brain but they suffer of instability in biological environment. After addition of dextran in the formulation, these particles showed to have good stability in physiologically relevant media preserving the permeation properties and the favourable drug release which characterise these type of particles[300]. Steric stabilization has a few advantages compared with the electrostatic repulsion. For instance, it is not sensitive to surface charge and salt concentration, it is suitable for non-aqueous suspensions and it is effective even for

highly concentrated samples. However, surface chemistry is not an easy choice, since it often requires multi-step reactions along with purification and characterisation steps that are not always straightforward, making this method sometimes laborious, expensive and time consuming.

Hydrothermal treatment

When specific types of particle are used (iron, magnetic silica nanoparticles, etc.) an alternative technique can be used to give a more stable suspension. Through hydrothermal treatment of the synthesised particles, the aggregation process can be significantly reduced, limiting the formation of aggregates even once the particles are exposed to unfavourable situations, such as highly salted buffers of complex medium[301-303]. Despite the good results achieved using this approach, the high temperature and the particular conditions required by the procedure mean that the hydrothermal treatment is still not considered as a valuable alternative to stabilise colloidal systems.

Lyophilisation

A further technique widely used to stabilize small molecules, proteins and colloidal systems over long-time storage is lyophilisation. Freeze drying (FD) is a common technique which involves a dehydration process typically used to preserve and make material more convenient to transport. For the process to occur, the sample needs to be frozen and then, when placed under vacuum, the water sublimes to leave the sample in a dried form. As well as particles, proteins, enzymes and biological materials are also commonly stored in this dried form for long periods of time.

The process of freezing induces stress in the particles, so to avoid degradation and agglomeration of particles cryoprotectants or lyoprotectants are used as additives in the formulation. The theory behind the role of these protectors during the FD process is that they replace the water molecules. Analysing protein samples, it has been proved that the presence of water maintains the structure of these complex molecules, forming hydrogen bounds with their reactive groups. When the water is removed, the reactive sites become free and the protein aggregates due to the interactions between molecules. It has been proposed that protectors reduce the possibility of aggregation

by forming hydrogen bonds with the reactive sites of proteins, taking the place of water molecules after sublimation occurs[304,305].

Three main problems are related to the use of this technique for long-term stabilization of colloidal suspensions. First of all, depending by the type of particles, the method can be effective only when the correct type of cryoprotectant is used and then only at a specific concentration. Since the type and concentration of cryo-protectant needed are unknown, it is necessary to proceed by trial and error, making the method laborious and time-consuming. In some cases, mannitol, in specific concentrations, has proved to be the best choice,[306] although not when used for polymeric nanocapsules. Glucose and sucrose were also chosen in some circumstances[26], while BSA gave better results with SiNPs, allowing for easy re-dispersion of the particles in suspension and keeping them stable for a few hours. On the other hand, BSA is relatively expensive and not suitable for large-scale production[299]. The second problem related with FD is that cryo-protectants can affect the morphology of the NPs surface, especially if used at high concentrations. The type of particles and the type of cryo-ptrotectant used determines the severity of these changes. For instance, as shown in *Figure 103-a*, when liposome nanocapsules (LNC) are protected with mannitol, their surface appears more rough and porous than when they are formulated with maltodextrin[307]. It can be observed that different cryoprotectants have different effect depending on the particle surfaces, and the effect can be more or less intense depending on the material of which the particles are made off. Thirdly, an important requirement of the FD process is that the colloids can be easily re-dispersed into solution after reconstitution as single entities. Unfortunately, in some cases, this step requires time and, depending on formulation and process used, some aggregates can be present in the reconstituted sample or aggregation occurs immediately after[306]. For instance, as shown in *Figure 103-b,* the reconstitution ability depends on the combination of particle-cryoprotectant chosen. For instance, mannitol showed to be a good cryoprotectant only for lipid-nanocapsules (LCN). The freeze-thaw effect is measured using the S_f/S_i value, which characterizes the reconstitution ability of the lyophilizate. Indeed, S_i is the size before and S_f the size after redipsersion. $S_f/S_i = 1$ indicates a complete reconstitution, $S_f/S_i > 1.5$ is a sign of a poor reconstitution[307].
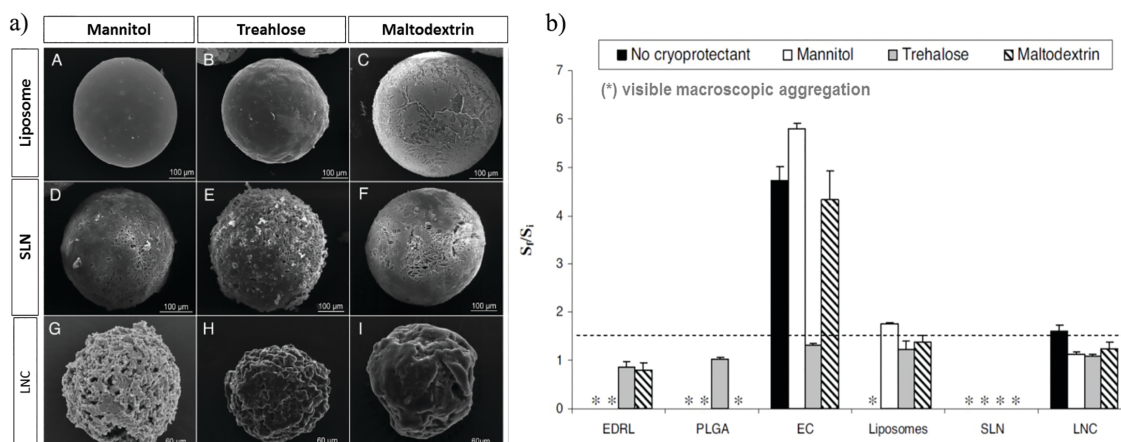
Figure 103: a) Surface alteration induced by cryoprotectants on the nanoparticle surfaces. b) Reconstitution ability of different lyophilizates formed by using different types of cryoprotectants (mannitol, trehalose and maltodextrin) with different particles (polymeric particles-EDRL, PLGA and EC; lipid nanoparticles-SLN; lipid nanocapsules-LNC and liposomes). Adapted from reference[307].

A possible alternative to FD is spray freeze drying (SFD), where the particles are sprayed in a cold environment and then frozen in order to keep them separated during the freezing process, thus reducing the stress. This method is apparently more reliable, but cryo-protectants are still necessary for the stabilisation to succeed, morphological alteration can be still noticed and it requires specific instrumentation[306,307]. Although FD overall can be considered a good option as a storage method, the cost of the instrumentation needed and the limitations discussed above leave the door open to innovations.

5.1.2 Nanomaterials on the market

The methods used for storing colloidal suspensions described above are commonly used by suppliers to stabilise nanomaterials produced on a large scale, before delivery to clients. More often than expected, users receive items with different properties to those claimed by the provider and some differences are noticeable between the nominal specifications and the actual characteristics of the nanomaterial. When this happens, the consequences can be deleterious for researchers who cannot rely on results acquired. It is always necessary to characterise the nanoparticles before using them for specific studies[308]. Moreover, information as NP size, mean size, size distribution and charge density is not always enough when the materials are employed in biological studies and manufacturers refuse to give the further information required causing sometimes artificial artefacts in biological testing[309].

5.1.2 When morphology matters

The use of NPs in nanomedicine implies the need for increased knowledge regarding particularly the interaction between the nanomaterial and living organisms and their cells. Three fundamental processes must occur for the NPs to interact with the cells. First of all they have to reach the cell, secondly they have to interact with cell surface and thirdly they must be internalised *(Figure 104)*. Each of these events occurs because of specific properties of the nanomaterial, highlighting the importance of maintaining their characteristics over time. Single particles, with lower density and smaller in size, diffuse in the environment better than the aggregates, enhancing the interaction with the cell surface and their uptake. However, since the diffusion process is time-dependent, the effect induced by the single particles takes longer to occur. Aggregates sediment on the cell surface in a shorter time, but they are not internalized since only cells belonging to the family of macrophages internalize particles bigger than 100 nm in diameter[310,311].
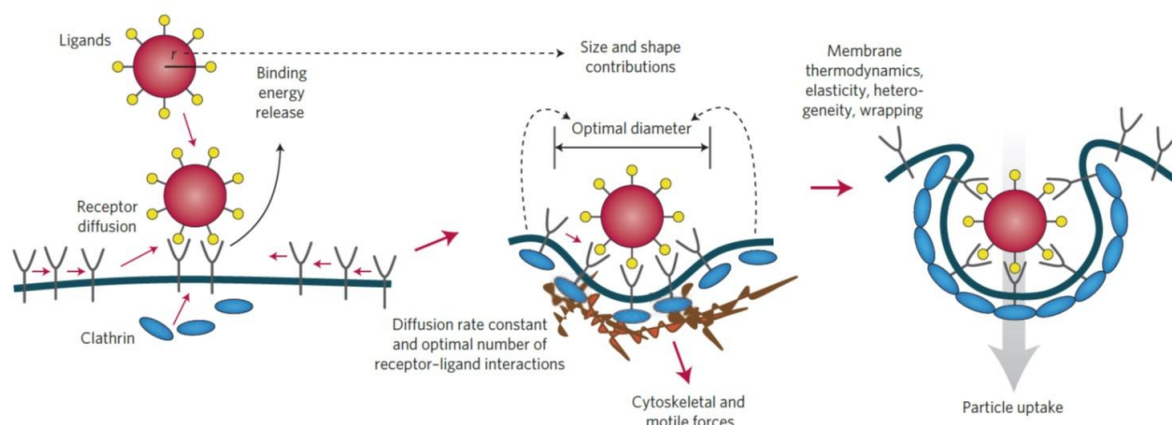
Figure 104: Size/shape of particle and specific/non-specific binding between ligand-receptor determine the wrapping around the particles and its internalisation. Adapted from reference[311].

The properties of the NP surface are fundamental for adsorption and cellular uptake. The cellular surface is predominantly negatively charged and, therefore, positively charged particles interact more efficiently with them compared to negatively charged and neutral particles[312-314]. However, it is well documented that positively charged particles tend to be unstable in water, buffers and cellular media[315]. Once nanoparticles are suspended in complex fluids (such as plasma, whole blood, urine), not only can they aggregate but a wide variety of proteins and salts can be adsorbed to their surface, forming the so-called hard and soft protein corona layers *(Figure 105).* The formation

of the protein corona can dramatically alter the biological activity of the particles, modifying their interaction with living cells, enhancing their toxicity, making both the opsonisation by macrophages and accumulation in the liver easier, thus reducing the half-life time of the nanomaterial in the body[287,313,316]. This has been observed for example by Salvati *et al.* which showed that SiNPs functionalised with transferrin (T$_f$) absorb different type of proteins on the surface once in contact with complex biological fluids. As shown in *Figure 105*, the protein corona formed hide the T$_f$ which can not interact with the transferrin receptor (T$_f$R) on the cell membrane therefore the particle lose specificity for the target[317]. Many research groups have tried to study the mechanism of formation of the protein corona, the proprieties of the surfaces that favourites its formation and the biological consequences[318]. Functionalising the surface with copolymers (PEG and dextran) has been shown to limit the formation of the protein corona on the surface[309,316,319].
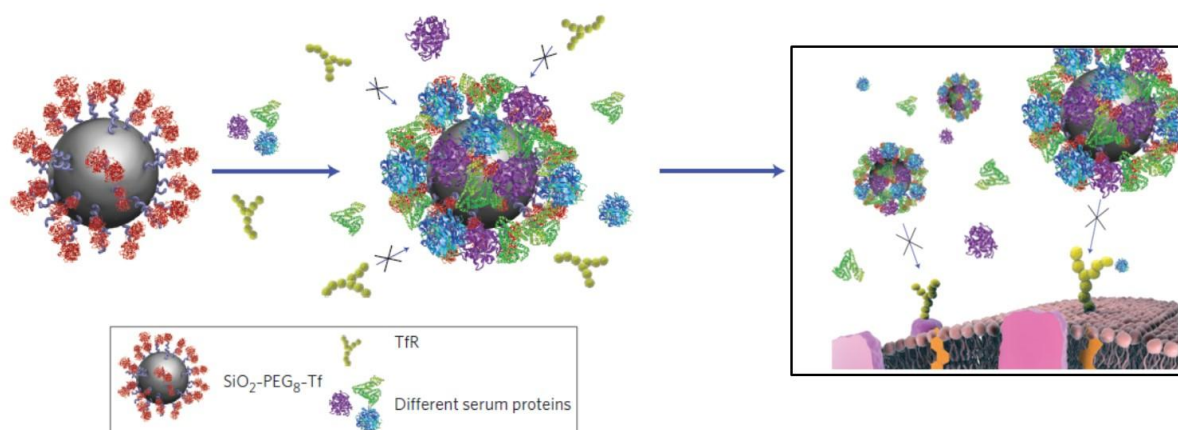
Figure 105: Formation of protein corona can alter the biological activity of the nanomaterial. Adapted from reference[317].

Despite the knowledge acquired, the prediction of stability of colloidal suspension in a complex environment such as culture cellular media or biological fluids is still a utopic goal[317]. The events that can occur which alter NPs properties are highly system dependent and many factors need to be evaluated. Considering the difficulties to foresee the behaviour of particles when added into a biological medium, it is fundamental to rely on the physico-chemical properties of the nanoparticles prior their use. The difference in surface area between an aggregate and monodispersed colloid, together with the alteration of the physico-chemical properties of their surface, can

heavily interfere with the cell interaction. Therefore, the characteristics of the material suspended must be thoroughly defined before further applications.

5.1.3 Storage methods proposed

Complex materials

In the last decades, materials scientists have turned their interest to the combination of known materials in order to enhance the properties of each component. The mutual benefits of combining materials have fascinated research groups belonging to different scientific fields. A variety of nanocomposite polymer hydrogels, with unique chemical, physical and biological properties, has been developed. NPs are sometimes used as building blocks or as cross-linkers for polymeric gel formation[320]. In other cases, the addition of NPs to the gel formulation confers to the hydrogel specific characteristics, such as responsiveness to mechanical, optical or thermal stimulation, increasing the number of possible applications of the material[321]. It is well documented that SiNPs increase the mechanical strength of polymeric gels. Numerous publications exist regarding the combination of different types of SiNPs and different polymeric gels, improving the proprieties of the gel matrix or developing new drug delivery systems[322-326].

Bearing in mind the attraction of enhancing the physical and biological characteristics of both materials, we combined NPs with hydrogels in order to exploit the organization of the gel network to keep individual particles separated and, thus, stabilizing the colloidal suspension. We propose a versatile method to stabilise colloidal systems in biological-friendly solvents, in order to maintain the chemical and physical characteristics of particles even after long-term storage. There is a plethora of NPs suitable to extrapolate key parameters that affect their stability in various formulations. In this work, we used dye-doped SiNPs as proxies to study the efficiency of the proposed method on reducing particle aggregation, evaluating the changes in their physico-chemical properties over time. We focused on SiNPs due to the ease with which is possible to modify their surface, increasing and decreasing their stability. In this way, we could better evaluate the robustness of the proposed method through synthesizing different types of SiNPs. In order to confirm the versatility of the proposed

model, some studies have also been done using AuNPs, which are widely used and normally stabilised in citric acid or PBS.

The correct scaffold

IUPAC defines a gel as a "non-fluid colloidal network or polymer network that is expanded throughout its whole volume by a fluid"[274]. Many features of gels are considered in their classification, as represented in *Figure 106*. Gels can be classified according to the composition of the solid network and the fluid continuous phase. If an organic solvent or an aqueous solution is used as liquid phase, we will hear about organo- or hydrogels, respectively. When considering the molecule forming the solid phase, gels are instead classified as polymeric (when the network is formed by long polymers) or as low molecular weight or supramolecular gels (if the gelator is a small molecule). One of the most relevant classifications of gel takes into account the interactions between the molecules forming the solid phase. Depending on these interactions, the network formed, and therefore the self-supportive gel reached, has different physical behaviours: when the network is formed by covalent cross-linking interactions between the gelators, we speak about non-reversible/chemical gels, while if weak, non-covalent interactions occur (hydrogen bonding, van der Waals forces, solvophobic interactions, etc.) the gel is considered to be a reversible/physical gel.
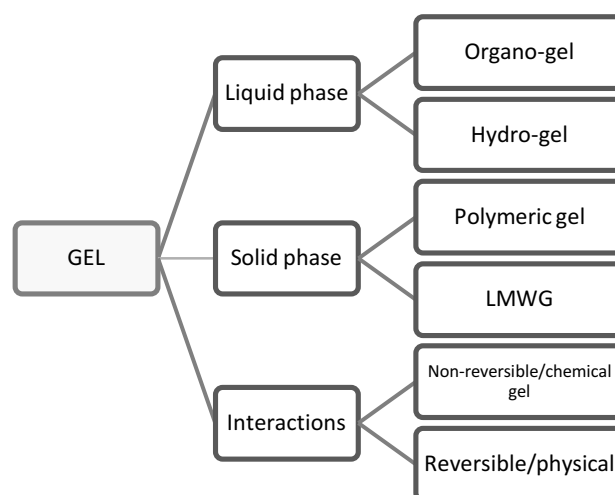
Figure 106: Schematic classification of gels accordingly to three main aspects: liquid phase, solid phase and interactions which lead to a self-supportive gel.

Many different types of gel are described in literature having different characteristics, but not all are suitable for the application herein described. We identify a few of main characteristics required for gel to be considered as a possible vehicle to store particles.

- It must be a hydrogel, since one of the main featured of the method proposed is to storage particles in an aqueous environment.

- The gelator must be inert to the particles and no strong interaction should occur between the particles and the gel so that the NPs are easily separated when required, without need for chemical alteration.

- The gel fibres must be biocompatible and non-toxic, such that once the gel has been broken and the particles are in back in suspension, the sample can be used directly for biological application, without any further manipulation.

- The gelation must be readily reversible and the material must show a good balance between stiffness and reversibility in order to resist until certain limits to mechanical stress for the sample to successfully be delivered.

Considering this, we decided to store silica nanoparticle in a low molecular weight hydrogel (LMWHG). These are made from relatively small molecules which form a three-dimensional network in water via non-covalent interactions, to give a reversible, self-supporting gel. LMWHs having the advantages of being easily designed, normally with biocompatibility and biodegradability, and have been widely applied in engineering, enzyme immobilisation, drug delivery, cell culture, etc. The structure of the molecule and the specific interaction needed for the network formation determine what triggers the formation of the self-supporting gel and what induces its degradation. In particular, we chose a responsive hydrogel formed by the amphiphilic molecule Fmoc-galactosamine (Fmoc-Gal, *Figure 107*) in which to trap the particles. This gelator has been well-studied and its various structural analogues have already been explored, for instance in the preparation of cell culture scaffolds[327]. The construction of the Fmoc-Gal gel is a fully reversible process, driven by a combination of non-covalent forces such as CH-π and T-stacking[328].
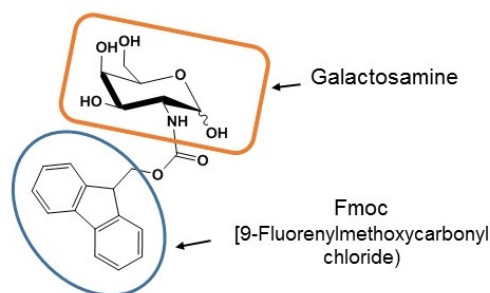
Figure 107: Structure of Fmoc-Gal gelator.

Fmoc-Gal forms stable gels at the minimum concentration of 2 mg/mL in water and has the characteristics we were looking for: (i) it should not interact chemically with the nanoparticles, (ii) it is easily formed and it can be reverted to solution by shaking it. In addition, (iii) since similar molecules have been used in biological assays, Fmoc-Gal is not expected to induce cytotoxicity. The most interesting feature of the Fmoc-Gal LMWH is that the gel forms quickly after sonication and the matrix can be broken by simply shaking/vortexing it, which nicely supports our requirements. In particular, by ultrasonication the single molecules of the gelator are exited at high energy level and oriented such that they interact between each other forming a self-supporting hydrogel. When instead the self-supporting hydrogel is shacked, the gel is broken since in this case the energy is lower and it is applied at the macroscopic level not at the molecular level. For instance, a thermos-responsive hydrogel[325] could be problematic, considering that requires the temperature to be constantly controlled and high temperatures could even damage the NPs its self or biomaterial on/into it. For similar reasons, the matrix of pH-responsive hydrogel could undesirably turn into solution in response to pH changes.

Theory behind the method

We believe that, on trapping the particles within the gel fibres, their mobility decreases. Therefore, phenomena such as aggregation, sedimentation and fusion would be drastically reduced. The principle underpinning this idea can be supported by analysis of the DLVO theory: suspended nanoparticles need to overcome the maximum energy peak defined by the stability profile in order to reach the primary minimum and therefore irreversible aggregate. This energy is determined by the mass of the particles, which is not a variable, and by their velocity in the sample. Einstein stated

that the Brownian motion of particles suspended in a liquid is governed by the diffusion coefficient, which is inversely proportional to the viscosity of the solvent. The higher the viscosity of the solvent, the lower the coefficient, and therefore Brownian motion of the particle in the solvent is more limited. Translating this in the DLVO profile, an increase in the energy needed for the particles to aggregate will enhance the stability of the suspension (*Figure 108)*.
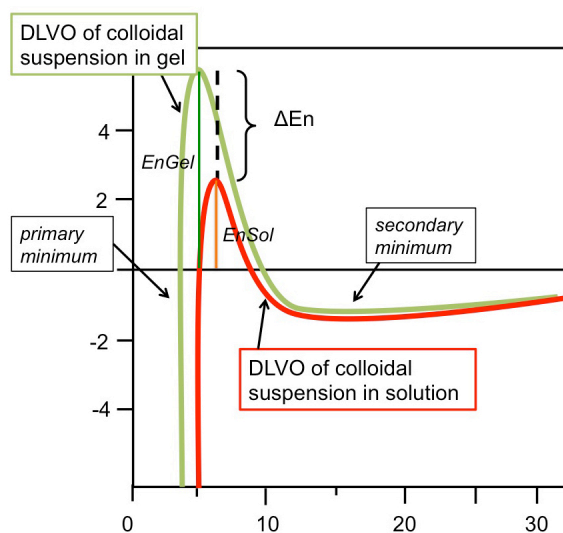
Figure 108: When particles are stored in gel the energy of the maximum peak will be higher than if stored in solution where particles are free to move (EnGel > EnSol), as result, the colloidal system when stored in gel is reasonably more stable than if stored in solution. Self-produce image.

5.1.4 Project aims

Based on this theoretical idea, a versatile approach to storage nanoparticle for long-term storage has been evaluated and the results are presented in this chapter. The proposed method is simple and it is presented in *Figure 109*: (i) the pellet of nanoparticle is re-dispersed in a solution of Fmoc-Gal and, after sonication, interactions between the gelator molecules occur and the solution turns into a self-supporting gel containing entrapped particles. When needed, (ii) by simply shaking or vortexing the sample the gel rupture can be induced to have the NPs back in suspension (iii). The stored sample of NPs can be used directly in biological experiment, without any further manipulations[i].

---

[i] An animation explaining the concept of the storage method proposed can be found on YouTube entitled 'Why would you store nanoparticles in responsive hydrogel?' [https://www.youtube.com/watch?v=EUQns52Q_q4].
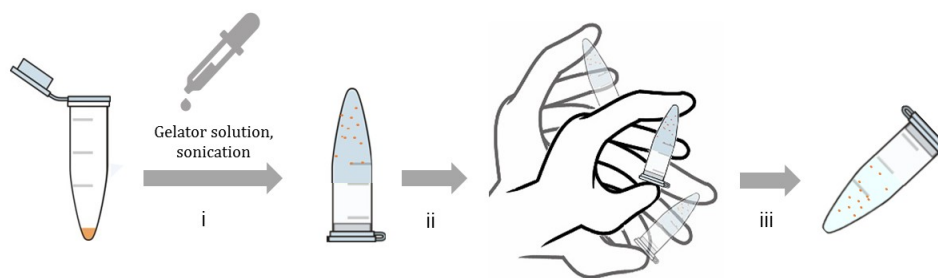
Figure 109: Schematic representation of the method: i) particles are suspended in the Fmoc-Gal solution and after sonication a self-supporting gel is formed. Ii) Gel can be broken by hand-shaking to have the particles back in suspension (iii).

Comparing NPs stored in solution *(Figure 110-A)* and in gel *(Figure 110-B)*, we have demonstrated that the method reduces changes in the colloidal system even after long-term storage in 'biological-friendly' solvents, such as water or PBS.
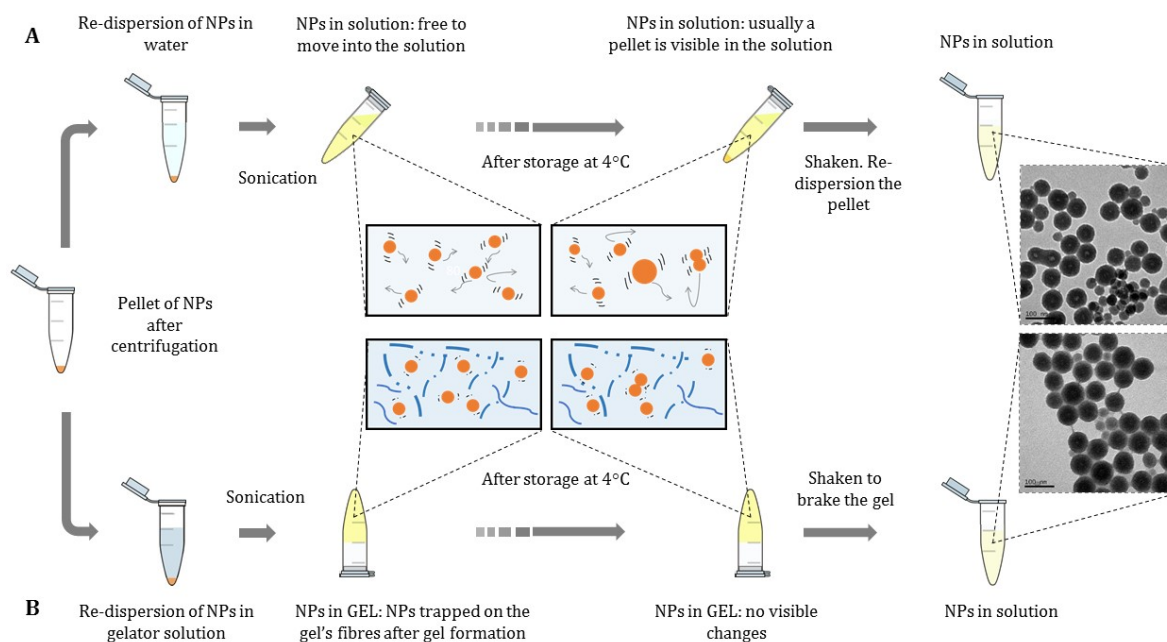
Figure 110: Evaluation of the efficiency of the method proposed by comparing the monodispersivity of SiNPs stored in solution (A) or in gel (B).

The versatility of the method has been evaluated using different type of NPs (*i.e.* AuNPs) in different environment (*i.e.* cell culture medium). The applicability of the method has been investigated instead by accomplishing *in vitro* and *ex ovo* toxicity studies. Toxicity studies were indeed demanded claiming that the sample of nanoparticles stored in gel can be used directly without needing to remove residual gel fibres.

In this chapter, it is also evaluated the possibility of reducing the leaching of the cargo from the particles during storage, which is particularly undesired when NPs are used as carrier for drug delivery systems (DDS). Such drug-loaded NPs may need to be stored for extended period of time before use and should therefore retain their cargo. It is important to limit the loss of drug during storage, since it will determine the dosage given in a therapeutic treatment. The process of leaching of a drug trapped in a delivery system is regulated by different factors. The drug solubility determines the chemical gradient across the solvent and therefore its diffusivity into it. Depending of the matrix chosen there will be a different penetration of the solvent into it and a different erosion of its structure[329]. Once again, freeze-drying is considered a suitable method, considering that removing the solvent not only decreases the diffusion of the drug into it but the matrix degradation can also be limited. However, during the drying process the drug loaded into the nanoparticles could migrate on the surface of the carrier, following the flow of the solvent during the evaporation. As a result, the drug will be more concentrated at the surface of the nanoparticles, leading to a higher 'burst release' when the nanoparticles interact with the solvent again[330].

We expected that, by increasing the viscosity of the medium in which the carriers are dispersed, the diffusion of the solvent through the matrix of the nanoparticles is dramatically reduced and, therefore, so is the undesired leaching of cargo. Furthermore, a mechanically stable gel also provides a more tortuous and resistant barrier to diffusion for the solvent, resulting in a slower release[331,332] *(Figure 111).*
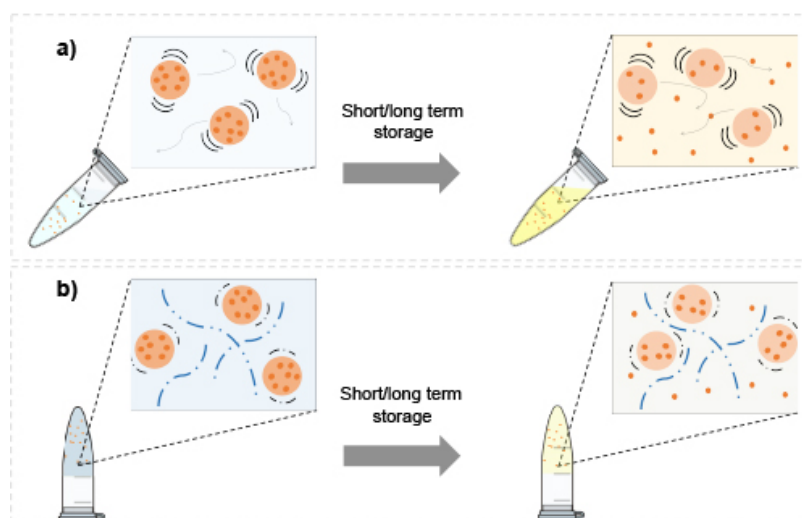
Figure 111: Schematic illustration of the differences leaching phenomenon observed between solution a) and gel b) samples.

5.1.5 Analytical techniques

Light scattering techniques are the techniques mostly used to analyse the size, polydispersity and surface charge of particles in suspension. Size and polydispersity are determined by monitoring fluctuations in the intensity of the light scattered from NPs in motion in the solution over the time. The way the light is scattered gives information on the size and dispersion of the NPs. Dynamic Light Scattering (DLS) is a straightforward analytical method and cutting-edge instruments are both available and affordable. However, while DLS data can be trusted entirely in the case of dilute and monodisperse suspensions, the limitations of the method become evident when concentrated and polydisperse samples are considered. In these cases, two issues are involved. Physical interactions between NPs could occur and a normal cumulative analysis would not give a reliable description of the droplets size in the sample; in this case, CONTIN analysis could be useful to obtain information about the entire distribution of the particle size. In the case of complex systems, it has been thoroughly explained that DLS data cannot be used alone to describe the real situation in the sample[336]. The consistency of the analysis can be improved using multi-angle DLS and static light scattering (SLS). The second issue related to polydisperse samples analysed with DLS is that, not being able to recognise the presence of different populations, even if only a few big particles are present, due to their higher scattering, the instrument will overestimate the average particles size. In such cases, the intensity-size distribution should be analysed together with the number-size distribution. In the latter, the number of NPs that give a specific signal are taken into consideration rather the intensity of the light scattered, reducing misinterpretation of the real sample.

Another analytical technique based on light scattering is Nanoparticle Tracking Analysis (NTA), which is based on similar principles to DLS, but presents a few crucial differences. Both techniques track the Brownian motion of particles in suspension to determine the diffusion coefficient, from which the software calculates the diameters at the given temperature and viscosity of the solvent by resolving the Stokes-Einstein equation. While DLS measures the size according to fluctuations in the scattered light, NTA does it through direct visualisation of the particles. Moreover, NTA analyses particle size and particle scattering intensity simultaneously, allowing the analysis of heterogeneous samples. NTA analysis is suggested when polydisperse samples are analysed or for low concentrations, while DLS remains the preferential solution for

quick and easy measurements. Since silica has a low refractive index, characterisation by NTA is not reported here. In order to track SiNPs it was necessary to considerably change specific parameters of the software and, for this reason, we decided not to rely on the result obtained. Thanks to their properties, AuNPs proved to be a good candidate for NTA analysis[275,336-339]

From the above considerations, Transmission Electrical Microscopy (TEM) was found to be the best technique by which to evaluate the efficiency of our proposed method. Using this technique, the sample is directly visualised allowing clear distinction between nanoparticles and gel fibres and the ability to highlight the presence of different populations. To determine the particle diameters, images acquired with the TEM camera were then processed with ImageJ software. While light scattering techniques calculate the diameter of particles in solution, for the TEM analysis the samples must be dried, which leads to small differences between the data obtained from TEM or DLS. The diameters measured by DLS are usually slightly larger due to the fact that some types of particle can absorb the solvent, but especially because DLS, and even NTA, measure the hydrodynamic diameter of particles, which is indicative of the apparent size of the dynamic hydrated/solvated particle. Indeed, light scattering techniques measure a hypothetical hard sphere formed by the particle of interest solvated by the solvent, which diffuses in the same fashion as the particle being measured *(Figure 112)*.
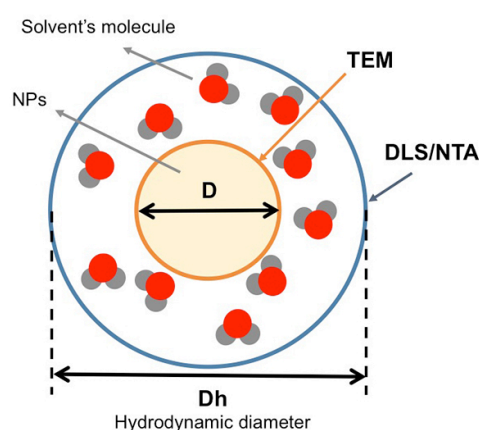
Figure 112: Representation of the different diameters measured using the different techniques.

TEM was used to evaluate the presence of aggregates (i.e. new entities with bigger size) in the SiNPs samples only. Since AuNPs agglomerate forming clusters of the original particles, it would't have been possible to clarify if the presence of agglomerates on the

TEM grid was due to the instability of the sample after storage or if the agglomeration occurred during the drying process required for the sample preparation. However, Scanning Electron Microscopy (SEM) was used to analyse AuNPs samples when exposed to unfavourable conditions. Since SEM allows a better analysis of the sample's surface, it was preferred for AuNPs in order to better distinguish between the particles, gel's fibres and NaCl residues. In *Table 36* are summarised the techniques used for NPs characterisation.

Table 36: Main differences between the analytical techniques used for the evaluation of the proposed storage method.

DLS	NTA	TEM
Light scattering technique		Microscopy technique
• Sample analysed in suspension • Hydrodynamic diameter		• Sample dried • Actual diameter
• Practical and generally automatic software • No concentration limits • Trustworthy only for monodispersed simple	• Many parameters need to be sated prior measurement • Concentration between 10^7-10^9 • Good for polydisperse sample allowing the recognition of different populations	• Different populations can be visualised directly • Allows to distinguish between NPs and gel fibres
Used for SiNPs and AuNPs	Used only for AuNPs	Used only for SiNPs

5.2 Experimental section

5.2.1 Materials

Cyclohexane (anhydrous, 99.5%), 1-hexanol (anhydrous, ≥99%), Triton® X-100, (3-aminopropyl)trimethoxysilane [APTMS] (97%), tetraethyl orthosilicate [TEOS] (99,99%), 3-(Trihydroxysilyl)propyl methylphosphonate [THPMP], monosodium salt solution 50 wt % in H2O, ammonium hydroxide solution (28% w/v in water, ≥99.99%), fluorescein isothiocyanate isomer (95%) [FITC], fluorescein sodium salt were purchased from Sigma Aldrich (Gillingham, UK). Methylene blue was purchased from Acros Organics (Loughborough, UK). Gold nanoparticles (diameter 30 nm and 80 nm; EM grade – OD1) were purchased from BBI Solutions (Wetzlar, Germany). Absolute ethanol, methanol, transparent Nunc Maxisorb 96 well plates, phosphate buffer saline tablets (one tablet dissolved in 200 mL DI water yields 0.01M phosphate buffer, pH 7.4) were purchased from Fisher Scientific (Loughborough, UK). Thereafter, the use of 'PBS' refers to 0.01 M PBS, pH 7.4. Deionised water (<18 MU) was prepared using 200 nm nylon membrane filters purchased from Millipore. Rhodamine B isothiocianate (mixture of isomers) [RBITC], Dextran (from *Leuconostoc spp.*; Mr ~ 40.000), sodium borohydrate (> 99.9%), sodium periodate (> 99.8%), N,N-dimethylformamide (anhydrous, 99.8%) [DMF]. All mentioned were purchased from Sigma Aldrich (Gillingham, UK). Dulcebbo's Modified Eagle Medium (DMEM) without phenol red and pyruvate and high level of D-Glucose was purchased from Gibico™. The model cell line U937 (human hematopoietic cell line histiocytic lymphoma) was sourced from European collection of cell culture. Human glioblastoma cell line (GBM) U87-MG (ATCC® HTB-14™, grade IV WHO classification) was obtained from American Type Culture Collection (ATCC®, Manassas, VA, USA). RPMI-1640 cell culture medium was purchased from Sigma Aldrich. DMEM with phenol red, antibiotic-antimycotic (containing 10,000 units/mL of penicillin, 10,000 μg/mL of stremptomycin and 25 μg/mL of Fungizone™), fetal bovine serum (FBS), Trypsin-EDTA were purchased from Gibico™ (Life Technologies). Carbon Tabs (12 mm Dia G3347N) and 0.5" Aluminium specimen Stubs were purchased from Agar Scientific. CellTiter 96® Aqueous One solution cell proliferation assay MTS was purchased from Promega. Poly(ethylene imine) coated nanoparticle (fluidMAG-PEI 750/O), Triton X-100, poly(ethylene imine)

(25 kDa), 4-(2-hydroxyethyl)-1-piperazineethanesulfonic acid (GlcHEPES) were purchased from chemicell GmbH (Berlin, Germany).

5.2.2 Synthetic methods

Synthetic procedures

Formation of Microemulsion: All nanoparticles were formed in a microemulsion prepared by combining cyclohexane (7.5 mL), 1-hexanol (1.133 mL), Triton® X-100 (1.894 g) and DI water (0.48 mL) in a 30 mL plastic bottle under constant stirring.

Dye Precursor Formation: In a dried glass vial, the fluorescent dye fluorescein isothiocyanate (FITC; 2.5 mg) was dissolved in 2 mL of 1-hexanol and APTMS (5.6 μL) was added. The reaction was allowed to proceed over 2 hours under a nitrogen atmosphere. After that, 0.666 mL of the mixture was collected and added into the pre-prepared microemulsion.

Synthesis of NP-FITC: Into the microemulsion described above, 100 μL of TEOS was added, followed by 0.666 mL of dye precursor solution. After 30 minutes, 40 μL of ammonium hydroxide was added to trigger the polymerisation. The mixture was stirred for further 24 hours. After this time, the microemulsion was broken by adding 30 mL ethanol. The formed silica cores were purified by centrifugation (14,000 rpm, 10 min) and re-dispersed in 30 mL ethanol (3×). After purification, the nanoparticles were stored in ethanol at 4°C.

Synthesis of NP-A-FITC-NH$_2$: The silica nanoparticle core was synthesised similarly to the NP-FITC protocol. After 24 h stirring, two 50 μL portions of TEOS were added to the mixture with a 30 minutes interval between additions. 30 minutes later, APTMS (25 μL) was added and the mixture was stirred. After 24 hours particles were purified as described above.

Synthesis of NP-B-FITC-NH$_2$: Similarly, to the protocol above, after 24 hours of stirring, one portion of 50 μL of TEOS was added to the microemulsion. After an additional 30 min, ATPMS (200 μL) was added and the mixture was stirred. After 24 hours particles were purified as described above.

Synthesis of NP-MB-NH$_2$ and NP-NaFlu-NH$_2$: Methylene blue and fluorescein sodium salt dyes were encapsulated in the nanoparticle cores by using 0.48 mL of their aqueous solutions (6.25 mM) as the water phase in the microemulsion. The rest of the procedure was as described for NP-B-FITC-NH$_2$.

Sample preparation

Preparation of Nanoparticle-loaded gels: The gelator was dissolved in filtered DI water via mechanical stirring at 30°C to give a concentration of 2 mg/mL. Meanwhile, 1 mg of nanoparticles was isolated from the stock solution by centrifugation. The pellet was then re-dispersed in 1 mL of gel solution by ultra-sonication for 20 s using the Sonics vibra-cell probe at 20% amplitude. This sonication step ensured maximum NP monodispersity and also triggered hydrogel formation, which normally occurred during the next few minutes. The formation of self-supporting gel could be observed by naked eye and was confirmed simply by inversion of the vial.

Preparation of aqueous NP solutions: Aqueous solutions of nanoparticles were prepared in a similar manner to the nanoparticle gel-samples, but omitting Fmoc-Gal, using simple DI water.

Preparation of AuNPs-loaded gels: A solution of Fmoc-Gal was prepared as described above. 2 mL of 30 nm and 80 nm of AuNPs solutions (2×10^{11} particles/mL and 1.1×10^{10} particles/mL respectively) were centrifuged and washed several times with water in order to remove the stabilising solution in which the AuNPs are normally stored. The soft pellet obtained after centrifugation was then re-dispersed in the Fmoc-Gal solution and sonicated as described above to allow the formation of the self-supporting gel.

Preparation of aqueous AuNP solutions: Aqueous NP solutions were prepared in a similar manner to AuNPs gel-samples, but omitting Fmoc-Gal, using simple DI water.

Synthetic procedures of Dextran-coated SiNPs (SiNP-Dex):

Dye Precursor Formation (Rho-APTMS): In a dried glass vial fluorescent dye Rhodamine B isothiocyanate (RBITC; 1.47 mg) was dissolved in 1 mL of 1-hexanol and APTMS (5.6 µL) was added. The reaction was allowed to proceed over 2 hours under nitrogen atmosphere.

Synthesis of SiNP-Rho: NPs were formed in a microemulsion prepared by combining Cyclohehexane (7.5 mL), 1-hexanol (1.133 mL), Triton® X-100 (1.894 g), DI water (0.48 mL) in a 30 mL plastic bottle under constant stirring. To the mixture 100 µL of TEOS was added followed by 0.666 mL dye (Rho-APTMS) precursor solution. After 30 min 40 µL of ammonium hydroxide was added to trigger polymerisation. After 24 h stirring 50 µL of TEOS was added to the microemulsion, followed, after 30 min, by the addition of 40 µL of THPMP whit 5 minute as interval 10 µL of ATPMS. The mixture was stirred for further 24 h. After that, the microemulsion was broken by adding 30 mL ethanol. Formed SiNPs were purified by centrifugation (14000 rpm, 10 min) and re-dispersion in 30 mL ethanol (3×). After purification the nanoparticles were stored in ethanol solution at 4°C.

Coating with dextran: 1 µg of 40 kDa dextran were redispersed in 0.5 ml of 10 mM of sodium periodate in water and mixed at room temperature. After 1.5 hours the solution was used to redispersed a pellet of 1 mg of SiNP and the suspension was shacked for 1 hour. 0.5 ml of 10 mM solution of sodium borohydride in DMF was added to the suspension and shacked for another 30 minutes. The samples were then centrifuged (1400 rpm, 10 min) to isolate the particles form the solution and the pellet was washed once with water. The dextran-coated particles were stored in water at 4°C.

Sample preparation

Preparation of nanoparticle-loaded gels and aqueous nanoparticle solutions: Both samples (gel and solution) were prepared following the same protocol mentioned previously with the exception that only 0.5 mg of NPs were used for the sample preparation.

5.2.3 Analytical methods

Dynamic Light Scattering (DLS)

DLS experiments were performed using a Malvern Zetasizer. Nanoparticle size and ζ-potential were used to characterise the particles at the day of synthesis and to evaluate their stability during storage. Particles were dispersed in ethanol or DI water during analysis and measurements were taken at room temperature at concentration of 0.5 or 0.25 mg/mL (as specified for each experiment). All measurements were carried using in DTS1070 disposable cell.

Transmission Electron Eicroscopy (TEM)

TEM micrographs were obtained using a Jeol JEM-3200FS transmission electron microscope operated at 150 kV. Sample preparation involved carefully pipetting water solution (5 μL) of NP onto 'Carbon Films on 400 Mesh Grids Copper' from Agar Scientific. No staining was necessary, as the NPs were electron dense enough to provide sufficient contrast.

5 μL of solution/gel sample were carefully added to the TEM grids and allowed to evaporate. Using ImageJ software, at least 100 NPs per image were analysed statistical values for NP diameter. Values are reported as average (n = 100) ± SD. The normal distribution of NP's size was determined using Excel.

Scanning Electron Eicroscopy (SEM)

SEM micrographs were obtained using a FEG-SEM Hitachi SU8030. Samples were pipetted on Carbon Tabs (12 mm Dia G3347N) and the grid were then placed on 0.5" Aluminium specimen Stubs.

Evaluation of efficiency of storage method by DLS and TEM: Prior to TEM and DLS analysis every samples, independently from the type (SiNP, AuNP or dextran-coated SiNPs) both solution- and gel-semples were vortexed for the same amount of time, procedure required to brake the gel and have the particles back in suspension. The samples were then diluted with DI water reaching the desired concentration (usually 0.5 or 0.25 mg/mL NPs).

Microscopes

The interaction AuNP-hydrogel's fibres and the dissolution of the gel after dilution were visualised by dark-field microscopy using Axio Imaginer A1.m Zeiss, 50 x Objective. For the visualisation of the stability of SiNPs pumped through the microfluidic chip was used epifluorescence microscope Axio Imaginer A1.m Zeiss, 10 x Objective using filter set – 77HE from Zeiss. The video were recorded with PCO camera.

Evaluation of SiNP-Dex-sol and SiNP-Dex-gel diluted in DMEM: 5 solution-samples (SiNP-Dex-sol) and 5 gel-samples (SiNP-Dex-gel) were prepared following the procedure mentioned above. After one week of storage, both solution and gel samples were vortexed for 10 s to break the gel matrix, in the case of the gel-samples. One of the sample (t0) was diluted to concentration of 0.25 mg/mL with DI water and analysed by DLS and TEM. The remaining samples were diluted with 1 ml of DMEM to 0.25 mg/mL of NPs and stored at 4°C. After 2, 4, 6 and 8 hours the samples were analysed using DLS and TEM. After further dilution with filtered DI to 0.125 mg/mL of NPs, the particles were pumped through a microfluidic chip featured at zig-zag shaped microchannel at 0.3 µL/min (geometrical parameters of the channel: width = 150 µm, depth = 40 µm). The flow of NPs was recorded by epifluorescence microscopy (Axio Imaginer A1.m Zeiss, 10 x Ojective, Filter set – 77HE from Zeiss, PCO camera).

Nanoparticles Tracking Analysis (NTA)

All measurements were performed on NanoSight LM10-HS instrument. Videos were recorded with CCD camera and processed using Nanoparticles Tracking Analysis software. Only AuNPs samples were analysed with this technique. Samples were diluted twice with DI water and injected in the caber by 1 mL syringe.

UV-Vis analysis

A Tecan Infinite M200 Pro Safire microplate reader was used for the majority of absorbance and fluorescence emission measurements. 0.2 mL of samples were added to Nunc Maxisorb 96 well plates before being read. Measurements were done in triplicates if not differently stated; values are reported as average ± SD.

Depending on the experiment and the type of dye loaded into SiNPs different λ_{ex}/ λ_{em} wavelengths were used:

- FITC-loaded particles (NP-FITC, NP-A-FITC-NH$_2$, NP-B-FITC-NH$_2$): 490-525 nm (λ_{ex}/ λ_{em})

- NaFlu-loaded partiles (NP-NaFlu-NH$_2$): 456-518 nm (λ_{ex}/ λ_{em})

- MB-loaded particles (NP-MB-NH$_2$): 660 nm (Abs)

- MTS assay: 490 nm (Abs)

Analysis of dye-leaching during storage in water and ethanol of SiNPs: 1 mg of NP-B-FITC-NH$_2$, NP-NaFlu-NH$_2$ and NP-MB-NH$_2$ were suspended in 1 mL of DI water or ethanol and the signal (fluorescence/absorbance) was recorded for each samples. After 24 hours of storage at 4°C, all samples were centrifuged (10 min, 14 000 rpm) the supernatant was completely removed and discarded. The pellet isolated for each sample was then resuspended in 1 mL of water or ethanol and the signal was measured. The same procedure was repeated on day 2, day 7, day 14 and day 21.

Analysis of dye-leaching of gel-/solution-sample after storage in water and PBS: Solution- and gel-samples of each type of NPs tested (NP-B-FITC-NH$_2$, NP-NaFlu-NH$_2$ and NP-MB-NH$_2$) were prepared following the procedure described above using DI filtered waterand PBS 0.01 M as media. After 28 days of storage at 4°C, both solution- and gel-sample were vortexed to brake the gel and release the particles beck in suspension. The samples were centrifuged (10 min, 14 000 rpm), 600 μL of the supernatant from the top-part of the tube was collected and the amount of dye was quantified using the calibration curves of the corresponding dye (FITC, NaFlu or MB). The remaining supernatant was discarded. The pellet of NPs was redispersed in equal amount of solvent 1 mL and sonicated. 200 μL of supernatant and NP-suspension were pipetted into 96-well plate and fluorescence and absorbance values were recorded. Values are reported as average (n = 3) ± SD.

UV/Vis of AuNPs: In order to characterise AuNPs, the absorbance spectrum was recorded using water suspension of AuNPs (both 30 and 80 nm) at concentration of 0.1 mg/mL in a 96-well plate. A scan range or 400-700 nm, and a wavelength step size of 1 nm, was employed for the sbsorbace spectra measurements.

Incubators:

HERA cell 150 Thermo electron Corporation was used to incubate both U-937 and U87MG during culturing and MTS assay. Temperature was set at 37°C in humidified atmosphere containing 5% CO_2. Red blood cells and embryos were incubated using WTC Binder Tüttlingen (Germany).

Micro injector for ex-ovo assay was obtained from Sutter Instrument Company, Novato, USA.

5.2.4 Toxicity assays

MTS assays:

MTS with U937 cell line: The cells were cultured in RPMI-1640 medium supplemented with 1% FBS and antibiotics. The cytotoxicity was analysed for the three different samples. NP-gel, NP-solution and Gel alone were prepared as mentioned previously using filtered water as solvent. All samples were shaken by hand (to break the gel) and vortexed for 1 min at 500 rpm. They were then diluted by up to a factor of 4, using the cell culture medium (RPMI). The cells were plated at a density of 3×10^3 per well in a sterile 96-well plate. In each well, the cells were treated with 20 μL of each sample, reaching a concentration of 50 μg of SiNPs per well and a total volume of 100 μL/ well. All plates were incubated at 37 °C in humidified atmosphere containing 5% CO_2 for up to 4 hours. After 1, 2 and 4 hours, respectively, 20 mL of MTS solution was added to the each well. The plate was then incubated for further 2 hours to allow the MTS reagent to react. The absorbance was read at 490 nm to determine the cell viability. As negative control, were used untreated cells.

MTS with U87MG cell line: The human cell line GBM cell line U87-MG (ATCC® HTB-14™, grade IV WHO classification) was cultured in a monolayer in a flask. U87MG cells were maintained in DMEM supplemented with FBS 10%, antibiotics 1% and sodium pyruvate 1%. Cells were kept at 37°C in humidified atmosphere containing 5 % CO_2. Cells were seeded into the wells of sterile 96-well plate at a density 8×10^3 cell/well and allowed to adhere for 24 hours. NP-sol, NP-gel and Gel were then diluted to appropriate concentrations with medium and immediately applied to the cells from which the old medium was removed. Untreated cells were used as negative control.

Incubation assay: cells were incubated for different times (2, 4, 8 and 12 hours) with the same concentration of samples, 50 µg/well.

Concentration assay: Samples were incubated for 2 hours with cells at concentrations of 100, 50 and 25 µg/well to evaluate the dose/survival conditions. The values were calculated as mean ± standard division (n=3). In both experiments, after incubation the samples were carefully removed from the wells and 100 mL of fresh medium were added, followed by addition of 20 mL of MTS reagent, and the plate was incubated for a further 2 hours. The absorbance was read at 490 nm.

In vitro haemocompatibility tests:

The hemolytic activity and the aggregation of erythrocytes were determined using an *in-vitro* red blood cell assays according to Bauer *et al.*[333]. Briefly, heparinized sheep blood samples were purified and washed several times by centrifugation (2800×*g*, 7 min, 3 times) to remove the plasma and to collect the red blood cells. The washing steps were performed with an isotonic 5% glucose solution buffered with 10 Mm 4-(2-hydroxyethyl)-1-piperazineethanesulfonic acid (GlcHEPES) adjusted to pH 7.4. RBCs and all samples tested were diluted to the desired concentration using the above-mentioned solution. The values were calculated as mean ± standard division (n=6).

RBCs aggregation assay: To analyze the red blood cell aggregation after interaction with the samples, the red blood cell stock solution was adjusted to 20000 erythrocytes/ml in GlcHEPES solution. All samples (NP-sol, NP-gel and Gel) were diluted with double-distilled water to the test concentrations. Samples were pipetted in a 96well-plate and mixed with the red blood cells to the final concentrations 3.125, 6.25, 12.5, 25, 50 and 100 µg/mL. Gel samples were liquefied using a vortex and diluted afterwards. The mixture of erythrocytes and samples was incubated for 2 h at 37°C under continuous shaking (1300 rpm). After incubation, the plates were analyzed by light microscopy and by spectrophotometric measurements at 645 nm to quantify the RBC aggregation. As positive control a poly(ethylene imine) coated nanoparticle (160 µg/Ml) was used, since this type of particle was proven to cause significant aggregations due to its positive surface charge[333]. The negative control (GlcHEPES with erythrocytes), the blank (GlcHEPES without erythrocytes) and the sample controls (samples without erythrocytes) were used in each experiment. To quantify the

erythrocyte aggregation, Δabs was calculated from the absorbance at 645 nm using the following equation according to Schlenk *et al.*[334]:

$$\Delta\text{abs} = \left(Abs_{negative\ control} - Abs_{blank}\right) - \left(Abs_{sample} - Abs_{sample\ control}\right) \quad (1)$$

Haemolysis assay: The hemolytic activity of the samples was analyzed by the quantification of the released hemoglobin by spectrophotometric measurement. The red blood cell stock solution was adjusted to 1.000.000 cells/μL and mixed (1:1) with the samples to the final test concentrations 3.125, 6.25, 12.5, 25, 50 and 100 μg/Ml. After 60 min incubation at 37 °C, the red blood cells were removed by centrifugation at 2250*xg* and the supernatant was spectrophotometrically quantified at 544 nm. Blank values were determined measuring only the GlcHEPES solution without cells. Particle test samples diluted with GlcHEPES were tested in similar concentrations without erythrocytes (sample control) in order to exclude any influence on the absorption measurement. Cells treated with 1% solution of the nonionic surfactant Triton X-100 was used as positive control. Untreated cells served as negative control. The percentage of the released hemoglobin in relation to the positive control was determined using following equation:

$$Haemolysis\ [\%] = \frac{\left(Abs_{sample} - Abs_{sample\ control}\right) - \left(Abs_{negative\ control} - Abs_{blank}\right)}{\left(Abs_{positive\ control} - Abs_{blank}\right)} \times 100 \quad (2)$$

According to the ASTM F756-00 standard, the hemolytic activity of the samples was classified as 0-2% non-hemolytic, 2-5% slightly hemolytic or >5% for hemolytic activity. Experiments were run in triplicates, data of the RBC aggregation and haemolysis assay are represented as mean ± SD.

Ex ovo hen's egg test on chick area vasculosa (HET-CAV):

To investigate the effect of the particles in a dynamic complex biological test system, we used a shell less hen's egg test on the chick area vasculosa (HET-CAV) according to Schlenk *et al.*[334]. Fertilized eggs were incubated for 72 h at 37 °C. After incubation, eggs were transferred into petri dishes containing Chick Ringer's solution pH 7.0 and incubated for further 24 h. For the experiments only eggs with a well-developed chick area vasculosa according to Hamburger and Hamilton stages 14-17 were selected[335]. Test samples (NP-sol, NP-gel and Gel) were stored in a stock solution of 1 mg/mL and

diluted to the test concentration (50 or 125 μg/mL) with DI water. The gel samples were liquefied by mechanical shaking using a vortex and diluted equally to the final test concentrations. A volume of 2 μL of each sample was injected into the upper or lower vitelline vein of the embryos chick area vasculosa (CAV) using a micro injector. According to the recommendations of the Interagency Coordinating Committee on the Validation of Alternative Method (ICCVAM) for the HET-CAM test 0.9% sodium chloride was used as negative control. Since samples were diluted with DI water it was run as solvent control in each experiment. As a positive control a solution of branched poly(ethylene imine) (25 kDa, 25 mg/mL) was used. Each sample was tested at least in two independent experiments with a minimum total number of 8 eggs. Eggs were analyzed after 0, 1, 2, 4, 8 and 24 h for thrombosis, haemorrhage, vascular lysis or embryonic lethality.

5.3 Results and Discussion

5.3.1 SiNPs synthesis and characterisation

SiNPs were prepared using a well-known, water-in-oil reverse microemulsion method, which is discussed in detail in Chapter 4 (*4.3.1)*. In order to better evaluate the versatility of our method, different types of SiNPs were synthesised. All particles have the same core, formed by polymerisation of tetraethyl orthosilicate (TEOS), but differ according to their shells and the dyes loaded. The protocol normally followed to synthesise highly stable SiNPs with the microemulsion method is based on the use of TEOS, THPMP and APTMS used for formation of the shell[340,341]. Using these silanes, the surface of the nanoparticle presents amino (APTMS) and phosphate groups (THPMP), respectively, which leads to the formation of an overall negative surface charge, as the ratio of silanes was used favours THPMP (2:1 molar ratio).

In order to prove that the proposed storage method is successful, we tested its efficiency in stabilising samples that would otherwise tend to aggregate. The protocol was therefore slightly modified to give positively charged particles, which are known to be colloidally unstable, especially in aqueous and salted solvents. Hence, NP-B-FITC-NH_2, NP-NaFlu-NH_2 and NP-MB-NH_2 were modified on the surface with a relatively thick shell consisting of polymerized TEOS:APTMS molecules in a ratio of 1:4 (by volume). SiNPs with a thicker shell and without shell were also synthesised (NP-A-FITC-NH_2 and NP-FITC, respectively) in order to evaluate the relationship between stability and particle size. The structure and characteristics of the SiNPs synthesised and used for this analysis are depicted in *Figure 113*. The first type of particle, NP-FITC, has no shell; this should lead to small neutral particles, but the surface charge is actually negative due to the spontaneous hydrolysis of TEOS used for the core formation, which leads to the presence of silanol groups on the surface. The second type, NP-A-FITC-NH_2, is composed of the silica core and by a thicker shell, since 100 μL rather than 50 μL of TEOS were used for its synthesis, which should give bigger particles. The positive charge of the particles has been obtained using only APTMS. In this case the molar amount of APTMS used is the sum of the molar amounts of THPMP and APTMS used in the standard protocol. For the remaining particle types, the shell was synthesised using 50 μL of TEOS and APTMS in excess (200 μL), leading to highly

positively charged particles. Positively charged, APTMS-coated silica nanoparticles (with a high density of -NH$_2$/-NH$_3^+$ groups) are known to aggregate readily in aqueous suspensions, which created a great opportunity for us to test the ability of the hydrogel to stabilize these colloidally 'highly unstable' SiNPs.
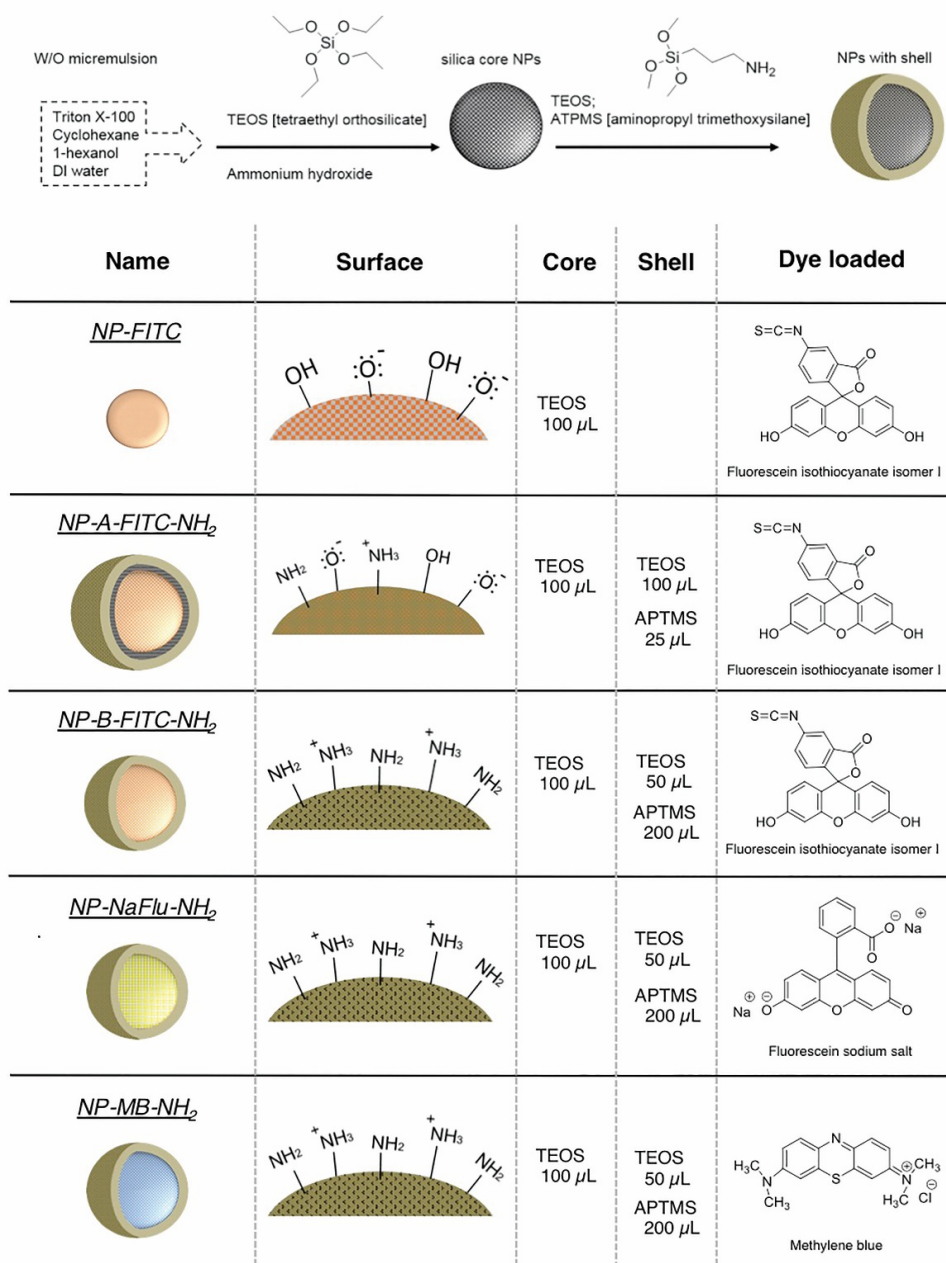
Figure 113: The scheme on the top gives a simple explanation of the microemulsion method used for the SiNPs synthesis. NP-FITC, NP-A-FITC-NH$_2$ and NP-B-FITC-NH$_2$ are loaded with FITC. NP-NaFlu-NH$_2$ and NP-MB-NH$_2$ are loaded respectively with NaFlu and MB, respectively. NP-FITC doesn't have shell, NP-A-FITC-NH$_2$ has a double shell while NP-B-FITC-NH$_2$, NP-NaFlu-NH$_2$ and NP-MB-NH$_2$ have a shell formed only of APTMS, which make their surface highly positively charged.

All particle types were characterised by DLS, both in water and in ethanol. Their size, polydispersity and shape were then corroborated using TEM, with representative results shown in *Figure 114*.
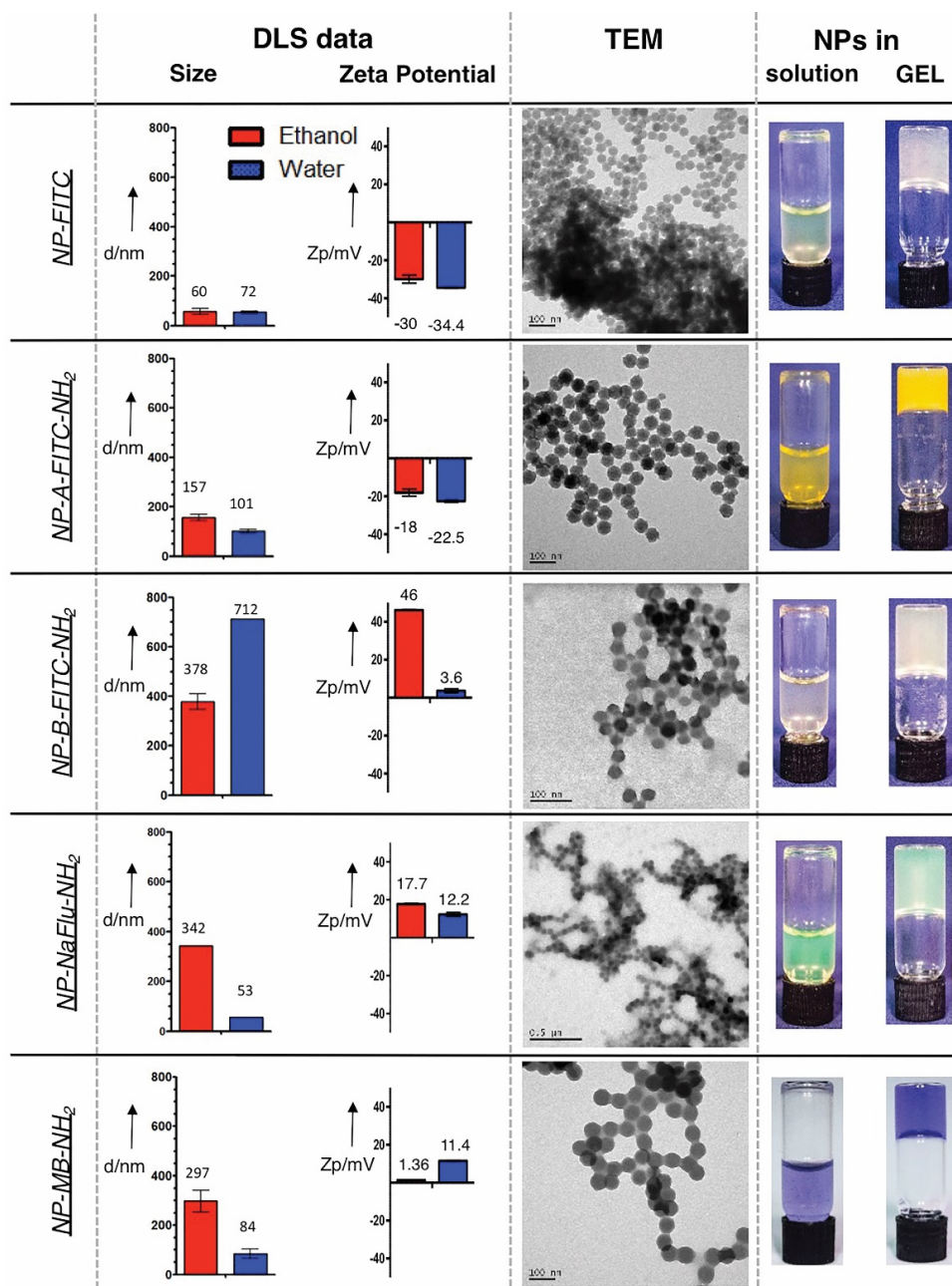
Figure 114: DLS analysis of diameter and zeta potential of particles in ethanol (red bars) and water (blue bars) are plotted in the graphs. Average values are reported (n = 3) ± SD. TEM images show the morphology and polydispersity of the samples and on the right column are showed all solution-sample and gel sample at day1.

The results are summarized in *Table 37*. The plain NP-FITC had a diameter of 60 nm/72 nm and ζ-potential of -30/-34.4 mV in ethanol and water, respectively, when analysed by DLS, while the size of the individual SiNPs measured by TEM was 38 nm. The

discrepancy between the two techniques is attributed to the fact that the TEM images were acquired in vacuum from SiNPs dried on the copper grid.

The thick layer of TEOS grafted on the SiNPs surface caused the NP-A-FITC-NH$_2$ to have a diameter of 157nm/101nm, with surface charge of -18/-22.5 mV, in ethanol and water, respectively. Interestingly, the presence of shell resulted in NPs with a much brighter yellow/orange colour when compared to the NP-FITC without the shell (*Figure 115, right column*). This visible 'brightness' increase can presumably be attributed to the different capacity for entrapment and retention of the cargo between the particle types.

The fact that the positively charged NPs (i.e. NP-B-FITC-NH$_2$, NP-NaFlu-NH$_2$ and NP-MB-NH$_2$) tend to aggregate in solution is evident from *Figure 115*. Although the TEM pictures show that size of the individual SiNPs is still in the range of 62-89 nm, DLS data indicate significant aggregation, with average size in the range of 297-378 nm in ethanol and even larger range in water.

Table 37: DLS and TEM values of the different SiNPs types. DLS values were measured both in ethanol (first column) and in water (central column). Values are reported as average (n = 3) ± SD. ImageJ software was used to obtain particle diameters from the TEM images. Values are reported as average (n = *c.a.* 100) ± SD.

	Ø DLS [nm]	PDI	ζ [mV]	Ø DLS [nm]	PDI	ζ [mV]	Ø TEM [nm]
	ethanol			water			vacuum
NP-FITC	64 ± 24	0.382	-30	72 ± 6	0.374	-34.4	38 ± 6
NP-A-FITC-NH$_2$	157 ± 13	0.373	-18	101 ± 8	0.249	-22.5	68 ± 14
NP-B-FITC-NH$_2$	378 ± 31	0.918	46	712 ± 1	0.754	3.6	89 ± 10
NP-NaFlu-NH$_2$	342 ± 1	0.112	17.7	53 ± 5	0.148	12.2	62 ± 11
NP-MB-NH$_2$	297 ± 44	0.179	1.36	84 ± 19	0.286	11.4	80 ± 17

SiNPs are often used as carriers for drug delivery and, therefore, to better evaluate the dye leaching during storage, all particle types were loaded with dyes using different loading methods or different dyes. FITC was covalently loaded after conjugation to APTMS (NP-B-FITC-NH$_2$). Fluorescein sodium salt was physically entrapped in the silca

matrix (NP-NaFlu-NH$_2$), in order to evaluate if the loading method used can affect the leaching of the cargo. The importance of cargo's properties has been considered through comparison of the leaching of methylene blue (hydrophobic dye) and fluorescein sodium salt (hydrophilic dye) from, respectively, NP-MB-NH$_2$ and NP-NaFlu-NH$_2$.

5.3.2 SiNPs: colloidal stability after long-term storage

Stability study

The in-house prepared SiNPs samples were formulated into an aqueous suspension (in water) and hydrogels. Solution- and gel-samples were prepared at a concentration of 1 mg/mL of particles, which corresponds to approximately ~1×10^{12} NPs/mL. For the preparation of the gel samples, the NPs pellet was re-dispersed by sonication in 2 mg/mL of the Fmoc-Gal gelator solution. For the preparation of the solution-samples, the pellet was instead re-dispersed in water and sonicated. Both the aqueous and hydrogel formulations were stored at 4°C for varying lengths of time. After storing the NPs, both the solution- and gel-samples were shaken by hand to convert the hydrogel back to liquid. After dilution, the samples were analysed with the appropriate techniques. *Figure 115* shows how all samples of SiNPs appeared after 8 days storage in solution and gel, respectively. In some cases, such as **NP-A-FITC-NH$_2$** and **NP-MB-NH$_2$**, aggregates were already visible in the solution-samples after storage using the naked eye. Conversely, for particles stored in gel, no differences were found between the sample on day of preparation and after 8 days.
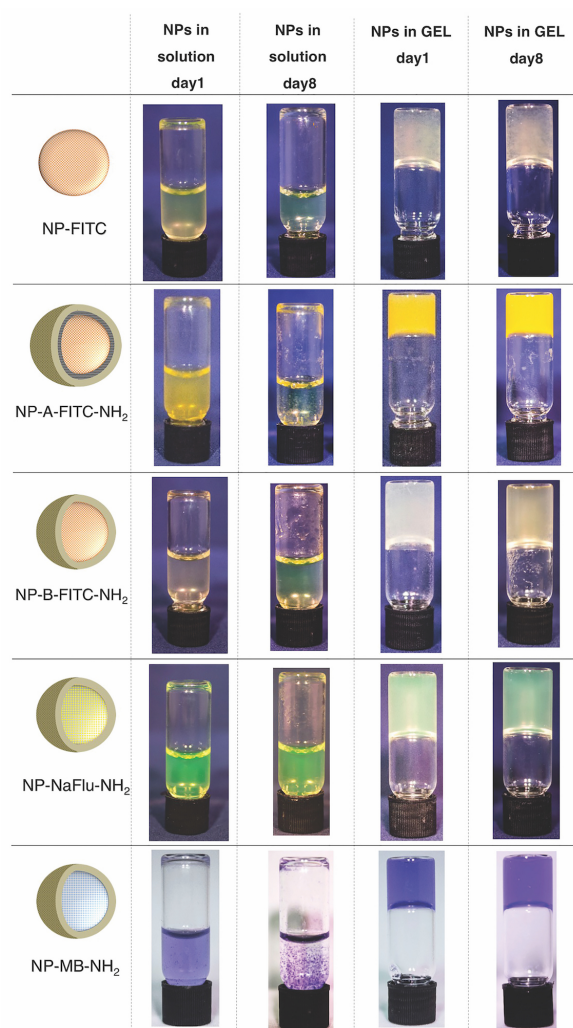
Figure 115: Evaluation of SiNP samples by naked eye after 8 days of storage in solution and gel at 4°C.

To better evaluate the morphology of the particles, after 30 days samples were shaken to convert the hydrogel back to liquid. The solution samples were also shaken in order to guarantee the same sample manipulation and a reliable comparison with the gel samples. All samples were then diluted to 0.5 mg of NP/mL, the optimal concentration for accurate analysis of the particle size and polydispersity.

As mentioned in the previous section, DLS analysis proved not to be a good method to analyse the polydispersity of the samples. The main problem was related to the presence of the residual gel fibers which, having scattering proprieties, disturbed the calculation of the average size. A better picture of the samples was obtained using the number-size distribution, overcoming the issues related to the overestimation of the particle size, due to the presence of the gel fibres, given by the intensity-size distribution. *Figure 116* gives an example of the different interpretations of samples when intensity or numbering distributions were considered. The two cases presented

are the analysis of two gel samples where both nanoparticles (smaller peak) and gel fibres (bigger peak) are present, increasing the polydispersity of the samples. It is clear that when using the intensity-size distribution, more 'importance' is given to the highly scattering gel fibres[338,342]. Using the number-size distribution instead the result is the opposite, since appears that almost no fibres are present in the sample (0,1 and 0% respectively in case1 and case2) and that only one population of particles is present in the sample (99,9 and 100% respectively in case1 and case2).
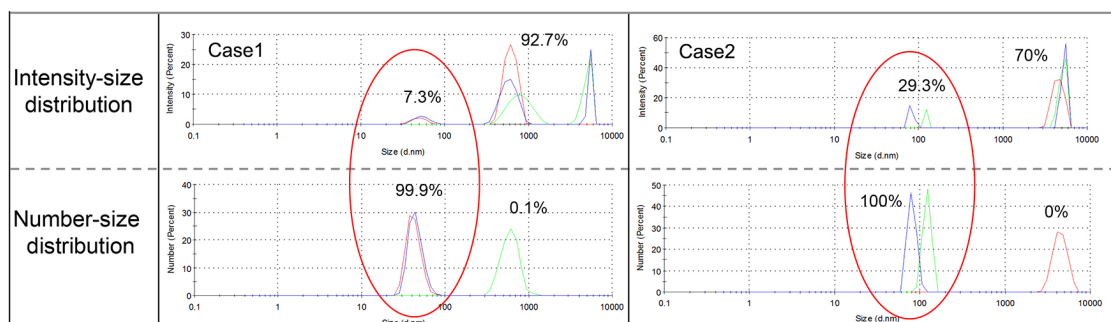
Figure 116: Case1 and case2 are two independent samples of SiNPs stored in gel analysed by DLS after dilution. These data are showed as example of the difference between the same data processed by intensity-size distribution or number-size distribution. Both cases highlighted that considering the intensity values the samples can easily wrongly interpreted.

To have a more robust interpretation of the sample and to better evaluate of the polydispersity of the samples, we chose to use TEM as main analytical technique. By directly visualizing the samples, it was indeed possible to point out that when the particles were stored in gel the aggregation process was dramatically reduced, while the morphology of the SiNPs stored in solution changed drastically. It is noteworthy that different populations were observed in the solution-samples for **NP-A-FITC-NH₂** and **NP-B-FITC-NH₂** *(Figure 117, red circles)*, while when formulated in gel the same particles did not experience any relevant changes in morphology. Using ImageJ software, the particles size was calculated from the TEM image of each sample. The normal distribution of the measurements *(Figure 117, right column)* confirms the presence of different populations in the solution samples (green line) since the bell curve is very broad. On the contrary, curve representing particles stored in gel (blue line) is sharper and it is not shifted remarkably from the curve representing the particles on the day of synthesis (red line).
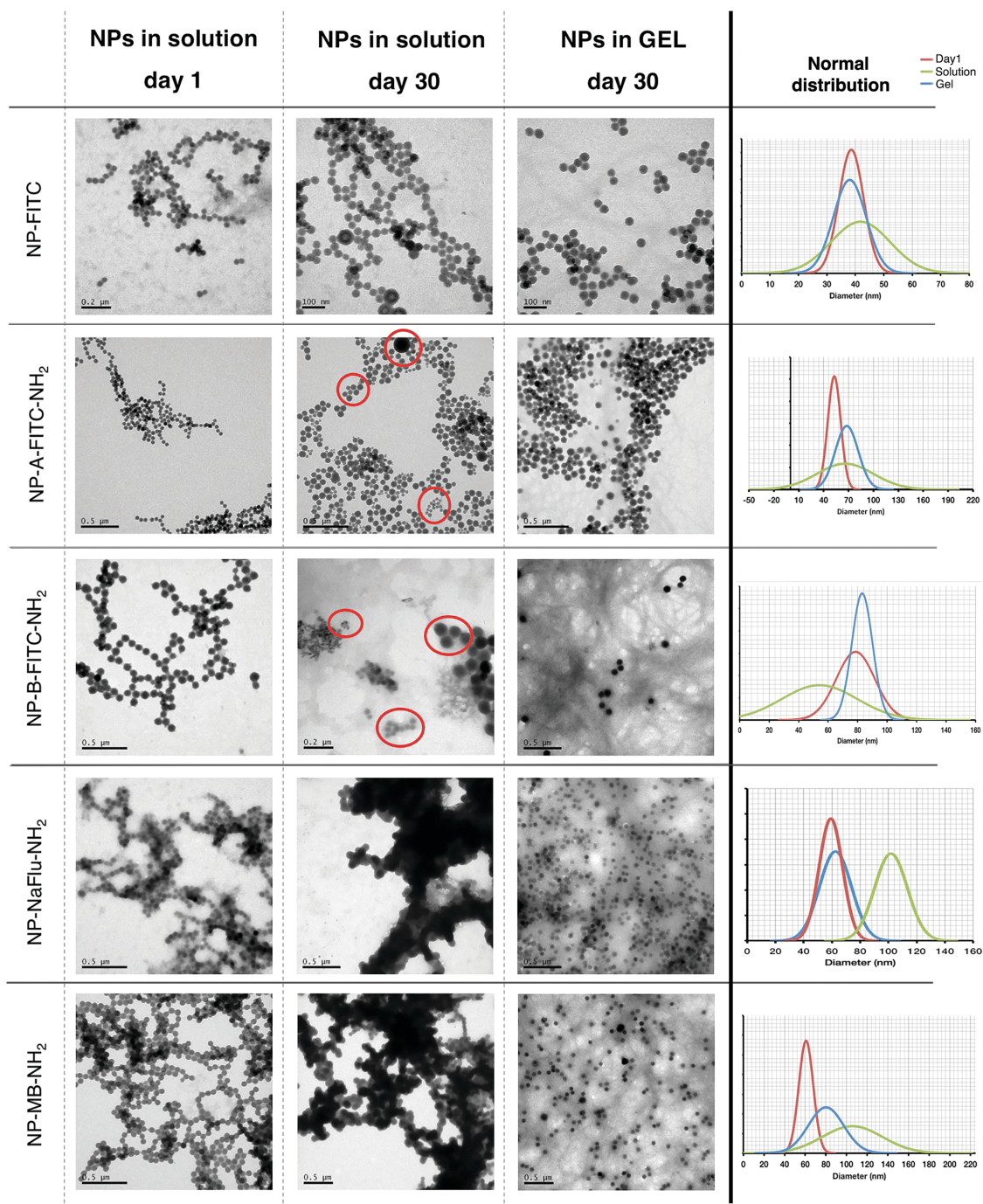
Figure 117: TEM evaluation of the NP's morphologies after 30 days of storage in solution (middle column) or in gel (right column). Red circles highlight the presence of different populations in the solution-samples. On the right, the normal distribution of particles size (*ca. ~ 100* of particles analysed) are plotted for each sample (SiNP at day of synthesis – red line; SiNP after 30 days in water – green line; storage in gel – blue line).

Dye leaching

It has been shown that the method proposed to store nanoparticles is efficient and represents a good option, especially for the storage of certain types of nanoparticles. As mentioned in the introduction, one of the many applications of nanoparticles is drug delivery. In particular, SiNPs, due to their high loading capacity, have been intensively investigated as drug delivery systems. A critical feature for any successful drug delivery system (DDS) is the possibility to regulate the amount of cargo loaded and, obviously, the ability to retain the clinically relevant concentration of the drug while in storage.

Firstly, the capacity of **NP-B-FITC-NH₂**, **NP-NaFlu-NH₂** and **NP-MB-NH₂** to retain their cargo when stored in both ethanol and water, for 3 weeks, was studied in order to mimic storage conditions and to evaluate the size of the problem. The leaching was evaluated after 1, 2, 7, 14 and 21 days which refer in the graph in Figure 119 to 1st, 2nd, 3th, 4th and 5th wash, respectively. At each time-point the pellet was isolated, re-dispersed in 1 mL of water/ethanol and fluorescence/absorbance of the particles was measured. The signal given by the particles isolated by centrifugation at each time-point indicates the amount of drug still present inside the NPs *(Figure 118).* The differences in dye-leaching between the studied solvents were quite remarkable. All three studied dyes leached relatively slowly when the NPs were stored in ethanol, but the rate of leaching was significantly accelerated in water. Furthermore, the loading method used appeared to interfere with the undesired leaching during storage. It can be noticed that when stored in ethanol, the fluorescent values of the pellet isolated every time-point for **NP-B-FITC-NH₂** decreased slowly *(Figure 118-a)* while after two days no fluorescence signal was measured for the **NP-NaFlu-NH₂** *(Figure 118-b).* This indicates that the leaching during storage is reduced if the dye is covalently loaded inside the particles *(***NP-B-FITC-NH₂**) while it is remarkably high if the dye is only physically entrapped (**NP-NaFlu-NH₂**). In the case of methylene blue (**NP-MB-NH₂**, *Figure 118-c)*, the study showed that, due to its hydrophobicity, the leaching is limited when in an aqueous environment while MB leach gradually when stored in ethanol.
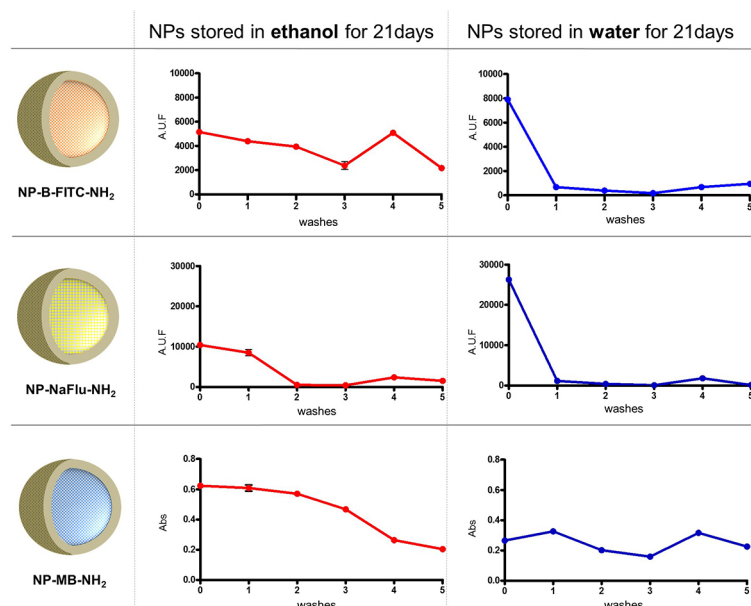
Figure 118: Evaluation of the retention capacity of dyes when SiNPs are stored in ethanol (red) or water (blue) for 21 days. NP-B-FITC-NH$_2$: 490-525 λ_{ex}/ λ_{em}; NP-NaFlu-NH$_2$: 456-518 λ_{ex}/ λ_{em}; NP-MB-NH$_2$: 660 abs.

To demonstrate the advantage of the hydrogel approach, **NP-B-FITC-NH$_2$**, **NP-NaFlu-NH$_2$** and **NP-MB-NH$_2$** were stored for 28 days at 4°C in both a water-based Fmoc-Gal hydrogel and a PBS-based Fmoc-Gal hydrogel. As a reference, an identical procedure was followed with NPs stored in water and PBS in the absence of the gelator. On the 28th day, all samples were gently shaken by hand, the resulting suspension was diluted to 0.5 mg of NP/mL and centrifuged. The leaching occurred during storage was evaluated in this case measuring the signal in the supernatants. In *Figure 119-a* are shown solution- and gel-samples as they looked after storage and after being shaken and diluted. By naked eye was possible to notice the differences between the stabilisation effect of the gel in the case of NP-FITC-NH2 and NP-MB-NH2 were aggregates were clearly visible in the solution-sample while the gel-samples appeared homogeneous. In Figure 119-b are shown fluorescence and UV/Vis values achieved measuring the supernatant after centrifugation of the solution- and gel-samples. For NP-B-FITC-NH2 the leaching was partially reduced when stored in gel while noteworthy is the case of NP-NaFlu-NH2, for which the efficiency of the gel in limiting the dye leaching during storage is evident. For both water and PBS formulations, the amount of NaFlu measured in the supernatant of gel-sample was three times lower than the one measured for solution-sample. Remarkably, despite that the hydrophobic methylene blue leached out of the NPs very slowly in both formulations, the differences in the colloidal stability of **NP-MB-NH$_2$** stored in water and gel were enormous and,

even after reconstitution and dilution, aggregates were still visible in the solution sample while the gel sample looked stable.
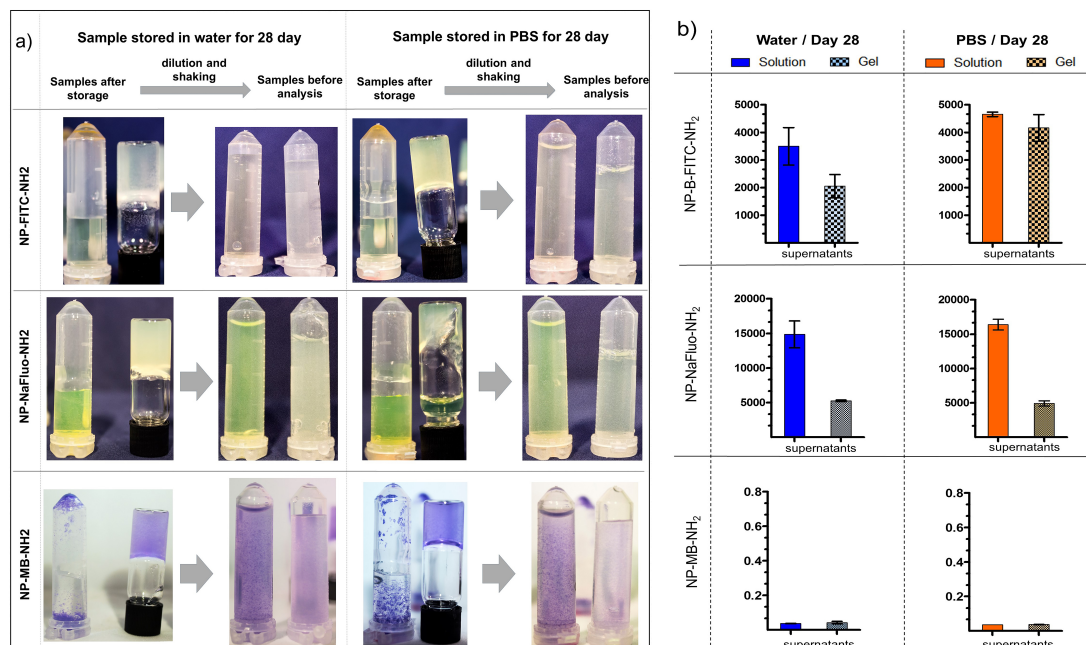
Figure 119: a) Representation of solution- and gel-samples after storage in water (left) and in PBS (right). The first image shows the samples as they looked after storage and the second one after being shaken and diluted. b) Measuremenst of the dye leached out the particles when stored in solution or gel for both formulation in water (blue bars) and PBS (orange bars). Values are reported as average ± SD, n=3.

5.3.3 AuNPs

Data obtained at the Leibniz - Institute of PHotonic Technology, Jena, Germany.

Two sizes of commercially sourced AuNPs were used for the study, 30 and 80 nm, named **30-AuNPs** and **80-AuNPs** respectively. Both types of particle were characterised using DSL and NTA and by UV/Vis spectroscopy. The analyses of the particles were carried out after several washes with water in order to remove any stabiliser that can be present in the stock solution. 2 mL of 30 nm and 80 nm of AuNPs stock solutions were chosen as the sample concentrations, which corresponded, according to information from the provider, to approximately 4×10^{11} and 2.5×10^{10} particles, respectively. The characterisation of the samples is shown in *Figure 120.*
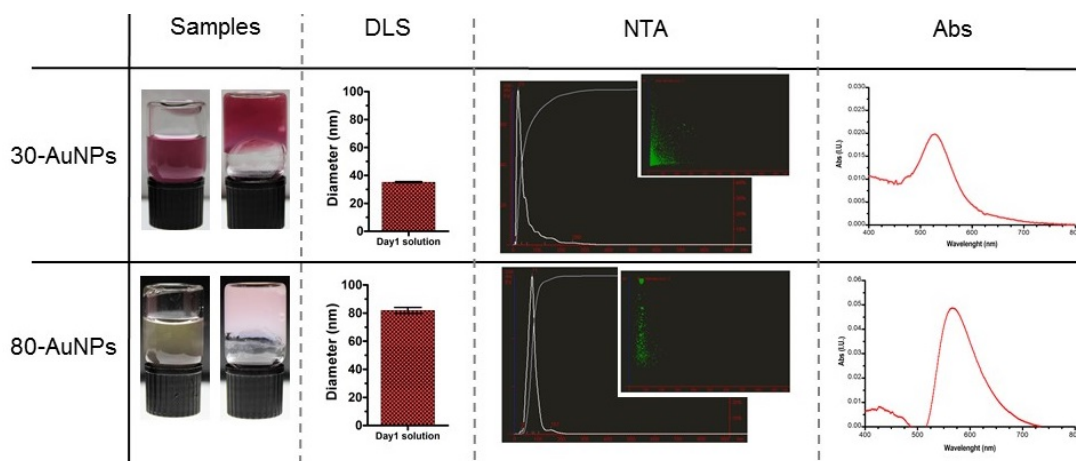
Figure 120: 30-AuNPs and 80-AuNPs were characterised using DLS, NTA and their absorbance spectrum were recorded. Results achieved by the different techniques all showed that both type of particles were monodispersed in suspension at day1. In the first column is showed how solution (on the left) and the gel (on the right) looked at the day of preparation. DLS values are reported as average ± SD, n=3.

Stability study of AuNPs stored in gel and solution

AuNPs are known to be unstable since they possess no surface charge. Commercialised AuNPs are therefore stabilised, usually by citrate adsorption on the surface or suspended in PBS, in order to form stable suspensions of negatively charged particles. To prove the efficacy of our method, we used high concentrations of **30-AuNPs** and **80-AuNPs** which were washed several times with water prior to use in order to remove as much stabiliser as possible. Using organic solvents or PBS would increase the efficiency of the washing process, but the particles would agglomerate immediately, making them unsuitable for our purpose. Solution and gel samples were prepared using 2 mL of **30-AuNPs** and **80-AuNPs** stock solutions (4×10^{11} and 2.5×10^{10} particles respectively). The particles were washed five times by centrifugation and re-dispersion in water. After the final wash, the solution samples were prepared by dispersing the pellet in 1 mL of water, while the gel samples were prepared dispersing the pellet in 1 mL of the gelator solution (2 mg/mL). After one week of storage at room temperature, the samples were analysed by DLS and NTA. It was possible to notice by naked eye that some agglomerates were present in the solution samples and that sedimentation on the bottom of the vial was noticeable, as shown in *Figure 121*. The gel samples showed no difference after storage. However, after shaking and dilution, the agglomerates and sediment in the solution samples were no longer visible.
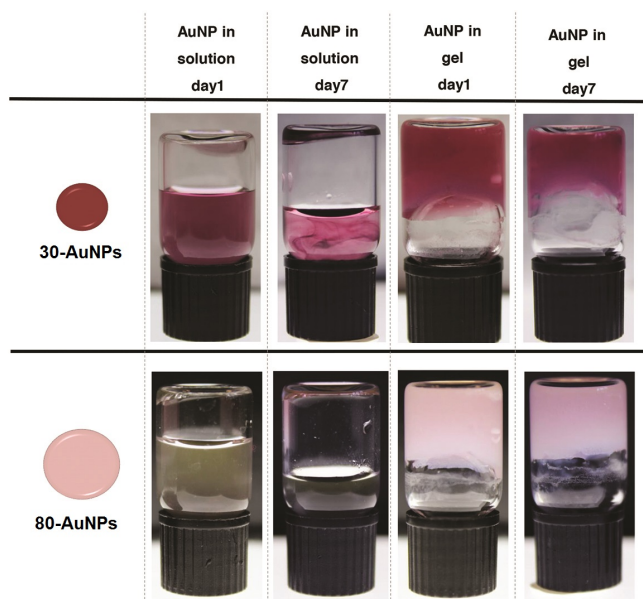
Figure 121: Visual comparison of solution and gel samples at day of synthesis and after 7 days of storage at room temperature.

Once the particles have been returned to suspension, the samples were analysed more thoroughly. DLS data were analysed by considering the most abundant peak in the number-size analysis, in order to reduce the influence of the gel fibres in the gel-stored samples. According to these results, little difference was found between the solution and gel samples for **80-AuNPs**. In the case of the **30-AuNPs** particles gel appear to slightly reduce the agglomeration process since 105.7 nm and 177.2 nm were the average values measured for the gel-sample and solution sample, respectively *(Figure 122-a)*. A clearer characterisation of the sample was given by NTA analysis, where it is possible to highlight the presence of different populations in the solution-sample in comparison with the gel-sample. In particular, NTA allowed for better identification of the presence of different populations in the samples, characterising each population by abundance *(main graph in Figure 122-b)* and intensity of the peak *(inset in Figure 122-b)*. Data showed that more populations were present in the solution-samples in comparison with the gel-samples, leading to the conclusion that, even if with less evidence, the gel method can be used to stabilise AuNPs.
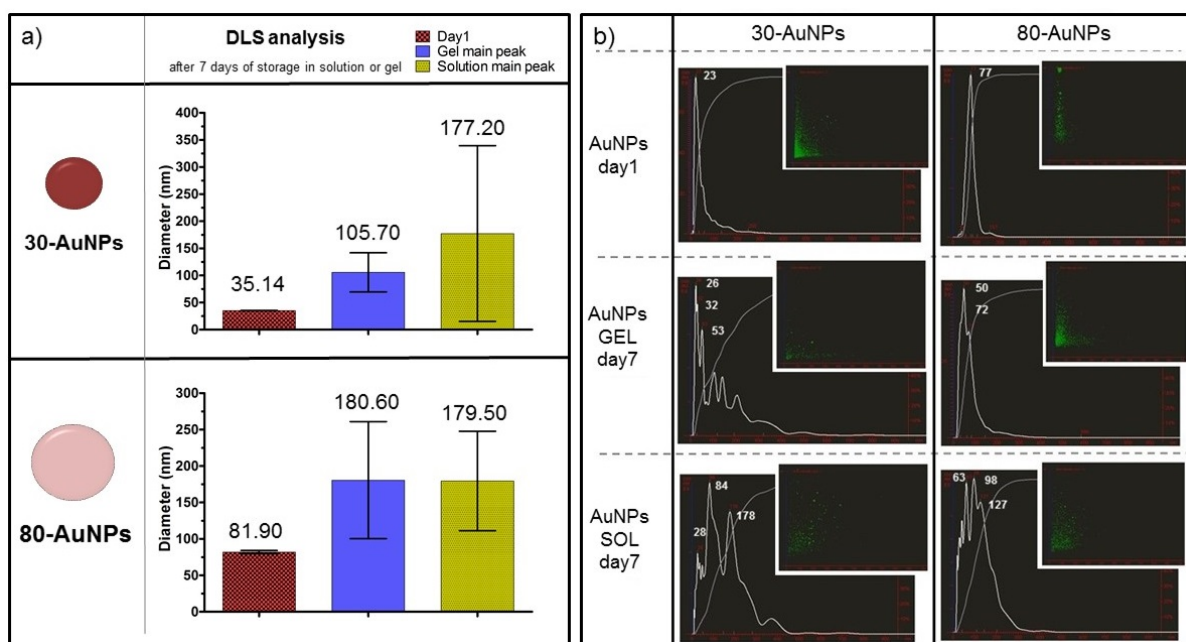
Figure 122: (a) After 7 days of storage, solution-samples (green bar) and in gel-samples (blue bar) of both 30-AuNPs and 80-AuNPs were characterised by DLS. Values are reported as average ± SD, n=3. (b) NTA data recorded for the particles at day one and after storage in solution and gel. The main graph represents the size versus abundance of the population in the sample while the insert image shows the size versus intensity.

Despite the difficulties encountered in analysing the proposed storage method using AuNPs, given their tendency to be stable, DLS and particularly NTA data showed that gel-stored AuNPs are stabilised to a greater extent than their solution-stored counterparts, even if the difference is not drastic in this case.

During the analysis, another interesting observation was made: AuNPs interact with the gel fibres. On analysing the samples after the gel had been broken under dark-field microscopy, it was clear that some particles were adhering the gel fibres, with only some of them being free in suspension. We concluded that the slightly enhanced grade of stabilisation of the particles when stored in gel is related with their interaction with the fibres. This interaction could be due to presence on the NPs surface of stabiliser, which could lead to the formation of reversible electrostatic interactions, or with the absence of charge on the particles surface after the washing process. However, as previously mentioned, one of the main requirements for the gel to be suitable for the requirement of storage colloidal systems is that irreversible interactions should not occur between nanomaterial and gel matrix. Therefore, it became necessary to further evaluate the intensity of the AuNP-fibres interactions. As shown in *Figure 123* further diluting the gel-sample with organic solvents, such as methanol, which dissolve the residual fibres, AuNPs are gradually released into the solvent, becoming available for

further applications. The experiment proved that AuNPs can be stored in gel if needed, but in order to release the particles back in suspension the sample needs to be diluted with organic solvent or with high amount of water in order to dissolve the gel's fibres.
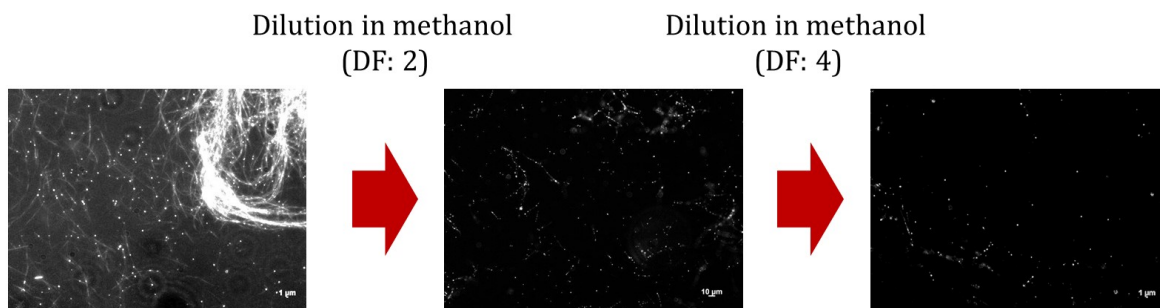
Figure 123: Microscope evaluation of AuNPs stored in gel. Diluting the sample with methanol in which the fibres are soluble, a progressive release of the particles in suspension is noticeable (second and third image).

As mentioned in the introduction, AuNPs are commonly electrostatically stabilised. This method makes them stable in water, but the stability is lost if highly salted solutions are added. Considering that the AuNPs interact reversibly with the Fmoc-Gal fibres, the possibility to improve the stability of the particles in highly salted environment was investigated. 2 mL of **80-AuNPs** were used to prepare solution- and gel- samples (respectively vial *a* and *b* in *Figure 124*). Once the gel was broken (*vial c and d* for solution- and gel-sample respectively), both solution- and gel-samples were diluted with 1 mL of 400 mM solution of NaCl. After only 5 minutes, particles in **80-AuNPs** in solution aggregate (*Figure 124 vial e*) and some precipitation was visible after 24 hours at the bottom of the vial (*vial g*). The aggregation was noticeable by naked eye, with the samples changing colour from the usual purple to violet, while no colour change was observed for **80-AuNPs** in gel (*vial f-h*), which indicate that the interaction between particles and fibres favours the stability of the AuNPs when exposed to highly unfavourable solutions.
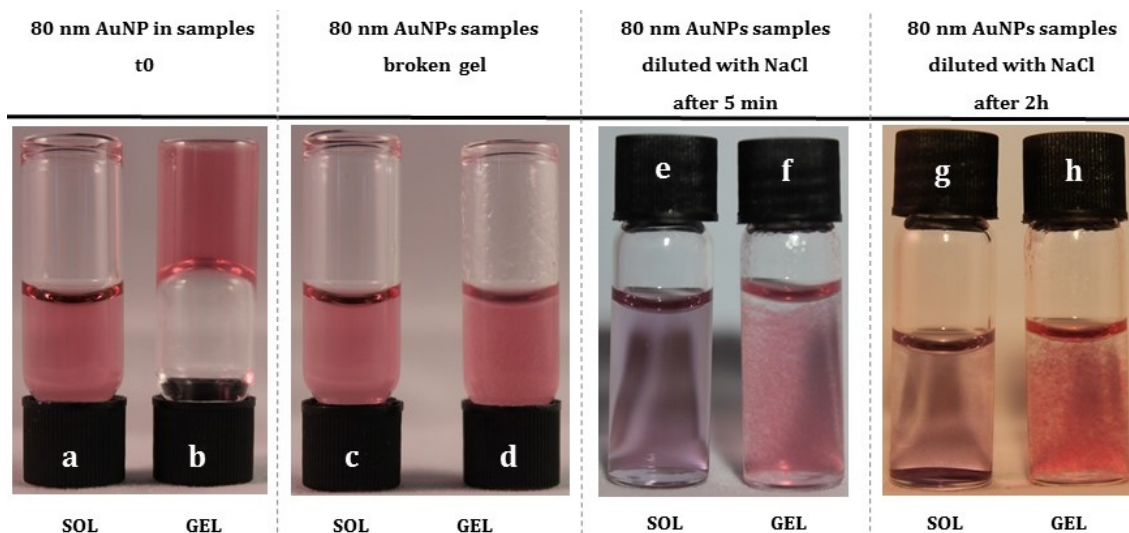
Figure 124: Solution- and gel-sample once prepared (vial a and b respectively) and when the gel was subsequently broken (c and d). In the third and last column, the two samples were analysed after 5 min (e and f) and 2 h (g nf h) of NaCl addition (1 mL of 400 mM NaCl).

Both samples were further analysed by DLS and UV-vis measurments. The values for the number-size distribution obtained by DLS confirmed that **80-AuNPs** in solution agglomerated dramatically after dilution with NaCl solution, forming agglomerates with diameters of *ca.* 1166 nm *(Table 38).*

Table 38: DLS values measured during the study. Values are reported as average ± SD, n=3.

	Ø (nm)	PDI	ζ (mV)
AuNPs t_0	89.14 ± 1.38	0.492	-18.5 ± 1.96
AuNPs in solution	1166 ± 379.3	0.741	-8.53 ± 0.14
AuNPs in gel	70.10 ± 9.5	1.00	-4.29 ± 1.44

The DLS data were supported by the UV/Vis absorbance spectrum measured for each of the sample types. The broad peak given by the **80-AuNPs** solution-sample (green line) contrasts with the sharp one given by the gel-sample (blue line), as shown in *Figure 125*.
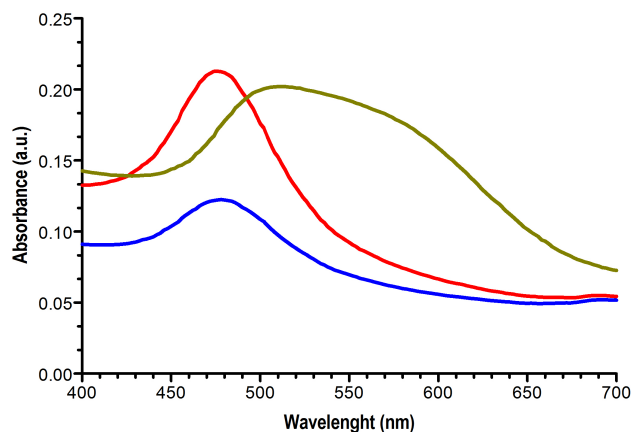
Figure 125: Absorbance values measured for 80-AuNPs at t_0 (red line), when NaCl was added to the solution-sample (green line) and to the gel-sample (blue line).

The difference between solution and gel samples was even more apparent when analysing the samples by SEM. As can be seen in *Figure 126*, **80-AuNPs** interacting with the gel fibres are protected from agglomeration even if exposed to salt solution, while in solution the agglomeration process is dramatically evident. The adhesion to the fibres ensures that **80-AuNPs** are maintained at sufficient distance from each other to avoid the formation of agglomerates. The possibility of stabilising **80-AuNPs** in highly salted solutions could be useful for some specific applications or for particular procedures of surface functionalization.

Figure 126: SEM analysis of gel- and solution-sample after dilution with 400 mM NaCl solution.

5.3.4 Stability of dextran-coated SiNPs in cell culture medium

Data obtained at the Leibniz - Institute of PHotonich Technology, Jena, Germany.

Steric hindrance is a common method used to stabilise nanoparticles and involves coating their surfaces with polymers, such as dextran, polyethylene glycol[292,312,322,343,344], biotin[345], with lipids[24,271,346] or by complex surface modifications[297]. As mentioned previously, these approaches have been shown to improve the stability of certain colloids in simple solvents, such as water or PBS. However, these methods show limitations when the particles are surrounded by complex media, such as biological fluids[296]. As discussed in the introduction to the present chapter, a further issue that needs to be overcome when designing nanomaterials for biological applications such as the formation of the protein corona on the nanoparticle surface, alteration of the NPs morphology and aggregation/agglomeration. Although coating NPs with bulky polymers can enhance their stability during *in vitro* experiments, once in complex biological fluids the fate of the particles is difficultly predictable.

In this section, the stability of dextran-coated SiNPs have been evaluated after storage and once diluted with cell culture medium (DMEM), reproducing a real situation in which, after storage, samples of SiNPs are prepared for biological assays.
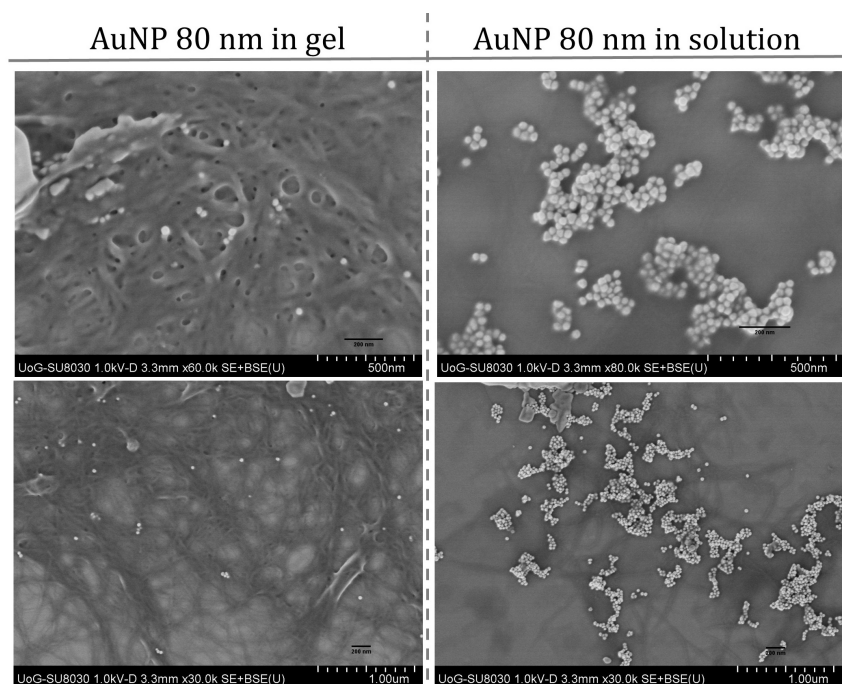
Synthesis of dextran-coated SiNPs

SiNPs were synthesised following the well-established protocol already mentioned, covalently loading in their matrix rhodamine B isothiocyanate (RBITC) rather than FITC to better visualise the particles in the epifluorescence microscope[303]. The silica core was formed by polymerisation of TEOS and the shell was synthesised, as previously, by addition of TEOS, THPMP and APTMS in the ratio 5:4:1 (% v/v) to give negatively charged silica particles also bearing amino groups on the surface. The amino groups on the surface were necessary in this case as an anchor for coating the particles with dextran. Dextran is a well-known polymer, widely used for coating nanomaterial surfaces and it can be readily functionalised with biomolecules such as antibodies to provide cell-targeting capabilities[347]. It is a water-soluble polysaccharide and some favourable proprieties, such as its biocompatibility and biodegradability, make it suitable for *in vivo* applications[348,349]. The 40 kDa dextran was activated using sodium

periodate ($NaIO_4$) to form an aldehyde-functionalised macromolecule. Once activated, the dextran was reacted with the amino groups on the NP surface. The formation of the Schiff base (imine) is a reversible process, therefore reduction with sodium borohydride ($NaBH_4$) was necessary to form a stable N-C bond[299] *(Figure 127).*
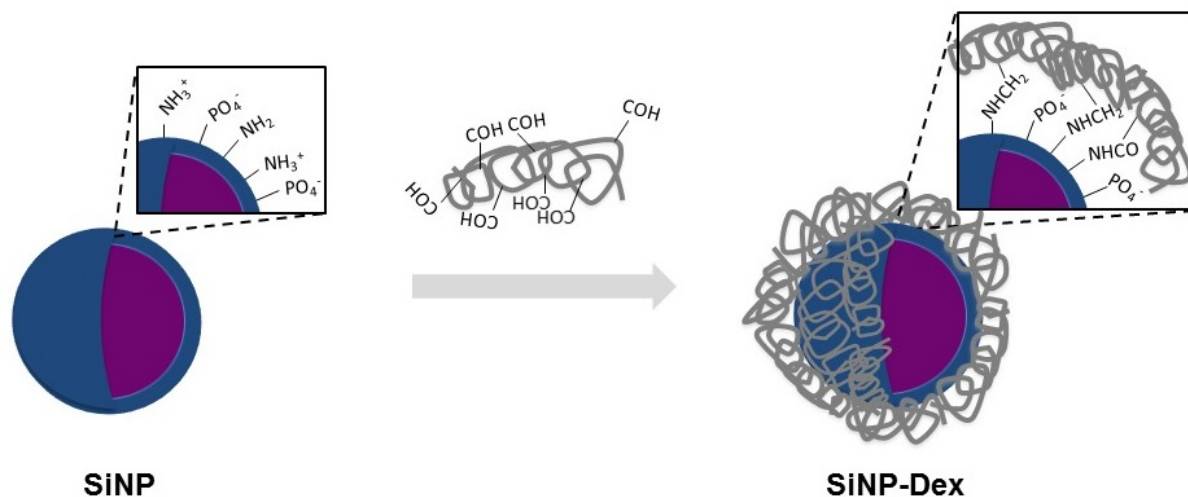
Figure 127: Representation of the coating process of SiNPs with 40kDa dextran. The coating occurs after the activation of the carboxylic groups of the dextran to aldehydes, which can then couple with the amino groups exposed on the NPs surface. The N-C bound formed are then stabilised by reduction.

Dextran-coated and uncoated SiNPs loaded with Rhodamine B (respectively named **SiNP** and **SiNP-Dex**) were characterised with respect to their size and surface charge by DLS and TEM. The DLS data showed that the **SiNP** have an average diameter of 157.0 nm and a negative surface charge (-32.4 mV). After coating with dextran, the diameter of the particles increases only slightly (160.2 nm) and the absolute value of the ζ increased to -25.1 mV as expected. The changes in ζ-potential towards a more positive value can be related to the shielding of the negative phosphate groups by the uncharged dextran coating and agrees with previous findings[262] *(Table 39).* The presence of dextran on the NP's surface is not visible by TEM, due to the low density of the coating. Nevertheless, the diameter of coated and uncoated particles was measured by processing the TEM images with ImageJ *(Table 39)* confirming the slight increase in particle diameter after dextran coating observed by DLS.

Table 39: Comparison of size and polydispersity of uncoated and coated SiNPs (SiNP and SiNP-Dex respectively) prepared by microemulsion method measured by DLS and TEM in water at concentration of 0.25 mg/mL. Measurements are reported as average values (n=3) ± SD.

	DLS			TEM
	Ø (nm)	PDI	ζ (mV)	Ø (nm)
SiNP	157.0 ± 48.2	0.277	-32.4 ± 0.872	59.30 ± 16
SiNP-Dex	160.2 ± 29.7	0.287	-25.1 ± 0.55	63.35 ± 13

Stability study of SiNP-Dex diluted in cell culture medium

Once synthesised and characterised, **SiNP-Dex** were stored for one week in solution (**SiNP-Dex-sol**) and in gel (**SiNP-Dex-gel**). As mentioned above, due to steric effects, dextran-coated particles are considerably stable in aqueous solution, but a further slight improvement is observed when the particles were stored in gel. DLS and TEM reported in *Table 40* show negligible increase in diameter for the particles stored in solution (133.0 nm DLS; 109 nm TEM) in comparison with the particles in the stored in gel (126.1 nm DLS; 91 nm TEM).

Table 40: Comparison of size and polydispersity of the SiNP-Dex stored in solution or in gel for 1 week, DLS and TEM measurements were accomplished in water at concentration of 0.25 mg/mL. Measurements are reported as average values (n=3) ± SD

	DLS			TEM
	Ø (nm)	PDI	ζ (mV)	Ø (nm)
SiNP	157.0 ± 48.2	0.277	-32.4 ± 0.872	59 ± 16
SiNP-Dex	160.2 ± 29.7	0.287	-25.1 ± 0.55	63 ± 11
SiNP-Dex-sol (1week)	133.0 ± 42.3	0.238	-27.5 ± 1.84	109 ± 19
SiNP-Dex-gel (1week)	126.1 ± 21.2	0.354	-11.5 ± 2.24	91 ± 28

Of note is that the TEM analysis showed the presence of holes in the silica matrix of the particles after storage. The dissolution and hollowing of the silica matrix are highly unwelcome effects, especially when SiNPs are designed as vehicles for encapsulation

of drugs in nano-drug delivery systems or with contrast agents (e.g. fluorescence, MRI or luminescence) for *in vivo* imaging applications. Importantly, the nanoparticle degradation effect was negligible for **SiNP-Dex-gel** after 1 week of storage compared with the one observed for **SiNP-Dex-sol**. Therefore, **SiNP-Dex-gel** will presumably retain their cargo for much longer period of time when compared to the same nanoparticles stored in solution *(Figure 128)*.
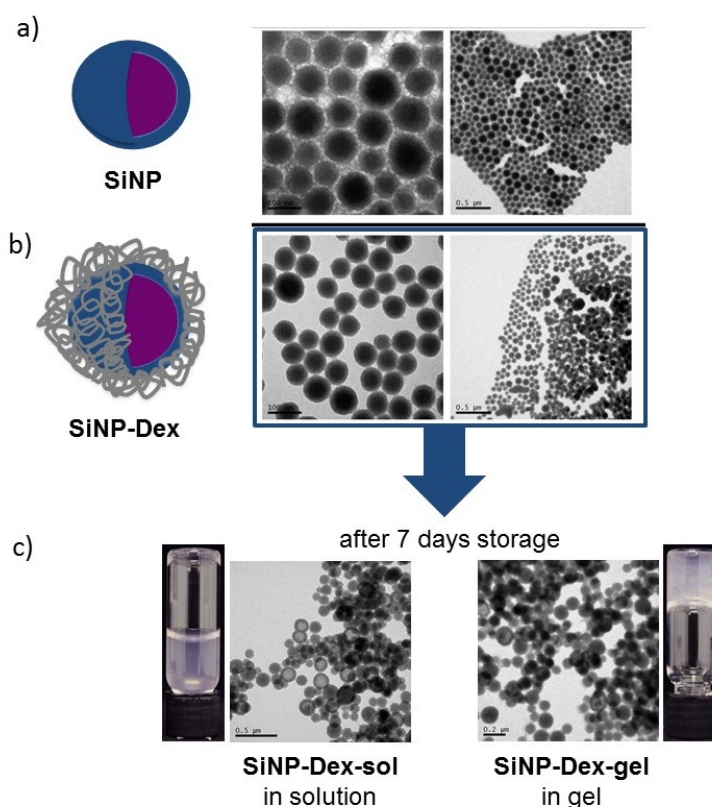
Figure 128: a) TEM images of the SiNP and (b) TEM images of the SiNP-Dex and also SiNP-Dex-sol and SiNP-Dex-gel after 1 week of storage at 4°C in the dark.

These results show that the gel-storage method can improve the stability of already quite stable NPs (such as the dextran-coated SiNPs) but, more interestingly, it can also better maintain their morphology. The presence of the gel matrix, limiting the diffusion of the medium into the SiNPs, reduced the particle degradation, phenomenon much more evident when the particles were stored in solution.

The main aim of this specific study was to further investigate the effect of biological media on SiNPs and to evaluate if the presence of the gel fibres could lead to some improvements in terms of colloidal stability and morphological changes. Since there is no need to store particles in a biological medium, NP features were evaluated when in

contact with complex solvents for a few hours, simulating the hypothetical situation where, after synthesis, the particles are diluted in the desired medium to proceed with biological applications.

After 7 days storage in solution and in gel, each sample (**SiNP-Dex-sol** and **SiNP-Dex-gel**) was diluted with 1 ml of cellular medium. DMEM was used in the present study, which is a variation of EMEM, the minimal essential medium. Indeed, DMEM has approximately four times as much of the vitamins and amino acids present in the original formula and double the amount of glucose. DMEM is widely used in biology since it can be used for different cell lines. As well as the high level of salt, which can interfere with the NPs morphology, the amino acids present in DMEM can be adsorbed onto the NPs surface depending on their positive/negative charge and their polar/hydrophobic chains. The diluted samples were kept at 4°C and, after 2, 4, 6 and 8 hours of the dilution in DMEM, their colloidal stability and morphology was evaluated by DLS, TEM and optical microscopy. On analysing the TEM images *(Figure 129)*, a degradation process of the NPs was noticed and, interestingly, it appears to be less dramatic in the case of the gel-stored samples. This could be due to the fact that the remaining matrix of the gel gives to the broken-gel sample a certain viscosity, which limits the rate of the dissolution process decreasing the diffusion of the solvent though the particles. For both samples, the dissolution of the silica matrix is already partially evident after 2 hours. However, the hollowing effect, 'bridging' of individual particles and the evolution of the nanoparticles into larger agglomerates or even an undefined polymer matrix that would no longer fit to definition of nanoparticle is arguably accelerated with **SiNP-Dex-sol**. The **SiNP-Dex-gel** also experienced hollowing and dissolution but, after 8 hours in DMEM, it is still possible to recognize individual nanoparticles, albeit with a wider size distribution than at the beginning of the experiment (time = 0h).
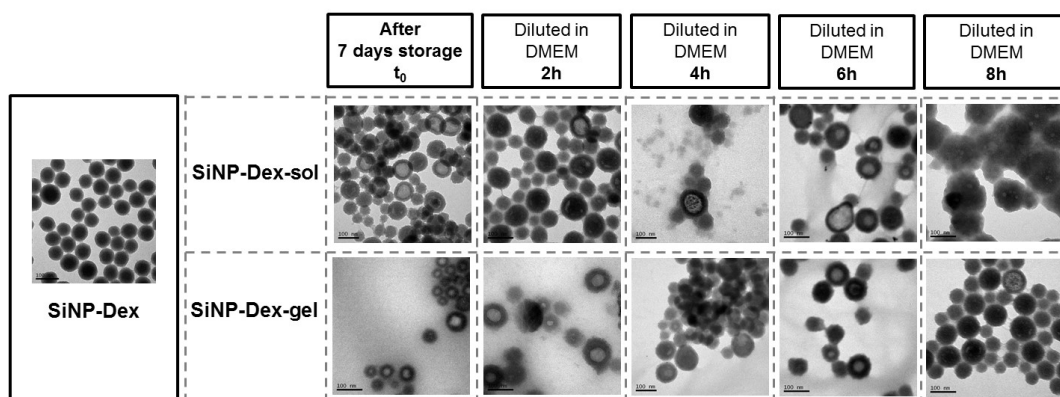
Figure 129: TEM analysis of particles during the stability study in DMEM: coating, storage and dilution in DMEM.

Once in the DMEM, no noticeable aggregation was noticed for either the solution or the gel samples, but DLS measurements indicate that in the gel-sample the NPs properties are better preserved compared with the particles stored in solution. This conclusion can be reached through consideration of both the size and zeta potential measurements. Indeed, as shown in *Table 41*, the diameter and charge of particles stored in gel are more stable over 8 hours in DMEM than when the particles were stored in solution. Prior DLS measurement, samples were diluted with DI water to a concentration of 0.1 mg/mL of particles to limit the interferences related with the complex medium.

Table 41: DLS data of particles stored in solution (SiNP-Dex-sol) and gel (SiNP-Dex-gel) after 2, 4, 6 and 8 hours in DMEM. Samples were diluted to a concentration of 0.1 mg/mL with water. The most abundant peak of the intensity-size analysis was considered for each sample. Average values are reported (n=3) ± SD.

	SiNP-Dex-sol			SiNP-Dex-gel		
	Ø (nm)	PDI	ζ (mV)	Ø (nm)	PDI	ζ (mV)
2 hour DMEM	141.7 ± 50.8	0.392	-17.9 ± 0.53	128.0 ± 24.0	0.522	-27.4 ± 1.42
4 hour DMEM	147.9 ± 20.5	0.438	-23.1 ± 1.17	166.0 ± 64.3	0.466	-27.5 ± 1.36.
6 hour DMEM	186.7 ± 86.9	0.243	-25.1 ± 2.84	150.8 ± 48.8	0.324	-25.9 ± 2.21
8 hour DMEM	197.2 ± 95.79	0.276	-23.4 ± 0.93	133.6 ± 43.9	0.330	-27.5 ± 1.61

In order to visually compare the degree of agglomeration between **SiNP-Dex-sol** and **SiNP-Dex-gel**, a simple qualitative test was designed using a model microfluidic chip. Since the **SiNP** were labelled with a fluorescent dye (RBITC), it was possible to image

the flow of the nanoparticles by epifluorescence microscopy. **SiNP-Dex-sol** and **SiNP-Dex-gel** samples diluted with DMEM and stored at 4°C for 2, 4, 6 and 8 hours respectively were evaluated in this study. At each time-point both solution- and gel-samples were slowly pumped through the zig-zag shaped microchannel (geometrical parameters of the channel: width = 150 μm, depth = 40 μm) while the fluorescence images were recorded (*Figure 130*)[ii].
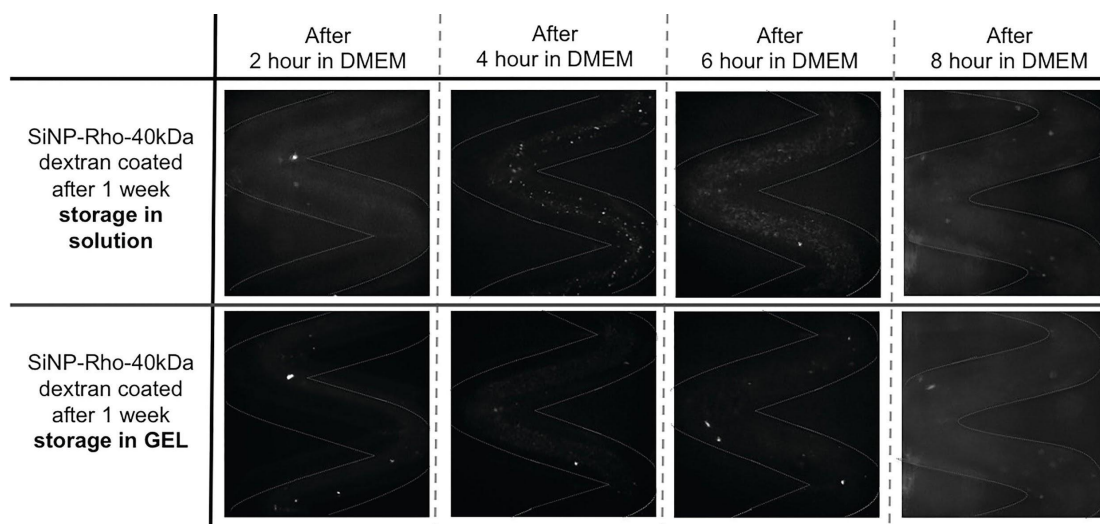

Figure 130: Microscope images of SiNP-Dex-sol and SiNP-Dex-gel samples 2, 4, 6 and 8 hours after the dilution in DMEM were flowing through the microfluidic chip. The particles were analysed at concentration of 0.125 mg/mL and samples were pumped through the channel at 0.3 μL/sec as flow rate.

It is important to mention that, due to the size of the original particles and the camera resolution, it was impossible to observe the individual nanoparticles. It was, however, possible to identify very clearly any agglomerates. **SiNP-Dex-gel**, reconstituted in DMEM, showed the occasional agglomerate flowing through the channel, even after 8 hours of being in a DMEM solution. This was stark in contrast with the DMEM solution of **SiNP-Dex-sol**, which showed a significant number of visible objects flowing through the channel. Interestingly, the images after 8 hours in DMEM medium show fewer aggregates for **SiNP-Dex-sol** than at time 4hr and 6 hr. This is presumably due to the nanoparticle dissolution and hollowing effect described earlier. After 8 hours in DMEM, the **SiNP-Dex-sol** were experiencing the aforementioned hollowing and disintegration, which has two consequences: a) the loss of the RBITC from the particle cores rendering

---

[ii] The videos recorded showing the samples flowing in the microchip can be found on YouTube entitled 'Nanoparticles flowing through microchannels' [https://www.youtube.com/watch?v=EmAzEVbGbGE].

them fluorescence invisible and b) silica dissolution means that the number of individual nanoparticles was significantly reduced, which also reduced the probability of forming agglomerates.

The fluorescent appearance of the agglomerates/aggregates has been exploited to approximately quantify the instability process in each sample. The values shown in *Table 42* represent the relative fluorescent intensity values measured in the channel for each sample at each time point, giving a quantitative indication of the agglomeration/aggregation. As noticeable, this analysis confirms that the destabilisation effect induced by complex medium (DMEM) is reduced even if the gel has been broken, indeed comparing the relative intensity values the one related to the solution samples are always two times higher than the one calculated for the gel samples.

Table 42: Relative intensity values of fluorescence measured from the images of each samples at each time point. The intensity was measured using ImageJ software and the values have been calculated using as 100% the higher intensity value, which corresponded to SiNP-Dex-sol after 8 hours in DMEM.

	SiNP-Dex-sol	SiNP-Dex-gel
After 2 hours in DMEM	65%	19%
After 4hours in DMEM	33%	17%
After 6 hours in DMEM	44%	24%
After 8 hour in DMEM	100%	58%

5.3.5 Evaluation of toxicity effect of gel-samples

The hallmark of the storage method proposed is the possibility to use the sample for further applications without any additional manipulation. Indeed, the storage method proposed was designed in order to allow the gel-sample to be directly used for *in vitro* assays or *in vivo* analysis, after reconstitution of the NPs suspension and appropriate dilution. However, proceeding with the studies it was clear that, after shaking and dilution, some gel fibres were still present in the solution although the sample looked clear by eye. In order to show the possibility of using the gel sample directly without further manipulation, it became clear that there was a need to prove that the presence of the gel fibres does not interfere with the biological activity of the NPs and also does

not induce any cytotoxicity effect. As shown in (*Figure 131)* fewer dilutions (dilution facto - DF 10) are required to dissolve the fibres if ethanol is used, due to the greater solubility of the gelator molecule in organic solvents while only after a DF 100 is require to dissolve the fibre with simple water.
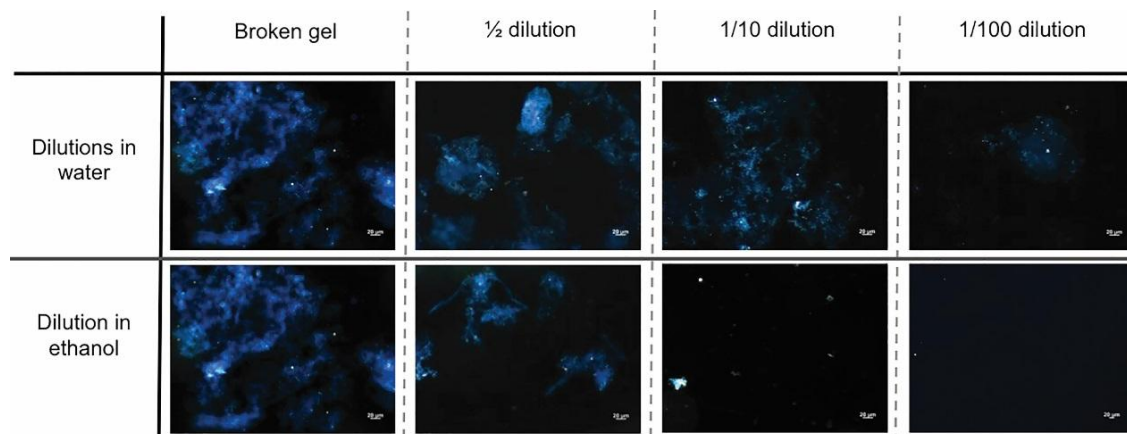

Figure 131: Gel sample was diluted of DF 2, 10 and 100 in water and ethanol. In order to dissolve the fibres, the sample needed to be diluted of factor 100 or 10 using water or ethanol respectively.

In all the toxicity experiments presented herein, the dilution of the samples used was calculated considering that the typical concentrations of silica NPs used either for animal studies or in *in vitro* assays ranges between 1 - 0.001 mg of NPs/mL. To obtain cytotoxicity data, three formulations were studied in all experiments: SiNPs stored in gel (**NP-gel**), SiNPs stored in solution (**NP-sol**) and hydrogel alone (**Gel**).

MTS assays

The MTS assay is a cell proliferation assay, which allows evaluation of cell viability by determining their metabolic activity. If cells are alive and metabolically active, they produce mitochondrial dehydrogenase. This enzyme reduces the MTS reagent (a tetrazolium salt), forming a product that absorbs light at 490 nm (formazan). Therefore, the higher is the absorbance, the greater is the cell viability *(Figure 132).*
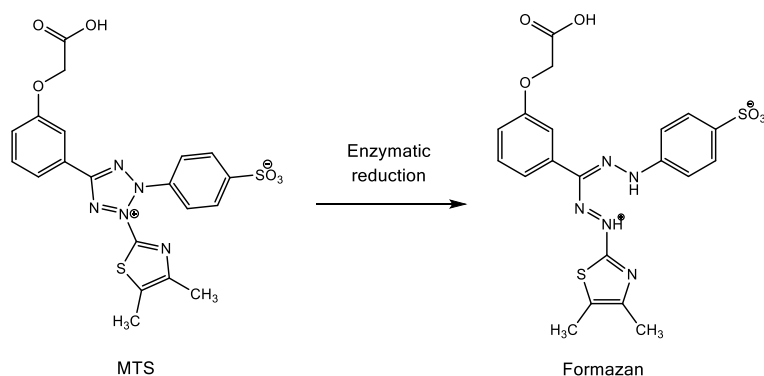
Figure 132: Conversion of MTS reagent in formazan, brown dye whose absorbance can be read at 490 nm.

Two different MTS assays were accomplished using two different cell lines and two different protocols in order to increase the robustness of the study. As one cell line is non-adherent and the other one can adhere to the 96-well plate, two different protocols were designed: in the case of U-937 (non-adherent cells), after incubation with the samples studied, the MTS reagent was added directly to the wells. Using instead U87MG (adherent cells), the samples were gently removed from the plate, and only after addition of fresh medium the MTS reagent was added. In this way two possible interactions sample-cell could be observed and it was possible to limit the interferences between the particles/gel and the MTS reagent.

MTS assay with non-adherent cells (U-937)

The U-937 is a neoplastic, histiocytic cell line derived from patients with generalized histiocytic lymphoma. The cells were plated at a density of 3×10^3 per well in a sterile 96-well plate. In each well, the cells were treated with 20 μL of each diluted sample, reaching a concentration of 50 μg of NPs per well. **NP-sol**, **NP-gel** and **Gel** were allowed to incubate with the U-937 cells in a 96-well plate format in cell culture medium for 1, 2 and 4 hours. At these three time-points, MTS was added and, after a further 2 hours incubation, the UV/Vis absorbance was read at 490 nm. From the value measured the % of cell viability was calculated considering value achieved for the negative control (untreated cells) as the 100%. As shown in *Figure 133* this very basic cytotoxicity study revealed that neither the **NP-sol** (red bars), **NP-gel** (green bars) nor **Gel** (blue bar) had a significant effect on U-937 cell growth over the course of 4 hours.
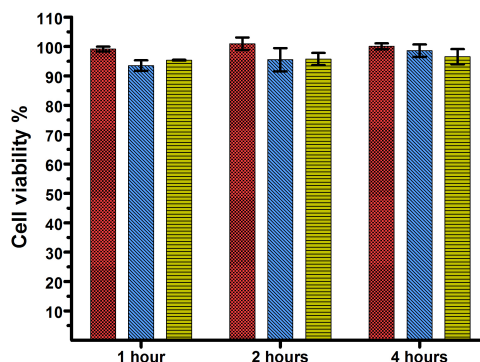
Figure 133: Cell viability measured by MTS assay with U937 human hematopoietic cell line incubated with NP-sol (red bars), NP-gel (green lines) and the Gel (blue bars) for 1, 2 and 4 hours. Values are reported as average ± SD, n=3.

MTS assay with adherent cells (U87MG)

U87MG is a human glioblastoma astrocytoma hematopoietic cell line which has been chosen for the following experiment because they adhere well to surfaces. This property allows removal of the analysed sample after incubation with cells. A first preliminary experiment was accomplished to determine the best incubation time for this type of cell. Cell alone were used as negative control and the absorbance measured after MTS reagent addition was regarded as 100% of cell viability. In *Figure 134-a* it is possible to notice that the **Gel** (grey bars) induced toxicity to these cells at the concentration used (50 μg/mL) after 8 hours incubation (cell viability drops below 80%). All samples (**NP-sol**, **NP-gel** and **Gel**) were then incubated for 2 hours with cells at different concentrations (100, 50 and 25 μg/mL) to determine the dose-response relationship. Negligible reduction of the cell viability was observed for **NP-sol** (green-bars). When incubated with **Gel** (grey bars) and **NP-gel** (blue bars) a reduction of the cell viability was calculated at concentration of 100 μg/mL. However, the samples can be considered non-toxic at the concentrations tested since the cell viability never dropped below 80% (*Figure 134-b*). As noticeable, especially when treated with **NP-sol**, the cell viability value calculated is above 100% indicating a stimulatory/hermetic response. This is phenomenon has been often observed treating cells with NPs[350], where particles appear to stimulate cellular metabolism. Although the phenomenon more visible for **NP-sol** it was observed even for **NP-gel** when used at 100 μg/mL.
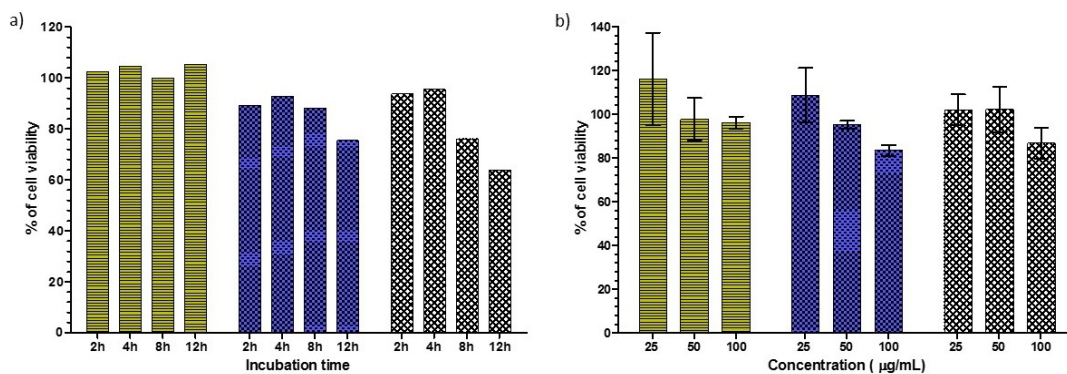
Figure 134: (a) U87MG cells were incubated for different time 2, 4, 8 and 12 hours with 50 μg/well of particles. (b) U87MG cells were incubated with different concentration of samples 25, 50 and 100 μg/well. NP-sol (green bar); NP-gel (blue bar); Gel (grey bars). Values are reported as average ± SD, n=3.

In addition to the MTS assay, we have qualitatively investigated the cell morphology before and after incubation with all samples (*Figure 135*). No significant changes in the cell morphology were observed, even when treated with the highest concentration of the nanomaterial. The cells appear spherical at lower degrees of confluence and more "star-like/branch out" at higher degrees of confluence indeed before incubation there are more spherical-shape cells, which indicate that the cells are not adhering at the bottom of the well although they are still healthy.
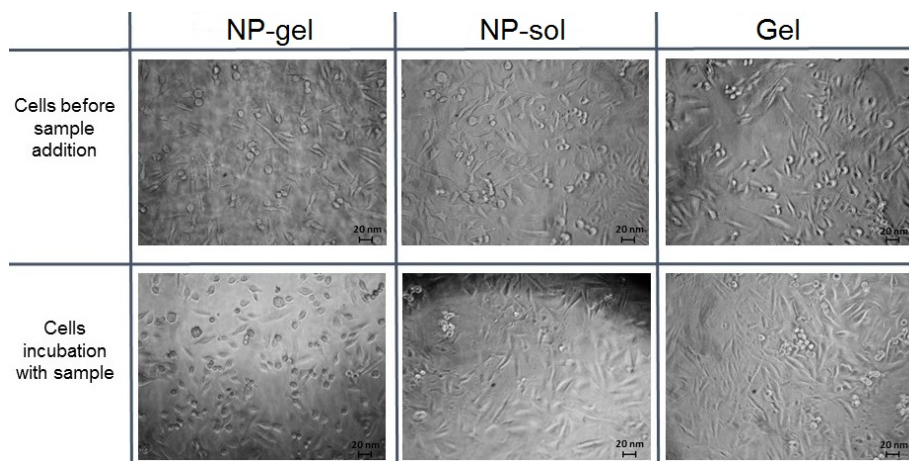

Figure 135: Evaluation of cell morphology during MTS assay

In vitro haemo-compatibility

Data obtained with the help of Paul Warncke (PhD) for the setup of the experiments and data interpretation, at the Institute fur Pharmazie, Friedrich-Schiller-Universitat, Jena, Germany.

Blood is composed of a multitude of cell types, ranging from simple oxygen-carrying erythrocytes to sophisticated antigen-specific lymphocytes. The various cells participate in a vast array of functions, including tissue repair and immune responses as well as oxygen transport. After the systemic injection of the particles, they can interact with blood components such as red blood cells (RBCs) as the major component of the blood cell pool possibly causes severe aggregation and haemolysis. Haemocompatibility tests are used to evaluate the possible adverse effects that can occur when blood enters into contact with foreign materials.

Two assays were performed to evaluate the haemocompatibility of the storage method, testing the samples on red RBCs isolated from heparinized sheep blood. RBCs have been selected since they are the most abundant cells in the blood and the sheep blood was preferred to human due to its ready availability. All samples (**NP-sol**, **NP-gel** and **Gel**) were tested at different concentrations between 3.125 μg/mL up to 100 μg/mL.

Haemolysis assay

Haemolysis can occur when the interaction between negatively charged cells and the nanomaterial leads to a disruption in the continuity of the cell's membrane, with the consequent release of RBC's content into the surrounding fluid. The haemolytic effect induced by the samples tested was quantified by measuring the release into the surrounding environment of haemoglobin, which adsorbs visible light at 535 nm. The haemolytic effect is quantified as the percentage of the effect given by the positive control, as shown in equation 2 (see *experimental section, 5.2.4*). A 1% solution of Triton X-100 was used as positive control following established protocols[333]. As shown in *Figure 136*, up to a concentration of 100 μg/mL, neither **NP-gel** solution nor **Gel** showed haemolytic effect (haemolysis < 2%) with RBCs in comparison to the positive control. According to the ASTM F756-08 standard, the activity of the samples tested is therefore classifiable as non-haemolytic.
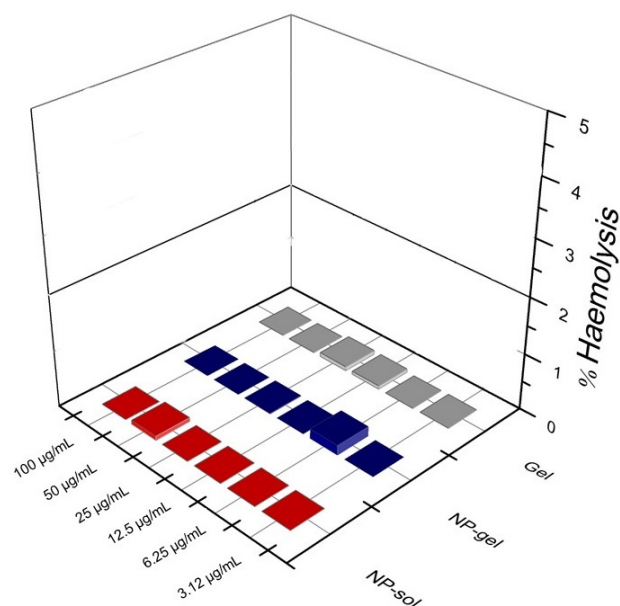
Figure 136: Haemolytic effect induced by SiNPs stored in solution (NP-sol) in gel (NP -Gel) and the gel alone (Gel). All samples are considerable non-haemolytic (< 2%) at all tested concentrations from 3.125 up to 100 µg/mL.

RBCs aggregation assay

The membrane of the RBCs is mainly negatively charged due to the presence of glycoproteins and phospholipids. This feature makes the cells relatively stable in suspension since electrostatic stabilisation occurs. When positively charged particles are added to the cell suspension, the repulsive forces fail and the cells quickly aggregate. This process was qualitatively (by light microscopy) and quantitatively (spectrophotometrically) evaluated by incubating RBCs with the samples (**NP-sol**, **NP-gel** and **Gel**) at the tested concentrations (between 3.125 µg/mL up to 100 µg/mL). The qualitative test is based on the different amount of light that passes through a suspension of well-dispersed RBCs compared with a sample of agglomerated cells. Indeed, since cells scatter light, when they are well suspended and the sample is analysed using a spectrophotometer, only part of the light will reach the detector. Conversely, if the RBCs are agglomerated in the samples, the scattering effect is less intense and more light will reach the detector, giving a higher absorbance signal at 645 nm. Agglomeration induced by each sample is proposed as the difference (ΔAbs) between the absorbance related to the maximum agglomeration event (measured from the positive control) and the signal measured for each sample, as shown by equation 1 (see *experimental section, 5.2.4*). Qualitative evaluation of aggregation by light microscopy was grouped into 3 stages: at stage 1 no aggregation was detectable and all erythrocytes stayed discrete in suspension; stage 2 indicated moderate aggregation

with rouleaux formation, but the majority of the erythrocytes were still discrete in suspension; in stage 3 almost all erythrocytes were aggregated to big clusters and no free cells remained discrete in suspension. Due to the aggregation of almost all erythrocytes in clusters (qualitative analysis: stage 3), the positive control (PC) showed the highest ΔAbs value (0.208 ± 0.012) of all samples. **NP-sol** and **NP-gel** as well as **Gel** showed no aggregation up to a concentration of 50 µg/mL (ΔAbs-values < 0.05, *Figure 137-i*). Whereas **NP-gel** (ΔAbs = 0.075 ± 0.028) and **Gel** (ΔAbs = 0.058 ± 0.025) caused no RBCs aggregation (stage 1) in a concentration of 100 µg/mL, **NP-sol** caused moderate aggregations (stage 2) accompanied by slightly increased ΔAbs values (ΔAbs = 0.088 ± 0.016). Observing directly by microscopy the samples tested at the highest concentration (100 µg/mL), no agglomeration was observed, especially when comparing the tested samples with the effect observed for the positive control *(Figure 137-ii).*
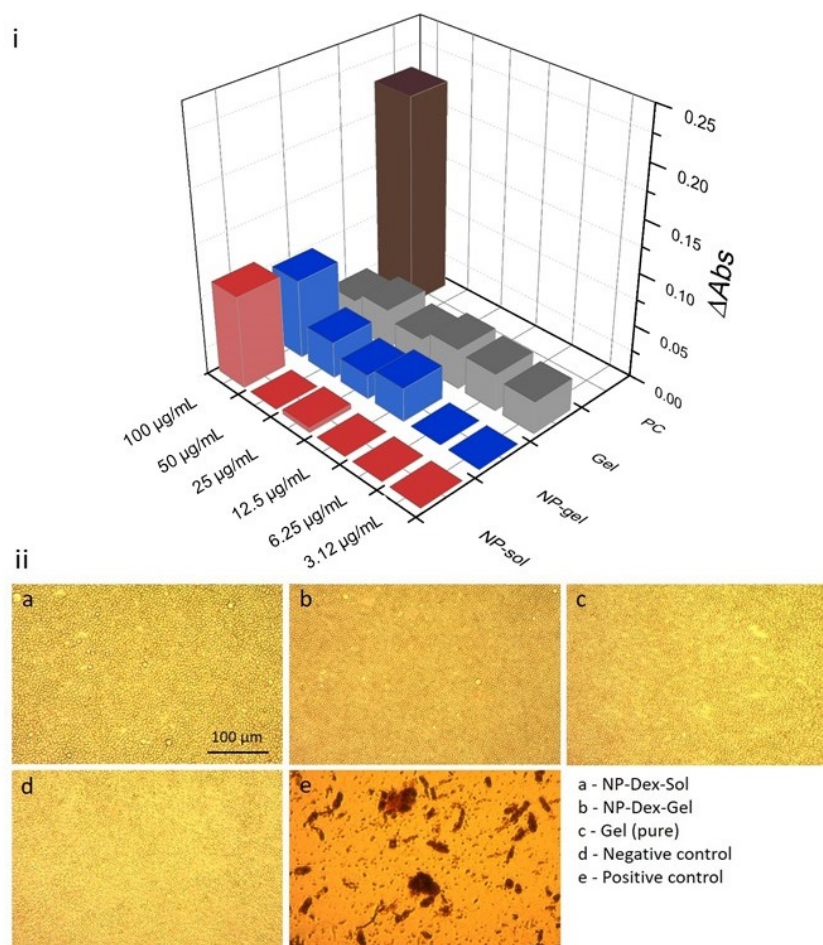

Figure 137: i) ΔAbs values for each sample in concentrations between 3.125-100 µg/mL. Values of the samples are considerably lower in comparison with positive control (PC), indicating no aggregation of the samples. ii) Example pictures from the qualitative analysis of the red blood cell aggregation assay. The test samples (a, b, c in the maximum concentration of 100 µg/mL) and the negative control (d) showed no aggregation (stage 1). In contrast, the positive control (e) triggered strong aggregation with large erythrocytes aggregates (stage 3).

Hen's egg test on the chick area vasculosa ex ovo

Using a hen egg model, it was possible to better simulate *in vivo* conditions. Thus, the samples were tested under dynamic conditions after injection into the blood stream of a chicken embryo, which represents a more complex biological system. The hen's egg test (HET) is accepted by ICCVAM (Interagency Coordinating Committee on the Validation of Alternative Methods, a federal research and regulatory agency) as a valid alternative to animal methods to scientifically evaluate the health and safety of substances. While the HET-CAM (chick embryo chorioallantoic membrane)[351,352] assay is performed by implanting a membrane or coverslip containing the compound evaluated over the chorioallantoic membrane through a hole in the shell, the HET-CAV (chick area vasculosa) method offers the advantage of observing the entire vascular network and the heartbeat over a long period of time. In this model, the embryo is cultivated outside the shell and, once it has reached a certain stage of development, the sample can be injected into the bloodstream and the effect induced can be observed micro- or macroscopically. The chick area vasculosa comprises the central vascular region of the vitelline membrane, which extends around the yolk. The shell-less cultivation of chick embryos at the development stage was initially described by Dunn[353] in 1974 and later further explored[354] and successfully used especially for the evaluation of the angiogenesis process and as model to study neovascularization. Of note is that it cannot be used for the evaluation of inflammatory response, given that the chick immune system develops only after 7 days[355].

The experiment was accomplished according to the protocol established by Schlenk *et al.*[334]. Briefly, fertilized eggs were incubated for at 37°C and at 80% relative humidity in a horizontal position. After 72 hours embryos were transferred to sterile Petri dishes containing 7 mL Chick Ringer's solution (pH=7.0) and incubated for further 24 hours. **NP-sol**, **NP-gel** and **Gel** samples were diluted at of 50 and 125 µg/mL with double-distilled water. 2 µL of each sample was injected into the upper or lower vitelline vessel of the embryo's CAV using a micro injector. According to the ICCVAM protocol for the HET-CAM test, 0.9% sodium chloride solution was used as a negative control, while double-distilled water (WFI) was used as the solvent control. As a positive control, a solution of branched poly(ethylenimine) (25 kDa, 25 mg/mL) was used, since it leads to thrombosis and consequently death of the embryo by inducing RBCs aggregation. Each sample was tested in two independent experiments with a minimum total

number repetition of 8 eggs. Eggs were analyzed by optical microscope at 0, 1, 2, 4, 8 and 24 hours, respectively, to check for the severe effects thrombosis, haemorrhage, vascular lysis or embryonic lethality (heart failure).

In *Figure 138* is showed the cluster-gram representing the evaluation of the effects observed for the samples over time. The black-scale is proportional to the number of eggs in which the event occurred, ranging from a minimum (0% - black) to a maximum (100% - white) of egg interested. The negative control (NaCl) and the solvent control (WFI) have similar results showing mild haemorrhagic events (1/11 eggs), which can be related micro injury caused by the injection itself. In the case of solvent control 1/10 embryo died between 8-24 h what is comparable to our lab historical data and related to the shell-less incubation and variances in biological systems. The injection of the positive control as expected (bPEI) strongly induced thrombotic events (directly after injection) what causes lethality in 11/11 eggs after 1 h. It can be seen that thrombosis and vascular lysis do not occur with any of the samples tested, while mild and reversible hemorrhagic events have been observed with higher frequencies with the **NP-gel** used at higher concentration (125 µg/ml) and with **Gel** at lower concentration (50 µg/ml). However, since no trend can be seen in the occurrence of haemorrhagic events and since some have been noticed even in the negative and solvent controls, a true connection between the sample tested and the induction of hemorrhage cannot be established. Embryonic lethality occurs after 24 hours in both concentration of **NP-sol** (1/10 and 1/12 respectively for 50 and 125 µg/ml), in the lower concentration of **NP-gel** (1/10) and after injection of the higher concentration of the **Gel** (1/10).
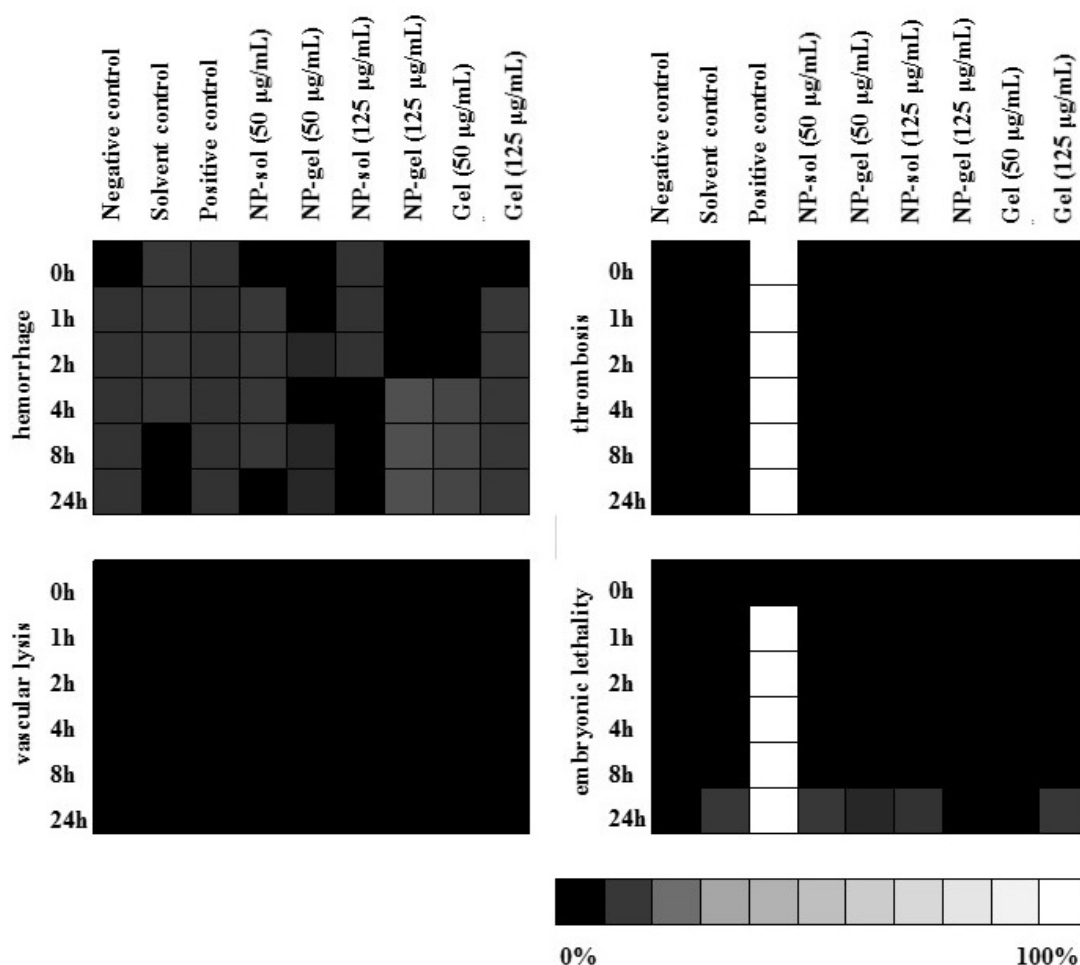
Figure 138: Clustergram showing the time-dependent toxic effects of intravenously applied nanoparticles or gel. The columns represent the time after injection of the sample, whereas the rows quantify the time-dependent toxic effects. The brightness of the squares is proportional to the number of infected eggs.

In summary, the MTS, haemocompatibility and HET-CAV tests used to evaluate the applicability of the storage method proposed were conform with each other, enhancing the robustness of the evaluation of the possible toxic effect induced by SiNPs if stored with the method proposed. All tests indicated that the gel-sample could safely be used directly for biological applications after reconstitution of the suspension and appropriate dilution. Indeed, no several toxicity effects was observed for both gel-samples and gel alone after appropriate dilution.

5.3.6 Hydrogel stability

The properties that have been considered when Fmoc-Gal was chosen as suitable gel for our application was its stability while being stored 'still' (i.e. without shaking or

245

strong vibrations) for long time and, on the other hand, the little effort required to turn it back into a viscous solution. However, the need to test the ability of the new formulation to retain the protective, gel-like properties, as a function of time and external factors, was soon understood, looking towards the possible requirement for samples to be delivered from a laboratory to another. Three studies were accomplished in order to prove the capability of the hydrogel matrix to retain stability under external mechanical stress, evaluating whether temperature and the concentration of NPs used could represent a limitation for the stability of the self-supporting gel.

Resistance to mechanical stress

In order to mimic a possible situation when particles are delivered, all NPs were formulated in gels using the usual concentration (1 mg of particles) and after 9 days storage at 4°C, they were all exposed to strong vibrations using a simple orbital shaker. The conversion of the hydrogel into a solution as a function of shaking speed and time was then qualitatively compared. The following experiments were accomplished at room temperature. All gels were shown to retain their matrix when shaken at 600 rpm and so, after 6 hours, the speed of the shaking was increased to 700 rpm. At this speed, only the weakest gel, **NP-NaFluo-NH₂** (*Figure 142)* started to show instability. Further increase of the shaking rate was needed to destroy the **NP-FITC** (*Figure 139)* and **NP-A-FITC-NH₂** (*Figure 140)* gel matrices, respectively 800 and 1200 rpm. In the case of **NP-B-FITC-NH₂** (*Figure 141)* and **NP-MB-NH₂** (*Figure 143)*, the shaking was increased to 1200 rpm (which is the maximum reachable speed of the instrument available), but after 30 hours the gel structure was not even partially damaged. Interestingly, two trends were observed when the nanoparticles and hydrogel were combined. Firstly, the gel stability positively correlated with increased ζ-potential of the SiNPs, and secondly, the more hydrophobic the dye, the more stable the gel appeared to be. The first trend is evident comparing results recorded for positively charged **NP-B-FITC-NH₂** (ζ= +3.6mV), which retained its self-supporting gel characteristic even after 30 hours of shaking at 1200 rpm, with the highly negatively charged **NP-FITC** (ζ= -34.4mV) instead converted to a suspension at 800 rpm and after *ca.* 7 hours of shaking. The second trend was pointed out observing *Figure 142* and *Figure 143*: **NP-MB-NH₂**, loaded with the hydrophobic methylene blue, greatly increased the strength of the gel matrix, while the fluorescein sodium salt-loaded particles (**NP-NaFlu-NH₂**)

contributed to the easier deterioration of the gel integrity. A possible explanation for these trends can be given considering that the gel matrix forms due to reversible and weak interactions (van der Waals forces, hydrogen bonds, etc.). Presumably, the presence of positively or negatively charged particles enhances or disturbs these interactions. Similarly, fluorescein sodium salt, which leaches out easily from the particles to the surrounding environment, could disturb the interactions between the fibres, making the gel more susceptible to mechanical stresses.
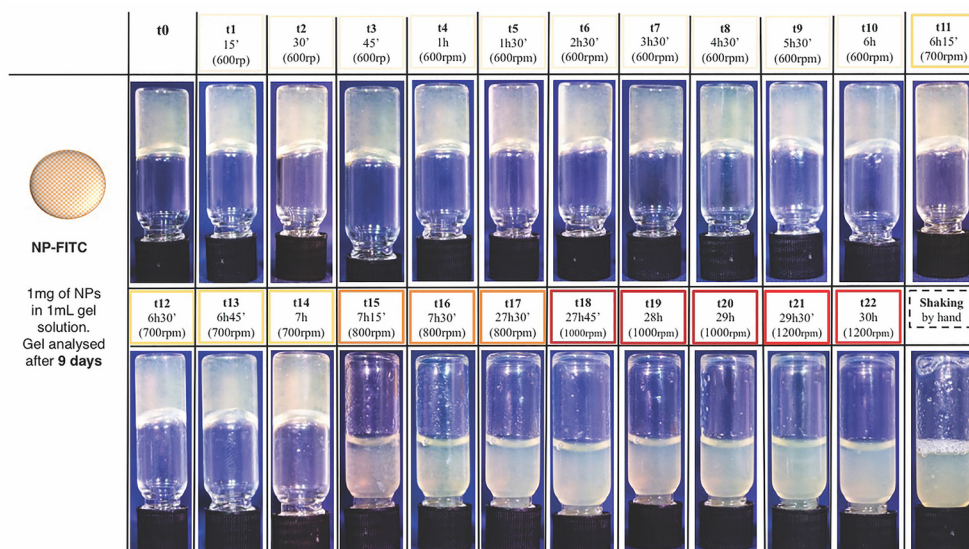
Figure 139: The NP-FITC gel sample showed to be stable for 7 hours until 700 rpm. The relative weakness of this sample could be related with the negativity of the nanoparticles surface
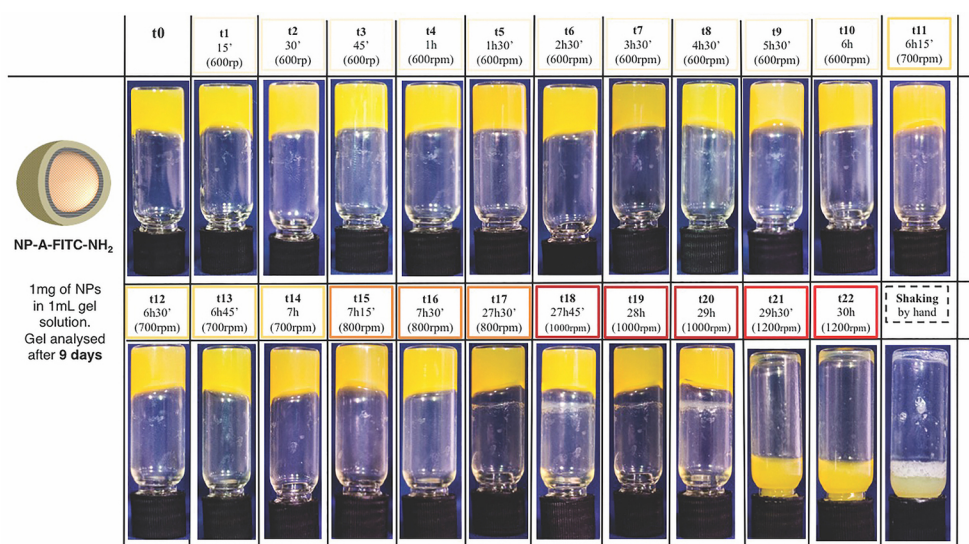
Figure 140: NP-A-FITC-NH₂ showed to be a strong gel since it turned into suspension only after more then 29 hours at the maximum shaking speed reachable.
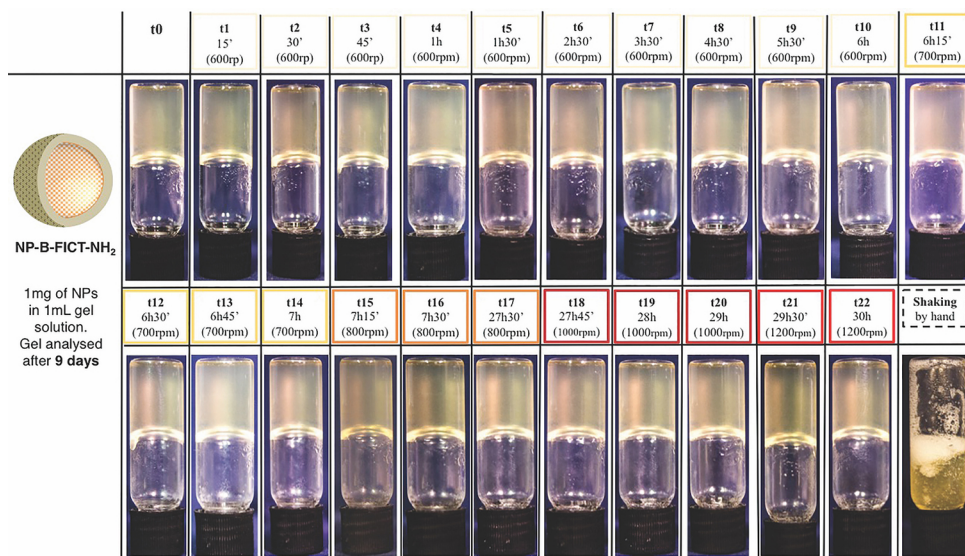
Figure 141: NP-B-FITC-NH$_2$ showed to be a very resistant gel, since it maintained its self-supportive state even after long time at the maximum shaking speed.
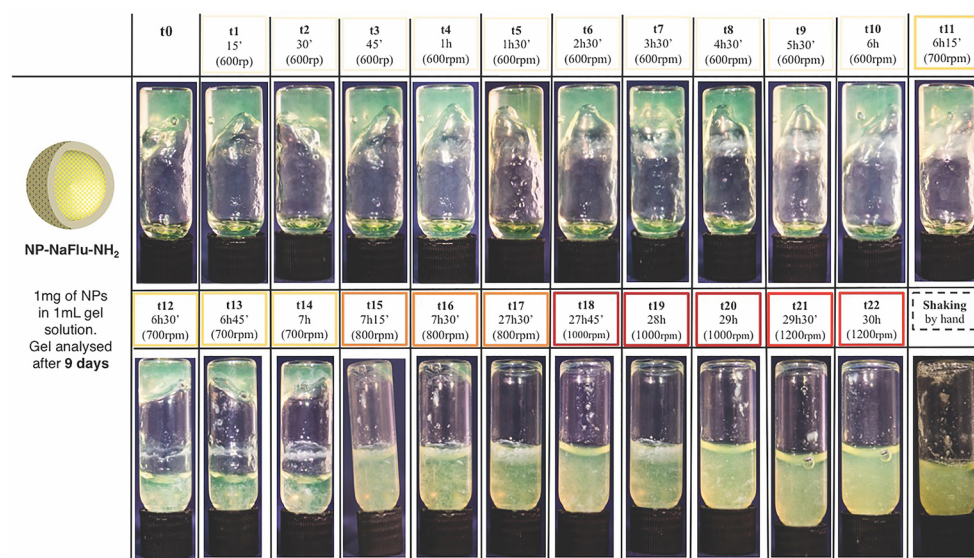

Figure 142: The mechanical stress study showed that NP-NaFLuo-NH$_2$ is the weakest gel tested. A possible explanation for this is that the presence of the highly water-soluble fluorescein sodium salt can destabilise the interaction that allows the formation of the self-supportive gel.
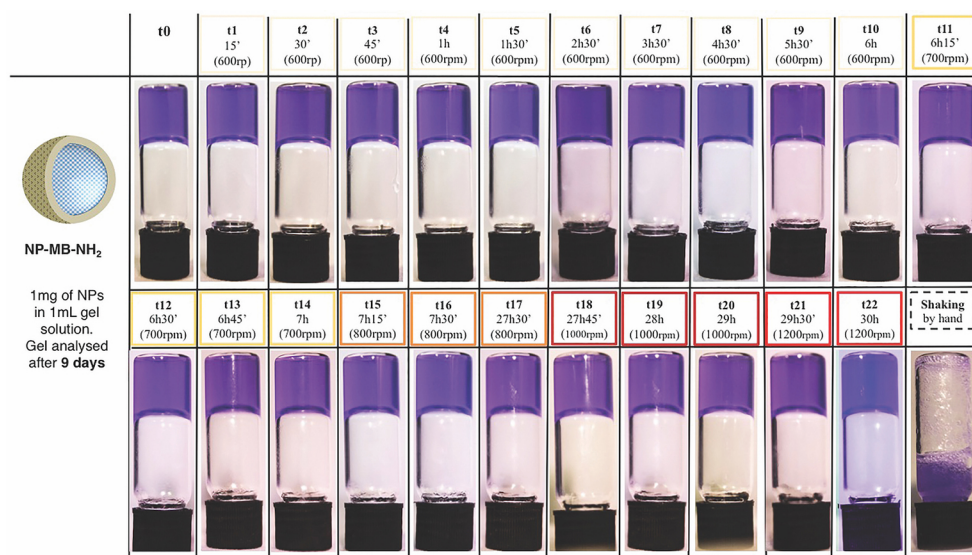
Figure 143: NP-MB-NH₂ showed to be one of the strongest gel in this study. In this case two are the factors that contribute to make the gel strong: the slightly positive surface charge and the presence of hydrophobic dye loaded inside the particles.

Nanoparticle concentration limit

In order to prove the versatility of the storage method, a further test was carried to define if the concentration of particles trapped into the gel could be varied without losing the self-supporting properties of the gel. For study, **NP-A-FITC-NH₂** were used as example. Thanks to their intermediate surface charge and the fact that FITC covalently is loaded inside the matrix, using this type of particles only the concentration of particles was expected to interfere with the gel stability and not the surface charge or dye leaching. Following the protocol always used for the preparation of gel-samples, 2.5, 3, 3.5, 4 and 4.5 mg of **NP-A-FITC-NH₂** were isolated by centrifugation and formulated in the gel samples by re-dispersion in 1 mL of Fmoc-Gal solution. After 30 minutes, gelation was obtained for all samples. The possibility to increase the concentration of nanoparticles in the samples could be interesting in order to favour the gel dissolution: increasing the NPs concentration in the gel-sample means that higher dilution is needed to reach the desired concentration (normally very low for biological applications), leading to a better dissolution of the residual gel fibres in the final sample. As shown in *Figure 144*, increasing the concentration of particles up to 4.5 mg/mL (which corresponds to *ca.* $4,5 \times 10^{12}$ NPs/mL), the stability of the gel is not even partially altered, which may point to the possibility that even higher concentrations could be trapped into the gel matrix, if required, without compromising the stability of the gel.
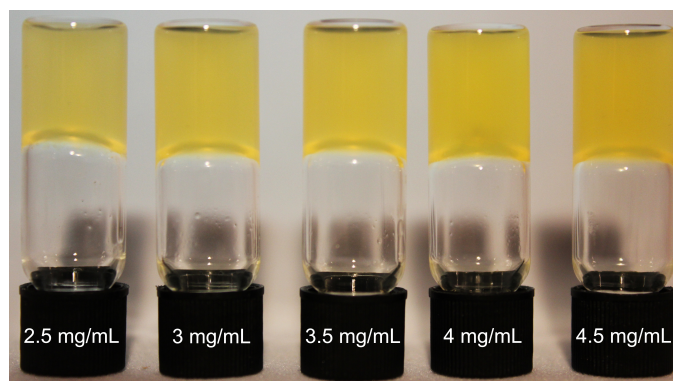
Figure 144: Different concentrations of NP-A-FITC-NH2 were formulated in gel: 2.5, 3, 3.5, 4 and 4.5 mg/mL of gelator solution. After 30 minutes all samples turned into gel without showing any stability problem.

Temperature stability

To guarantee the stability of biological and non-biological samples, it is normally suggested to store them under refrigeration (approximated at 4°C). Although the it is possible to deliver samples under controlled temperature conditions, the stability of the hydrogel was evaluated at different temperatures. For this particular study, the hydrogel alone was tested, without nanoparticles trapped into the matrix. Hydrogel samples were formulated following the same procedure as previously and the gel stability was tested at 4°C, room temperature (R.T. *c.a.* 25°C) and at 37°C, which represent the conditions at which the samples can potentially be exposed during storage or delivery. Each day, the stability of the gel was qualitatively evaluated by vial inversion. The study was carried on in triplicate, which means that three gel samples were stored at each temperature. As shown in *Figure 145*, no relevant alteration of the gel structure was observed at R.T. and 4°C during course of the experiment, while only after 6 days at 37°C did the gel matrix appear to become slightly weaker, although the integrity cannot be considered completely altered.
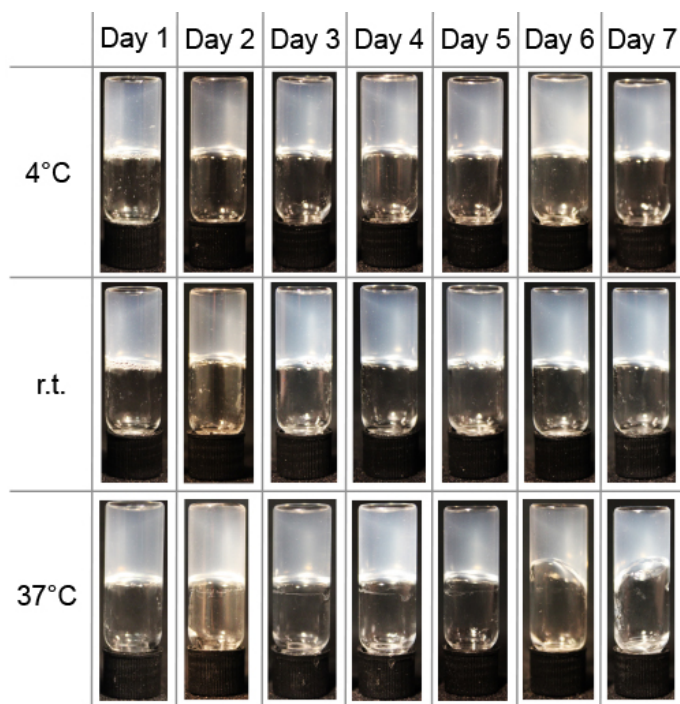
Figure 145: Each day, an image of the gel was taken to visually analyse the structure of the gel. It is clearly visible that the gel is perfectly stable at 4°C and at r.t. for 7 days. When stored at 37°C it became weaker after 5 days however the effect is not enough to consider its integrity altered.

It is therefore possible to conclude that the Fmoc-Gal hydrogel could eventually maintain its integrity even if not stored under refrigeration but at R.T. or at 37 at least for one week. However, it is recommended to store gel-samples under refrigeration, when possible, to prudently prevent contamination that in an aqueous environment could easily occur, especially at high temperature.

5.4 Conclusions

Storing nanoparticles in an Fmoc-Gal hydrogel has been shown to be an effective method to better maintain mondispersity of the suspension and to preserve the morphology and physic-chemical characteristics of the nanomaterial. The stabilisation effect obtained using the hydrogel is remarkable, especially for highly unstable particles such as positively charged SiNPs. **NP-MB-NH₂** in particular, were visibly aggregated when stored in suspension after 30 days, while in the gel-sample the particles were still nicely monodisperse. The novel storage method showed to be efficient even in reducing the dye leaching during storage of highly soluble dyes (**NP-NaFlu-NH₂)** which is particular important considering that NPs are often used as DDS.

When the method was evaluated with more stable colloidal systems, AuNPs and dextran-coated SiNPs, the gel showed to only slightly increase the stability of the nanoparticles; however, more interesting findings were noticed in these cases.

Coating SiNPs with dextran is a common and efficient technique used to stabilise this type of suspension. However, it was shown that hollowing and degradation processes, which occurred when the SiNP were stored and subsequently diluted with a complex solvent (cellular medium), are limited if the particles are stored in gel rather than in solution.

In the other case studied, it was observed that AuNPs interact with the gel fibres. Only by diluting the sample, hence dissolving the residual fibres, the particles are gradually released back into suspension. More interestingly, thanks to these reversible interactions, the AuNP were stabilised in a highly salted environment. The possibility of using salted solutions with AuNPs, while avoiding agglomeration, could widen the applicability of these nanomaterials, which has until now been limited by the specific conditions required during the handling of this susceptible nanomaterial.

Once the stabilisation effect achievable with the proposed method had been proven, two further issues needed to be investigated.

First of all, since the intention was that the sample stored in gel could be used for biological applications directly, without further manipulation, the evaluation of toxicity induced by residual fibres inevitably present in the sample was claimed as necessary. *In vitro* and *ex ovo* assays were carried out to evaluate the cytotoxicity and biocompatibility of the samples previously stored using the proposed method. All assays led to the same conclusion, i.e. that the residual gel fibres do not induce any toxicity effect at the concentrations tested, proving the applicability of the method.

Secondly, the stability of the self-supporting gel was tested under different conditions. Very often the laboratory, department and even the geographical location where nanomaterials are produced is not the same as the one where they are tested for their activity or used for further applications. Therefore, samples need to be stable even during transportation. To prove that nanoparticles stored in gel can be safety transported, the hydrogel stability was tested under mechanical stress and at different temperatures, reproducing possible scenarios that can take place during transport. The

hydrogel was shown to maintain its self-supporting matrix under high-speed shaking and when exposed to different temperatures for 7 days. The possibility of trap high concentrations of nanoparticles in the gel matrix was further proven, making this storage method adaptable for any specific condition and need.

5.5 Future work

In order to better evaluate the efficiency of the method, home-made AuNPs should be used considering the difficulties encountered trying to remove the stabilisers from the samples purchased. Furthermore, it would be interesting to evaluate the possibility of stabilise in the hydrogel matrix other type of particles, such as liposomes, for which the instability in suspension is still considered an issue. The following step will be to effectively test the method in a real scenario. NPs designed for a particular application, such as ELISA-like assay, should be formulated in gel and their activity tested after reconstitution of the suspension. If the gel-stored particles will show the same or better activity compared with the 'normal' sample, then the proposed storage method should really be considered as a valuable alternative to the common storage techniques herein discussed.

Chapter 6

Overview

Incredible amounts of effort and resources have been spent worldwide in developing nanoproducts with the final goal of improving healthcare and to give new tools for medical research. Since 2000, governments in the U.S.A., Europe, Japan and other Asian nations have invested millions of dollars on nanotechnology, supporting both private and public research centres. Thanks to the development of nanotechnology, it is now possible to measure, design and manipulate materials at the nanoscale. This allows the preparation of novel entities with specific properties, with control at the atomic, molecular and supramolecular level. Furthermore, an expanding array of tools has become accessible for characterizing materials at the nanoscale.

Medicine and healthcare could be revolutionized by the application of nanotechnology to the life sciences. A new era in biotechnology and biomedical engineering is emerging with use of nanoscale structures for diagnosis, gene sequencing and drug delivery. Nanotechnology has the potential to enable us to learn about the detailed processes, which occur inside individual cells and tissues, giving key information with which living systems could be re-engineered *in vitro*.

As discussed in Chapter 1, three applications of nanotechnology are particularly suited to nanomedicine: diagnostic techniques, bio-imaging and drug delivery. In the present work, we have considered two important aspects related with nanomaterials: bio-application of NPs *in vitro* and *in vivo* and their stability. Although distinct, these two aspects are intimately related. The bio-activity and efficiency of NPs is strictly

dependent on their physico-chemical properties and morphology. Indeed, the formation of aggregates/agglomerates can alter the activity of NPs, especially when intended for *in vitro* and *in vivo* applications.

Chapter 2 presents the development of an 'on/off' fluorescence probe for the detection of bacteria. The detection is achieved by using switchable substrate whom fluorescent signal is 'turned on' only when reacts with a specific enzyme (β-glucosidae). Similar substrates are commercially available and are based on the use of 4-methy umbelliferone (4-MU) as switchable fluorophore. The limitations of 4-MU were firstly discussed and 7 novel alternative umbelliferone-derivatives were synthesised. Almost all of the compounds showed better fluorescent properties under the conditions required for biological assays in comparison with 4-MU. Compound **1** was further modified to obtain the substrate β-4-AAUG, which showed to be highly selective for the specific enzyme β-glucosidase. When tested in bacterial experiments, the substrate was able to detect low amounts (75-1 CFU/mL) of *E. coli, Enterococcus* and *K. pneumonia* in 2-3 hours.

Chapter 3 is a continuation of the previous project. In this case a fluorescent nanoprobe for bacterial detection were synthesised functionalising the particles surface with the 'on/off' probe synthesised in the previous chapter. The goal of the project was to evaluate the possibility of enhance the limit of detection exploiting nanoparticles properties. It was observed that functionalizing the NP's surface with the fluorescent substrates did not afford significant improvements compared to the free β-4-AAUG. Good results were obtained with **Glu-5-strpt-MNs**, synthesised anchoring the substrate **5** on streptavidin-coated magnetic particles followed by a glycosylation step. Treating them with bacteria a prompt increase of fluorescence was measurable. However, the pathway chosen for the surface functionalization led to the presence on the particle's surface of both α- and β- anomers of the glucose, which caused a loss in enzymatic-specificity.

Due to their high loading capacity, ease of manipulation and biocompatibility, SiNPs are considered as valuable carriers for drug delivery. In Chapter 4, preliminary studies are presented, in which the applicability of SiNPs as carrier for oral administration is evaluated. Different types of particles were synthesised varying the ration of silica derivatives (TEOS:ETEOS) used for the silica core formation in order to evaluate if

changing the particle matrix a different pH-sensitivity could be achieved. Additionally, three different drug-model dyes were loaded inside the particles, by covalent incorporation or by physical entrapment. The suitability of such particles for oral drug deliver was evaluated by testing dye release and dissolution when incubated at pH 4, 6 and 7.4, which mimic the environments encountered along the GI tract, i.e. fed stomach, duodenum and jejunum respectively. The importance of the loading method was firstly highlighted. Indeed, FITC-SiNPs series having FITC covalently loaded into the silica matrix showed to have a higher loading capacity and better control on the dye release compared with the other types of particles in which the dye was only physically entrapped. The kinetic of dye release observed for FITC-SiNPs showed to be strongly pH-dependent. In particular, no release was observed at pH 4, while it increased at pH 6 and peaked at pH 7.4. Therefore, using this type of carrier, the drug is protected from the harsh conditions of the stomach, while it is released in the intestine, where absorption takes place. While the release profiles of the model drugs form the differently formulated NPs was similar, there were clear differences in the dissolution mechanism. FITC-SiNP$_{100TEOS}$ degraded via a hollowing process, while FITC-SiNP$_{100ETEOS}$ simply dissolved without the formation of holes. Although preliminary results are promising, more studies are required in order to prove that SiNPs can be applied for oral drug delivery. The capability of SiNPs in protecting the cargo should be tested re-creating the physiological environment by adding enzymes, e.g. peptidase, in the system. Additionally, in order to better simulate the *in vivo* conditions, the kinetic or release should be accomplished in larger volume and in a more dynamic model.

Working with NPs, we often had to deal with colloidal stability issues. Addressing this problem, in Chapter 5 an alternative method to stabilise colloidal systems has been discussed. The aim of the project was to develop an alternative method of storing NPs, capable of preserve their physico-chemical properties over time in aqueous suspension. Simply trapping the particles in the matrix of a reversible hydrogel, thus limiting the potential for aggregation, highly unstable SiNPs were successfully stored for long-term storage, maintaining their morphology and monodispersity. Additionally, it was observed that by trapping the particles in the gel matrix, the undesired leaching of the cargo was remarkably reduced, which is particularly important when NPs are used in drug delivery. Various *in vitro* and *ex ovo* assays were used to evaluate the applicability of the method. The data obtained indicated that, after

storage, no further manipulation of the sample is required since the gel's fibres do not induce toxicity effects after appropriate dilution. In order to test the versatility of the method, gel-samples of AuNPs were also prepared, stored and analysed. AuNPs were shown to be stable in the hydrogel even when exposed to unfavourable conditions, such as saline solution. Besides the promising results obtained, further studies are needed in order to claim that the method can be applied even for other types of particles, in addition to SiNPs.

6.1 General discussion

During the development of the projects described in this thesis, I had the opportunity to work with a number of different materials. I have been particularly intrigued by the fascinating word of complex materials, through combining nanoparticles with hydrogels and by the possibility of changing behaviour and properties of materials only through minor changes in its formulation. It would be interesting to design libraries of new nano/micro-products characterizing their properties and find for them an application accordingly to the result.

Considering this, as future research-prospects, I would like to deeper investigate the potential in the combination of both nano- and soft materials: the tunability, responsiveness and hydrogel's biocompatibility on one hand and, on the other hand, the possibility of surface functionalization, loading and protection of drugs in the nanoparticle's matrix. Combining nanoparticles and hydrogels could be applied to the development of novel drug delivery systems, sensing devices, responsive patches and many other applications. In particular, I think the possibility of combining biosensing NPs or drug-loaded NPs in the matrix of a gel could be useful for the development of novel responsive patches as either diagnostic tools or reservoir-based delivery systems, respectively. Furthermore, combining NPs and gels, it is possible to create a composite third material having different behaviour and stimuli responsiveness to the individual components, which increases the attraction of such complex materials.

6.2 Personal prospective on nanomedicine

Nanomedicine is undoubtedly a promising field. There are many advantages in nanotechnology when applied in medicine, as discussed in Chapter 1. However, it appears evident that biocompatibility and the efficiency of the nano-products when used *in vivo* is still a challenge. Many intricate nanomaterials have been designed. They are often characterised by complicated and ambitious architectures and sometimes uncertain applications. Some of them fail the preliminary studies or are not stable under the required conditions. In other cases, nano-products succeed in their aim when tested *in vitro*, but the story changes once they are applied *in vivo*. The fate of the nanomaterial once in a biological environment and the interaction of NPs with cells are the fundamental aspects that need to be considered during the design and fabrication of the nanomaterial.

It is worth recognising that the *in vivo* limitations of nanotechnology no longer represent issues when the particles are design for external uses. The application of nanotechnology in the development of diagnostic sensors and "lab on a chip" devices has boomed in recent years. There are a few reasons for this: (i) the large variety of instruments available for signal detection, (ii) the relative ease by which the particles' bio-activity can be tracked and, finally, (iii) the minor interferences encountered when the particles are used outside the body. Such external devices are usually suitable for analysis of human samples such as blood, urine and sweat. Therefore, the main limitations are the interference of other species present in the same sample and the low concentration of the analyte. The NP's properties allow to increase the sensitivity/selectivity of the recognition event and it has often been exploited to amplify the signal reached when detection occurs.

Personally, I see greater potential in nanotechnology applied for the development of diagnostic devices rather than for *in vivo* applications. I have been inspired by observing the variety of impressive sensing devices that have been developed in recent years, either by reading about published works or from attending international conferences. The research effort in the field is supported/pushed by relevant industrial investment, where the interest is obviously more concrete and realistic. Investors from the industrial sector are obviously more attracted by products that have an

easier/broader target rather than investing in developing tools for diagnose diseases. Their priority is to launch the new personalized wearable devices (e.g. watches, bracelets) to monitor overall wellbeing (e.g. how your body feels, what you should drink and for how long you should walk). However, it is clear that over the last decade society has moved further into the belief that 'prevention is better than cure', which is fundamental to support the development of advanced diagnostic devices. The investments coming from public and private resources, which are already increasing exponentially, will certainty guarantee further progress in this promising field.

During the three years of my PhD I think I have acquired knowledge that allows me to recognize pros and cons of nanotechnology when applied in medicine. The unlimited potential, the financial support and the fundamental social empathy forecast a certain success for nanotechnology in the development of diagnostic devices. On the other hand, the uncertain fate of NPs *in vivo* and the lack of appropriate *in vitro* studies should be the aspect on which efforts need to be focused in order to turn 'blue sky' science into a concrete reality.

REFERENCES

1 A. P. Alivisatos, *Science,* 1996, **271**, 933-937.

2 https://www.nano.gov/nanotech-101/what/definition.

3 O. Salata, *J. Nanobiotechnol.,* 2004, **2**, 3

4 P. Satalkar, B. S. Elger and D. M. Shaw, *Sci. Eng. Ethics,* 2016, **22**, 1255-1276.

5 E. H. Chang, J. B. Harford, M. A. W. Eaton, P. M. Boisseau, A. Dube, R. Hayeshi, H. Swai and D. S. Lee, *Nanomedicine: Past, present and future – A global perspective*, 2015.

6 A. Tivnan, W. S. Orr, V. Gubala, R. Nooney, A. M. Davidoff and R. L. Stallings, *PloS one,* 2012, **7**, e38129

7 M. Rasekh, C. Young, M. Roldo, F. Lancien, J. C. Le Mével, S. Hafizi, Z. Ahmad, E. Barbu and D. Gorecki, *J. Mater. Sci-Mater M.,* 2015, **26**, 256.

8 G. Tosi, T. Musumeci, B. Ruozi, C. Carbone, D. Belletti, R. Pignatello, M. A. Vandelli and G. Puglisi, *J. Drug Deliv. Sci. Tec.,* 2016, **32**, 66-76

9 D. Napierska, L. C. J. Thomassen, V. Rabolli, D. Lison, L. Gonzalez, M. Kirsch-Volders, J. A. Martens and P. H. Hoet, *Small,* 2009, **7**, 846-853.

10 X. Gao, Y. Cui, R. M. Levenson, L. W. K. Chung and S. Nie, *Nat. Biotechnol.,* 2004, **22**, 969-976.

11 A. Khademhosseini, J. P. Vacanti and R. Langer, *Sci. Am.,* 2009, **300**, 64-71.

12 M. Stevens and H. J. George, *Science,* 2005, **310**, 1135-1138.

13 A. De Carvalho, G. Veronese, A. V. José, F. Carvalho, E. Barbu, A. C. Amaral and E. Trovatti, *Cellulose,* 2016, **23**, 3399-3405.

14 X. Gao and S. Nie, *Anal. Chem.,* 2004, **76**, 2406-2410.

15 L. Faucher, M. Tremblay, J. Lagueux, Y. Gossuin and M. Fortin, *ACS Appl. Mater. Inter.,* 2012, **4**, 4506-4515.

16 J. Lin, X. Chen and P. Huang, *Graphene-based nanomaterials for bioimaging*, 2016.

17 Q. Liu, B. Guo, Z. Rao, B. Zhang and J. R. Gong, *Nano Lett.,* 2013, **13**, 2436-2441.

18 S. K. Bhunia, A. Saha, A. R. Maity, S. C. Ray and N. R. Jana, *Sci. Rep.,* 2013, **3**, 1473.

19 H. Shi, X. He, K. Wang, Y. Yuan, K. Deng, J. Chen and W. Tan, *Nanomedicine: NBM,* 2007, **3**, 266-272.

20.https://bio.libretexts.org/TextMaps/Map%3A_Microbiology_(OpenStax)/20%3A_Laboratory_Analysis_of_the_Immune_Response/20.4%3A_Enzyme_Immunoassays_(EIA)_and_Enzyme-Linked_Immunosorbent_Assays_(ELISA).

21 C. Schofield, R. Field and D. Russell, *Anal. Chem.,* 2007, **79**, 1356-1361.

22 Z. Fan, D. Senapati, A. K. Singh and P. C. Ray, *Mol. Pharmaceut.,* 2013, **10**, 857-866.

23 D. Napierska, L. C. J. Thomassen, V. Rabolli, D. Lison, L. Gonzalez and M. Kirsch-Volders, *Small,* 2009, **5**, 846-853.

24 D. Bobo, K. J. Robinson, J. Islam, K. J. Thurecht and S. R. Corrie, *Pharm. Res.,* 2016, **33**, 2373-2387.

25 M. A. Dobrovolskaia, *Pre-clinical immunotoxicity studies of nanotechnology-formulated drugs: Challenges, considerations and strategy*, 2015.

26 V. Rabolli, C. J. Thomassen, C. Prince, D. Napierska, L. Gonzales, J. Martens and D. Lison, *Nanotoxicology,* 2010, **4**, 307-318.

27 J. Zaloga, C. Janko, R. Agarwal, J. Nowak, R., S. Odenbach, S. Lyer and C. Alexiou, *Int. J. Mol. Sci.,* 2015, **16**, 9368-9384.

28 W. Abdelwahed, G. Degobert and H. Fessi, *Eur. J. Pharm. Sci.,* 2006, **63**, 87-94.

29 S. P. J. Higson, S. M. Reddy and P. M. Vadgama, *Eng. Sci. Educ. J.,* 1994, **3**, 41-48.

30 D. Fraser, *Med. Device Technol.,* 1994, **5**.

31 D. R. Thévenot, K. Toth, R. A. Durst and G. S. Wilson, *Biosens. Bioelectron.,* 2001, **16**, 121-131.

32 B. Garipcan, M. Caglayan and G. Demirel, *New Genereation Biosensors based on Ellipsometry*, Pier Andrea Serra, 2011.

33 IUPAC, *International Union of Pure and Applied Chemistry,* 2014.

34 L. Syedmoradi, M. Daneshpour, M. Alvandipour, F. A. Gomez, H. Hajghassem and K. Omidfar, *Biosens. Bioelectron.,* 2017, **87**, 373-387.

35 J. R. North, *Trends Biotechnol.,* 1985, **3**.

36 P. S. Mohanty and E. Kougianos, *IEEE Potentials,* 2006.

37 A. Wendel, *Biosensors Based on Biological Nanostructures*, Intechopen.

38 A. Mahara, R. Iwase, T. Sakamoto, K. Yamana, T. Yamaoka and A. Murakami, *Angew. Chem.-Int. Edit.,* 2002, **41**, 3648-3650.

39 M. Sharma and N. K. Gohil, *Eng. Life Sci.,* 2010, **10**, 304-310.

40 J. H. Kim, S. Y. Lim, D. H. Nam, J. Ryu, S. H. Ku and C. B. Park, *Biosens. Bioelectron.,* 2011, **26**, 1860-1865.

41 Y. Hori, T. Norinobu, M. Sato, K. Arita, M. Shirakawa and K. Kikuchi, *JACS,* 2013, **135**, 12360-12365.

42 M. E. Vazquez, J. B. Blanco and B. Imperiali, *JACS,* 2004, **127**, 1300-1306.

43 M. Pellerano, D. Naud-Martin, M. Peyressatre, C. Prével, M. -. Teulade-Fichou, M. Morris and F. Mahuteau-Betzer, *ChemBioChem,* 2016, **17**, 737-744.

44 H. Lai, Y. Xiao, F. Tian, C. Zhong, Y. Liu, X. Weng and X. Zhou, *RSC Analyst,* 2014, **139**, 1834-1838.

45 J. Liu, J. Ren, X. Bao, W. Gao, C. Wu and Y. Zhao, *Anal. Chem.,* 2016, **88**, 5865-5870.

46 C. Jing and V. Cornish, *ACS Chem. Biol.,* 2013, **8**, 1704-1712.

47 E. K. Fauster and T. E. Glass, *JACS,* 2003, **125**, 16174-16175.

48 Y. Wang, H. Jiang, F. Zhu, X. Wang and T. Geng, *B. Mater. Sci.,* 2017, **40**, 187-193.

49 J. Han, A. Loudet, R. Barhoumi, R. C. Burghardt and K. Burgess, *JACS,* 2009, **131**, 1642-1643.

50 Y. Kurishita, T. Kohira, A. Ojida and I. Hamachi, *JACS,* 2010, **132**, 13290-13299.

51 A. Majzoub, C. Cadiou, I. Dechamps-Olivier, B. Tinant and F. Chuburu, *Inorg. Chem.,* 2011, **50**, 4029-4038.

52 P. Ashokkumar, V. T. Ramakrishnan and P. Ramamurthy, *J. Phys. Chem. A,* 2011, **115**, 14292-14299.

53 K. Secor, J. Plante, C. Avetta and T. Glass, *J. Mat. Chem.,* 2005, **15**, 4073-4077.

54 X. Li, H. Ma, S. Dong, X. Duan and S. Liang, *Talanta,* 2004, **62**, 367-371.

55 X. Li, H. Ma, L. Nie, M. Sun and S. Xiong, *Anal. Chim. Acta,* 2004, **515**, 255-260.

56 H. Yu, Y. Xiao, H. Guo and X. Qian, *Chem. Eur. J.,* 2011, **17**, 3179-3191.

57 R. Wang, F. Fabiao Yu, P. Liua and L. Chen, *Chem. Commun.,* 2012, **48**, 5310-5312.

58 K. Xu, X. Liu, B. Tang, G. Yang, Y. Yang and L. An, *Chem. Eur. J.,* 2007, **13**, 1411-1416.

59 C. Sun, W. Shi, Y. Song, W. Chen and H. Ma, *Chem. Commun.,* 2011, **47**, 8638-8640.

60 K. S. Lee, T. Kim, J. Lee, H. Kim and J. Hong, *Chem. Commun.,* 2008, , 6173-6175.

61 H. Kwon, K. Leea and H. Kim, *Chem. Commun.,* 2011, **47**, 1773-1775.

62 D. Gong, Y. Tian, C. Yang, A. Iqbal, Z. Wang, W. Liu, W. Qin, X. Zhu and H. Guo, *Biosens. Bioelectron.,* 2016, **85**, 178-183.

63 M. Hoshiyama, K. Kubo, T. Igarashi and T. Sakurai, *J. Photoch. Photobio. A,* 2001, **138**, 227-233.

64 G. Jones II, W. R. Jackson, C. Choi and W. Bergmark, *J. Phys. Chem.,* 1985, **89**, 294-300.

65 C. Wheelock, *JACS,* 1958, **81**, 1348.

66 J. Richard, M. Massonneau, P. Renard and A. Romieu, *Org.Lett.,* 2008, **10**, 4175-4178.

67 Y. Meyer, J. Richard, M. Massonneau, P. Renard and A. Romieu, *Org. Lett.,* 2008, **10**, 1517-1520.

68 R. K. Singh, T. Mandal, N. Balasubramanian, G. Cook and D. K. Srivastava, *Anal. Biochem.,* 2011, **408**, 309-315.

69 H. Huang, K. Wang, S. Huang, H. Lin and C. Lin, *Biosens. Bioelectron.,* 2011, **26**, 3511-3516.

70 S. Huang, C. Teng, Y. Lee, J. Wu, K. Wang and C. Lin, *Anal. Chem.,* 2010, **82**, 7329-7334.

71 G. Chen, D. J. Yee, N. G. Gubernator and D. Sames, *JACS,* 2005, **127**, 4544-4545.

72 J. M. Conly and B. L. Johnston, *Can. J. Infect. Dis, Med.,* 2005, **16**, 159-160.

73 H. W. Boucher, G. H. Talbot, D. B. E. Murray, R. A. Bonomo and D. Gilbert, *IDSA pubblications,* 2013, **56**, 1685-1694.

74 IDSA, *IDSA pubblications,* 2004.

75 D. Deak, K. Outterson, J. Powers and S. Kesselheim, *Annals of Internal Medicine,* 2016, **165**.

76 H. D. Isenberg, *J. Clin. Microbiol.,* 2003, **41**, 917-918.

77 T. Braine, *Race against time to develop new antibiotics*, 2011.

78 A. Horan, *Tackilng antimicrobial resistence*, 2015.

79 A. Cunha, A. Almeida, Coelho, F J R C, N. C. M. Gomes, V. Oliveira and A. L. Santos, in *Current Research, Technology and Environmental Topics in Applied Microbial Biotechnology*, ed. nonymous , A.Mendez-Vilas, 2010, p. 124.

80 Kim D.H., Kang H.J., Park S.H., Kobashi K., *Biol. Pharm. Bull.,* 1994, **17**, 423-426.

81 V. Veena, P. Poornima, R. Parvatham, K. Sivapriyadharsini and K. Kalaiselvi, *Afr. J. Biotechnol.,* 2011, **10**, 14907-14912.

82 http://proteopedia.org/wiki/index.php/Beta-glucosidase#Structure_and_function.

83 A. L. James and P. Yeoman, *Zentralblatt für Bakteriologie Mikrobiologie und Hygiene,* 1987, **267**, 188-193.

84 J. D. Perry, K. A. Morris, A. L. James, M. Oliver and F. K. Gould, *J. Appl. Microbiol.,* 2006, **102**, 4100-415.

85 J. D. Perry, A. L. James, K. A. Morris, M. Oliver, K. F. Chilvers, R. H. Reed and F. K. Gould, *J. Appl. Microbiol.,* 2006, **101**, 977-985.

86 A. Kaufhold, R. Lütticken and U. Schwien, *Zentralblatt für Bakteriologie,* 1989, **272**, 191-195.

87 K. Panosian and S. Edberg, *J. Clin. Microbiol.,* 1989, **27**, 1719-1722.

88 X. Wei, Q. Wu, J. Zhang, Y. Zhang, W. Guo, M. Chen, Q. Gu, Z. Caie and M. Lue, *Chem. Commun,* 2017, **53**, 103-106.

89 Y. Li, H. Wang, J. Li, J. Zheng, X. Xu and R. Yang, *Anal. Chem.,* 2011, **83**, 1268-1274.

90 K. F. Chilvers, J. D. Perry, A. L. James and R. H. Reed, *J. Appl. Microbiol,* 2001, **91**, 1118-1130.

91 Y. Yang and K. Hamaguchi, *J. Biochem.,* 1980, **87**, 1003-1014.

92 C. Malet, J. L. Viladot, A. Ochoa, B. Gallégo, C. Brosa and A. Planas, *Carbohyd. Res.,* 1995, **274**, 285-301.

93 N. Baggett, M. A. Case, P. R. Darby and J. Gray, *Enz. Microbiol.,* 1993, **15**, 742-748.

94 J. C. Paton and A. W. Paton, *Clin. Microbiol. Rev.,* 1998, **11**, 450-479.

95 http://www.phac-aspc.gc.ca/lab-bio/res/psds-ftss/escherichia-coli-pa-eng.php.

96 K. Fisher and C. Phillips, *Microbiology,* 2009, **155**, 1749-1757.

97 L. M. Teixeira, M. G. S. Carvalho, P. L. Shewmaker and R. R. Facklam, in *Bacetriology*, ed. nonymous.

98 http://www.phac-aspc.gc.ca/lab-bio/res/psds-ftss/enterococcus-eng.php#endnote2.

99 http://www.phac-aspc.gc.ca/lab-bio/res/psds-ftss/klebsiella-eng.php#footnote1.

100 R. Podschun and U. Ullmann, *Cli. Macrobiol. Rev.,* 1998, **11**, 589-603.

101 A. Banerjee and T. K. Danger, *World J. Microb. Biot.,* 1995, **11**, 618-620.

102 http://www.phac-aspc.gc.ca/lab-bio/res/psds-ftss/pseudomonas-spp-eng.php.

103 J. Klockgether, N. Cramer, L. Wiehlmann, C. F. Davenportand and B. Tümmler, *Front. Mocrobiol,* 2011, **2**, 1-18.

104 http://www.phac-aspc.gc.ca/lab-bio/res/psds-ftss/staphylococcus-aureus-eng.php.

105 S. Y. C. Tong, J. S. Davis, E. Eichenberger, T. L. Holland and V. G. Fowler, *Clin. Microbiol. Rev.,* 2015, **28**, 603-661.

106 A. Bren, J. Park, B. Towbin, E. Dekel, D. Rabinowitz and U. Alon, *Sci. Rep.,* 2016, **6**.

107 J. Weber, A. Kayser and U. Rinas, *Microbiology,* 2005, **151**, 707-716.

108 M. Ramsey, A. Hartke and M. Huycke, in *Enterococci: From Commensals to Leading Causes of Drug Resistant Infection [Internet]*, ed. nonymous , Gilmore MS, Clewell DB, Ike Y, et al., Boston: Massachusetts Eye and Ear Infirmary, 2014.

109 J. A. Simons, Teixeira De Mattos, M J and O. M. Neijssel, *J. Gen. Microbiol.,* 1991, **137**, 1479-1483.

110 F. Rojo, *FEMS Microbiol. Rev.,* 2010, **34**, 658-684.

111 F. Chen, *Metabolism of Pseudomonas aeruginosa Under Simultaneous Aerobic Respiration and Denitrification*, University of Akron, Akron, 2005.

112 M. T. Ferreira, A. S. Manso, P. Gaspar, M. G. Pinho and A. R. Neves, *PLOS ONE,* 2013, **8**, 1-12.

113 J. Kim and K. Cho, *Comput. Biol. Chem.,* 2006, **30**, 438-444.

114 C. I. L. Justino, A. C. Duarte and T. A. P. Rocha-Santos, *TrAC Trends Anal. Chem.,* 2016, **85**, 36-60

115 H. Zhang, L. Liu, X. Fu and Z. Zhu, *Biosens. Bioelectro.,* 2013, **42**, 23-30

116 I. Cho, A. Bhunia and J. Irudayaraj, *Int. J. Food Microbiol.,* 2015, **206**, 60-66

117 L. Hung, J. Chang, Y. Tsai, C. Huang, C. Chang, C. Yeh and G. Lee, *Nanomedicine: NBM,* 2014, **10**, 819-829

118 H. Ju, X. Zhang and J. Wang, in , ed. nonymous , Springer New York, 2011, p. 535.

119 A. Martín, J. Hernández-Ferrer, L. Vázquez, M. Martínezb and A. Escarpa, *RSC Advance,* 2014, **4**, 132-139.

120 F. Liu, G. Xiang, R. Yuan, X. Chen, F. Luo, D. Jiang, S. Huang, Y. Li and X. Pu, *Biosens. Bioelectro.,* 2014, **60**, 210-217

121 C. Li, M. Curreli, H. Lin, B. Lei, F. N. Ishikawa, R. Datar, R. J. Cote, M. E. Thompson and C. Zhou, *JACS,* 2005, **127**, 12484-12485.

122 A. Ambrosi, F. Airo and A. Merkoci, *Anal. Chem.,* 2010, **82**, 1151-1156.

123 J. Li, H. Gaoa, Z. Chena, X. Wei and C. F. Yang, *Anal. Chim. Acta,* 2010, **665**, 98-104.

124 J. W. Chung, K. Lee, C. Nikirk, C. M. Nelson and R. D. Priestley, *Small,* 2012, **8**, 1693-1700.

125 H. Dong, W. Gao, F. Yan, H. Ji and H. Ju, *Anal. Chem.,* 2010, **82**, 5511-5517.

126 D. Geißler, L. J. Charbonnière, R. F. Ziessel, N. G. Butlin, H. Löhmannsröben and N. Hildebrandt, *Angew. Chem. Int. Ed.,* 2010, **49**, 1396-1401.

127 G. M. Ganea, P. E. Kolic, B. El-Zahab and I. M. Warner, *Anal. Chem.,* 2011, **83**, 2576-2581.

128 C. Lei, Z. Qiao, Y. Fu and Y. Li, *Anal. Methods.,* 2016, **8**, 8079-8083.

129 W. Su, M. Cho, J. Nam, W. Choe and Y. Lee, *Electroanal.,* 2013, **25**, 380-386.

130 H. Zhou, D. Yang, N. P. Ivleva, N. E. Mircescu, R. Niessner and C. Haisch, *Anal. Chem.,* 2014, **86**, 1525-1523.

131 V. Raj, A. N. Vijayan and K. Joseph, *Sens. Bio-Sens. Res.,* 2015, **5**, 33-36

132 S. J. Richards, E. Fullam, G. S. Besrab and Gibson M.I., *J. Mat. Chem. B,* 2014, **2**, 1490-1498.

133 L. Otten, E. Fullamb and M. Gibson, *2016,* 12, **341**, 344.

134 R. Zhang, X. Cai, G. Feng and B. Liu, *Faraday Discuss.,* 2017, **196**, 363-375.

135 Y. Chen, Y. Xianyu, Y. Wang, X. Zhang, R. Cha, J. Sun and X. Jiang, *ACS Nano,* 2015, **9**, 3184-3191.

136 Y. Wang and E. Alocilja, *J. Biol. Eng.,* 2015, **9**, 1-7.

137 R. Wang, Y. Xu, T. Zhang and Y. Jiang, *Anal. Methods,* 2015, **7**, 1701-1706.

138 H. Zhang, X. Ma, Y. Liu, N. Duan, S. Wu, Z. Wang and B. Xu, *Biosens. Bioelectron.,* 2015, **74**, 872-877

139 S. Qiu, Z. Lin, Y. Zhou, D. Wang, L. Yuan, Y. Wei, T. Dai, L. Luo and G. Chen, *Analyst,* 2015, **140**, 1149-1154.

140 Y. Zhao, Y. Li, K. Jiang, J. Wang, W. L. White, S. Yang and J. Lu, *Food Control,* 2017, **71**, 110-116

141 Z. Chen, L. Cai, M. Chen, Y. Lin, D. Pang and H. Tang, *Biosens. Bioelecton.*, 2015, **15**, 95-102.

142 J. Chen, Z. Jiangb, J. D. Ackermanb, M. Yazdanib, S. Houb, S. R. Nugena and V. M. Rotello, *Analyst,* 2015, **140**, 4991-4996.

143 L. Kern, J. Spreckels, A. Nist, T. Stiewe, C. Skevaki, B. Greene, M. Mernberger and H. Elsässer, *Cell Tissue Res.,* 2016, **366**, 651-665.

144 R. Anet, *Can. J. Chem.,* 1962, **40**, 1249-1257.

145 R. Hoffman, P. Welis and H. Morrison, *J. Org. Chem.,* 1971, **36**, 1971.

146 K. Belfield, M. V. Bondar, Y. Liu and O. Przhonska, *J. Phys. Org. Chem.,* 2003, **16**, 69-78.

147 F. Lewis and S. V. Barancyk, *JACS,* 1989, **111**, 8653-8661.

148 S. R. Trenor, A. R. Shultz, B. J. Love and T. E. Long, *Chem. Rev.,* 2004, **104**, 3059-3078.

149 N. Yonezawa, T. Yoshida and M. Hasegawa, *J. Chem. Soc., Perkin Transaction 1,* 1983, 1083-1086.

150 V. V. Khutoryanskiy, *Nat. Mater.,* 2015, **14**.

151 B. J. Aungst, *AAPS Journal,* 2011, **14**, 10-18.

152 Y. S. Youn, S. Y. Chae, S. Lee, M. J. Kwon, H. J. Shin and K. C. Lee, *Eur. J. Pharma. Biopharm.,* 2008, **68**, 667-675

153 B. F. Choonara, Y. E. Choonara, P. Kumar, D. Bijukumar, L. C. du Toit and V. Pillay, *Biotechnol. Adv.,* 2014, **32**, 1269-1282

154 J. F. Liang and V. C. Yang, *Biochem. Biophys. Res. Commun.,* 2005, **335**, 734-738

155 S. Lee, S. Y. You, Y. Byun and K. C. Lee, *Diabetologia,* 2006, **49**, 1608-1611.

156 S. Y. Chae, Y. G. Chun, S. Lee, C. Jin, E. S. Lee, K. C. Lee and Y. S. Youn, *Journal of Pharm. Sci.*, 2009, **98**, 1556-1567.

157 M. Doyle and J. M. Egan, *Pharmacol. Ther.,* 2007, **113**, 546-593.

158 M. Teng, M. Johnson, J. Holst and J. Lau, *Bioorg. Med. Chem. Lett.,* 2007, **17**, 5472-5478

159 Y. Li, W. Xu, L. Tang, M. Gong and J. Zhang, *Peptides,* 2011, **32**, 1408-1414

160 D. Malkov, R. Angelo, H. Z. Wang, E. Flanders, H. Tang and I. Gomez-Orella, *Curr. Drug Deli.,,* 2005, **2**, 191-197.

161 T. W. Leonard, J. Lynch, M. J. McKenna and D. J. Brayden, *Expert Opin. Drug Deliv.,* 2006, **3**, 685-692.

162 O. C. Farokhzad and R. Langer, *ACS nano,* 2009, **3**, 16-20.

163 W. Xu, P. Ling and T. Zhang, *J. Drug Deliv.,* 2013, .

164 G. Xu, C. Wang and P. Yao, *Food Hydrocolloids,* 2017, **71**, 108-117.

165 E. Blanco, H. Shen and M. Ferrari, *Nat. Biotechnol.,* 2015, **33**, 941-951.

166 K. Tahara, T. Sakai, H. Yamamoto, H. Takeuchi, N. Hirashima and Y., *J. Pahr.,* 2009, **382**, 198-204.

167 C. Schmidt, E. C. Collnot, C. Bojarski, M. Schumann, J. D. Schulzke, M. O. Khan and A. Stallmach, *Gastroenterology,* 2010, **138**.

168 J. Baek and C. Cho, *Eur. J. Pharm. Biopharm.,* 2017, **117**, 132-140

169 D. Bhadra, S. Bhadra, S. Jain and N. K. Jain, *Int. J. Pharm.,* 2003, **257**, 111-124

170 L. Ould-Ouali, M. Noppe, X. Langlois, B. Willems, P. Te Riele, P. Timmerman, M. E. Brewster, A. Ariën and V. Préat, *J. Control. Release,* 2005, **102**, 657-668

171 J. M. Koziara, T. R. Whisman, M. T. Tseng and R. J. Mumper, *J. Control. Release,* 2006, **112**, 312-319

172 C. Fonseca, S. Simões and R. Gaspar, *J. Control. Release,* 2002, **83**, 273-286

173 J. E. Kipp, *Int. J. Pharm.,* 2004, **284**, 109-122

174 M. Dawson, E. Krauland, D. Wirtz and J. Hanes, *Biotechnology Progress,* 2004, **20**, 851-857.

175 N. Reuel, A. Dupont, O. Thouvenin, D. C. Lamb and S. M. Strano, *ACS nano,* 2012, **6**, 5420-5428.

176 H. Jin, D. A. Heller and M. S. Strano, *Nano Lett.,* 2008, **8**, 1577-1585.

177 J. Suh, Y. An, C. B. Tang, C. Dempsey, F. Huang and J. Hanes, *Micros.Res. Tech.,* 2012, **75**, 691-697.

178 D. Peer, J. Karp, S. Hong, O. Farokhzad, R. Margalit and R. Langer, *Nat. Nanotechnol.,* 2007, **2**, 751-760.

179 P. Colombo, F. Sonvico, G. Colombo and R. Bettini, *Pharm. Res.,* 2009, **26**, 601-611.

180 M. Han, Q. Fang, H. Zhan, T. Luo, W. Liang and J. Gao, *J. Pharm. Sci.,* 2009, **98**, 2626-2635

181 X. Wang and Q. Zhang, *Eur. J. Pharm. Sci.,* 2012, **82**, 219-229

182 R. K. Kankala, Y. Kuthati, H. Sie, H. Shih, S. Lue, S. Kankala, C. Jeng, J. Deng, C. Weng, C. Liu and C. Lee, *J. Colloid Interf. Sci.,* 2015, **458**, 217-228.

183 Y. Lin, C. Chang, Y. Wu, Y. Hsu, S. Chiou and Y. Chen, *Biomaterials,* 2009, **30**, 3332-3342.

184 M. J. Dew, P. J. Hughes, M. G. Lee, B. K. Evans and J. Rhodes, *Br. J. Clin. Pharmacol,* 1982, **14**, 405-408.

185 A. Makhlof, Y. Tozuka and H. Takeuchi, *Eur. J. Pharm. Sci.,* 2009, **72**, 1-8.

186 L. Han, Y. Zhao, L. Yin, R. Li, Y. Liang, H. Huang, S. Pan, C. Wu and M. Feng, *AAPS PharmSciTech,* 2012, **13**, 836-845.

187 J. Raiman, S. Törmälehto, K. Yritys, H. E. Junginger and J. Mönkkönen, *Int. J. Pharm.,* 2003, **261**, 129-136.

188 A. Bernkop-Schnürch, C. E. Kast and D. Guggi, *J. Control Release,* 2003, **93**, 95-103.

189 J. M. Smith, M. Dornish and E. J. Wood, *Biomaterials,* 2005, **26**, 3269-3276.

190 M. Torres-Lugo, M. García, R. Record and N. A. Peppas, *J. Control Release,* 2002, **80**, 197-205.

191 A. Weissenböck, M. Wirth and F. Gabor, *J. Control Release,* 2004, **99**, 383-392.

192 X. Wang, R. Koller, M. Wirth and F. Gabor, *Sci. Pharm.,* 2014, **82**, 193-205.

193 F. Gabor, E. Bogner, A. Weissenboeck and M. Wirth, *Adv. Drug Deliv. Rev.,* 2004, **56**, 459-480.

194 C. A. Hart, R. M. Batt and Saunders, J.R., Getty, B., *Scand. J. Gastroentero.,* 1988, **23**, 1153-1159.

195 B. Carreno-Gómez, J. F. Woodley and A. T. Florence, *Int. J. Pharm.,* 1999, **183**, 7-11.

196 G. J. Russel-Jones, *Crit. Rev. Ther. Drug,* 1998, **15**, 557-586.

197 G. J. Russell-Jones, L. Arthur and H. Walker, *Int. J. Pharm.,* 1999, **179**, 247-255.

198 S. Li, W. G. Mallet and F. M. Brodskt, in *Endocytosis*, ed. nonymous, M. Marsh, Oxford University Press, 2001, p. 1-25.

199 Y. Dong and S. Feng, *Biomaterials,* 2005, **26**, 6068-6076.

200 S. Hariharan, V. Bhardwaj, I. Bala, J. Sitterberg, U. Bakowsky and N. V. Ravi Kumar, *Pharm. Res.,* 2006, **23**, 184-195.

201 A. Makhlof, M. Werle, Y. Tozuka and H. Takeuchi, *J. Control. Release,* 2011, **149**, 81-88.

202 K. Yoncheva, L. Guembe, M. A. Campanero and J. M. Irache, *Int. J. Pharm.*, 2007, **334** (1-2), 156-165.

203 K. Yoncheva, E. Lizarraga and J. M. Irache, *Eur. J. Pharm Res.,* 2005, **24**, 411-419.

204 M. Song, L. Li, Y. Zhang, K. Chen, H. W. Wang and R. Gong, *React. Funct. Polym.,* 2017, **117**, 10-15.

205 C. Prego, M. Babre, D. Torres and M. J. Alonso, *Pharm. Res.,* 2006, **23**, 549-556.

206 L. Agüero, D. Zaldivar-Silva, L. Peña and M. L. Dias, *Carbohydr. Polym.,* 2017, **168**, 32-43.

207 A. M. Omer, T. M. Tamer, M. A. Hassan, P. Rychter, M. S. Mohy Eldin and N. Koseva, *Int. J. Biol. Macromol.,* 2016, **92**, 362-370.

208 J. Chen, W. L. Yang, G. Li, J. Qian, J. L. Xue, S. K. Fu and D. R. Lu, *World J. Gastroentrol.,* 2004, **10**, 112-116.

209 M. Garcia-Fuentes, D. Torres and M. J. Alonso, *Int. J. Pharm.,* 2005, **296**, 122-132.

210 R. Coco, L. Plapied, V. Pourcelle, C. Jérôme, D. J. Brayden, Y. Schneider and V. Préat, *Int. J. Pharm.,* 2013, **440**, 3-12.

211 C. Prego, D. Torres, E. Fernandez-Megia, R. Novoa-Carballal, E. Quiñóá and M. J. Alonso, *J. Control. Release,* 2006, **111**, 299-308.

212 W. Zauner, N. A. Farrow and A. M. R. Haines, *J. Control. Release,* 2001, **71**, 39-51.

213 T. Jung, W. Kamm, A. Breitenbach, E. Kaiserling, J. X. Xiao and T. Kissel, *Eur. J. Pharm. Sci.,* 2000, **50**, 147-160.

214 A. d. Rieux, E. G. E. Ragnarsson, E. Gullberg, V. Préat, Y. Schneider and P. Artursson, *Eur. J. Pharm. Sci.,* 2005, **25**, 455-465.

215 K. Yin Win and S. Feng, *Biomaterials,* 2005, **26**, 2713-2722.

216 L. Tang, N. Gabrielson, F. Uckun, M. Fan and J. Cheng, *Molec. Pharm.,* 2013, **10**, 883-892.

217 F. Szoka and D. Papahadjopulos, *Proc. Natl. Acad. Sci. U.S.A.,* 1978, **75**, 4194-4198.

218 I. V. Zhigaltsev, N. Belliveau, I. Hafez, A. K. Leung, J. Huft, C. Hansen and P. R. Cullis, *Langmuir,* 2012, **28**, 3633-3640.

219 G. Gregoriadis, *FEBS Letter,* 1973, **36**, 292-296.

220 Z. Vujaskovic, D. W. Kim, E. Jones, L. Lan, L. McCall, M. W. Dewhirst, O. Craciunescu, P. Stauffer, V. Liotcheva, A. Betof and K. Blackwell, *Int. J. Hypertherm.,* 2010, **26**, 514-521.

221 T. M. Allen and L. G. Cleland, *BBA - Biomembranes,* 1980, **597**, 418-426.

222 P. R. Cullis, *FEBS Letter,* 1976, **70**, 223-228.

223 X. Guo and F. C. Szoka, *Bioconjugate Chem.,* 2001, **12**, 291-300.

224 D. C. Drummond, O. C. Noble, Z. Guo, K. Hong, J. W. Park and D. B. Kirpotin, *Cancer Res.,* 2006, **66**, 3271-3277.

225 M. J. Johnston, K. Edwards, G. Karlsson and P. R. Cullis, *J. Lipo. Res.,* 2008, **18**, 145-157.

226 I. V. Zhigaltsev, G. Winters, M. Srinivasulu, J. Crawford, M. Wong, L. Amankwa, M. A. Ciufolini, P. R. Cullis and N. Maurer, *J. Control. Release,* 2010, **144**, 332-340.

227 T. M. Allen and P. R. Cullis, *Adv. Drug Deliv. Rev.,* 2013, **65**, 36-48.

228 W. Situ, X. Song, S. Luo and Y. Liang, *Food Chem.,* 2017, **228**, 219-225.

229 B. Clares, A. C. Calpena, A. Parra, G. Abrego, H. Alvarado, J. F. Fangueiro and E. B. Souto, *Int. J. Pharm.,* 2014, **473**, 591-598.

230 N. P. Aditya, A. S. Macedo, S. Doktorovova, E. B. Souto, S. Kim, P. Chang and S. Ko, *LWT - Food Sci. Technol.,* 2014, **59**, 115-121.

231 G. Yoon, J. W. Park and I. S. Yoon, *Int. J. Pharm. Invest.,* 2013, **43**, 353-362.

232 M. K. Rawat, A. Jain and S. Singh, *J. Pharm. Sci.,* 2011, **100**, 2366-2378.

233 N. Naseri, H. Valizadeh and P. Zakeri-Milani, *Adv. Pharm. Bull.,* 2015, **5**, 305-313.

234 C. A. Das S, *AAPS PharmSciTech,* 2011, **12**, 62-76.

235 Y. S. Elnaggar, M. A. El Massik and O. Y. Abdallah, *Int. J. Nanomed.,* 2011, **6**, 3195-3205.

236 S. Galindo-Rodriguez, E. Allemann, H. Fessi and E. Doelker, *Crit. Rev. Thera.Drug,* 2005, **22**, 419-464.

237 M. Tobio, A. Sanchez, A. Vila, I. Soriano, C. Evora, J. L. Vila-Jato and M. J. Alonso, *Colloids Surf. B,* 2000, **18**, 315-323.

238 Y. Y. Wang, S. K. Lai, J. S. Suk, A. Pace, R. Cone and J. Hanes, *Angew. Chem. Int. Ed.,* 2008, **47**, 9726-9729.

239 M. J. Dar, H. Ali, A. Khan and M. Khan J. *Drug Targeting,* 2017, **25**, 582-596.

240 C. B. Woitiski, R. A. Carvalho, A. J. Ribeiro, R. J. Neufeld and F. Veiga, *BioDrugs,* 2008, **22**, 223-237.

241 F. Alexis, E. Pridgen, L. Molnar K. and O. C. Farokhzad, *Mol. Pharm.,* 2008, **5**, 505-515.

242 S. Wang, R. Su, S. Nie, M. Sun, J. Zhang, D. Wu and N. Moustaid-Moussa, *J. Nutr. Biochem.,* 2014, **25**, 363-376.

243 R. P. Bagwe, C. Yang, L. Hilliard R. and W. Tan, *Langmuir,* 2004, **20**, 8336-8342.

244 Y. Jin, S. Lohstreter, D. T. Pierce, J. Parisien, M. Wu and C. Hall, *Chem. Mater.,* 2008, **20**, 4411-4419.

245 J. Lu, Z. Li, J. I. Zink and F. Tamanoi, *Nanomedicine: NBM,* 2012, **8**, 212-220.

246 X. He, H. Nie, K. Wang, W. Tan, X. Wu and P. Zhang, *Anal. Chem.,* 2008, **80**, 9597-9603.

247 D. Napierska, L. C. J. Thomassen, V. Rabolli, D. Lison, L. Gonzalez and M. Kirsch-Volders, *Small,* 2009, **5**, 846-853.

248 T. Liu, L. Li, X. Teng, X. Huang, H. Liu, D. Chen, J. Ren, J. He and F. Tang, *Biomaterials,* 2011, **32**, 1657-1668.

249 M. Mahkam, *Cur. Drug Deliv.,* 2011, **9**, 607-611.

250 M. Mohammadpour, M. Jabbarvand, H. Hashemi and E. Delrish, *Adv. Biomed. Res.,* 2015, **4**.

251 T. López, G. Bata-García, D. Esquivel, R. Ortiz-IslasGonzalez, J. Ascencio, P. Quintana, G. Oskam, F. J. ÁlvarezCervera, F. J. Heredia-López4 and J. L. Góngora-Alfaro, *Int. J. Nanomed.,* 2011, **6**, 19-31.

252 J. Peng, X. He, K. Wang, W. Tan, H. Li, X. Xing and Y. Wang, *Nanomedicine: NBM,* 2006, **2**, 113-120.

253 T. Y. Ohulchanskyy, I. Roy, Y. Chen, E. Bergey, R. Pandey, A. Oseroff and P. Prasad, *Nano Lett.,* 2007, **7**, 2835-2842.

254 I. Roy, Y. Ohulchanskyy, H. Pudavar, E. Bergey, A. Oseroff, J. Morgan, T. Dougherty and P. Pras, *JACS,* 2003, **125**, 7860-7865.

255 T. Andreani, A. L. R. d. Souza, C. P. Kiill, E. N. Lorenzón, J. F. Fangueiro, A. C. Calpena, M. V. Chaud, M. L. Garcia, M. P. D. Gremião, A. M. Silva and E. B. Souto, *Int. J. Pharm.,* 2014, **473**, 627-635.

256 T. Andreani, C. P. Kiill, A. L. R. d. Souza, J. F. Fangueiro, L. Fernandes, S. Doktorovová, D. L. Santos, M. L. Garcia, M. P. D. Gremião, E. B. Souto and A. M. Silva, *Colloids Surf. B,* 2014, **123**, 916-923.

257 S. Bale, S. Kwon, D. Shah, A. Banerjee, J. Dordick and R. Kane, *ACS nano,* 2010, **4**, 1493-1500.

258 J. Lofgrenn and G. Ozin, *Chem. Soc.y Rev.,* 2014, **43**, 911-933.

259 W. Stober and A. Fink, *J. Colloid. Interf. Sci.,* 1968, **26**, 62-69.

260 J. Wang, A. Sugawara-Narutaki, M. Fukao, T. Yokoi, A. Shimojima and T. Okubo, *ACS Appl. Mater. Interfaces,* 2011, **3**, 1538-1544.

261 F. J. Arriagada and K. Osseo-Asare, *J. Colloid. Interf. Sci.,* 1999, **211**, 210-220.

262 C. Moore, H. Monton, R. O'Kennedy, D. E. Williams, C. Nogues, C. Crean and V. Gubala, *J. Mater. Chem. B,* 2015, **3**, 2043-2055.

263 R. Bagwe, L. Hilliard and W. Tan, *Langmuir,* 2006, **22**, 4357-4362.

264 G. Giovannini, F. Kunc, C. Piras, O. Stranik, A. Edwards, A. Hall and V. Gubala, *RSC Advance,* 2017, **7**, 19942-19933.

265 C. Moore, G. Giovannini, F. Kunc, A. Hall and V. Gubala, *J. Mater. Chem. B,* 2017, **5**, 5564-5572.

266 S. Park, Y. Kim and S. Park, *Langmuir,* 2008, **24**, 12134-12137.

267 T. Zhang, J. Ge, Y. Hu, Q. Zhang, S. Aloni and Y. Yin, *Angew. Chem. Int. Ed.,* 2008, **47**, 5806-5811.

268 H. C. Zeng, *Curr. Nanosci.,* 2007, **3**, 177-181.

269 H. Yamada, C. Urata, Y. Aoyama, S. Osada, Y. Yamauchi and K. Kuroda, *Chem. Mater.,* 2012, **24**, 1462-1471.

270 A. Abouelmagd, B. Sun, A. Chang, J. Ku and Y. Yeo, *Molec. Pharm.,* 2015, **12**, 997-1003.

271 C. Vasti, D. Bedoya, R. Rojas and C. Giacomelli, *J. Mater. Chem. B,* 2016, **4**, 2008-2016.

272 A. Albanese and C. W. Chan, *ACS nano,* 2011, **5**, 5478-5489.

273 M. D. Haw, *J Phys Cond. Mater.,* 2002, **14**, 7769-7779.

274 https://goldbook.iupac.org/pages/about.html.

275 S. V. Sokolov, K. Tschulik, C. Batchelor-McAuley, K. Jurkschat and R. G. Compton, *Anal. Chem.,* 2015, **87**, 10033-10039.

276 http://www.colloid.ch/index.php?name=dlvo.

277 S. N. Olsen, K. B. Andersen, T. W. Randolph, J. F. Carpenter and P. Westh, *Biochim. Biophys. Acta,* 2009, 1058-1065.

278 R. J. Stol and P. L. De Bruyn, *J. Colloid Interface. Sci.,* 1980, **75**.

279 M. Iijima, M. Kobayakawa, M. Yamazaki, Y. Ohta and H. Kamiya, *JACS,* 2009, **131**, 16342-16343.

280 R. Roij and M. Dijksrta, *Physic. Rev. E,* 1999, **59**.

281 R. Roij, *J. Phys. Cond. Mater.,* 2000, **12**, A263-A267.

282 D. Chan, P. Linse and S. Petris, *Langmuir,* 2001.

283 *Encyclopedia of Colloid and Interface Science*, Tadros, Tharwat, 2013.

284 J. Park and J. Shumaker-Parry, *JACS,* 2014, **136**, 1907-1921.

285 S. Skoglund, T. Lowe, J. Hedberg, E. Blomberg, O. Wallinder, S. Wold and M. Lundin, *Langmuir,* 2013, **29**, 8882-8891.

286 R. Maccuspie, A. J. Allen and V. Hackley, *Nanotoxicology,* 2011, **5**, 140-156.

287 T. Moore, L. Rodriguez-Lorenzo, V. Hirsch, S. Balog, D. Urban, C. Jud, B. Rothen-Rutishauser, M. Lattuada and A. Petri-Fink, *Chem. Soc. Rev.,* 2015, **44**, 6287-6305.

288 A. Hajdú, E. Illés, E. Tombácz and I. Borbáth, *Colloids Surf. Physicochem. Eng. Aspects,* 2009, **347**, 104-108.

289 Q. Huo, J. Liu, L. Wang, Y. Jiang, T. Lambert and E. Fang, *JACS,* 2006, **128**, 6447-6453.

290 H. Kamiya and M. Iijima, *Sci. Technol. Adv. Mater.,* 2010, **11**.

291 L. Wang, L. Wu, S. Lu, L. Chang, I. Teng, C. Yang and J. Ho, *ACS nano,* 2010, **4**, 4371-4379.

292 A. Ruiz, Y. Hernaandez, C. Cabal, E. Gonzalez, S. Veintemillas-Verdaguer, E. Martınez and M. P. Morales, *Nanoscale,* 2013.

293 M. S. Grunér, U. Kauscher, M. B. Linder and M. B. Monopoli, *J. Proteomics,* 2016, **137**, 52-58.

294 K. Herynková, E. Podkorytov, M. Šlechta and O. Cibulka, *Physica Status Solidi C,* 2016, **13**, 142-145.

295 R. Nooney, A. White, C. O'Mahony, C. O'Connell, S. Kelleher, S. Daniels and C. McDonagh, *J. Colloid Interface Sci.,* 2015, **456**, 50-58.

296 C. Oliviera, F. Veiga, C. Varela, F. Roleira, E. Taveres, I. Silveira and A. Ribeiro, *Colloids and Surfaces B: Biointerfaces,* 2016.

297 C. Fang, N. Bhattarai, C. Sun and M. Zhang, *Small,* 2009, **5**, 1637-1641.

298 L. Wang, L. Wu, S. Lu, L. Chang, T. Teng, C. Yang and A. Annie Ho, *ACS nano,* 2010, **4**, 4371-4379.

299 C. J. Moore, H. Mont´on, R. O'Kennedy, D. E. Williams, C. Nogu´es, C. Crean and V. Gubala, *J. Mater. Chem. B,* 2015, **3**, 2043-2055.

300 D. Ibegbu, A. Boussahel, S. C. Cragg, J. Tsibouklis and E. Barbu, *Int. J. Polym. Mater. Polym. Biomater.,* 2017, **66**, 265-279.

301 K. Hurley, Y. Lin, J. Zhang, S. Egger and C. L. Haynes, *Chem. Mater.,* 2013, **25**, 1968-1978.

302 Y. Lin, N. Abadeer, K. Hurley and C. Haynes, *JACS,* 2011, **133**, 20444-20457.

303 Y. Lin, N. Abadeer and C. Haynes, *Chem. Commun.,* 2011, **47**, 532-534.

304 J. A. Rupley and G. Careri, *Adv. Protein Chem.,* 1991, **41**, 37-172.

305 H. G. Nagendra, N. Sukumar and M. Vijayan, *Proteins,* 1998, **32**, 229-240.

306 K. Kho and K. Hadinoto, *Powder Technol.,* 2010, **198**, 354-363.

307 M. A. Ali and A. Lamprecht, *Int. J. Pharm.,* 2017, **516**, 170-177.

308 M. Lundqvlst, J. Stlgler, G. Ella, I. Lynch, T. Cedervell and K. Dawson, *Proc Natl Acad Sci U S A,* 2008, **105**, 14265-14270.

309 R. H. Muller, D. Ruhl, M. Luck and B. -. Paulke, *Pharm. Res.,* 1997, **14**, 18-24.

310 V. Hirsch, C. Dinner, L. Rodriguez, C. A. Monnier, B. Rothen, S. Balgo and A. Petri, *Nanoscale,* 2014, **6**, 7325.

311 A. Nel, L. Mädler, D. Velegol, T. Xia, E. V. Hoek, P. somasundaran, F. Klaessig, V. Castranova and M. Thompson, *Nat. Mater. Rev.,* 2009, **8**, 543-557.

312 C. Graf, Q. Gao, I. Schutz, C. Noufele, W. Ruan, U. Posselt, E. Korotianskiy, D. Nordmeyer, F. Rancan, S. Hadam, A. Vogt, J. Lademann, V. Haucke and E. Ruhl, *Langmuir,* 2012, **28**, 7598-7613.

313 C. Wilhelm, F. Gazeau, J. Roger, J. Pons and J. -. Bacri, *Langmuir,* 2002, **18**, 8148-8155.

314 A. Asati, S. Santra, C. Kaittanis and J. M. Perez, *ACS nano,* 2010, **4**, 5321-5331.

315 K. Kim, H. Kim, C. Lee, T. Kim, J. Lee, J. Jeong, S. Peak and J. Oh, *Int. J. Nanomed.,* 2014, **9**, 29-40.

316 M. Lundquvist, I. Sethson and B. Jonsson, *Langmuir,* 2004, **20**, 10647.

317 A. Salvati, A. S. Pitek, P. Monopoli, K. Prapainop, F. Baldelli Bomelli, D. R. Hirstov, A. Kelly C., P.M., E. Mahon and K. A. Dawson, *Nat. Nanotechnol.,* 2013, **8**, 137-143.

318 F. Turci, E. Ghibaudi, M. Colonna, B. Boscolo, I. Fenoglio and B. Fubini, *Langmuir,* 2010, **20**, 8336-8346.

319 B. Ratner and S. Bryant, *Annual Rev. Biomed. Eng.,* 2004, **6**, 41-75.

320 P. Tongwa and B. Baojun, *J. Petrol. Explor. Prod. Technol.,* 2015, **5**, 201-210.

321 M. Bikram, A. M. Gobin, R. E. Whitmire and J. L. West, *J. Controlled Release,* 2007, **123**, 219-227.

322 W. Loyens, P. Jannasch and F. H. J. Maurer, *Polymer,* 2005, **46**, 915-928.

323 N. Negrete-Herrera, J. Putaux and E. Bourgeat-Lami, *Prog. Solid State Chem.,* 2006, **34**, 121-137.

324 E. A. Stefanescu, P. J. Schexnailder, A. Dundigalla, I. I. Negulescu and G. Schmidt, *Polymer,* 2006, **47**, 7339-7348.

325 C. Silverira, L. M. Apolinario, W. Favaro, A. J. Paula and N. Duran, *ACS Biomater. Sci. Eng.,* 2016, **2**.

326 S. Nie, W. Hsiao, W. Pan and Z. Yang, *Int. J. Nanomed.,* 2011, **6**, 151-166.

327 M. Zhou, A. M. Smith, A. K. Das, N. W. Hodson, R. F. Collins, R. V. Ulijn and J. E. Gough, *Biomaterials,* 2009, **30**, 2523-2530.

328 L. Birchall, S. Roy, V. Jayawarna, M. Hughes, E. Irvine, G. Okorogheye, N. Saudi, E. De Santis, T. Tuttle, A. Edwards and R. Ulijn, *Chem. Sci.,* 2011, **2**, 1349.

329 M. V. S. Varma, A. M. Kaushal and A. Garg, *Am. J. Drug Deliv.,* 2004, **2**, 43-57.

330 K. Yoncheva, B. Tzankov, M. Popova, V. Petrova and N. Lambov, *J. Dispers. Sci. Technol.,* 2016, **37**, 113-118.

331 J. Kowalczuk, S. Jarosz and J. Tritt-Go, *Tetrahedron,* 2009, **65**, 9801-9806.

332 L. W. S. Cheong, P. W. S. Heng and L. F. Wong, *Pharm. Res.,* 1992, **9**, 1510.

333 M. Bauer, C. Lautenschlaeger, K. Kempe, L. Tauhardt, U. S. Schubert and D. Fischer, *Macromol. Biosci.,* 2012, **12**, 986-998.

334 F. Schlenk, S. Werner, M. Rabel, F. Jacobs, C. Bergmann, J. Clement and D. Fischer, *Arch. Toxicol,* 2017, , 1-16.

335 V. Hamburger and H. L. Hamilton, *J. Morphol,* 1951, **88**.

336 J. Gross, S. Sayle, A. R. Karow, U. Bakowsky and P. Garidel, Eur. J. Pharm Biopharm., 2016, **104**, 30-41.

337 V. Filipe, A. Hawe and W. Jiskoot, *Pharm. Res.,* 2010, **27**, 796-810.

338 C. Cascio, D. Gilliland, F. Rossi, L. Calzolai and C. Contado, *Anal. Chem.,* 2014, **86**, 12143-12151.

339 B. Halamoda-Kenzaoui, M. Ceridono, P. Colpo, A. Valsesia, P. Urban, I. Ojea-Jimenez, S. Gioria, D. Gilliland, F. Rossi and A. Kinsner-Ovaskainen, *PLOS,* 2015, 1-18.

340 Y. Lin, N. Abadeer and C. Haynes, *Chem. Commun.,* 2011, **47**, 532-534.

341 E. J. W. Verwey, *J. Phys. Chem.,* 1947, **51**, 631-636.

342 A. Sikora, Shard A G and Minelli Caterina, *Langmuir,* 2016, **21**, 2224.

343 S. Wang, T. Xu, Y. Yang and Z. Shao, *ACS Appl. Mater. Interfaces,* 2015, **7**, 21254-21262.

344 K. Emoto, J. M. Van Alstine and J. M. Harris, *Langmuir,* 1998, **14**, 2722-2729.

345 V. Balan, A. I. Petrache, I. M. Popa, M. Butnaru, E. Barbu, J. Tsibouklis and L. Verestiuc, *J. Nanopart. Res.,* 2012, **14**, 730.

346 P Sanchez-Moreno and J AMachal, *Biomaterials,* 2015, **61**, 266-278.

347 M. Peng, H. Li, Z. Luo, J. Kong, Y. Wan, L. Zheng, Q. Zhang, H. Niu, A. Vermorken, W. Van de Ven, C. Chen, X. Zhang, F. Li, L. Guob and Y. Cui, *Nanoscale,* 2015, **7**, 11155-11162.

348 C. Tassa, S. Shaw and R. Weissleder, *Acc. Chem. Res.,* 2011, **44**, 842-852.

349 M. Yu, S. Huang, K. Jun-Yu and A. Clyne, *Int. J. Mol. Sci.,* 2012, **13**, 5554-5570.

350 M. Davoren, E. Herzog, A. Casey, B. Cottineau and G. Chambers, *Toxicol. in Vitro,* 2007, **21**, 438-448.

351 N. P. Luepke, *Food Chem. Toxicol,* 1985, **23**, 287-291.

352 A. Brantmer, F. Quehenberger, A. Chakraborty, J. Polligger, S. Sosa and R. Della Loggia, *Altex,* 2002, **19**, 51-56.

353 B. Dunn, *Poultr. Sci.,* 1974, **53**, 409-412.

354 R. Stewart, J. Nelson and D. Wilson, *J. Anat.,* 1990, **172**, 81-87.

355 A. L. Romanoff, *The avian embryo. Structural and functional development*, The Macmillan Co, New York and London, 1960.

APPENDIX

Table of Contents

A2.1 Characterisation of compound d

Figure A-1: ¹H NMR of compound d**¹H NMR** (400 MHz, DMSO-d_6): δ 6.85 (s, 1H), 5.4 (d, ^3J = 4.1 Hz, 1H), 5.14 (dd, ^2J = 5.13, ^3J = 4.1 Hz, 1H), 4.36 (dd, ^2J = 12.13 ^3J = 7.01, Hz, 1H), 4.44 (m, 1H), 4.18 (dd, ^2J = 12.22. ^3J = 3.16, 1H), 2.06 (s, 3H), 2.05 (s, 3H), 2.04 (s, 3H), 2.01 (s, 3H) ppm.
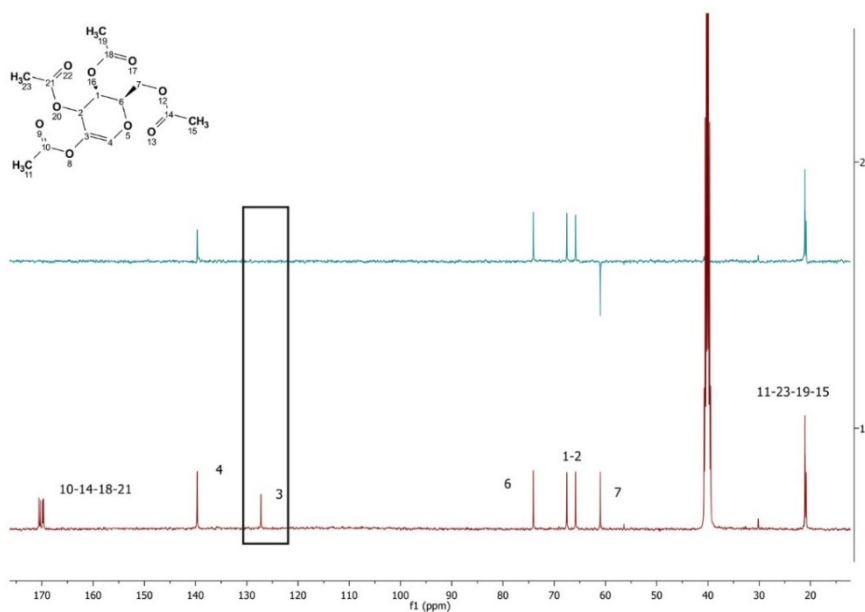
Figure A-2: ¹³C NMR of compound d: **¹³C NMR** (100 MHz, DMSO-d_6): δ 170.54 (C=O), 170.27 (C=O), 169.83 (C=O), 169.67 (C=O), 139.68 (C=C), 127.23 (C=C), 74.06 (C-H), 67.52 (C-H), 65.81 (C-H), 61.00 (CH₂), 21.35 (CH₃), 21.08 (CH₃), 21.06 (CH₃), 21.02 (CH₃), 20.81 (CH₃) ppm.

A2.2 Auto-hydrolysis of 'on-off' fluorescent substrates

The auto-hydrolysis, which leads to an increase of fluorescence in absence of either enzymes or bacteria of each substrate, was evaluated in water and in broth. As shown in *Figure A-3* and *A-4* the auto-hydrolysis in water is almost negligible for β-4-AAUG and α-4-MUD while it increases for β-4-MUD.
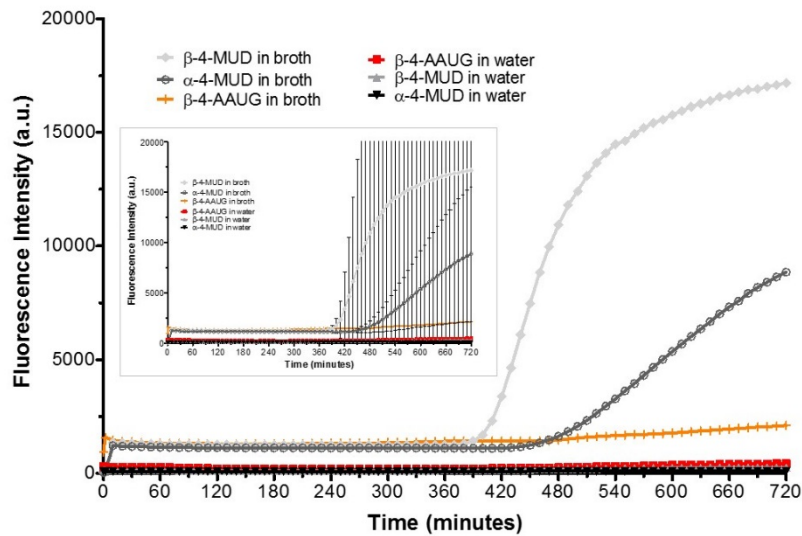
Figure A-3: Auto-hydrolysis of substrates in water and LB-broth. When broth was used, the auto-hydrolysis phenomenon was much more evident in particular for β-4-MUD substrates which appear to be quite unstable. As noticeable β-4-AAUG tends to be stable in each environment while in broth α-4-MUD but mainly β-4-MUD suffer of auto-hydrolysis after 6 hours.
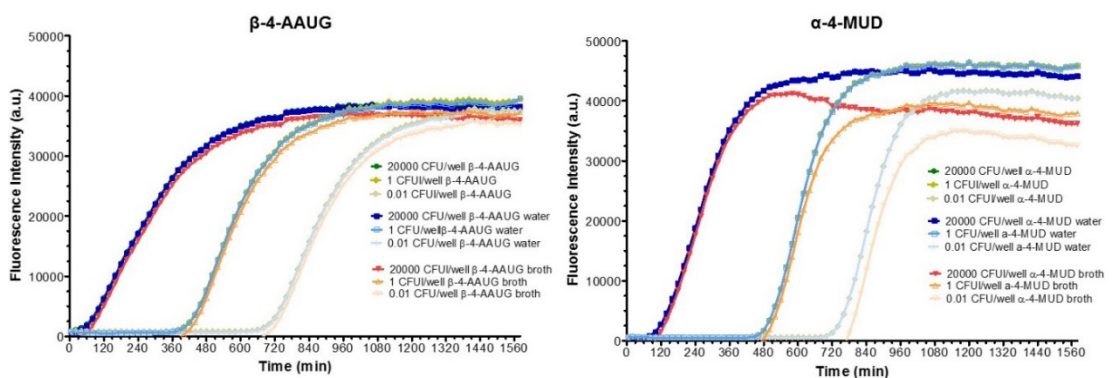
Figure A-4: Fluorescent measurements obtained after normalised with auto-hydrolysis in water (blue grades), in broth (red grades) and not normalised (green grades) when 50 μM of β-AAUG or α-MUD were treated with 20000, 1, 0.01 CFU/mL of *E.coli*. The only case when a considerable difference was observed was in the case of α-4-MUD when normalised with the broth. However, the difference is negligible.

A2.3 Nanoprobe synthesis: first step of functionalisation

After the first step of functionalisation all particles were intensively washes with repeated cycles of centrifugation and re-dispersion in water until no fluorescence signal was measured in the supernatant indicating that all the non-bonded fluorophore was removed (*Figure A-5*).
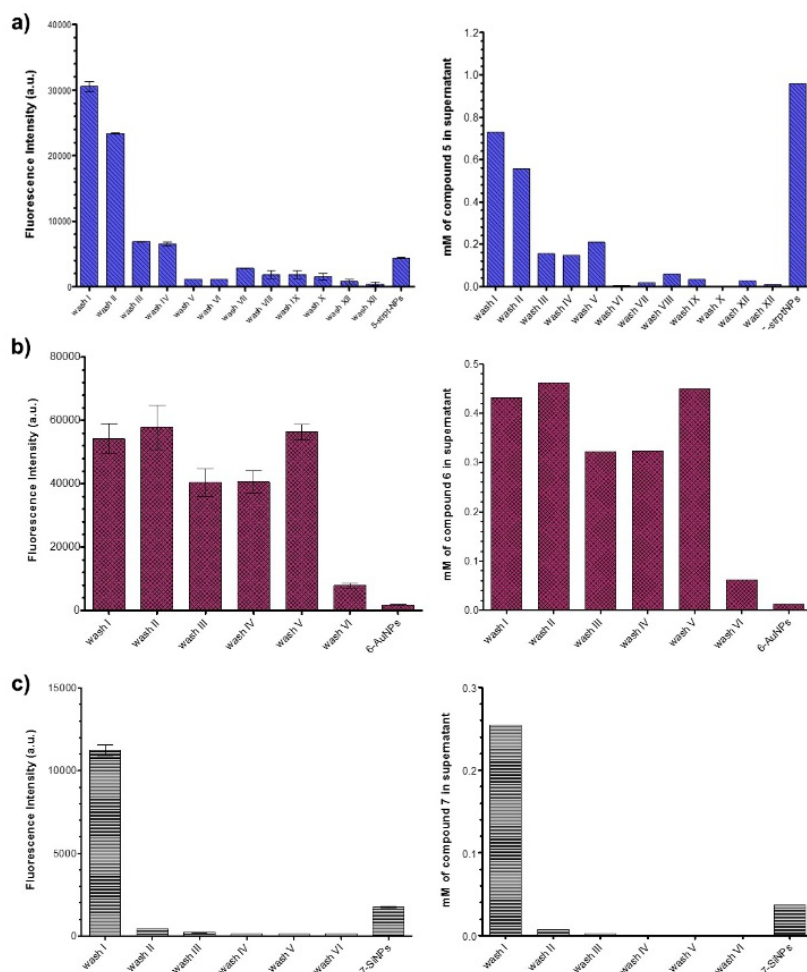
Figure A-5: Work up of the functionalisation for a) 5-strept-NPs b) 6-AuNPs and c) 7-SiNPs respectively. The amount of 4-AAU derivatives (compound 5, 6 and 7 respectively), measured in the supernatants during purification, was quantified from the fluorescent signal measured at $\lambda_{ex}/\lambda_{em}$: 327/460 nm.

A2.4 Nanoprobe synthesis: second step of functionalisation

The quantification of the glucose in the supernatants after the glycosylation step of NPs was accomplished by measuring the absorbance at 340 nm after treatment with a solution of 1.5 mM NAD, 1.0 mM ATP, 1 unit/mL of hexokinase and 1.0 unit/ml of

glucose-6-phosphate dehydrogenase (Glucose Assay Reagent Kit, G3293, Sigma). This mixture allows the production of NADH which is quantified by measuring the absorption at 340 nm. In particular, the enzyme hexokinase transfers a phosphate group from ATP to the glucose. In presence of NAD and glucose-6-phosphate, a red-ox reaction is induced by glucose-6-phosphate dehydrogenase with formation of NADH which can be quantified by UV/Vis absorbace. Since the stoichiometry of the reaction is 1:1 in each step, the amount of NADH determine is equivalent to the amount of glucose in first place[1].
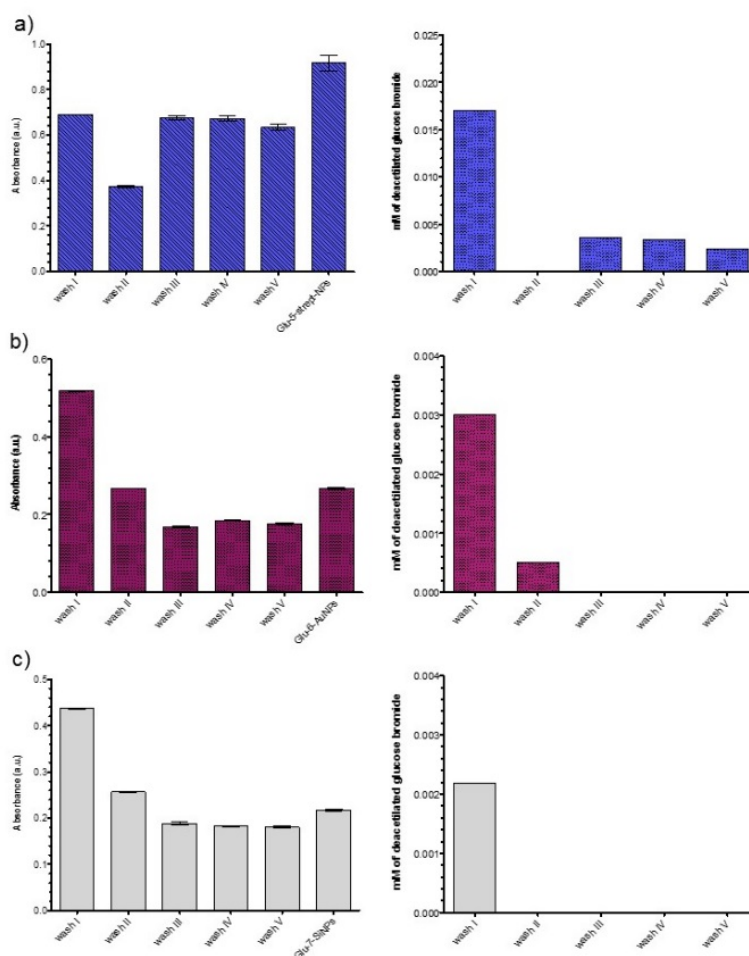
Figure A-6: After the work up of the glycosylation step for Glu-5-strept-NPs and Glu-7-SiNPs, the quantification of unbonded glucose in the supernatant indicated that it was completely removed after the first wash. The quantification of the glucose attached on the particles surface is not trustable since the absorbance of the fluorophore could interfere with this measurement, making the obtained value not reliable.

A2.5 Quantification of functionalisation

Quantification of substrate on the nanoprobe surface following Method 1 and Method 2 are shown in *Table A-1.* The values are expressed both as µmol of substrate per mg of nanoprobe. As expected, appears that Method 1 overestimates the values while Method 2 underestimates the amount of substrate present on the surface. As such, the average of the values obtained with the two methods have been considered to determine the concentration used in the enzymatic and bacterial experiments.

Table A-1: Quantification of the corresponding fluorophores on the surface of each particles by method1 and method2

	Glu-5-strpt-NPs,	Glu-6-AuNPs	Glu-7-SiNPs
Method 1	1.2 µmol/mg	0.12 µmol/mg	0.46 µmol/mg
Method 2	0.73 µmol/mg	0.074 µmol/mg	0.067 µmol/mg
Average	1.965 µmol/mg	0.097 µmol/mg	0.264 µmol/mg

A2.6 Glu-7-SiNP: results of bacterial experiment

The result of the bacterial experiment using **Glu-7-SiNPs** confirmed the negative results achieved in the enzymatic assay. As shown in *Figure A-7* **Glu-7-SiNPs** exhibited no detecting properties due to the unsuccessful functionalisation.
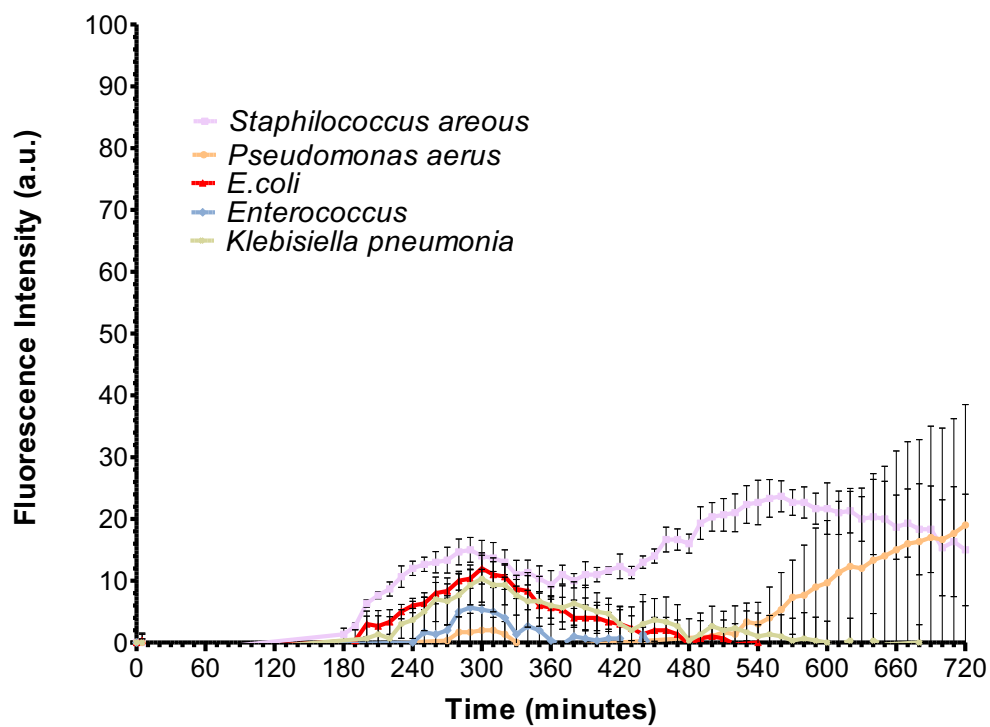
Figure A-7: 75 CFU of each type of bacteria was treated with 50 µM of **Glu-7-SiNPs** (calculated as the substrate on the surface) and incubated at 37°C. Every 10 min the fluorescence signal was measured. Highlighting the scale used in the graph, it can be noticed that an increase in fluorescence is evident only after 3 h and most importantly, the fluorescence measured is negligible.

A2.7 Characterisation of umbelliferone derivatives

A2.7.1 Compound 1
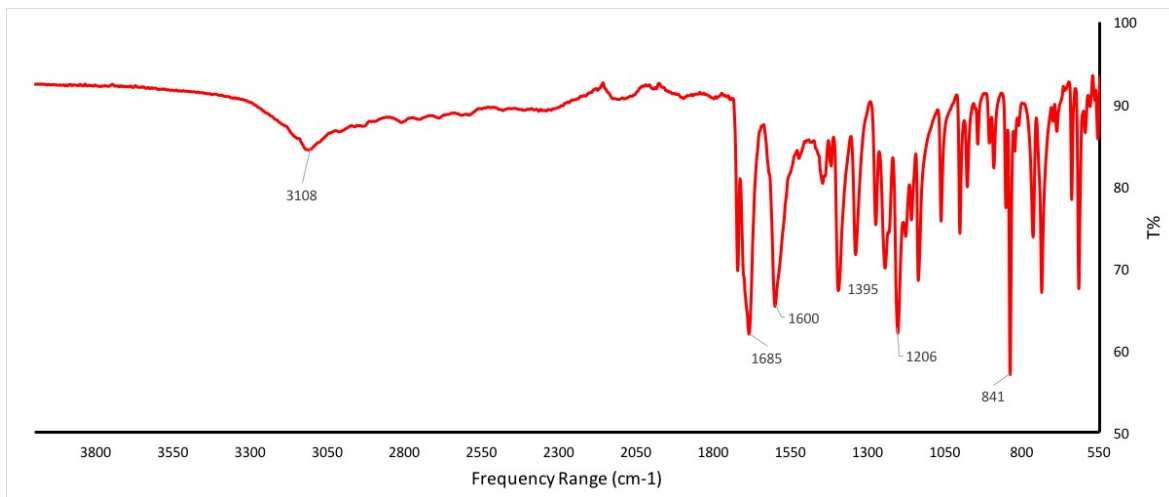
FT-IR **compound 1**. **IR**: 3108, 1684, 1600, 1395, 1206, 841 cm^{-1}.
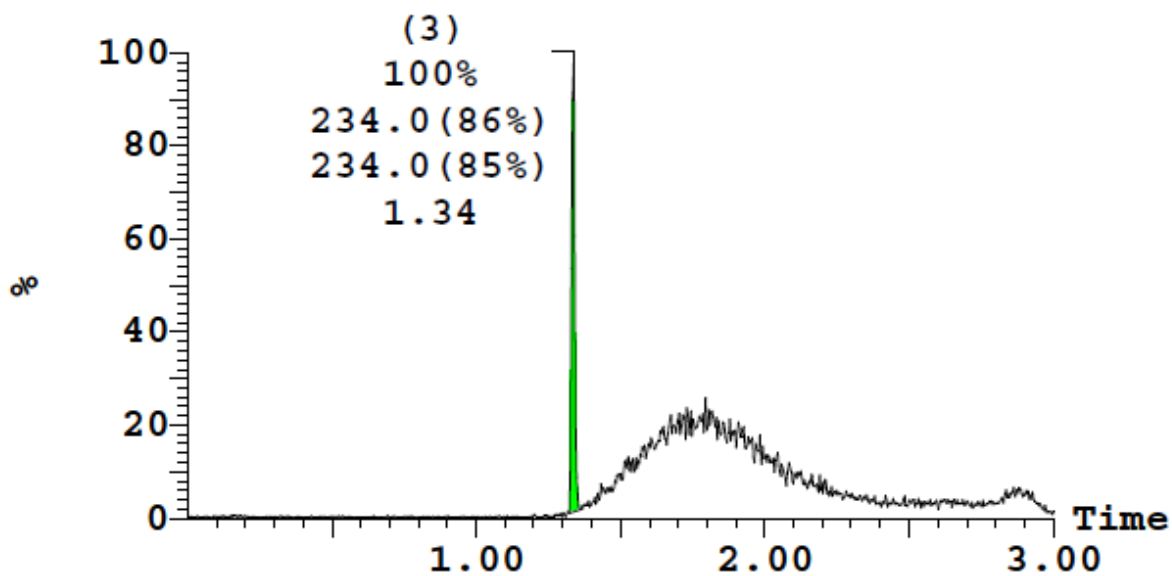
High resolution-MS spectrum of **compound 1.** HR-MS (ESI-TOF): m/z for $C_{12}H_{10}O_5^+$ [M+H]$^+$ calculated 234.18 found 234.0
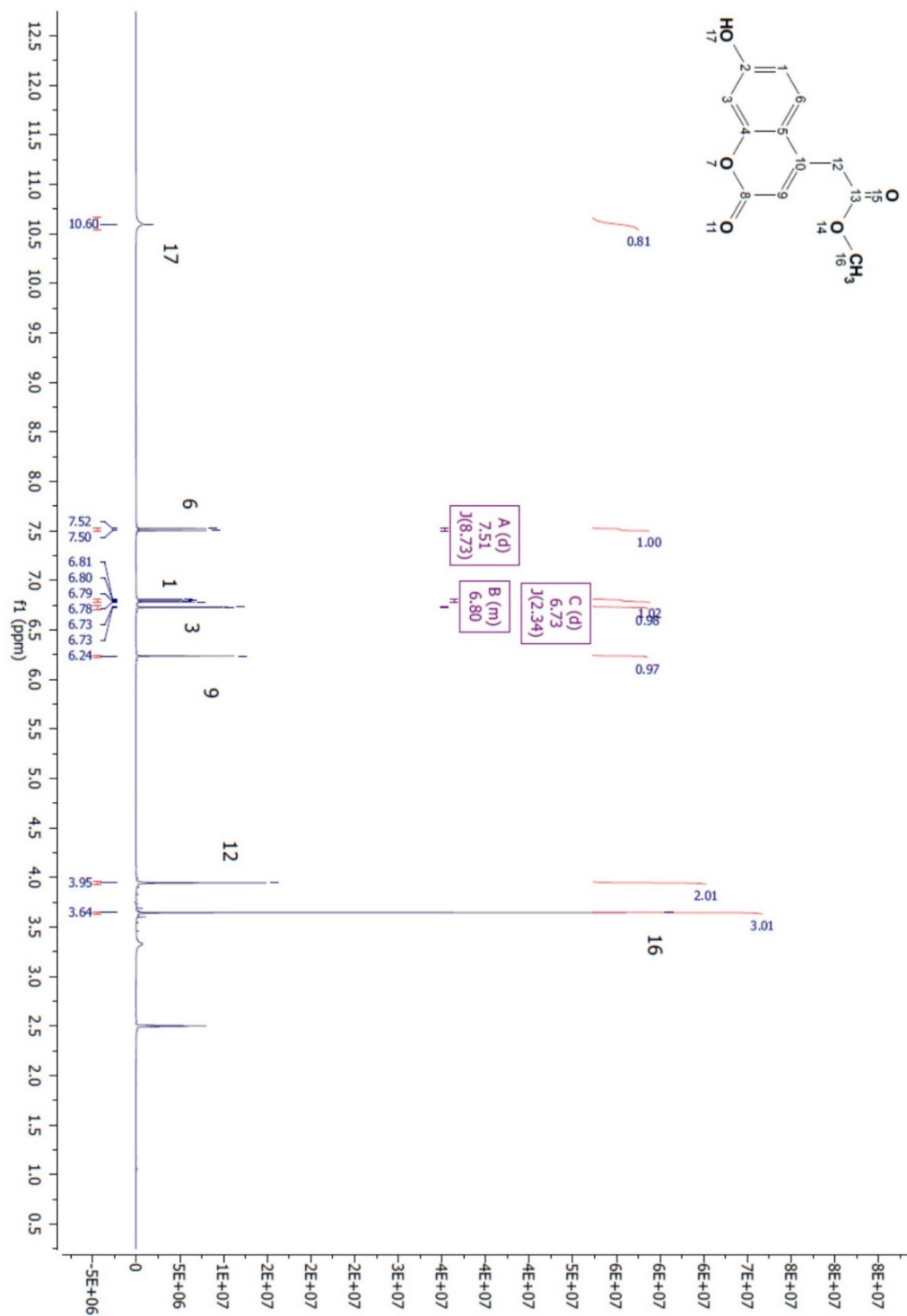
^{1}H-NMR spectrum of **compound 1**: **^{1}H NMR** (400 MHz, DMSO-d_6): δ 3.64 (s, 3H), 3.95 (s, 2H), 6.24 (s, 1H), 6.73 (d, J = 2.3 Hz, 1H), 6.81-6.78 (q, 1H), 7.50 (d, J = 8.7 Hz, 1H), 10.6 (s, 1H) ppm.
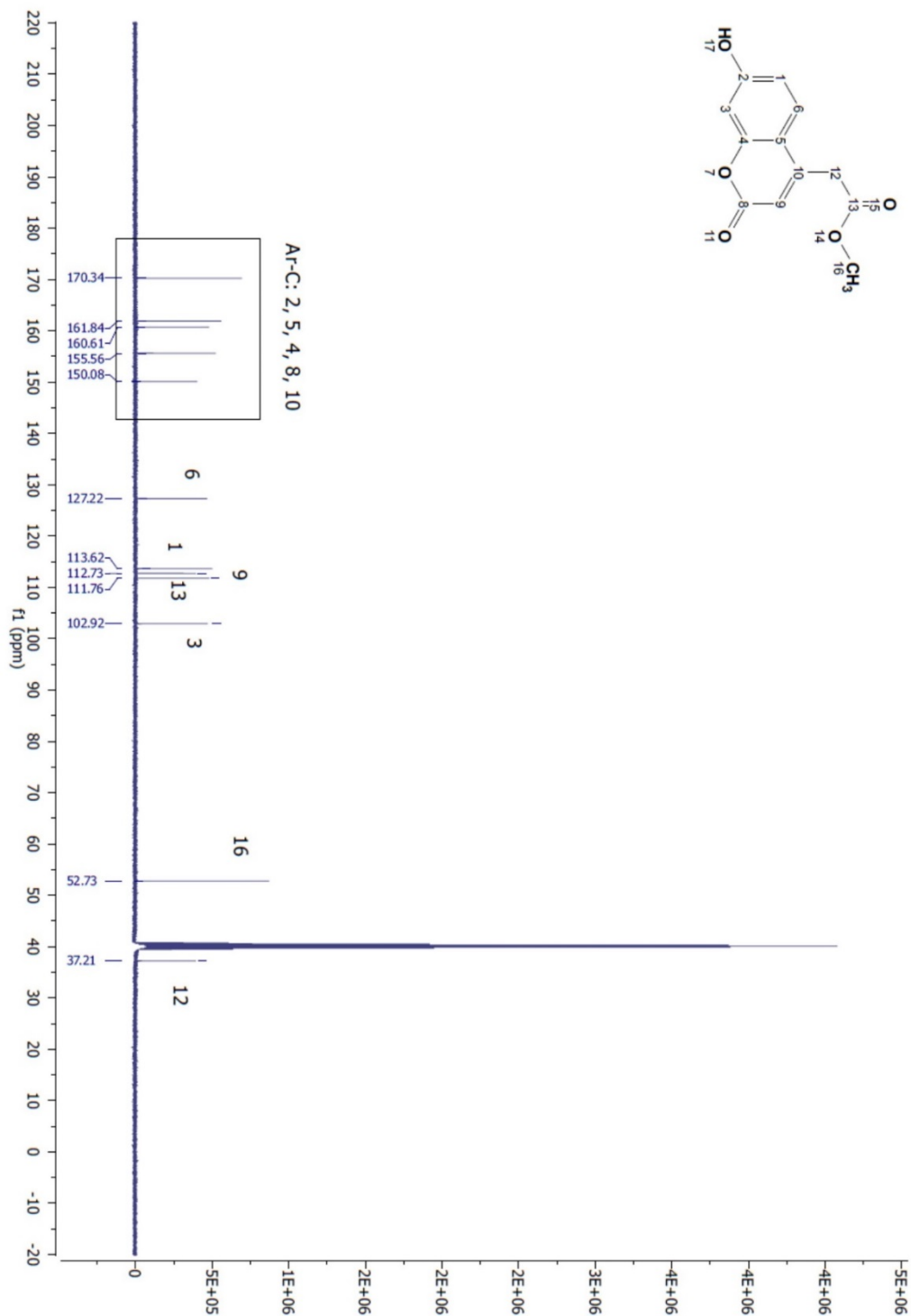
¹³C-NMR spectrum of **compound 1**: **¹³C NMR** (100 MHz, DMSO-*d₆*): δ 37.21 (-CH₂-), 52.73 (-CH₃), 102.92 (CH-Ar), 111.76 (C=O), 112.73 (CH-Ar), 113.62 (CH-Ar), 127.22 (CH-Ar), 150.08 (-C-OH), 155.56 (C-Ar), 160.61 (C-Ar), 161.84 (C-Ar), 170.34 (C-Ar) ppm.
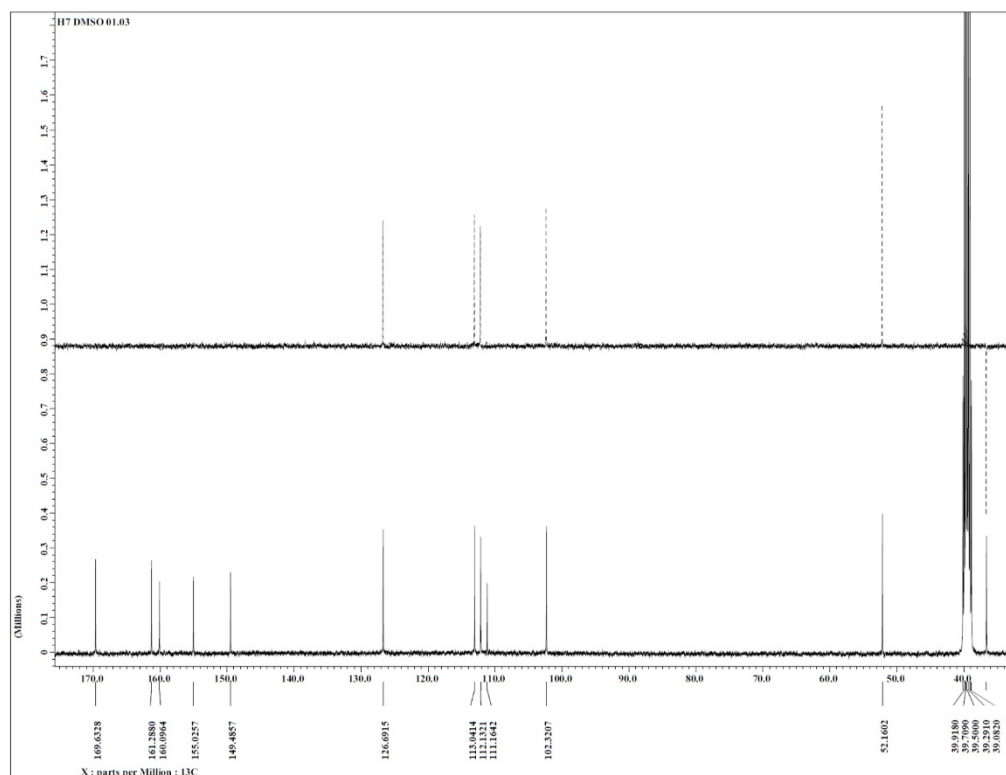
^{13}C- DEPT135 spectrum of **compound 1**
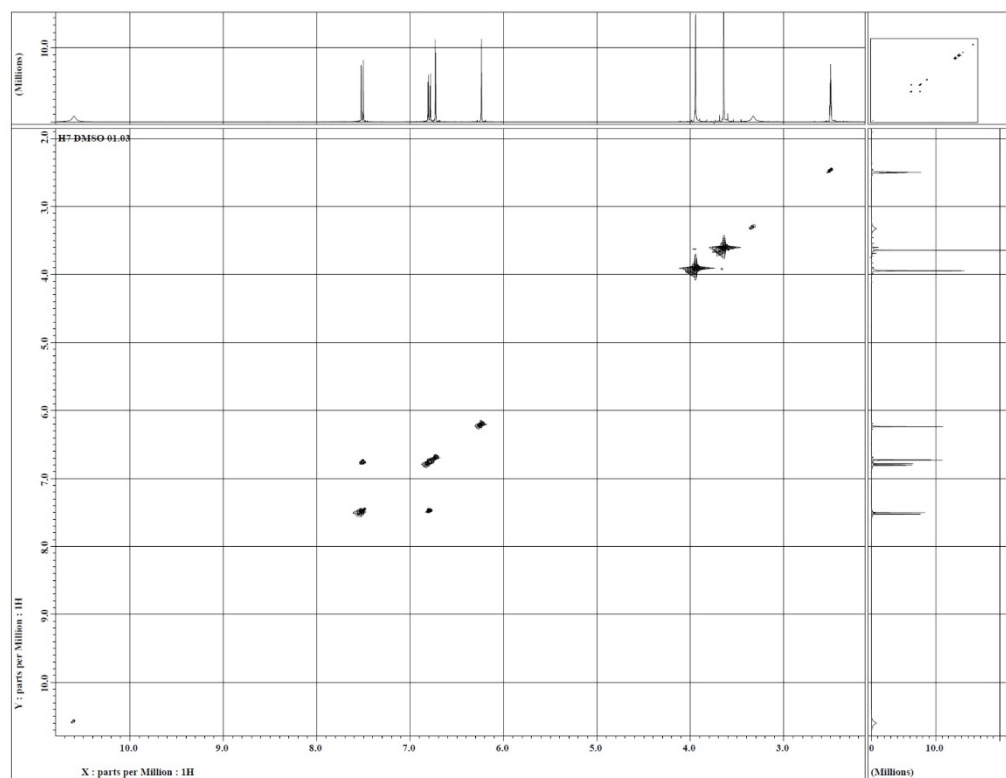
COSY spectrum of **compound 1**

A2.7.2 Compound 1'
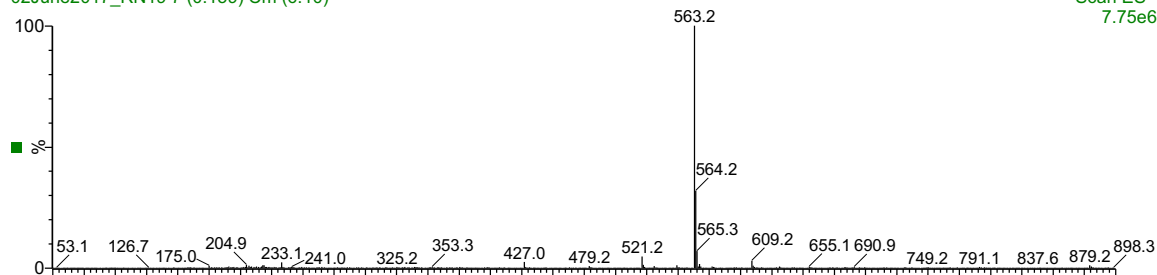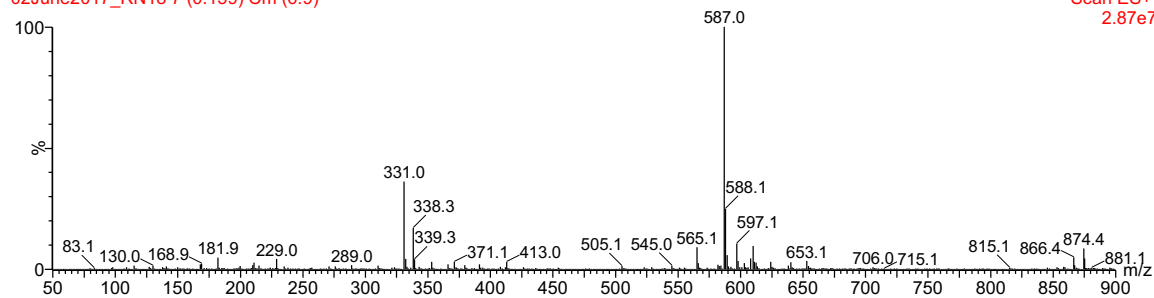
Low resolution-MS spectrum of **compound 1'**: MS (ES-): m/z 563.2 [M$^-$ - H$^+$]; MS (ES+): m/z 587.0 [M$^+$ + Na$^+$].
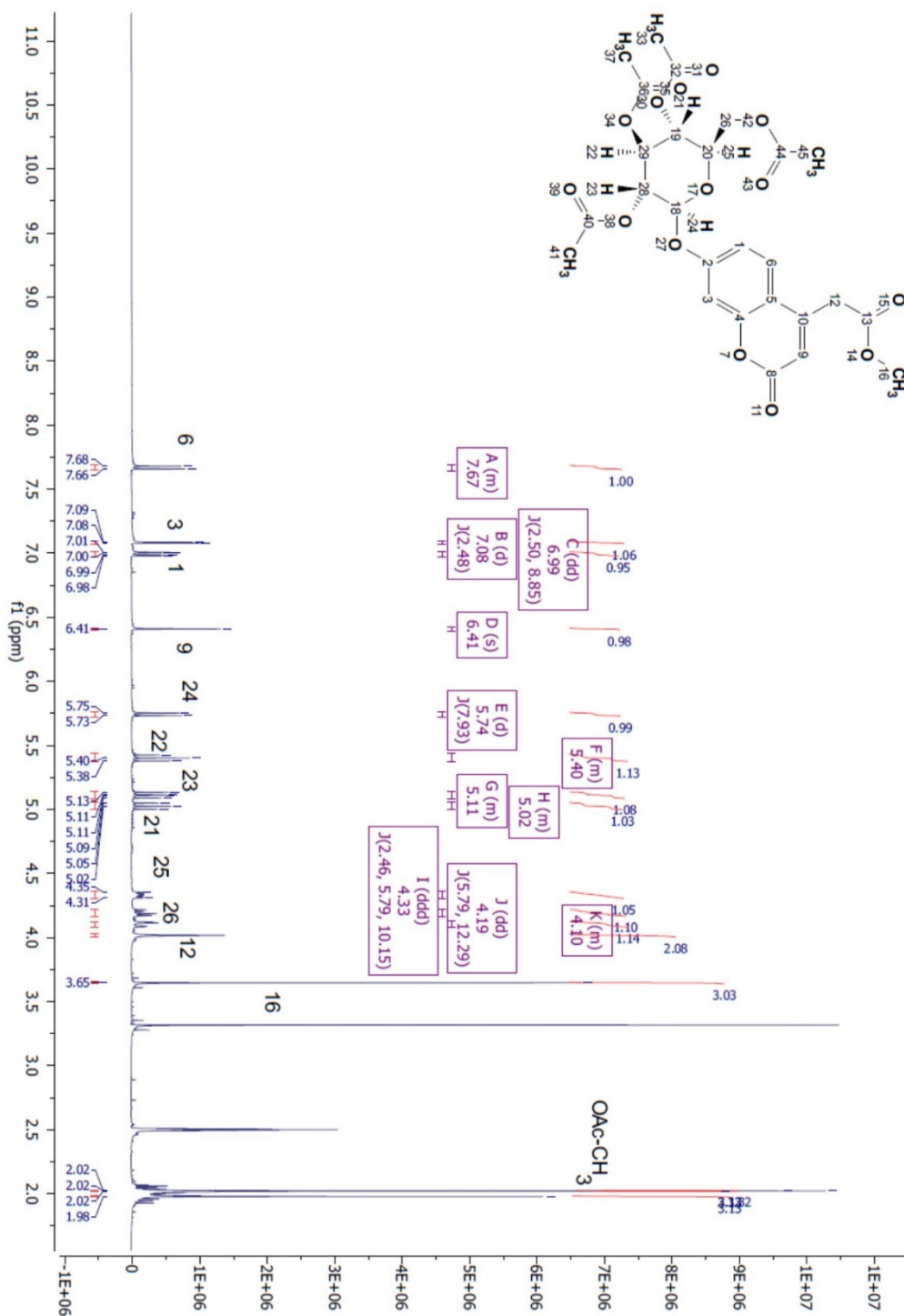
¹H-NMR spectrum of **compound 1'**: **¹H NMR** (400 MHz, DMSO-d_6): δ 1.98 (s, 3H), 2.02(s, 9H), 3.65 (s, 3H), 4.02 (s, 2H), 4.13-4.08 (q, 1H), 4.17-4.22 (dd, J = 12.3, J = 5.8 Hz, 1H), 4.33 (m, J = 10.2, 5.8 , 2.5 Hz, 1H), 5.0-5.05 (m, 1H), 5.14-5.08 (m, 1H), 5.44 – 5.37 (m, 1H), 5.73 (d, J = 7.93, Hz, 1H), 6.99 (dd, J = 8.9, 2.5 Hz, 1H), 6.41 (s, 1H), 7.01-6.98 (dd, J = 2.50, 8.85 Hz, 1H), 7.08 (m, J = J = 2.5 Hz, 1H), 7.68 (d, J = 2.5 Hz, 1H) ppm.

¹³C-NMR spectrum of **compound 1'**: **¹³C NMR** (100 MHz, DMSO-d_6): δ 20.87 (-CH$_3$), 37.16 (-CH$_2$-), 52.77 (-CH$_3$), 62.19 (-CH$_2$-), 68.5-72.47 (C-Glu), 97.08 (C-Glu), 103.98 (Ar-CH), 114.03 (C=O), 114.65 (Ar-CH), 114.90 (Ar-CH), 127.53 (Ar-CH), 149.72 (Ar-C), 155.05 (Ar-C), 159.38 (Ar-C), 160.26 (Ar-C), 169.69 (C-Glu), 169.90 (C=O), 170.11 (C=O), 170.17 (C=O), 170.56 (C=O) ppm.
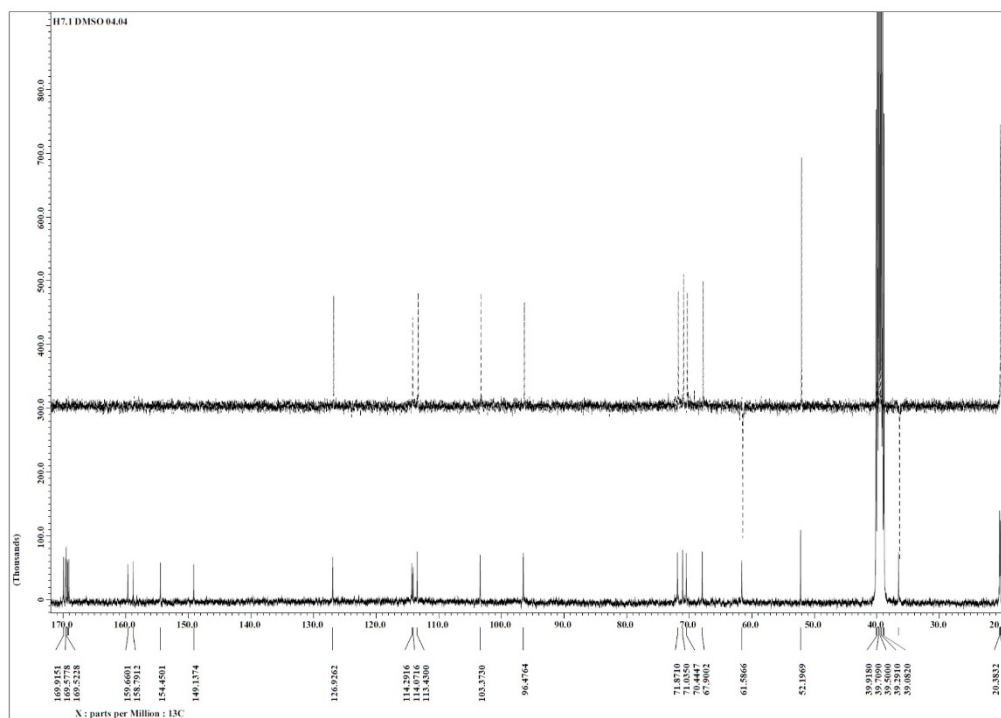
^{13}C- DEPT135 spectrum of **compound 1'**
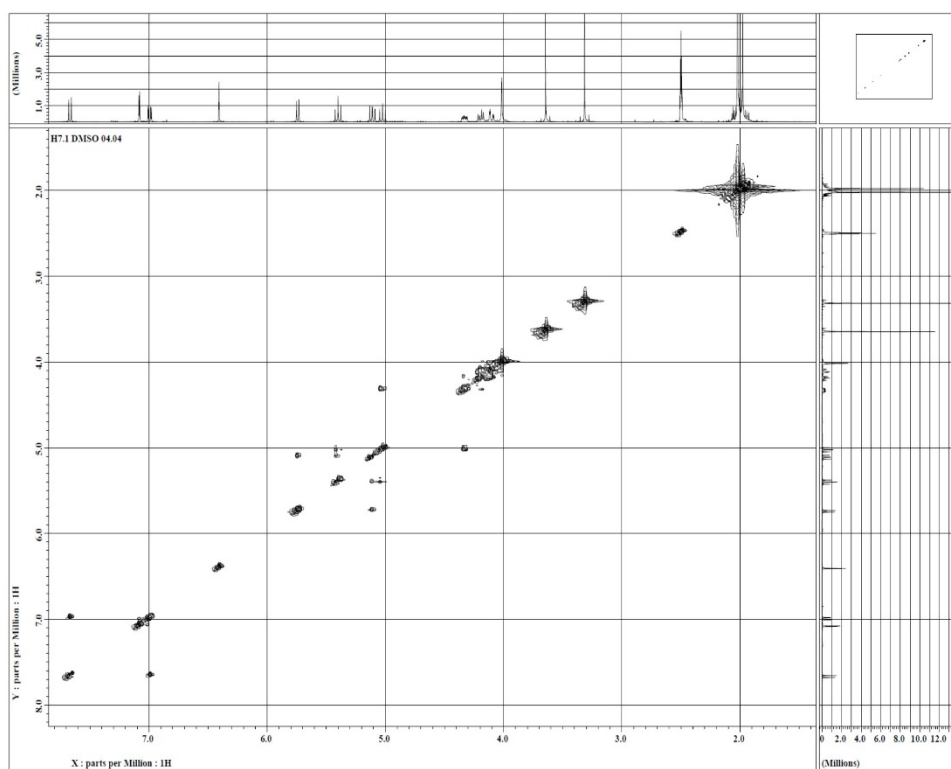
COSY spectrum of **compound 1'**

A2.7.3 Compound 8 (β-4-AAUG)
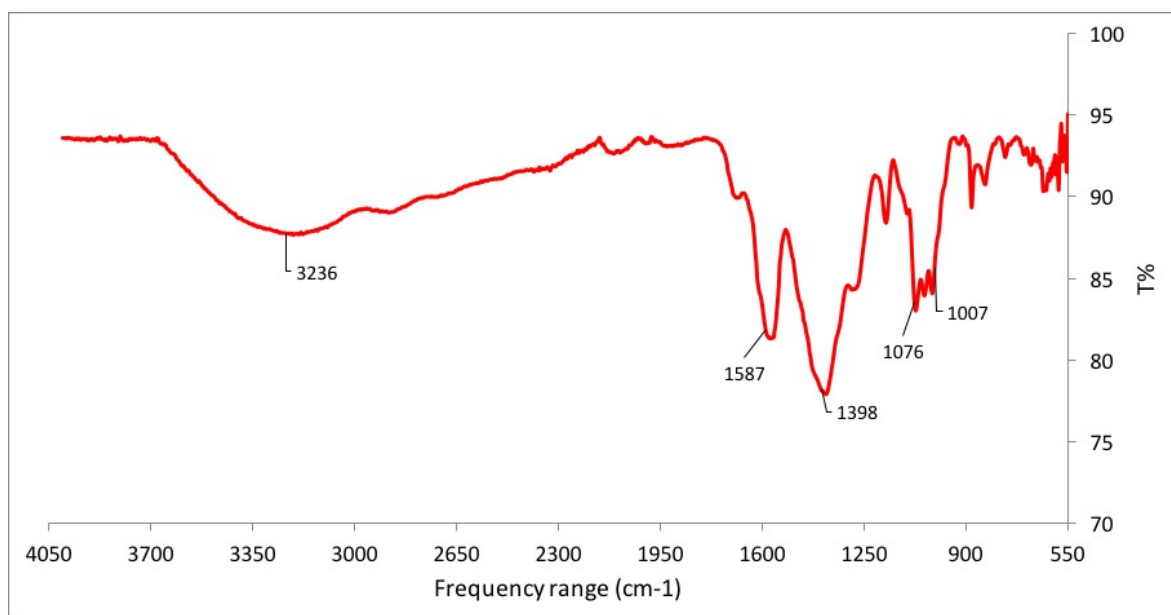
FT-IR spectrum of **compound 8 (β-4-AAUG)**: **IR:** 3236, 1587, 1398, 1076-1007 cm^{-1}.
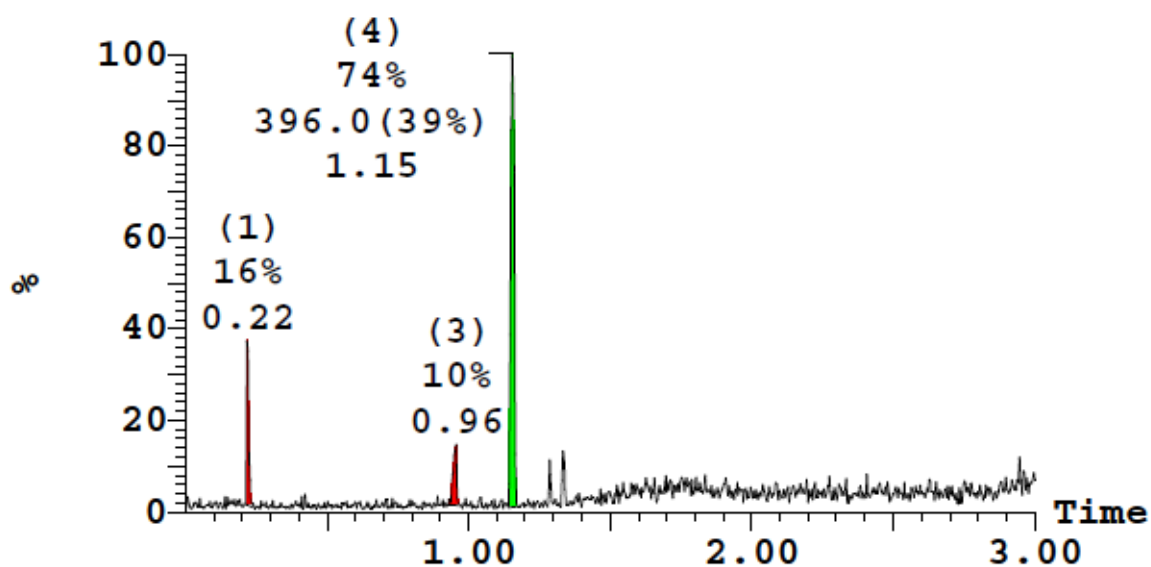
High resolution-MS spectrum of **compound 8 (β-4-AAUG):** HR-MS (ESI-TOF): m/z for $C_{17}H_{18}O_{10}^+$ [M+H]$^+$ calculated 396.31 found 396.0.
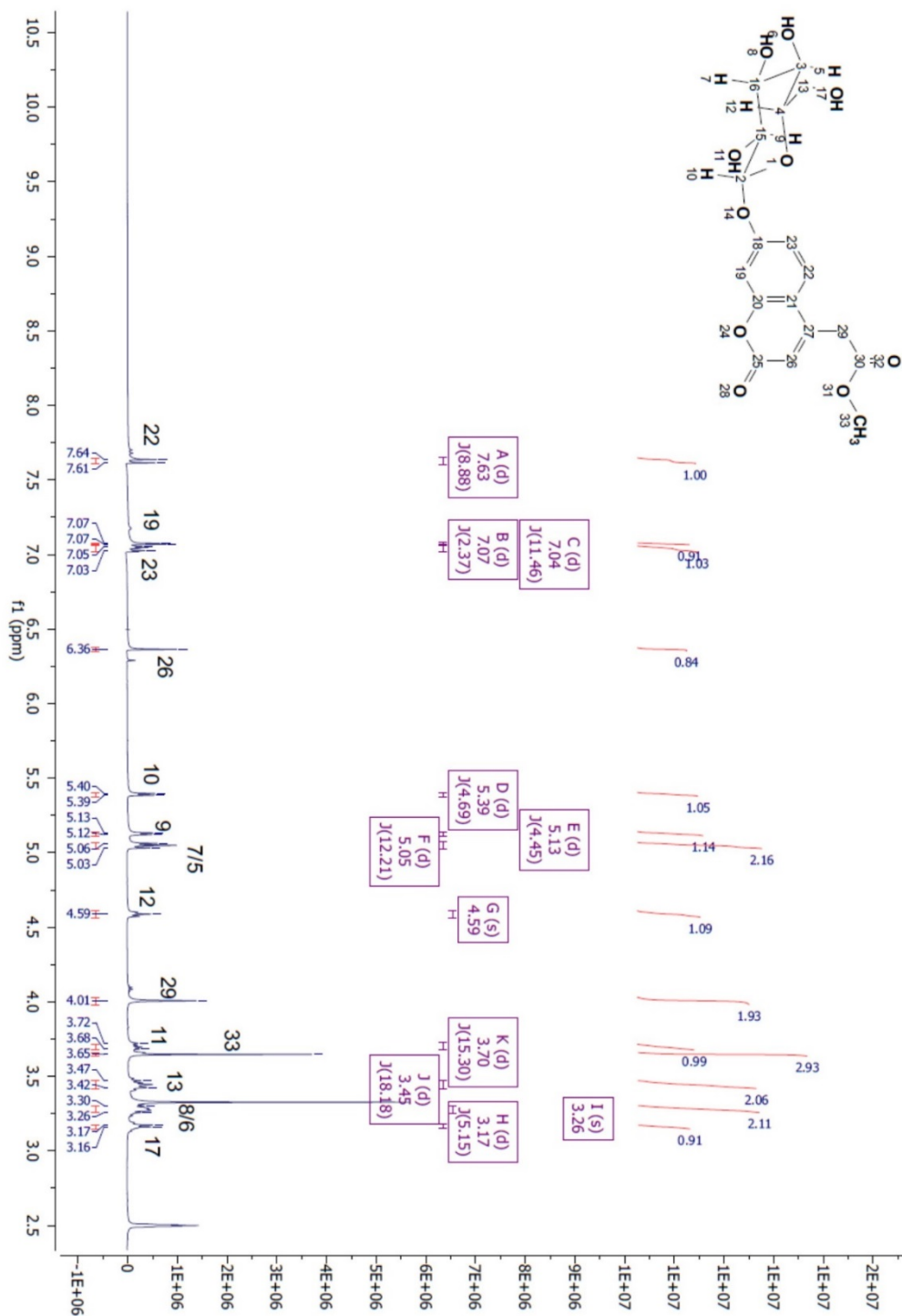
^{1}H-NMR spectrum of **compound 8 (β-4-AAUG)**: **^{1}H NMR** (400 MHz, DMSO-D6) δ 7.63 (d, J = 8.9 Hz, 1H), 7.07 (d, J = 2.4 Hz, 1H), 7.04 (d, J = 11.5 Hz, 1H), 6.36 (s, 1H), 5.39 (d, J = 4.7 Hz, 1H), 5.13 (d, J = 4.5 Hz, 1H), 5.05 (t, J = 12.2 Hz, 2H), 4.59 (t, J = 5.45, 1H), 3.70 (d, J = 15.3 Hz, 1H), 4.01 (s, 2H), 3.70 (m, J = 15.3, 1H), 3.65 (s, 2H), 3.45 (m, J = 18.2 Hz, 2H), 3.28 (m, J = 18.72, 2H), 3.17 (m, J = 5.2 Hz, 1H) ppm.
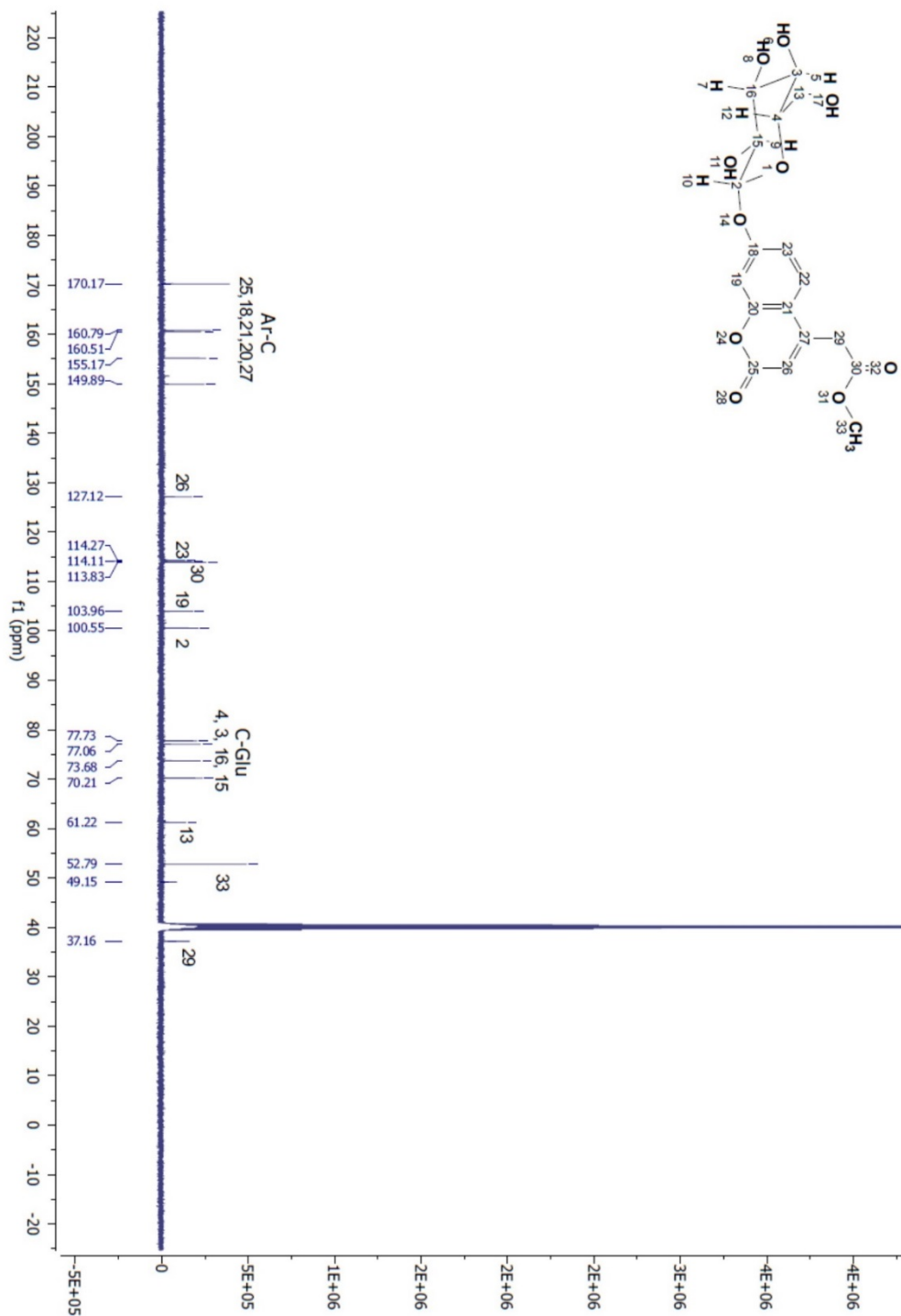
^{13}C-NMR spectrum of **compound 8 (β-4-AAUG)**: **^{13}C NMR** (101 MHz, DMSO-D6) δ 170.17 (C-Ar), 160.79 (C-C), 160.51 (C-C), 155.17 (C-Ar), 149.89 (C-Ar), 127.12 (Ar-CH), 114.27 (Ar-CH), 113.83 (C=O), 103.96 (Ar-CH), 100.55 (C-Glu), 77.73 (C-Glu), 77.06 (C-Glu), 73.68 (C-Glu), 70.21 (C-Glu), 61.22 (-CH$_2$-), 52.79 (-CH$_3$-), 37.16 (-CH$_2$-) ppm.
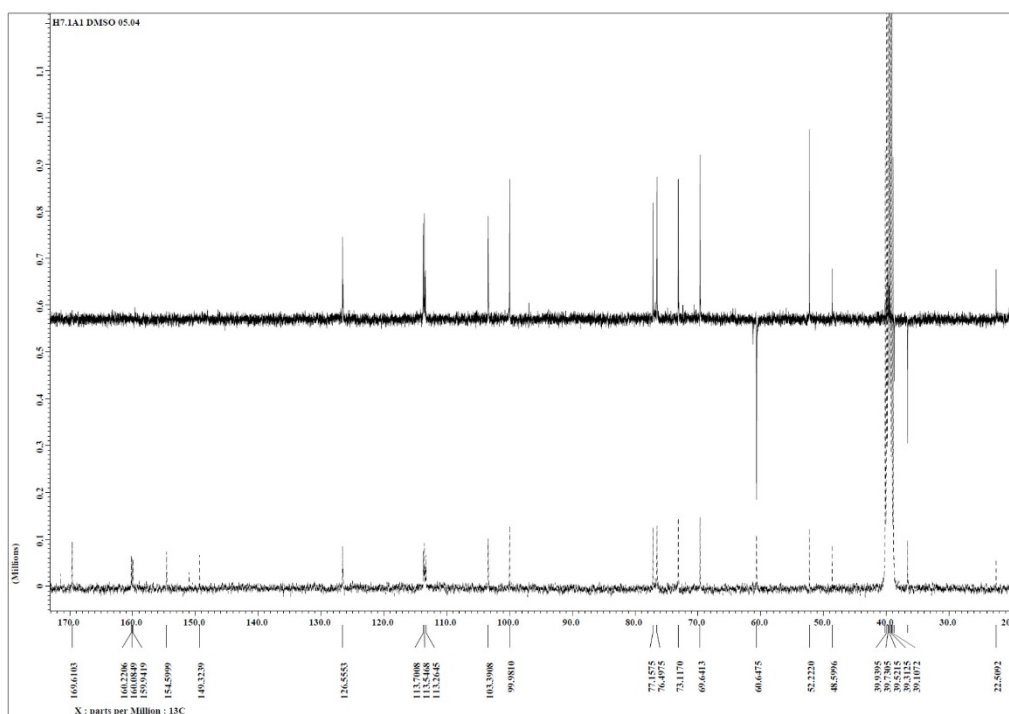
^{13}C- DEPT135 spectrum of **compound 8 (β-4-AAUG)**
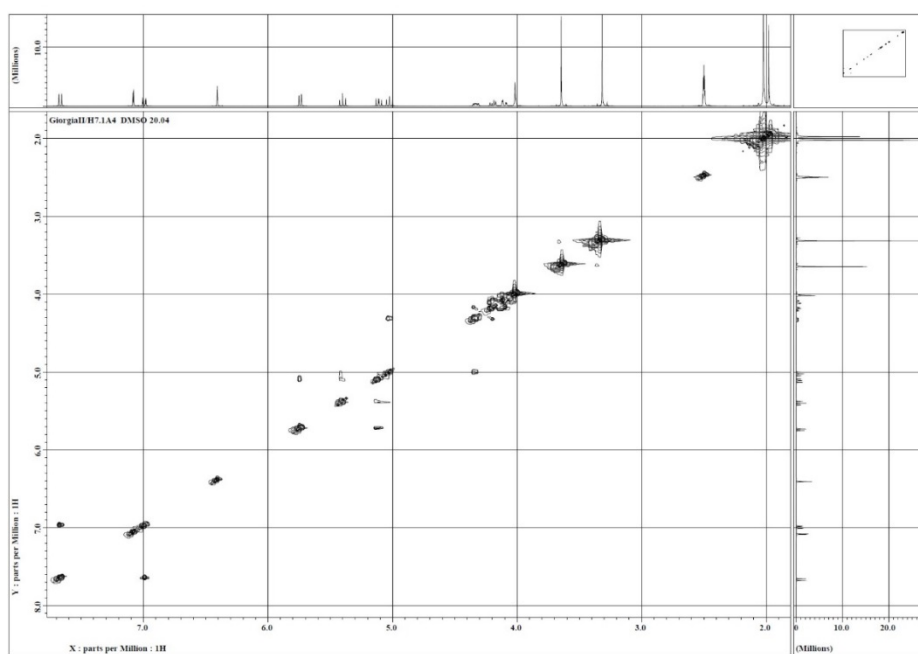
COSY spectrum of **compound 8 (β-4-AAUG)**

A2.7.4 Compound 2
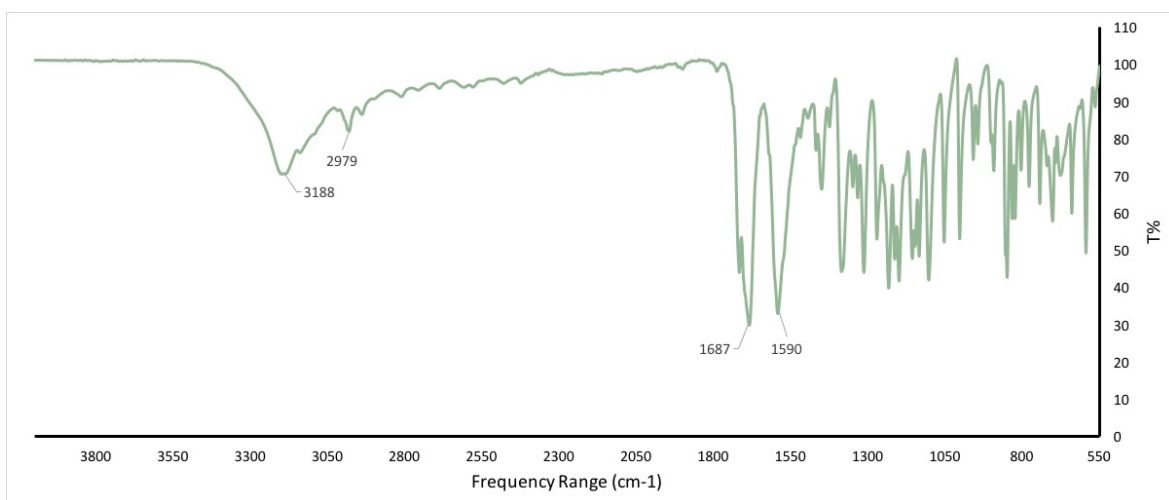
FT-IR spectrum of **compound 2. IR**: 3188, 2979, 1684, 1596, 1480-1440 cm^{-1}.
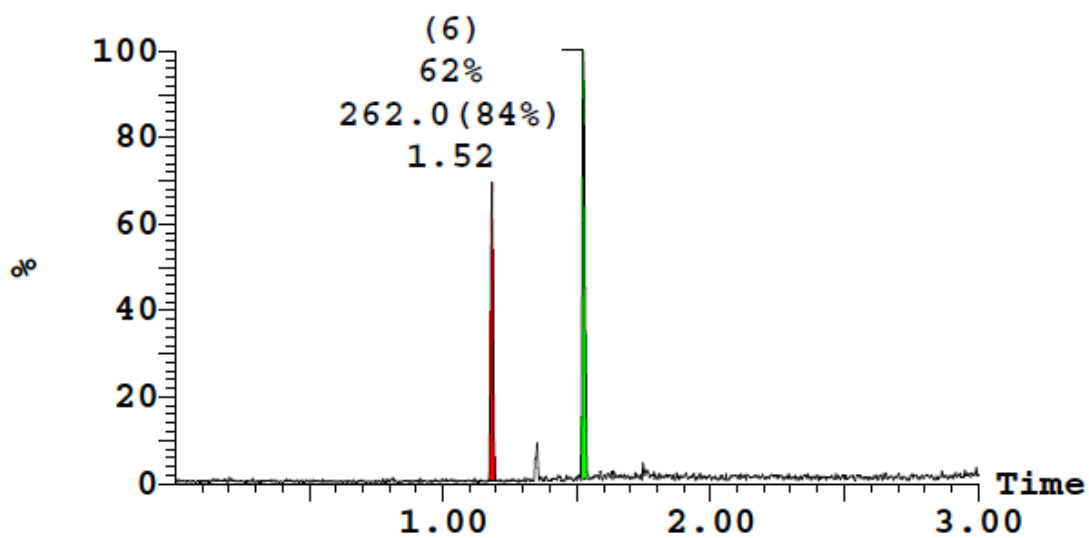
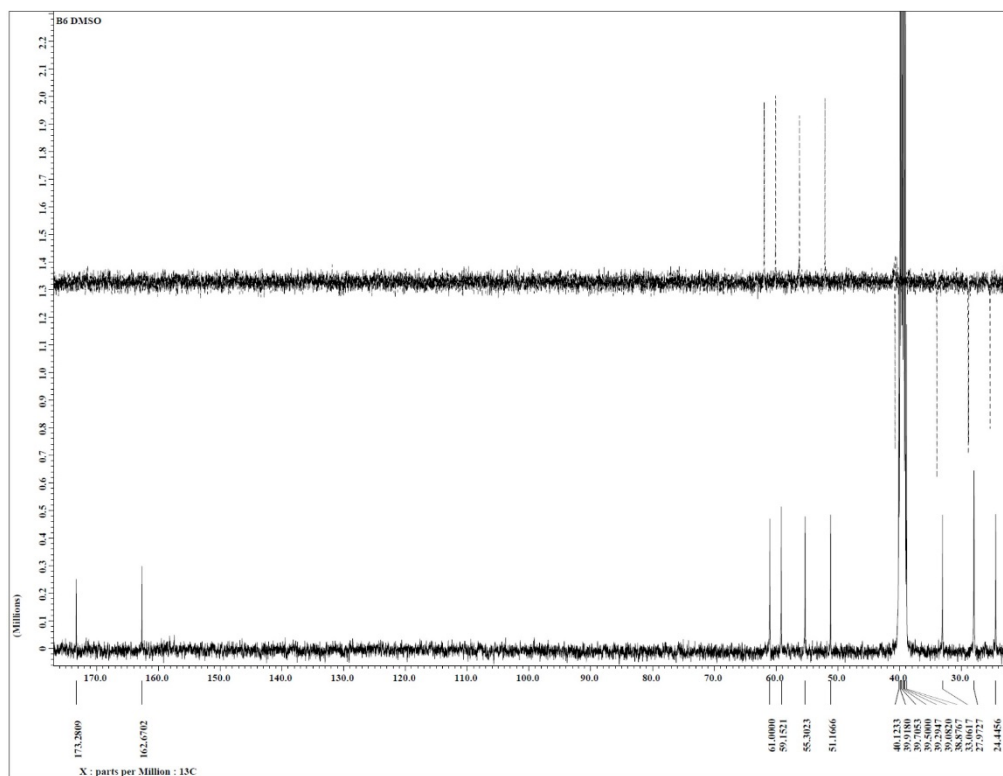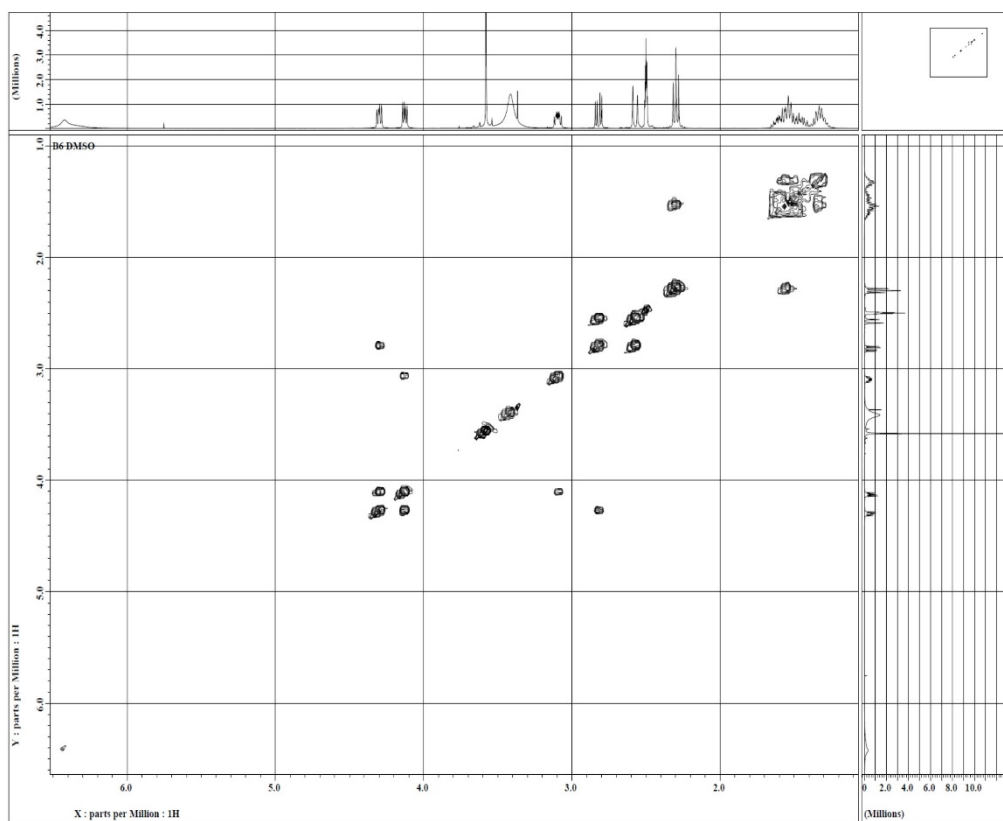High resolution-MS spectrum of **compound 2**: HR-MS (ESI-TOF): m/z for $C_{14}H_{14}O_5^+$ [M+H]$^+$ calculated 262.18 found 262.0.
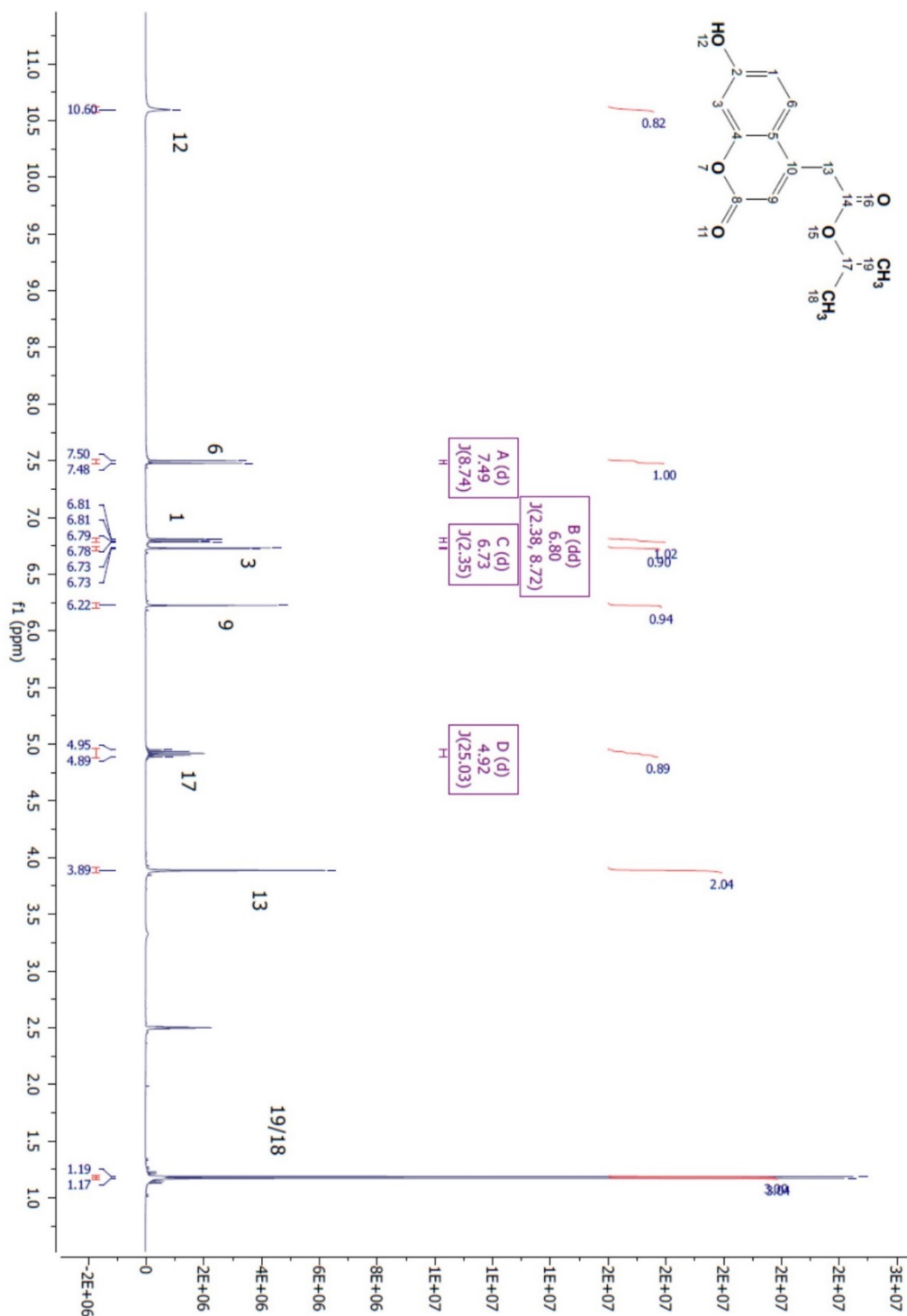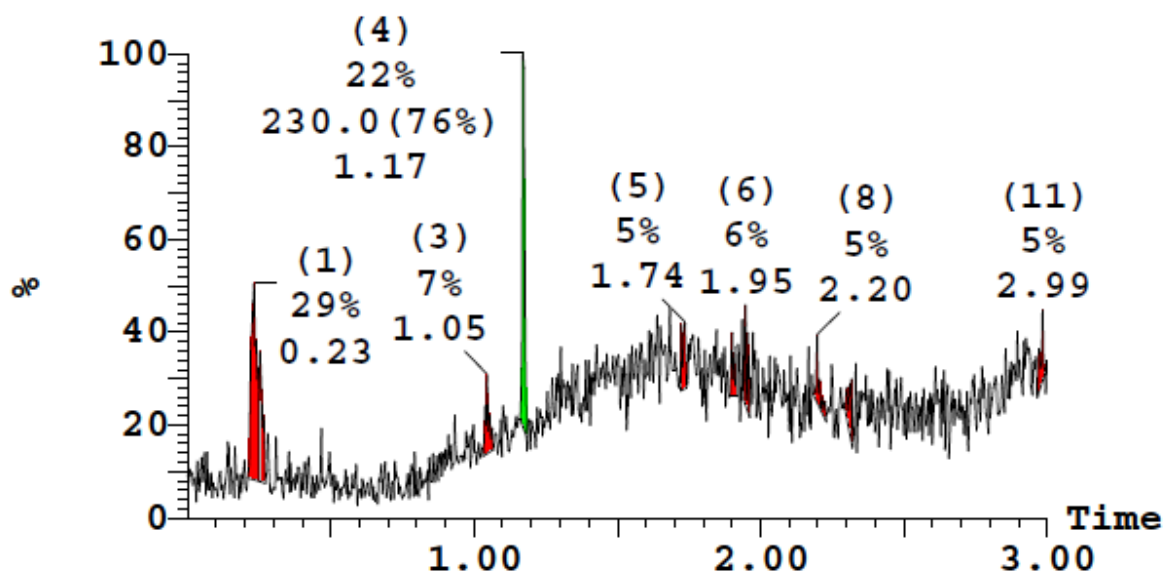
¹H-NMR spectrum of **compound 2**: **¹H NMR** (400 MHz, DMSO-D6) δ 10.6 (s, 1H), 7.51 (d, J = 8.7 Hz, 1H), 6.79 (dd, J = 8.72, 2.38, 1H), 6.73 (d, J = 2.3 Hz, 1H), 6.23 (s, 1H), 4.05 (t, J = 6.5 Hz, 1H), 3.93 (s, 1H), 1.50 (m, J = 12.6 Hz, 2H), 1.24 (m, J = 14.9 Hz, 2H), 0.82 (t, J = 7.4 Hz, 3H) ppm.
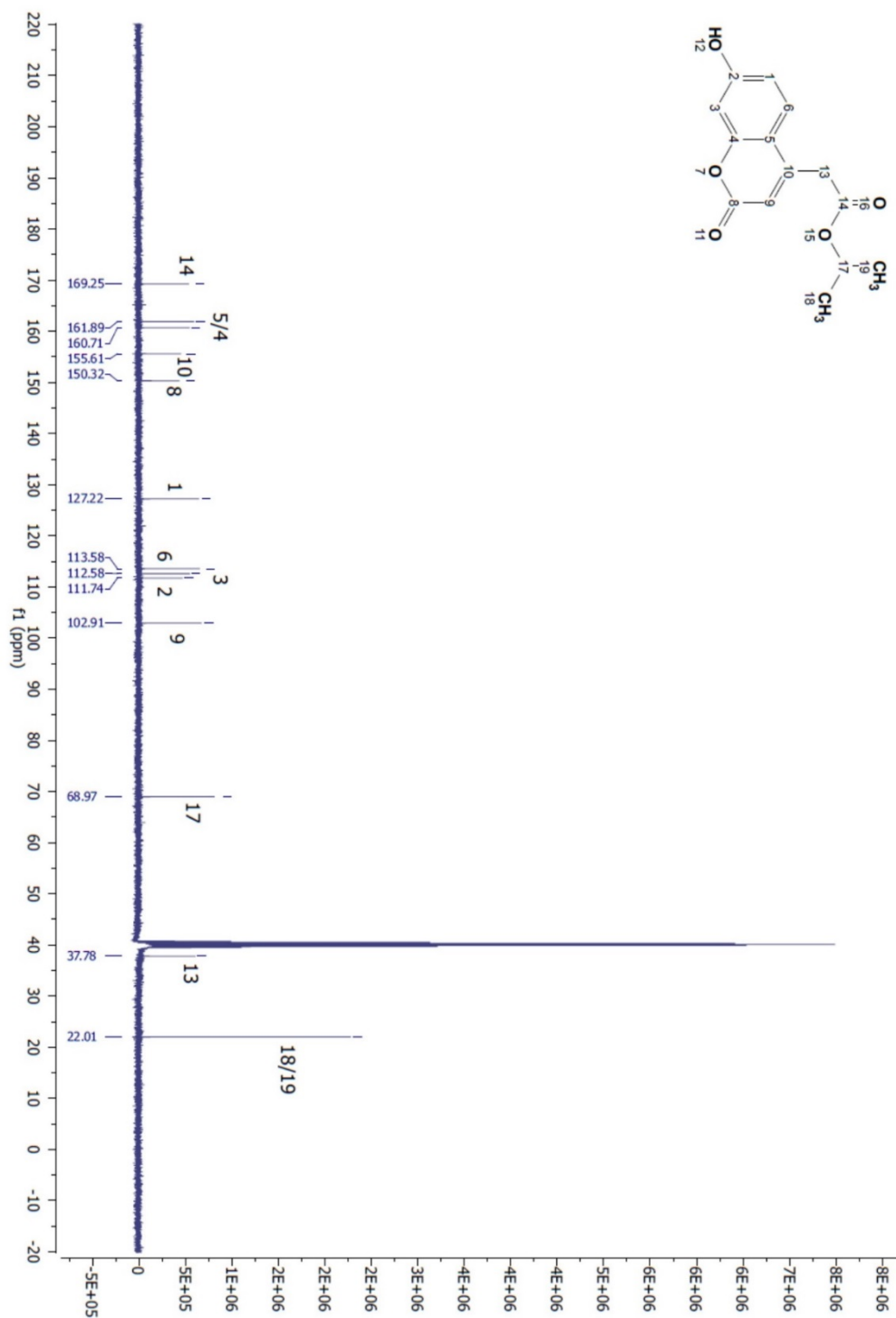
^{13}C-NMR spectrum of **compound 2**: **^{13}C NMR** (101 MHz, DMSO-D6) δ 169.75 (C=O), 161.88 (-C-C-), 160.71 (-C-C-), 155.61 (Ar-C), 150.23 (C=O), 127.25 (Ar-C), 113.56 (Ar-C), 112.63 (Ar-C), 111.75 (Ar-C-OH), 102.90 (Ar-C), 65.03 (-CH$_2$-), 37.52 (-CH$_2$-), 30.59 (-CH$_2$-), 19.04 (-CH$_2$-), 14.01 (-CH$_3$) ppm.
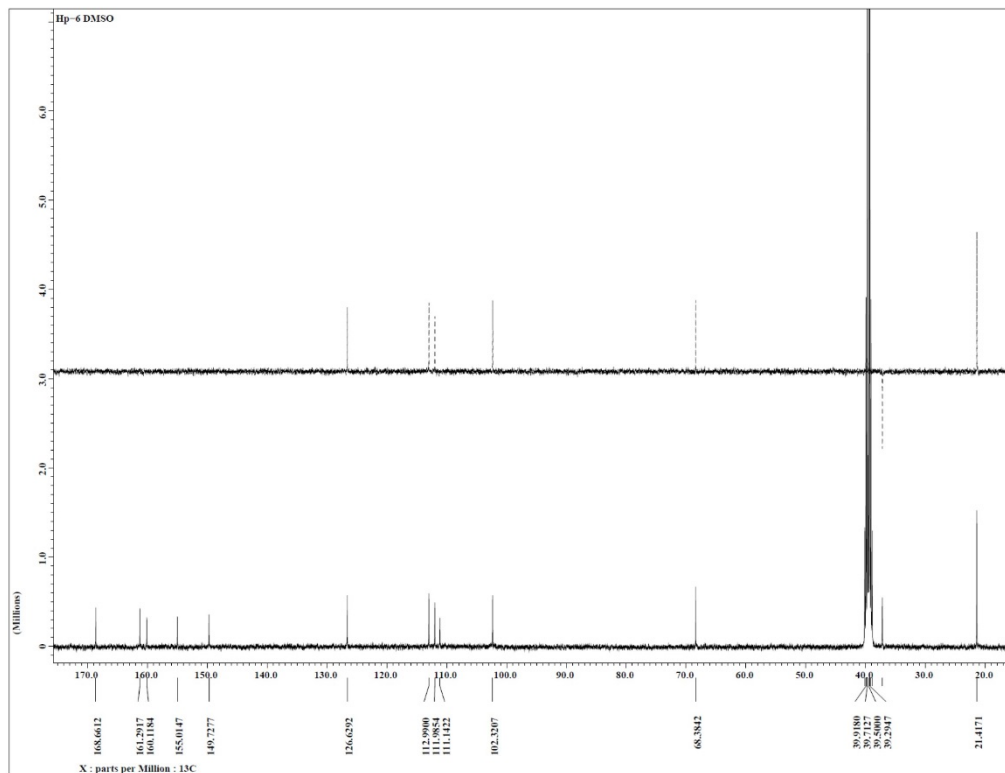
^{13}C- DEPT135 spectrum of **compound 2.**
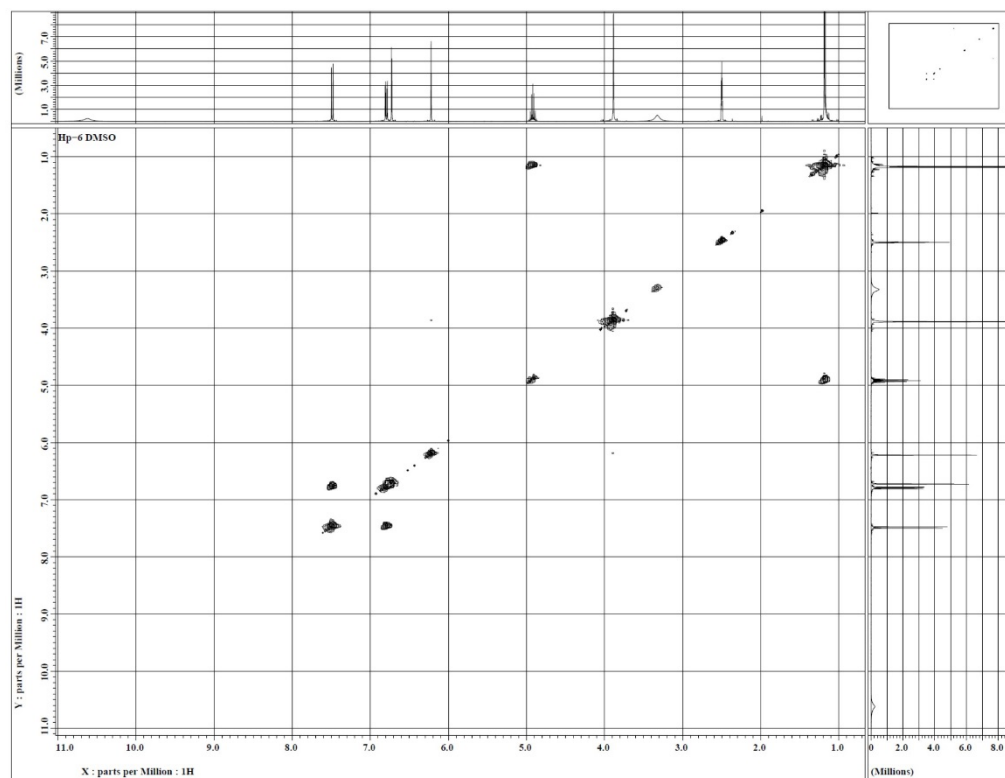
COSY spectrum of **compound 2.**

A2.7.5 Compound 3
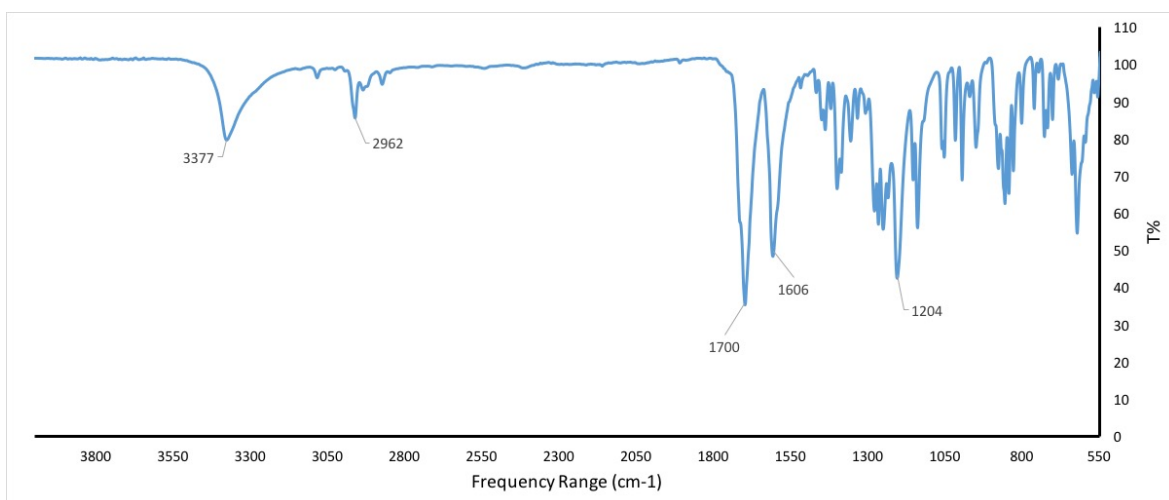
FR-IR spectrum of **compound 3**. **IR:** 3377, 2962, 1700, 1606, 1204 cm^{-1}.
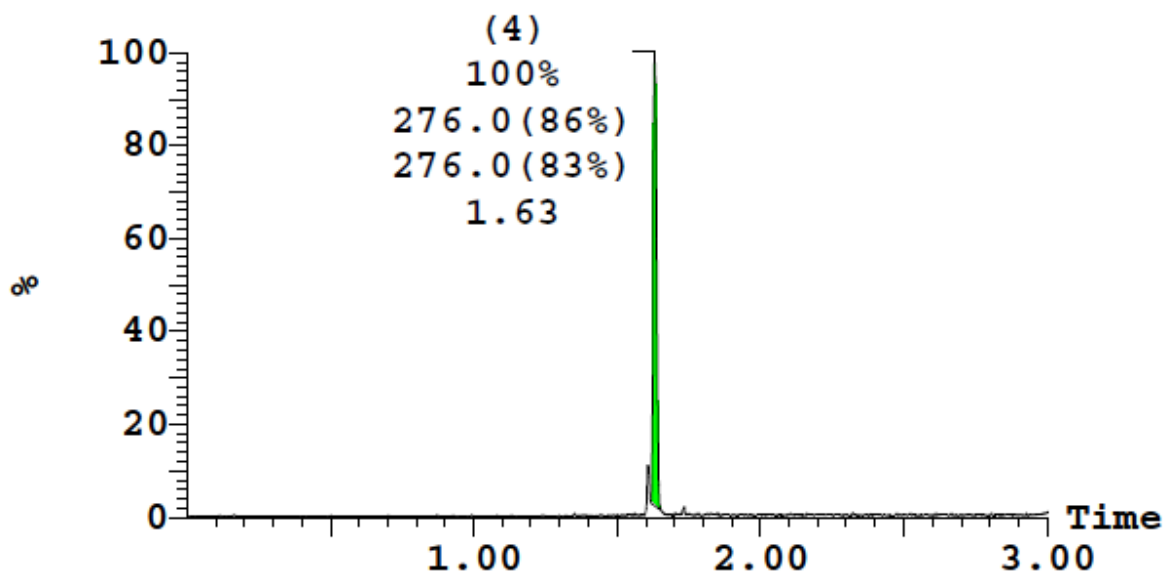
High resolution-MS spectrum of **compound 3**: HR-MS (ESI-TOF): m/z for $C_{15}H_{16}O_5^+$ [M+H]$^+$ calculated 276.18 found 276.0.
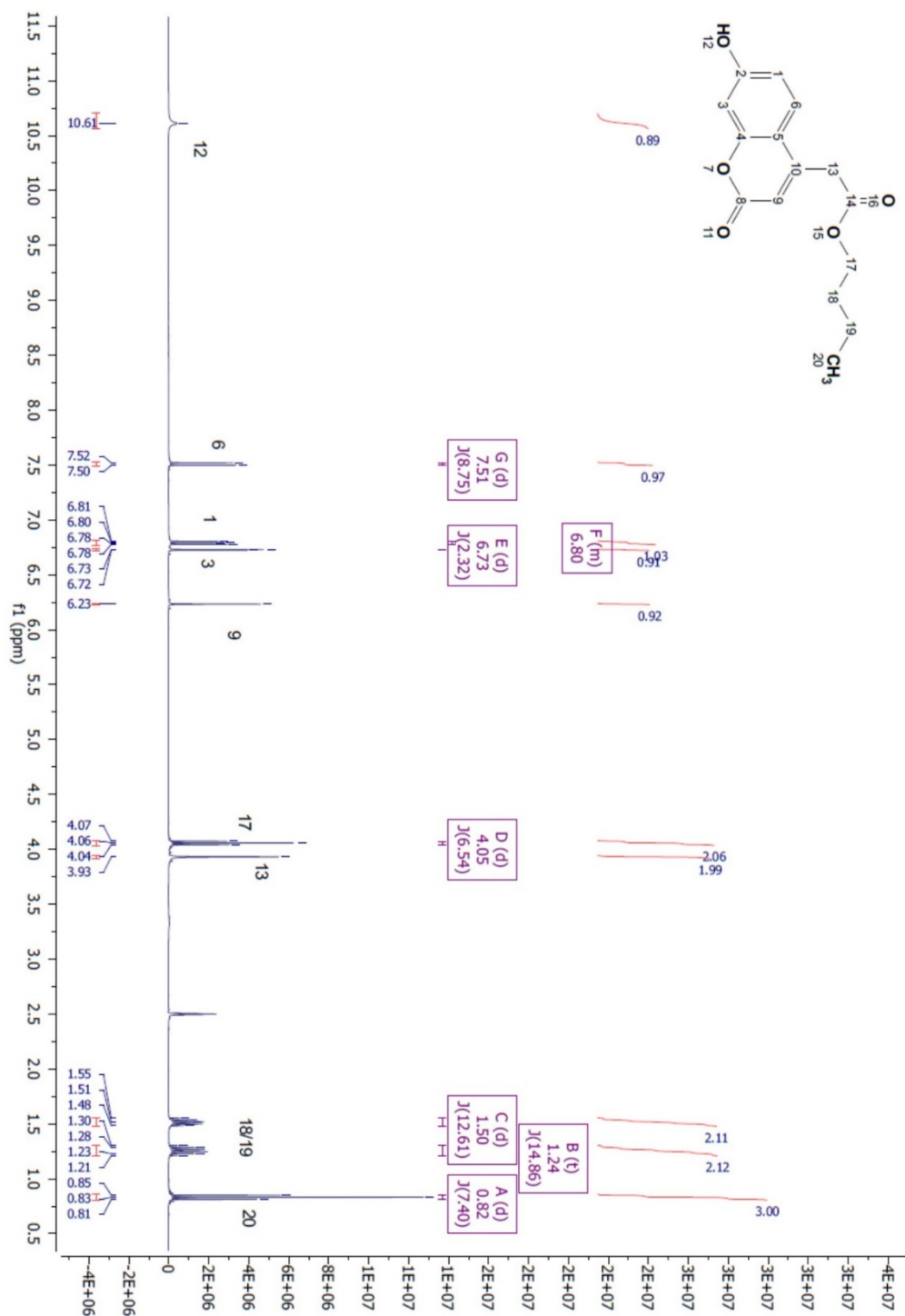
^{1}H-NMR spectrum of **compound 3**: **^{1}H NMR** (400 MHz, DMSO-D6) δ 10.6 (s, 1H), 7.51 (d, J = 8.7 Hz, 1H), 6.79 (dd, J = 8.72, 2.38, 1H), 6.73 (d, J = 2.3 Hz, 1H), 6.23 (s, 1H), 4.05 (t, J = 6.5 Hz, 1H), 3.93 (s, 1H), 1.50 (m, J = 12.6 Hz, 2H), 1.24 (m, J = 14.9 Hz, 2H), 0.82 (t, J = 7.4 Hz, 3H) ppm.
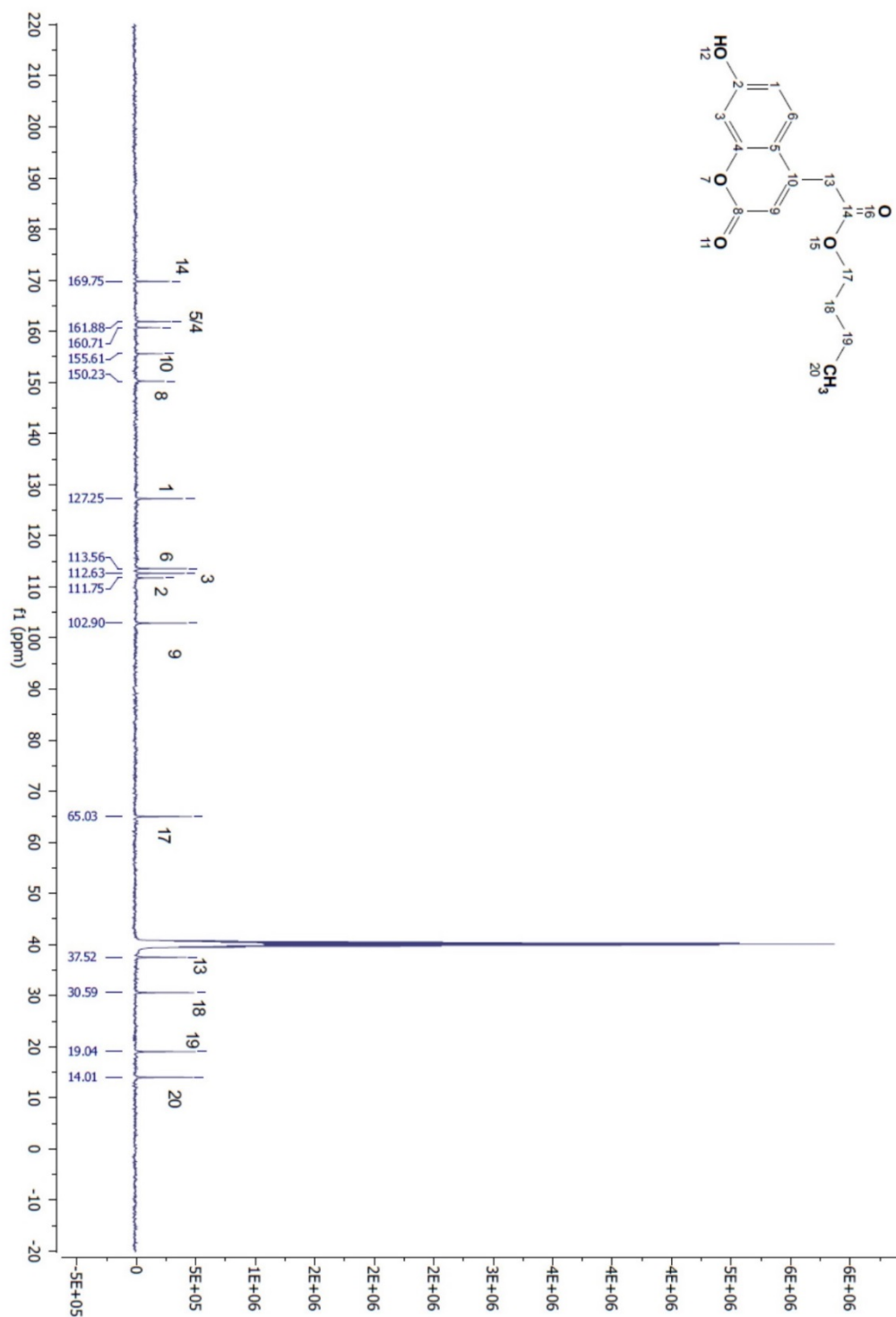
^{13}C-NMR spectrum of **compound 3**: **^{13}C NMR** (101 MHz, DMSO-D6) δ 169.75 (C=O), 161.88 (-C-C-), 160.71 (-C-C-), 155.61 (Ar-C), 150.23 (C=O), 127.25 (Ar-C), 113.56 (Ar-C), 112.63 (Ar-C), 111.75 (Ar-C-OH), 102.90 (Ar-C), 65.03 (-CH$_2$-), 37.52 (-CH$_2$-), 30.59 (-CH$_2$-), 19.04 (-CH$_2$-), 14.01 (-CH$_3$) ppm.
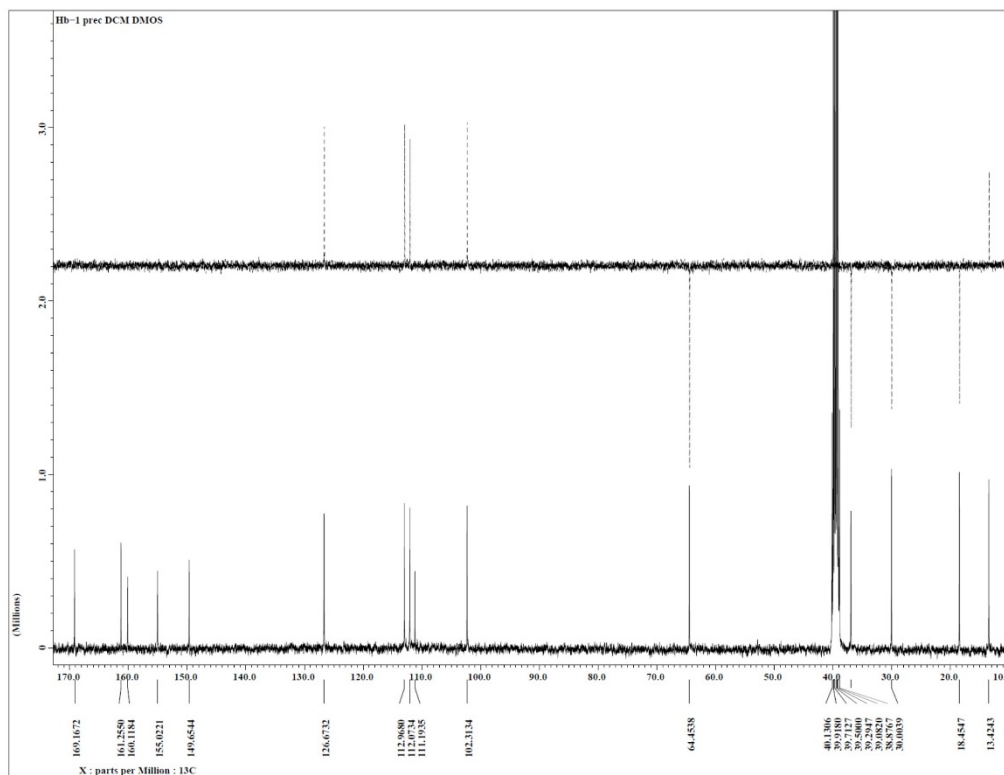
^{13}C- DEPT135 spectrum of **compound 3**
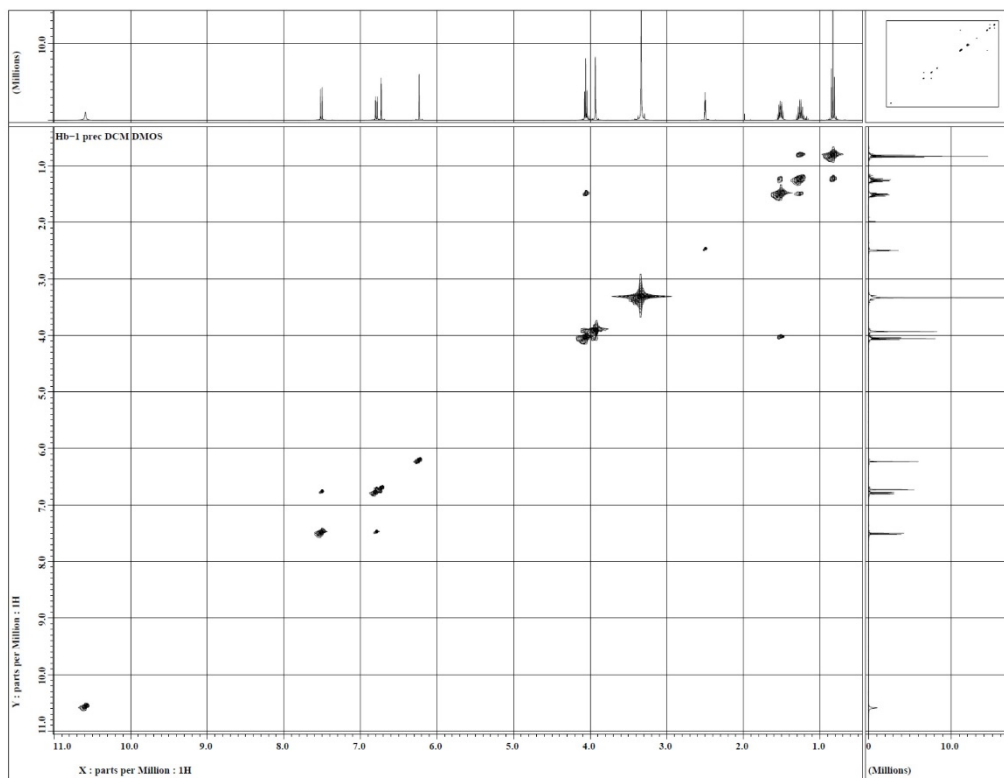
COSY spectrum of **compound 3**

A2.7.6 Compound 4
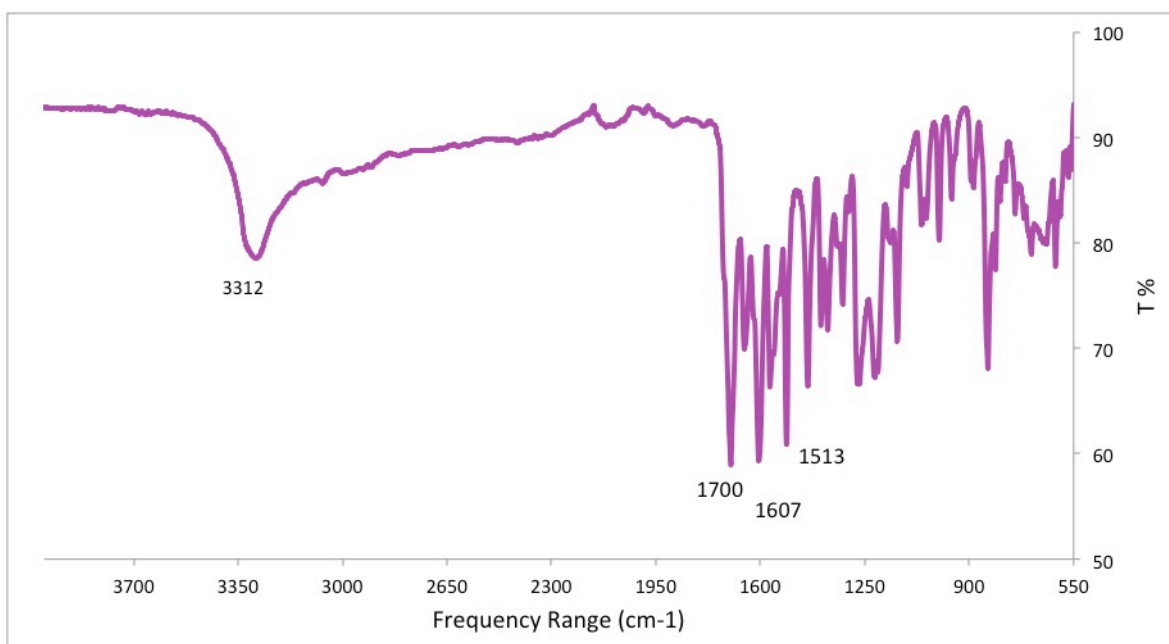
FT-IR spectrum of **compound 4. IR:** 3312, 1700, 1607, 1513 cm^{-1}.
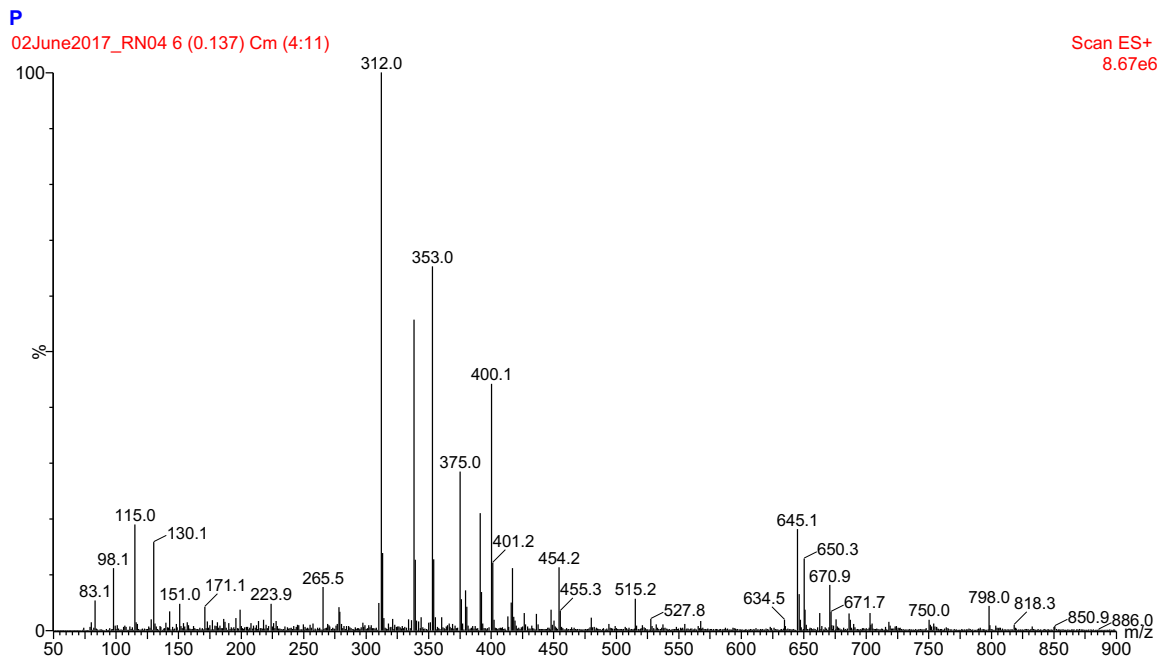
Low resolution-MS spectrum of **compound 4**: MS (ES+): m/z 312.0 [M$^+$ + H$^+$].

^{1}H-NMR spectrum of **compound 4**: **^{1}H NMR** (400 MHz, DMSO-d_6): δ 10.04 (s, 1H), 7.66 (d, J = 8.8 Hz, 1H), 7.35 (m, 2H), 6.82 (dd, J = 2.38, 8.73 Hz, 1H), 6.74 (d, J = 2.36 Hz, 1H), 6.70 (m, 2H), 6.23 (s, 1H), 3.83 (s, 2H), ppm.
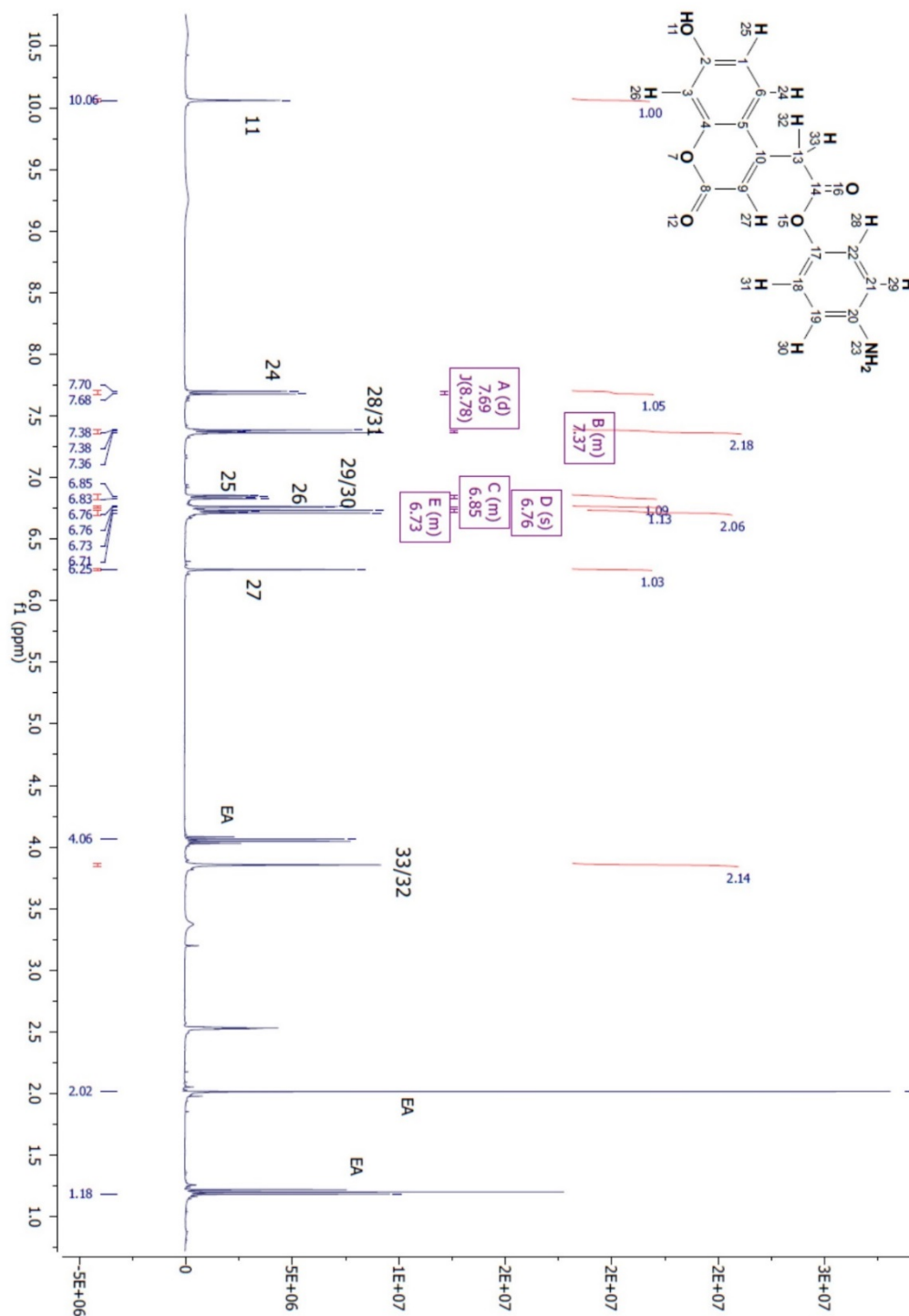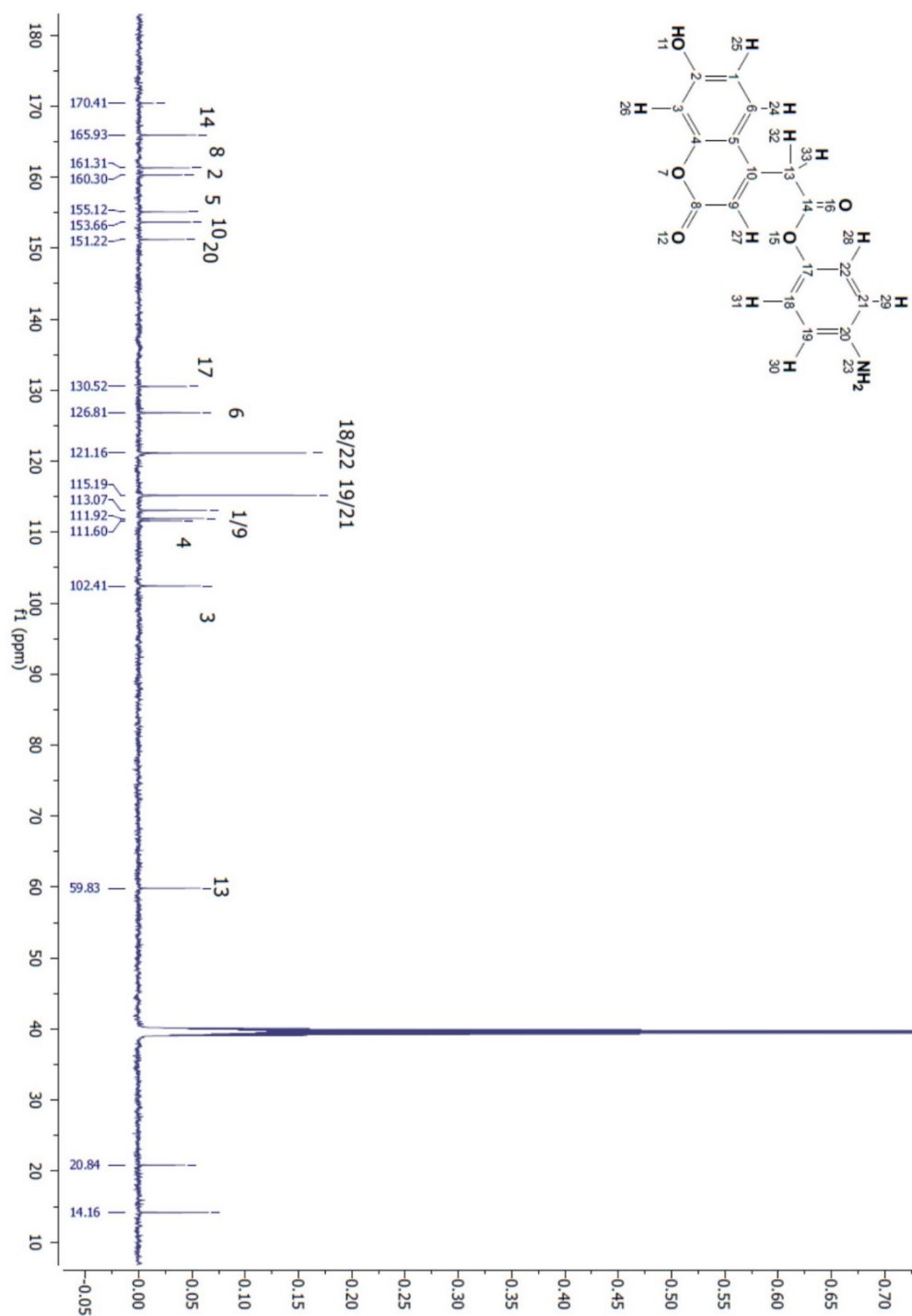
^{13}C-NMR spectrum of **compound 4**: **^{13}C NMR** (100 MHz, DMSO-d_6): δ 165.93 (C=O), 161.31 (C=O), 160.30 (Ar-C-OH), 155.12 (C=C), 153.66 (Ar-CH$_2$-), 151.22 (Ar-NH$_2$), 130.52 (Ar-O), 126.81 (Ar-C), 121.16 (Ar-C), 115.19 (Ar-C), 113.07 (Ar-C), 11.92 (Ar-C), 111.60 (C=C), 102.41 (Ar-C), 59.83 (-CH$_2$-) ppm.
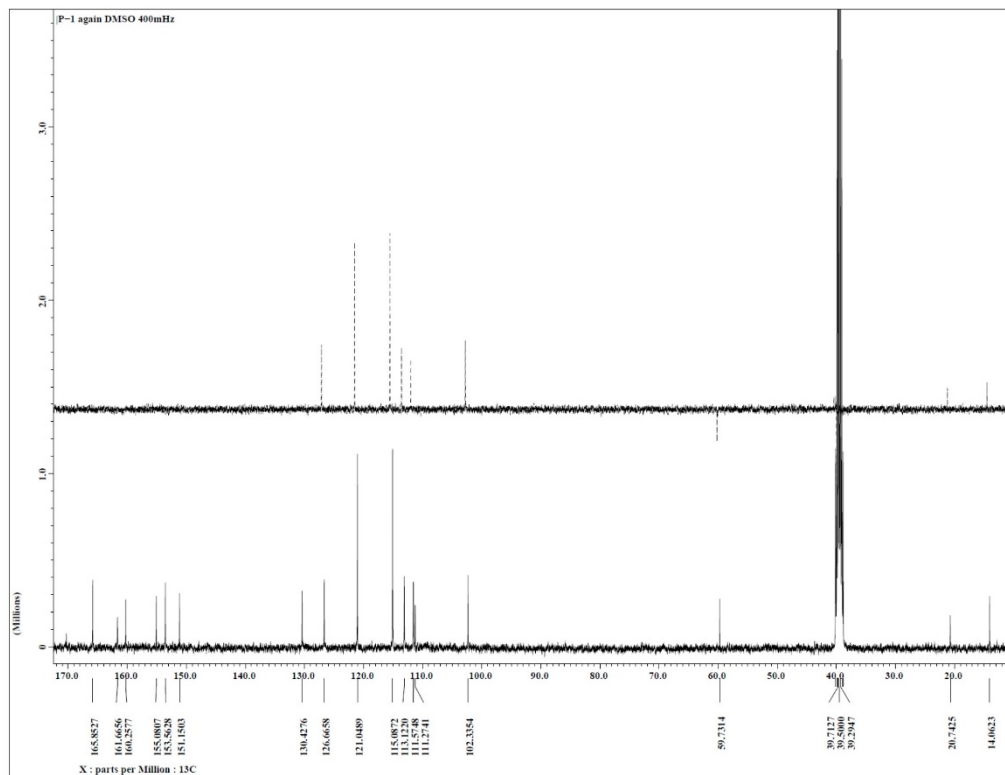
^{13}C- DEPT135 spectrum of **compound 4**.
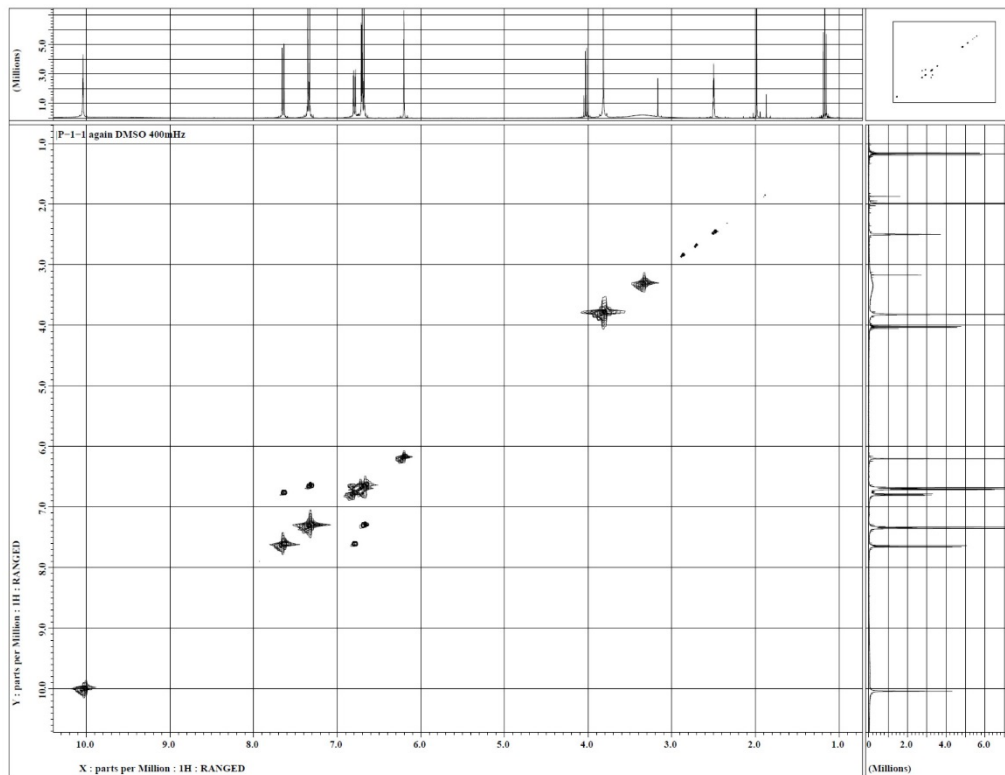
COSY spectrum of **compound 4**

A2.7.7 Compound 5'
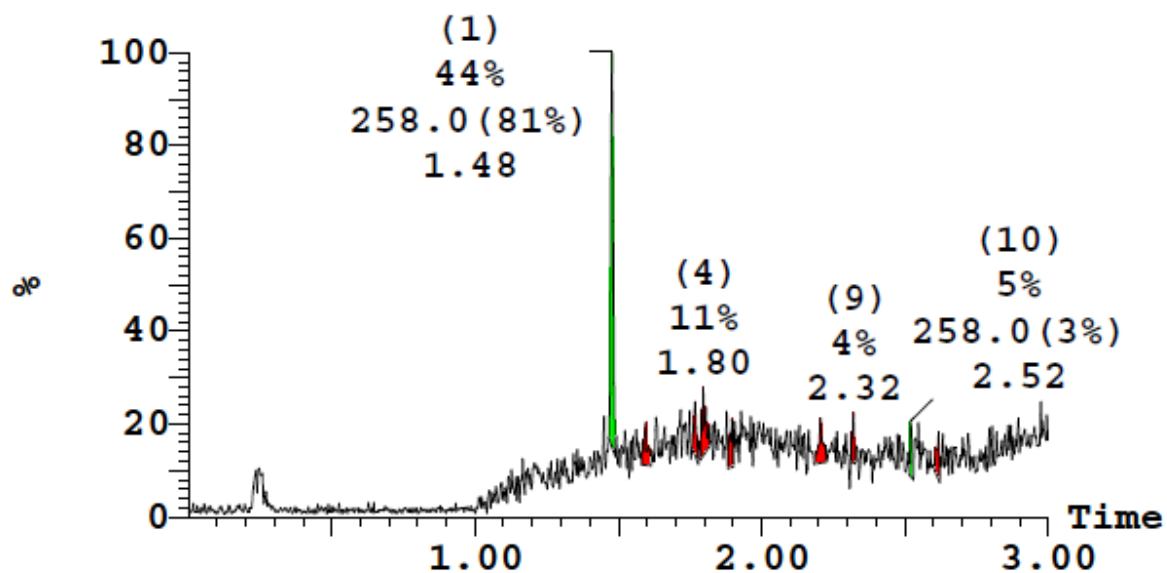
High resolution-MS spectrum of **compound 5'**: HR-MS (ESI-TOF): m/z for $C_{11}H_{18}N_2O_3S^+$ [M+H]$^+$ calculated 258.32 found 258.0.
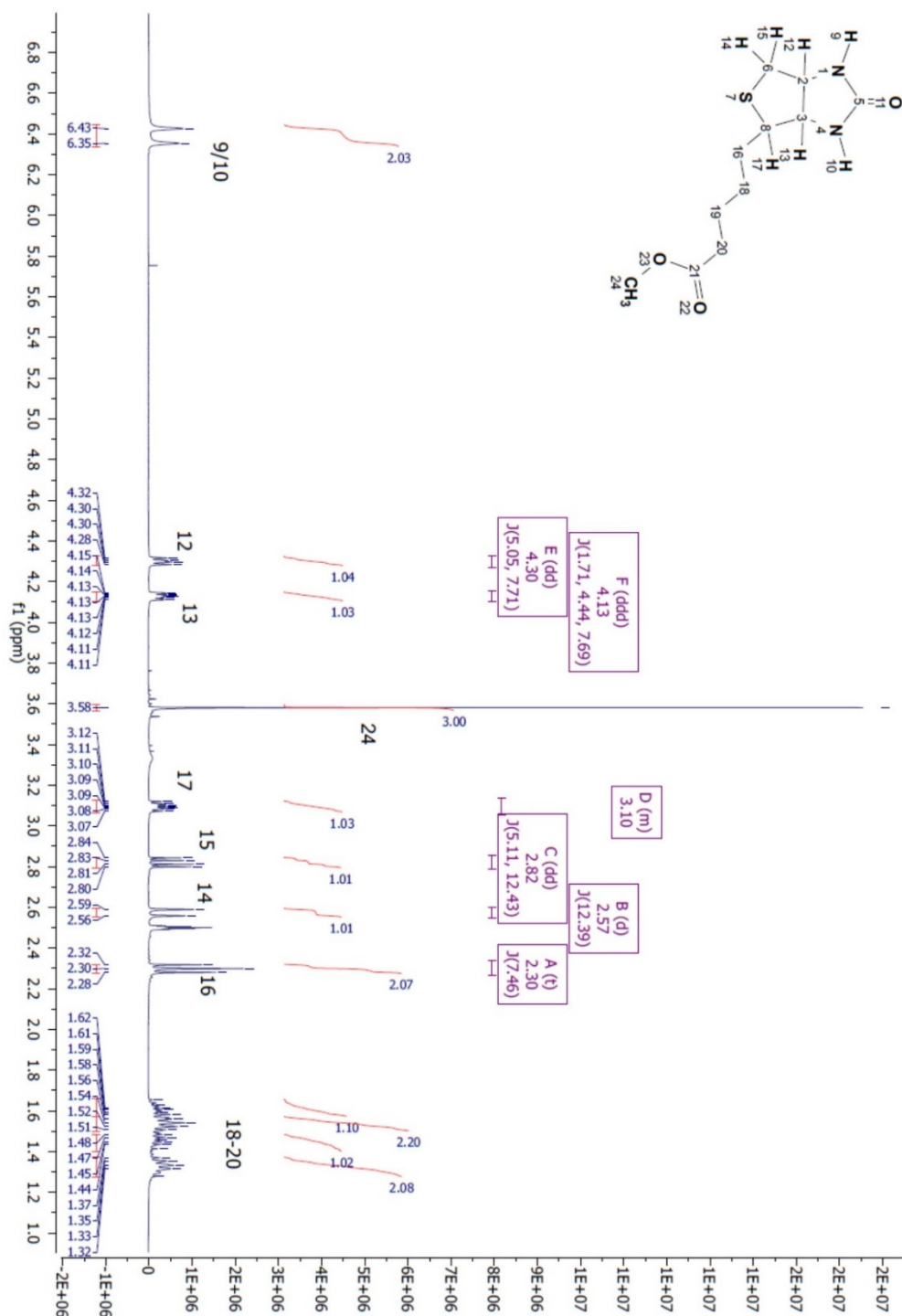
¹H-NMR spectrum of **compound 5'**: **¹H NMR** (400 MHz, DMSO-d_6): δ 6.43 (s, 1H), 6.35 (s, 1H), 4.30 (dd, J = 7.7, 5.0 Hz, 1H), 4.13 (m, 1H), 3.58 (s, 3H), 3.10 (m, 1H), 2.82 (dd, J = 12.4, 5.1 Hz, 1H), 2.57 (d, J = 12.4 Hz, 1H), 2.30 (t, J = 7.5 Hz, 2H), 1.61 (m, 1H), 1.53 (m, 2H), 1.45 (m, 1H), 1.33 (m, 2H) ppm.
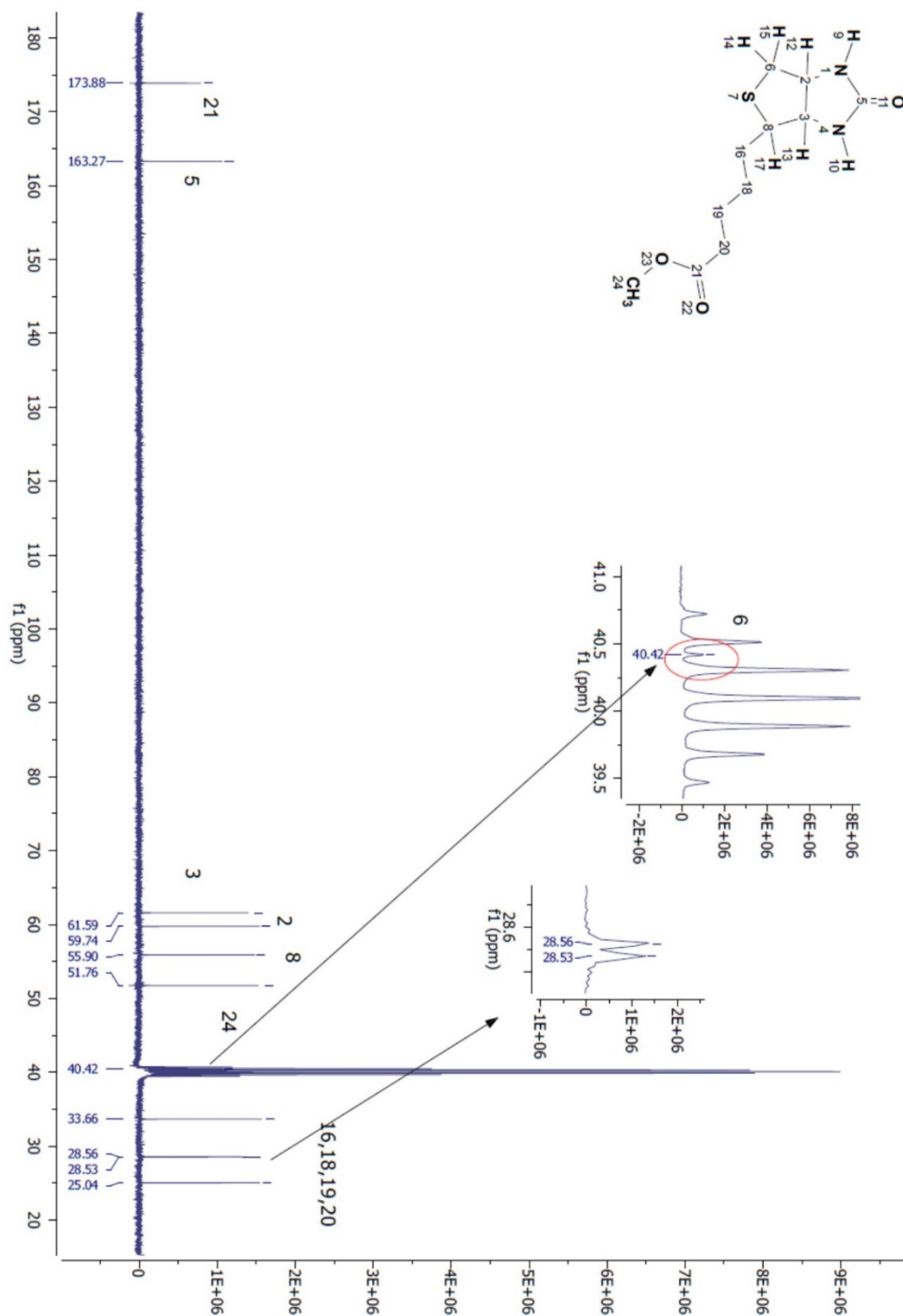
^{13}C-NMR spectrum of **compound 5'**: **^{13}C NMR** (100 MHz, DMSO-d_6): δ 173.88 (C=O), 163.27 (C=O), 61.59 (C-H), 59.74 (C-H), 55.90 (C-H), 51.76 (CH$_3$), 40.42 (C-H$_2$), 33.66 (CH$_2$), 28.56 (CH$_2$), 28.53 (CH$_2$), 25.04 (CH$_2$) ppm.

^{13}C- DEPT135 spectrum of **compound 5'**

COSY spectrum of **compound 5'**

A2.7.8 Compound 5"
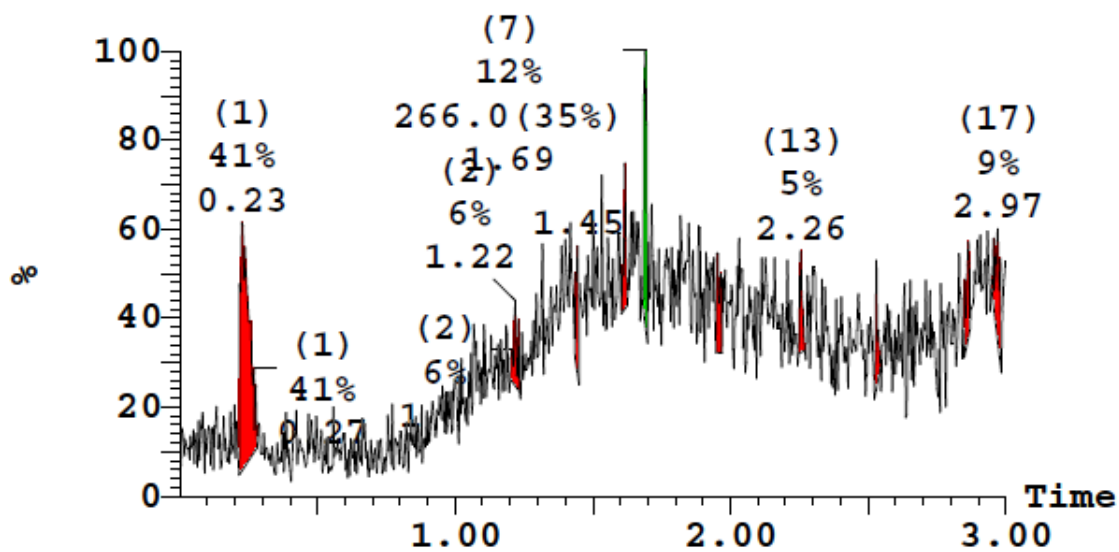

High resolution-MS spectrum of **compound 5":** HR-MS (ESI-TOF): m/z for $C_{10}H_{18}N_2O_2S^+$ [M+H]$^+$ calculated 230.32 found 230.0.
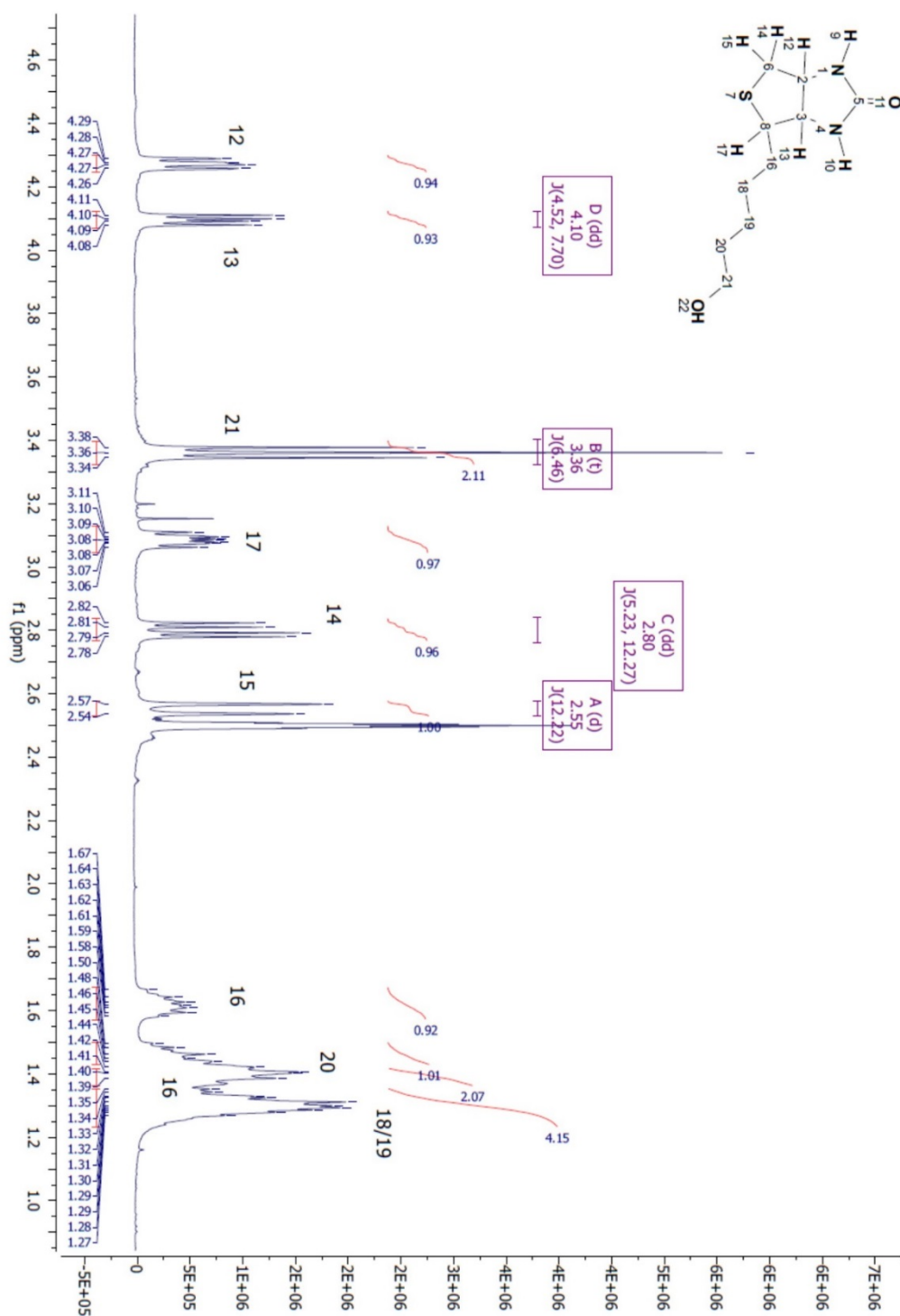
¹H-NMR spectrum of **compound 5'': ¹H NMR** (400 MHz, DMSO-d_6): δ 4.27 (m, 1H), 4.10 (dd, J= 7.70, 4.52, 1H), 3.36 (t, J = 6.5 Hz, 2H), 3.08 (m, 1H), 2.80 (dd, J = 12.27, 5.2 Hz, 1H), 2.55 (d, J = 12.2 Hz, 1H), 1.62 (m, 1H), 1.47 (m, 1H), 1.41 (m, 2H), 1.30 (m, 4H) ppm.
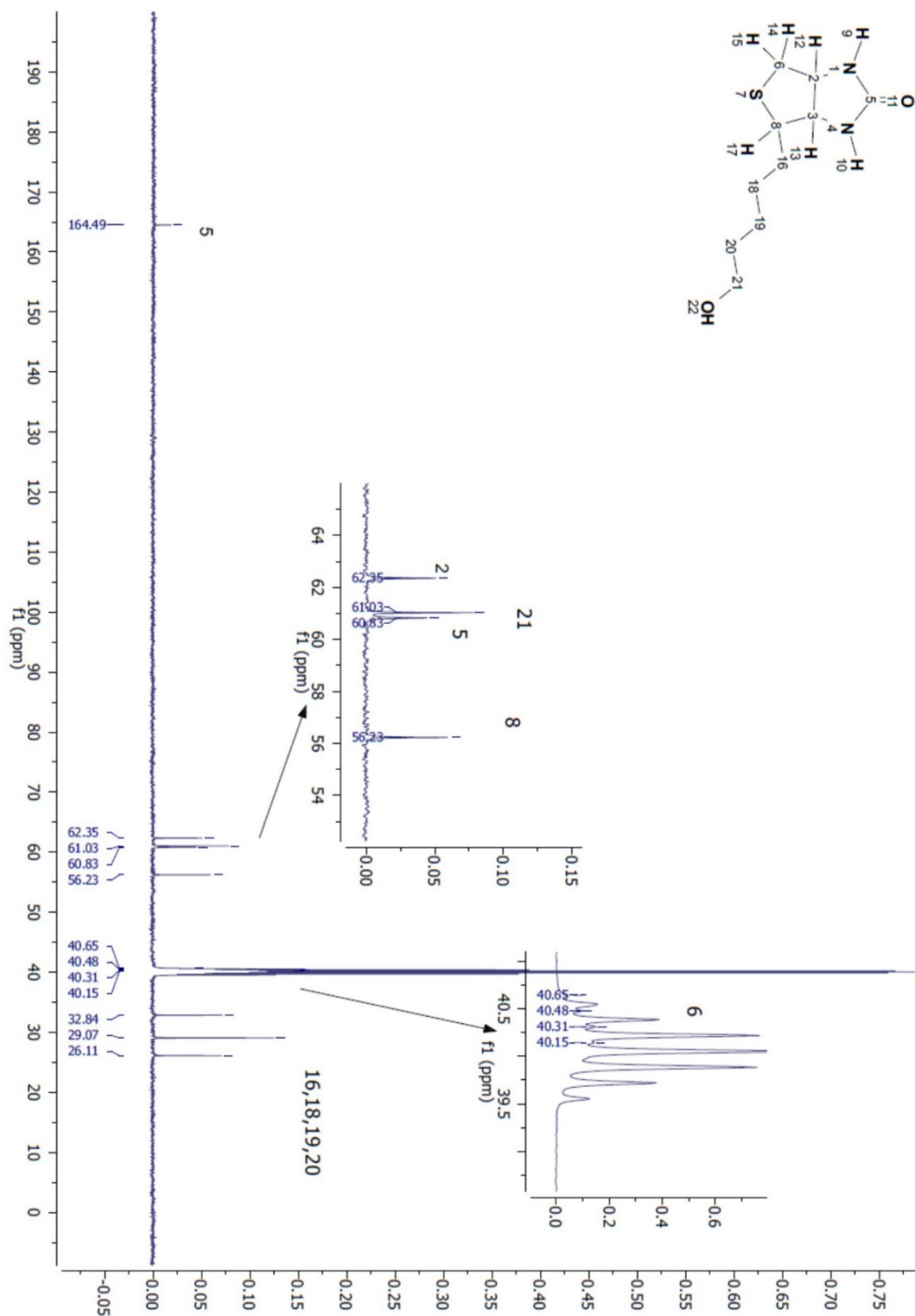
^{13}C-NMR spectrum of **compound 5":** **^{13}C NMR** (126 MHz, DMSO-d_6): δ 164.49 (C=O), 62.35 (C-H), 61.03 (CH$_2$), 60.83 (C-H), 56.23 (C-H), 40.5 (CH$_2$), 32.84 (CH$_2$), 29.07 (CH$_2$), 26.11 (CH$_2$) ppm.
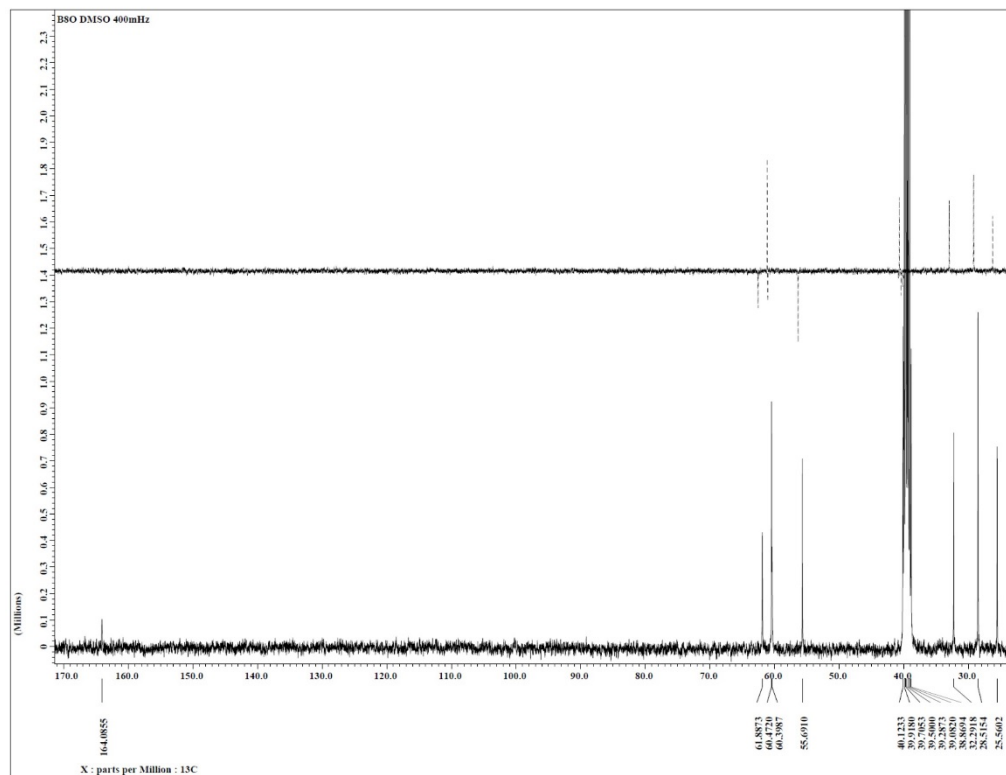
^{13}C- DEPT135 spectrum of **compound 5'':**
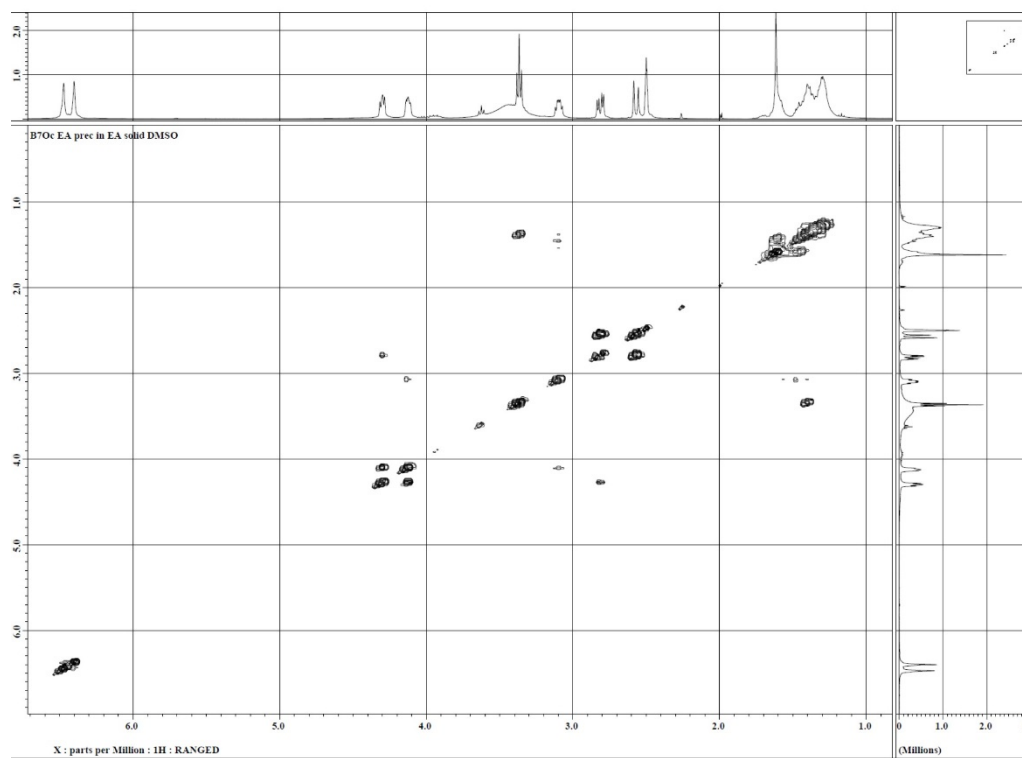
COSY spectrum of **compound 5'':**

A2.7.9 Compound 5
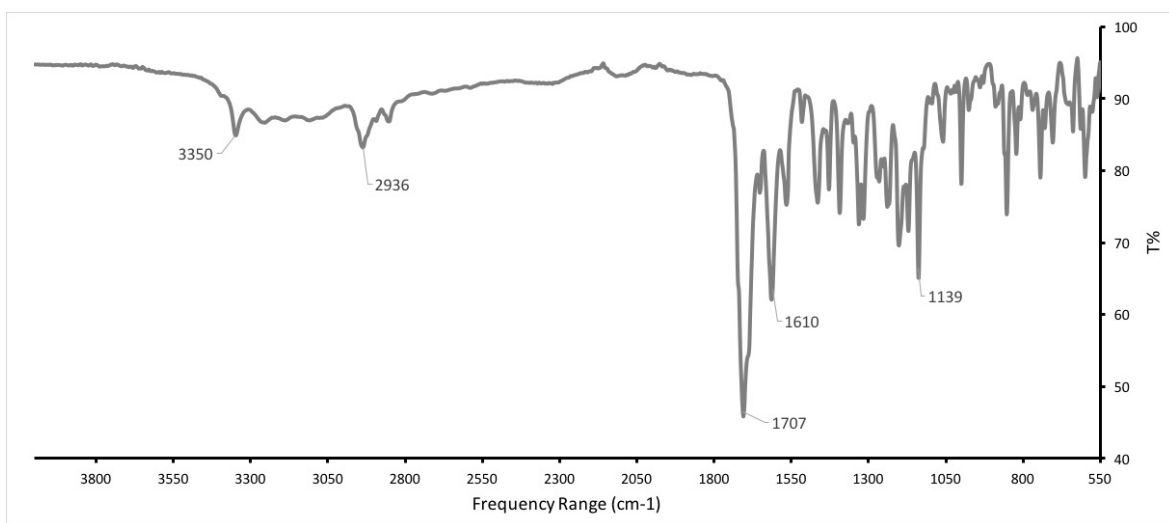
FT-IR spectrum of **compound 5**. **IR:** 3350, 2936, 1707, 1610, 1139 cm^{-1}.
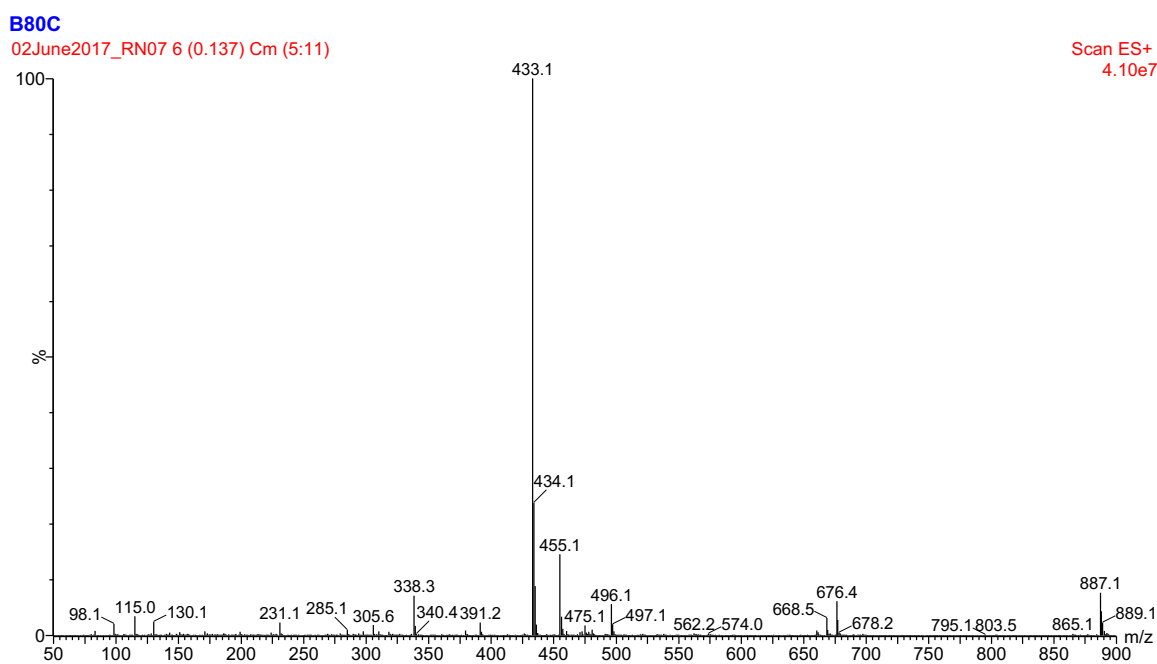
Low resolution-MS spectrum of **compound 5**: MS (ES+): m/z for $C_{21}H_{24}N_6O_2S^+$ [M+H]$^+$ calculated 432.49 found 433.1.
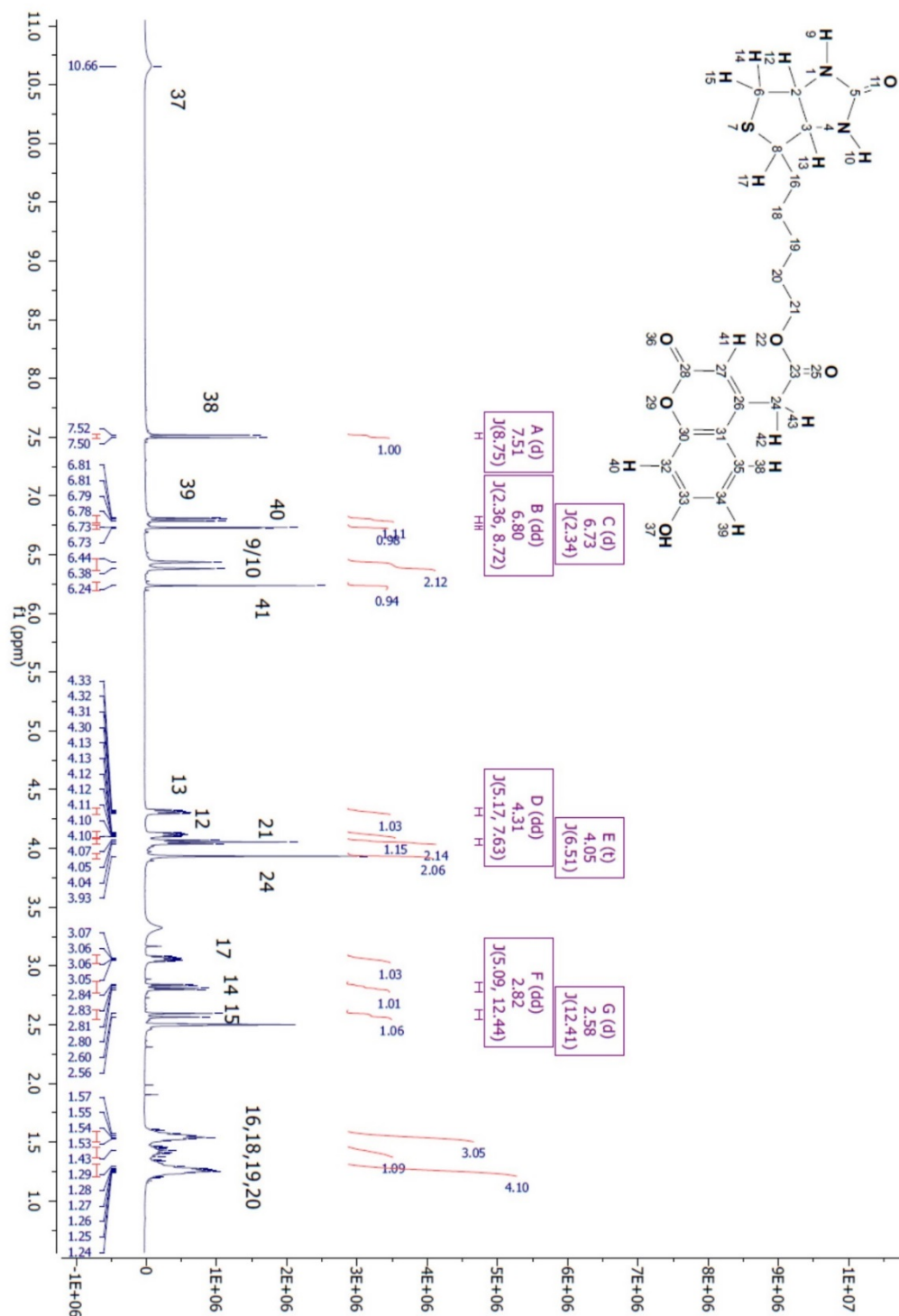
¹H-NMR spectrum of **compound 5**: **¹H NMR** (400 MHz, DMSO-d_6): δ 10.66 (s, 1H), 7.51 (d, J = 8.7 Hz, 1H), 6.80 (dd, J = 8.7, 2.4 Hz, 1H), 6.73 (d, J = 2.3 Hz, 1H), 6.44 (s, 1H), 6.38 (s, 1H), 6.24 (s, 1H), 4.31 (dd, J = 7.6, 5.2 Hz, 1H), 4.12 (m, 1H), 4.05 (t, J = 6.5 Hz, 2H), 3.39 (s, 2H), 3.06 (m, 1H), 2.82 (dd, J = 12.4, 5.1 Hz, 1H), 2.58 (d, J = 12.4 Hz, 1H), 1.54 (m, 3H), 1.45 (m, 1H), 1.25 (M, 4h) ppm.

^{13}C-NMR spectrum of **compound 5: ^{13}C NMR** 169.74 (C=O), 163.33 (C=O), 161.92 (C=O), 160.72 (Ar-OH), 155.62 (C=C), 150.23 (Ar-C), 127.24 (Ar-H), 113.60 (Ar-H), 112.65 (C=O), 111.74 (Ar-H), 102.92 (Ar-H), 65.27 (CH$_2$), 61.60 (C-H), 59.79 (C-H), 55.98 (C-H), 40 (CH$_2$), 37.56 (CH$_2$), 28.74 (CH$_2$), 28.68 (CH$_2$), 28.38 (CH$_2$), 25.86 (CH$_2$) ppm.
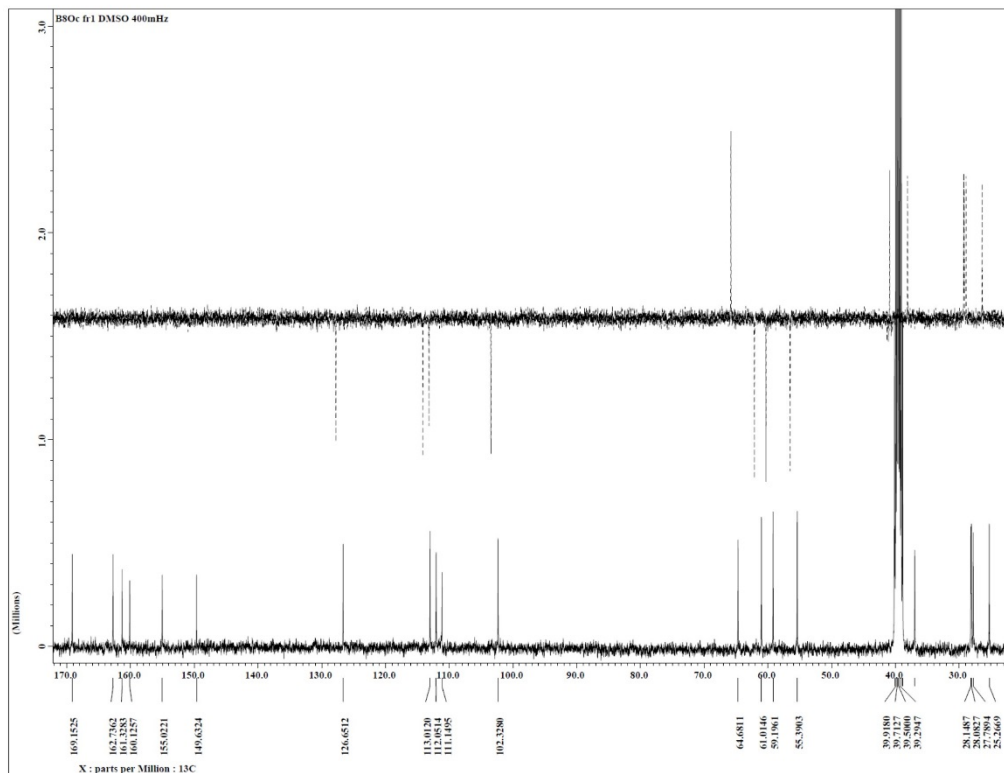
^{13}C- DEPT135 spectrum of **compound 5**
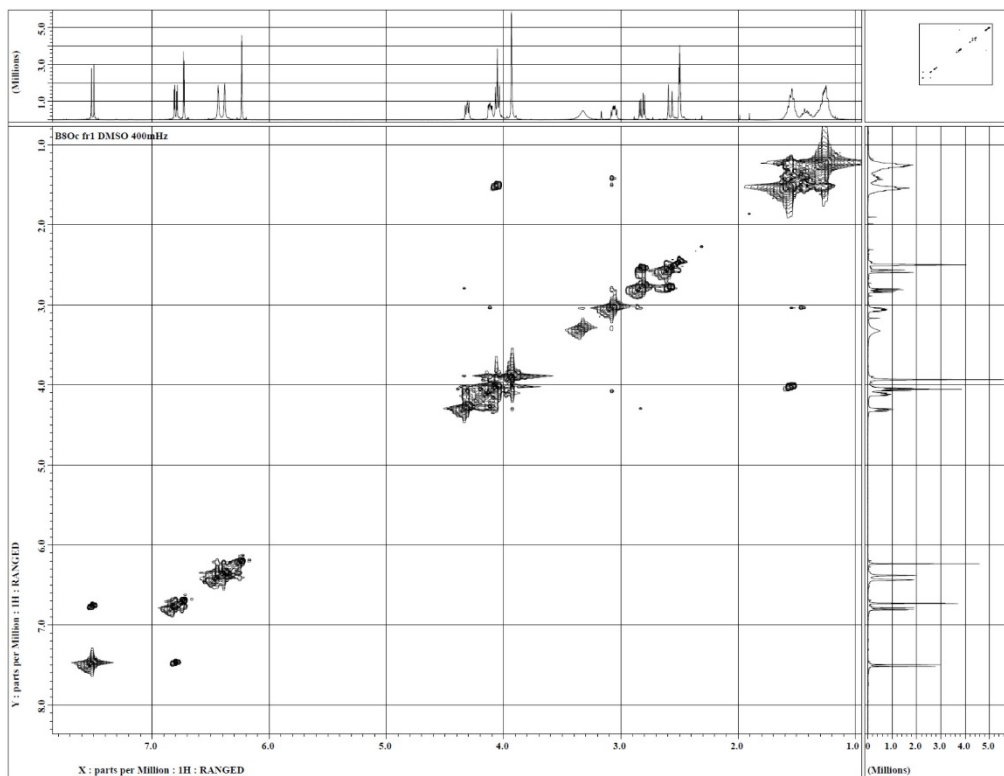
COSY spectrum of **compound 5**

A2.7.10 Compound 6'

High resolution-MS spectrum of **compound 6':** HR-MS (ESI-TOF): m/z for $C_{12}H_{28}O_2S_2{}^+$ [M+H]$^+$ calculated 266.48 found 266.0.
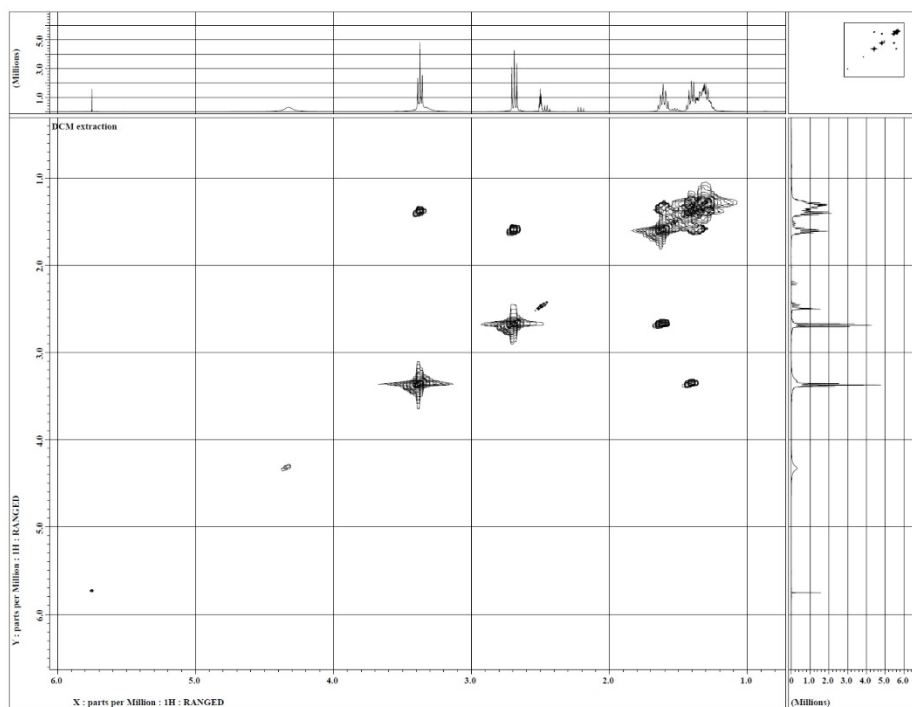
COSY spectrum of **compound 6':**
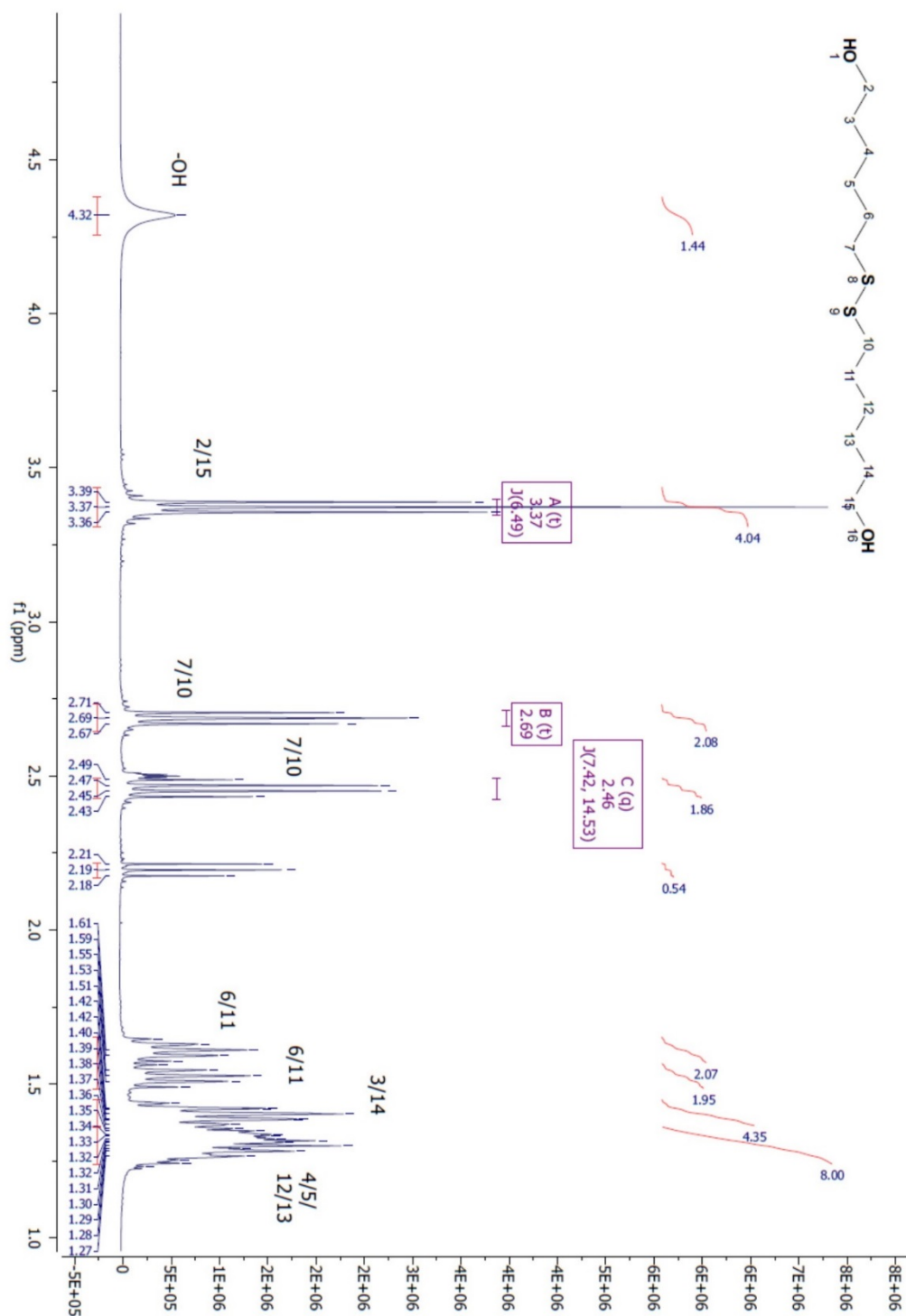
^{1}H-NMR spectrum of **compound 6'**: **^{1}H NMR** (400 MHz, DMSO-d_6): δ 4.32 (s, 2H), 3.37 (t, J = 6.5 Hz, 4H), 2.69 (t, J = 8, 2H), 2.46 (q, J = 8 Hz, 2H), 1.61 (m, 2H), 1.53 (m, 2H), 1.40 (m, 4H), 1.30 (m, 8H) ppm.
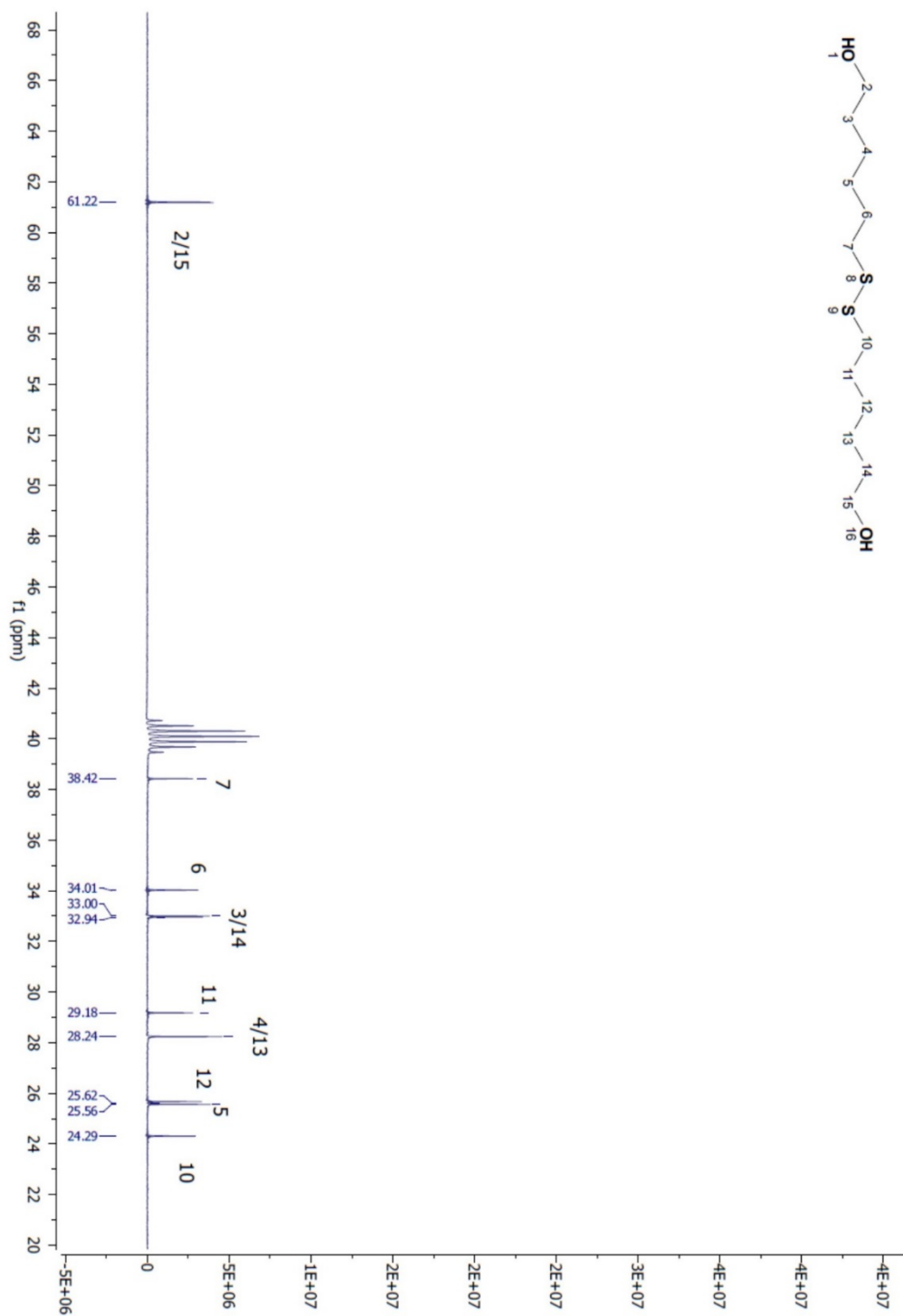
^{13}C-NMR spectrum of **compound 6'**: **^{13}C NMR** (100 MHz, DMSO-d_6): δ 61.22 (C-OH), 38.42 (CH-S-S), 34.01 (CH$_2$), 33.00 (CH$_2$), 32.94 (CH$_2$), 29.18 (CH$_2$), 28.24 (CH$_2$), 25.62 (CH$_2$), 25.56 (CH$_2$), 24.29 (-S-S-CH) ppm.
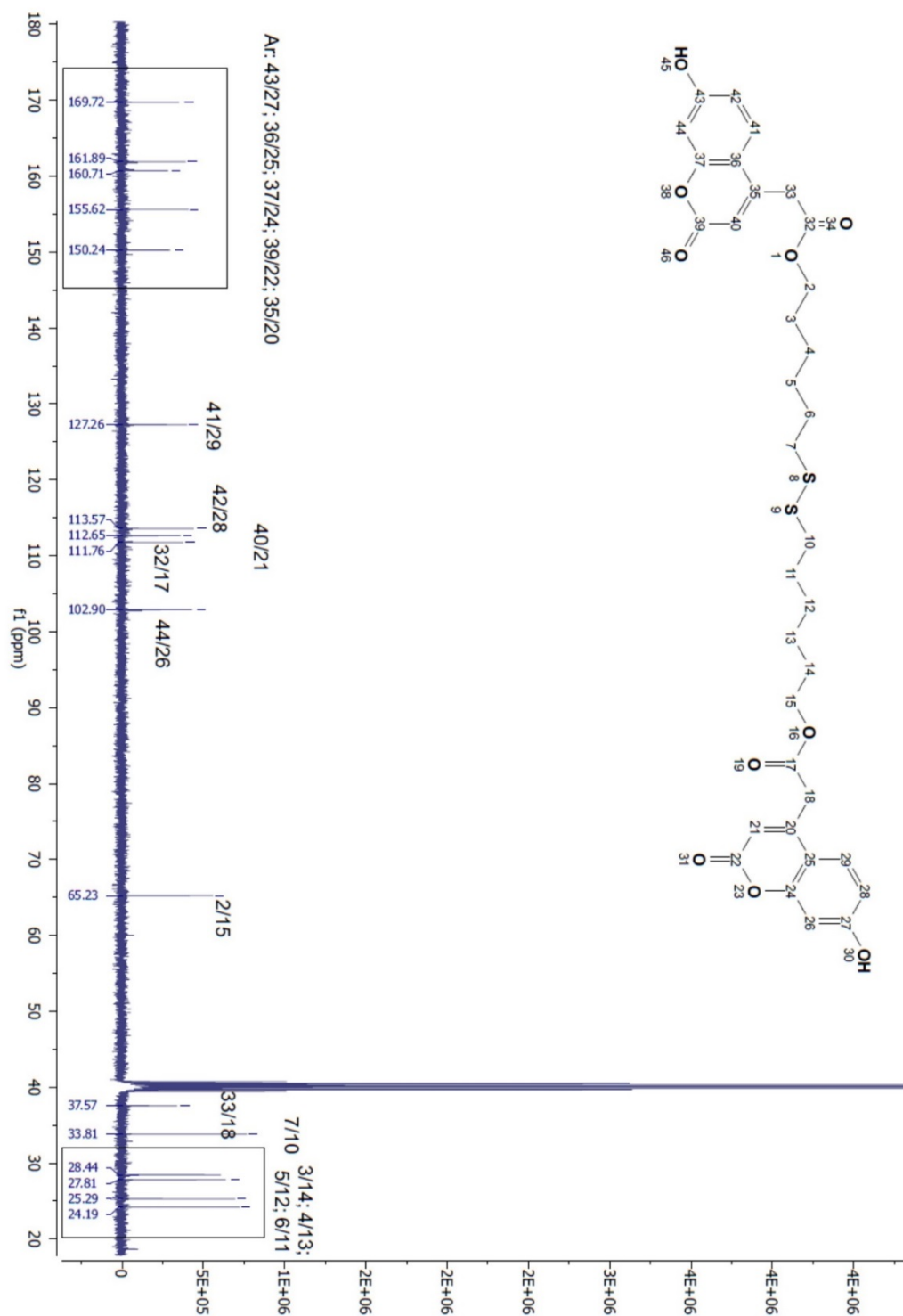
A2.7.11 Compound 6"
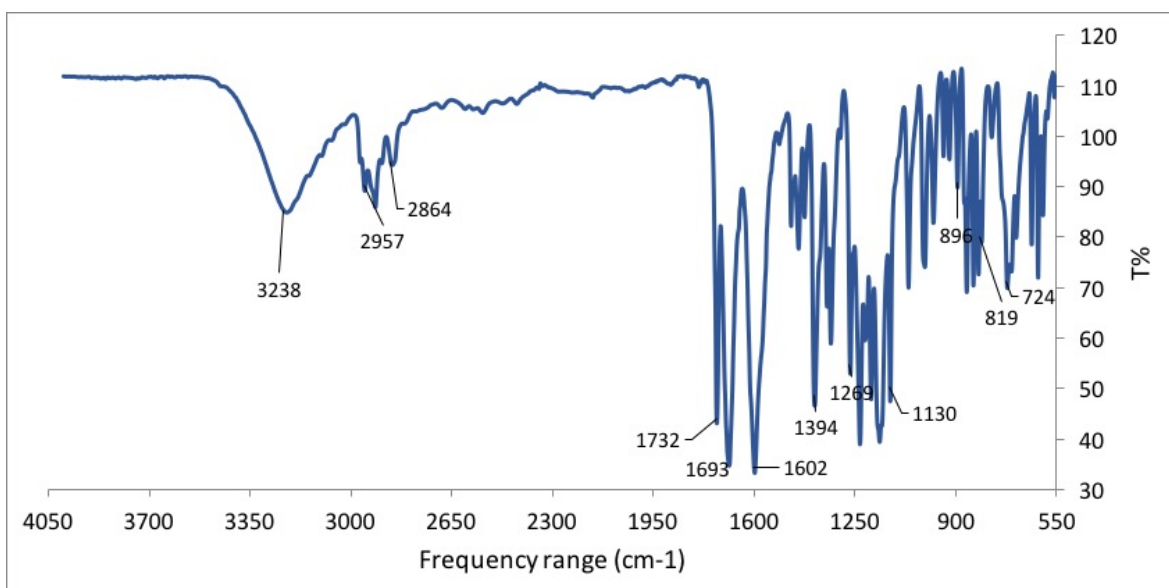
FT-IR spectrum of **compound 6". IR:** 3238, 2957-2864,1732, 1693, 1602, 1394, 1269-1130, 896-819, 724 cm^{-1}.
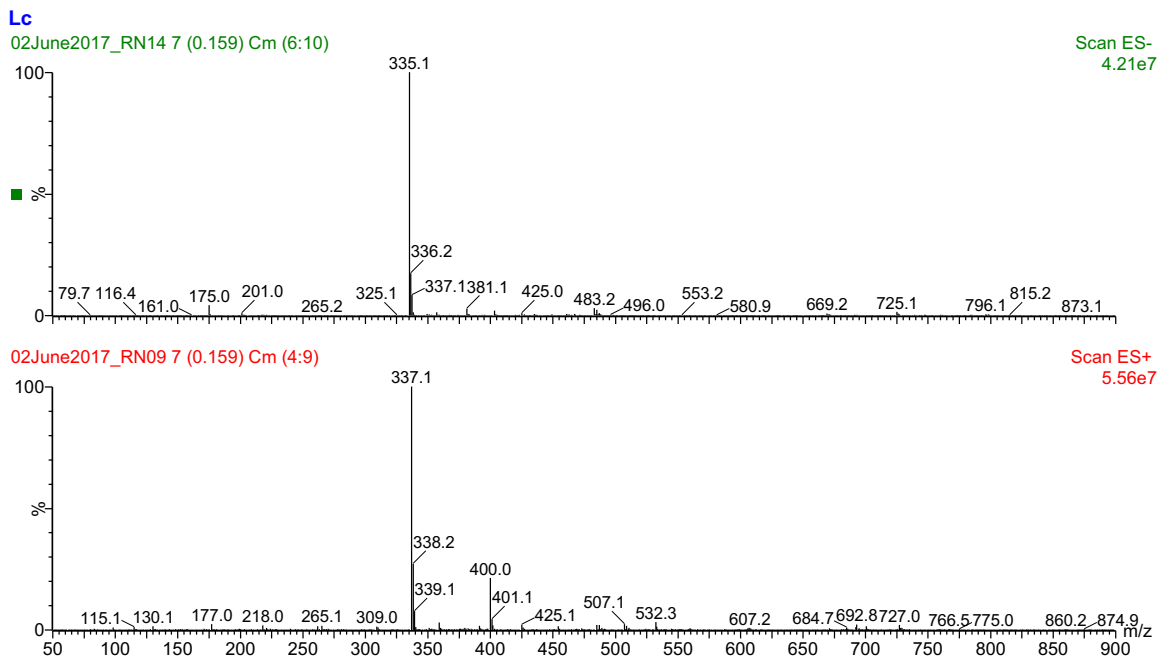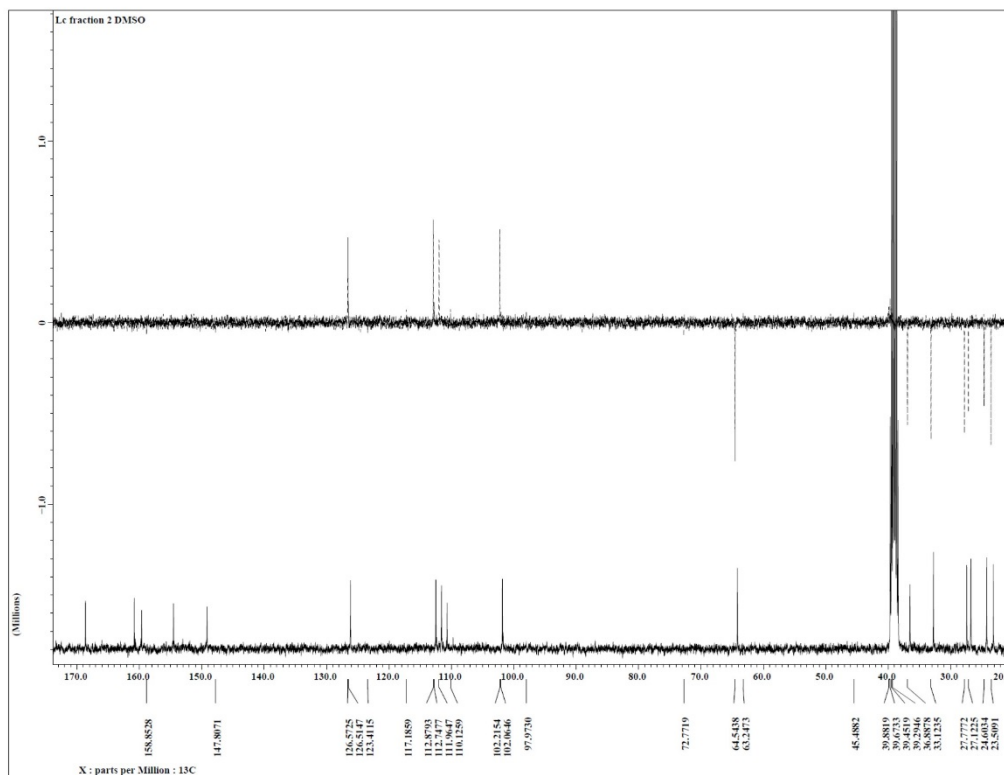

Low resolution-MS spectrum of **compound 6".** Compound 6 MS (ES^{-}): m/z 335.1 [M/2 - H]$^{+}$; MS (ES^{+}): m/z 337.1 [M/2 + H]$^{+}$.
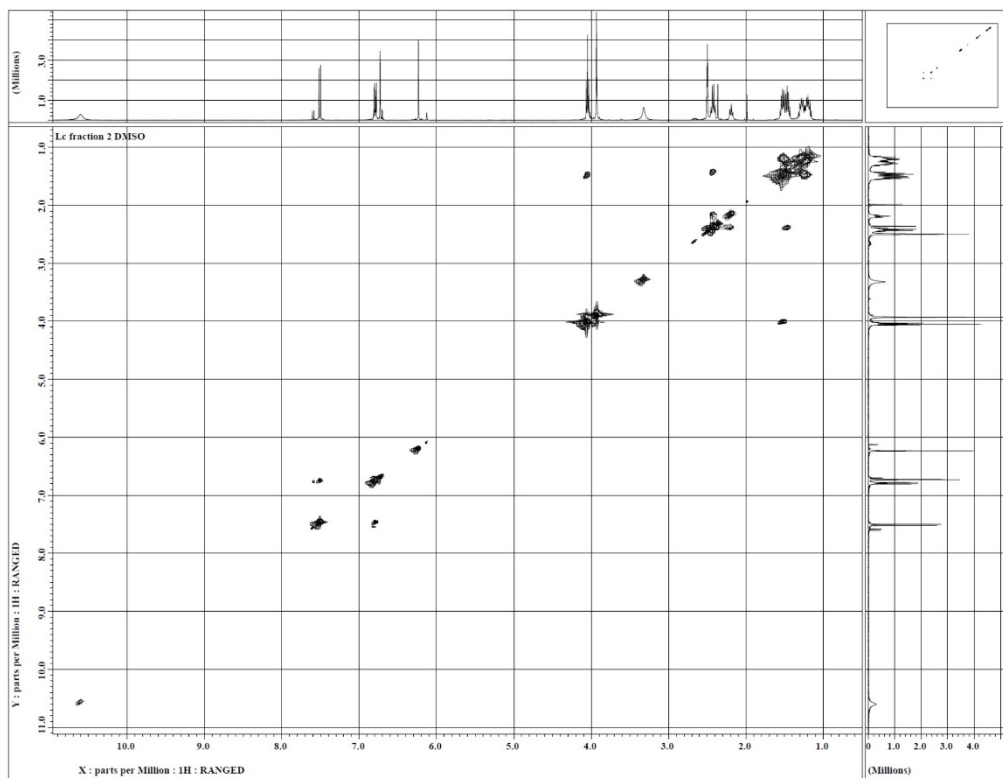
¹H-NMR spectrum of **compound 6".** **¹H NMR** (400 MHz, DMSO-d_6): 10.62 (S, 2H), δ 7.50 (d, J = 8.7 Hz, 2H), 6.78 (dd, J = 8.7, 2.3 Hz, 2H), 6.72 (d, J = 2.3 Hz, 2H), 6.23 (s, 2H), 4.05 (t, J = 4.0 Hz, 4H), 4.02 (s, 4H), 2.64 (t, J = 8.0 Hz, 4H), 1.55 – 1.51 (m, 8H), 1.28-1.17 (m, 8H) ppm.

^{13}C-NMR spectrum of **compound 6"**. **^{13}C NMR** (100 MHz, DMSO-d_6): δ 169.72 (Ar-C-OH), 161.89 (C-C), 160.71 (C-C), 155.62 (Ar-C=O), 150.24 (Ar-C-CH$_2$), 127.26 (Ar-CH-), 113.57 (Ar-CH-), 112.65 (Ar-CH-), 111.76 (-O-C=O), 102.90 (Ar-CH-), 65.23 (CH$_2$), 37.57 (Ar-CH$_2$), 33.81 (CH$_2$), 28.44 (CH$_2$), 27.81 (CH$_2$), 25.29 (CH$_2$), 24.19 (CH$_2$) ppm.
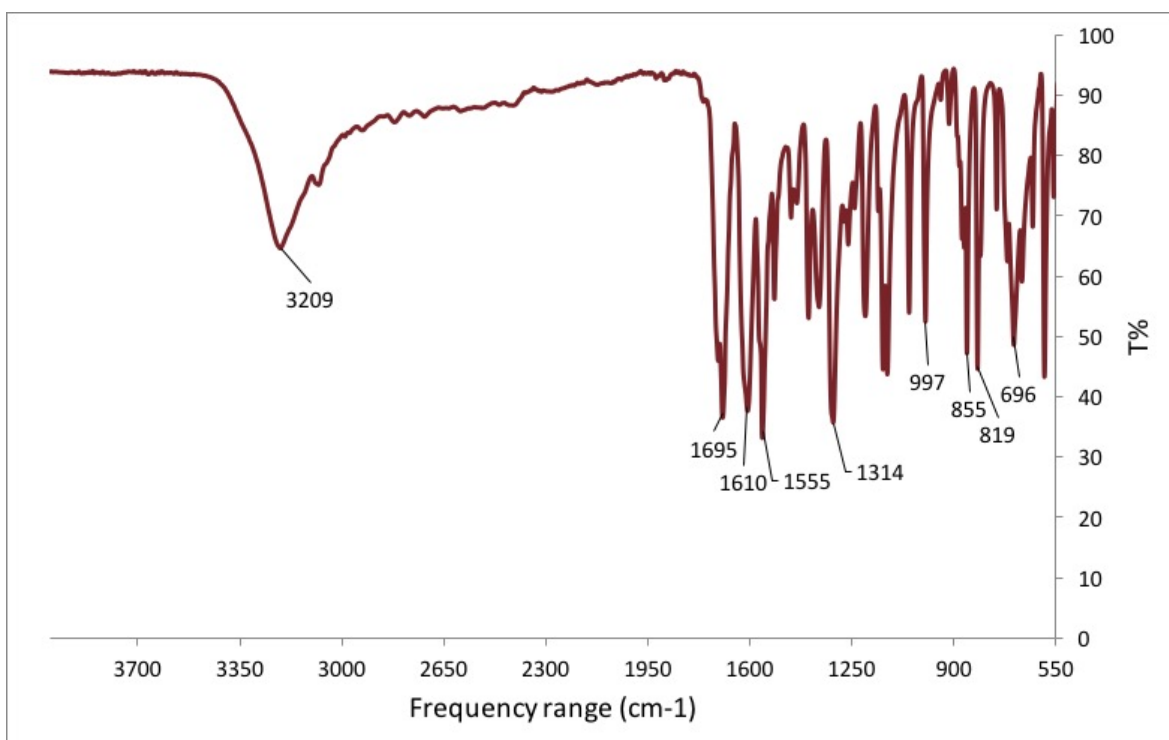
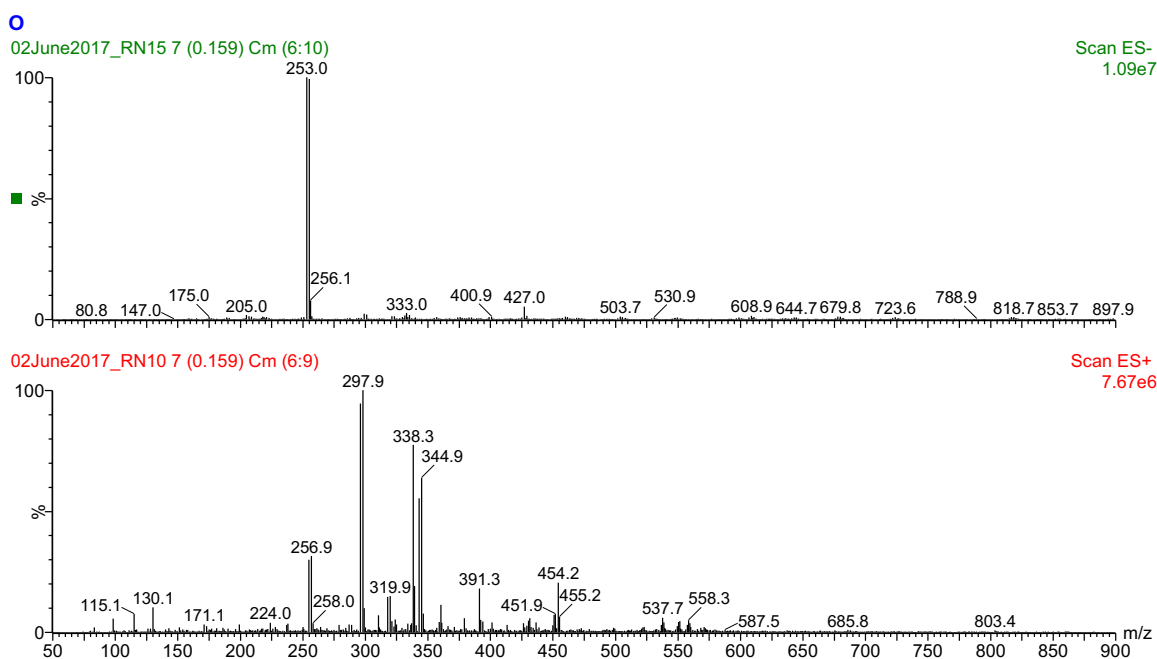^{13}C- DEPT135 spectrum of **compound 6".**

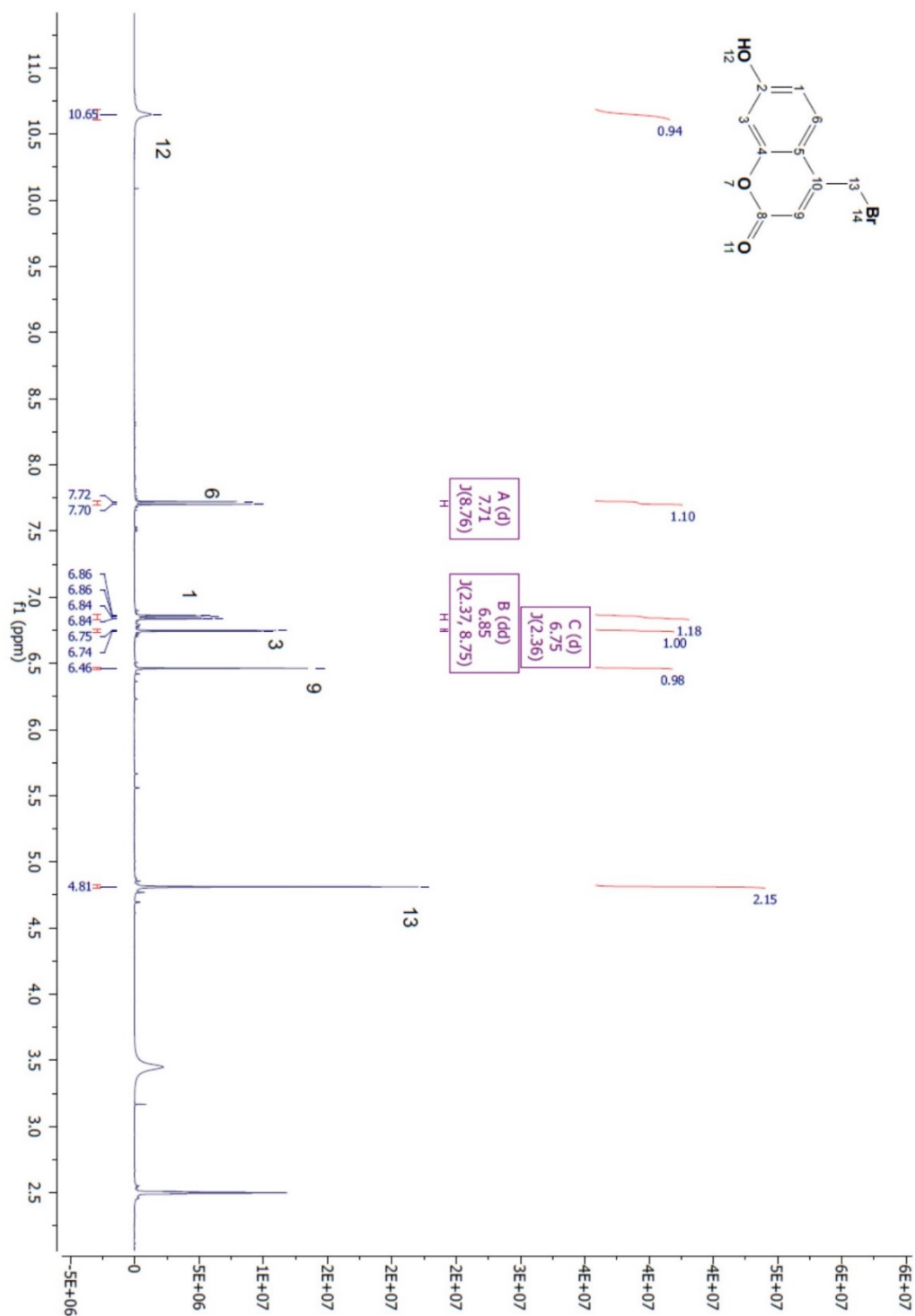COSY spectrum of **compound 6".**
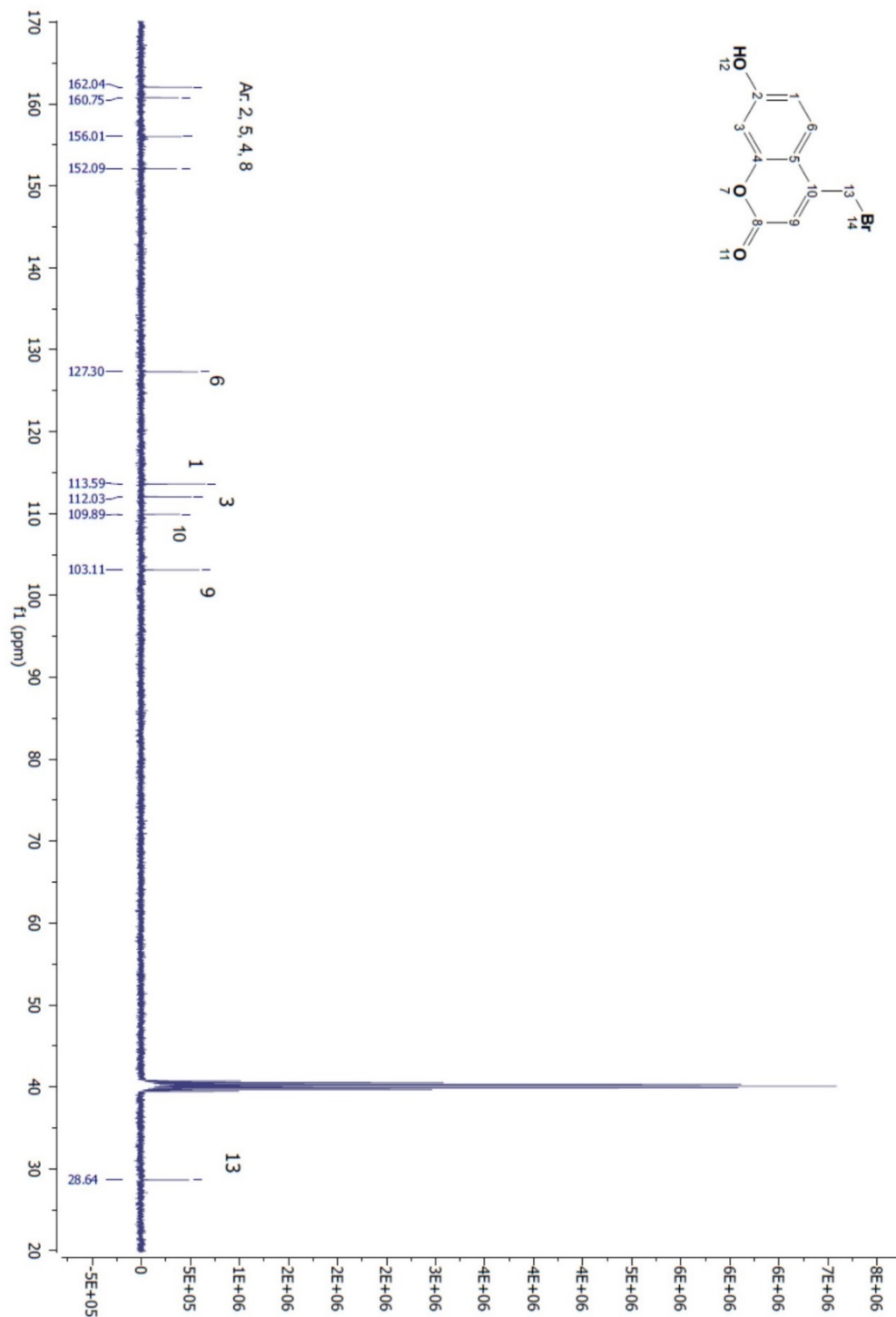
A2.7.12 Compound 7

FT-IR spectrum of **compound 7**. **IR:** 3209, 1695, 1610, 1555, 1314, 1128, 997, 855-819, 696 cm^{-1}.

Low resolution-MS spectrum of **compound 7**: MS (ES$^-$): m/z 255 [M$^-$ - 2H$^+$]; MS (ES$^+$): m/z 256.9 [M$^-$ + H$^+$].
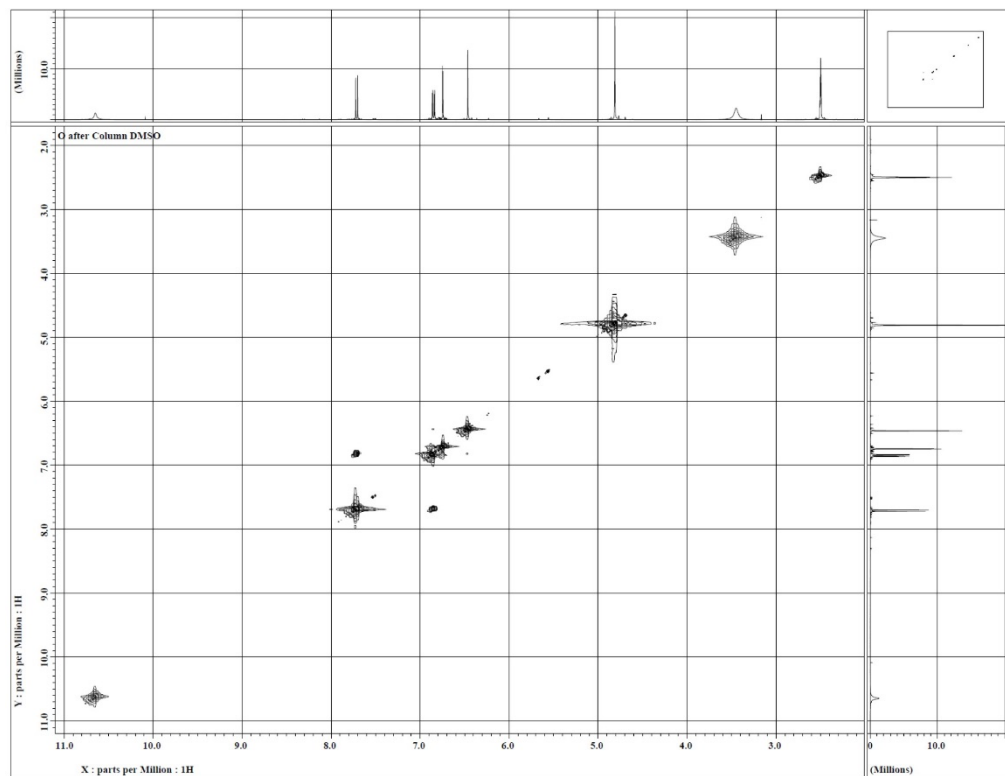
^{1}H-NMR spectrum of **compound 7**: **^{1}H NMR** (400 MHz, DMSO-d_6): δ 10.65 (s, 1H), 7.71 (d, J = 8.8 Hz, 1H), 6.85 (dd, J = 8.8, 2.4 Hz, 1H), 6.75 (d, J = 2.4 Hz, 1H), 6.46 (s, 1H), 4.81 (s, 2H) ppm.

^{13}C-NMR spectrum of **compound 7**: **^{13}C NMR** (100 MHz, DMSO-d_6): δ 162.04 (Ar-CH), 160.75 (-C-C-), 156.01 (-C-C-), 152.09 (Ar-C=O), 127.30 (Ar-CH), 113.59 (Ar-CH), 112.03 (Ar-CH), 109.89 (Ar-C-), 103.11 (Ar-CH), 28.64 (-CH$_2$-). ppm.
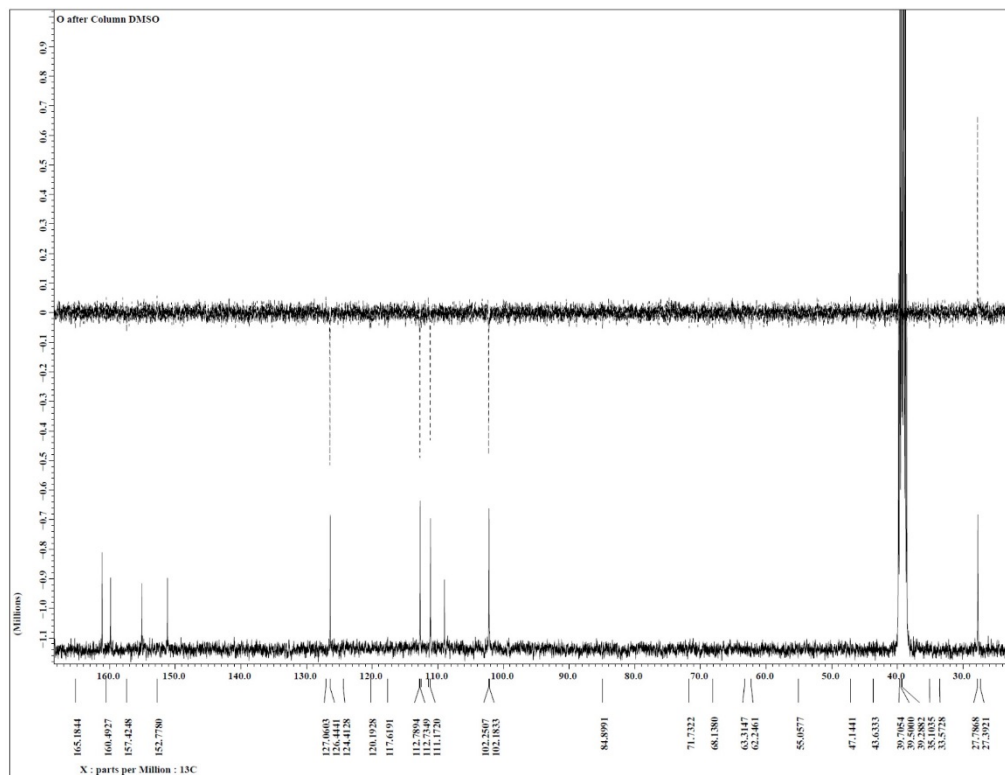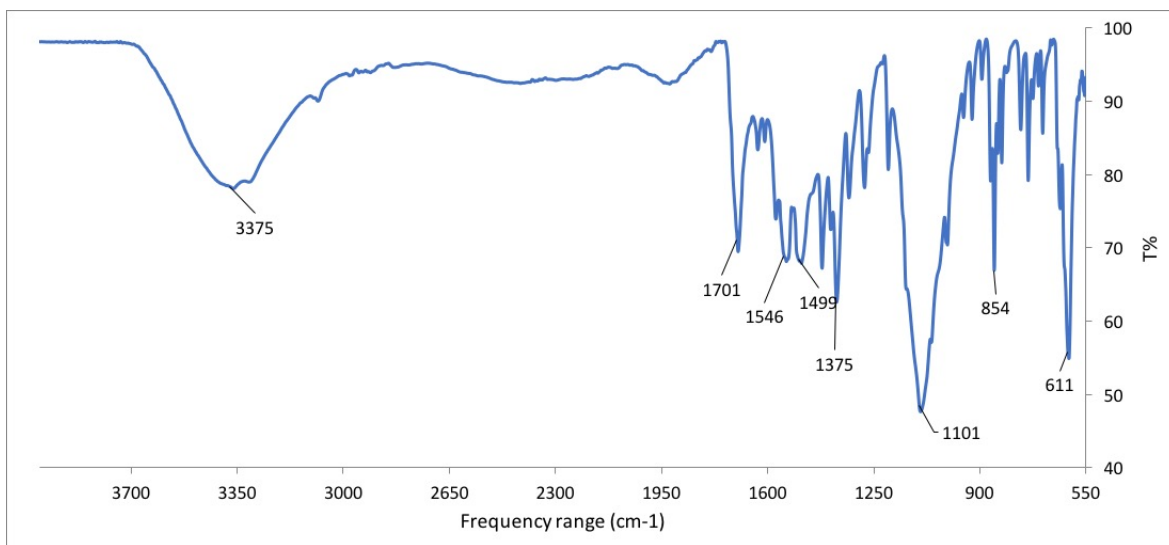
^{13}C- DEPT135 spectrum of **compound 7.**

COSY spectrum of **compound 7.**

A2.7.13 Compound 4-MU

FT-IR spectrum of compound **4-MUD. IR:** 3375, 1701, 1546, 1499, 1375, 1101, 854, 611 cm^{-1}

Mp: 211°C (from literature).
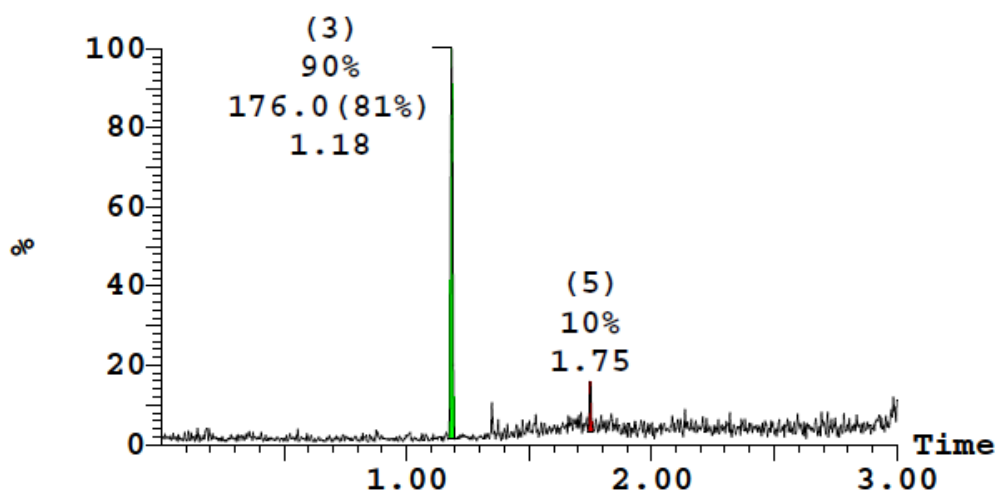
High resolution-MS spectrum of compound **4-MUD**: **HR-MS (ESI-TOF)**: m/z for $C_{10}H_8O_3^+$ [M+H]$^+$ calculated 176.17, found 176.0.
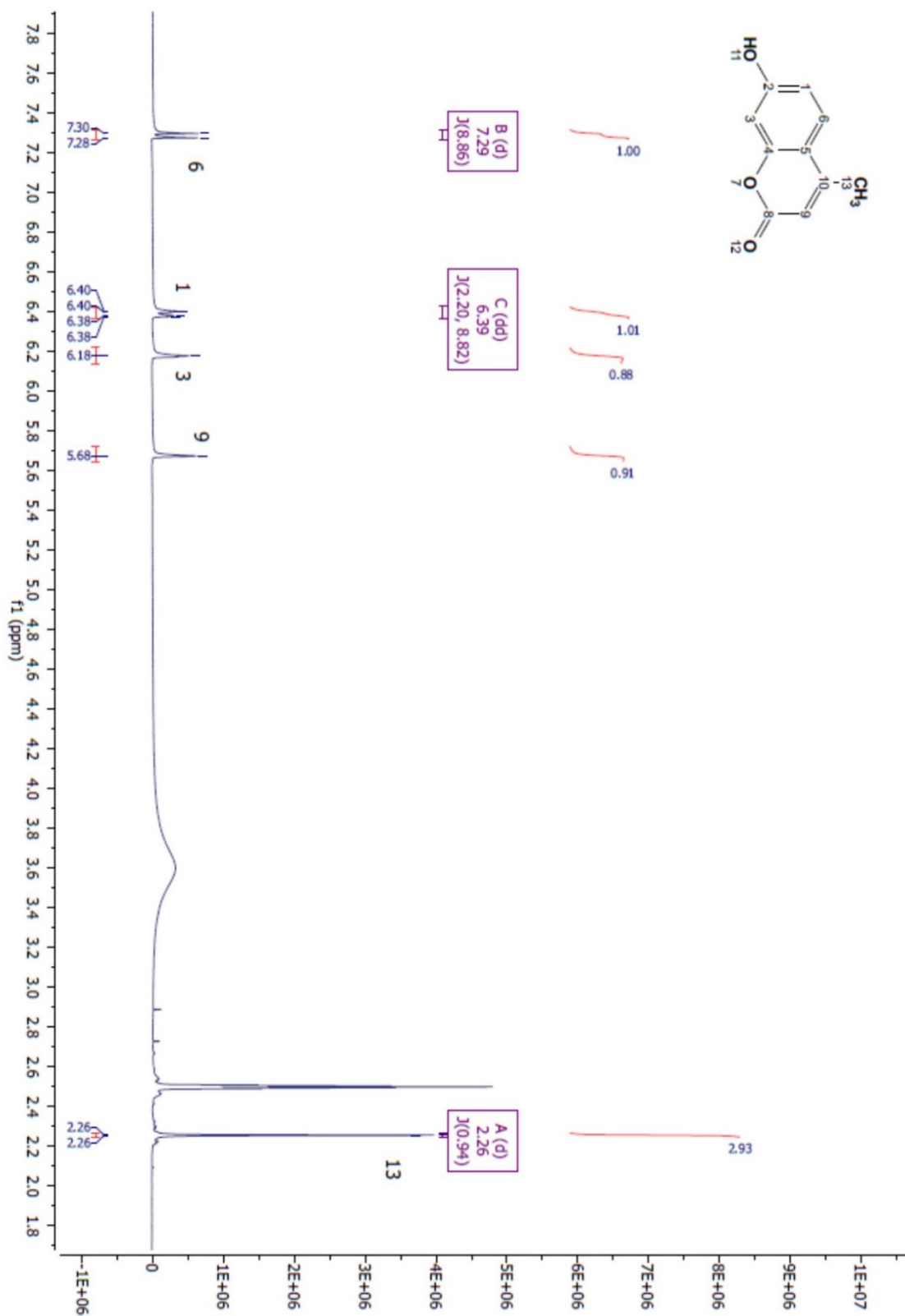
¹H-NMR spectrum of **4-MU**: **¹H NMR** (400 MHz, DMSO-d_6): δ 7.29 (d, J = 8.86, 1H), 6.39 (dd, J = 8.82, 2.20, 1H), 6.18 (s, 1H), 5.68 (s, 1H), 2.26 (s, 3H).
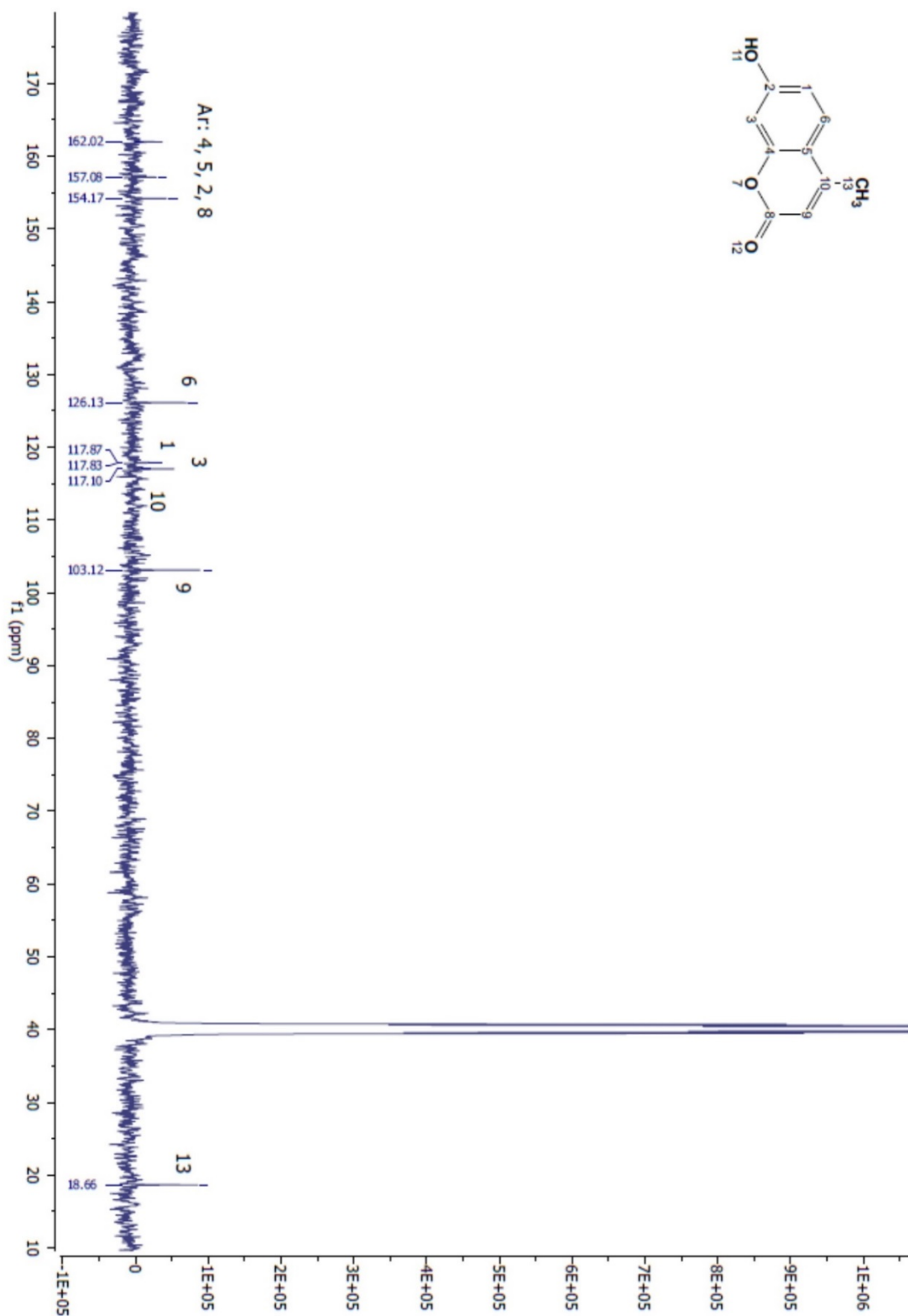
^{13}C-NMR spectrum of **4-MU. ^{13}C NMR** (100 MHz, DMSO-d_6): δ 162.02 (Ar-CH), 157.08 (-C-C-), 154.17 (-C-C-), 126.13 (Ar-CH), 117.87 (Ar-CH), 117.83 (Ar-CH), 117.10 (Ar-C-CH$_3$), 103.12 (Ar-CH), 18.66 (-CH$_3$) ppm.

A2.7.14 Compound 9 (β-4-MUD)

4-AAU
7-hydroxy-4-coumarin acetic acid

1

1a

9/ -4-MUD

Synthesis of compound 9 (β-4-MUD)

Synthesis of methyl 2-(7-hydroxy-2-oxo-2H-chromen-4-yl)acetate; **_(7-hydroxy-4-coumarin methoxy acetic acid)(1):_** 7-hydroxy-4-coumarin acetic acid 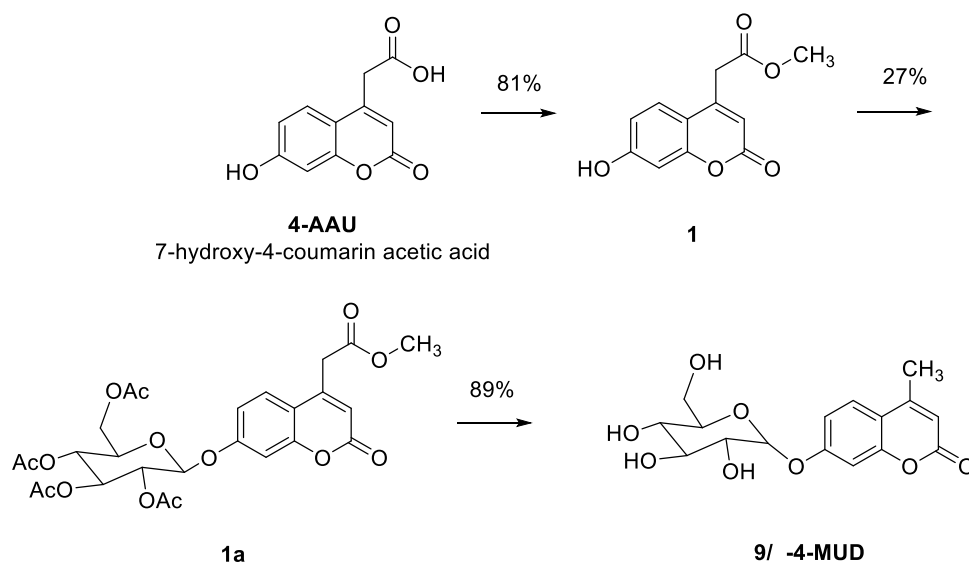(1 g, 4.54 mmol) was dissolved in methanol (200 mL). Thionyl chloride (1.47 ml) was added under stirring at 0°C for a while, then at room temperature. The reaction was left react overnight. Next day, the solvent was evaporated under vacuum and the received residue was dissolved in EA solid immediately formed. After a few hours in the fridge the solid was filtered and dried under vacuum overnight reaching compound **1** as pale yellow solid (0.86 g, 81%, MW 234.18 gmol^{-1}). **^{1}H NMR** (400 MHz, DMSO-d_6): δ 3.64 (s, 3H), 3.95 (s, 2H), 6.24 (s, 1H), 6.73 (d, J = 2.3 Hz, 1H), 6.81-6.78 (q, 1H), 7.50 (d, J = 8.7 Hz, 1H), 10.6 (s, 1H). **^{13}C NMR** (100 MHz, DMSO-d_6): δ 37.21 (-CH$_2$-), 52.73 (-CH$_3$), 102.92 (CH-Ar), 111.76 (C=O), 112.73 (CH-Ar), 113.62 (CH-Ar), 127.22 (CH-Ar), 150.08 (-C-OH), 155.56 (C-Ar), 160.61 (C-Ar), 161.84 (C-Ar), 170.34 (C-Ar) ppm.

Synthesis of (2R,3R,4S,5R)-2-(acetoxymethyl)-6-((4-(2-methoxy-2-oxoethyl)-2-oxo-2H-chromen-7-yl)oxy)tetrahydro-2H-pyran-3,4,5-triyl triacetate (7-aceto-β-glucopyranoseide-4-coumarin acetyl methoxyde) (1') : compound **1** (0.86 g, 3.68 mmol) was dissolved in acetone (20 ml) and a NaOH 1M solution was added (4.5 ml). After 15 minutes the aceto-α-glucopyranoside-bromide (1.8 g, 4.5 mmol) was dissolved in acetone (50 mL) and added to the reaction dropwise over 30 minutes in the dark. The reaction was left react for 24 hours under inert atmosphere in dark. After 24 hours the

solvent was removed under vacuum and the water layer (50 mL) was extracted five times with chloroform (50 mL). The combined organic phases were distilled under vacuum to obtain a brown oil, which was suspended in EA and after sonication the compound precipitated. After filtration, the product (1') was isolated as pale yellow solid (0.639 g, 27%, MW 564.18 gmol^{-1}). **^{1}H NMR** (400 MHz, DMSO-d_6): δ 1.98 (s, 3H), 2.02(s, 9H), 3.65 (s, 3H), 4.02 (s, 2H), 4.13-4.08 (q, 1H), 4.17-4.22 (dd, ^{2}J = 12.3, ^{3}J = 5.8 Hz, 1H), 4.33 (m, ^{2}J = 10.2, ^{2}J = 5.8 , 2.5 Hz, 1H), 5.0-5.05 (m, 1H), 5.14-5.08 (m, 1H), 5.44 – 5.37 (m, 1H), 5.73 (d, J = 7.93, Hz, 1H), 6.99 (dd, ^{2}J = 8.9, ^{3}J = 2.5 Hz, 1H), 6.41 (s, 1H), 7.01-6.98 (dd, ^{2}J = 2.50, ^{3}J = 8.85 Hz, 1H), 7.08 (m, J = 2.5 Hz, 1H), 7.68 (d, J = 2.5 Hz, 1H). **^{13}C NMR** (100 MHz, DMSO-d_6): δ 20.87 (-CH$_3$), 37.16 (-CH$_2$-), 52.77 (-CH$_3$), 62.19 (-CH$_2$-), 68.5-72.47 (C-Glu), 97.08 (C-Glu), 103.98 (Ar-CH), 114.03 (C=O), 114.65 (Ar-CH), 114.90 (Ar-CH), 127.53 (Ar-CH), 149.72 (Ar-C), 155.05 (Ar-C), 159.38 (Ar-C), 160.26 (Ar-C), 169.69 (C-Glu), 169.90 (C=O), 170.11 (C=O), 170.17 (C=O), 170.56 (C=O) ppm.

Synthesis of 4-methyl-7-(((2R,3S,4R,5R,6R)-4,5,6-trihydroxy-2-(hydroxymethyl)tetrahydro-2H-pyran-3-yl)oxy)-2H-chromen-2-one **(9; β-4-MUD):** compound **1'** (0.415 g, 0.73 mmol) was suspended in dried methanol (30 mL) and stirred for a couple of minutes under dinitrogen atmosphere. Sodium methoxide (0.238 g, 4.4 mmol) was solubilised in dried methanol (10 mL) and added to the reaction. After 4 h of stirring under nitrogen, the solution was neutralised and concentrated under vacuum. The crude was precipitated in EtOH reaching compound **9** as pale yellow solid (0.22 g, 89%, MW 338.10 gmol^{-1}). **^{1}H NMR** (400 MHz, DMSO-$d6$) δ 7.71 (d, J = 9.45 Hz, 1H), 7.05 (s, 1H), 7.02 (d, J = 2.44 Hz, 1H), 6.25 (s, 1H), 5.39 (d, J = 4.39 Hz, 1H), 5.14 (d, J = 4.49 Hz, 1H), 5.07 (d, J = 5.42 Hz, 2H), 5.03 (d, J = 7.32, 1H), 4.59 (t, J = 5.64 Hz, 1H), 3.72 (dd, ^{2}J = 4.69, ^{3}J = 10.25, 1H), 3.46 (m, 1H), 3.43 (m, J = 7.47 Hz, 2H), 3.29 (m, 2H), 2.41 (s, 3H). **^{13}C NMR** (101 MHz, DMSO-$d6$) δ 160.69 (C-C), 160.63 (C-C), 154.94 (C-Ar), 153.87 (C-Ar), 126.94 (Ar-CH), 114.61 (Ar-CH), 113.92 (C=O), 112.23 (Ar-C$_H$-CH3) 103.75 (Ar-CH), 100.54 (C-Glu), 77.68 (C-Glu), 77.02 (C-Glu), 73.66 (C-Glu), 70.17 (C-Glu), 61.18 (-CH$_2$-), 18.66 (-CH$_3$) ppm. **MS(ES-):** m/z 337.1 [M - H]$^+$ **IR**: 3378, 3280, 1690, 1608, 1391, 1024, 837 cm^{-1}. **M.p.:** 185-190°C (from literature).
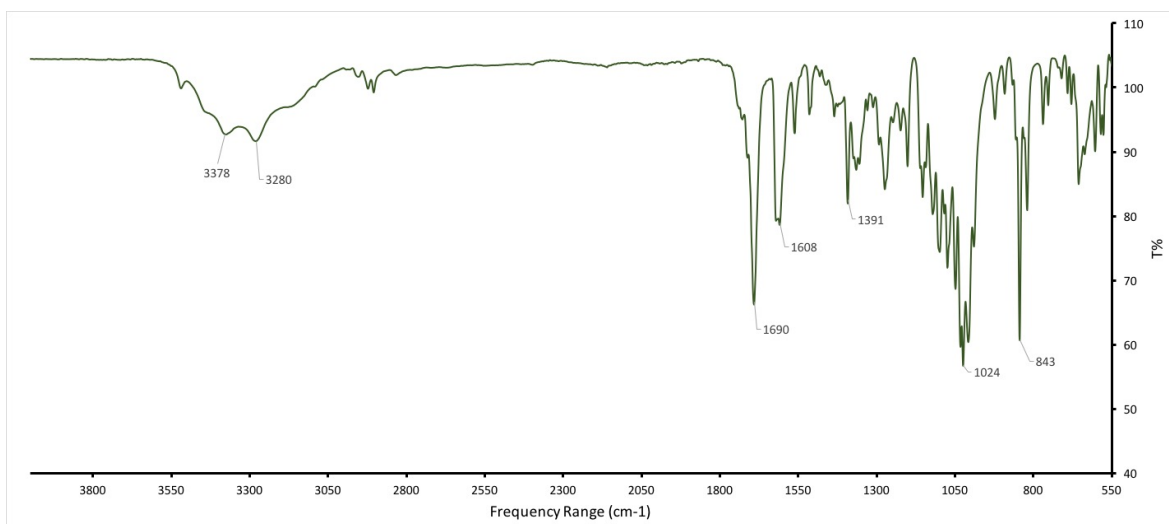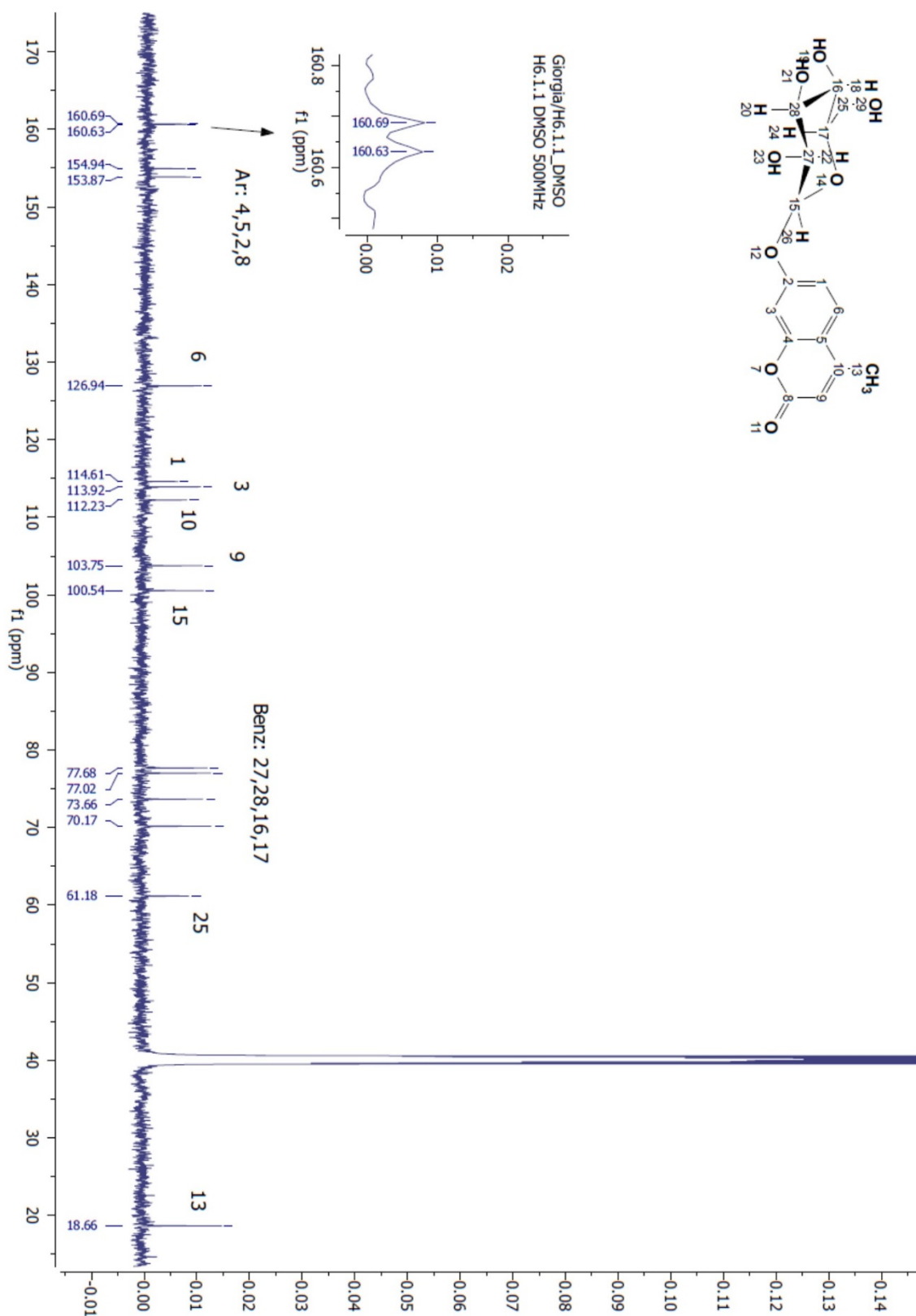
FT-IR spectrum of **compound 9 (β-4-MUD): IR**: 3378, 3280, 1690, 1608, 1391, 1024, 843 cm^{-1}
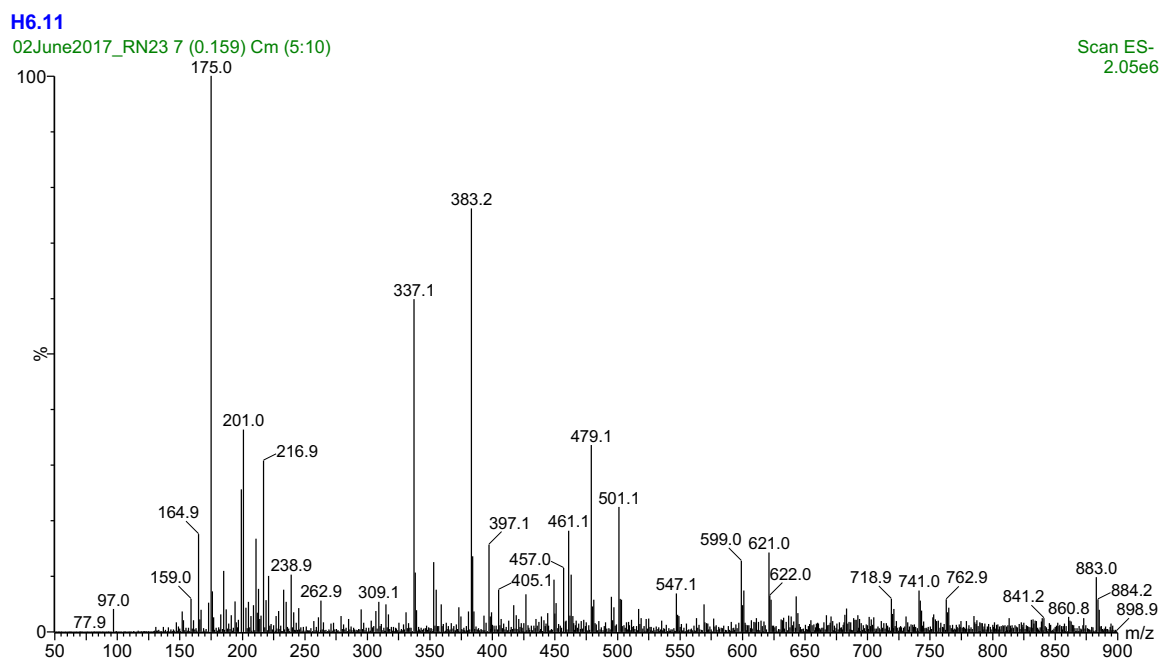
Low resolution-MS spectrum of **compound 9 (β-4-MUD):** MS(ES-): m/z 337.1 [M - H]$^+$
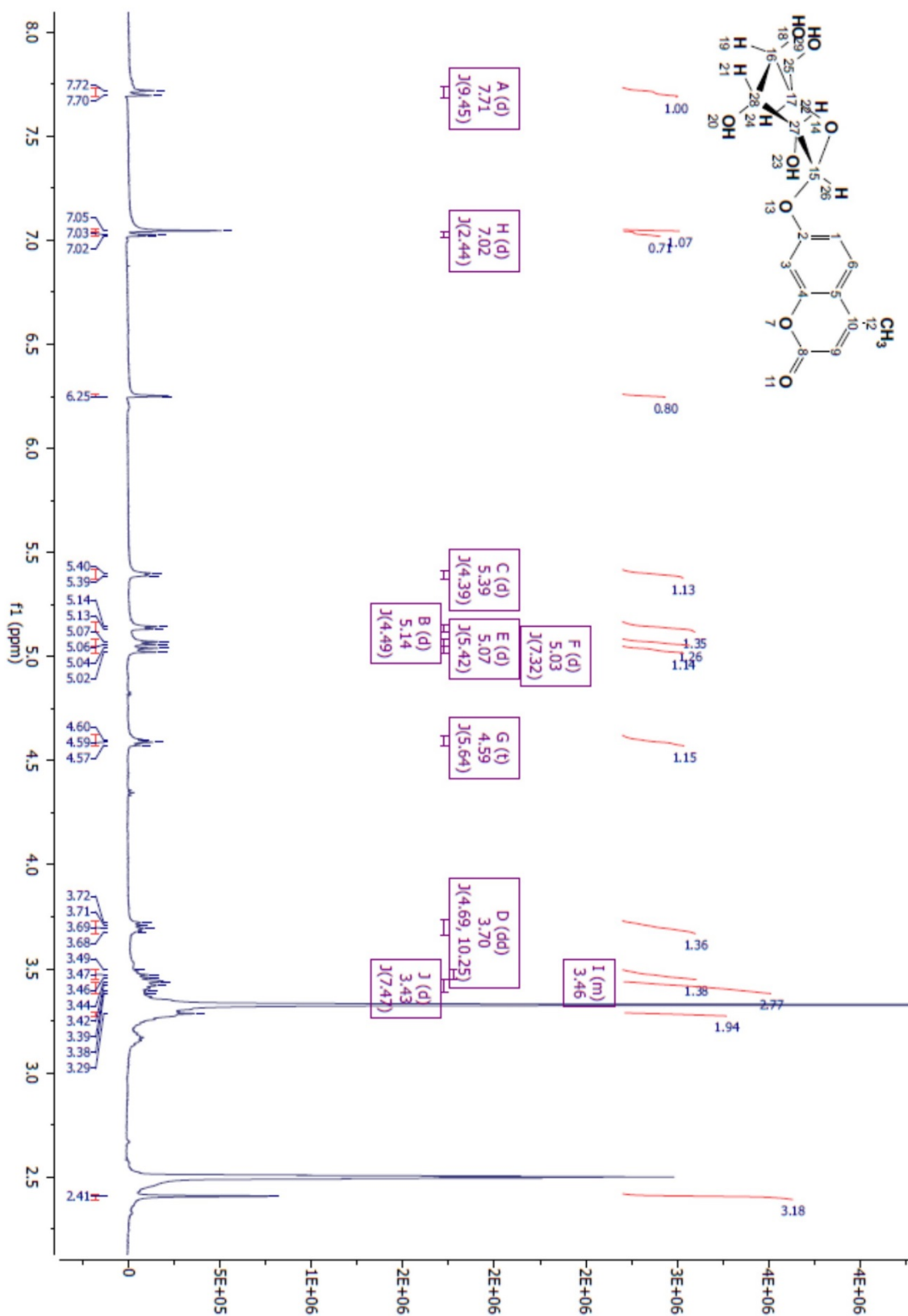
^{1}H-NMR spectrum of compound **9 (β-4-MUD):**

^{13}C-NMR spectrum of compound **9 (β-4-MUD).**

A3.1 Example of calculation of number of dye per NPs

	TEM Ø (nm)	µM FITC per 200 µg of SiNPs		
FITC-SiNP$_{100TEOS}$	72 ± 8	1.107	0.580	0.981
FITC-SiNP$_{75TEOS}$	79 ± 16	1.282	0.646	1.001
FITC-SiNP$_{50}$	80 ± 13	1.019	0.475	0.950
FITC-SiNP$_{75ETEOS}$	58 ± 20	0.805	0.602	0.827
FITC-SiNP$_{100ETEOS}$	50 ± 31	0.295	0.298	0.217

mol FITC per 200 µg of SiNPs		
1.11E-09	5.80E-10	9.81E-10
1.28E-09	6.46E-10	1.00E-09
1.02E-09	4.75E-10	9.50E-10
8.05E-10	6.02E-10	8.27E-10
2.95E-10	2.98E-10	2.17E-10

Avogadro's number = 6.02E+23

	number of molecule of FITC per 200 µg of SiNPs		
FITC-SiNP$_{100TEOS}$	6.669E+14	3.495E+14	5.909E+14
FITC-SiNP$_{75TEOS}$	7.719E+14	3.890E+14	6.027E+14
FITC-SiNP$_{50}$	6.137E+14	2.859E+14	5.723E+14
FITC-SiNP$_{75ETEOS}$	4.850E+14	3.625E+14	4.979E+14
FITC-SiNP$_{100ETEOS}$	1.779E+14	1.795E+14	1.306E+14

density of 1 SiNP = 2.4 g/cm^3
M = dV

	Volume of 1 SiNPs	Mass of 1 SiNPs (µg)	number SiNPs in 200 µg
FITC-SiNP$_{100TEOS}$	195333.12	4.688E-10	4.266E+11
FITC-SiNP$_{75TEOS}$	258023.74	6.193E-10	3.230E+11
FITC-SiNP$_{50}$	267946.67	6.431E-10	3.110E+11
FITC-SiNP$_{75ETEOS}$	102108.61	2.451E-10	8.161E+11
FITC-SiNP$_{100ETEOS}$	65416.67	1.570E-10	1.274E+12

number of molecule of FITC in 1 SiNP

	number of molecule of FITC per SiNP			Average		SD
FITC-SiNP100TEOS	1563.314314	819.2043974	1385.073726	1256	±	389
FITC-SiNP75TEOS	2389.957719	1204.317092	1866.233113	1755	±	576
FITC-SiNP50	1973.361244	919.3816066	1840.144677	1578	±	574
FITC-SiNP75ETEOS	594.241573	444.1785147	610.0556047	550	±	92
FITC-SiNP100ETEOS	139.6787886	140.8742726	102.4952975	122	±	27

Figure 146: Example of calculations required for the determination of molecule of FITC/SiNP. The calculations require the assumption that the density (ρ) of one SiNP is 2.4 g/cm^3 as reported elsewhere[2,3]

REFERENCES

1 L. Kern, J. Spreckels, A. Nist, T. Stiewe, C. Skevaki, B. Greene, M. Mernberger and H. Elsässer, *Cell Tissue Research,* 2016, **366**, 651-665.

2 J. Chen, M. Liu, C. Chen, H. Gong and C. Gao, *ACS Applied Material and Interface,* 2011, **3**, 3215-3223.

3 C. Moore, G. Giovannini, F. Kunc, A. Hall and V. Gubala, *Journal of Material Chemistry B,* 2017, **5**, 5564-5572.